A Coupled Petrological and Petrophysical Study of High Pressure Dehydration Reactions in Subduction Settings

Insights from the Betic Cordillera and the Kohistan Paleo-Arc

JOSÉ ALBERTO PADRÓN NAVARTA

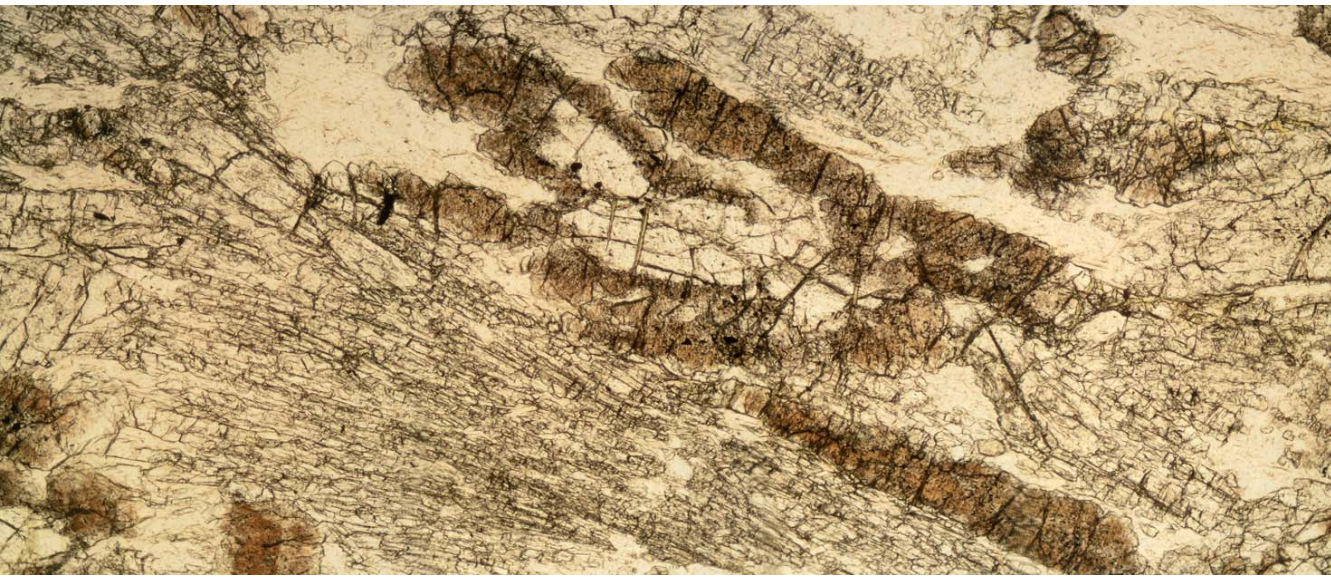

ugr
Tesis Doctoral 2010
Universidad de **Granada**
Departamento de Mineralogía y Petrología

Departamento de
Mineralogía y Petrología

UNIVERSIDAD DE GRANADA

A COUPLED PETROLOGICAL AND PETROPHYSICAL STUDY OF HIGH PRESSURE DEHYDRATION REACTIONS IN SUBDUCTION SETTINGS:

Insights from the Betic Cordillera and the Kohistan Paleo-Arc

TESIS DOCTORAL · Ph. D. Thesis

Memoria de Tesis Doctoral presentada por el Licenciado en Geología
D. José Alberto Padrón Navarta para optar al Grado de Doctor por la
Universidad de Granada

Granada, 23 de febrero de 2010

Fdo. José Alberto Padrón Navarta

VºBº del Director	VºBº del Director	VºBº del Director
Fdo. Dra. María Teresa Gómez Pugnaire	Fdo. Dr. Carlos J. Garrido Marín	Fdo. Dr. Vicente López Sánchez-Vizcaíno

Editor: Editorial de la Universidad de Granada
Autor: José Alberto Padrón Navarta
D.L.: GR 2966-2010
ISBN: 978-84-693-2563-6

Abstract

Our understanding of subduction zones relies on our ability to integrate observations at diverse spatial and temporal scales in these settings. Volatiles are perhaps one of the most distinctive features of subduction zones, which are, in turn, the flagships of Earth's tectonics. A key process in subduction zones is the cycling of volatiles from the hydrated incoming slab and their recycling back into the Earth's surface through arc volcanism. The cycling of volatiles in these settings depends crucially upon metamorphic reactions involving volatile-bearing phases. Our ability to understand the transfer of volatiles in subduction settings therefore relies on our understanding of devolatilization reactions in these settings. Unfortunately, the paucity in the geological record of fossilized examples of arrested devolatilization reactions hampers a better understanding of devolatilization processes deep in the subduction factory.

In this Ph. D. thesis I have selected two specific dehydration reactions that are fundamental in the volatile cycling of subduction zones: the breakdown of amphibole in the lower arc crust, and the breakdown of antigorite deeper in the mantle wedge-slab. The originality of this work relies on the study of two unique outcrops worldwide where these breakdown reactions occur in arrested, dehydration fronts: (i) the dehydration-melting of amphibole as recorded in the Jijal Complex (Kohistan paleo-arc Complex, NW Pakistan); and (ii) the dehydration of antigorite as recorded in the Cerro del Almirez ultramafic massif (Nevado-Filábride Complex, Betic Cordilleras, SE Spain). The study of such fronts provides a unique opportunity to investigate in detail how these reactions operate in nature and what are the allied petrological, physical and chemical modifications induced by these reactions. Field mapping and sampling of reactants and products across the arrested reaction fronts make it possible to compare textural and chemical changes during the progression of the reactions and to unravel the mechanism of devolatilization. The methodology followed in the present research consists of detailed field mapping (in the case of the Cerro del Almirez ultramafic massif), combined with the application of basic petrological tools and state-of-the-art instrumental techniques (Transmission Electron Microscopy, TEM; Electron Backscattered Diffraction, EBSD, High-Pressure experiments, etc.). The study of mineral phase relations, as well as phase diagrams derived from computational thermodynamics, has been also an important part of this Ph.D. thesis. This methodology was used to estimate the pressure and temperature conditions at which both reactions took place and to constrain the possible mechanisms controlling mineral growth and textural development.

The first case study is the high-pressure antigorite dehydration reaction, based on the detailed mapping of the Cerro del Almirez ultramafic massif (Nevado-Filábride Complex, Betic Cordillera, SE Spain). In this massif, the antigorite breakdown took place during the Alpine collision when serpentinite (antigorite + magnetite ± olivine ± tremolite/diopside) was subducted to depths of up to 70 km, and transformed into Chl-harzburgite (olivine + orthopyroxene + magnetite ± tremolite). TEM observations of the antigorite microstructure show that, prior to the transformation, antigorite is exceptionally ordered and consists of the polysome m = 17 with no polysomatic defects.

Close to the dehydration front, however, limited disorder features occur, mainly as (001) twins, reaction rims and reduction of *m* down to 14-15. Moreover, the observed, locally incomplete, breakdown of titanclinohumite in olivine-rich veins supports that serpentinite was annealed at high pressure conditions and very close to its maximum thermal stability. Furthermore, the peak pressure and temperature have been experimentally constrained at 680-710ºC and 1.6-1.9 GPa. This experimental work also put important constrains on the phase relation of silica-rich serpentinite, demonstrating that in such lithology dehydration starts at lower temperatures than the terminal antigorite reaction. Detailed mapping of the Atg-serpentinite to Chl-harzburgite arrested, dehydration front in Cerro del Almirez reveals the presence of a layer of a transitional lithology made up of antigorite-chlorite-orthopyroxene-olivine. This transitional lithology, which delineates the devolatilization front, shows a sequence of mineral assemblages that, together with their mineral composition variation, demonstrates an increase of the metamorphic grade from the Atg-serpentinite to the Chl-harzburgite. An important finding of this Ph.D. thesis is the discovery of metric-to-decametric alternations of contrasting texture of the prograde Chl-harzburgite assemblage and the preservation of serpentinite lenses downstream the devolatilization front. Three textural varieties of Chl-harzburgite have been recognized: granofels, spinifex-like, and recrystallized textures. The former textural variety is crystallized near the atg-breakdown equilibrium, whereas the spinifex texture grew under faster growth rates at a high affinity of the atg-breakdown equilibrium. Recrystallization of these two textures is interpreted, on the basis of field and detailed microstructural observations, as due to brittle deformation, most probably due to hydrofracturing at high pressure conditions. The spatial alternation of granofelsic and spinifex-like textures is interpreted as reflecting the cyclic evolution of the fluid pore pressure excess during the development and advancement of the atg-dehydration front. It witnesses for different fluid expulsion mechanisms operating in subduction environments.

The second case study is the arrested transformation of hornblende gabbronorite to opx-free, garnet granulite, involving the coeval breakdown of amphibole and orthopyroxene, and the formation of garnet and quartz in the lower crust of a Paleo-Island arc (Jijal Complex, Kohistan paleo-arc Complex, NW. Pakistan). Close to the reaction front, clinopyroxene from the granulite displays a strong Ca-tschermark zoning with lower Al-contents in the rims. REE zoning of clinopyroxene and pseudosection diagrams indicate that only clinopyroxene rims reflect chemical equilibrium with garnet in the reaction front metamorphic conditions (P = 1.1 ± 0.1 GPa, T = 800 ± 50ºC). Clinopyroxene cores retained high-Al contents inherited from precursor gabbronorite clinopyroxene and remained in chemical disequilibrium. Further beyond the reaction front, the garnet granulite mineral assemblage is, nevertheless, completely re-equilibrated. Pseudosections calculations indicate that hornblende gabbronorite assemblages are highly metastable at lower arc crust depths. The transformation to garnet granulite was therefore substantially overstepped in terms of pressure and temperature. A key observation is the preservation of the original magmatic foliation in the garnet granulite. This suggests that the gabbronorite-granulite transformation took place at static conditions. In fact, product garnet displays a strong lattice preferred orientation, attesting for a topotactic replacement of amphibole and orthopyroxene from the igneous protholith. Thus, in the absence of deformation, the orientation of mafic precursor phases conditioned the nucleation site and the crystallographic orientation of

garnet. Topotaxial transformation reactions and homoepitaxial growth of garnet occurred during the formation of high-pressure, mafic garnet-granulite after low-pressure mafic protoliths. This result shows that metastable low-pressure lithologies can be buried down the root of the island arc crust, where amphibole dehydration melting reactions triggers their transformation into dense mafic garnet granulites. This process attests for an intra-crustal recycling of volatiles and provides a mechanism for the development of dense roots in island arc. Delamination of such dense roots has important petrological and geochemical consequences for the evolution of mature island arcs.

Resumen

El conocimiento de las zonas de subducción se basa en nuestra destreza para integrar observaciones a diversas escalas espaciales y temporales en este tipo de contextos geológicos. Los volátiles son, quizás, una de las características más distintivas de las zonas de subducción, que, constituyen en sí mismas una peculiaridad de la tectónica de la Tierra. Uno de los procesos claves en las zonas de subducción es el reciclado de volátiles procedentes de la deshidratación de la placa que subduce y su transporte hacia la superficie de la Tierra a través del vulcanismo de arco. El reciclado de volátiles en estos contextos depende de manera crucial de las reacciones metamórficas que involucran a minerales hidratados. Nuestra capacidad para entender la transferencia de volátiles en las zonas de subducción radica, por tanto, en nuestra comprensión de las reacciones de dehidratación. Desafortunadamente, la escasez de ejemplos fosilizados de reacciones de deshidratación en el registro geológico ha impedido una completa caracterización de la influencia de estos procesos en las regiones profundas de las zonas de subducción.

En esta Tesis Doctoral he seleccionado dos reacciones concretas de deshidratación que son fundamentales en el reciclado de volátiles en las zonas de subducción: la desestabilización de anfíbol en la corteza inferior y la desestabilización de antigorita en la placa que subduce y en la cuña mantélica. La originalidad de este trabajo reside en el estudio de dos afloramientos únicos a nivel mundial en el que estas reacciones aparecen 'congeladas' en forma de frentes de reacción: (i) la deshidratación-fusión del anfíbol observada en el Complejo de Jijal (Complejo de Paleo-arco de Kohistán, NO Pakistán) y (ii) la deshidratación de la antigorita presente en el macizo ultramáfico del Cerro del Almirez (Complejo Nevado-Filábride, Cordilleras Béticas, SE España). El estudio de estos frentes permite investigar en detalle cómo operan estas reacciones en la naturaleza, así como las modificaciones petrológicas, físicas y químicas que están asociadas a éstas. La cartografía y muestreo de los reactantes y productos a lo largo del frente de reacción detenido hace posible comparar los cambios químicos y texturales durante la progresión de las reacciones para dilucidar, de este modo, los mecanismos de deshidratación. La metodología seguida en el presente trabajo de investigación consiste en una cartografía detallada (en el caso del macizo ultramáfico del Cerro del Almirez), combinada con la aplicación de herramientas petrológicas fundamentales y modernas técnicas instrumentales (Microscopía Electrónica de Transmisión, TEM, Difracción de Electrones Retrodispersados, EBSD; experimentación a alta presión, etc.). El estudio de las relaciones de fase, así como de los diagramas de fase obtenidos a partir de cálculos termodinámicos, han sido igualmente una parte importante de esta Tesis. Esta metodología combinada ha sido utilizada para estimar las condiciones de presión y temperatura a las cuales ambas reacciones tuvieron lugar, así como para estimar los posibles mecanismos que controlaron el crecimiento cristalino y el desarrollo de la textura de las rocas.

El primer caso estudiado es el de la deshidratación de antigorita en condiciones de alta presión, basado en la cartografía detallada del macizo ultramáfico del Cerro del Almirez (Complejo Nevado-Filábride, Cordillera Bética, SE España). En este macizo, la

antigorita se desestabilizó durante la colisión continental alpina donde serpentinitas (antigorita + magnetita ± olivino ± tremolita/diópsido) fueron subducidas hasta profundidades de hasta 70 km y transformadas en harzburgitas con clorita (olivino + orthopyroxeno + magnetita ± tremolita). Observaciones mediante microscopía electrónica de transmisión de la microestructura de la antigorita muestran que, antes de la desestabilización, la antigorita posee una ordenación cristalina excepcional y está constituida por el polisoma *m* = 17. Cerca del frente de reacción, sin embargo, aparecen defectos cristalinos con una distribución limitad, principalmente maclas según los planos (001), bordes de reacción y reducción del polisoma *m* hasta valores de 14-15. Por otra parte, las condiciones de alta presión a las que las serpentinitas fueron sometidas se han deducido independientemente a través del estudio de la desestabilización de la clinohumita titanífera que aparece en venas de olivino. Adicionalmente, las condiciones del pico metamórfico de presión y temperatura han sido determinadas experimentalmente: 680-710ºC y 1.6-1.9 GPa. Este trabajo experimental restringe de manera significativa las relaciones de fase posibles para serpentinitas rica en sílice, demostrando que litologías de este tipo son estables a temperaturas por debajo de la desestabilización de la antigorita. La cartografía detallada del frente de reacción en el Cerro del Almirez, revela la presencia de una litología transicional, constituida esencialmente por antigorita-clorita-ortopiroxeno-olivino. Esta litología transicional, que delinea el frente de reacción, muestra una secuencia de asociaciones minerales que, junto con la variación sistemática de la composición química de los minerales, demuestra que fue necesario un incremento en el grado metamórfico desde las serpentinitas con antigorita a las harzburgitas con clorita. Otro descubrimiento importante de esta Tesis es el hallazgo de una alternancia, a escala métrica a decamétrica, de dos texturas muy diferentes de la asociación prograda de las harzburgitas con clorita, así como de la preservación de lentes de serpentinitas más allá del frente de reacción. Se han establecido tres variedades texturales en las harzburgitas con clorita: (i) "granofels", (ii) de tipo spinifex y (iii) recristalización de las texturas previas. La primera variedad textural cristalizó en condiciones cercanas al equilibrio, mientras que la textura de tipo spinifex lo hizo con altas velocidades de crecimiento y altas tasas de afinidad química de la reacción de desestabilización de la antigorita. La recristalización de ambas texturas es interpretada, a partir de observaciones de campo y microstructurales de detalle, como consecuencia de deformación frágil, muy probablemente ligada a hidrofracturanción en condiciones de alta presión. La alternancia de las texturas granofélsicas y de tipo spinifex es interpretada como el reflejo de la evolución cíclica de la presión de fluidos en los poros, producida durante el desarrollo y avance del frente de deshidratación de la antigorita. Esta alternancia atestigua la existencia de diferentes mecanismos de expulsión de fluidos metamórficos que han de operar en las zonas de subducción.

El segundo caso de estudio se centra en la transformación inhibida de una gabronorita con anfíbol a una granulita con granate, involucrando la desestabilización del anfíbol y el ortopiroxeno para formar granate y cuarzo en la corteza inferior de un paleo-arco de islas (Complejo de Jijal, Complejo de Kohistán, NO de Pakistán). Cerca del frente de reacción, los clinopiroxenos de las granulitas muestran una fuerte zonación de Ca-Tschermaks, con menores contenidos de alumninio en los bordes. La zonación de tierras raras en los clinopiroxenos y las pseudosecciones calculadas indican que tan sólo los bordes de estos clinopiroxenos del frente de reación reflejan equilibrio químico con el granate (P = 1.1 ± 0.1 GPa, T = 800 ± 50ºC). Los núcleos de estos clinopiroxenos del

frente de reacción preservan altos contenidos en aluminio del precursor (gabronorita con hornblenda). Más allá del frente de la reacción, sin embargo, la asociación está completamente reequilibrada. Las pseudosecciones calculadas indican que la asociación de la gabronorita con hornblenda era altamente metaestable en las condiciones de alta presión y temperatura correspondientes a la corteza inferior del arco. La transformación de éstas a granulitas con granate fue substancialmente sobrepasada en términos de afinidad de la reacción. Una observación clave es la preservación de una foliación magmática original en las granulitas con granate. Esto último sugiere que la transformación grabronorita-granulita tuvo lugar en condiciones estáticas, explicándose de esta manera las relaciones de reemplazamiento topotáctico del anfíbol y el ortopiroxeno del protolito ígneo. Por tanto, en ausencia de deformación, la orientación de las fases precursoras máficas condicionó los lugares de nucleación y la orientación cristalográfica del granate. El crecimiento del granate se produjo durante el reequilibrio a alta presión mediante reacciones de transformación topotácticas y crecimiento homoepitáctico. Estos resultados muestran que litologías con asociaciones de baja presión pueden permanecer metaestables en la corteza inferior de arcos de islas, hasta que la deshidratación/fusión del anfíbol produce su transformación casi instantánea en granulitas máficas más densas. Este tipo de procesos explicaría el reciclado intra-cortical de volátiles y proporcionaría un mecanismo para explicar el desarrollo de raíces corticales densas en arcos de islas. La delaminación de estas raíces más densas conlleva importantes consecuencias petrológicas y gequímicas durante el desarrollo y evolución de arcos de islas maduros.

Index

Part I

Part II

Part IV

1 Introduction

This work deals with the role played by volatiles in some metamorphic reactions occurring in subduction settings. Volatiles are one of the most important the distinctive feature of subduction zones, which, in turn, can be considered as the main fingerprint of the Earth tectonics. Subduction[1] is the process taking place at convergent plate margins (Fig. 1.1) by which lithosphere is underthrusted, sinking into the Earth's mantle. Convergent plate margins represent >55,000 km (Lallemand, 1999), almost equal to that of mid-ocean ridges (60,000 km, Stern 2002 and references therein). Subduction zones, thus, account for most of the paroxistic phenomena on the Earth's surface, including explosive volcanic activity, high-magnitude earthquakes, fast morphological evolution, and deeply contrasting thermal fields (Poli and Schmidt, 2001). Moreover, subduction zones have been considered as the main site for the formation of juvenile crust in the Phanerozoic (e.g. McLennan and Taylor, 1985; Rudnick, 1995; Condie and Chomiak, 1996). Subduction zones can be envisaged as the three-dimensional manifestation of convective asthenosphere downwelling and the largest recycling system in the Earth (Stern 2002), being promoted by extreme chemical, thermal, and mechanical gradients for an extended period of time[2]. Ambitious international and interdisciplinary research programs, such as the National Science Foundation's MARGINS Program (first initiated in 1998), and the Integrated Ocean Drilling Program (IODP)-Initial Science Plan (ISP), have established individual science plans specifically focused on subduction zones, certainly attesting for the pertinence of priority research on these highly geological active settings.

Nowadays, the popular "Subduction Factory" term (e.g. Tatsumi 2005) graphically describes the so-called machinery of subduction zones, where raw inputs are processed into arc magmas and, eventually, into continental crust. More specifically, the term Subduction Factory has been used to encompass the fluxes of material into and out of subduction zones. Raw materials - seafloor sediments, oceanic crust, and mantle lithosphere - are fed into the Subduction Factory at deep sea trenches. In the wedge

[1] the term *Subduction* was first introduced in the geological literature by André Amstutz in 1951 from field observations in the Penninic Alps (e.g. Dewey et al. 1973). The interested reader is referred to White et al. (1970) for an historical review of the subduction concept that can be traced as far as the beginning of 20th century, well before the global tectonic theory.

[2] the classic continental-type subduction margin of central and southern Andes, for example, has been active since the early Triassic (c. 250 Ma), when the Pangea supercontinent was fully assembled.

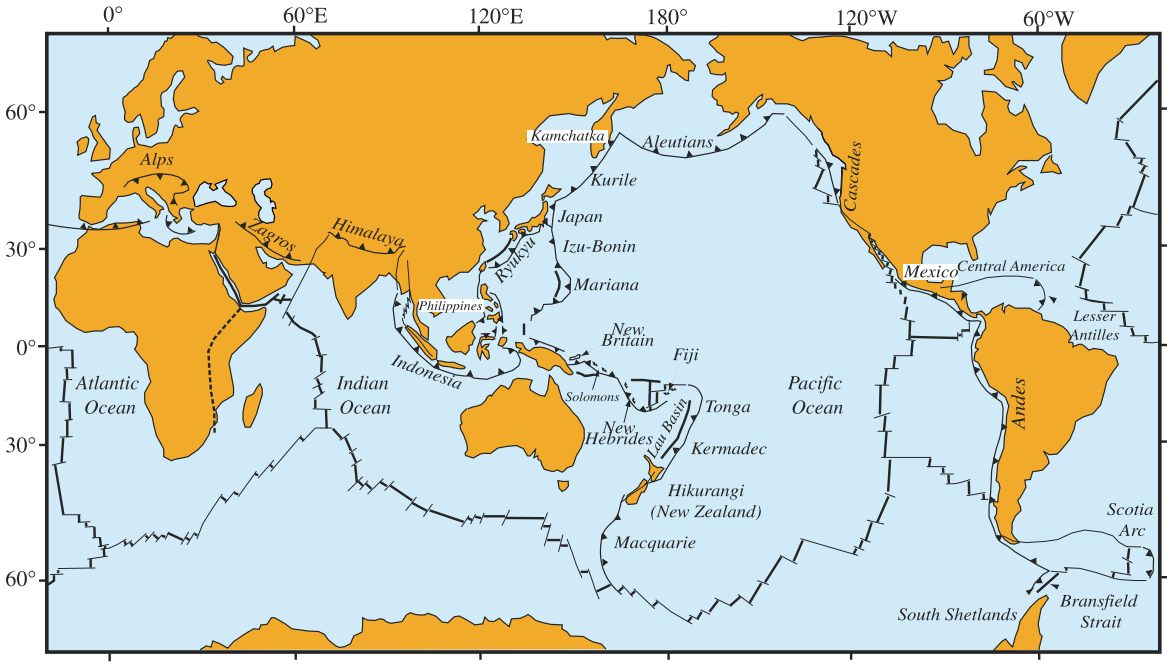

Figure 1-1. Subduction zones and convergent plate margins on Earth (modified after Lallemand, 1999).

above the slab, subducted materials are mixed with mantle rocks, supplied by convection from the landward side of the arc. Output products - melts, aqueous fluids, metalliferous deposits, serpentine diapirs, volcanics, continental crust, gases, back-arc seafloor - emerge from the Factory on the upper plate. The remainder of the material sinks deep into the mantle, and, eventually, is resurrected as mantle plumes.

Subduction zones are generally subdivided into four interrelated components: (1) incoming plate, (2) downgoing plate (subducting lithosphere), (3) mantle wedge, and (4) arc-trench Complex or magmatic arc. Figure 1.2 shows a cross section of an idealized subduction zone[3], where these components are distinguished. It is worth to notice that the evolution of subduction zone systems is intimately related to petrological reactions occurring in all these four components and, more importantly, that these reactions usually involve volatiles. This Thesis is devoted to two specific dehydration reactions, mainly relevant for the downgoing plate and the lower part of the arc-trench Complex, with the aim of improving our knowledge about the work some pieces do in the subduction machinery. The first reaction (Part II) is the high pressure antigorite breakdown, relevant for the hydrated ultramafic composition of the mantle lithosphere downgoing slab and the mantle serpentinized forearc (Fig. 1.2). The second reaction discussed in this Thesis (Part III), occurs in the lower mafic crust of arc-trench Complex (Fig. 1.2). Before that, the influence of volatiles in subduction zones will be briefly outlined, in order to better perceive the implication of these reactions in a general context.

[3] it should be noticed that subduction zones can be extended from the Earth surface down to the 660 km transition zone and thence to the core-mantle boundary; only the shallower (<150 km) is introduced here as the devolatilization reactions studied here are only relevance for this frame.

1.1. Devolatilization reactions in subduction zones

The link between devolatilization reactions and fluid flow is crucial to unravel important geodynamic processes in subduction zones. Deformation and element transfer are highly controlled by the presence of water. Aqueous, supercritical, or melt flow (for a comprehensive revision of this terminology see Hermann et al., 2006) has been claimed, for example, (1) to produce the double seismic zones and forearc seismic tremor observed in some subduction zones (Yamasaki and Seno, 2003; Peacock, 2001; Hacker et al., 2003; Brown et al., 2005); (2) to generate supra-subduction, arc-related, mantle derived magmas (e.g. Ulmer, 2001); or (3) to transfer crustal signatures to continental crust in arcs (e.g. Tatsumi and Eggins, 1995). Furthermore, the release of fluid from the downgoing slab has been recently suggested as the driving force controlling the style of subduction itself (Regenauer-Lieb et al., 2001; Gerya et al., 2008). Moreover, hydration-induced rheological weakening in the mantle wedge (Mackwell et al., 1985, Mei et al., 2002, Arcay et al., 2005) has been considered to change the subduction dynamics, producing extensive thinning of the upper plate (Arcay et al., 2006) or development of cold diapirs in the wedge (Gerya and Yuen, 2003), affecting the overriding crust. For example, extensive thinning of the upper plate would result in extremely high temperature gradients at relatively shallow depths and has profound consequences for the stability of the lower island-arc crust and, eventually, for the evolution of the continental crust itself (Garrido et al., 2006), as discussed in Chapter III. Fluid migration at a wide range of pressure and temperature (PT) conditions is, thus, required in order to explain all these observations at different stages of the subduction machinery.

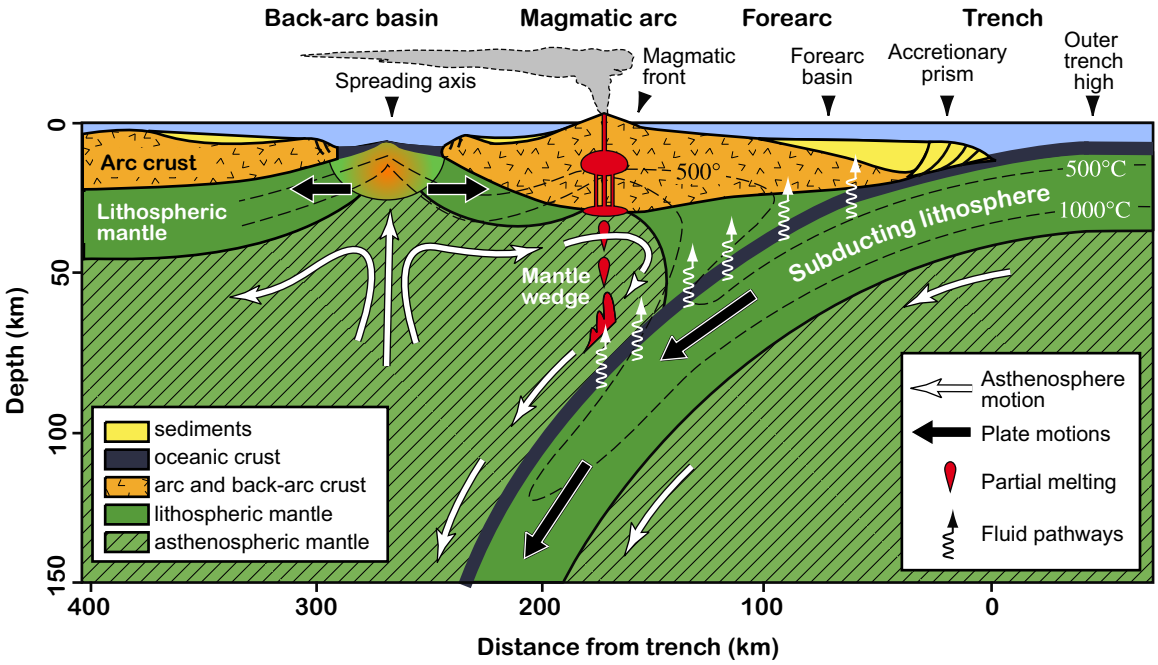

Figure 1-2 Schematic section through the upper 150 km of an idealized subduction zone, showing the principal crustal and upper mantle components and their interactions. Note that the "mantle wedge" is that part of the mantle beneath the overriding plate comprised between the trench and the most distal part of the arc where subduction-related igneous or fluid activity are found (modified from Stern, 2002).

Subduction of pore fluids and hydrous minerals in oceanic sediments, altered basalt and hydrated ultramafic upper mantle, their distillation at depth, transport through the mantle, and re-emission from arcs can be seen as the Earth's deepest hydrologic cycle, having a profound impact on the global budgets of volatiles such as H_2O and CO_2. The critical role of "fluids" in subduction zone environments has been intensively surveyed since the early 1970s, when the global plate tectonic framework, modern geochemistry, and high-pressure experimental petrology provided a consistent indication of major processes occurring at convergent plate margins (Poli and Schmidt, 2001). The release of aqueous and carbonic fluids from subducted sediments, crust, and mantle is a capital issue in order to understand how the Subduction Factory operates.

Most of the water dragged to depth in subduction zones is bounded as hydrous minerals in sediments (e.g. biotite, phengite, chloritoid and zoisite), mafic oceanic crust (e.g. amphibole, biotite, lawsonite, zoisite) and in the hydrous mantle (e.g. antigorite, chlorite, 10Å-phase, and humite series minerals)[4,5]. Water is also stored in nominally anhydrous minerals (NAMs), like olivine and orthopyroxene, and controls a wide range

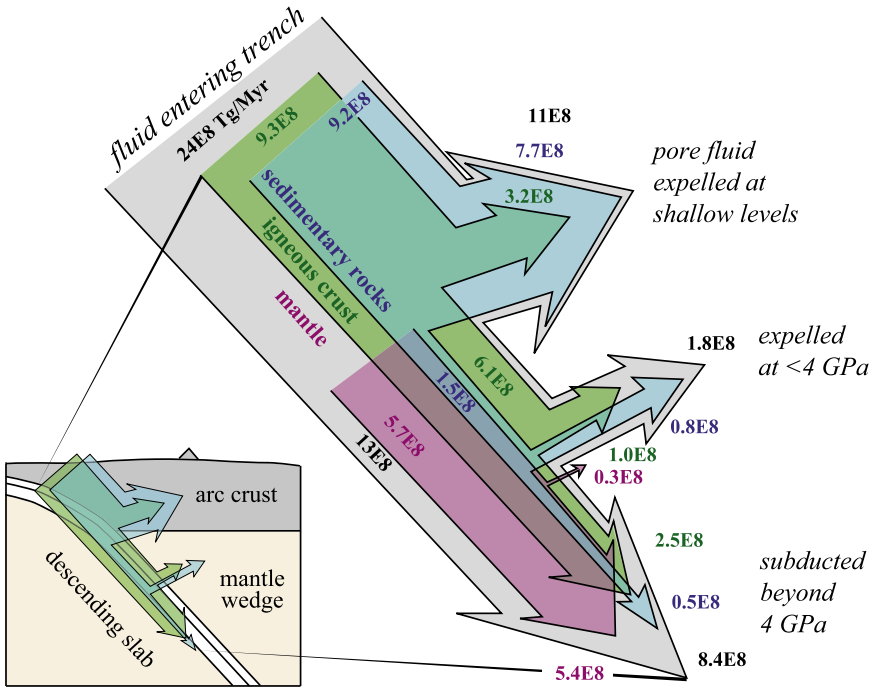

Figure 1-3 Simplified global H_2O flux, from trench to postarc depths, for oceanic lithosphere. Widths of arrows are scaled to flux magnitudes, which are given in Tg/Ma. Of the H_2O subducted at trenches in oceanic lithosphere (24E8 Tg/Ma), 46% is driven off by the closure of pores (11E8 Tg/Ma), another 19% (4.6E8 Tg/Ma) is driven off by devolatilization at pressures <4 GPa, and 35% (8.4E8 Tg/Ma) is subducted beyond 4 GPa (from Hacker, 2008).

[4] the reader may wish to refer to Herman and Spander (2008) and Ulmer and Trommsdorff (1999) for a review on phase relations in subducted sediments and hydrous mantle, respectively.
[5] see Appendix (section 14.1) for a list of mineral formulae and abbreviations used in this Thesis.

of physical and chemical properties of the Earth's mantle. Although only a limited amount of "water" (more concisely hydroxyl species like OH) can be incorporated in NAMs, it may affect partial melting, rheology, diffusion, electrical conductivity, and seismic wave attenuation (e.g. Kovács et al., 2008 and references therein). Nevertheless, it must be stated that the presence of even small amounts of serpentinite in the subducting mantle lithosphere and mantle wedge represent the most important source for the cycling of water through subduction zones. Equal volumes of serpentinite carry an order of magnitude more water than hydrated mafic crust (13 wt % H_2O versus 1–2% in hydrated mafic crust). Additionally, serpentinite is stable to much greater pressures (7 GPa or more versus ~3 GPa; Ulmer and Trommsdorf, 1995). Therefore, the breakdown of antigorite to olivine, orthopyroxene and water in the subducted lithospheric mantle results in a significant density increase as it releases a considerable amount of water (13 wt %) and the reaction products are denser than antigorite. Based on phase diagram calculations, rock physical properties, and a range of appropriate bulk compositions, Hacker (2008) estimated an idealized global H_2O flux in subduction zones (Figure 1.3). Hydrous peridotite is considered to deliver the greatest postarc slab H_2O flux (60 wt %) (cf. Schmidt and Poli, 1998; Rüpke et al., 2004), whereas hydrous plutonic rocks deliver 28 wt % and sediment only 5 wt % (Hacker, 2008). Although these values are critically-dependent on the thermal structure of the subduction zone considered,

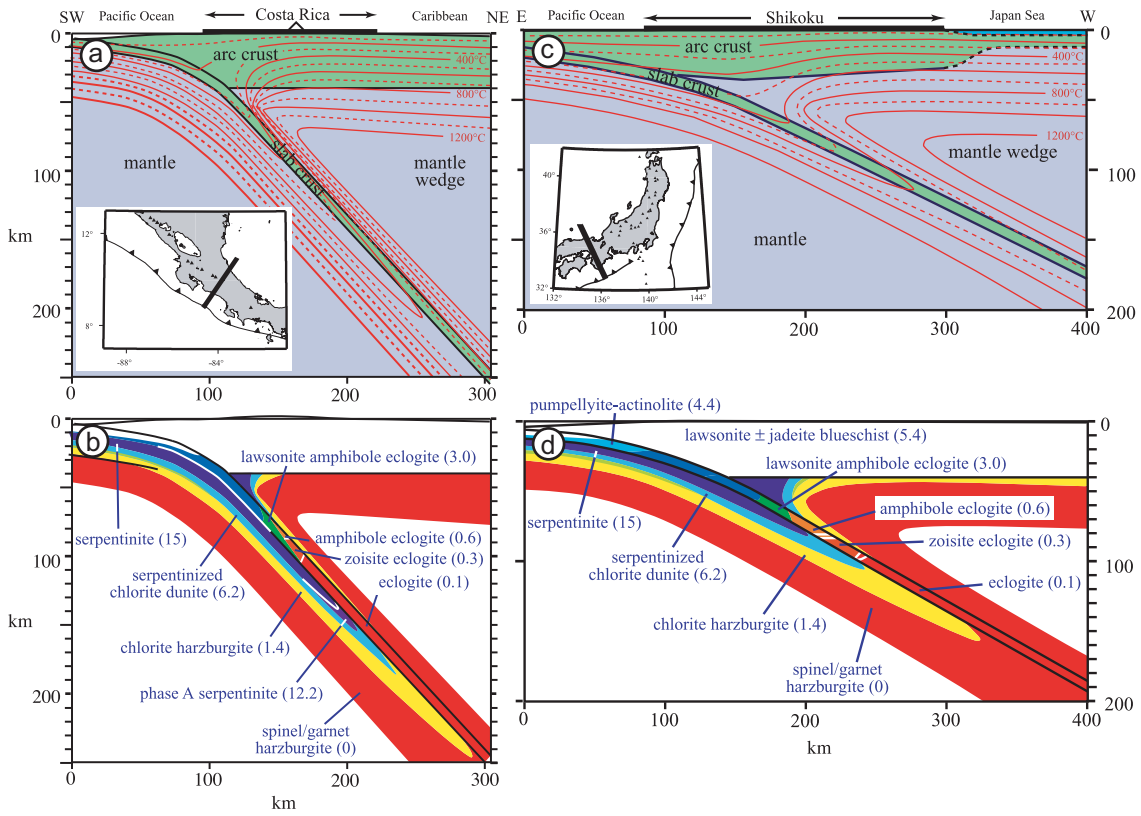

Figure 1-4 Thermo-petrological models for two types of subduction zone: a) thermal and b) metamorphic facies for a cold-type subduction zone (Costa Rica), c) and d) the same for a hot-type subduction zone (Shikoku). Modified from Hacker et al. (2003).

they strongly highlight the potential of hydrated ultramafic rocks as H_2O-carrier. As a matter of fact, and depending on the thermal regime of the subduction zone, antigorite may be stable up to pressures of 8 GPa, ~250 km deep in subduction zones (Ulmer and Trommsdorf, 1995), providing an effective way to transport water to great depths.

Thermal petrologic models of subduction zones (e.g. Hacker et al. 2003, Gerya et al., 2002, 2003, 2008) enable to predict a 2-D arrangement or mapping of metamorphic facies for different bulk compositions. Figure 1.4 shows an example of such models (Hacker et al., 2003) and clearly illustrates the contrasting extension of mineral assemblages for different subduction thermal structures. This provides a basis for constructing realistic models for rock behavior as a function of physical conditions (Connolly, 2005). In order to unravel geodynamic processes in subduction zones, this integrated approach (viz. equilibrium phase calculation combined with mechanical properties) results in an essential first step for a more holistic modeling of the thermal, compositional, density, seismological, and rheological structure in the deep Earth. Nowadays, this methodology represents an emerging and challenging research field (e.g. Afonso et al., 2008; Fullea et al., 2009; Gerya et al., 2002, 2003, 2008). Regarding this issue, 3-D geophysical-petrological modeling software (Fullea et al., 2009) is already available and promises future progress in our knowledge of the physical state of the Earth interior.

1.2. Volatiles, lithosphere erosion and granulite metamorphism

Volatiles released from the breakdown of hydrous minerals in the downgoing slab have a profound influence on the chemistry and rheology of the mantle wedge, modifying its thermal structure and dynamics. This is because even traces of water are sufficient to decrease significantly the mantle rock strength (e.g. Hirth and Kohlstedt, 1996, Mei and Kohlstedt, 2000). Viscous flow in the mantle wedge generates a trenchward horizontal asthenospheric flow, at the base of the overriding lithosphere. This flow ("corner flow") significantly modifies the structure of the overlapping plate (Peacock, 1990; Furukawa, 1993; Peacock and Wang, 1999), and it can heat the upper plate base near the wedge tip. Hot thermal state of the upper plate is not only restricted to volcanic arc, but also occurs below backarc region, even if no recent extension has been recorded (Currie et al. 2004). In order to explain this generalized hot overriding thermal state, lithosphere erosion by thermal convection is required (Currie et al. 2003; Honda and Saito, 2003) and could be triggered by weakening associated to the slab dehydration (Arcay et al. 2005, 2006).

This postulated high thermal gradient at the base of the overriding plate can potentially cause granulite metamorphism at relatively shallow depths. While the thermal regime of arcs has been traditionally considered too cool for granulite metamorphism, there are increasing geological and numerical modeling evidences indicating that the lower crust of arcs is much hotter than previously anticipated (Arcay et al., 2006; Behn & Kelemen, 2006; Garrido et al., 2006; Jull & Kelemen, 2001; Kelemen et al., 2003; Yoshino & Okudaira, 2004). This scenario is explored in Part III of the present Thesis by studying the arrested metamorphic transition of hydrated mafic rocks at the base of a paleo-island arc.

1.3. Reaction and textures during devolatilization

As stated before, this Thesis focuses on the petrological and petrophysical results of two dehydration reactions. Textures and microstructures of the resulting prograde assemblages have been studied by applying several instrumental techniques, described in parts 4.1, 4.5 and 5.2. Although the study of prograde assemblages from a initial protolith is one of the fundamental aim of metamorphic petrology, the study of reaction fronts (either as isograd, kinetic front, etc.) is usually hampered by their scarcity in the geological record.

The two reaction fronts described here, thus, represent a matchless opportunity to survey how textures are developed during devolatilization reactions. The texture of prograde assemblages has a profound effect on a wide range of physical properties as most of the rock-forming minerals are physically anisotropic, e.g. in terms of velocity, thermal or conductivity propagation. Moreover, the thermodynamic treatment of dehydration reactions is, indeed, extremely difficult because of pore pressure deviations and dilatational strain is usually disregarded in conventional phase diagram calculations (Connolly 2009). For example, it is well known that fluid pressure can vary independently of the confining pressure during hydration and dehydration reaction (e.g. Hacker, 1997). Connolly (1997), based on numerical modeling, showed that time-dependent fluctuation of fluid pressure can produce also a fluctuation of the reaction rate at the scale of millions of years. These overturns are ultimately controlled by fluid migration (Connolly 1997, Connolly and Podladchikov, 1998, Miller and Nur 2000; Miller et al. 2003) and, thus, by the rheology of the rock being dehydrated.

Compactation-driven fluid flow seems to be an intrinsic mechanism of viscoelastic rocks. Indeed, it has been recognized for a long time that deformation is coupled with melt migration in partially molten systems. A wide variety of melt migration morphologies has been explained by combining different end-members of the melt driving force (shear stress vs. buoyancy) and the matrix rheology (viscous vs. elastic-brittle) (Phipps Morgan and Holtzman 2005, Phipps Morgan, 2001). Nevertheless, and despite the large implications of deformation/fluid-migration mechanisms for the interpretation of reaction fronts and fluid transport at lower temperatures, a conclusive confirmation by petrological and textural evidences in metamorphic terrains, is still lacking.

1.4. Geological setting of the two studied cases

The geological setting of the two studied natural examples (the Cerro del Almirez ultramafic massif and the Kohistan gabbronorites) is introduced in the corresponding sections of Part II and Part III, respectively. A more general context and a short review of previous works are presented here.

1.1.1 Cerro del Almirez ultramafic massif

Detail geological descriptions of the Cerro del Almirez ultramafic massif will be given in each section of Part II. Apart from the well-known Ronda peridotite massif, ultramafic

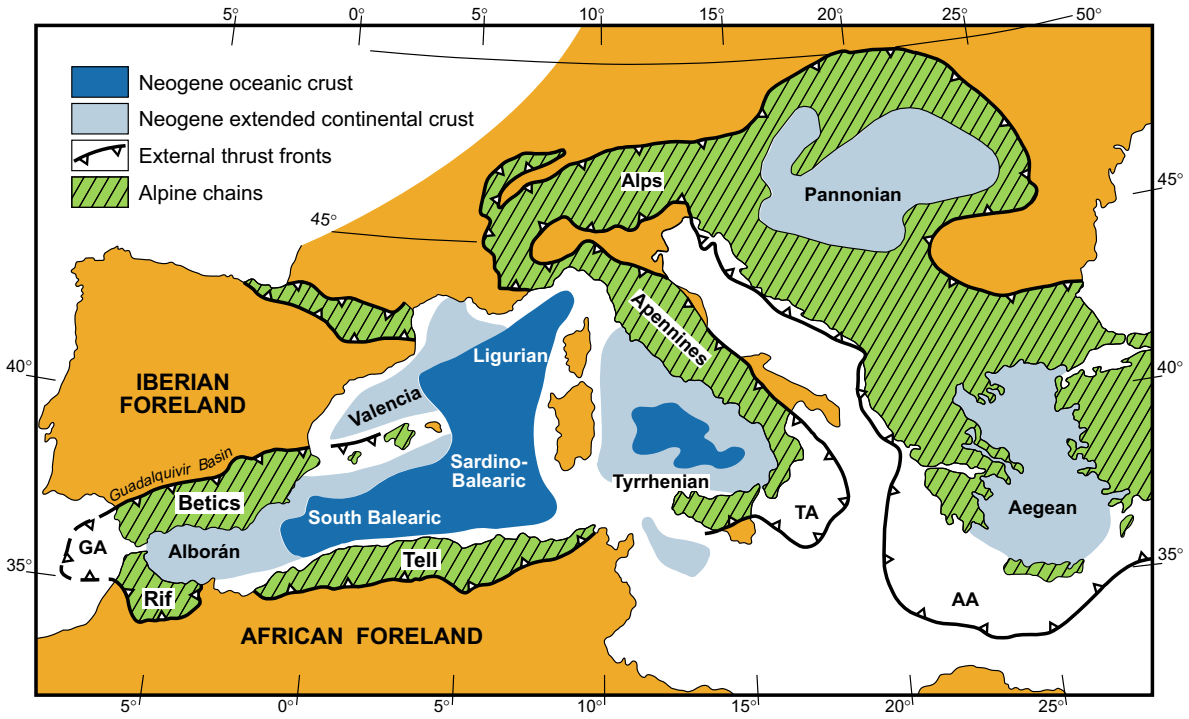

Figure 1-5 Tectonic sketch of the Mediterranean Sea, showing Neogene extensional basins and external front of surrounding Alpine thrust belts. AA = Aegean Arc, GA = Gibraltar Arc, TA = Tyrrhenian Arc (Comas et al. 1999).

lithologies have been recognized for a long time in the Betic Cordillera[6]. There is a vast literature about the structure and metamorphic evolution of the Betic Cordillera. Only a brief outline of this alpine chain and of the metamorphic Complex where the ultramafic rocks crop out (Nevado-Filábride Complex), will be given here. The interested reader is referred to the recent reviews by Azañón et al. (2002) and Vera (2004).

The Betic Cordillera

The Betic Cordillera (Fig. 1.5) forms part the Betic-Rifean orogen (or peri-Alborán orogenic system), an arc-shaped collisional mountain belt bordering the Alborán Sea, which constitutes the westernmost segment of the peri-mediterranean Alpine orogenic system in southern Europe. This orogen was generated during convergence between the African and Iberian plates in Tertiary times (Dewey et al., 1989) and underwent large scale extensional collapse in the Early Miocene (Platt and Vissers, 1989; Galindo-Zaldívar et al., 1989, among many others). Three paleogeographic domains are distinguished: (i) paleomargins of the Iberian plate and the northern part of the African forelands (traditionally called 'External Zones') (ii) deep-water flysh sediments and (iii) Alborán Domain (traditionally called 'Internal Zones') (see Fig. 8.2a in chapter 8 for location of these three domains). On the other side, three metamorphic Complexes have been conventionally distinguished in the Alborán Domain of the Betic Cordillera. In ascending order, these are: (1) The Nevado-Filábride Complex (Egeler 1963); (2) the

[6] mapping and first descriptions of serpentinites can be found at the end of 19th century in one of the first geological surveys of Sierra Nevada (Von Drasche 1879, pags. 358-359 and corresponding map).

Alpujárride Complex (Van Bemmelen 1927); and (3) the Maláguide Complex (Blumenthal 1927). They consist mainly of metasedimentary Mesozoic and pre-Mesozoic rocks (Egeler and Simon, 1969; Gómez-Pugnaire et al., 1982). These Complexes underwent pervasive Alpine deformation and metamorphism that obliterated most of the effects of pre-Alpine deformational events.

The Nevado Filábride Complex

The Nevado-Filábride Complex (NFC) is the structural lowermost metamorphic Complex of the Betic Cordillera, cropping out within large antiformal structures. Nowadays there is not consensus about the number of tectonic units comprising the NFC, which vary between different areas and according to different authors. For brevity the following scheme is adopted here[7]. The Nevado-Filábride Complex may be divided into two lithological units (Fig. 1.6 b, c). The lower unit mainly consists of a (>2 km) thick and monotonous sequence of graphite-bearing metapelites with intercalated quartzites and scarce graphite-bearing marbles (up to 1 m thick). This unit constitutes more than 90% of the outcrops in the western part of Sierra Nevada. This lower unit has been assumed to be Palaeozoic or older in age on the basis of the occurrence of Middle Devonian fauna

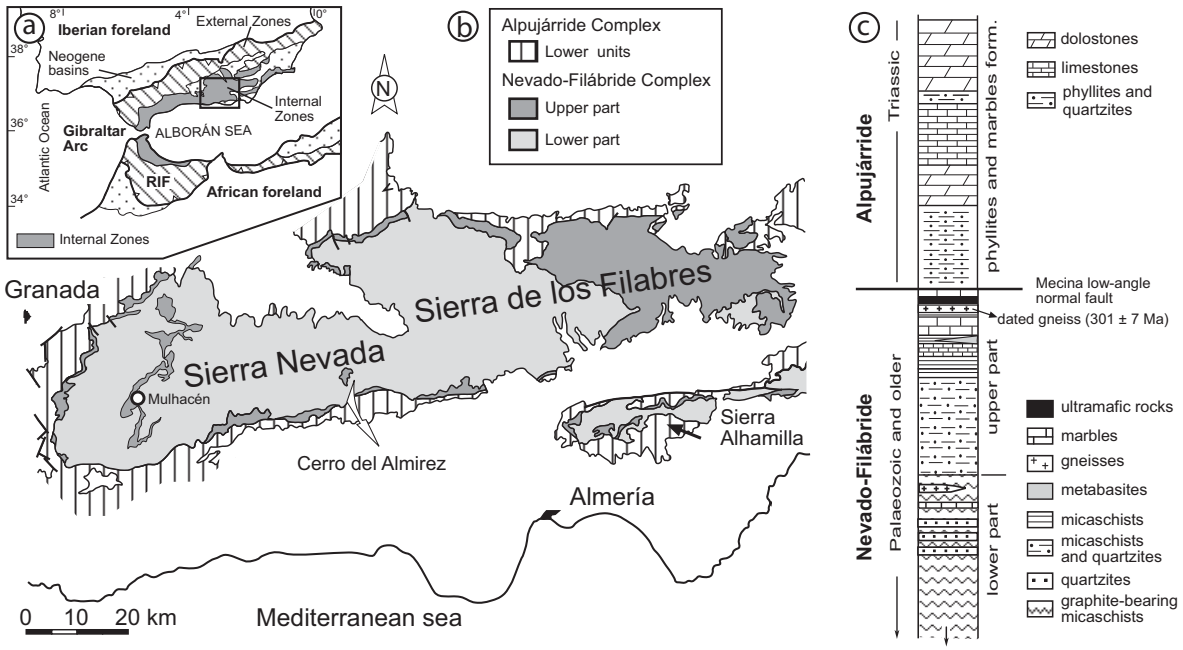

Figure 1-6 (a) Sketch map of the Betic Cordillera. (b) Sketch map of the Nevado-Filábride Complex (NFC) with location of the Cerro del Almirez ultramafic massif. (c) Lithological succession observed in western Sierra Nevada with location of ultramafic rocks in the upper part of the Nevado-Filábride Complex. The Mecina low-angle normal fault separates the underlying NFC from the overlying Permian-Triassic phyllites and Triassic marbles of the Alpujárride Complex. The lower arrow indicates that the thickness of the graphite bearing metapelites is higher but unknown.

[7] It is beyond the scope of this introduction to review or justify the preference of the author among other interpretations of the NFC. Alternative geological maps for the whole NFC is presented in Part II.

(Lafuste and Pavillon, 1976) and Pre-Cambrian (Gómez-Pugnaire et al., 1982) fossils in marbles and metapelites. Ages of metagranitic bodies intruded in the graphite-bearing metasediments range from 307±34 Ma (Sm/Nd, Nieto et al., 1997) to 269±6 Ma (Rb-Sr whole-rock, Priem et al., 1966, Andriessen et al, 1991). They indicate a Late Carboniferous to Late Permian age for both the host rocks and the metagranites.

Palaeozoic and Pre-Cambrian lower series of the Nevado-Filábride Complex are overlain by light-coloured metasediments, up to several hundred meters. They consist, from bottom to top, of quartzites and micaschists (Tahal schists, Nijhuis, 1964) followed by marbles and calcschists (e.g. López Sánchez-Vizcaíno, 1994). Small (several meters) discontinuous bodies, dykes (millimeters to meters in size) and sheets (up to 5 meters thick) of mafic and acid igneous rocks occur within these upper metasediments and comprise small bodies of eclogites, amphibolites and gneisses. Ultramafic rocks form lenses of variable dimensions, up to hundreds of meters thick, most of them completely serpentinised.

Gómez Pugnaire et al., 2004 have reported SHRIMP U-Pb analyses on zircons from gneisses in several outcrops of the upper unit of the Nevado-Filábride Complex, where original intrusive contacts with marbles and other rocks are preserved. Zircon crystals display igneous oscillatory-zoned domains, with an age of 301±7 Ma (95% c.l.), rimmed by dark, unzoned overgrowths of metamorphic origin (mean age of 16.5±0.4 Ma). The former age is interpreted as dating the crystallization of the granitic protoliths of the gneiss. This implies a pre-Permian age for the Nevado-Filábride marbles, traditionally considered to be Triassic, and a Palaeozoic age for the complete sequence of the upper part of the Complex.

The igneous and sedimentary rocks of the Nevado-Filábride Complex underwent Alpine metamorphism. Relics of pre-Alpine structures and minerals appear locally in the graphite bearing metapelites from the lower unit (e.g. Gómez-Pugnaire and Franz, 1988). Pressure - temperature (P-T) conditions of the early alpine high-pressure event commonly range in metabasites between 12 and 14 kbar and 550-600ºC (Gómez-Pugnaire and Fernández-Soler, 1987). Higher pressures and temperatures, however, have locally been determined in several different rock types (more than 18 kbar and 650-700ºC, Gómez-Pugnaire et al., 1994; Trommsdorff et al., 1998; Puga et al., 2002). High-pressure metamorphism occurred during the Middle Miocene, as revealed by SHRIMP U-Pb analysis of zircon in a pyroxenite layer of the Cerro del Almirez ultramafic rocks (Nevado-Filábride Complex, Southern Spain) resulting in an age of 15.0 ± 0.6 Ma (95 % c.l.) (López Sánchez-Vizcaíno et al., 2001). Later uplift produced a decompressional path that is not well constrained (Bakker et al. 1989, Augier et al. 2005, Gómez-Pugnaire et al., 2004). For most authors, decompression occurred with initial heating conditions followed by slight cooling in the amphibolite facies (see Gómez-Pugnaire et al., 2004 for a summary and for different cases of contrasting decompressional paths).

The observed succession from the Nevado-Filábride Complex is overlain by the Alpujárride Complex (Fig. 1.6b), consisting of phyllites, quartzites and carbonates (Fig. 1c), which have been dated with fossils as Middle to Upper Triassic (Barrois and Offert, 1889; Martín and Braga, 1987). The phyllites immediately on top of the Nevado-Filábride Complex show high-pressure mineral assemblages formed at up to 9-10 kbar

and 450-480 ºC (Azañón and Goffé, 1997). The proposed ages and metamorphic evolution are consistent with an original contact between the Nevado-Filábride and the phyllites and quartzites from the Alpujárride Complexes that can be considered as normal from a stratigraphic point of view (Gómez-Pugnaire et al., 2004). However, the main contact separating the Nevado-Filábride and Alpujárride Complexes is, at present, a low-angle normal fault (the Mecina Fault) (Fig. 1.6c), which was formed during exhumation, as were all of the ductile and brittle structures identifiable in the Nevado-Filábride Complex, and the brittle ones in the Alpujárride Complex. Most of the deformational structures of the Nevado-Filabride Complex were associated with the activity of the Alpujárride / Nevado-Filábride contact. For this reason, deformation gets more intense in the Nevado-Filábride Complex towards the contact with the Mecina Fault, which behaved as a ductile shear zone during the earlier stages of its development (Galindo-Zaldívar et al., 1989; Jabaloy et al., 1993). The sequence of structures that progressively formed in the Nevado-Filábride Complex, including the low-dipping main foliation and an associated stretching lineation, was related to the extensional detachment that overprinted the sparse relics of previous penetrative structures.

1.1.2 Kohistan arc Complex

The Kohistan arc Complex (KAC) of northern Pakistan is tectonically sandwiched between the Karakoram and Indian plates (Tahirkheli et al. 1979, Bard 1983, Coward et al. 1986, Treolar 1996). This cretaceous arc developed in the neo-Thetys due to northward subduction of oceanic lithosphere at the leading edge of the Indian plate. Closure of the marginal basin to the north welded the arc to the Karakoram plate. From then on the Kohistan arc became an Andean-type continental margin. Continued subduction resulted in complete consumption of the leading oceanic edge of the Indian plate, resulting in Eocene collision between the arc and the Indian continent at the site of the Indus suture (Treloar et al. 1989). The deformation associated with the two collision events folded and tilted the arc so that the basal arc crust is now exposed in southern Kohistan in the hangingwall of the Indus suture. The phases of magmatism associated with the two stages of arc growth are compositionally distinct. The arc sequence developed during the intraoceanic stage comprises mainly ultramafic-mafic igneous rocks, while magmatism in the continental-margin stage was intermediate to felsic in composition.

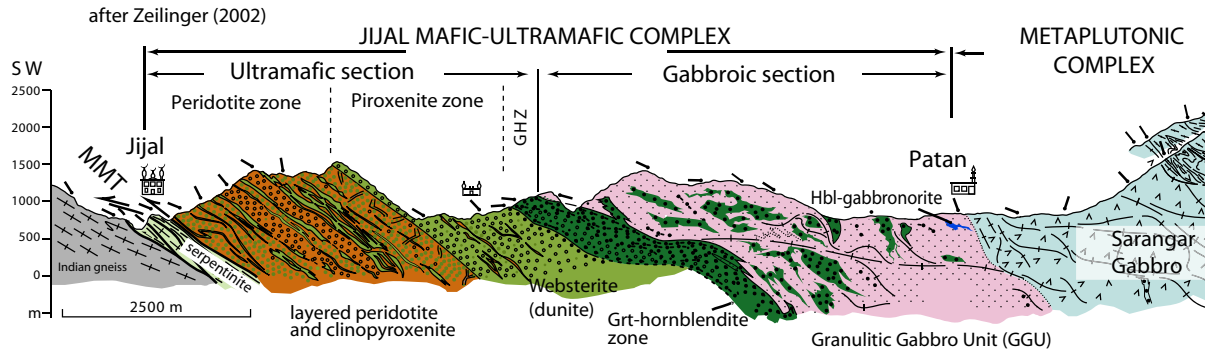

Figure 1-7 Geological section along the Indus valley, showing the Jijal mafic ultramafic Complex (after Zeilinger, 2002).

The KAC is subdivided into six distinct units (Jijal Complex; 'Kamila amphibolite belt' or 'metaplutonic Complex'; Chilas Complex; Kohistan Batholith; Jaglot and Utror-Chalt groups; Yasin group, see Fig. 9.1a for a simplified geological map of the Kohistan arc) from south to north along a transect spanning >200 km. This study focuses on the Jijal Complex consisting of a lower ultramafic section and an upper mafic section (Fig. 1.7) (Jan, 1979, Bard, 1983, Miller and Christensen, 1994, Burg et al., 1998). The upper mafic section or 'granulitic gabbro unit' (GGU) is dominated by garnet-bearing metagabbroic rocks (garnet granulite), which suffered high-pressure granulitic metamorphism (T=700–>950 °C, P>1 GPa) at ca. 96–91 Ma (Yamamoto, 1993; Yamamoto and Nakamura, 1996; Yoshino et al., 1998; Ringuette et al., 1999; Yamamoto and Nakamura, 2000; Anczkiewicz et al., 2002). Geochemical and isotope variations observed between the plutonic crust and the underlying ultramafic section discard a crystal fractionation model from a single parental magma between Jijal mafic and ultramafic basal section of KAC (Garrido et al. 2007, Dhuime et al. 2007, 2009).

2 Aims and Thesis structure

1.1 Statement of the problem

This study was motivated by two, exceptionally well preserved, metamorphic reaction fronts. These two reaction fronts involve hydrous minerals (antigorite and amphibole) and release of fluids and hydrous melt, respectively, and provide a matchless opportunity to survey processes of a great importance in subduction zones at very different scales.

The Cerro del Almirez ultramafic massif (Nevado-Filábride Complex, Betic Cordillera, southern Spain) is a unique locality to survey the high-pressure antigorite dehydration reaction, as both the prograde and product rocks (antigorite serpentinite and chlorite harzburgite, respectively) are preserved here in contact with each other. The general reaction forming the isograd of antigorite dehydration (antigorite-out) is:

antigorite → olivine + orthopyroxene + chlorite + H_2O
(serpentinite) → (chlorite harzburgite)

This metamorphic reaction was first described by Trommsdorff and coworkers (1998) in the Cerro del Almirez ultramafic massif, which is considered the only field occurrence of the high-pressure antigorite breakdown worldwide. The profound implications (see Chapter 1) of this reaction in subduction zones motivated this Thesis (Part II) in great extent.

This work is completed with the study of another, well preserved, sharp reaction front in rocks of the lower crust of a paleo-island arc (Jijal Complex, Kohistan):

amphibole + plagioclase + quartz → garnet + clinopyroxene + hydrous melt
(hornblende-gabbronorite) → (orthopyroxene-free, garnet granulite)

1.2 Aims

The main aim of the present Ph. D. Thesis is to contribute to the knowledge of devolatilization reactions at high pressure conditions (≥ 1.0 GPa). This study is focused on the following three goals:

- To describe the morphology of the reaction fronts at the outcrop, thin section, micro- and submicroscopic scales.

- To provide mineral chemistry, bulk rock analyses and microstructural data in order to assess the metamorphic conditions (pressure and temperature) prevailing during the hydrous breakdown.

- To discuss the implications of reactions involving-volatiles in subduction zone settings, among others: (i) the stability of antigorite in different natural systems and the factors controlling its breakdown reaction; (ii) the occurrence of other dehydration events at lower temperature in Si-metasomatized, subducted ultramafic rocks; (iii) hydrofracturing events allowing fluid transport at the initial stage of dehydration reactions; (iv) stability of amphibole in basic plutonic rocks and their metamorphic evolution in the lower island-arc crust.

1.3 Approach

Different approaches have been followed to deal with several specific goals in the study of the two cases. Methodology used has been very similar (see Chapter 3). A considerable large variety of instrumental techniques has been applied to the elemental, and essential, petrographic study. The antigorite breakdown has been examined with a detailed field work. The resulting observations and mapping of the antigorite isograd is the product of four years of field investigations, complementary of previous field work made within the research group I belong to. Structures were examined using both field and microscopic observations. Petrography and description of microstructures combined with SEM and EPM-analyses of the minerals were done on selected samples. Whole rock composition has been determined by XRF for major and trace elements. Transmission electron micropcopy observations were carried out in order to fully characterize crystallographic-microstructural features and crystallographic relationships (epitaxy) between reactant and product minerals. Microstructures (at thin section scale) were quantitatively measured by means of the Electron Backscattered Diffraction technique. An experimental petrology study was addressed to constrain pressure, temperature conditions and phase relations for an uncommon but relevant mineral assemblage (Si-metasomatized ultramafic rocks).

1.4 Organization of the Thesis

This Thesis has been subdivided in four parts. In Part I, some introductory concepts relevant to focus the studied problem were summarized, in addition to the description of methodology used (Chapter 3). Part II and III are the main body of the text and comprise several chapters (Chapters from 4, to 8, in Part II and Chapters 9 and 10 in Part III). Each chapter (see below) of Part II and III tackles with an specific topic about

the antigorite and amphibole dehydration, respectively, and have been published or submitted for publication to an international peer-reviewed journal, with exception of chapter 4. In Part IV, conclusions, afterthoughts and future perspectives are presented. A brief outline of the chapters in parts II and III is given here for a better understanding of the text:

PART I

- Chapter 4. 'Textural record of dynamic fluid expulsion in a subduction setting: the high-pressure antigorite dehydration front in Cerro del Almirez ultramafic massif (Nevado-Filábride Complex, S. Spain)'. Field and petrographic observations of several textures along the antigorite isograd and the prograde Chl-harzburgite are presented together with major analysis of main mineral phases and bulk rock compositions. An explanation of the very contrasting textures in the prograde assemblage is proposed.

- Chapter 5. 'Highly ordered antigorite from Cerro del Almirez HP–HT serpentinites'. Assessment of the high-pressure nature of the antigorite prior to its breakdown was performed by measuring the crystallographic ordering and microstructural features, like polysomatic defects, by Transmission Electron Microscopy (TEM). This chapter has been published in Contributions to Mineralogy and Petrology, 2008 (156, 679-688).

- Chapter 6. 'Breakdown mechanisms of titanclinohumite in antigorite serpentinite (Cerro del Almirez massif, S. Spain): A petrological and TEM study' Further assessments of the pressure and temperature conditions attained in antigorite serpentinite are presented here by studying the breakdown mechanism of titanclinohumite (an important minor phase in ultramafic rocks) by TEM observations. Breakdown reaction mechanisms of titanclinohumite and their implications for subduction zones are discussed. This chapter has been published in Lithos, 2009 (107, 216-226).

- Chapter 7. 'An experimental investigation of antigorite dehydration in natural silica-enriched serpentinite'. The occurrence of a new compositional lithology found during field survey (Si-enriched serpentinite) motivated an experimental work dealing with the phase relations of this new lithology. Silica-enriched serpentinite is expected to be relevant in subduction zones where silica-metasomatism is envisaged. Additionally, this work enabled a better constrain of the peak metamorphic conditions of the prograde Chl-harzburgite. This chapter has been published in Contributions to Mineralogy and Petrology, 2010 (159, 25-42).

- Chapter 8. 'Fluid transfer into the wedge controlled by high-pressure hydrofracturing in the cold top-slab mantle'. This chapter is focused on the structures of deformation observed in the prograde assemblage. Based on microstructural observations and crystal preferred orientations (CPO) mapping, these structures are interpreted as a record of brittle deformation (microcraking)

of the prograde assemblage, probably induced by hydrofracturing at high pressure and relative low temperature conditions (680-710ºC). In this chapter the implications of fluid-flow by hydrofracturing in subduction zones are discussed. This chapter has been submitted to Earth and Planetary Science Letters.

PART II

- Chapter 9. 'The Arrested Metamorphic Transition of Metastable Hornblende Gabbronorite to Mafic Opx-Free, Garnet Granulite in the lower Crust of a Paleo-Island Arc (Jijal Complex, Kohistan, north Pakistan)'. The mineral chemistry and high-pressure granulite metamorphism of hornblende-gabbronorite are presented in this chapter. Amphibole dehydration versus dehydration-melting scenarios is discriminated in light of thermodynamic calculations. Geodynamic implications of amphibole breakdown at the roots of island arcs are discussed. This chapter has been submitted to Journal of Petrology.

- Chapter 10. 'Oriented Growth of Garnet by Topotactic Reactions and Epitaxy in High-Pressure, Mafic Garnet Granulite formed by Dehydration Melting of Metastable Hornblende-Gabbronorite (Jijal Complex, Kohistan Complex, north Pakistan)'. Microstructural and topotaxial relationships between products and reactants are established by combining petrographic and TEM observations with EBSD data. Kinetic inhibition is proposed here to explain very sharp reaction fronts, as well as the textural inheritance in the garnet preferred orientation from the precursor hornblende gabbronorite. This chapter has been published in Journal of Metamorphic Geology, 2008 (26, 855-870).

PART IV

- Chapter 11. General conclusions.

3 Methodology

3.1 Field work and sampling

This Thesis is based on the study of two natural examples located in two different countries (Spain and Pakistan). Field observations corresponding to Part III (Jijal-Patan Complex, Kohistan) build upon detail field work on the frame of the collaborative research project. Samples used in this Thesis are well-characterized samples reported in previous works and belong to the collection of the IACT (Dr. CJ Garrido) and the ETH and the University of Montpellier.

Field work concerning Part II (Cerro del Almirez, Betic Cordillera) has been carried out by the author through a series of campaigns, extending from 2006 to 2009. The area investigated is situated in south-eastern Spain, in the western part of the Almería province. Bounded approximately by latitudes 37º05'36" and 37º04'00" and longitudes 2º55'52" and 2º53'51", the area covers ca. 7.5 square kilometers. Geographically, it is located in the eastern termination of the Sierra Nevada mountain range. The highest elevation is located in the so-called "Cerro del Almirez" with two twin peaks (2519m and 2517m).

Sample and outcrop positions were acquired with a Garmin e-Trex GPS and exported to *.kml (Keyhole Markup Language, used by Keyhole and Google Earth) by using CompeGPS Land™ software (*.wpt) and the free conversion tool software GPSBabel. Silva Ranger 15 compass was used for retrieve structural information.

A complete sample list with a brief rock description, UTM coordinates (European Datum 1950) and other useful information is shown in Appendix (section 14.2) and A total of 169 samples were collected. The weight of most of them is above 2-3 kg to ensure a homogeneous and representative bulk rock analysis. Sectioning and cleaning of raw samples with a diamond saw were done by the author. Most of the sections prepared for petrographic analysis were cut normal to the foliation plane and parallel to the lineation (when possible) in the case of foliated rocks. Additionally, plane-parallel sections were etched by dilute hydrochloric acid with the aim of revealing macroscopic lineation.

3.2 Electron Probe Microanalyses (EPMA)

Major element compositions of minerals were obtained by Electron Probe Microanalyses (EPMA) in ~30 μm thick, standard thin sections, using the following electron microprobes from different institutions:

- CAMECA SX-50[8] and CAMECA SX-100 instruments at the "Centro de Instrumentación Científica" (CIC, University of Granada, Spain).
- CAMECA SX-100 instrument at Geosciences Montpellier (CNRS-Université de Montpellier 2, France).
- CAMECA SX-100 instrument at the Research School of Earth Sciences (RSES, Australian National University, Australia).

A more detailed description of analytical routines, detection limits and errors is presented here for the CAMECA SX-100 at CIC (University of Granada). For experimental conditions of the other instruments the reader can refer to chapters 7 (SX-100, RSES) and 9 (SX-50, CIC and SX-100, GM).

Two different analytical routines were used: (1) a general routine for silicates and (2) a routine for olivine and orthopyroxene. The latter routine was specifically designed to detect small minor elements in olivine (Ti) and in orthopyroxene (Al) and illustrates how slight variations in the counting time are propagated in the detection limit (see below). Excitation voltage (15 kV), beam current (15 nA) and standards used for element calibrations were the same for the two routines: Al_2O_3 (Al), quartz (Si), periclase (Mg), diopside (Ca), albite (Na), $MnTiO_3$ (Mn), rutile (Ti), hematite (Fe), chromite (Cr), NiO (Ni), barite (Ba), fluorite (F), sanidine (K) and vanadinite (V). Peak and background counting times for each element in the two routines is shown in Table 3.1. Note that the counting time for Al, Ca and Ti has been increased in routine 2.

Table 3.1. Peak and background counting times for routine 1 and 2.

			Routine 1		Routine 2	
Element line	Spectrometer	Crystal	Peak Time (s)	Background Time (s)	Peak Time (s)	Background Time (s)
Na $K\alpha_1$	Sp4	LTAP	20	10	20	10
Mg $K\alpha_1$	Sp4	LTAP	50	25	50	25
Si $K\alpha_1$	Sp5	LTAP	30	15	30	15
Al $K\alpha_1$	**Sp5**	**LTAP**	**40**	**20**	**60**	**30**
K $K\alpha_1$	Sp1	LPET	20	10		
Fe $K\alpha_1$	Sp3	LLIF	20	10	20	10
Mn $K\alpha_1$	Sp3	LLIF	20	10	20	10
Cl $K\alpha_1$	Sp1	LPET	20	10		
Ca $K\alpha_1$	**Sp1**	**LPET**	**20**	**10**	**40**	**20**
Ti $K\alpha_1$	**Sp1**	**LPET**	**20**	**10**	**60**	**30**
Ba $L\alpha_1$	Sp1	LPET	20	10		
F $K\alpha_1$	Sp2	LPC0	30	15	30	15
Cr $K\alpha_1$	Sp3	LLIF	30	15	30	15
Ni $K\alpha_1$	Sp3	LLIF	30	15	30	15

Limit of detection and standard deviation of each measurement is routinely calculated by CAMECA software, based on a series of parameters like counting time in the peak and in the background and in the column conditions (excitation voltage and beam current). The equations used by the CAMECA software are presented here only in an

[8] replaced by a CAMECA SX-100 instrument in 2006.

abbreviated manner and are based on the work by Ancey and coworker (1978)[9]. For a more comprehensive and rigorous exposition, the interested reader is referred to Merlet and Bodinier (1990).

Table 3.2. Examples of limit of detection (ppm) and standard deviation of the concentration (wt. %) for routines 1 and 2 (cf. Table 3.1).

Mineral	Atg		Chl		Ol		Opx	
Sample	Al06-45		Al07-15		Al06-05a		Al08-22	
	Routine 1		Routine 1		Routine 2		Routine 2	
measurements	25		19		54		44	
limit of detection (ppm)								
	average	σ	average	σ	average	σ	average	σ
Na	140	4	138	3	148	4	147	4
Mg	74	1	75	1	78	1	77	1
Si	77	1	78	1	78	1	77	1
Al	**71**	**1**	**71**	**1**	**61**	**1**	**59**	**1**
Fe	557	17	547	23	572	18	585	19
Mn	527	23	523	19	536	20	554	23
Ca	**184**	**5**	**183**	**4**	**142**	**3**	**136**	**2**
Ti	**236**	**5**	**234**	**5**	**154**	**2**	**141**	**2**
F	777	21	780	25	730	20	784	23
Cr	396	14	397	16	406	13	412	15
Ni	580	14	576	11	597	17	609	15
K	163	5	156	4				
Cl	387	24	366	16				
Ba	745	15	712	14				
precision at 3σ relative to the concentration (wt. %)								
	average	σ	average	σ	average	σ	average	σ
Na	0.012	<0.001	0.012	0.002	0.013	<0.001	0.012	<0.001
Mg	0.272	0.011	0.119	0.062	0.368	0.004	0.121	<0.001
Si	0.109	0.007	0.096	0.018	0.111	0.002	0.144	<0.001
Al	0.029	0.012	0.053	0.009	0.005	<0.001	0.005	<0.001
Fe	0.158	0.003	0.153	0.031	0.234	0.013	0.215	0.002
Mn	0.047	0.002	0.045	0.009	0.053	0.001	0.067	0.002
Ca	0.015	0.001	0.015	0.003	0.011	<0.001	0.013	<0.001
Ti	0.020	<0.001	0.020	0.004	0.013	0.002	0.012	<0.001
F	0.066	0.001	0.066	0.013	0.064	0.001	0.067	0.001
Cr	0.055	0.016	0.081	0.016	0.041	0.012	0.035	0.001
Ni	0.054	0.002	0.057	0.011	0.066	0.001	0.052	0.001
K	0.015	<0.001	0.015	0.003				
Cl	0.043	0.005	0.034	0.006				
Ba	0.062	0.001	0.059	0.012				

Detection limit ($C_{min,}$ ppm)**:** The definition of the Detection Limit is related with the "statistical confidence level" based on the two following parameters:

- α : Probability of considering C > 0 when the actual value is C = 0
- β : Probability of considering that C = 0 when the actual value is C > 0

[9] detection limit can optionally be calculated with the method described by Ziebold (1967).

These parameters are usually set at $\alpha = \beta = 0.05$ or $\alpha = \beta = 0.01$ for a statistical confidence level of 95% or 99%, respectively. The detection limit (C_{min}) is calculated using the following expression:

$$C_{\min} = \left(\frac{C_e}{P_e - \gamma_e B_e} \right) * \left(\frac{\lambda(\alpha,\beta)}{2} \sqrt{1 + \frac{4 B_e \gamma_e (1+\gamma_e)}{\lambda(\alpha,\beta)}} \right)$$

where C_e is the concentration in the sample, P_e and B_e are the peak and background counts in the samples, γ_e is the square root of the ratio between the background counts in the sample and in the standard, and parameter $\lambda(\alpha,\beta)$ is taken from Ancey et al. (1978).

Standard deviation (StdDev wt %). The precision at 3σ relative to the concentration C_e is calculated, based on: (1) the concentration in the sample C_e (wt. %), (2) the number of counts per sec per nA in the sample (λ_e) and in the standard (λ_s) and (3) the variance on the emission of the sample (σ^2_e) and of the standard (σ^2_s). The precision of the standard deviation (StdDev wt %) corresponds to a confidence of 95% in the interval of 3σ, given as a result.

$$3\sigma = 3\left(\frac{C_e}{\lambda_e} \right) \left(\sigma_e^2 + \left(\frac{\lambda_e}{\lambda_S} \right)^2 \sigma_s^2 + \right)^{1/2}$$

The limit of detection and standard deviation slightly vary from mineral to mineral and sample to sample for constant column conditions. As an example, Table 3.2 shows the detection limit and precision at 3σ relative to the concentration for antigorite, chlorite, olivine and orthopyroxene, based on several measurements made in the same sample and in the same day (i.e. under roughly constant column conditions). Limit of detection values are rather similar for routines 1 and 2, except for Al, Ca, Ti, which are lower in routine 2 (Table 3.2), as a result of higher counting times at the peak and background for these elements in this routine (cf. Table 3.1).

X-rays maps of samples KG-03 and BKI-158 (chapter 9) were performed in a Cameca SX100 Superprobe at Géosciences Montpellier (CNRS-Université de Montpellier II, Montpellier, France). The counting time per point for Ca, Na, K, Fe, Mg, Al and Si cations was 20 milliseconds.

3.3 Laser Ablation inductively Coupled Plasma-Mass Spectrometry (LA-ICPMS)

In situ trace element analyses of clinopyroxene (chapter 10) were carried out by LA-ICP-MS in an Agilent-7500a ICPMS coupled to a 213 nm wavelength Nd-YAG Mercantek® laser at the CIC (University of Granada, Granada, Spain). This instrument can measure more than 70 elements with a typical precision of 5% for a concentration of 100 ppm. It is especially suitable for elements heavier than Ga. Isotopic relations can also be

measured with a precision around 0.2% (1σ) in the best situation. Laser spots can be varied from 10 to 160 μm. Small spot diameter leads to low sensibility as the accuracy depends on the ablated volume. For instance, spot size of 30 m results in detection limits around 1 ppm.

Laser ablation analyses were done on thick sections (~ 80 μm), using laser spots of c. 60 μm. Ablation was done in a He atmosphere. Data were acquired for 60 s and the laser repetition rate was 10 Hz. Silica, determined by EPMA, was used as internal standard, whereas the external standards were glasses NIST-610 and ML3B-G. Data were reduced using software and procedure described by Bea et al. (2006). Figure 3.1 shows a good correlation between the measured and preferred value for glass ML3B-G (Jochum 2006).

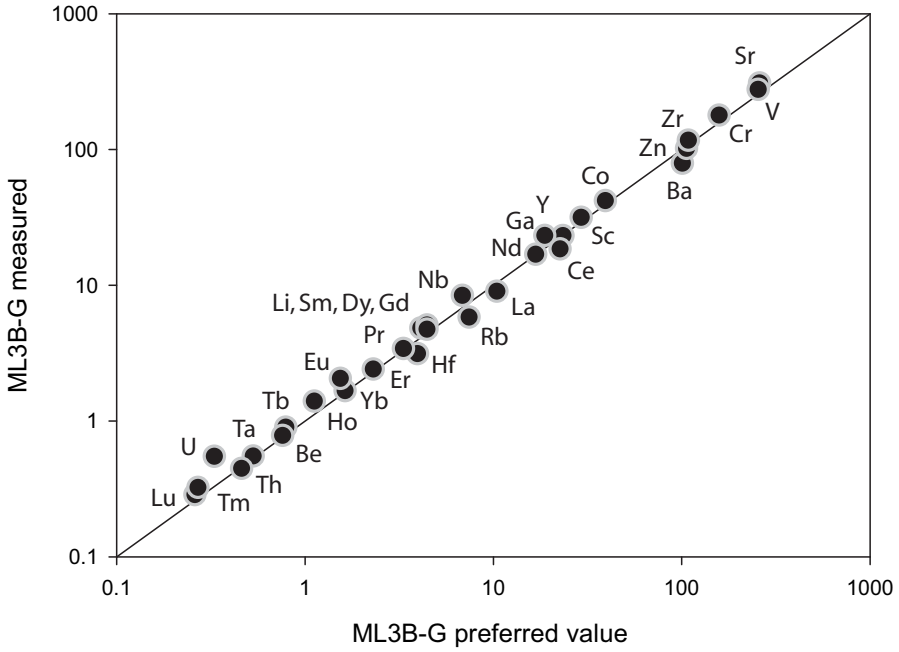

Figure 3-1. Measured and preferred values (in ppm) for trace elements in the glass ML3B-G. Preferred values are taken from Jochum (2006).

3.4 X-ray Fluorescence (XRF)

Large blocks of samples (usually >2 kg) were cleaned and cut in parallelepipeds (4–6 cm in length) with a diamond saw. Final parallelepipeds (0.5–1 kg) where crushed in steel jaw crusher and quartered several times in a riffle-splitter. Sample aliquots were powdered in an agate ring mill. Whole rock major elements were analysed using standard X-ray fluorescence procedure (XRF) in the Geoscience Laboratories (GeoLabs), Ontario Geological Survey, Sudbury, Canada. The samples were first run for loss on ignition and then fused with borate flux to produce a glass bead. Transition metals were measured in pressed pellets. Ferrous iron was determined in the same laboratory by potentiometric analysis using potassium permanganate as oxidation agent. Ferric iron

was calculated from the difference of the total iron measured by XRF and the measured ferrous iron.

3.5 Transmission Electron Microscopy (TEM)

TEM studies have been carried out to investigate antigorite (chapter 5), Ti-clinohumite microstructure in olivine veins in serpentinites (chapter 6) and garnet coronas (chapter 10). TEM specimens have been prepared following standard procedures, selecting study areas by gluing copper rings with 1000 μm hole over the thin sections. The detached sample grids have been ion-thinned by a Gatan DuoMill apparatus and finally carbon coated. The TEM data have been acquired with a Philips CM20 analytical TEM, equipped with microanalytical STEM-EDS, at the CIC facilities of the University of Granada and Siena.

Microanalytical data were acquired in STEM modalities, alternatively using small or large scan windows (1000×200 Å and 10000×2000 Å). Raw data were corrected by the Cliff and Lorimer (1975) method, using experimental proportionality factors, determined for each element on mineral standards. Precision in the final, calculated atomic contents ranges from 1 to 5% relative, depending upon elemental abundances and window size.

3.6 Scanning Electron Microscopy (SEM)

Scanning electron microscope (SEM) observations were performed by secondary and back-scattered electron imaging in carbon-coated, polished, thin sections, using the following instruments: (1) Zeiss DMS instrument at the Centro de Instrumentación Científica (CIC) of the Universidad de Granada (Spain); (2) LEO 1430-VP at CIC; (3) Phillips Quanta 400 instruments at CIC and (3) JEOL JSM 6400 scanning electron microscope (Electron Microscopy Unit, ANU, Canberra).

X-ray mapping was performed (section 5.1) in order to identify small patches and microveins of potassium feldspar. X-ray mapping for K, Na Mg, Fe, Ca, Si, Ti, and O were made at CIC by EDS-SEM in a LEO 1430-VP instrument under an acceleration voltage of 20 kV, a beam current of 20 nA, and a beam diameter of 2 μm. Time counting for a frame was 105.8 seconds for a 1024x1024 pixel images.

Mineral compositions in the experimental runs (chapter 7, Appendix, section 14.3) were measured with the JEOL JSM 6400 scanning electron microscope, equipped with a LINK-ISIS energy dispersive spectrometer (EDS), operated at 15-kV accelerating voltage, 1-nA beam current and a working distance of 39 mm, with counting time of 100 s. No differences were observed using a spot or defocused beam due to the low alkalis concentration in the hydrous phases

3.7 Electron Backscattered diffraction (EBSD)-SEM

Crystal preferred orientations (CPO) in olivine and orthopyroxene (chapter 8) and garnet, clinopyroxene, orthopyroxene, and amphibole (chapter 10) were measured by indexing backscattered pattern diffraction or Kikuchi patterns. Backscattered diffraction is one of a variety of possible interactions produced when a sample is incided by high-energy electrons of an electron beam (Prior et al. 1999). This effect is enhanced by tilting

the sample ~70º (for an acceleration voltage of 20 kV). To improve the quality of Kikuchi diffraction patterns, standard diamond-polished (0.25 lm grain size) thin sections were further polished during 5 min with a chemical–mechanical procedure, using a colloidal silica suspension (Buehler™ Mastermet™). EBSD patterns were acquired by using the SEM-EBSD systems at Geosciences Montpellier (CNRS-Université de Montpellier 2, France). Indexing was performed by automatic EBSD mapping of whole thin sections on a JEOL JSM 5600, using a regular grid step of 30-35 μm for chapter 8 and 100 μm for chapter 10. Detailed mapping of selected areas in sample Al06-05b was performed using the CamScan X5000FE CrystalProbe in a low vacuum mode and a grid step of 12 μm.

EBSD patterns were indexed automatically using CHANNEL 5 software package from HKL Technology. Lattice orientation by CHANNEL 5 software is achieved by automatic indexation of Kikuchi patterns, using the Hough transform and six to nine detected band edges and their zones axis in the diffraction pattern. The following post-acquisition data treatment (Tommasi et al. 2008) was used in order to increase the indexation rate:

(i) Filling the non-indexed pixels that have up to 8 identical neighbors with this orientation.
(ii) Repeating this operation using respectively 7, 6, and 5 identical neighbors.
(iii) Identifying the grains, i.e., continuous domains characterized by an internal misorientation <15°.
(iv) Within each olivine crystal, searching and correcting for systematic indexation errors due to the olivine hexagonal pseudosymmetry, which results in similar diffraction patterns for orientations differing by a rotation of 60° around [100].

Pole figures are represented using average Euler angles for each grain instead of individual measurements to avoid overrepresentation of larger grains on the thin section. The EBSD data were processed and contoured as conventional CPO pole figures for selected crystallographic planes and directions using the software PFCH5 (Mainprice, 1990, 2007; Mainprice & Humbert, 1994).

Figure 3-2. CamScan X500FE CrystalProbe installed at "Service commun de microscopie électronique et analytique" l'Université Montpellier 2. Picture courtesy of David Mainprice.

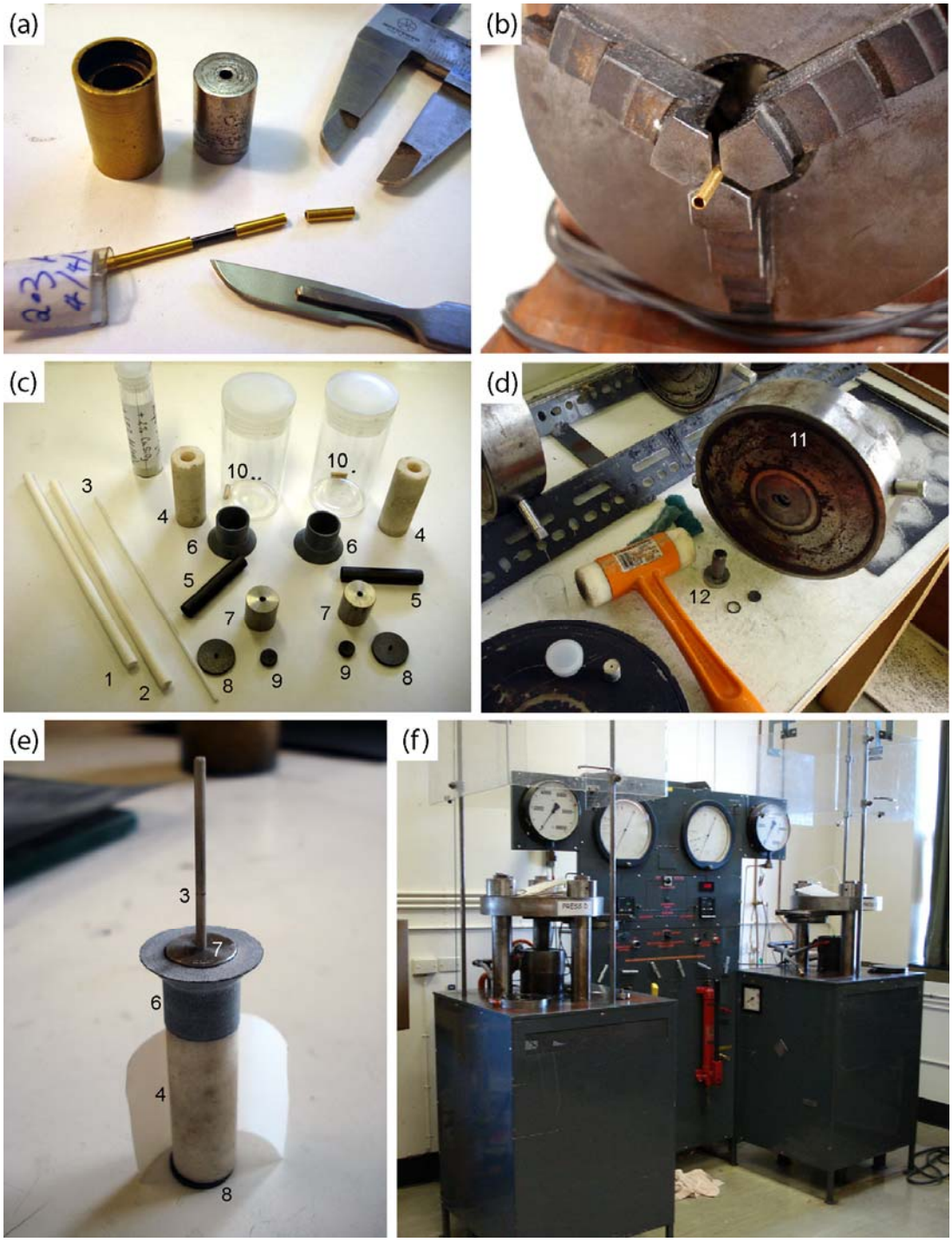

Figure 3-3. Step by step procedure for the preparation of high- pressure experiments **(a)** 2.3 mm ∅ gold tubes are sliced into open capsules **(b)** one side of the capsule is closed and welded. Then the starting material is filled into the capsule and the other end is welded **(c)** elements needed for two assemblies: (1) MgO-rod, (2) MgO-tube, (3) Mullite 2-bore tube, (4) two NaCl sleeves, (5) two graphite heaters, (6) two pyrophyllite caps, (7) two steel plugs, (8) two graphite outer discs, (9) two graphite inner discs (10), two welded gold capsules **(d)** vessel (11) with a 32-mm length bore with the assembly already inserted and piston (12) **(e)** final arrangement of the furnace assembly with the Teflon insulator and the 2-bore mullite rod (3) where the thermocouple wires are inserted. Same labels as in (c) **(f)** Piston cylinder apparatus with two presses. All pictures were taken by the author in the experimental laboratories at the Research School of Earth Science (ANU, Canberra, Australia).

3.8 High-Pressure experiments

The experiments reported in chapter 7 are conventional quenching experiments conducted in a range of 1.6–2.5 GPa and 600–700ºC. Sample containers were Au-capsules with an outer diameter of 4.3 and 6–7 mm in outer length, resulting in cylindrical samples of 4–6 mm in length (Fig. 3.3a and b). Experiments were performed in 0.5-inch (12.7 mm), end-loaded piston cylinder apparatuses at the Research School of Earth Science (The Australian National University) using a vessel with a 32-mm length bore (Fig. 3.3d), employing pure NaCl, low friction assemblies (Fig. 3.3c and e).

Gold capsules were placed in a MgO tube, inside a Teflon coated NaCl-graphite assembly (Fig. 3.3c and e). Figure 3.4 shows the dimensions of each part of the furnace assemblage used in the high-pressure experiments. The use of a gold capsule and the "dry" furnace assembly produces conditions close to the Ni–NiO transition (Hermann and Spandler 2008), which are similar to the FMQ buffer in the investigated temperature range. Capsules were welded, shut and tested for leakage prior to the experiment. A disk of 1-mm MgO was placed between the thermocouple end-point and the capsule to avoid reaction between them (Figs. 3.3 and 3.4).

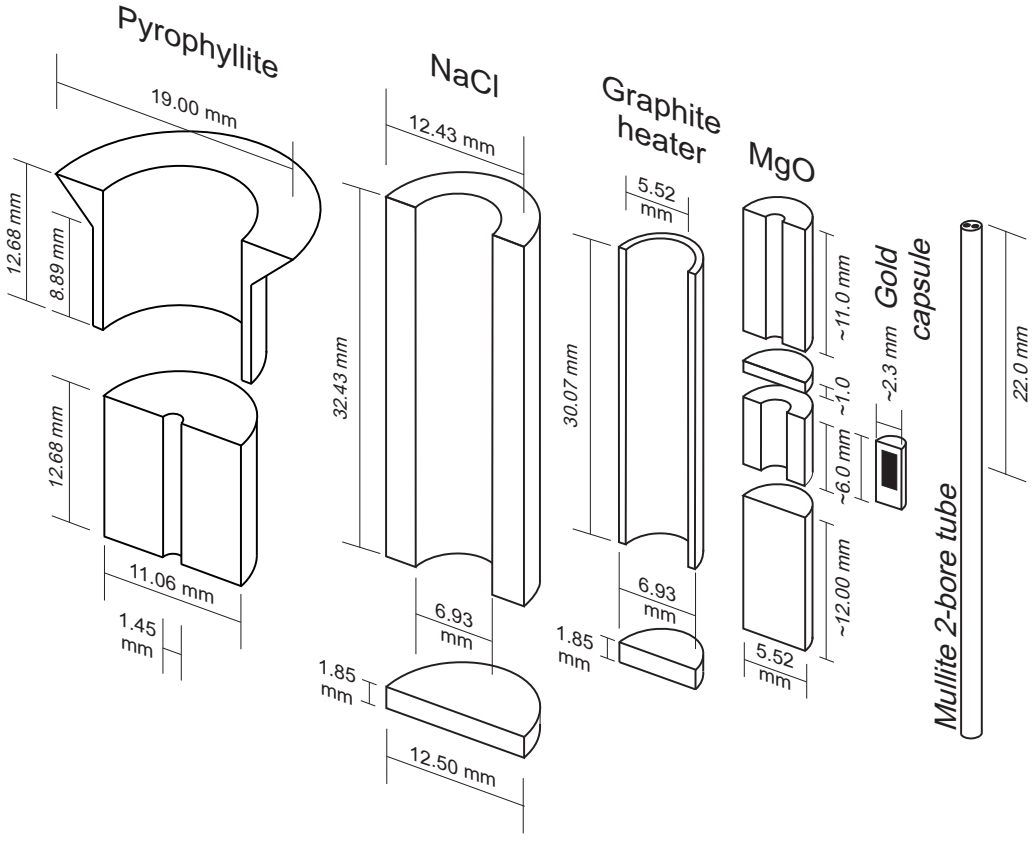

Figure 3-4. Sectioning of the ½" furnace assembly for end loaded pyston cylinder used in the high pressure experiments. (drawn by the author, see also Fig. 3-3).

Pressure was measured directly, converting the load in the cell to pressure for a low friction assembly and was kept constant during the experiments. No pressure corrections were applied because of the low friction behaviour of the NaCl cells and the relatively long run durations. Measurements on piston travel have shown that in such an assembly and given run temperatures, friction dissipates within the first 24–36 h. From this, we estimate that pressure is accurate within ±0.1 GPa.

Temperatures were measured using type B thermocouples ($Pt_{94}Rh_6$–$Pt_{70}Rh_{30}$), protected by two bore mullite tubes. The thermocouple precision is better than ±2ºC and accuracy is ±10ºC. The samples were quenched at the end of the runs by turning off the power of the furnace. Afterwards the experiments capsules were pinched and dried in the oven for 4 h. They were mounted in epoxy and ground down until a representative section was exposed.

3.9 Phase diagrams calculation (Perplex)

Thermodynamic calculations presented in many of the following chapters have been computed by using Perple_X software (Connolly 1990, 2005). PerpleX calculation strategy is based on a linearized formulation of the free energy minimization problem in a multi-level grid used to map and recover phase relations and physical properties. The preference for Perple_X over other petrological-oriented software (e.g. Thermocalc, Theriak-domino, etc.) mainly resides in the possibility to compute physical properties (e.g. density, specific heat capacity, P- and S-wave veolocities, etc.) simultaneously with the phase diagram calculation. The ability of PerpleX to perform this kind of petrophysical calculation has revealed as a powerful tool in the geodynamic modeling (Connolly, 2005).

Another virtue of Perple_X is that it is based on a thermodynamic generalization. In this generalization, the thermodynamic components are extended in order to construct phase diagrams independently of the chosen variables, and enable to compute phase diagrams for a broad range of physico-chemical systems. In this way, Perple_X can manage isochoric, adiabatic or chemically open systems with the same computational strategy as for conventional isochemical systems (Connolly, 1990). Moreover, the algorithm for the linearization of the free energy surface permits robust and relatively fast computation times even for Complex systems. There are only two basic types of phase diagram variables:

(1) 'Potentials' defined by the partial derivate of one extensive propertiy with respect to another. For example: pressure (P), temperature (T) and chemical potential of the j^{th} component (μ_j). All of them are potential state functions (θ).

(2) 'Compositions', defined arbitrary as a ratio of extensive properties. For example: number of moles of the j^{th} component (n_j), internal energy (U), enthalpy (H), entropy (S) and volume (V). All of them are extensive state functions (ψ).

Although each variable has a different physico-chemical significance, both can be treated in the same way from a computational point of view. This serves as a basis for the

method of calculating phase diagram used in Perple_X. In the frame of the generalized thermodynamics (Connolly, 1990), the notion of component is associated with each independent conservative extensity of a system[10]. Variation in the state and extent of an equilibrium system can be described by the relation:

$$d\Omega = \sum_{j=1}^{c} \theta_j d\psi_j - \sum_{j=c+1}^{n} \psi_j d\theta_j$$

where Ω is a generalized state function, and ψ_j and θ_j represent respectively, the extensities and potentials of the system. For isochemical systems[11] Ω is known as Gibbs free energy (G) and the former expression can be formulated for the independent variables {-P, T, n_1, ... n_j, … n_c} in a more conventional way as:

$$dG = VdP - SdT + \sum_{j=1}^{c} \mu_j dn_j$$

In practice, Perple_X finds the amounts and compositions of the phases that minimize the Gibbs energy of a system (G^{sys}) at constant pressure and temperature (Connolly, 2005). The Gibbs energy of the system is expressed in terms of the phases possible in the system as:

$$G^{sys} = \sum_{i=1}^{\Pi} \alpha_i G^i$$

where G^i is the Gibbs energy of an arbitrary quantity, here chosen to be a mole, of the i^{th} phase, and α_i is the amount of the phase. The Gibbs energy of a solution phase is a nonlinear function of its composition and is represented in Perple_X by a series of compounds, designated 'pseudocompounds'; defined such that each compound has the thermodynamic properties of the solution at a specific composition. Figure 3.5 illustrates the distinction between the non-linear Gibbs surface of phases β and γ and its corresponding

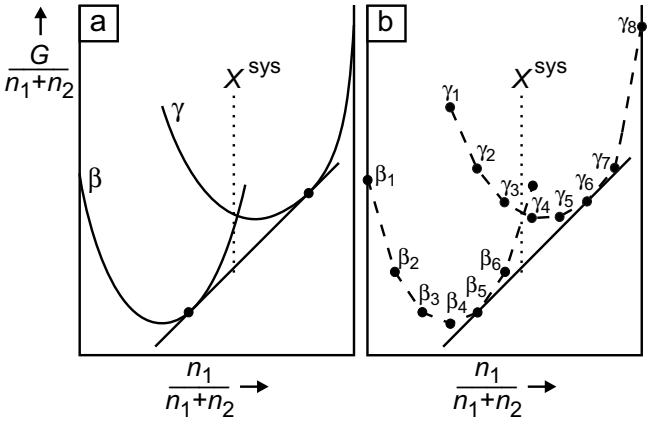

Figure 3-5. Schematic isobaric–isothermal free energy-composition diagrams for a binary system illustrating the distinction between the non-linear solution to the phase equilibrium problem (a) and its linear approximation (b) (from Connolly, 2005).

[10] for example, n_j in closed systems, V in isochoric s

[11] an isochemical systems is a system with P and T a moles of the components as conservative properties.

linear approximation by a finite number of pseudocompounds {β_1, ..., β_6, γ_1, …, γ_8). For composition X^{sys} the algorithm would identify $\beta_4+\gamma_6$ as the stable phase assemblage. A multilevel Cartesian grid strategy is used for mapping phase diagram sections. The stable assemblage is computed for each grid node at different iteration steps[12].

An attractive option of Perple_X is the possibility of computing phase diagrams for a particular bulk composition (commonly referred as pseudosection). Pseudosections contain information about mineral assemblages and changes in the mineral assemblages with variations in the intensive variables, showing only those equilibria that are relevant to one bulk composition. These diagrams are probably the best way to illustrate the dependence of mineral assemblages on, for example, pressure and temperature. Therefore, these diagrams are very useful to document the metamorphic history of a specific rock. Pseudosections can be used to link features observable in hand specimens and thin sections, such as mineral assemblages, reaction textures etc., with the metamorphic history experienced by a rock. In this Thesis, pseudosection calculations are used in this way, as an invaluable tool to unravel pressure and temperature conditions and reconstruct PT paths. Detailed discussion about possible factors affecting the final results (e.g., effective bulk composition, thermodynamic data or solid solution models) are discussed in each specific case.

[12] In the current version (Perple_X 07) calculations involving solution phases are done in two cycles, an exploratory stage used to estimate the range of phase compositions and an auto-refinement stage in which these estimates are refined (Connolly, 2009). This enables higher pseudocomponent resolution for shorter times.

PART TWO

4. Textural record of dynamic fluid expulsion in a subduction setting: the high-pressure antigorite dehydration front in Cerro del Almirez ultramafic massif (Nevado-Filábride Complex, S. Spain)

5 Highly ordered antigorite from Cerro del Almirez HP–HT serpentinites, SE Spain

6 Breakdown mechanisms of titanclinohumite in antigorite serpentinite (Cerro del Almirez massif, S. Spain): A petrological and TEM study.

7 An experimental investigation of antigorite dehydration in natural silica-enriched serpentinite

8 Fluid transfer into the wedge controlled by high–pressure hydrofracturing in the cold top-slab mantle

4 Textural record of dynamic fluid expulsion in a subduction setting: the high-pressure antigorite dehydration front in Cerro del Almirez ultramafic massif (Nevado-Filábride Complex, S. Spain)

Padrón-Navarta, JA[1*] · López Sánchez-Vizcaíno, V[2] · Garrido CJ[3] · Gómez-Pugnaire MT[1,3] ·

Although the cyclic nature of metamorphic dehydration events is subduction zones is attested by intermediate-depth seismicity, the hydrodynamics of fluid expulsion during the high-pressure, breakdown of antigorite and its potential on the development of dehydration events in these settings are still barely known. This is due to the Complexity of the system and the paucity in the geological record of arrested dehydration fronts where this process can be investigated on the field. The high pressure antigorite dehydration front in the Almirez ultramafic massif (Nevado-Filábride Complex, Betic Cordillera, SE Spain) offers an unique opportunity to investigate the dynamics of expulsion of large amount of deserpentinization fluids (~ 9 wt %) during the prograde breakdown of atg-serpentinite to chl-harzburgite. In this massif, the transition between atg-serpentinite and the prograde product assemblage (ol+opx+chl, chl-harzburgite) is well preserved and consist of chlorite-antigorite-olivine-serpentinite, which grades to (2) chlorite-antigorite-olivine-orthopyroxene serpentinite. The final prograde assemblage is chl-harzburgite showing two contrasting textures: granofelsic (with coarse, round olivine) and spinifex-like (dentritic-like, cm-sized olivine and orthopyroxene). Both textures occur as interspersed, m-sized boudins behind the antigorite dehydration front. We ascribe these textures to shifts of the growth rate of reaction products due to temporal and spatial fluctuations of the affinity of the antigorite-breakdown reaction. The granofelsic texture represents near equilibrium crystallization conditions, whereas the spinifex-like texture crystallizes at large overstepping of the atg-breakdown reaction. These fluctuations of affinity of the atg-breakdown reaction are driven by cyclic variations of the excess fluid pressure in the dehydrating system, which are ultimately controlled by the hydrodynamics of deserpentinization fluid expulsion. Crystallization at a low affinity of the reaction, corresponding to the granofelsic texture, may be attained if fluids are slowly drained out the dehydration front. During the advancement of the dehydration front, which constitutes a permeability barrier, overpressured domains are left behind. These low permeability, overpressure domains preserve atg-serpentinite that is highly metastable relative to surrounding lithostatic fluid pressure domains. Brittle failure in these domains results in a sudden increase of its permeability, a drop of the fluid pressure towards hydrostatic pressure, and a displacement of atg equilibrium towards the prograde products that crystallizes at a high affinity of the reaction. This mechanism accounts for strong, disequilibrium growth of chl-harzburgite products leading to the spinifex chl-harzburgite. The textural bimodality of chl-harzburgite in the Almirez massif hence witnesses a unique example of the feedbacks between the cyclic dynamic of metamorphic fluid expulsion, the reaction rate and crystallisation of the atg-dehydrating system.

1. Departamento de Mineralogía y Petrología, Universidad de Granada, Spain.
2. Departamento de Geología, Universidad de Jaén Linares, Spain.
3. Instituto Andaluz de Ciencias de la Tierra (IACT), Granada, Spain.

4.1 Introduction

The link between devolatilization reactions and fluid flow is crucial to unravel important geodynamic processes in subduction zones as deformation and element transfer are strongly controlled by the presence of water (e.g. Yamasaki and Seno 2003, Ulmer 2001, Arcay et al. 2005). Moreover, the endothermic effect of devolatilization reactions may contribute to regulate the thermal structure evolution of subduction zones itself. At high confining pressure, and due to their rather limited permeability, reacting rocks being dehydrated induce a certain increase in the fluid pore pressure (Thompson and Connolly 1990, Connolly 1997). Although a rigorous treatment of non-hydrostatic equilibrium prevents a straightforward relationship to be established between the environmental conditions and the microscopic state of stress within the solid phases (Dahlen 1992), it can be stated that the locus of dehydration is strongly dependent on fluid pressure and temperature. In fluid-dominated dehydration reactions (where the total volume change of reactions is positive, Hacker 1997), fluid drainage is a first order requirement that ultimately controls the progression of reactions that, otherwise, would be retarded or eventually quenched. In other words, reaction rate kinetics are mainly controlled by the drainage rate and, consequently, by the fluid flow mechanism. Even simple, two limiting cases can be envisaged: compacting and non-compacting scenarios (Connolly, 2010). The former is an intrinsic mechanism occurring during devolatilization of viscolastic rocks if compactation is shorter than the metamorphic time scale (Connolly 1997). The latter would occur when the threshold tensile strength of the rock is exceeded, providing an essentially instantaneous mechanism for regulating supra-lithostatic fluid pressures (e.g. Sibson 1992, 2004). Despite these two scenarios should be texturally recorded in dehydrated prograde assemblages in a very contrasting way, a conclusive confirmation of these processes by petrological and textural evidences in metamorphic terrains has been hampered by the rare occurrence of devolatilization fronts in the geological record.

Evidences of high-pressure antigorite dehydration found at the Cerro del Almirez ultramafic massif (Betic Cordillera, Spain) represent a noteworthy exception. Here, the transition between the hydrous protolith (antigorite serpentinite) and the prograde product assemblage (olivine + orthopyroxene + chlorite, chlorite harzburgite) is very well preserved and can be surveyed in detail. This transition between antigorite serpentinite (Atg-serpentinite in the following) and chlorite harzburgite (Chl-harzburgite) has been interpreted as the antigorite-out isograd (Trommsdorff et al., 1998). Antigorite dehydration was accompanied by release of high amounts of high–pressure water-rich fluids (~ 9 wt % fluid) (Padrón-Navarta et al., submitted b, Chapter 8, this thesis). The maximum stability of antigorite in these rocks has been experimentally determined at ~680ºC at 1.6-1.9 GPa (Padrón-Navarta et al., 2010, Chapter 7).

Recent field work and detailed mapping of the antigorite-out isograd reveals, nevertheless, a more Complex scenario than previously reported. In this work, we describe a variety of newly found textures and transitional lithologies, linked to the antigorite breakdown and the prograde growth of Chl-harzburgite. These features can be interpreted in the light of fluid migration and overpressure release and can be important for understand fluid flow mechanism in subduction zones.

4.2 Geological Setting of The Cerro del Almirez Ultramafic massif

The Cerro del Almirez ultramafic massif is the largest (~2.3 km^2) of several small and, mostly, strongly deformed ultramafic sheets or lenses, which are found throughout the upper lithological sequence of the Nevado-Filábride Complex (Fig. 4-1), the lowermost tectonometamorphic unit of the Internal Zones of the Betic Cordillera (Southern Spain). Ultramafic rocks appear in the upper part of this sequence, intercalated with quartzites and light-coloured micaschists (Tahal schist, Fig. 4-1), marbles and, locally, with orthogneisses. This unit overlays a lower lithological unit (Montenegro, Fig. 4-1), mainly consisting of a thick and monotonous sequence of graphite-bearing metapelites, intercalated quartzites, and scarce graphite-bearing marbles (Gómez-Pugnaire et al., 2004 and references therein). The whole sequence was metamorphosed during the Miocene under eclogite facies conditions. During exhumation, the high-pressure rocks

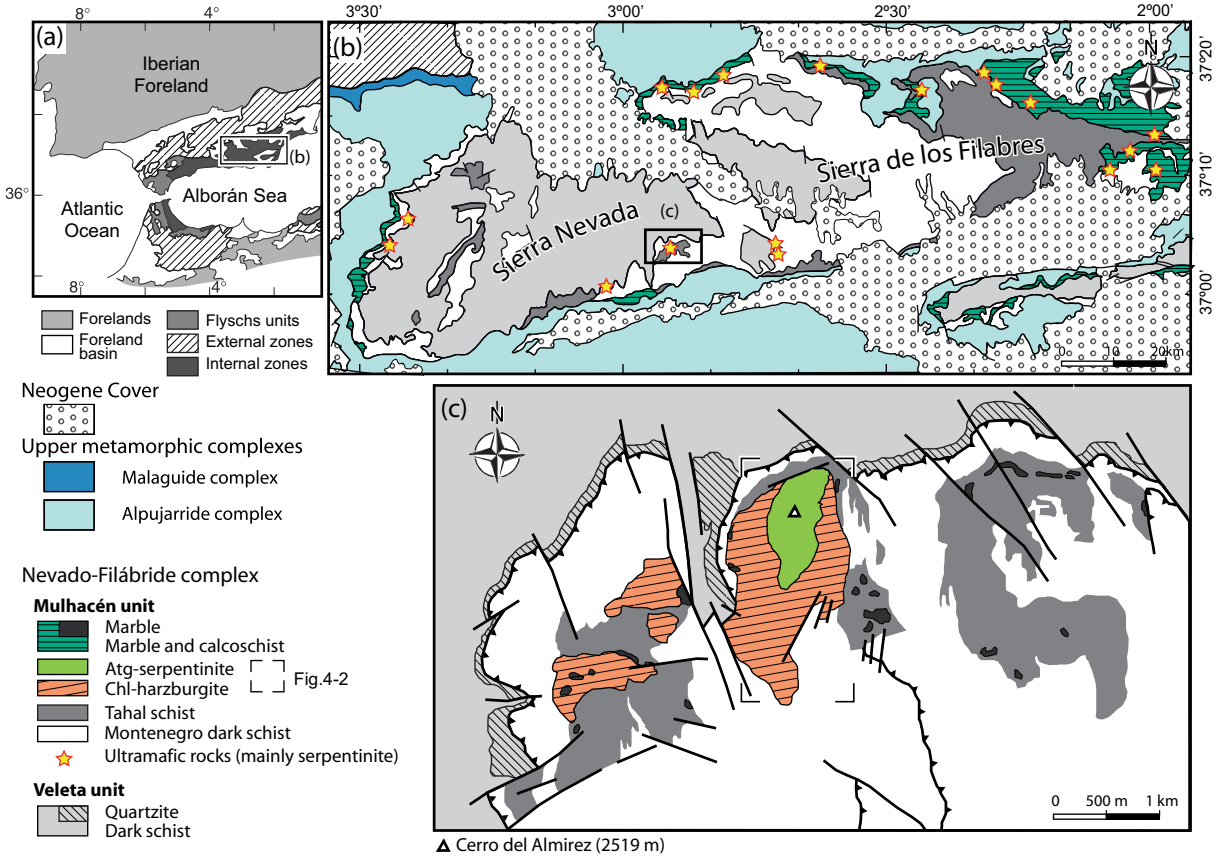

Figure 4-1. (a) Simplified geological map showing the main tectono-metamorphic domains of the Betic Cordillera; **(b)** Main tectonic and lithologic units of the Nevado-Filábride Complex and location of the Cerro del Almirez ultramafic massif (inset) together with other smaller ultramafic bodies (mainly serpentinite, stars) cropping out in this Complex (modified from López Sánchez-Vizcaíno 1994); **(c)** Geological map of the field area where the Cerro del Almirez and two adjacent smaller ultramafic massifs crop out (modified from IGME 1981, Schönbächer 1999, Hürlimann 1999 and own field observations).

were partially overprinted by amphibolite and greenschist facies retrograde assemblages (Gómez-Pugnaire et al., 2004 and references therein).

The Nevado-Filábride rocks underwent a Complex, alpine, tectonic evolution (Gómez-Pugnaire and Fernández-Soler 1987, Gómez-Pugnaire and Franz 1988, Bakker et al. 1989, Jabaloy et al., 1993, De Jong et al, 1993, Puga et al., 2002, Augier et al., 2005, Booth-Rea et al. 2005). The main extensional, shear deformation, event postdated high-pressure metamorphism and produced a strong thinning of the upper lithological sequence of the Complex, perpendicular to the transposed bedding (Jabaloy 1993, González-Lodeiro et al., 1996, Martínez-Martínez et al, 2002). This accounts for the extremely reduced thickness (less than 20 m) of marbles and clear schists in the Cerro del Almirez area, when compared with their thickness in the eastern part of the Complex (several hundreds of meters in the Sierra de los Filabres), as well as for the discontinuous character of the outcrops of both ultramafic rocks and metasediments (Fig. 4-1).

The Cerro del Almirez ultramafic massif and its lithological variety were earliest reported by Jansen (1936). Detailed mapping of the enclosing metasediments, the ultramafic bodies and the internal contact between serpentinites and chlorite harzburgites were published by Burgos et al., (1980) and IGME (1981). Morten and Puga (1984) interpreted the characteristic blades of olivine and orthopyroxene in Chl-harzburgite as produced by melt quenching. A secondary, metamorphic origin, for this spinifex-like texture was later proposed by Bodinier et al. (1993). However, the observed transition from the antigorite serpentinite to the olivine-enstatite rocks (the Chl-harzburgite term was introduced by Garrido et al., 2005) was first interpreted as due to a prograde, high pressure, metamorphic reaction by Trommsdorff et al. (1998). In this latter paper, the boundary between serpentinite and spinifex-like rocks is described as "sharp, but irregular, with no intermediate tectonic discontinuity" and it is stated that "the two rock types grade into each other over a distance of no more than a few tens of metres". Concerning the olivine-enstatite rocks, the variety with spinifex-like texture is considered by these authors as the dominant one and the harzburgites with granular textures are always attributed to deformation-induced recrystallisation.

From the publication of the Trommsdorff et al. (1998) paper up to the present several works came out with an extensive description and mapping of the ultramafic bodies from the Cerro del Almirez (Hürlimann, 1999, Schönbächler, 1999) and other nearby areas (Cerro Blanco and Montenegro ultramafic outcrops). Several, more specific studies were also published in recent years with reference to: the age of the high-pressure metamorphic peak in these rocks (López Sánchez-Vizcaíno et al., 2001); their metamorphic evolution (Puga et al., 1999); the silicate and oxide exsolution in pseudo-spinifex olivine (Ruiz Cruz, et al., 1999); the geochemical characterization of the Chl-harzburgite and Atg-serpentinite and their implications for subduction settings (Scambelluri et al., 2001a, 2007; Garrido et al., 2005); the metamorphic evolution of titanclinohumite in both the serpentinite and the Chl-harzburgite (López Sánchez-Vizcaíno et al., 2005, 2009); the microstructural characterization of antigorite (Padrón-Navarta et al., 2008); the experimental investigation of antigorite dehydration and the constrain of antigorite maximum stability conditions (Padrón-Navarta et al., 2010); the determination of antigorite compressibility at high-pressure conditions (Nestola et al., in

press); and the description of high-pressure hydrofracturing of Chl-harzburgite and the implications for fluid transfer into the mantle wedge in subduction settings (Padrón-Navarta et al., submitted, b).

All these papers provide a growing number of field, petrographic and chemical evidences supporting the exceptional nature of the Cerro del Almirez utramafic massif as a unique example in the world, were observations can be made concerning the significance of dehydration reactions in subduction zones and how these reactions were affected by different bulk-rock compositions and Complex kinetic and deformational factors. In all these works, however, the boundary between serpentinites and harzburgites keeps being interpreted as the antigorite-out dehydration isograd at high-pressure and temperature conditions, without further considerations. It is the aim of the present paper to investigate in detail this devolatilization front and its link with the development of textures recorded in the prograde assemblage.

4.3 Field Relationships of Ultramafic Rocks

In this work, we account for new results obtained after thorough mapping and sampling of all the rock outcrops found along, and several meters above and below, the antigorite-out isograd in the Cerro del Almirez ultramafic massif. Field and structural relationships are shown in the map from Figure 4-2, as well as the sampling location for the most significant rock types studied in the present contribution. In the following sections we make a detailed description of newly discovered lithologies and textural relationships associated to the Atg-serpentinite - Chl-harzburgite transition in the Cerro del Almirez ultramafic massif. From top to bottom, we describe: (1) Atg-serpentinite, including some of the mineralogical and textural features that can, occasionally, be preserved during the prograde evolution of the rocks; (2) a series of transitional assemblages and textures occurring between Atg-serpentinite and Chl-harzburgite; and (3) three types of Chl-harzburgite with highly contrasting textures. The mineralogical composition and the main macroscopic and textural features of these rocks are summarized in Table 4-1.

4.3.1 Serpentinites

The upper part the of the Cerro del Almirez massif consists of a ca. 200 m thick sequence of well foliated *antigorite serpentinites* (Table 4-1; Trommsdorff et al., 1998; Padrón-Navarta et al. 2008). The overall structure of the serpentinite sequence is characterized by a shallowly dipping foliation (20-30º), defining an open NNE-SSW trending synclinal (Fig 4-2). Minor, WNW-ESE trending folds with rare crenulation cleavage are superimposed. A weak lineation can be rarely found, defined by stretched magnetite and/or chlorite aggregates. Olivine and clinopyroxene abundance is very variable, even at metric scale. Prograde *olivine-rich veins* are widespread, in some cases together with titanclinohumite (López Sánchez-Vizcaíno et al., 2005, 2009). Their thickness ranges from several millimetres to 10 centimetres. They are commonly folded by the main foliation and, in some cases, even transposed and boudinaged. Olivine also appears as clusters of individual, rock-forming, xenomorphic to prismatic idiomorphic porphyroblasts with up to 10 cm in length (ol^A in Fig. 4-3a). *Metadunites* (> 90 vol. %

Table 4-1. Summary of the main lithologies cropping out at the Cerro del Almirez ultramafic massif.

	Rock name	Mineral assemblage	Macroscopic description	Textural relationships
Serpentinite	Atg-serpentinite	atg^A + mag ± ol^A ± cpx ± tr ± chl ± Ti-chu	Dark-green-coloured, well foliated serpentinite with weak magnetite stretching lineation and very rare crenulation cleveage. Irregular occurrence of ol ± Ti-chu veins and ol porphyroblasts.	Atg^A interpenetrating blades texture, transposed by disjunctive cleavage defined by fine-grained, shape preferred, oriented atg^A along narrow shear bands (Fig. 4-6a). Oriented mag aggregates. Porphyroblasts or aggregates of ol^A, cpx, and tr in very variable ammounts.
	Opx-Ol-serpentinite	atg^O + ol^O + opx^O (tlc) + mag + tr	Dark-green, well foliated serpentinite with abundant ol^O veins cutting the foliation. Large ol^O and opx^O porphyroblasts (Figs 4-3b). Preserved as an isolated lens within Chl-harzburgite.	Subhedral porphyroblasts of ol^O. Euhedral porphyroblast of opx^O, partial or totally replaced by tlc. Fine grained atg^O matrix. (Fig. 4-6c)
Transitional lithologies	Chl-serpentinite	atg^T + chl^T + ol^T + mag + tr	Dark-brownish, foliated serpentinite with coarse grained atg^T, chl^T and ol^T (Fig. 4-5c). Sharp contact with Atg-serpentinite (Fig. 4-4).	Three textural domains: (1) fine grained atg^A+ol^A; (2) big euhedral atg^T with subhedral chl^T plates in the core; (3) coarse grained ol^T with interstitial atg^T. Mag and tr in domains (1) and (2) (Fig. 4-6b)
	Atg-Chl-Opx(Tlc)-Ol schist	atg^T + chl^T + ol^T + opx^T(tlc) + mag + tr	Indicated in the field by the ocurrence of prismatic opx^T. Progressively less foliated, with increasing grain size and richer in opx^T and chl^T towards Chl-harzburgite.	More recrystallized than Chl-serpentinite. Ol^T granoblasts; prismatic opx^T porphyroblasts, partially replaced by tlc; big platy chl^T; variable ammounts of atg^T. Straight grain boundaries (Fig. 4-6d).
Chl-harzburgite	Granofels	ol^G + opx^G(tlc) + chl^G + mag + tr ± Ti-chu	Massive, medium to coarse grained rock. Chl^G flakes and opx^G prisms can be easily identified with naked eye. The only Chl-harzburgite in contact with transitional rocks.	Atg lacking. Coarse grained opx^G and chl^G with intergranular texture confined by ol^G grains (Fig. 4-6f). Relic ol^R and opx^R porphyroblasts from serpentinites.
	Spinifex-like	ol^S + opx^S(tlc) + chl^S + mag + tr ± Ti-chu	Fine to very coarse grained rock with randomly oriented spinifex-like texture (Fig. 4-3e). Dark, arborescent ol^S; radial opx^S aggregates (usually weathered to tlc); elongated strings of mag. Alternating in the field with granofels bodies (Fig. 4-3d).	Brown pleochroic, elongated ol^S grains, overgrowing in some places relic colourless ol^R porphyroblasts. Opx^S as coarse-grained aggregates or radial acicular crystals. Also idioblastic opx^R relics. Fine-grained chl^S in the matrix and as inclusions in ol and opx. Prismatic tr grains. (Fig. 4-6g).
	Recrystallized	ol + opx(tlc) + chl + mag + tr ± Ti-chu	Dark green, weakly to strongly foliated rocks, mostly with spinifex-like and granofelsic relic domains. Foliation is defined by spaced interconected bands, millimetric to metric in thickness.	Grain size reduction. Granoblastic aggregates of colourless ol and chl. Relic prismatic opx. Ol shape preferred orientation defining the foliation.

olivine) sporadically occur (Fig. 4-2) as metric lenses intercalated in the serpentinite. They are easily recognized by their reddish colour in weathered surfaces, large grain size (mm to 8 cm) and poor foliation. *Clinopyroxene-tremolite rich serpentinites* are also poorly foliated or massive. They appear as widespread layers, especially in the southern and eastern parts of the massif. Tremolite can be commonly observed in them as non oriented, small (2-5 mm), prismatic grains. In places, dark green, up to 0.5 m thick *clinopyroxenite boudins* can be found. They consist of coarse grained aggregates of, originally mantelic, clinopyroxenes with a very conspicuous cleavage. Metamorphic recrystallisation of thin clinopyroxenite layers may give place to the limited occurrence of light-coloured *diopside + chlorite schist* with well developed S-C structures. *Metarodingite* boudins (up to 5 m long and 1.5 m thick), accompanied by chlorite-amphibole blackwalls, are also relatively common through the whole sequence (Trommsdorff et al. 1998).

Atg-serpentinite also occurs preserved as decametric lenses beyond the antigorite-out reaction front, intercalated within the Chl-harzburgite sequence in the Southern face of the body (Fig. 4-2). Lenses crop out as a poorly foliated or massive serpentinite with cm-sized, prismatic tremolite, olivine porphyroblasts, magnetite, and rare chlorite. According to their shape and the general structure of the ultramafic body (Fig. 4-2), the present location of these lenses can not be explained by tectonic processes (folds). Thus, it might be suggested (see below) that they were preserved as metastable relics beyond the antigorite maximum stability conditions.

A different outstanding case of relic serpentinites preserved within the Chl-harzburgite is that of a single isolated lens (c. 50 m long and 3 m thick) of *orthopyroxene-olivine serpentinite* found in the Western face of the ultramafic body, about 70 m below the antigorite-out devolatilization front (black triangle with white dot in Fig. 4-2). This rock displays contrasting mineralogical and textural features with Atg-serpentinite (Table 4-1; Padrón-Navarta *et al.*, 2010). In the field, it appears as a foliated serpentinite with abundant, almost horizontal brown coloured olivine veins (up to 2 cm thick) cross cutting the main foliation. Rounded or subhedral olivine grains (2-3 cm long) occur scattered throughout the antigorite matrix without any preferred orientation (ol^O in Fig. 4-3b). In the veins, prismatic, up to 4 cm long, crystals of orthopyroxene nucleate perpendicular to the vein walls towards the antigorite matrix. Similar orthopyroxene grains appear also in the matrix (opx^O in Figs. 4-3b and 4-5b). The contact of the orthopyroxene-olivine serpentinite lens with Chl-harzburgite is very sharp and without evidences of tectonic origin.

4.3.2 Transitional lithologies to Chl-harzburgite

A sequence of distinctive lithologies and textures occur through an approximately 8 m thick sequence between Atg-serpentinite and Chl-harzburgite (Table 4-1) in the best preserved outcrops (Fig. 4-4a), scattered along the antigorite-out devolatilization front (black stars in Fig. 4-2). The first and more conspicuous rock type, *chlorite-serpentinite* (hereafter Chl-serpentinite; Padrón-Navarta et al., 2008) is more massive and darker in colour than Atg-serpentinite and consists of coarse grained (single grains can be distinguished with naked eye) antigorite, chlorite, and olivine. The transition between normal Atg-serpentinite and Chl-serpentinite is sharp and clearly oblique to the Atg-serpentinite main foliation (Padrón-Navarta et al., 2008). These relationships between

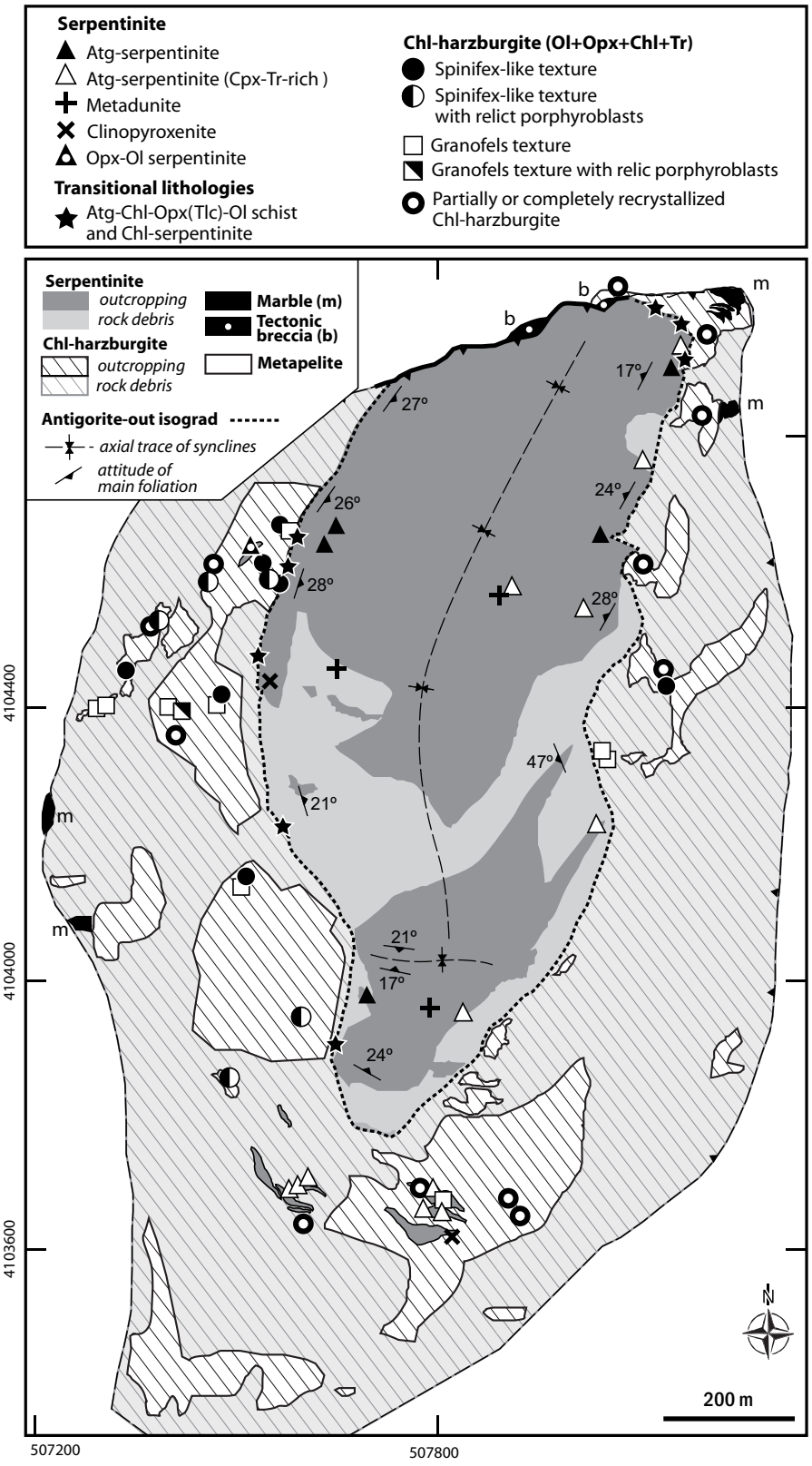

Figure 4-2. Detailed geological map of the antigorite-out isograd in the Cerro del Almirez massif, with location of the main in-situ outcrops of the lithologies (symbols) relevant for the study of the Atg-serpentinite – Chl-harzburgite transformation.

the two rock types can be neatly observed at outcrop (Fig. 4-4b) or, even, hand specimen scales (sample Al06-45, Fig. 4-5a). The occurrence of the second rock type (*Atg-Chl-Opx(Tlc)-Ol schist*), about 20-30 cm away from Chl-serpentinite (sample Al06-43, Fig. 4-4a), is indicated by the appearance of prismatic orthopyroxene grains in rocks externally very similar to Chl-serpentinite: dark colour and penetrative foliation. Transition towards clearly identifiable granofelsic Chl-harzburgite (see below) takes place progressively through a 1-2 m thick rock section (Fig. 4-4a), characterised by: (i) the increasing amount of orthopyroxene and the associated lighter colour of the rock, due to the orthopyroxene replacement by talc; (ii) the disappearance of antigorite (not to be observed in the field); (iii) increasing grain size, especially in the case of orthopyroxene and chlorite; and, accordingly, (iv) the change from a roughly foliated to a granofelsic structure.

4.3.3 Chlorite-harzburgite

The lower part of Cerro del Almirez ultramafic massif (Fig. 4-2) and the other three minor ultramafic bodies West of the Cerro del Almirez (Fig. 4-1) consist mainly of olivine + orthopyroxene + chlorite + magnetite ± tremolite ± titanclinohumite rocks (Chl-harzburgite), together with minor orthopyroxene-rich veins, clinopyroxenite boudins and metarodingite boudins. On the basis of their textural features, we recognize three varieties of Chl-harzburgite (Table 4-1): granofels (reported for the first time in this work), spinifex-like (Trommsdorff et al., 1998), and recrystallized (Padrón-Navarta et al., submitted, b see Chapter 8).

Chl-harzburgite granofels

It crops out as a medium- to coarse-grained rock with weak or, most commonly, completely lacking, foliation or lineation, thus matching the granofels term originally proposed by Goldsmith (1959) and recently countersigned by the IUGS Subcommission on the Systematics of Metamorphic Rocks (Brodie et al., 2007). The occurrence of conspicuous, coarse chlorite flakes (2-3 mm) and orthopyroxene prisms can be used to identify this Chl-harzburgite type in the field (Fig. 4-3c). This granofels rock is the only Chl-harzburgite variety to be found in direct contact with the above described transitional lithologies, close to the antigorite-out reaction front.

⇒ **Fig. 4-3.** Representative field and textural features of ultramafic rocks from the Cerro del Almirez ultramafic massif. **(a)** Atg-serpentinite with olivine porphyroblasts. **(b)** Scanned polished-surface of a orthopyroxene-olivine serpentinite with olivine and orthopyroxene porphyroblasts within a fine-grained antigorite matrix. **(c)** Typical field appearance of a coarse-grained Chl-harzburgite granofels. **(d)** Sharp contact in the field between granofels and spinifex-like Chl-harzburgites. Rock colours were enhanced for the shake of clarity. **(e)** Spinifex-like textured Chl-harzburgite. Elongated dark minerals are olivine, white zones are rich in orthopyroxene weathered to talc; **(f)** Spinifex-like texture preserving relic olivine (ol^R) and orthopyroxene (opx^R) porphyroblasts similar to those from the orthopyroxene-olivine serpentinite from b. **(g)** Fine –grained Chl-harzburgite granofels preserving relic olivine (ol^R) and orthopyroxene (opx^R) porphyroblasts similar to those from the orthopyroxene-olivine serpentinite from b. Superscript letters accompanying mineral names in a, b, e, f, and g refer to the rock type these minerals belong to and the mineral assemblage they equilibrated with: ^{A}: Antigorite-serpentinite; ^{O}: Orthopyroxene-olivine serpentinite; ^{G}: granofels Chl-harzburgite; ^{S}: spinifex-like Chl-harzburgite; ^{R}: relic porphyroblast.

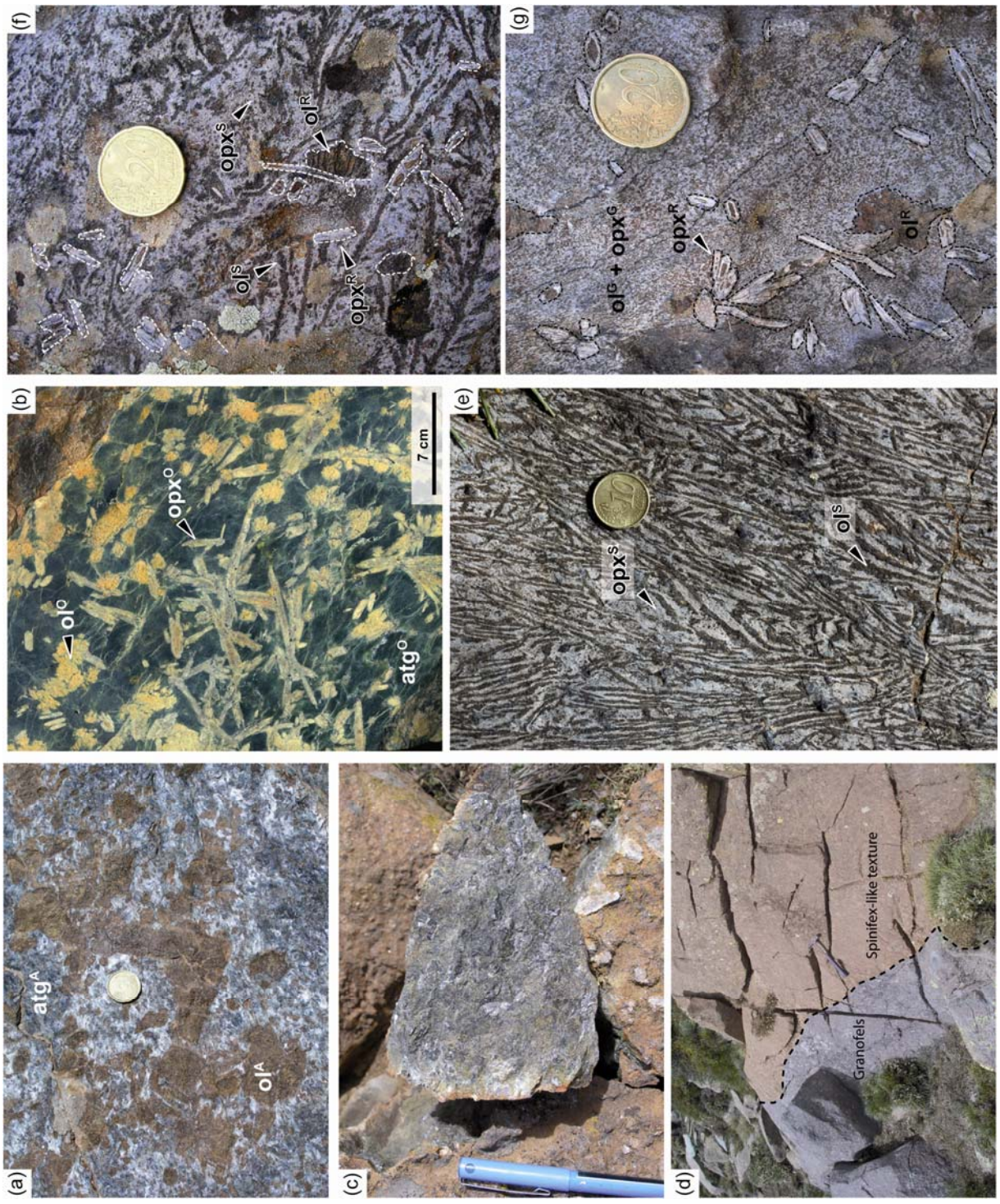
(a)
atg^A
ol^A
(b)
ol^O
opx^O
atg^O
7 cm
(c)
(d)
Spinifex-like texture
Granofels
(e)
opx^S
ol^S
(f)
opx^S
ol^R
ol^S
opx^R
(g)
ol^G + opx^G
opx^R
ol^R

and centrimetric radial aggregates of orthopyroxene (Fig. 4-3e). Both the grain size and the orientations of olivine and orthopyroxene crystals can vary at centimeter to meter observation scale in the field. Strong shape preferred orientation of olivine crystals producing a typical fish-tail texture is usually observed in rocks with large and highly anisomorphic olivine crystals (up to 10 cm in length and aspect ratios of 50:1). More radial/arborescent or even random oriented textures tend to correspond to olivine crystals with a smaller grain size (5-10 mm) and lower aspect ratio (~6:1) (Padrón-Navarta et al., submitted, b). The ol:opx modal proportion is similar (~1:1) in both textures (strongly and randomly oriented). Although very strong shape preferred orientations exist locally, there is not a general orientation pattern of the spinifex texture at the scale of the massif. Exceptionally magnetite occurs as elongated strings evoking the weak lineation observed in serpentinites.

In places, both the spinifex-like and the granofels textured Chl-harzburgites enclose large (up to 4 cm) subhedral and euhedral porphyroblasts of olivine and/or prismatic orthopyroxene (ol^R and opx^R in Fig. 4-3f, g, see also Fig. 4-5f). These porphyroblasts are randomly oriented and heterogeneously scattered through the rock. In the field, they are very similar to those occurring in the above described Atg-serpentinite (olivine porphyroblasts) and in the orthopyroxene-olivine serpentinite (olivine and orthopyroxene porphyroblasts). In the following, they will be referred to as relic porphyroblasts. Figure 4-3 shows that relic porphyroblasts may occur both in spinifex-like and granofels Chl-harzburgite when the two rock types are found in contact with each other.

Granofels and spinifex-like textures alternate in intricate metric or even decimetric bodies through the Chl-harzburgite sequence without a recognizable distribution pattern. Direct contact between the granofels and spinifex-like varieties is sharp and slightly convoluted. However, it can be only exceptionally observed without disruption at the outcrop scale (Fig. 4-3d). In those cases, no clear relationships can be established between the boundary and the orientation of arborescent olivine from the spinifex-like Chl-harzburgite.

Recrystallized Chl-harzburgite

In wide areas of the Cerro del Almirez body, especially in the Southern and Eastern zones (Fig. 4-2), the above described two varieties of Chl-harzburgite may locally occur affected by recrystallisation along spaced bands with a thickness ranging from millimetric to metric. Contacts between recrystallised and undeformed zones are sharp at the outcrop scale. Recrystallized domains are characterized by: (i) partial to complete obliteration of previous textures; (ii) significant grain size reduction of olivine, resulting in greenish fine grained (< 200 µm) olivine aggregates; and (iii) local development of a rough foliation. These features have been described in detail in a separated paper (Padrón-Navarta *et al.*, submitted, b; see Chapter 8).

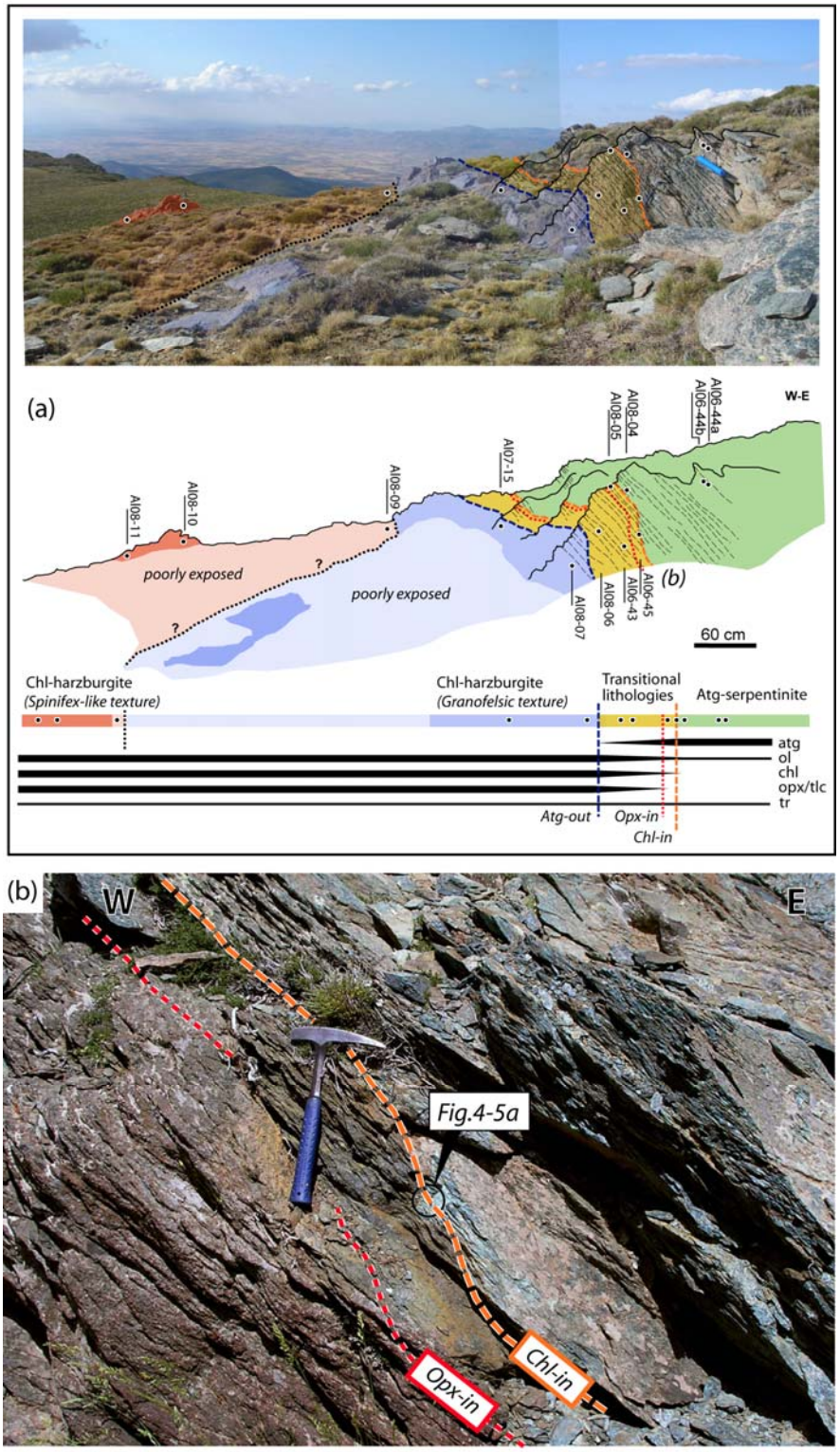

Figure 4-4. (a) Sketch drawing showing field relationships between Atg-serpentinite (right hand side; green colour), transitional lithologies (narrow yellow band) and Chl-harzburgites (granofels in violet and spinifex-like in pink). Black dots represent the location of studied samples. **(b)** Outcrop detail showing the contact (Chl-in orange line) between Atg-serpentinite (greenish rocks in the right hand side) and Chl-serpentinite (brownish rocks), and between the latter and Atg-Chl-Ol-Opx schist (Opx-in red line).

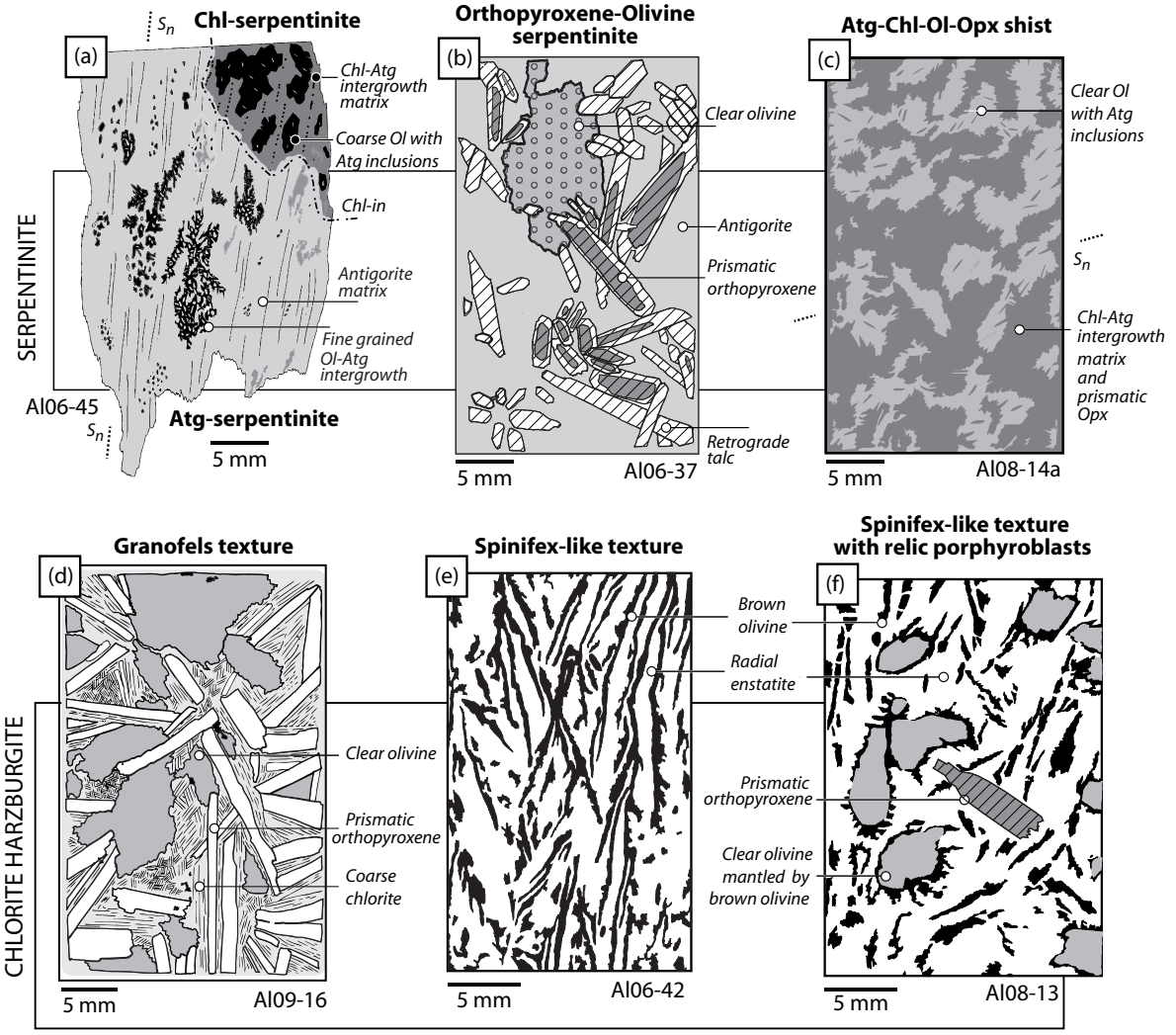

Figure 4-5. Thin section sketches highlighting the main textural features of the studied ultramafic rocks. **(a)** Contact between fine-grained Atg-serpentinite (lower left) and coarser grained Chl-serpentinite (upper right). The appearance of chlorite (Chl-in) crosscuts the subvertical foliation trace (S_n) (sample Al06-45, see Fig. 4a for the exact location of this sample and Fig. 4b for field occurrence). **(b)** Orthopyroxene-olivine serpentinite. **(c)** Atg-Chl-Ol-Opx schist (sample Al06-14a). The foliation trace can still be recognized due to preferred orientation of olivine rich domains. **(d)** Chl-harzburgite granofels with coarse (1-2 mm) chlorite and orthopyroxene intergranular texture confined by olivine grains (sample Al08-16). **(e)** Chl-harzburgite with spinifex-like texture; the thin section was cut parallel to the maximum olivine elongation [001] (sample Al06-42). Olivine is typically brown coloured. **(f)** Spinifex-like Chl-harzburgite with large relic porphyroblasts of clear olivine and orthopyroxene.

4.4 Petrography

4.4.1 Serpentinite

Antigorite serpentinite

Atg-serpentinite with variable amounts of clinopyroxene, tremolite or titanclinohumite is described in detail by Trommsdorff et al. (1998); López Sánchez-Vizcaíno et al. (2005), and Padrón-Navarta et al. (2008). Clinopyroxene-poor Atg-serpentinite, like the one found directly in contact with Chl-serpentinite in the best outcrops displaying the transitional lithologies (Western face, Fig. 4-2; samples Al06-44 and Al08-04 in Fig. 4-4), is composed almost exclusively by antigorite and minor magnetite. In these rock, serpentinite foliation is developed by a shape preferred orientation of fine grained antigorite (atg^A) blades along subparallel disjunctive shear bands (Fig. 4-6a). These narrow cleavage domains transpose an otherwise well developed antigorite interpenetrating texture (O'Hanley, 1996, Wicks & Whittaker, 1977). It must be stated that chlorite is a very uncommon mineral in Atg-serpentinite; it appears rarely, associated to magnetite.

Orthopyroxene-olivine serpentinite

This serpentinite was previously described by Padrón-Navarta et al. (2010). It is composed of Opx(Tlc) + Ol + Atg + Tr + Mgt (Table 4-1) and consists of large, inclusions-free porphyroblasts of olivine and orthopyroxene, randomly oriented within a fine-grained antigorite matrix with interpenetrating texture and disjunctive shear bands (Fig. 4-5b). Orthopyroxene (opx^O) occurs as isolated euhedral prismatic crystals (up to 4 cm long) and as very characteristic radial-palmate aggregates (up to 8 cm long) of elongated prisms. Orthopyroxene can be partially or completely replaced by aggregates of platy talc and minor olivine, leading to talc pseudomorphs with nice euhedral shapes (Fig. 4-6c). Strings of small magnetite grains and rare tremolite tend to concentrate in the rim of these pseudomorphs. Chlorite is completely lacking in orthopyroxene-serpentinite.

4.4.2 Transitional lithologies

Chlorite serpentinite

Chl-serpentinite consists of Atg + Chl + Ol + Tr + Mgt (Table 4-1). Three differentiated, but irregularly distributed, domains can be distinguished at thin section scale, based on their mineral assemblages and textural relationships (Figs. 4-5a and 4-6b): (1) Chlorite-lacking domains with fine-grained antigorite blades (atg^A), defining the foliation, and minor olivine and magnetite. This domain is strictly equivalent to Atg-serpentinite. (2) Chlorite-bearing domains characterized by large, unoriented, euhedral antigorite (atg^T) flakes (up to 3 mm long) and by subhedral plates (up to 2 mm long) of chlorite (chl^T) surrounded by antigorite flakes. Fine grained inclusions of antigorite can be found in the largest chlorite cores, rimmed in turn by large antigorite flakes. Fine grained aggregates of antigorite and chlorite can also occur in the core of big antigorite crystals. (3) Coarser grained olivine-rich (ol^T) domains, when compared with olivine from domain (1), with interstitial antigorite grains. Magnetite and interstitial tremolite are also relatively common in domains (2) and (3).

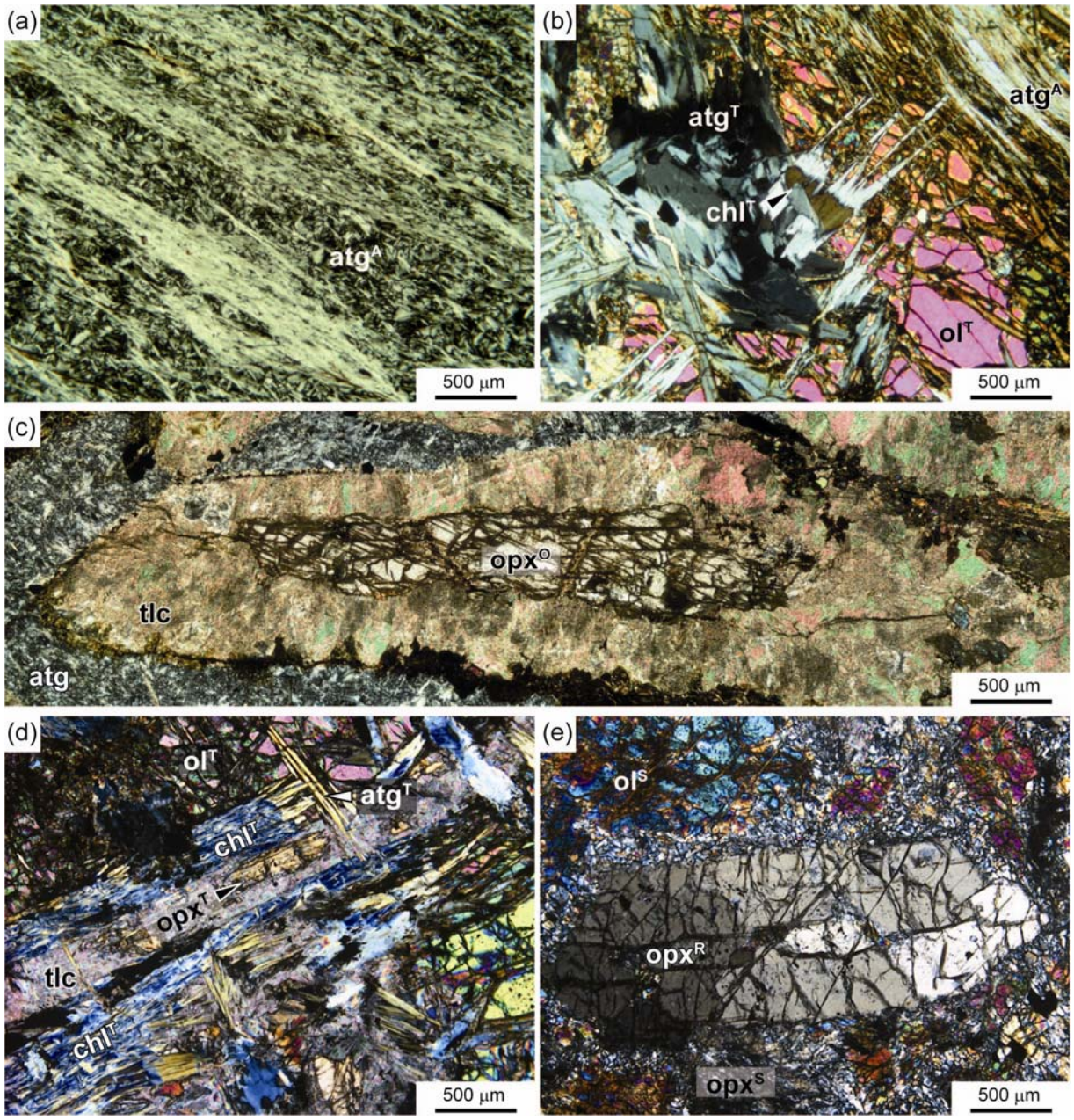

Figure 4-6. Microphotographs with representative textures of the Cerro del Almirez ultramafic rocks (see text for details). **(a)** Pure Atg-serpentinite. **(b)** Chl-serpentinite with two antigorite generations (atg^A and atg^T) and chlorite plates in the core of atg^T. **(c)** Prismatic orthopyroxene porphyroblast, partially replaced by talc, within a fine-grained antigorite matrix. **(d)** Highly recrystallized Atg-Chl-Ol-Opx schist with straight grain boundaries between chlorite and orthopyroxene. **(e)** Relic idioblastic and prismatic orthopyroxene porphyroblast in a spinifex-like Chl-harzburgite. **(f)** Coarse grained Chl-harzburgite granofels. Compare texture with that of d. **(g)** Spinifex-like Chl-harzburgite with elongated brown olivine (ol^S) overgrowing relic clear olivine porphyroblasts (ol^R). High relief colourless minerals are orthophyroxene grains, intercalated with chlorite (opx^S + chl^S). This latter mineral also concentrates as monomineralic aggregates (chl^S) and in the contact between olivine and orthopyroxene. Superscript letters accompanying mineral names refer to the rock type these minerals belong to and the mineral assemblage they equilibrated with: ^{A}: Antigorite-serpentinite; ^{O}: Orthopyroxene-olivine serpentinite; ^{T}: transitional rocks; ^{G}: granofels Chl-harzburgite; ^{S}: spinifex-like Chl-harzburgite; ^{R}: relic porphyroblast.

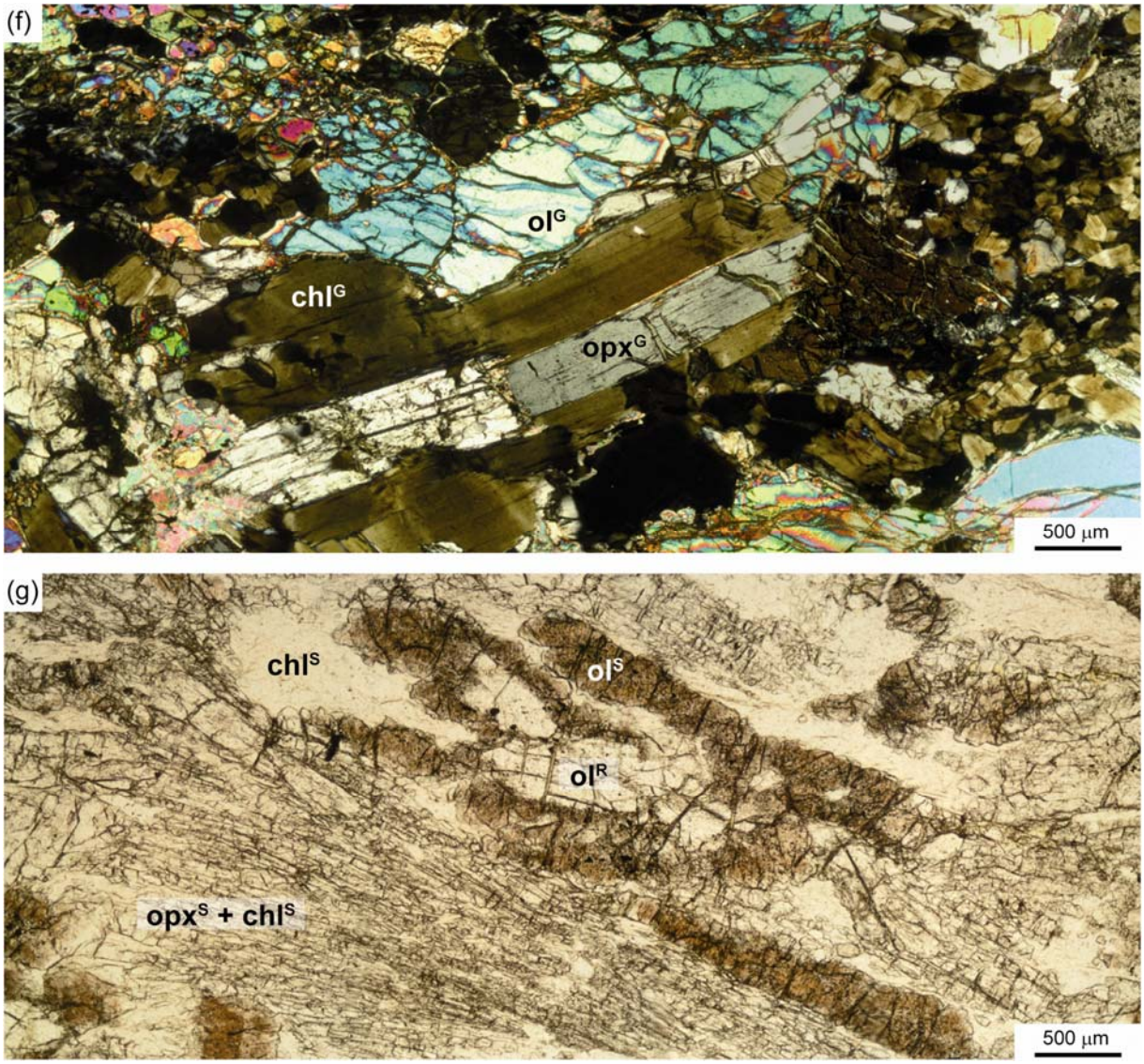

Figure 4-6. Continuation (see opposite page for figure caption description).

At the microscope, this rock may look very similar to Chl-serpentinite but for the occurrence of orthopyroxene, frequently replaced by talc (Table 4-1; Fig. 4-5c), and the higher degree of recrystallisation. Two domains can be distinguished: (1) domains composed of coarse subhedral olivine (ol^{T}; up to 3 mm in size), commonly including large tapered antigorite (atg^{T}) blades (up to 2 mm in length, Fig. 4-6d). Preferred orientation of these olivine-rich domains may give place to a weak foliation. (2) Chlorite and orthopyroxene rich domains (Fig. 4-6d). Orthopyroxene (opx^{T}) occurs as elongated prisms (up to 3 mm in length) partial or totally replaced by talc (tlc). Close to the contact with Chl-serpentinite, chlorite (chl^{T}) – antigorite (atg^{T}) relationships are identical to those reported for the latter rock type. Modal abundance and grain size of orthopyroxene increase away from Chl-serpentinite, concomitant with the gradual disappearance of antigorite. Thus, near the Chl-harzburgite, antigorite is almost completely consumed from the rock matrix and it may only remain as thin rims around chlorite plates or as

blades parallel to cleavage from this latter mineral. Tremolite and granular aggregates of chlorite and magnetite are also to be found. Due to the high degree of recrystallisation of this rock, mineral grain boundaries are straight and, in cases, result in chlorite and olivine grains with three faceted shapes.

4.4.3 Chlorite harzburgite

Orthopyroxene-olivine-chlorite granofels

Irrespective of grain size, Chl-harzburgite granofels is characterized by the complete lack of antigorite in the matrix and by a well developed opx-ol-chl intergranular texture with mostly planar interfaces (Figs. 4-5d, 4-6f). Olivine (ol^G) appears as colourless, inclusions-free granoblasts, whereas orthopyroxene (opx^G) forms elongated, prismatic, single crystals, only locally replaced by secondary talc. Chlorite (chl^G) can be found with two highly contrasting textures: as large (2-5 mm) flakes in between olivine and orthopyroxene (central part of Fig. 4-6f) and as smaller-sized granular decussate aggregates (right hand side of Fig. 4-6f). In both cases chlorite grains are patchy zoned and may, rarely, contain antigorite lamelar inclusions like the ones from atg-chl-ol-opx schist. This, together with the common occurrence of three faceted shapes (in 2D) of olivine and chlorite, suggests that granofelsic harzburgite is directly formed from atg-chl-ol-opx schist, thus, explaining why they always occur together in the field in the immediate contact between the transitional lithology and Chl-harzburgite. Relic orthopyroxene and olivine porphyroblasts from previous serpentintes can be easily identified, by their, already described, especial textural features and by their diferentiating chemical composition (Fig. 4-3g, see below)

Spinifex-like texture

Despite having the same mineral assemblage (Table 4-1), there are strong textural differences between granofelsic and spinifex-like Chl-harzburgites (compare Figs 4-5d and 4-5e and Figs 4-6f and 4-6g). Olivine in spinifex textured rocks may occur in three generations (Trommsdorff et al., 1998) that overgrow each other, although not in every studied sample. First generation olivines (ol^R) reported by these authors correspond to the above described relic porphyroblasts inherited from either Atg-serpentinites or Opx-serpentinites (Fig. 4-6g). They appear as colourless xenomorphic olivines rimmed by the, second generation, typical spinifex-like olivine (ol^S). This is characterised by an outstanding brownish pleochroism, resulting from numerous oriented submicroscopic inclusions of magnetite, chromian magnetite and ilmenite, in some cases concentrated in lamellae parallel to (001) and (100) (Trommsdorff et al., 1998), as well as orthopyroxene and talc (Ruiz Cruz *et al.*, 1999). Small microscopic inclusions of chlorite and chromian magnetite are very common. Titanclinohumite microscopic lamellae have been also reported (López Sánchez-Vizcaíno *et al.*, 2005). Individual crystals of spinifex-like olivine are very elongated along the [001] crystallographic axis, and form curved laths where the shorter section is parallel to the [100] olivine axis (Padrón-Navarta et al., submitted, b see Fig. 8-7 in Chapter 8). These elongated spinifex-like olivines can be found as isolated grains or aggregates within the orthopyroxene and chlorite matrix or growing perpendicular to the original border of relic, colourless, olivine porphyroblasts (Fig. 4-6g). Irrespective of their position, brown olivine borders can be extraordinarily lobulated when in contact with chlorite, but they tend to be straight when in contact with orthopyroxene. Finally, the third generation olivine appears as a colourless rim around

brown olivine produced at the onset of late recrystallisation processes. In strongly recrystallised Chl-harzburgites, previous spinifex-like or porphyroblastic olivines can be partial or totally replaced by a fine-grained, granoblastic aggregate of colourless olivine. For a detailed study of recrystallisation processes and textures see Padrón-Navarta et al., submitted, b (Chapter 8).

Orthopyroxene (opx^S) occurs as coarse-grained aggregates (up to 8 cm in length) of radial acicular crystals (50-100 μm wide and 0.5-2 mm long) with a common orientation (Fig. 4-6g). These aggregates are texturally and compositionally (see below) very different from relic orthopyroxene porphyroblasts. In fact, the latter display euhedral shapes and are almost completely free of inclusions (Figs. 4-5f and 4-6e). In some places, relic orthophyroxene also forms aggregates, exactly resembling those described in the Opx-serpentinites (compare Fig. 4-3b with 4-3g and h).

Chlorite (chl^S) is always relatively fine grained, commonly 200-300 μm in length, and occurs as (1) single crystals or aggregates randomly hosted in olivine and, more commonly, in orthopyroxene (opx^S + chl^S aggregate in Fig. 4-6g) and (2) as monomineralic aggregates concentrated along grain boundaries (Fig. 4-6g). Magnetite is generally associated to chlorite in semigraphic irregular clots. In places, prismatic tremolite grains can also be found.

4.5 Bulk-Rock Composition

4.5.1 Methods

Large blocks of representative samples (usually > 2 kg) were cleaned and cut in parallelepipeds (4-6 cm in length) with a rock diamond saw. Final parallelepipeds (0.5-1 kg) where smashed in a steel jaw crusher and quartered several times in a riffle-splitter. The resulting aliquots were pulverized in an agate ring mill. Whole rock major elements were analyzed using standard X-ray fluorescence procedure (XRF) in the Geoscience Laboratories (GeoLabs), Ontario Geological Survey, Sudbury, Canada. The samples were first run for loss on ignition (LOI) and then fused with borate flux to produce a glass bead. Ferrous iron was determined in the same laboratory by potentiometric analysis using potassium permanganate as oxidation agent. Ferric iron was calculated from the difference of the total iron measured by XRF and the measured ferrous iron.

4.5.2 Bulk-rock composition

Representative bulk-rock compositions and estimated modal contents of the previously described lithologies are shown in Table 2. Basic relationships among mineral and bulk compositions are plotted in the enstatite-forsterite-clinochlore (x3) phase diagram from Figure 4-7. Only Ca-poor compositions have been considered in this work. Distribution of Ca-rich (clinopyroxene and or tremolite-bearing) rocks is very heterogeneous through the whole ultramafic massif. This might be due to inhomogeneous shearing and mixing of former clinopyroxenite layers with very variable thickness (centimetric to metric) in

Table 4-2. Representative bulk compositions and modal estimations of different types of serpentinite and chl-harzburgite and th anhydrous equivalents (in italics).

Type*	A		O		T		G		G		S		R	
Sample	Al06-44		Al06-37		Al06-43		Al06-12		Al08-16		Al06-17		Al06-19	
Major elements determined by XRF (wt%)														
SiO_2	40.34	*45.81*	45.07	*49.26*	41.57	*46.53*	42.97	*45.12*	42.45	*45.13*	42.18	*45.67*	45.44	*47.45*
TiO_2	0.10	*0.11*	0.08	*0.09*	0.10	*0.11*	0.13	*0.14*	0.09	*0.10*	0.08	*0.09*	0.07	*0.07*
Al_2O_3	2.81	*3.19*	2.19	*2.39*	2.61	*2.92*	2.79	*2.93*	2.39	*2.54*	3.51	*3.80*	2.41	*2.52*
FeO	2.87	*3.26*	3.78	*4.13*	3.34	*3.74*	5.10	*5.36*	4.75	*5.05*	4.89	*5.29*	4.63	*4.83*
Fe_2O_3	4.26	*4.84*	3.08	*3.37*	4.25	*4.76*	2.84	*2.98*	3.71	*3.95*	3.44	*3.72*	3.83	*4.00*
MnO	0.09	*0.10*	0.09	*0.10*	0.13	*0.15*	0.10	*0.11*	0.12	*0.13*	0.11	*0.12*	0.12	*0.13*
MgO	37.48	*42.56*	36.98	*40.42*	36.98	*41.39*	41.10	*43.16*	40.49	*43.05*	37.75	*40.87*	39.07	*40.80*
CaO	0.07	*0.08*	0.16	*0.17*	0.29	*0.32*	0.11	*0.12*	0.04	*0.04*	0.32	*0.35*	0.10	*0.10*
Na_2O	0.04	*0.05*	0.05	*0.05*	0.05	*0.06*	0.07	*0.07*	<0.01	-	0.06	*0.06*	0.07	*0.07*
K_2O	<0.005	-	0.01	*0.01*	0.01	*0.01*	0.01	*0.01*	<0.01	-	<0.005	-	0.01	*0.01*
P_2O_5	<0.005	-	<0.005	-	0.01	-	0.01	*0.01*	0.01	*0.01*	0.02	*0.02*	0.01	*0.01*
LOI	11.47	-	7.71	-	10.24	-	4.18	-	5.73	-	6.60	-	4.81	-
Total	99.5	*100.0*	99.2	*100.0*	99.6	*100.0*	99.4	*100.0*	99.8	*100.0*	99.0	*100.0*	100.6	*100.0*
mg-no.	0.93		0.91		0.92		0.89		0.90		0.89		0.89	
FeO/Fe$_2$O$_3$	0.67		1.23		0.79		1.80		1.28		1.42		1.21	
Mode (vol %)														
atg	94		66		53		-		-		-		-	
ol	3		9		13		41		42		38		31	
chl	-		-		20		22		21		22		18	
opx	-		5		-		34		35		37		48	
tlc†	-		(18)		(10)		-		-		-		-	
tr	-		1		2		1		1		2		1	
mgt	3		1		2		2		1		1		2	
Trace elements determinated by XRF (ppm)														
Ba	<20		<20		<20		<20		<20		<20		<20	
Rb	<1		<1		<1		1		<1		<1		<1	
Sr	<2		2		4		6		2		4		4	
Pb	<3		<3		<3		<3		<3		<3		<3	
Nb	<2		<2		<2		2		<2		<2		<2	
Y	2		1		2		1		2		1		1	
Zr	<3		<3		<3		<3		3		<3		<3	
V	69		63		67		82		58		89		70	
Cr	2970		3481		2612		3034		2877		2823		2801	
Ni	1834		2190		1753		1943		2115		1766		1834	
Co	98		107		101		87		107		111		108	
Cu	10		35		6		10		5		169		147	
Zn	42		32		63		49		59		58		66	
Ga	<3		<3		<3		3		<3		3		3	
Sc	12		10		9		15		12		14		10	
Ta	11		11		9		9		<7		8		9	

* A: atg-serpentinite; O: opx-ol serpentinite, T: transitional lithology (Atg-Chl-Opx(Tlc)-Ol schist); G: Chl-harzburgite with granofelsi texture; S: Chl-harzburgite with spinifex-like texture; R: Spinifex-like texrture with relic orthopyroxene and olivine porphyroblast.
** mg-no. MgO/(FeO + MgO) and FeO/Fe_2O_3 in wt%
† retrograde talc replacing orthopyroxen

the former serpentinite body. Variable bulk amounts of Ca, nevertheless, may affect the modal amount of tremolite, but do not alter the main phase relations at the pressure and temperature conditions relevant for this massif (Padrón-Navarta et al. 2010, chapter 7). Bulk compositions of samples Al06-37 (Opx-Ol-serpentinite) and Al06-43 (Atg-Chl-Opx-Ol-schist) (Table 4-2) have been recalculated in order to discard the Si-enrichment produced by intense retrograde replacement of talc for orthopyroxene. Recalculated analysis are not shown in Table 4-2, but note the significant displacement in Figure 4-7 of the plotted recasted analyses towards compositions more consistent with those of other analysed rocks.

Apart from the obvious contrasting water content between serpentinite and Chl-harzburgite, major elements contents in both protolith and products are remarkably

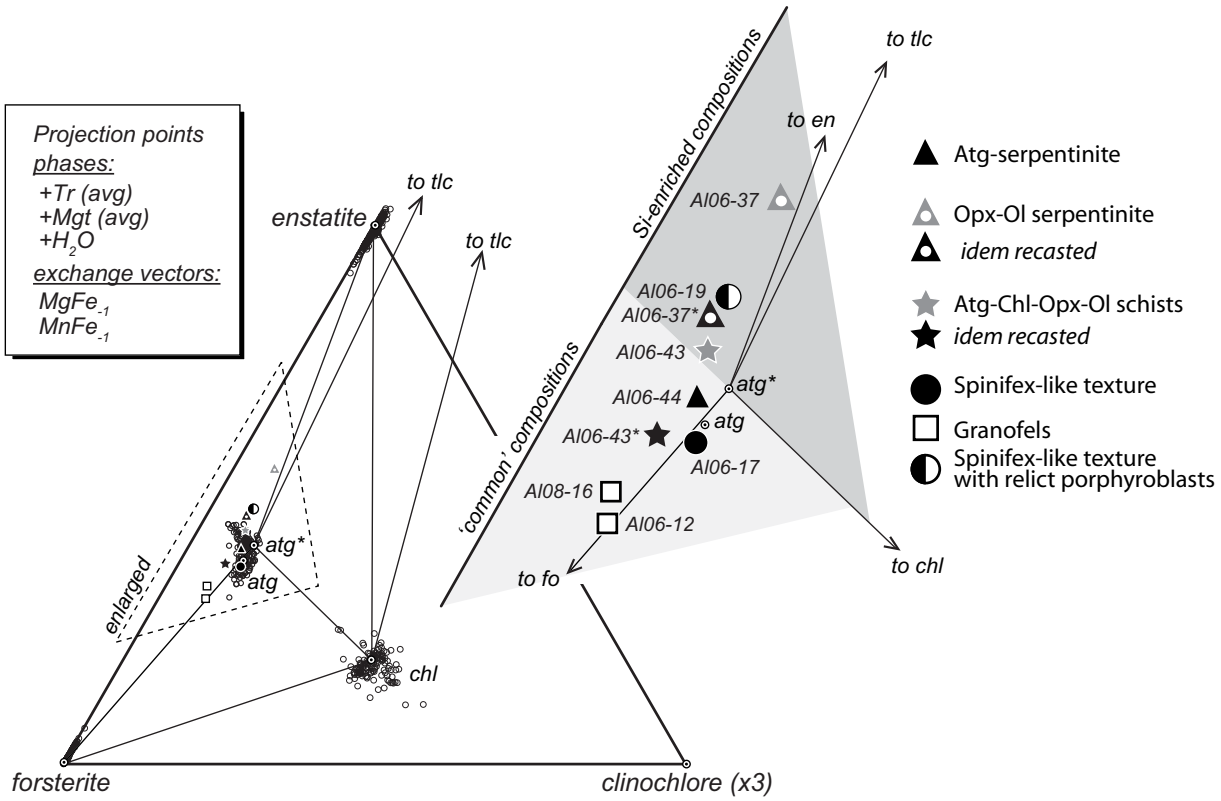

Figure 4-7. Projected composition of samples (same symbols as in Fig. 1) and phases (○) into a condensed triangular phase diagram from the system MnO-CaO-FeO-MgO-Al_2O_3-SiO_2-H_2O-Fe_2O_3 (MnCFMASHO), constructed after projection from a combination of phases (average composition, avg) and exchange vectors (see adjacent box for details). Right: enlarged area showing the location of samples in two groups: (1) 'common' compositions and (2) silica-enriched compositions. Measured compositions of samples Al06-43 and Al06-37 (grey symbols) have been recasted taking into account the Si-enrichment due to the replacement of orthopyroxene by retrograde talc (black symbols, see table 2). Tie-lines only join average phase compositions and arrowed tie-lines point to talc (plotting in negative coordinates after projection). Average composition of antigorite (atg) is biased by the unknown oxidation state of iron in antigorite from Cerro del Almirez. For reference, the same average antigorite composition is also tentatively plotted (atg*), by assuming the same redox state determined for the Elba antigorite (83-88 % of total iron as Fe^{2+}, Mellini et al. 2002). Mapping and diagram generated using program CSpace, Torres-Roldán et al. (2000).

similar. Good comparison is even more evident when the normalized anhydrous compositions are considered (second column in italics for each bulk analysis in Table 4-2). Nevertheless, two exceptions arise: an Opx-Ol serpentinite (sample Al06-37) and a Chl-harzburgite with relic orthopyroxene and olivine porphyroblasts (sample Al06-19). Both lithologies are significantly rich in silica (Table 4-2) and plot within the Si-enriched compositions field of Figure 4-7. Si-enriched compositions are defined here as those plotting in the field with Si/Mg ratios above the chl-atg projection on the fo-en line (dark grey field in Fig. 4-7). However, two average antigorite compositions can be considered: (1) antigorite with total ferrous iron (atg in Fig. 4-7) and (2) antigorite in which the oxidation state of iron is considered (atg* in Fig. 4-7). Owing to the lack of own oxidation state determinations, we tentatively assumed results by Mellini et al. (2002) for the Elba antigorite: ~ 86 wt% of total iron as Fe^{2+}. The second antigorite average composition (atg*) matches better the composition of sample Al06-44, an almost pure Atg-serpentinite with magnetite and minor amounts of olivine (but not talc). Note that if a line was traced from chl to the fo-en line through atg and not atg* the Al06-44 composition would plot in the field of the Si-enriched compositions. That is the reason for considering atg* as a more appropriate reference for defining the limit of Si-enriched compositions in Figure 4-7. It is important to note that Atg-serpentinite (Al06-44), transitional lithologies (Al06-43*) and spinifex-like Chl-harzburgite with no orthopyroxene relics (Al06-17) plot gathered in the 'common' composition domain (light grey filed in Fig. 4-7). However, it is also clear that Chl-harzburgite granofels samples Al08-16 and Al06-12 are richer in the forsterite component compared with the analyzed spinifex-like textured Chl-harzburgite (Al06-17) (Fig. 4-7). These differences might be explained rather by former, casual bulk compositional heterogeneities of the protholith than by sistematic bulk compositions differences between these two textural types. In fact all transitions have been observed in the field from pure Atg-serpentinite to metadunite. This should be, eventually, also reflected in compositional heterogeneities of their equivalent prograde Chl-harzburgite. A final outstanding difference between Atg-serpentinite and prograde lithologies is the significant change in their oxidation state. FeO/Fe_2O_3 ranges from 0.67-0.79 in Atg-serpentinite to 1.23 in Opx-Ol-serpentinite and 1.21-1.80 in Chl-harzburite (Table 4-2). First consequence of these differences is the higher magnesium number of Atg-serpentinites (0.91-0.93) when compared with those of prograde rocks: 0.89-0.90 (Table 4-2).

4.6 Mineral Chemistry

Average compositions from the most important minerals present in the studied rocks are summarized in Tables 4-3 to 4-6.

4.6.1 Methods

Mineral analyses were performed using a Cameca SX100 electron microprobe at the CIC (University of Granada) with operating conditions of 15kV acceleration voltage, 15 nA beam current, and 5 μm beam diameter. Natural and synthetic minerals and glasses were used as standards. A special routine was set up to increase precision and accuracy in electron microprobe analyses for Ti in olivine and Al in orthopyroxene by using LPET and LTAP crystals and a peak counting time of 60 s, thus yielding detection limits at

around 140-150 ppm and 60-70 ppm, respectively, and errors of 150 ppm (3σ). Detection limits in olivine and orthopyroxene for Cr, Ni and Mn were 400-600 ppm and errors of 350-650 ppm (3σ).

4.6.2 Antigorite

In the Cerro del Almirez ultramafic massif, antigorite occurs in four different rock types (Table 4-1): Atg-serpentinite (atg^A), Opx-Ol-serpentinite (atg^O), and transitional rocks, divided in turn in Chl-serpentinite (atg^A and atg^T) and Atg-Chl-Opx-Ol schist (atg^T). Antigorite composition in all these rocks is Al- and Cr- rich (Table 4-3; Trommsdorff et al. 1998, Padrón-Navarta et al., 2008, 2010), but, in both cases, the highest contents correspond to atg^A and atg^O (up to 4.2 wt % Al_2O_3 and 1.3 wt % Cr_2O_3) when compared with atg^T from transitional rocks (Table 4-3).

Table 4-3. Antigorite compositions (average and 1σ) from representative serpentinite and transitional samples.

	A	A	O	T	T	T
Sample	Al95-20	Al06-45	Al06-37	Al06-45	Al06-43	Al08-14
Type	Atg^A	Atg^A	Atg^O	Atg^T	Atg^T	Atg^T
	(*n* = 31)	(*n* = 7)	(*n* = 25)	(*n* = 8)	(*n* = 51)	(*n* = 16)
SiO_2	41.41 (0.38)	41.60 (0.22)	41.54 (0.59)	41.78 (0.80)	42.56 (0.70)	42.86 (0.47)
TiO_2	0.02 (0.01)	0.02 (0.01)	0.01 (0.01)	0.01 (0.01)	0.01 (0.01)	0.01 (0.01)
Al_2O_3	3.45 (0.35)	3.03 (0.13)	3.44 (0.53)	2.91 (0.10)	2.74 (0.58)	2.33 (0.36)
Cr_2O_3	0.34 (0.14)	0.44 (0.03)	0.55 (0.11)	0.18 (0.11)	0.18 (0.21)	0.21 (0.15)
FeO	3.32 (0.25)	3.98 (0.05)	3.99 (0.17)	4.20 (0.10)	4.39 (0.28)	4.55 (0.32)
NiO	0.11 (0.03)	0.14 (0.03)	0.10 (0.03)	0.14 (0.03)	0.16 (0.03)	0.15 (0.03)
MgO	37.69 (0.41)	36.72 (0.30)	37.20 (0.75)	36.61 (0.63)	37.36 (0.48)	36.54 (0.29)
MnO	0.06 (0.02)	0.08 (0.06)	0.05 (0.01)	0.07 (0.02)	0.05 (0.01)	0.05 (0.02)
CaO	0.01 (0.01)	0.00 (0.01)	0.01 (0.01)	0.00 (0.01)	0.00 (0.01)	0.01 (0.01)
Na_2O	0.01 (0.01)	0.00 (0.00)	0.01 (0.01)	0.00 (0.00)	0.01 (0.01)	0.01 (0.00)
Cl	0.04 (0.01)	0.13 (0.01)	0.16 (0.06)	0.11 (0.02)	0.16 (0.05)	0.14 (0.03)
F	0.07 (0.04)	0.03 (0.02)	0.00 (0.01)	0.04 (0.02)	0.02 (0.04)	0.02 (0.02)
H_2O calc	11.90 (0.07)	11.81 (0.08)	11.92 (0.16)	11.80 (0.20)	12.00 (0.12)	11.90 (0.04)
Total	98.4 (0.6)	98.0 (0.6)	99.0 (1.3)	97.9 (1.5)	99.6 (0.9)	98.8 (0.4)
O	6.824	6.824	6.824	6.824	6.824	6.824
OH	3.647	3.647	3.647	3.647	3.647	3.647
Si	1.903 (0.013)	1.926 (0.005)	1.905 (0.025)	1.937 (0.007)	1.939 (0.022)	1.969 (0.018)
Ti	0.001 (0.000)	0.001 (0.000)	0.000 (0.000)	0.000 (0.000)	0.000 (0.000)	0.000 (0.000)
Al	0.187 (0.019)	0.165 (0.007)	0.186 (0.028)	0.159 (0.005)	0.147 (0.031)	0.126 (0.019)
Cr	0.012 (0.005)	0.016 (0.001)	0.020 (0.004)	0.006 (0.004)	0.006 (0.008)	0.008 (0.005)
Fe	0.128 (0.010)	0.154 (0.002)	0.153 (0.007)	0.163 (0.005)	0.168 (0.012)	0.175 (0.012)
Ni	0.004 (0.001)	0.005 (0.001)	0.004 (0.001)	0.005 (0.001)	0.006 (0.001)	0.005 (0.001)
Mg	2.583 (0.024)	2.535 (0.005)	2.544 (0.025)	2.530 (0.004)	2.538 (0.019)	2.503 (0.012)
Mn	0.002 (0.001)	0.003 (0.002)	0.002 (0.000)	0.003 (0.001)	0.002 (0.001)	0.002 (0.001)
Ca	0.000 (0.000)	0.000 (0.000)	0.001 (0.000)	0.000 (0.000)	0.000 (0.000)	0.000 (0.000)
Na	0.001 (0.001)	0.000 (0.000)	0.000 (0.001)	0.000 (0.000)	0.000 (0.001)	0.001 (0.000)
Sum cation	4.821	4.806	4.815	4.804	4.807	4.788
$*X_{Mg}$	0.953 (0.004)	0.943 (0.001)	0.943 (0.003)	0.940 (0.002)	0.938 (0.004)	0.935 (0.004)

* A: atg-serpentinite; O: opx-ol serpentinite, T: transitional lithology (Atg-Chl-Opx(Tlc)-Ol schist).
$*X_{Mg}$=Mg/(Fe+Mg)

Slight differences, in terms of Al and Si contents, between antigorite from Atg-serpentinite (atg^A) and that from Opx-Ol-serpentinite (atg^O) are controlled by the occurrence or not of clinopyroxene and tremolite in the former rock type. Al-contents in atg^O (dotted triangle; Fig. 4-8a) and atg^A coexisting with clinopyroxene and tremolite (white triangle), have a common range from 0.15 to 0.22 Al atoms per formula unit (apfu) / 6.834 O (Fig. 4-8a), but atg^O can be Si-richer (up to 1.93 apfu / 6.834 O). Composition of atg^A in almost pure (cpx- and tr- lacking) Atg-serpentinite (black triangles) expands, nevertheless, towards lower Al and higher Si contents (0.145 Al and 1.94 Si apfu / 6.834 O, respectively; Fig. 4-8a). As a general trend, Si and Al are negatively correlated, but they depart slightly from pure tschermaks exchange (Fig. 4-8a).

Antigorite from transitional rocks displays a wide compositional range (Fig. 4-8b), especially in the case of Chl-serpentinite. In this rock, antigorite occurs in two texturally and compositionally different domains (Fig. 4-6b). Fine-grained antigorite is Al-rich and matches the composition of atg^A from Atg-serpentinite (white stars in Fig. 4-8b with Al > 0.15 apfu / 6.834 O, superposed on the dark grey field (I) corresponding to black triangles from Fig. 8a). Big euhedral atg^T blades (Al06-45, Table 4-3) mantling chlorite flakes and large antigorite blades included in coarse olivine have distinctive lower Al (0.09-0.15 apfu / 6.834 O) and higher Si contents (up to 1.98 apfu / 6.834 O; white stars outside field I in Fig. 4-8b; Table 4-3). Atg^T from Atg-Chl-Opx-Ol schist (black stars), where the fine grained domain is lacking, is also Al-poor (<0.15-0.09 apfu / 6.834 O) and even Si-richer (up to 1.99 apfu / 6.834 O). In Figure 4-8b, the tschermaks parallel general trend is more evident, although offset towards higher Si contents. This offset might, however, be the effect of normalizing all the antigorite structural formulae to the highest polysome number *m* (the number of tetahedra along a wave, Mellini et al. 1987) found in the Cerro del Almirez Atg-serpentinites, that is polysome *m* = 17 (Padrón-

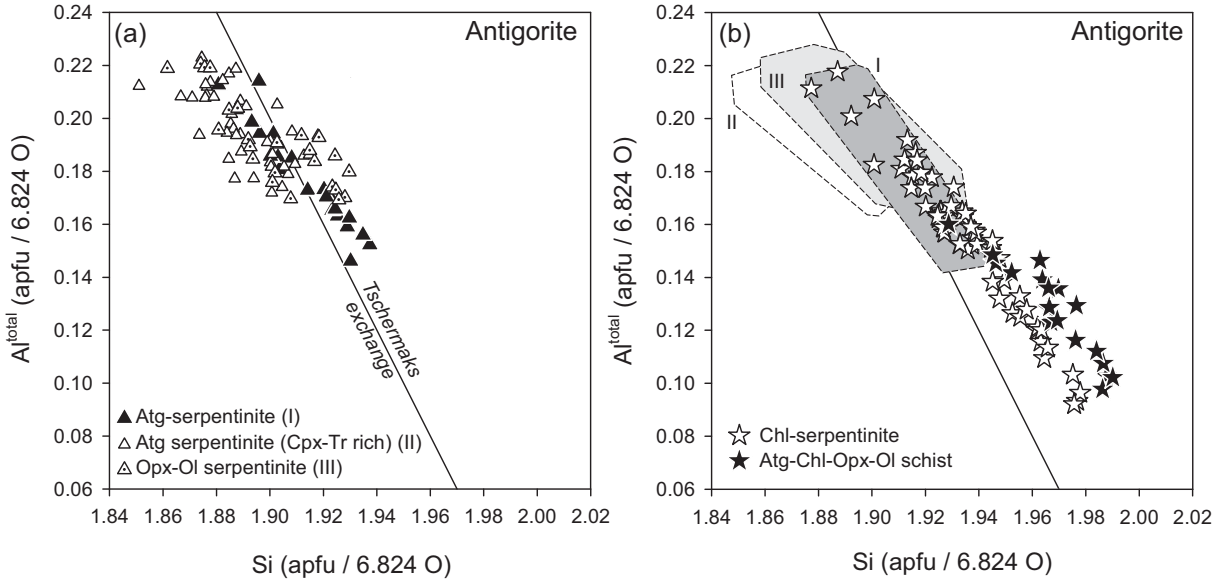

Figure 4-8. Antigorite composition in terms of Al^{total} versus Si, calculated on the basis of the ideal antigorite formula (m = 17) and normalized to 4.824 total cations. The line represents the ideal Tschermak exchange. **(a)** Antigorite in serpentinites. **(b)** Antigorite in transitional lithologies at the devolatilization front. Labelled fields in (b) are taken from (a).

Navarta et al. 2010). In fact, these authors reported a reduction of *m* in antigorite, ranging from 17 in Atg-serpentinites down to 14 in antigorite the transitional lithologies (sample Al06-43, *m* = 14-16, Padrón-Navarta et al. 2010, see Chapter 5). The effect of normalizing the antigorite structural formulae in Fig. 4-8 to lower *m* values is a displacement of Si towards lower values.

4.6.3 Olivine

Olivine occurs in all the studied rocks. Different textural and compositional types can be distinguished (Tables 4-1 and 4-4). Some of their main compositional trends were already shown by Trommsdorff et al. (1998; their Fig. 4-8) and López Sánchez-Vizcaíno et al. (2005).

Magnesium number [X_{Mg} = Mg/(Fe + Mg)] in olivine from Atg-serpentinite (ol^A) ranges from 0.885±0.001, in clinopyroxene and tremolite lacking samples (black triangles), to 0.913±0.005 in samples containing these minerals (white triangles; Fig. 4-9a; compare also fields I and II). In both cases, ol^A is relatively rich in Mn (0.006-0.009 apfu / 4 O) and poor in Ni (0.004-0.007 apfu / 4 O) (Fig. 4-9b and Table 4-4). Olivine

Table 4-4. Olivine mineral compositions (average and 1σ) from representative serpentinite and Chl-harzburgite samples.

	A	O	T	G	S	R	R
Sample	Al06-45	Al06-37	Al08-07	Al08-16	Al06-42	Al08-13	Al08-21
Type	Ol^A	Ol^O	Ol^T	Ol^G	Ol^S	Ol^R	Ol^R
	(*n* = 8)	(*n* = 42)	(*n* = 7)	(*n* = 10)	(*n* = 43)	(*n* = 10)	(*n* = 4)
SiO_2	40.67 (0.06)	40.47 (0.42)	41.17 (0.13)	41.24 (0.24)	40.41 (0.34)	40.67 (0.07)	40.94 (0.14)
TiO_2	0.01 (0.01)	0.01 (0.01)	0.00 (0.00)	0.01 (0.03)	0.05 (0.04)	0.00 (0.00)	0.00 (0.01)
Al_2O_3	0.00 (0.00)	0.01 (0.01)	0.00 (0.00)	0.00 (0.00)	0.00 (0.00)	0.00 (0.00)	0.00 (0.00)
Cr_2O_3	0.01 (0.01)	0.00 (0.01)	0.01 (0.01)	0.01 (0.02)	0.17 (0.21)	0.00 (0.01)	0.01 (0.01)
FeO	11.03 (0.11)	10.96 (0.50)	10.49 (0.33)	9.37 (0.14)	9.81 (0.18)	10.64 (0.25)	10.07 (0.34)
NiO	0.28 (0.03)	0.26 (0.03)	0.35 (0.07)	0.44 (0.04)	0.21 (0.03)	0.28 (0.04)	0.29 (0.03)
MgO	47.80 (0.08)	48.35 (0.44)	47.83 (0.50)	48.44 (0.30)	49.15 (0.36)	48.08 (0.18)	46.94 (0.24)
MnO	0.33 (0.04)	0.16 (0.02)	0.19 (0.04)	0.12 (0.03)	0.11 (0.02)	0.20 (0.04)	0.34 (0.04)
CaO	0.01 (0.01)	0.01 (0.01)	0.01 (0.01)	0.01 (0.00)	0.01 (0.01)	0.00 (0.00)	0.01 (0.00)
Total	100.1 (0.1)	100.2 (0.7)	100.1 (0.3)	99.6 (0.2)	99.9 (0.5)	99.9 (0.2)	98.6 (0.2)
O	4	4	4	4	4	4	4
Si	1.002 (0.001)	0.996 (0.004)	1.011 (0.002)	1.012 (0.006)	0.993 (0.004)	1.002 (0.001)	1.018 (0.001
Ti	0.000 (0.000)	0.000 (0.000)	0.000 (0.000)	0.000 (0.001)	0.001 (0.001)	0.000 (0.000)	0.000 (0.000
Al	0.000 (0.000)	0.000 (0.000)	0.000 (0.000)	0.000 (0.000)	0.000 (0.000)	0.000 (0.000)	0.000 (0.000
Cr	0.000 (0.000)	0.000 (0.000)	0.000 (0.000)	0.000 (0.000)	0.003 (0.004)	0.000 (0.000)	0.000 (0.000
Fe	0.227 (0.002)	0.226 (0.010)	0.215 (0.008)	0.192 (0.003)	0.201 (0.004)	0.219 (0.005)	0.209 (0.007
Ni	0.006 (0.001)	0.005 (0.001)	0.007 (0.001)	0.009 (0.001)	0.004 (0.001)	0.006 (0.001)	0.006 (0.001
Mg	1.756 (0.003)	1.774 (0.015)	1.751 (0.011)	1.772 (0.010)	1.800 (0.008)	1.766 (0.005)	1.741 (0.007
Mn	0.007 (0.001)	0.003 (0.000)	0.004 (0.001)	0.002 (0.001)	0.002 (0.000)	0.004 (0.001)	0.007 (0.001
Ca	0.000 (0.000)	0.000 (0.000)	0.000 (0.000)	0.000 (0.000)	0.000 (0.000)	0.000 (0.000)	0.000 (0.000
Sum cation	2.998	3.004	2.989	2.988	3.005	2.998	2.982
*X_{Mg}	0.885 (0.001)	0.887 (0.005)	0.890 (0.004)	0.902 (0.001)	0.899 (0.002)	0.890 (0.003)	0.893 (0.004

* A: atg-serpentinite; O: opx-ol serpentinite, T: transitional lithology (Atg-Chl-Opx(Tlc)-Ol schist); G: Chl-harzburgite w granofelsic texture; S: Chl-harzburgite with spinifex-like texture; R: Spinifex-like texrture with relic orthopyroxene and olivi porphyroblast.
*X_{Mg}=Mg/(Fe+Mg)

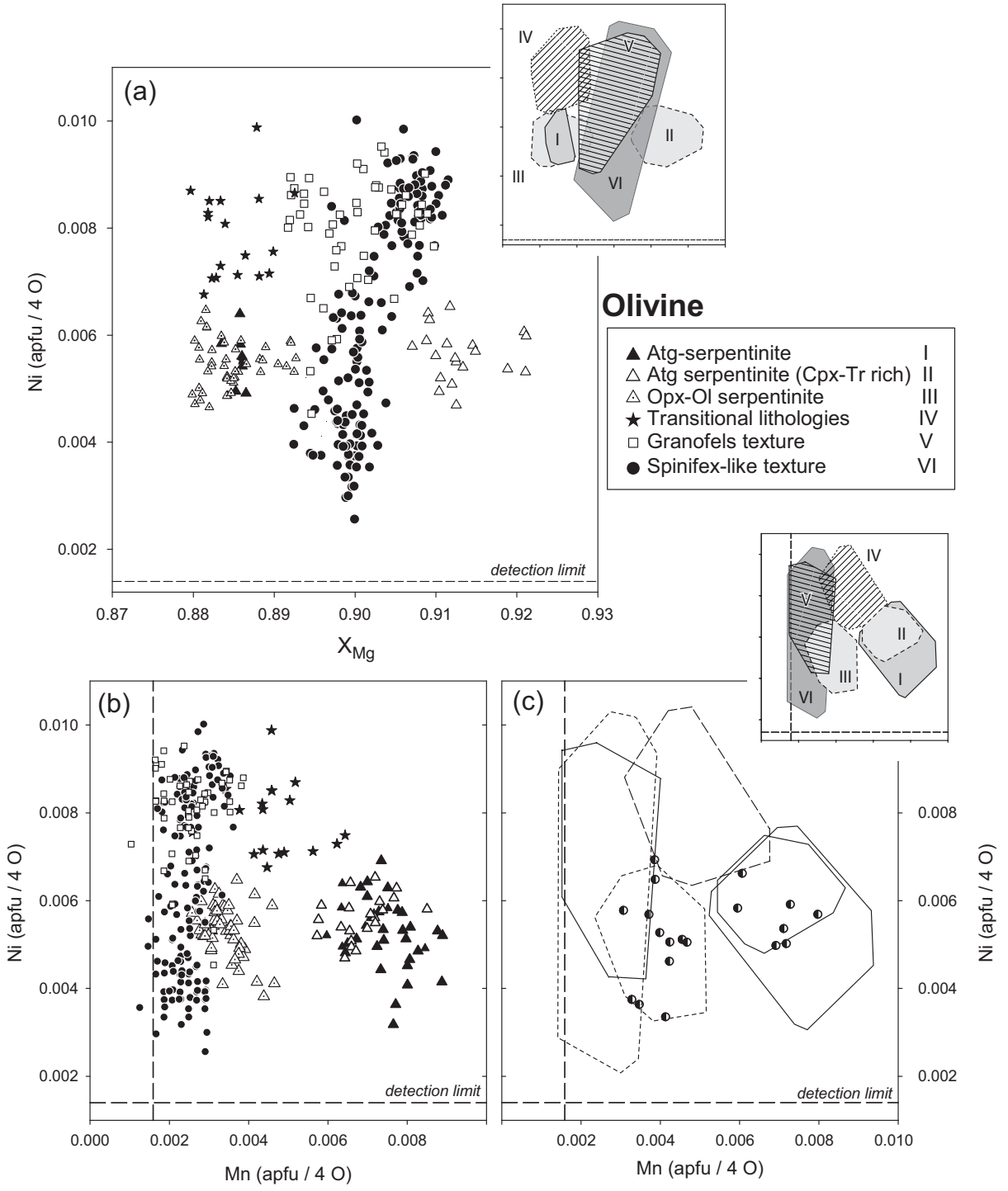

Figure 4-9. Compositional features of olivine in different rock types. **(a)** X_{Mg} versus Ni atoms per formula unit, normalized to 4 oxygen (apfu / 4 O). Labelled fields in the above inset were outlined from the compositional range of each rock type. **(b)** Ni versus Mn for olivine in the same rock types as in (a). **(c)** Ni versus Mn for olivine porphyroblasts of two different origins preserved in Chl-harzburgite. Outlined fields from (b) are shown for comparison. Mn and Ni detection limits indicated by dashed lines.

porphyroblasts from Opx-Ol serpentinite (ol^O) have X_{Mg} (0.886±0.005) and Ni (0.004-0.006 apfu / 4 O) contents similar to those of ol^A, but much lower Mn (0.001-0.005 apfu / 4 O) (dotted triangles in Fig. 4-9a, b).

Olivines from Chl-harzburgite are Fo-rich (X_{Mg} = 0.902±0.005). They are also characterized by very low Mn contents (0.002±0.001 apfu / 4 O) and a highly scattered Ni-content range (0.003-0.010 apfu / 4 O). Olivine from granofelsic (ol^G, white squares) and spinifex-like (ol^S, black dots) textures can not be discriminated in terms of X_{Mg} or Mn contents. However, Ni contents in ol^S scatter in a very wide compositional range, including very low values, whereas most ol^G analyses plot above 0.007 Ni apfu / 4 O (Fig. 4-9a, b). Anomalous high Ti- and Cr-contents in ol^S (Table 4-4) can be explained by the abundant microscopic to submicroscopic inclusions of ilmenite and chromite in brown spinifex-like olivine (Ruiz Cruz et al. 1999), some of them derived from the breakdown of Ti-Chu intergrowths (López Sánchez-Vizcaíno et al., 2005). Olivine from transitional lithologies (ol^T) has low Fo-contents (X_{Mg} = 0.886±0.005), similar to those of ol^A (Fig. 4-9a) However, in the Mn vs Ni diagram (Fig. 4-9b) ol^T plots scattered in an intermediate field (black stars) between those of ol^A (black and white triangles) and those of ol^G (with squares) and ol^S (black dots).

Relic olivine (ol^R), irrespective of the rock type it belongs to, has relatively low X_{Mg} (0.888±0.005) and Ni-contents (0.004-0.007, Fig. 4-9c). However, two different ol^R populations can be distinguished in terms of Mn content (Fig. 4-9c, Table 4-4). Population (1) has Mn > 0.005 apfu / 4 O and corresponds to samples where olivine is the only relic porphyroblast (e.g. Al06-13, Table 4-4). Population (2), with Mn < 0.005 apfu / 4 O, is found in samples with both relic olivine and orthopyroxene porphyroblasts (e.g. Al06-21). The former group exactly overlaps the compositional field of olivine porphyroblasts (ol^A, Fig. 4-9c light grey field; cf. Fig. 4-3a) found in Atg-serpentinite, whereas the latter matches the field corresponding to olivine from Opx-Ol serpentinite (ol^O, Fig. 4-9c, dark grey field, cf. Fig. 4-3b).

4.6.4 Orthopyroxene

Orthopyroxene composition in equilibrium with antigorite (opx^O) in Opx-Ol-serpentinite (white dotted triangles) is very contrasting compared with orthopyroxene from the two Chl-harzburgite textural types: granofels (opx^G, white squares) and spinifex-like (opx^S; black dots) (Table 4-5, Fig. 4-10a and b). Opx^O has comparatively low X_{Mg} (0.88-0.89) and is remarkably rich in Mn (0.008-0.015 apfu / 6 O) (Fig. 4-10a). The opposite is true for opx^G and opx^S (Fig. 4-10a), which are again indiscernible in terms of X_{Mg}, Mn or Al. Opx^T from Atg-Chl-Opx-Ol schist plots in between these two groups (black stars and dotted outlined field in Fig. 4-10a). As in the case of olivine, relic orthopyroxene composition (opx^R) nicely overlaps that of opx^O, i.e. low X_{Mg}, high Mn-content (Fig. 4-10a) and Al below detection limit (Fig. 4-10b).

Aluminium content can be used to easily discriminate orthopyroxene compositions in equilibrium with antigorite (Fig. 4-10b). Both opx^O and opx^R have Al-content below detection limit whereas orthopyroxene from other lithologies scatters in a wide field (from nearly zero to 0.011 apfu / 6 O, Fig. 4-10b). The occurrence of Al-free

Table 4-5. Orthopyroxene mineral composition (average and 1σ) from representative serpentinite and chl-harzburgite samples.

	O	S	T	G	R
Sample	Al06-37c	Al06-42	Al08-07	Al08-16	Al08-22
Type	Opx^O (n = 22)	Opx^S (n = 18)	Opx^T (n = 8)	Opx^G (n = 12)	Opx^R (n = 50)
SiO_2	57.83 (0.64)	57.80 (0.32)	58.58 (0.17)	58.67 (0.16)	58.33 (0.20)
TiO_2	0.02 (0.01)	0.02 (0.01)	0.03 (0.01)	0.02 (0.01)	0.01 (0.01)
Al_2O_3	0.04 (0.07)	0.11 (0.06)	0.10 (0.04)	0.11 (0.08)	0.04 (0.12)
Cr_2O_3	0.01 (0.01)	0.08 (0.04)	0.07 (0.03)	0.09 (0.05)	0.03 (0.04)
FeO	7.95 (0.23)	6.70 (0.10)	7.08 (0.13)	6.42 (0.17)	7.68 (0.22)
NiO	0.04 (0.01)	0.04 (0.02)	0.05 (0.02)	0.07 (0.03)	0.03 (0.02)
MgO	34.79 (0.39)	35.02 (0.13)	34.25 (0.25)	34.37 (0.20)	33.65 (0.24)
MnO	0.38 (0.03)	0.14 (0.02)	0.18 (0.04)	0.18 (0.02)	0.40 (0.09)
CaO	0.12 (0.02)	0.07 (0.01)	0.13 (0.08)	0.07 (0.02)	0.08 (0.01)
Total	101.2 (0.8)	100.0 (0.3)	100.4 (0.3)	100.0 (0.2)	100.3 (0.3)
O	6	6	6	6	6
Si	1.985 (0.011)	1.994 (0.005)	2.011 (0.003)	2.016 (0.002)	2.013 (0.005)
Ti	0.000 (0.000)	0.001 (0.000)	0.001 (0.000)	0.000 (0.000)	0.000 (0.000)
Al	0.002 (0.003)	0.004 (0.002)	0.004 (0.002)	0.005 (0.003)	0.001 (0.005)
Cr	0.000 (0.000)	0.002 (0.001)	0.002 (0.001)	0.003 (0.001)	0.001 (0.001)
Fe	0.228 (0.006)	0.193 (0.003)	0.203 (0.004)	0.185 (0.005)	0.222 (0.006)
Ni	0.001 (0.000)	0.001 (0.001)	0.001 (0.001)	0.002 (0.001)	0.001 (0.001)
Mg	1.781 (0.021)	1.801 (0.008)	1.753 (0.009)	1.761 (0.008)	1.731 (0.011)
Mn	0.011 (0.001)	0.004 (0.001)	0.005 (0.001)	0.005 (0.001)	0.012 (0.003)
Ca	0.004 (0.001)	0.002 (0.000)	0.005 (0.003)	0.003 (0.001)	0.003 (0.000)
Sum cation	4.013	4.002	3.985	3.979	3.985
$*X_{Mg}$	0.886 (0.003)	0.903 (0.002)	0.896 (0.002)	0.905 (0.003)	0.886 (0.003)

* O: opx-ol serpentinite, T: transitional lithology (Atg-Chl-Opx(Tlc)-Ol schist); G: Chl-harzburgite with granofelsic texture; S: Chl-harzburgite with spinifex-like texture; R: Spinifex-like texrture with relic orthopyroxene and olivine porphyroblast.
$*X_{Mg}$=Mg/(Fe+Mg)

orthopyroxene in Opx-Ol-serpentinite is explained by preferential partitioning of Al into antigorite when antigorite reacts with talc to produce orthopyroxene (see Fig. 7-2 in Chapter 7, Padrón-Navarta et al., 2010, for the loci of this reaction). At higher temperature, when antigorite breaks down to olivine + orthopyroxene + chlorite, Al-content in orthopyroxene turns to be buffered by chlorite. Baker and Holland (1996) experimentally showed slight systematic variations of Al-content in chlorite in the MASH divariant opx + ol assemblage that they interpreted as due to Tschermaks exchange between chlorite and orthopyroxene. It remains unclear, however, if Al is incorporated into orthopyroxene in form of Tschermaks exchange as most of the tetrahedral site is fulfil by Si (Table 4-5). However, the scattered distribution of Al in opx^G and opx^S (Fig. 4-10b), may suggest that exchange equilibrium between orthopyroxene and chlorite was never attained. In fact, Baker and Holland (1996)

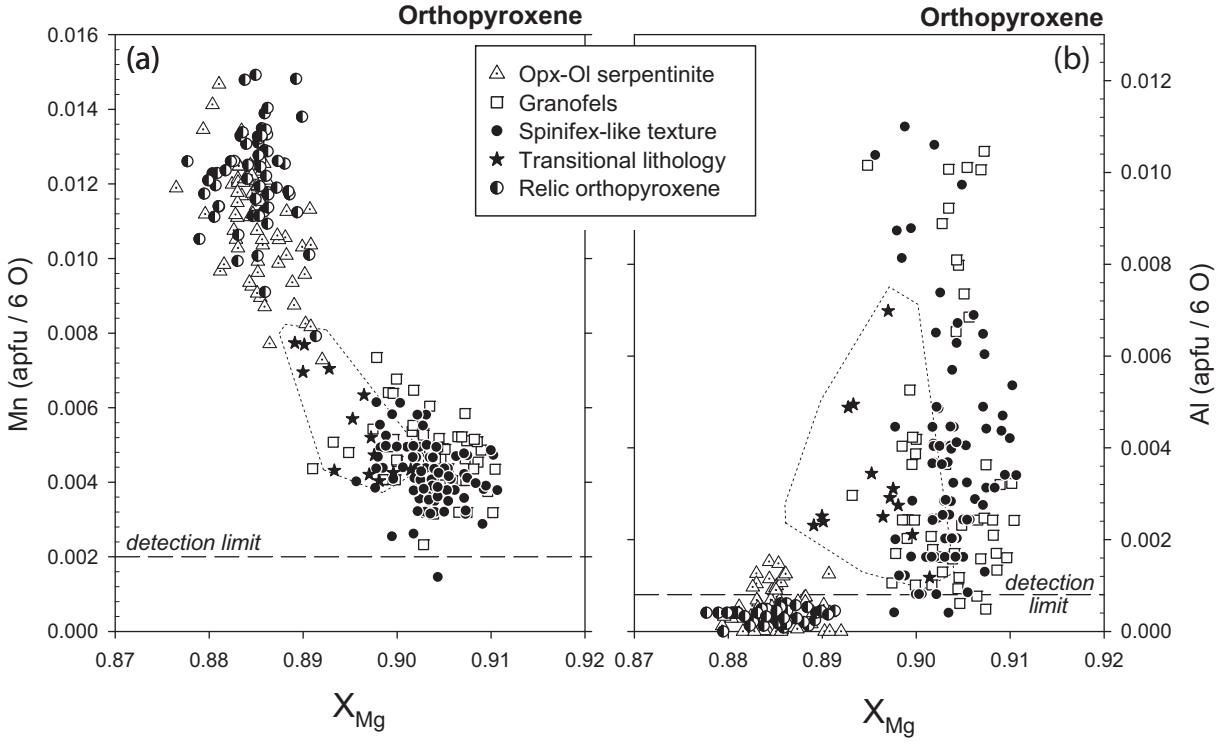

Figure 4-10. (a) Mn versus X_{Mg} and **(b)** Al versus X_{Mg} for different orthopyroxene generations in the referred rock types and relic porphyroblasts. The compositional field of orthopyroxene in transitional Atg-Chl-Opx-Ol schist is outlined by a short-dashed line. Mn and Al detection limits indicated by long-dashed lines.

recognized the possibility that orthopyroxene did not reequilibrate even at the relatively high temperature conditions used in their experiments (760-840ºC).

4.6.5 Chlorite

Chlorite has high magnesium contents (X_{Mg} = 0.941±0.006), Cr_2O_3 up to 2.7 wt % and Al_2O_3 ranging from 10 to 15 wt% (Table 4-6). Attending to the Al^{total} content (equivalent to the content of the clinochlore endmember) two populations can be discriminated (Fig. 11). Group (1) has low Al (< 3.05 apfu / 28 O) and good negative correlation with Cr ($CrAl_{-1}$); it corresponds to transitional lithologies (black and white stars) and some analyses from Chl-harzburgite granofels (white squares). Group (2) is characterized by higher Al^{total} (> 3.05 apfu / 28 O) contents, but with highly scattered distribution and poor Al-Cr correlation; it corresponds to chl^S from spinifex-like Chl-harzburgite (black dots) and chl^G from some granofels. The reported Cr/Al partitioning in chlorite from transitional lithologies might suggest that chlorite composition in these rocks was buffered by coexisting antigorite, thus pointing to equilibrium conditions. It is worth to note that chlorite from some granofels follows a similar Cr/Al pattern (Fig. 4-11), probably inherited from the Atg-Chl-Opx-Ol schist they derive from, after complete Atg disappearance and a high recrystallization degree. On the contrary, complete lack of

Cr/Al correlation in spinifex-like chlorite must be attributed to local control of Cr availability by the heterogeneous distribution of chromite and chromian magnetite.

Table 4-6. Chlorite mineral compositions (average and 1σ) from representative serpentinite and Chl-harzburgite samples.

	T	T	G	S
Sample	Al06-45	Al06-43	Al06-16	Al06-05
Type	Chl^T	Chl^T	Chl^G	Chl^S
	(*n* = 5)	(*n* = 23)	(*n* = 13)	(*n* = 10)
SiO_2	33.40 (0.19)	34.10 (0.51)	33.73 (0.30)	33.36 (0.54)
TiO_2	0.03 (0.01)	0.02 (0.01)	0.02 (0.01)	0.01 (0.01)
Al_2O_3	12.36 (0.23)	12.68 (0.41)	12.91 (0.28)	13.52 (0.72)
Cr_2O_3	1.62 (0.03)	1.43 (0.25)	1.48 (0.62)	1.31 (0.33)
FeO	4.21 (0.08)	4.15 (0.09)	3.56 (0.24)	3.29 (0.11)
NiO	0.22 (0.05)	0.24 (0.04)	0.26 (0.02)	0.25 (0.04)
MgO	33.26 (0.10)	33.81 (0.36)	33.13 (0.31)	33.16 (0.28)
MnO	0.02 (0.01)	0.04 (0.04)	0.01 (0.01)	0.02 (0.02)
CaO	0.01 (0.00)	0.01 (0.01)	0.01 (0.01)	0.02 (0.01)
Na_2O	0.01 (0.00)	0.03 (0.07)	0.00 (0.00)	0.02 (0.01)
Cl	0.04 (0.01)	0.05 (0.06)	0.02 (0.01)	0.06 (0.02)
F	0.02 (0.02)	0.01 (0.03)	0.04 (0.02)	0.05 (0.02)
H_2O calc	12.33 (0.02)	12.55 (0.15)	12.40 (0.05)	12.39 (0.04)
Total	97.5 (0.2)	99.1 (1.1)	97.6 (0.2)	97.5 (0.4)
O	28	28	28	28
OH	16	16	16	16
Si	6.498 (0.033)	6.517 (0.039)	6.527 (0.038)	6.456 (0.111)
Ti	0.004 (0.002)	0.003 (0.001)	0.003 (0.002)	0.002 (0.002)
Al	2.833 (0.055)	2.857 (0.075)	2.945 (0.056)	3.085 (0.160)
Cr	0.250 (0.004)	0.216 (0.038)	0.227 (0.095)	0.200 (0.050)
Fe	0.685 (0.012)	0.663 (0.018)	0.576 (0.040)	0.532 (0.018)
Ni	0.034 (0.007)	0.036 (0.006)	0.040 (0.004)	0.039 (0.006)
Mg	9.646 (0.026)	9.635 (0.067)	9.559 (0.058)	9.570 (0.084)
Mn	0.003 (0.002)	0.006 (0.007)	0.002 (0.002)	0.002 (0.003)
Ca	0.001 (0.001)	0.002 (0.003)	0.001 (0.002)	0.004 (0.002)
Na	0.002 (0.002)	0.012 (0.026)	0.001 (0.001)	0.009 (0.002)
Sum cation	19.955	19.947	19.882	19.898
X_{Mg}	0.934 (0.001)	0.936 (0.002)	0.943 (0.004)	0.947 (0.002)

* T: transitional lithology (Atg-Chl-Opx(Tlc)-Ol schist); G: Chl-harzburgite with granofelsic texture; S: Chl-harzburgite with spinifex-like texture
*X_{Mg}=Mg/(Fe+Mg)

4.6.6 Other phases

Other minor phases have little systematic compositional variations with changing assemblages or textures. A notable exception is the fluorine content in titanian clinohumite dicussed in detail by López Sánchez-Vizcaíno and coworkers (2005, 2009). Tremolite composition is very homogenous in all the rock types, with X_{Mg} = 0.961±0.005 and small amounts of alkalis (up to 0.6 wt% Na_2O and 0.2 wt% K_2O). Clinopyroxene is almost pure diopside (X_{Mg} = 0.970±0.006, and MnO < 0.1 wt%). Talc is the magnesium richest phase (0.980±0.001), having up to 0.2 wt% Al_2O_3 and appreciable amounts of nickel (up to 0.1 NiO wt%).

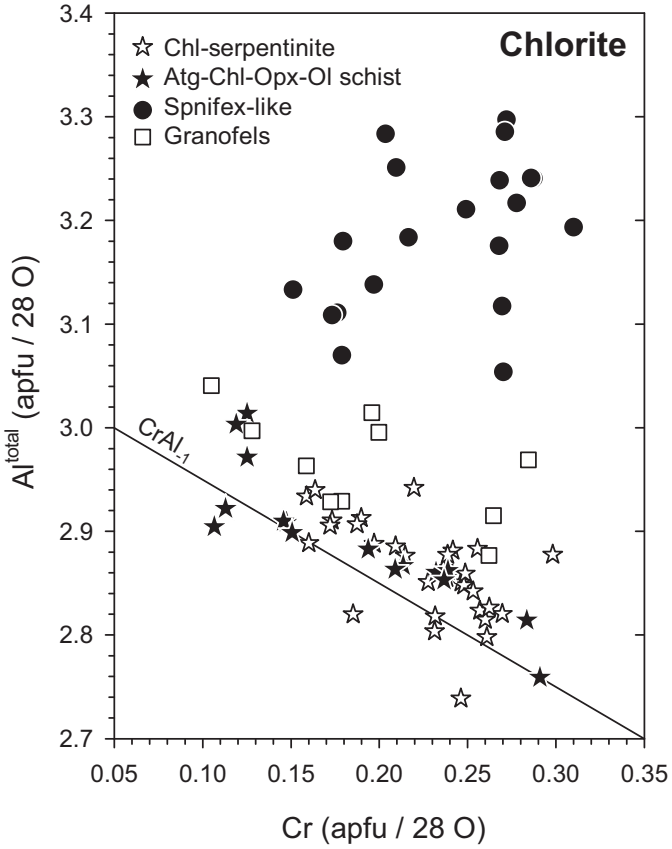

Figure 4-11. Al^{total} versus Cr for chlorite in transitional lithologies, and granofelsic and spinifex-like textured Chl-harzburgite. The line represents the $CrAl_{-1}$ exchange.

4.7 Discussion

The above reported field, petrographic and chemical data may contribute to enlighten with higher detail the formation process of the antigorite isograd and its evolution through time. Main peculiarities of the antigorite breakdown reaction and its associated lithologies are related with the fact that this is a dehydration reaction releasing as much as about 9 wt% H_2O (Padrón-Navarta et al., submitted, b). This allows considering the antigorite-out isogradic surface as a dehydration or devolatilization front.

4.7.1 Phase relationships in the devolatilization front

As already reported, Atg-serpentinite and Chl-harzburgite never occur in direct contact with each other in the Cerro del Almirez ultramafic massif. Instead, transitional lithologies are found (Chl-serpentinite and Chl-Atg-Opx-Ol schist) in a narrow band separating Atg-serpentinite from Chl-harzburgite with granofelsic texture (Fig. 4-4). Chl-serpentinite occurs in direct contact with Atg-serpentinite and is characterized by the sharp appearance of chlorite (even at mm scale; Fig. 4-5a) and by the growth of a

second generation of highly recrystallized antigorite. First occurrence of orthopyroxene takes place several centimetres to decimetres away from the contact with Atg-serpentinite (Fig. 4-4b), thus allowing to define the Chl-Atg-Opx-Ol schist. This second transitional rock is characterized by the increasing modal amount of orthopyroxene and the counterpart decreasing modal amount of antigorite towards the contact with Chl-harzburgite with granofelsic texture. In fact, the only significant difference between close to each other Chl-Atg-Opx-Ol schists and granofelsic Chl-harzburgites is the lack of antigorite in the latter rock type.

Accordingly, two different metamorphic reactions must be invoked in order to account for the first appearance of chlorite and orthopyroxene in these rocks. With the aim of defining these reactions, we appeal to qualitative compositional phase diagrams (Fig. 4-12) and mass balance calculations. As a starting point, we assume that changing topologies in these phase diagrams are essentially driven by an increasing metamorphic grade. This seems to be a realistic assumption when trying to explain the main metamorphic reactions observed to occur in the Atg-serpentinite from the Cerro del Almirez massif, as well as the Atg-serpentinite transformation into Chl-harzburgites (see phase diagram in Trommsdorff et al., 1998; pseudosections in López Sánchez-Vizcaíno et al., 2005 and 2009; and experimental determinations in Padrón-Navarta et al., 2010). Hence, most of the systematic changes in mineral chemistry reported here for transitional rocks can be also reasonably attributed to increasing temperature conditions (see also Fig. 4-13).

Phase relationships between antigorite, chlorite, olivine, orthopyroxene and water can be explained in a FeO-MgO-Al_2O_3-SiO_2-H_2O (FMASH) compositional system. We use, nevertheless, two sets of three-component phase diagrams (Fig. 4-12) for a better visualization of phase relationships. MAS diagrams (Fig. 4-12a) were constructed after projection from H_2O and $MgFe_{-1}$ exchange vector. They are best suited for depicting mineral compatibilities and compositional changes between antigorite and chlorite with increasing metamorphic grade. Note that antigorite and chlorite solid solutions are parallel, as they are mostly controlled by tschermaks substitution, but not collinear. A representative bulk composition of Atg-serpentinite (black triangle) is chosen and assumed to remain constant in all the diagrams; the symbol is changed, in accordance with the rock type assemblage stable in each diagram (Fig. 4-12a). At low temperature conditions, forsterite and Al-rich antigorite with a wide compositional range (Fig. 4-8a) coexist in Atg-serpentinite (black triangle). With increasing metamorphic grade, transition takes place from Atg-serpentinite to Chl-serpentinite (black star). Al-rich antigorite (atg^A) reacts with forsterite giving place to Al-poorer antigorite (atg^T) and to the first appearance of chlorite. Within Chl-serpentinite and with increasing

⇒ **Fig. 4-12.** Sequence of **(a)** MAS (projected from H_2O and $MgFe_{-1}$ exchange component) and **(b)** FMS (projected from H_2O and average chlorite composition from Chl-serpentinite) compositional phase diagrams depicting the mineral compatibilities with increasing temperature. Black dots are measured minerals compositions (corresponding to samples Al06-45, Al06-43 and Al08-07; see Fig. 4-4a for sample location); dotted white points are theoretical mineral end-members compositions; and large symbols are bulk-rock compositions (same symbols as in Fig. 4-2; see text for details). Appearance and disappearance of key phases are controlled by continuous reactions (limited by vertical dashed lines). Note that the Opx-in reaction is discontinuous in the MAS system (vertical solid line in a,) but continuous in the FMS system (b).

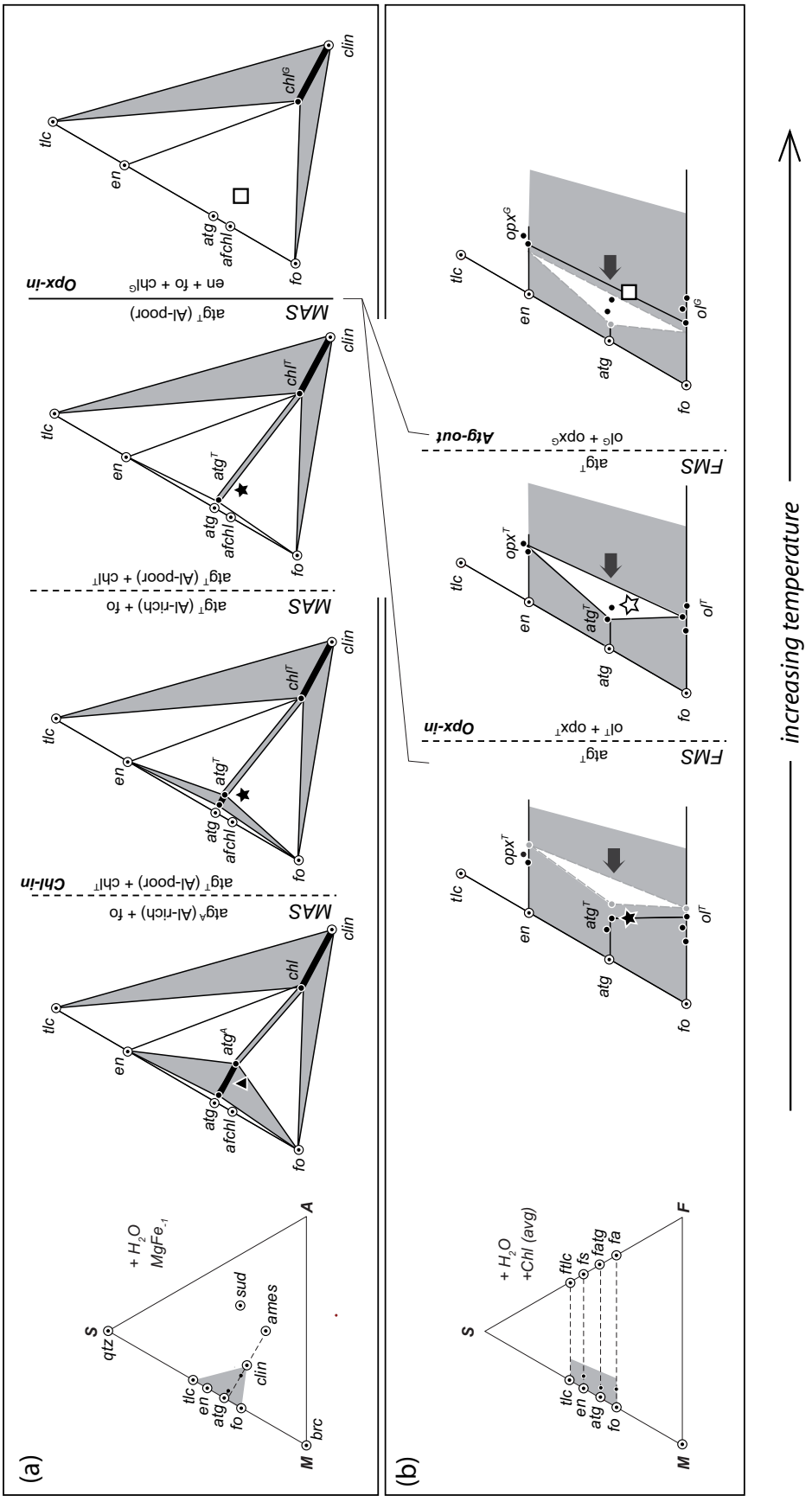
(a)
(b)
increasing temperature
Chl-in
Opx-in
Atg-out
MAS
FMS
clin
chl
chl^T
chl^G
atg^A
atg^T
afchl
tlc
en
atg
fo
opx^T
opx^G
ol^T
ol^G
qtz
sud
ames
brc
ftlc
fs
fatg
fa
S
A
M
F

metamorphic grade, antigorite composition keeps changing in a systematic way towards lower Al-contents (Fig. 4-8b). Chlorite composition may also change within Chl-serpentinite. These changes seem to be buffered by the coexisting antigorite composition, they always take place along the tschermaks substitution trend (thick black line in Fig. 4-12a) and do not affect the general topology of the MAS diagram. Chlorite formation is thus produced by a discontinuous reaction with increasing temperature conditions (dashed vertical lines). Reaction could be calibrated for the FMASH system, after mass balance calculation with C-Space software (Torres Roldán et al. 2000) and average mineral compositions from sample Al06-45:

$$1\ atg^{A} + 0.05\ ol + 0.09\ H_2O = 0.84\ atg^{T} + 0.05\ chl^{T} \qquad (1)$$

In the MAS system (last diagram in Fig. 4-12a), first enstatite formation (Opx-in reaction; continuous vertical line) takes place as a higher temperature, discontinuous metamorphic reaction, in which Al-poor atg^{T} breaks down to enstatite + forsterite + chlorite and gives place directly to the assemblage of Chl-harzburgite (white square, Fig. 4-12a), thus skipping the formation of Chl-Atg-Opx-Ol schists. It can be observed, nevertheless, that the mineral assemblage of the latter rock type can not be represented in a MAS diagram for antigorite, enstatite and olivine are colinear in it (Fig. 4-12a).

Phase relationships in Chl-Atg-Opx-Ol schists are mainly controlled by the $FeMg_{-1}$ exchange vector and can be better understood in a FMS phase diagram, after projecting from H_2O and the average chlorite composition in Chl-serpentinite (Fig. 4-12b). As already stated, chlorite composition is buffered by antigorite composition and does not change in a systematic way between Chl-serpentinite and Chl-Atg-Opx-Ol schist (Fig. 4-11). In this diagram, the Chl-serpentinite's bulk composition (black star) plots on the tie line connecting coexisting compositions of olivine and antigorite in this rock type. With increasing temperature, Opx-in reaction conditions are reached (first vertical dashed line in Fig. 4-12b) and atg^{T} breakdown takes place, together with crystallization of newly formed opx^{T} and ol^{T}, giving place to Chl-Atg-Opx-Ol schist (white star). This is, again, a continuous reaction, by which both remaining antigorite and newly formed olivine and orthopyroxene get progresively enriched in X_{Mg}. This reaction finishes with the complete antigorite consumption (Atg-out vertical dashed line) and the formation of Chl-harzburgite mineral assemblages (ol^{G} and opx^{G}, together with chlorite), in this case the ones with granofelsic textures (black square).

The calibrated reaction after mass balance with C-Space for the FMASH system and average mineral compositions from sample Al06-43 can be expressed as:

$$1.00\ atg^{T} = 0.45\ opx^{T} + 0.88\ ol^{T} + 0.03\ chl^{T} + 1.62\ H_2O \qquad (2)$$

Quantitative thermodynamic modeling of the Chl-in (1) and Opx-in (2) reactions is not possible due to the lack of thermodynamic data for the antigorite Al-rich end-member. P-T conditions for the above described phase relations can be only approximately estimated from previous pseudosections calculations in the CFMASH system with an Al-free solid solution model for antigorite (López Sánchez-Vizcaíno et al., 2005). In this work, a pseudodivariant field with coexisting Atg + Chl + Ol + Opx + Tr + H_2O (the same assemblage found in transitional lithologies) is predicted to occur

between the stability fields of Atg-serpentinite and Chl-harzburgite assemblages at 640°C and 1.7 – 1.9 Gpa. More precisely, experimental work by Padrón-Navarta et al. (2010) determines that the maximum stability of the Cerro del Almirez antigorite was reached at 680-710°C and 1.6 – 1.9 GPa.

Two additional points remain to be explained in transitional lithologies: the sharp contact with the above limiting Atg-serpentinites and the coarse grain size of the rocks. Chl-in reaction (1) is slightly water consuming: 0.09 moles of H_2O per each mole of reacting antigorite. Water availability from the Atg-serpentinite can be easily explained; most prograde reactions taking place in this rock at lower temperatures are dehydration reactions. These include the tremolite and olivine producing reaction after diopside and antigorite and the titanclinohumite breakdown reaction (López Sánchez-Vizcaíno et al., 2009). Pseudosections calculations by these authors demonstrate that the bulk H_2O content in Atg-serpentinite close to the antigorite breakdown temperature conditions was about 15 vol. % (equivalent to 5.5 wt. % H_2O). These amounts of water would contribute to trigger reaction (1) as soon as the appropriate P-T conditions were reached during prograde metamorphism of the serpentinites. This would probably help to explain the sharp contact with Atg-serpentinites.

The main textural feature of Chl-serpentinite, Atg-Chl-Opx-Ol schist and Chl-harzburgite granofels is, nevertheless, the large grain size of crystals. In the case of the first two rocks, this is particulary true for antigorite and chlorite. However, detailed textural observation in these two rocks reveals that fine grained intergrowths of chlorite and antigorite may locally remain preserved in the core of the very coarse-grained antigorite crystals, thus attesting for the original texture of Ch-serpentinite at the onset of reaction (1). Hence, it can be suggested that grain coarsening should have happened in an undetermined time after reaction (1) started. Padrón-Navarta et al. (2008) suggested that recrystallization in these rocks occurred under conditions dominated by fluids released from antigorite breakdown. This latter reaction corresponds to the above balanced reaction (2), taking place only a few centimetres away from reaction (1) and almost simultaneously. As already stated, reaction (2) is a continuous dehydration reaction, producing 1.62 moles of H_2O per reacting mole of antigorite, equivalent to about 9 wt % H_2O (Padrón-Navarta et al., 2008 and submitted, b). These huge amounts of water, concentrated in a relatively small volume of rock (Fig. 4-4), would be enough to recrystallize not only Chl-serpentinite and Atg-Chl-Opx-Ol schist, but also Chl-harzburgite granofels and to lead all these rocks to almost complete thermodynamic equilibrium, as indicated by their textural arrangement (Fig. 4-6b, d, f).

Explanation for fluid concentration in the limit with Atg-serpentinite might be derived from the fact that this rock was already completely equilibrated -as indicated by its mineral assemblage (fully stabilized in the field of tremolite) and its very homogeneous textural and microstructural arrangement (Padrón-Navarta et al., 2008)- and behaved as a fully impermeable barrier. In contrast, at a higher metamorphic grade, reactions (1) and (2) were operating in the transitional lithologies and these can be truly considered as the antigorite-out devolatilization front. Following Connolly (1997, 2010), devolatilization front is the only porous zone to be found in terrains being metamorphosed. Accordingly, transitional lithologies and resulting Chl-harzburgite

granofels should have been porous enough to host water released by antigorite breakdown and to attain metamorphic equilibrium (see below).

In conclusion, it has been demonstrated that in the Cerro del Almirez ultramafic massif, antigorite breakdown did not happen through a single discontinuous reaction giving place to a well defined, linear, antigorite-out isograd. Instead, two discontinuous reactions have been proven to occur - Chl-in (1) and Opx-in (2) – driven by increasing temperature through time and producing a decimetric thick transition zone between Atg-serpentinite and Chl-harzburgite granofels. This transition zone can be identified with the antigorite breakdown devolatilization front.

4.7.2 Preservation of relic porphyroblasts from precursor assemblages

An important finding of this work is the fact that olivine and/or orthopyroxene from the precursor serpentinite can be preserved beyond the complete antigorite breakdown. These relic porphyroblasts are characterized by contrasting compositional features with respect to prograde olivine and orthopyroxene from Chl-harzburgite (see above). Opx-bearing serpentinite with or without olivine has been experimentally determined to be stable at lower P-T conditions between (> 1.6 GPa, 640 - 680ºC) than those determined for antigorite breakdown (1.6-1.9 GPa, 680-710ºC)(Padrón-Navarta et al. 2010). The bulk composition of this rock type indicates enrichment in silica relative to common Atg-serpentinite (Fig. 4-7). Chl-harzburgite samples with relic orthopyroxene porphyroblasts are also Si-rich in bulk composition and they should have inherited it from a Si-rich serpentinite. Metamorphic peak in the prograde assemblages at Cerro del Almirez ultramafic massif was attained at relatively low temperature conditions (680-710ºC, Padrón-Navarta et al. 2010); in good agreement with the slow diffusion rates required for the preservation of olivine and orthopyroxene porphyroblasts in chemical disequilibrium with the Chl-harzburgite mineral assemblage. Moreover, the scattered distribution of undeformed, relic porphyroblasts certainly points to the lack of significant simple or pure shear deformation before and after the main devolatilization reaction. Otherwise these porphyroblasts would appear rotated with respect to foliation and with textural evidences of dynamic recrystallization. Preservation of relic porphyroblasts in both spinifex-like and granofels Chl-harzburgite (cf. Figs. 4-3f and 4-3g, respectively), suggests, as well, that mechanisms leading to the development of either textural type were independent of the bulk-rock composition of the serpentinite protolith.

4.7.3 Origin of granofelsic and spinifex-like textures

One the most striking features of Cerro del Almirez ultramafic massif is the presence of Chl-harzburgite with spinifex-like texture (Morten & Puga, 1984; Trommsdorff *et al.*, 1998; Puga *et al.*, 1999;). Although several authors have described similar textures in lower pressure, talc-bearing metaperidotite -mostly associated to contact metamorphism- (Evans & Trommsdorff, 1974; Snoke & Call, 1978; Oliver et al., 1972; Bakke & Korneliussen, 1986), the ultimate origin and meaning of spinifex-like texture after antigorite breakdown has not been addressed so far. In Cerro del Almirez, we show that spinifex and granofelsic Chl-harzburgite coexist in interspersed, metric to

decametric bodies and show sharp boundaries between both textural types (Fig. 3d). The challenge in Cerro del Almirez is to understand the cause of this textural alternation of atg-breakdown reaction products in space and its relationship to the development of the arrested, antigorite dehydration front.

Reaction affinity of antigorite dehydration reaction

It is well established that the reaction affinity –i.e. the reaction overstepping relative to the reaction equilibrium conditions, i.e. $\Delta G=0$ – determines the rate and mechanism of growth of the reaction products in solid-solid, solid-fluid and melt-solid reactions (Lasaga, 1998; Sunagawa, 1987). In Cerro del Almirez, the textural bimodality of the Atg-serpentinite dehydration products might be due to shifts of the growth rate of reaction products induced by temporal and/or spatial fluctuations of the overstepping of the antigorite-breakdown reaction. Equant olivine morphologies and rather constant opx-ol-chl dihedral angles in granofels are consistent with diffusion controlled-growth near-equilibrium, whereas spinifex-like olivine morphologies are indicative of interface controlled growth, far from equilibrium, under high supersaturation conditions (Donaldson, 1976; Lasaga, 1998; Sunagawa, 1987). The spinifex-like texture is characteristic of dentritic growth of a reacting system crystallizing under large overstepping at both non-isothermal or isothermal conditions (Asta *et al.*, 2009; Koss *et al.*, 2005). Therefore, the granofelsic to spinifex-like textural variation must attest for metamorphic crystallization of Chl-harzburgite at increasing overstepping, and these textures can be used as proxies for metamorphic crystallization under variable overstepping of the antigorite-dehydration reaction. The cause of the overstepping of the atg-breakdown reaction depends ultimately on spatial and/or temporal variations of intensive variables relative to the equilibrium reaction.

Field mapping in Cerro del Almirez ultramafic massif indicates that spinifex-like Chl-harzburgite occurs scattered downstream the atg-breakdown reaction front (Fig. 2), whereas granofelsic Chl-harzburgite occurs both downstream, interspersed with spinifex-like textured Chl-harzburgite, and at the reaction front associated with transitional lithologies. Where the transition of granofelsic to spinifex-like texture is observed, spinifex olivine grows over granofelsic olivine, indicating that spinifex texture crystallized after granofels. This spatial-temporal arrangement of the products of Atg-serpentinite dehydration reaction indicates that crystallization of reaction product at larger overstepping of the dehydration reaction, as recorded by crystallization of spinifex Chl-harzburgite, occurred downstream the reaction front, once the granofelsic texture was formed at the reaction front at low degrees of overstepping. The spatial recurrence of both textures throughout the Chl-harzburgite body must then reflect fluctuations of the antigorite breakdown reaction overstepping in time and space, related to the development of the dehydration front.

Geodynamic and thermal scenario

Space and temporal variations of the overstepping of the atg-breakdown reaction products must be due to fluctuations of intensive variables during the metamorphic prograde path. As in any other metamorphic reactions, the rate of the prograde atg-breakdown reaction is controlled by the energy input arising from large-scale

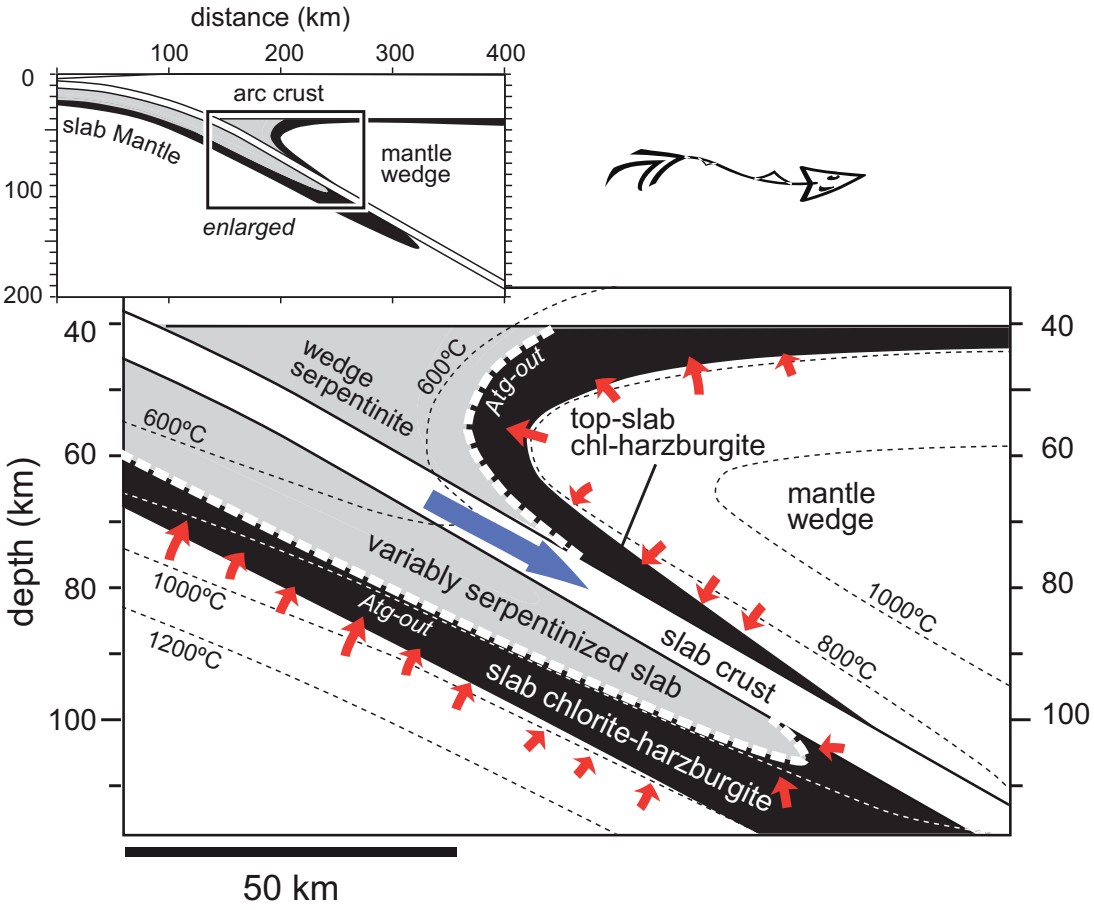

Figure 4-13. Ultramafic rocks metamorphic facies distribution in an intermediate age subduction zone setting (Nankai, SW Japan, modified from Hacker et al., 2003), highlighting the antigorite-out isograd (dashed white line), the loci of chlorite-harzburgite (black), the heat flux direction (small red arrows) and the direction of the "tectonic forcing" in the dynamics of the tectonic wedge-slab system (large blue arrow). Fish is not at scale.

geodynamic processes (Connolly, 1997; Connolly & Thompson, 1989) In Cerro del Almirez, the atg-breakdown reaction occurred at the peak conditions of a clockwise P-T-t path, recording the continental subduction of the Nevado-Filábride Complex in the Miocene (Gómez-Pugnaire *et al.*, 2004; Gómez Pugnaire & Fernández Soler, 1987; López Sánchez-Vizcaíno *et al.*, 2001). As plate tectonic movements in convergent settings are rapid relative to heat conduction, the prograde path of incoming rocks is slightly undercooled relative to the subduction steady-state geotherm (Fig. 4-13) (Connolly, 1997; Connolly & Thompson, 1989). Subsequent heat flow from the mantle as the geotherm relaxes toward the steady-state geotherm provides the necessary thermal driving force for the progress of the atg-breakdown reaction. Because the atg-breakdown reaction has a steep Clayperon slope, the resulting dehydration reaction front must be nearly parallel to the c. 680-710 ºC steady-state geotherm and, whatever the original tectonic position of the Almirez body, the reaction front must have been moved upstream the heat flux towards the Atg-serpentinite reactant (Fig. 4-13). In this setting, the degree of

temperature overstepping at which the atg-breakdown reaction proceeds is a combination of the rate of convergence and dynamics of the wedge-slab system ("tectonic forcing"), which drive the Atg-serpentinite across the 680-710 ºC steady-state isotherm at P~1.6-1.9 GPa, and the kinetic of the reaction, which establishes the advancement of the reaction front towards the steady-state geotherm. The very fast kinetic of the antigorite breakdown reaction (Perrillat *et al.*, 2005), together with the fact that dehydration reactions are highly endothermic (Connolly & Thompson 1989, Lyubetskaya and Ague 2009), implies that the dehydration reaction front evolved likely near equilibrium conditions.

In the above scenario, fluctuations of the overstepping relative to the atg-breakdown equilibrium might be caused either by tectonic forcing (García-Casco *et al.*, 2002; Gerya & Stockhert, 2006), or by variations of intensive parameters controlled by the hydrodynamic of the atg-breakdown devolatilization reaction (Connolly, 1997; Miller *et al.*, 2003; Wang & Wong, 2003). Variations of the convergence rate occurs at temporal scales that can account neither for a reaction overstepping causing the metric recurrence of spinifex-like and granofelsic Chl-harzburgite nor for the absence of spinifex-like textures at the antigorite breakdown reaction front. So, below we focus on fluctuations of intensive variables controlled by the hydrodynamic of the antigorite breakdown devolatilization as the potential cause for variations of the affinity of the antigorite breakdown reaction.

Deformation and pressure regimes

As the Clayperon slope of the atg-breakdown reaction is positive at the P-T interval of the development of this reaction front in the Cerro del Almirez ultramafic massif, the dehydration reaction results in a net decrease in the total solid volume, which implies an irreversible increase in porosity (Connolly, 1997; Connolly & Podladchikov, 1998; Ko *et al.*, 1997; Miller *et al.*, 2002; Miller *et al.*, 2003; Olgaard *et al.*, 1995; Wong *et al.*, 1997) (see also Chapter 8 for a estimation of the volume change for this reaction). If the dilation of the pore space is insufficient to provide storage for all the released fluid, then a pore pressure excess is generated, and if it becomes sufficiently high, it may lead to brittle fracturing and to drainage of the fluid out the system, with the subsequent a drop of the fluid pore pressure (Olgaard *et al.*, 1995; Wang & Wong, 2003; Wong *et al.*, 1997). Alternatively, if the system is compacting, fluids can be drained by high porosity waves (Connolly, 1997; Connolly & Podladchikov, 1998). The obstruction to fluid flow exerted by the rocks overlying a metamorphic devolatilization front causes the fluid pressure gradient in the reacting rock to diverge from lithostatic, thus producing deformation in viscoelastic rocks (Connolly 1997, Connolly and Podladchikov 1998). Viscoelastic deformation evolves with time by propagating the pressure anomaly upward, leading to underpressuring and densification at the reaction front (granofels texture) and to the detachment of a wave of anomalous fluid pressure and porosity (i.e. porosity wave). This situation induces spatiotemporal variations of the fluid pore pressure throughout the antigorite-breakdown reaction that are controlled ultimately by the hydraulics of the dehydrating system. Fluid overpressure would build up at the reaction front and/or at low permeability compartments downstream the reaction front. Sudden drops of the fluid pressure would occur when/where fluids were effectively drained from these overpressurized domains. Concerning the time scale, the fluid pressure generation and

the pore pressure excess can be maintained over long duration depending on the interplay of reaction kinetics and fluid drainage (Connolly, 1997; Olgaard *et al.*, 1995; Wang & Wong, 2003; Wong *et al.*, 1997). Although the structure and evolution of permeability in the deep mantle wedge of subduction settings is almost completely unknown, the existence of variable pore pressure in these settings is attested by intermediate depth earthquakes, most likely produced by dehydration embrittlement (Hacker *et al.*, 2003; Kirby *et al.*, 1991; Peacock, 2001).

Although the treatment of non-hydrostatic thermodynamic equilibrium is Complex, Dahlen (1992) has shown that dehydration equilibrium is almost completely dependent on fluid pressure and temperature. In such scenario, the fluid pressure (P_f), instead of the confining lithostatic pressure (P_0), becomes the relevant thermodynamic pressure in a standard P-T phase diagram (Connolly, 1997; Dahlen, 1992; Wang & Wong, 2003; Wong *et al.*, 1997). This means that, at hydrological development under an isothermal scenario, the affinity of the antigorite dehydration reaction (ΔG) is proportional to ($P_f - P_0$), where P_f is the actual fluid pore pressure and P_0 is the fluid pore pressure at the equilibrium temperature (see Fig. 1 of Wang & Wong (2003)). If $P_f = P_0$, $\Delta G = 0$ and the reaction will proceed toward the reaction products at near equilibrium conditions, or will be halted if there is not enough overstep in temperature for the reaction to progress. If $P_f > P_e$, $\Delta G > 1$, overpressure occurs and the reaction is driven back to the equilibrium where it may be halted or even reversed if the excess pressure does not induce the brittle failure of the system. A sudden drop of the P_f will favour crystallization of the reaction products under a high affinity of the dehydration reaction, leading to enhanced growth and, potentially, to modifications in the growth mechanism of reactants (Asta *et al.*, 2009; Koss *et al.*, 2005). In all the above scenarios, variations in the affinity of the atg-dehydration reaction are caused by fluctuations in the excess fluid pore pressure ($P_f - P_0$; where P_0 is the initial fluid pore pressure of the dehydrating system) that are ultimately set by the temporal and spatial variability of the permeability of the dehydrating system. In addition of disturbing the affinity of the dehydration reacting system, laboratory measurements in gypsum indicate that increasing fluid pore pressure in dehydrating systems dramatically decreases the reaction rate (Ko *et al.*, 1997). So, more sluggish dehydration reaction kinetics would be expected where or when overpressure is prevalent than where or when the excess fluid pore pressure is drained out the dehydrating system.

Evolution of the Cerro del Almirez dehydration front

In Figures 4-14 and 4-15 we sketch a working scenario for the development of Cerro del Almirez dehydration front, whereby the crystallization of the intermediate lithologies at the antigorite dehydration front, and of spinifex-like and granofelsic Chl-harzburgite are due to spatial-temporal variations of the excess pore fluids during the advancement of the dehydration front. In a first stage, the Atg-serpentinite is dragged down into a steady-state temperature geotherm in a convergent setting, thus providing the energy source to drive the dehydration reaction (t_o in Fig. 4-14). Dehydration of the Atg-serpentinite occurs when the Atg-serpentinite cross over the opx-in/chl-in reaction and some temperature overstep is allowed for the reaction to proceed (t_1 in Fig. 4-14). As the opx-in/chl-in reaction has a steep Clayperon slope (Fig. 4-15), the intermediate lithologies crystallize at a dehydration reaction front parallel to the steady-state

isotherm. This reaction front is perpendicular to the heat flux and advances upstream towards the steady-state geotherm of c. 680-710 ºC. At the initiation of the antigorite dehydration reaction, we envisage a system in lithostatic equilibrium with an initial fluid pressure (P_o) equal to the confining, lithostatic pressure ($P_o=P_f=P_l$, where P_l is the lithostatic pressure). Here, we neglect the presence of deviatory stresses. This simplification is partly supported by the lack of deformational textures in Chl-harzburgite and the preservation of scattered relic porphyroblasts with no evidences of recrystallization or rotation.

As the reaction progresses, dehydration of antigorite results in a net decrease in the total solid volume, leading to an irreversible increase in porosity and the generation of a fluid pore pressure excess ($P_f > P_o=P_l$; i.e. positive overpressure). In this scenario, the equilibrium is non-lithostatic and the thermodynamic pressure is not longer the confining pressure, but the excess fluid pore pressure (Dahlen, 1992). In a P-T diagram, the reaction path evolves at increasing P_f and is parallel to the Clayperon slope of the opx-in/chl-in reaction. The buildup of fluid overpressure leads to a permeability barrier at the dehydrating reaction front, which is coeval with the crystallization of transitional lithologies. If the system is undrained, the affinity and the rate of the dehydration reaction decreases, and the reaction stalls eventually, which brings to a halt in the advancement of the reaction front. If enough overpressure is build up at the front, the reaction may be even reversed. In Cerro del Almirez, buildup of fluid overpressures at antigorite breakdown reaction front may account for the overgrowth of large antigorite (Padrón-Navarta *et al.*, 2008) over prograde chlorite in the transitional lithologies (Fig. 4-6b) For the reaction to progress, the overpressure fluid must be drained from the dehydrating system. Draining of the excess fluid likely occurred differently at the reaction front and downstream the front, where fluid overpressure maintains the dehydrating system near the chl-in/opx-in equilibrium (t_2 in 4-14). At the reaction front, where compaction has taken place due to devolatilization, the escape of overpressure fluids can be accommodated by porosity waves, if the critical compaction length is attained and viscous compaction is operative (t_2 in Fig. 4-14) (Connolly, 1997; Connolly & Podladchikov, 1998; Connolly & Podladchikov, 2004). Dehydrating front draining decreases the fluid overpressure bringing back the P_f near the lithostatic pressure (Site 1 and t_0 to t_1 in Figs. 4-14 & 4-15). If draining is slow, the decrease of P_f towards P_l drives the P-T path toward crystallization of the ol-opx-chl assemblage in the

⇒ **Fig. 4-14.** Schematic general evolution with time (from t_0 to t_5) of the reaction front in the Cerro del Almirez ultramafic massif. Three sites are shown with contrasting fluid pressure evolution and giving place to three different rock types beyond the present location of the devolatilization front (see Fig. 4-15 and text for explanation). Site 1 (blue dot): slowly drained domain producing granofelsic Chl-harzburgite; Site 2 (red dot): fast drained domains, after episodic hydrofracturing, producing spinifex-like Chl-harzburgite; Site 3 (green dot): isolated non-reacted domains preserving Atg-serpentinite or Chl-serpentinite lenses within Chl-harzburgites. Vertical red arrows indicate upwards advance of the reaction front with time. Advance can be controlled by the presence of an indeterminate deep heat source (upwards pointing orange arrow). Alternatively, downward transport of serpentinite due to 'tectonic forcing' can be considered (downwards pointing orange arrow). In this case isotherms would remain stationary and roughly horizontal.

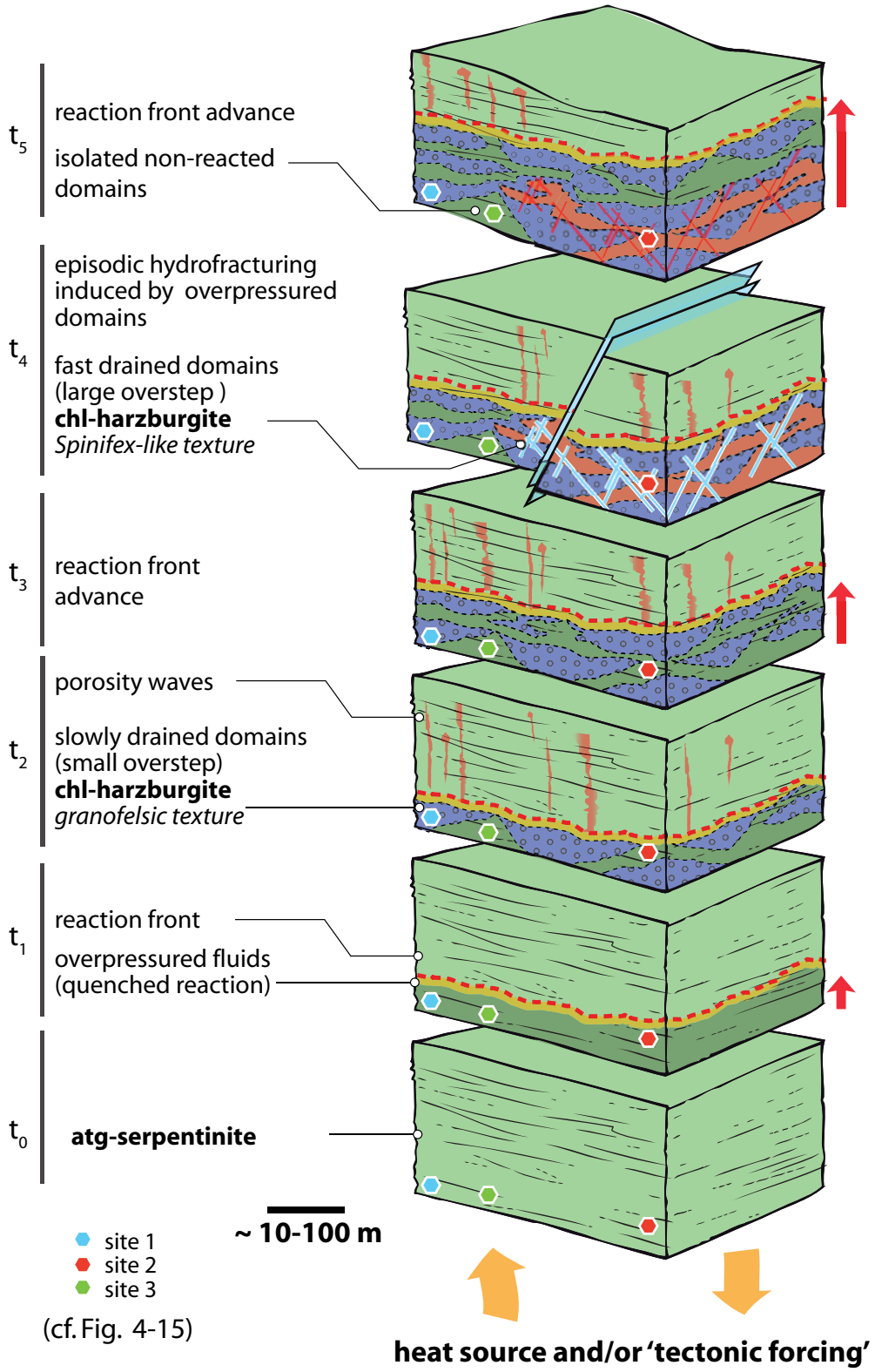
t5
reaction front advance
isolated non-reacted domains
t4
episodic hydrofracturing induced by overpressured domains
fast drained domains (large overstep)
chl-harzburgite
Spinifex-like texture
t3
reaction front advance
t2
porosity waves
slowly drained domains (small overstep)
chl-harzburgite
granofelsic texture
t1
reaction front
overpressured fluids (quenched reaction)
t0
atg-serpentinite
~ 10-100 m
site 1
site 2
site 3
(cf. Fig. 4-15)
heat source and/or 'tectonic forcing'

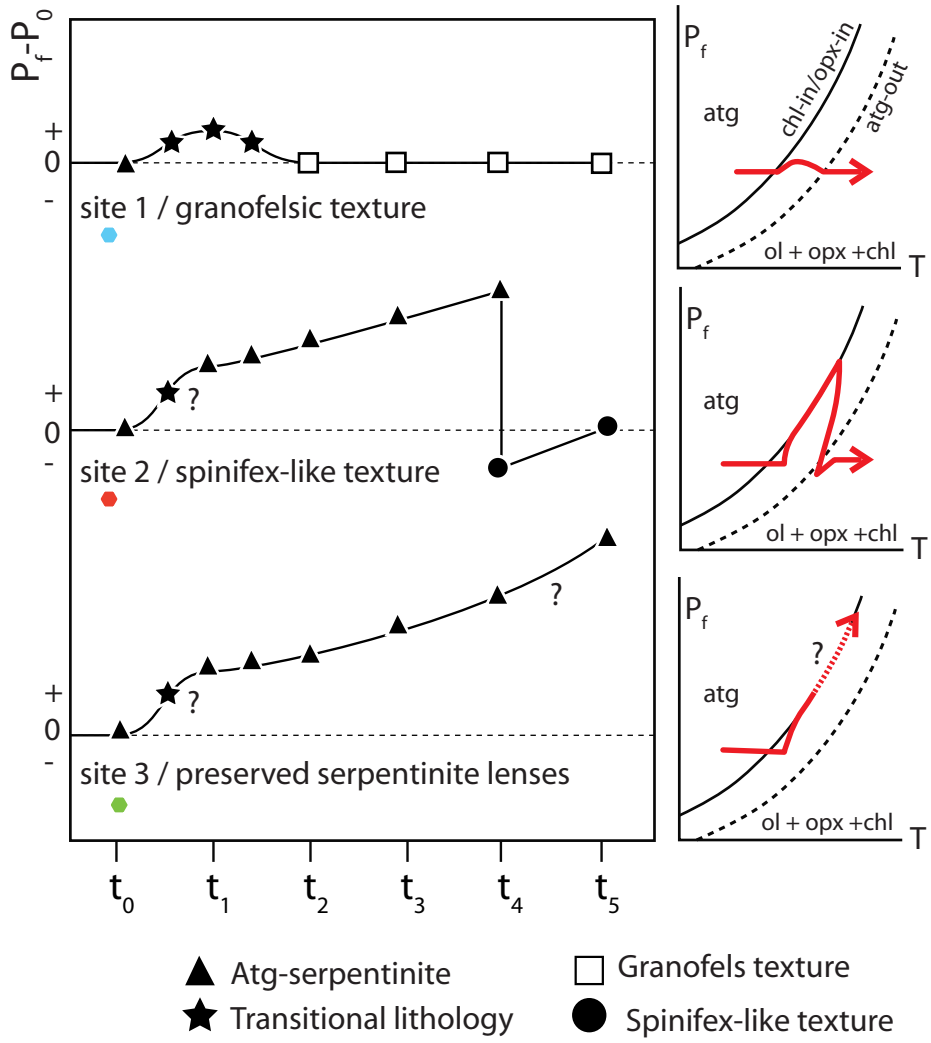

Figure 4-15. Left diagrams: schematic evolution with time (from t_0 to t_5) of the contrasting fluid porosity anomalies ($P_f - P_0$, where P_f is fluid pressure and P_0 is lithostatic pressure) generated during the devolatilization reaction for three different sites (see Fig. 4-14). Horizontal, short dashed, baseline corresponds to lithostatic pressure (P_0~1.6-1.9 GPa, Padrón-Navarta et al. 2010). Right diagrams: schematic P_fTt evolution for the three sites. Antigorite breakdown reaction is considered to occur in a divariant field delimited by the Chl-in and Opx-in reactions (roughly coincident at this representation scale) at low temperature and Atg-out at high temperature (see Fig. 4-12). Site 1 corresponds to slowly and continuously drained domains (giving place to the granofelsic texture at t_2). In site 2, the fluid overpressure quenches the reaction at t_1 and increases with time until t_4 when fluid overpressure exceeds the tensile strength of the rock causing hydrofracturing, fast drainaged and development of the spinifex-like texture. In site 3, drainage is never attained and serpentinite can be preserved thought time.

prograde Chl-harzburgite. At this stage, small fluid overpressures may occur as a result of a tradeoff between the kinetic of the reaction and the pace of fluid escape from the dehydration front (Site 1, Fig. 4-15). Slow draining of fluids at the dehydration front by means of fluid porosity waves would account for the crystallization of Chl-harzburgite near the lithostatic equilibrium and the growth of atg-breakdown products under a low affinity of the reaction. This scenario accounts for the texture of granofelsic Chl-harzburgite and for their occurrence at the dehydrating front, closely associated with transitional lithologies (Fig. 4-6b). The crystallization of granofelsic Chl-harzburgite at

the reaction front generates a permeability barrier that impedes the efficient draining of domains under overpressure downstream the reaction front (Sites 2 & 3 at t_2 in Fig. 4-14). In these overpressure compartments, the system is in non-lithostatic conditions nearby the opx-in/chl-in equilibrium, and the Atg-serpentinite is highly metastable relative to the lithostatic pressure equilibrium (Sites 2 & 3 in Fig. 4-15). In Cerro del Almirez ultramafic massif, the existence decametric lenses of Atg-serpentinite downstream the reaction front (Fig. 4-2) supports the presence of overpressured domains during the development of the antigorite dehydration front. Ii is difficult to ascertain how long this overpressure can be maintained, but it should be limited by the tensile strength of the surrounding rocks (~5 MPa, Gueguen and Palciauskas, 1994).

Eventually, the buildup of pore pressure excess in these domains may lead to failure stress and embrittlement (hydrofracturing), suddenly increasing the permeability of these domains and providing an essentially instantaneous mechanism for regulating supra-lithostatic fluid pressures (Gueguen and Palciauskas, 1994; Sibson 2004). This mechanism would effectively drain out the interconnected overpressure compartments (Site 2, t_4, Figs. 4-14 & Fig. 4-15). Under these conditions, the P_f might decrease drastically even below the P_l, as the P_f would be dominated by the regional hydrostatic gradient (Connolly, 1997; Connolly, 2010). The drop of P_f would induce fast crystallization of the the reaction products of antigorite breakdown (i.e., Chl-harzburgite) under a high reaction affinity. This scenario would account for supersaturation and enhanced growth of reaction products driven by an interface-growth mechanism, which would lead to spinifex-like textures in Chl-harzburgite. This rapid growth could occur at a much wider depth interval, because once failure takes place fluid pressure is more or less independent of total pressure (Connolly, 2010). When failure occurs, the P_f-T follows a hydrostatic gradient and the change in temperature due to this gradient is given by the Clapeyron slope of the dehydration reaction (Site 2, Fig. 4-15) (Connolly, 1997; Connolly, 2010). In this scenario, steady-state conditions can be envisaged on long time scales, which in detail consist of small fluid "jumps" associated with fracturing (Connolly, 2010) and in which each jump would create the spinifex-like Chl-harzburgite. Evidences for hydrofracturing affecting Chl-harzburgite have been reported in the Cerro del Almirez ultramafic massif and are described in detail in Chapter 8 of this Thesis.

Undrained domains (site 3 in Figs. 4-14 & 4-15) at the time of the halt of the reaction front would account in the Cerro del Almirez for the isolated Atg-serpentinite lenses downstream the reaction front. With further heat flux, advancement of the reaction front would proceed towards the Atg-serpentinite, thus starting a new loop of overpressure (t_5 in Fig. 4-14) and allied textural fluctuations in the reaction front linked to the hydraulic evolution of the atg-dehydrating front.

4.8 CONCLUSIONS

In the Cerro del Almirez ultramafic massif, field relationships, textural evolution and mineral chemistry all attest for near equilibrium conditions at the reaction front that records higher temperatures than those prevailing in the antigorite serpentinite. Nevertheless, the occurrence of two very contrasting textures in the final prograde assemblage of chlorite harzburgite, after antigorite breakdown, as well as the sporadic

preservation of serpentinite lenses indicate that the reaction front evolved differently in separated domains at the meter to decametre scale. As discussed before, very contrasting reaction rates may account for the textural differences recorded in Chl-harzburgite (granofels versus spinifex-like texture). Fast reaction rates and mineral growth are indicative of high reaction affinity during the growth of the spinifex-like texture. On the contrary, granoblastic texture in granofels points to a near equilibrium transformation from the transitional lithologies. This cyclic alternation in time and space of near equilibrium and disequilibrium textures symbolizes an outstanding paradox that is interpreted here as a consequence of contrasting evolution of the fluid pore pressure in temporally isolated, hydraulic compartments. Textural bimodality recorded by Chl-harzburgite from the Cerro del Almirez ultramafic massif witness for two contrasting mechanisms of metamorphic fluid expulsion likely operating in subduction settings.

Contrib Mineral Petrol (2008) 156:679–688
DOI 10.1007/s00410−008−0309−x
Received: 12 March 2008 / Accepted: 30 April 2008 / Published online: 22 May 2008

5 Highly ordered antigorite from Cerro del Almirez HP–HT serpentinites, SE Spain

Padrón-Navarta, JA[1*]· López Sánchez-Vizcaíno, V[2] · Garrido CJ[3] · Gómez-Pugnaire MT[1,3] · Jabaloy A· Capitani GC · Mellini M[5]

The Cerro del Almirez ultramafic massif offers an example of high pressure and high temperature antigorite serpentinites. A sharp antigorite-out isograd separates them from Chl–harzburgites, consisting of olivine + enstatite + chlorite. Antigorite is characterized by aluminium contents as high as 4 wt. % Al_2O_3. The microstructural study shows that, prior to the transformation, antigorite is exceptionally ordered and consists of the polysome m = 17. No polysomatic defect occurs in antigorite forming most of the Cerro del Almirez serpentinites. Close to the antigorite-out isograd, limited disorder features may occur, mainly as (001) twins, reaction rims and reduction of m down to 14-15. Here, local recrystallization phenomena lead to sporadic growth of large antigorite and chlorite crystals.

1. Departamento de Mineralogía y Petrología, Universidad de Granada, Spain.
2. Departamento de Geología, Universidad de Jaén Linares, Spain.
3. Instituto Andaluz de Ciencias de la Tierra (IACT), Granada, Spain.
4. Departamento de Geodinámica, Universidad de Granada, Spain
5. Dipartimento Geomineralogico, Universitá di Bari, , Italy.
6. Dipartimento di Scienze della Terra, Universitá di Siena , Italy

5.1 Introduction

During recent years, much interest has been focused on the stability of antigorite under high-pressure and high-temperature conditions, because of its potential role in subduction dynamics and volcanism and in the water recycling into the Earth mantle (e.g., Ulmer and Trommsdorff 1995; Scambelluri et al. 1995; Garrido et al. 2005; Ranero et al. 2003). Several studies have approached the high–pressure dehydration of antigorite from the experimental point of view (e.g., Ulmer and Trommsdorff 1995; Wunder and Schreyer 1997; Bromiley and Pawley 2003; Reynard and Wunder 2006; Perrillat et al. 2005; Hilairet et al. 2006a, b), while others have focused on the petrological and geochemical features of natural occurrences of antigorite serpentinites under variable pressure and temperature conditions (e.g., Scambelluri et al. 1995; Trommsdorff et al. 1998; Uehara 1998; Auzende et al. 2002, 2006).

The Cerro del Almirez ultramafic massif (Betic Cordillera, SE Spain) provides a matchless example of antigorite serpentinites metamorphosed under higher temperature and pressure conditions than any other antigorite occurrence reported worldwide (Trommsdorff et al. 1998; Puga et al. 1999; López Sánchez-Vizcaíno et al. 2001, 2005; Garrido et al. 2005). In this massif, a 200-m thick body of antigorite serpentinite schist crops out above a 200-m thick tabular body of chlorite-harzburgite (olivine + enstatite + chlorite + magnetite) with spinifex textured olivine and enstatite (Trommsdorff et al. 1998). These lithologies are separated from each other by a rather sharp boundary, interpreted as the antigorite-out dehydration isograd at high–pressure (1.7–2.0 GPa) and temperature (640ºC) conditions (Trommsdorff et al. 1998; López Sánchez-Vizcaíno et al. 2005).

Despite the increasing number of petrological and geochemical studies devoted to this massif, the textural and crystallographic features of antigorite in these HP–HT serpentinites are unknown. Previous studies have shown significant modifications in the structure and texture of antigorite in serpentinites metamorphosed at variable P and T conditions (Mellini et al. 1987; Viti and Mellini 1996; Auzende et al. 2002, 2006). It has been also argued that the structure and composition variations may play an important role in the stability of antigorite (Wunder and Schreyer 1997; Wunder et al. 2001) and may explain discrepancies in the breakdown conditions of antigorite reported by different experimental studies. The Almirez massif offers an extremely valuable natural case study for the investigation of the textural and crystallographic features of antigorite in the vicinity of the antigorite breakdown at high pressure and temperature conditions. The aim of our study is to investigate and characterize the microstructural features of antigorite at different distances from the antigorite-out isograd.

5.2 Field occurrence

The Cerro del Almirez ultramafic massif (0.4-km thick, and 2-km wide) is the largest body of ultramafic rocks occurring in the upper sequence of the Nevado–Filábride Complex of the Betic Cordilleras (Fig. 5-1a). Ultramafic rocks in the Nevado–Fila´bride Complex are surrounded by Paleozoic metasediments (Gómez-Pugnaire et al. 2000, 2004), where dominant pelitic rocks are interbedded with quartzite and minor marble

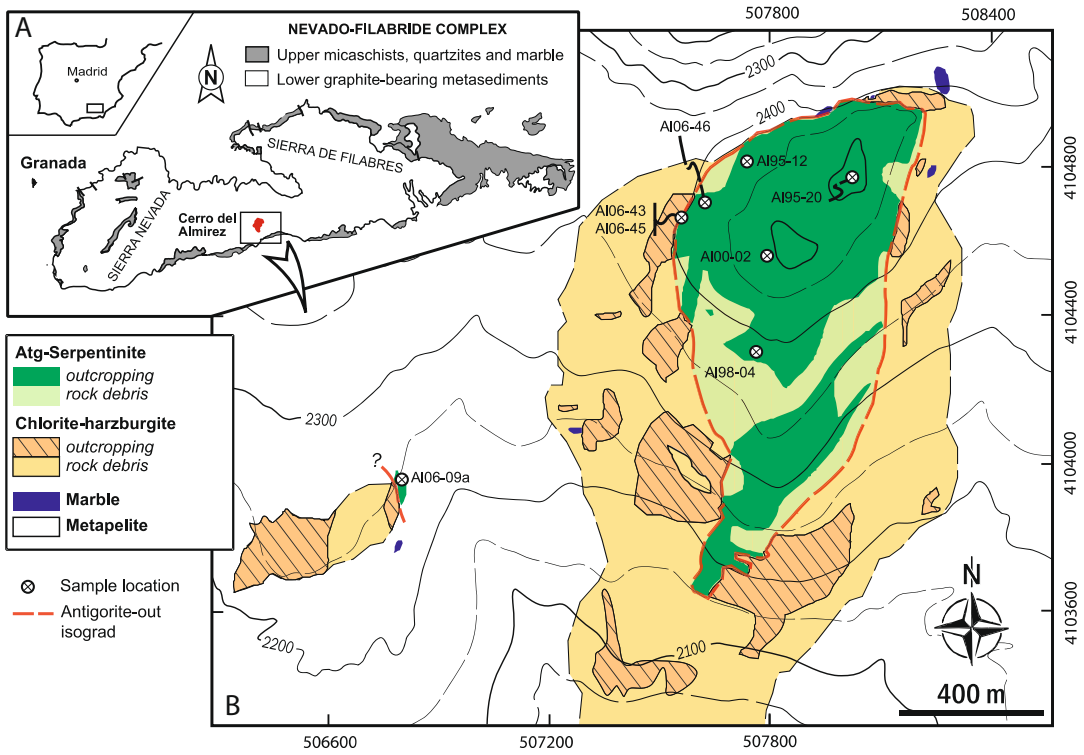

Figure 5-1. (a) Outline geological map of the Nevado–Filábride Complex of the Betic Cordilleras with location of the Cerro del Almirez outcrop. B Geological map of the Cerro del Almirez body (modified from Schönbächler 1999 and Hürlimann 1999) showing the distribution of the two main ultramafic rock types (antigorite serpentinite and chlorite harzburgite), the antigorite-out isograd and the location of the studied antigorite-bearing samples. Country rocks mainly consist of metapelites and small marble outcrops. Coordinate frame system is WGS (1984), UTM 30

(Hürlimann 1999; Schönbächler 1999). The whole sequence was metamorphosed during the Miocene under eclogite facies conditions, recording peak metamorphic conditions of ~2 GPa and ~650ºC (Trommsdorff et al. 1998; Puga et al. 1999; López Sánchez-Vizcaíno et al. 2005). Trommsdorff et al. (1998) have provided a detailed account of the petrology and field occurrence of the different lithologies of the Almirez massif. The massif is composed of two lithological domains: an upper domain of strongly foliated antigorite serpentinite schists (Atg-serpentinite) overlying a lower domain of variably textured (radial to granular) enstatite + olivine + chlorite rocks (Chl-harzburgite) (Fig. 5-1b) (Trommsdorff et al. 1998). The Atg-serpentinite domain, which extends from the antigorite--out isograd up to the summit of the massif (Fig. 5-1b), is lithologically and structurally homogeneous, despite thelocal occurrence of cm to dm-scale clinopyroxenite layers and lenses, veins of titanian clinohumite + olivine (López Sánchez-Vizcaíno et al. 2005), and minor boudins of rodingite. Oriented domains of antigorite define a low-dipping foliation, which locally contains a distinct stretching lineation defined by elongated magnetite-chlorite aggregates (Hürlimann 1999; Schönbächler 1999).

A sharp lithological boundary separates the Atg-serpentinite domain from the Chl-harzburgite domain below. This lithological boundary crosscuts the Atg-serpentinite foliation and constitutes the antigorite-out isograd (Trommsdorff et al. 1998). Atg-serpentinites close to the antigorite-out isograd display a variable appearance at the

outcrop and hand specimen scales. In most places (e.g., samples Al06-09a and Al06-46, Fig. 5-1b) they are texturally and lithologically similar to the overlying Atg-serpentinite. In some outcrops, however, the Atg-serpentinites and Chl-harzburgites are separated by a distinct, poorly foliated and dark lithology composed of coarse antigorite and chlorite flakes, visible to the naked eye, and variable amounts of olivine. Hereafter, we will refer to this lithology as Chl-serpentinite (samples Al06-43 and Al06-45). The transition between normal Atgserpentinite and Chl-serpentinite is sharp and oblique to the foliation of Atg-serpentinite.

5.3 Samples and petrography

We selected representative samples of Atg-serpentinite and Chl-serpentinite (Table 5-1; Fig. 5-1b for location of samples). Most of them come from the larger ultramafic body in the Cerro del Almirez; one sample (Al06-09a) comes from a smaller massif west of the main body and sampled in an Atg-serpentinite lens in contact with Chl-harzburgite. We studied only clinopyroxene-poor serpentinites in order to avoid any potential influence of modal variations of this mineral on the antigorite textures.

Atg-serpentinite is similar to other highly recrystallized alpine serpentinites (e.g., Trommsdorff and Evans 1972). It is characterized by flaky antigorite, with variable grain size and shape orientation, lower amounts of granular olivine and diopside, minor chlorite, and discontinuous strings of magnetite (Fig. 5-2a). Tremolite is also widespread. It may occur as thin rims surrounding diopside, as isolated subidiomorphic grains, or in olivine-magnetite-rich domains. Stability of tremolite in Almirez olivine-serpentinites allows accurate estimations of the minimum temperature of prograde metamorphism (i.e., T > 610ºC at P ~ 1.7– 2.0 GPa; López Sánchez-Vizcaíno et al. 2005). Accessory minerals in the serpentinites are pentlandite, pyrrhotite, ilmenite and titanian clinohumite.

Chl-serpentinite (samples Al06-43 and Al06-45) is poorly foliated and shows a remarkably different texture characterized by two distinct textural types of antigorite: (1) large and unoriented, euhedral antigorite grains with flakes and subhedral cores of chlorite, and (2) smaller, acicular antigorite grains with a preferred orientation 2006).

Table 5-1. Summary of petrographic and mineral features of the serpentinites from the Cerro del Almirez ultramafic body. Mineral abbreviations after Kretz (1983)

Sample	Lithology	Field occurrence	Mineral assemblage[1]						
			Atg	Ol	Di	Tr	Chl	Tlc	Mag
Al95-20	Atg-serpentinite	Foliated serpentinite. Upper part of the ultramafic body	x	x	x	x	(x)		x
Al00-02	Atg-serpentinite		x	x	x	(x)			x
Al98-04	Atg-serpentinite	Foliated serpentinite. Intermediate position in the ultramafic body	x	(x)		x			x
Al95-12	Atg-serpentinite		x	x					x
Al06-46	Atg-serpentinite	Foliated serpentinite. Near the antigorite-out isograd	x	x					x
Al06-09a	Atg-serpentinite	Foliated serpentinite. Just in the antigorite-out isograd. Small body to the W	x	(x)		x			x
Al06-43	Chl-serpentinite	Slightly foliated serpentinite. Coarse antigorite-chlorite grains. Just in the antigorite-out isograd	x	x		x	x	x	x
Al06-45	Chl-serpentinite		x	x		x	x	x	x

[1] minor phases in parentheses

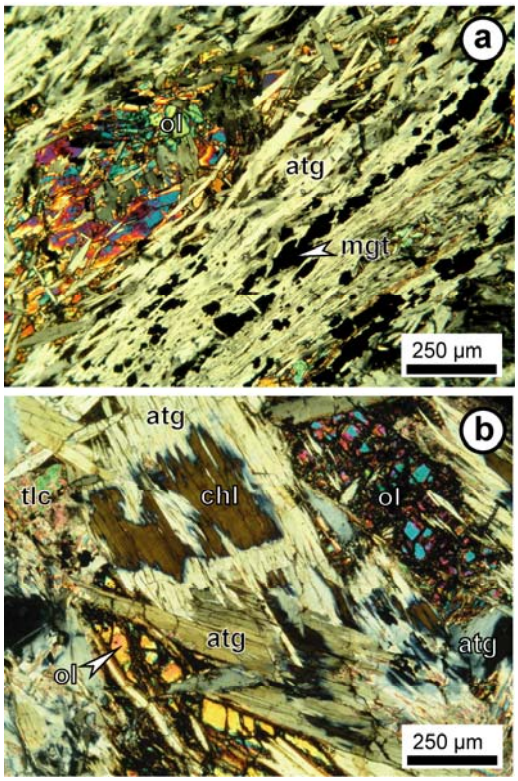

Figure 5-2: (a) Typical Atg-serpentinite with oriented antigorite, olivine aggregates and discontinuous strings of magnetite. **(b)** Representative texture of Chl-serpentinite (sample Al06-43) with large antigorite grains, chlorite cores and interstitial olivine. Mineral abbreviations after Kretz (1983).

(Fig. 5-2b). Chl-serpentinite also contains minor tremolite and interstitial olivine associated with the larger antigorite grains. Talc pseudomorphs after antigorite are common, partially replacing large euhedral antigorite, or totally replacing the smaller acicular ones. Chemical compositions of Cerro del Almirez antigorite Table 5-2 reports representative electron microprobe analyses (see López Sánchez-Vizcaíno et al. 2005 for analytical details) of antigorites in Atg-serpentinite (Al95-20) and Chl-serpentinite (Al06-43) samples from Cerro del Almirez. They are compared with a well-characterized alpine high-grade antigorite from theVal Malenco ultramafic massif (sample Mg159 of Capitani and Mellini 2004, 2006) and one of the many vein antigorites occurring in the Elba island serpentinite (sample # 7 of Viti and Mellini 1996). The Almirez antigorites of our study show compositions similar to those reported in previous studies (Trommsdorff et al. 1998). Their most important obvious feature is the high aluminium content, as evident by comparison with Val Malenco and Elba antigorites (Table 5-2). We have calculated the crystal-chemical formulae of antigorite using the ideal polysomatic formula

$$M_{3m-3}\,T_{2m}\,O_{5m}\,(OH)_{4m-6}$$

assuming m = 17, where m is the number of tetrahedral along a wave (Mellini et al. 1987), and then normalizing to the expected 4.824 total cations. The structural formula of Almirez antigorite for the lithologies and representative analyses reported in Table 5-2 are:

Atg-serpentinite:

$$(Mg_{2.584}\,Fe_{0.126}\,Al_{0.092}\,Cr_{0.016}\,Ni_{0.003}\,Mn_{0.002})_{\Sigma=2.824}\,(Si_{1.898}\,Al_{0.102})_{\Sigma=2.000}Cl_{0.003}$$

Chl-serpentinite:

$$(Mg_{2.553}\,Fe_{0.153}\,Al_{0.016}\,Cr_{0.005}\,Ni_{0.004}\,Mn_{0.002})_{\Sigma=2.824}\,(Si_{1.958}\,Al_{0.042})_{\Sigma=2.000}Cl_{0.012}$$

Using the same normalization, the structural formula of Val Malenco and Elba antigorite analyses reported in Table 5-2 are:

Val Malenco:

$$(Mg_{2.673}\,Fe_{0.113}\,Al_{0.035}\,Cr_{0.007}\,Ni_{0.003}\,Mn_{0.002})_{\Sigma=2.823}\,(Si_{1.997}\,Al_{0.003})_{\Sigma=2.000}$$

Elba:
$(Mg_{2.632}\ Fe_{0.169}\ Al_{0.005})\ \Sigma=2.806\ (Si_{2.019})\ \Sigma=2.019$

The antigorite formulae for the different Cerro del Almirez lithologies are rather similar. They are characterized by significant substitutions of Al for Si and Mg, and of Fe and Cr for Mg. The negative correlation of Al^{total} (a.p.f.u) with Si (a.p.f.u) displayed by the Cerro del Almirez antigorites (Fig. 5-3) supports a coupled substitution of Al for Si. This negative correlation holds for antigorite analyses within a single thin section and for those from the different lithologies altogether (Fig. 5-3). In detail, Atg serpentinite antigorites display higher Al^{total} contents compared with Chl-serpentinite antigorites (Fig. 5-3; Table 5-2). On the contrary, Cl contents are significantly higher in Chl-serpentinite antigorites than in those from Atg serpentinite (Table 5-2). As during optical and TEM analysis (see below) no evidence for any exotic phase included within antigorite was found, we discard the presence of Cl-bearing solid inclusions as the reason for the significant Cl amounts detected in Chl-serpentinite antigorites.

Cerro del Almirez antigorite formulae strongly differ from Al- and Cr-free antigorite from Elba. Cerro del Almirez antigorite formulae also display substantially higher Al and Cr contents than antigorite from Val Malenco. Cl contents are below detection limits in antigorite from both Elba and Val Malenco (Table 5-2).

Table 5-2. Chemical compositions of representative antigorites from Cerro del Almirez (Al#-#), compared with antigorite from Val Malenco (Mg159) and from Elba island (#7); n.d. = not determined.

Sample	Al95-20	Al06-43	Mg159	#7
Type	*Atg-serp.*	*Chl-serp.*		
SiO_2	41.16	42.54	42.75	44.82
TiO_2	0.02	0.01	0.01	n.d.
Cr_2O_3	0.43	0.14	0.38	n.d.
Al_2O_3	3.58	2.73	1.39	0.09
FeO	3.27	3.98	2.65	4.48
MgO	37.6	37.22	38.4	39.21
MnO	0.06	0.04	0.05	n.d.
NiO	0.09	0.11	0.09	n.d.
Cl	0.04	0.16	n.d.	n.d.
SUM	86.39	86.95	85.72	88.6

n.d. not determined

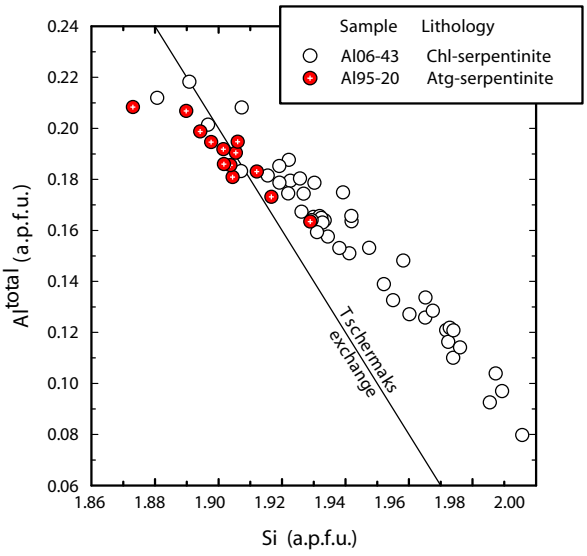

Figure 5-3: Chemical data for representative antigorites from different serpentinite types from Cerro del Almirez. Data are given as Al^{total} versus Si atoms, calculated on the basis of the ideal antigorite polysomatic formula (m = 17) and normalized to 4.824 total cations. The line represents the ideal Tschermak exchange line.

We have plotted the Tschermaks tie-line in Fig. 5-3, from $(Al_{0.06}Si_{1.97})$ to $(Al_{0.24}Si_{1.88})$. Represented data show Al excess for most of the Chl-serpentinite antigorites and for the Si-richest ones (Si>1.91) from Atg-serpentinite. For instance, 0.08 Al atoms are already present for Si = 2.00. As no tetrahedral site is available, Al excess may be expected to be octahedrally coordinated (^{VI}Al). All along the replacement, excess Al atoms seem to enter octahedral coordination.

This excess may become even more remarkable in the case that iron may occur, at least in part, as ferric iron. From this evidence, we draw two remarks:

(a) possible achievement of charge balance in Cerro del Almirez antigorites, through octahedral and/or H^+ vacancies (as already discussed for lizardite by Fuchs et al. 1998).

(b) stabilization of ^{VI}Al coordination under the HP conditions of the Almirez ultramafic rocks.

The high Al content of the Cerro del Almirez antigorites deserves further consideration because of its importance in the crystal chemistry and stability of serpentine minerals. Experimental work (Bromiley and Pawley 2003) has shown that a few percent of Al_2O_3 in antigorite shifts its stability field to significantly higher pressure and temperature. Thus, the high Al content of Cerro del Almirez antigorites may be a response to the high P and T conditions deduced for the Cerro del Almirez serpentinites (López Sánchez-Vizcaíno et al. 2005). Nevertheless, this point deserves careful consideration, because of the known association between antigorite and chlorite in the Cerro del Almirez thin sections (sample Al06-43). Preliminary X-ray powder diffraction pattern for a representative, pure antigorite from Atg-serpentinites, i.e., Al00-02, seems to favor the presence of isomorphous aluminium in antigorite, rather than the occurrence of intermixed chlorite lamellae, as no chlorite peak occurs. This conclusion seems further confirmed also by the observed contraction of the d_{001} spacing, with respect to that in Al-poor antigorites (e.g., Viti and Mellini 1996). The value of 7.216 Å measured for Al00-02 matches the 7.22 Å spacing determined by Bromiley and Pawley (2003) for their BM1913.87 specimen, which has 3.06 wt. % Al_2O_3.

At this stage, however, we may still wonder whether the aluminium content is a real fact of the Cerro del Almirez antigorites or an analytical artefact. Therefore, in order to check for any chlorite-antigorite fine intergrowth, we carried out detailed Transmission Electron Microscopy (TEM) analysis as reported below.

Table 5-3. Microstructural features for the Cerro del Almirez antigorites.

Sample	Order	Size	Twins	Offset	Wobbling	*m*	Other features
Al95-20	good	wide	no	no	no	17 (16)	
Al00-02	good	wide	no	no	no	17 (16)	
Al98-04	good	wide	no	no	no	16 (15)	
Al95-12	good	wide	no	no	no	17 (16)	
Al06-43	poor	lamellar	yes	rare	no	14 to 16	Two-layer polytypes
Al06-45	poor	lamellar	yes	rare	no	16	
Al06-09a	poor	lamellar	yes	rare	no	15 to16	reaction rims
Al06-46	poor	lamellar	yes	rare	no	16 (15)	reaction rims

"Order" refers to the absence of extended defects, such as polysomatic faults, twins, modulation dislocations and similar. "Wide" and "lamellar" in the Size column mean ordered domains larger than the observation field or lamellar appearance within the observation field, respectively. Numbers in brackets give the less abundant m values.

5.4 Order and disorder in the Cerro del Almirez antigorites

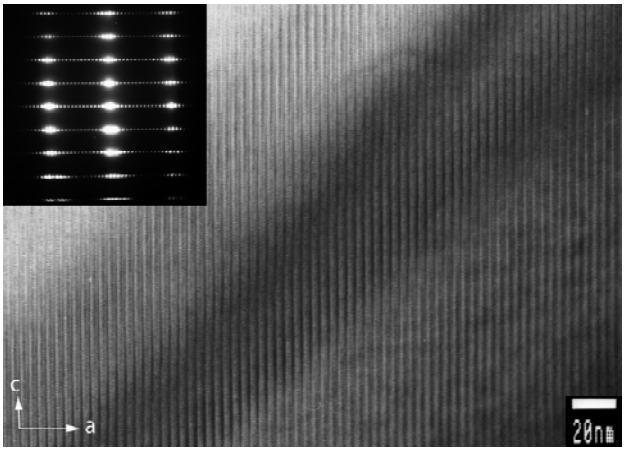

Figure 5-4. Lattice image with [010] beam incidence for ordered antigorite (m = 17) from Al95-20 Atg-serpentinite, with SAED in the inset. No structural defect can be seen.

On the basis of their TEM microstructures (summarized in Table 5-3), we have classified the Cerro del Almirez antigorites into two main groups: "ordered" and "disordered" antigorites. The first group contains samples Al95-20, Al00-02, Al98-04 and Al95-12, namely antigorites from Atgserpentinites cropping out from the summit of the Cerro del Almirez down to a few meters from the contact with Chl-harzburgites (Fig. 5-1). Disordered antigorites are found in Atg-serpentinites and Chl-serpentinites occurring within a narrow zone close to the boundary separating serpentinites from Chl-harzburgites (samples Al06-43, Al06-45, Al06-09a and Al06-46; Fig. 5-1). By "order"we refer to the absence of extended defects, such as polysomatic faults, twins, modulation dislocations and similar. Point defects or any other features affecting site-ordering are not considered as "disorder".

Antigorite crystals from top of Cerro del Almirez are exceptional in terms of their crystal order compared with antigorites from other occurrences worldwide (e.g., Veblen and Buseck 1979; Mellini et al. 1987; Otten 1993; Uehara and Kamata 1994; Viti and Mellini 1996; Uehara 1998; Auzende et al. 2002, 2006). Lattice images of Al95-20 and Al00-02 (Fig. 5-4) appear completely regular, with almost no evident polysomatic fault over micrometric distances. Lattice fringes run straight, without wobbling effect. No (001) twin may be found, at difference from their usual occurrence elsewhere. Selected Area Electron Diffraction (SAED) (inset of Fig. 5-4) confirms the previous appraisal, by showing well sharp spotty patterns, with many superlattice reflections and no offset.

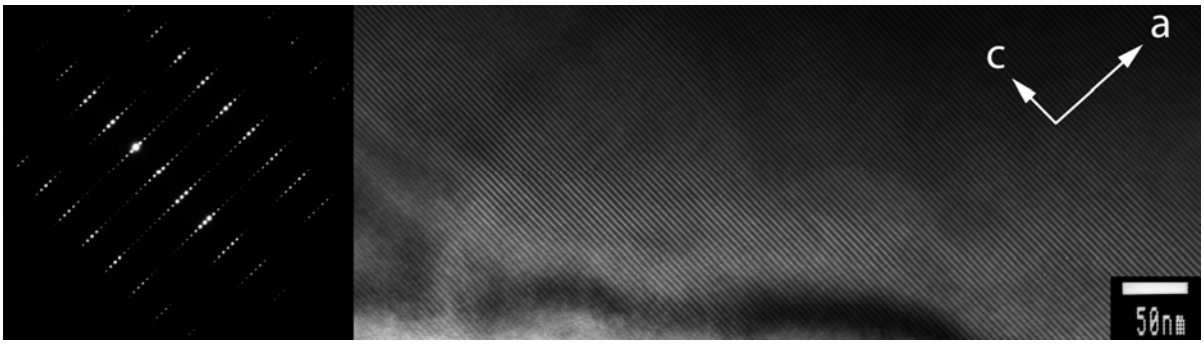

Figure 5-5. Lattice image with [010] beam incidence for ordered antigorite (m = 16) from Al98-4B Atg-serpentinite, with SAED in the inset. No structural defect can be seen.

Most of the SAED patterns of ordered antigorite reveal the presence of the polysomes m = 17 and some have m = 16. In contrast to lattice images, SAED patterns represent a synthetic view of wide regions. Due to this property, the antigorites from the top of Cerro del Almirez may produce SAED patterns still with sharp but doubled superlattice reflections. This feature, not evident in lattice images, may be interpreted as deriving from the association of domains with different polysomes close in modulation wavelength (e.g., m = 16 and 17). Strong polysomatic order characterizes also antigorites from samples Al98-04 and Al95-12 (Fig. 5-5), which were sampled at intermediate levels between the summit of the Cerro del Almirez and the contact with Chl-harzburgites (Fig. 5-1). Whereas antigorite in sample Al95-12 most commonly has polysomes with m = 17, m may decrease to 16 or even 15 in sample Al98-04.

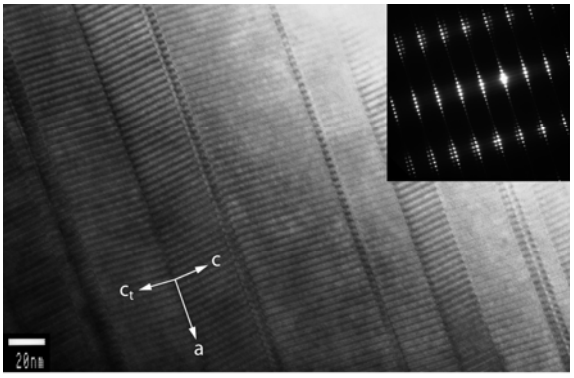

Figure 5-6 Lattice image for (001) twinned antigorite (m = 16) from Al06-46 Atg-serpentinite, with SAED in the inset. The specimen was sampled close to the contact (Fig. 1). Twin lamellae pervasively extend throughout the whole crystal

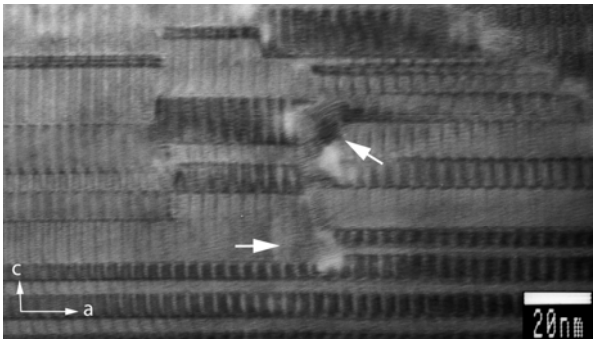

Figure 5-7. Lattice image for (001) twinned antigorite from Al06-46 Atgserpentinite. The specimen was sampled close to the contact (Fig. 1). Twin lamellae pervasively extend throughout the whole crystal. They are laterally interrupted, with transitional curved microstructures (arrows) accommodating the mismatching twin lamellae.

More disordered antigorites occur close to the contact (samples Al06-43, Al06-45, Al06-9A, Al06-46). By contrast with ordered antigorites, they show evident (001) twins (Fig. 5-6). Twin frequency is however limited, at least with respect to the usually polysynthetically twinned antigorites from localities other than Cerro del Almirez. SAED patterns (inset of Fig. 5-6) often reveal that one twin orientation may be dominant over the other, as also evident in low magnification images. Slight, rare offset may be present in the SAED. In some cases (mainly Al06-46 and Al06-9a) twin lamellae are laterally interrupted (Fig. 5-7). From one side of the interruption to the other, different twin patterns occur. Corresponding to the twin interruption, curved structural arrangements connect the two mismatching twin patterns. These irregular transitional structures are interpreted as the reaction rims of the antigorite recrystallization process. Rare evidence for doubled c polytypes (Grobéty 2003) may be found in Al06-43; the doubled periodicity may be seen both in the SAED pattern (inset of Fig. 5-8), as well as in the modified contrast of lattice fringes (Fig 5-8).

5.5 Discussion

5.5.1 Bimodal antigorite occurrence

The most striking feature of the Cerro del Almirez antigorites is their highly polysomatic ordered nature. Similar highordered antigorites have only been reported in sample Mg159 of the Val Malenco high-grade serpentinites (Mellini et al. 1987). However, order and disorder features distinguish all the serpentinites found more than a few meters away from the Chl-harzburgites, with respect to the serpentinites found in the narrow belt close to the boundary between serpentinites and Chl-harzburgites. In fact, at the TEM scale, upper antigorites are extremely ordered, with no evident disorder effect, while in contact antigorites (001) twins are common. Furthermore, contact specimens may show also other features, usually present in quickly grown, not equilibrated antigorites, such as offset SAED patterns, wobbling of lattice fringes, dislocation modulations (see Otten 1993, for definition of these terms), and intracrystalline suture zones akin to what was reported in Fig. 9 by Auzende et al. (2006).

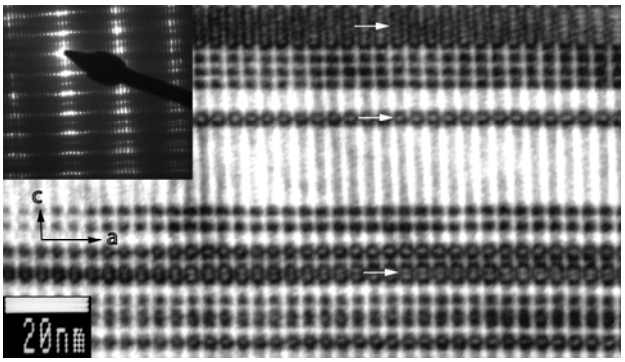

Figure 5-8. Lattice image for (001) twinned antigorite (m = 15) from Al06-43 Chl-serpentinite, with SAED in the inset. The specimen was sampled in the Chl-serpentinite pockets occurring at the Atg-serpentinite–Chl-harzburgite contact (Fig. 1). Two-layer polytypes are evident as doubled *c* periodicity in the SAED pattern; their occurrence is indicated by the arrows

Based upon field evidence, the contact between the overlying Atg-serpentinite and lower Chl-harzburgite is sharp and may be followed approximately all around the Cerro del Almirez Massif (Fig. 1). All our data seem to support the interpretation by Trommsdorff et al. (1998), favouring abrupt evolution from Atg-serpentinite to Chl harzburgite (antigorite-out boundary). The sharp discontinuity affects also the antigorite microstructure distributions. In fact, there is no variation within ordered antigorite from the top of the mountain down to a few meters from the contact. Only in this narrow region, antigorites from Atg-serpentinites (Al06-46 and Al06-9a) show disordered features (mostly appearance of twins and reaction rims) that anticipate the Atg-breakdown limit.

Chl-serpentinites occur as sporadic pockets, 1- or 2-m thick, where the normal fine-grained serpentinites change to large antigorite and chlorite crystals. We interpret Chl serpentinites as the result of recrystallization of Atg-serpentinites under-fluid dominated conditions near the Chlharzburgite- serpentinite boundary. The breakdown of serpentinites to Chl-harzburgites is accompanied by release of high amounts of high-temperature and high–pressure water-rich fluids (e.g., in the order of 9 wt.% in the case of a 25% chlorite modal content in the Chl-harzburgites) that circulate along the reaction boundary, locally enhancing dissolution and coarsening of fine-grained

antigorites, finally resulting in the very coarse antigorites observed in Chl-serpentinites pockets. Recrystallization explains the disordered features of antigorite in the Chl-serpentinite. In fact, they are formed by fast recrystallization of the previously annealed fine antigorites, close to the Chl harzburgite boundary. In addition, part of the antigorite aluminium content was partitioned into newly formed chlorite. On the contrary, and in the lack of any solid inclusions of minerals such as iowaite within antigorite, the observed Cl-enrichment of the Chl-serpentinite antigorites must be due to the concentration of Cl in the newly formed antigorite owing to preferential partitioning in this mineral with respect to newly formed chlorite (Cl<0.03 wt.%).

5.5.2 Antigorite and metamorphic grade

Cerro del Almirez antigorites show higher Al content, which may attain up to 28 mol% chlorite component in sample Al95-20 (Trommsdorff et al. 1998), compared with antigorites from other high-grade localities (Table 5-2). Our TEM study shows that no intermixed chlorite lamella occurs in ordered or disordered antigorites. We therefore conclude that the high aluminium contents of the Cerro del Almirez antigorites (Table 5-2; Fig. 5-3) have to be explained only by the isomorphic replacement of aluminium for silicon
and magnesium.

Earlier field and experimental works suggested variations in the polysomatism of antigorite; these variations have been related to metamorphic grade (Mellini et al. 1987). All the investigated Almirez antigorites present mvalues of, or close to, 17 (number of tetrahedra along a wave), with a slightly wider range, and shorter periodicities, in antigorites close to the contact with Chl-harzburgite. In particular, m is 15–17 and 14–16 in ordered and more disordered antigorite, respectively (Table 5-3). These ranges are narrower than found elsewhere. For instance, Mellini et al. (1987) found m = 14–19 in the Val Malenco antigorites (up to 23 if the Oberhalbstein/Platta antigorites are included). Wide ranges occur also in the Saganoseki specimens (m ~ 12–20; Uehara and Kamata 1994) or in the Elba vein antigorites (m between 13 and 19; Viti and Mellini 1996). In the case of Cuban antigorites, Auzende et al. (2002) found ordered specimens with lattice parameter of 37 Å (that should correspond to m = 14–15) in the Escambray serpentinites and a higher abundance of defects in the Zaza Zone antigorites, but with lattice parameter still around 37 Å. Finally, Auzende et al. (2006) reported m values varying between 16 and 20 for the Monviso antigorites, and between 16 and 21 for the Erro Tobbio ones.

The Cerro del Almirez antigorites have m values well within the known range, either in the case of slightly irregular antigorites from the contact or the very regular antigorites away from the contact. Furthermore, the latter have m values mostly close to 16–17. Apparently, these values characterize well-equilibrated antigorites, such as the ones occurring in the metamorphically annealed Mg159 specimen (Mellini et al. 1987; Capitani and Mellini 2004, 2006) in good agreement with the high-grade metamorphic evolution of Cerro del Almirez.

The slightly different polysomes occurring within Atg serpentinites [m = 17(16)] and in Chl serpentinites [m = 14(16)] might be interpreted in two different ways. By the first

one (schematized as "thermodynamic control", as based upon the existence of equilibrium even in Chl serpentinites), the difference might be interpreted as related with the slightly different chemical compositions. Namely, for the same P and T conditions, the m value would decrease with the decreasing Al-content, thus matching the m = 14 value experimentally determined for Al-free antigorite by Wunder et al. (2001). By the second approach (schematized as "kinetic control") the difference would be related only with the absence of a long annealing metamorphic history in Chl-serpentinites with respect to Atg-serpentinites, as previously observed in short-wave, low-temperature vein antigorites by Viti and Mellini (1996). In conclusion, the pervasive high-ordered nature of the Almirez antigorites, their high-aluminium contents and the narrow variations in the polysomatism are consistent with the high-pressure and high-temperature metamorphic evolution of this massif.

5.5.3 Importance for future research

Mg159 from Val Malenco has been an important reference specimen in the antigorite saga. In fact, its purity, its exceptional crystal order, its large crystal size has allowed us to overcome the experimental difficulties that previously prevented the crystal structure analysis (Capitani and Mellini 2004, 2006). Owing to its homogeneous ordered structural state, it has been successfully used also for controlled experimental investigation on the antigorite stability field (Ulmer and Trommsdorff 1995). In our opinion, the ordered Cerro del Almirez antigorites, cropping out far from the contact, possess the same potential and may well become another reference material in the study of the antigorite properties. In particular, taking into account the large aluminium content, they may be useful in the study of the serpentinites phase relations within the $FeO–MgO–Al_2O_3–SiO_2–H_2O$ (FMASH) system. We stress here also the absence of any low-grade serpentine mineral (such as chrysotile, polygonal serpentine or lizardite). This absence indicates that the Cerro del Almirez serpentinites did not experience any retrograde evolution, capable of obliterating or modifying the original features, and still increases the advantage in exploiting these specimens for future studies.

5.6 Conclusions

The Cerro del Almirez Atg-serpentinites are exceptional, being characterized by a very ordered antigorite, with m = 17. This exceptional antigorite crystallinity derives from the metamorphical annealing of the Cerro del Almirez ultramafic rocks under high-pressure and high-temperature conditions. These were very close to the maximal antigorite thermal stability conditions (640ºC at 1.7–2.0 GPa; Trommsdorff et al. 1998; López Sánchez-Vizcaíno et al. 2005).

These antigorites are also characterized by an important aluminium content (Al_2O_3 in the order of 3.5–4.0 wt %), that definitely contributes to the high-temperature stabilization of antigorite (Bromiley and Pawley 2003).

Owing to their extreme order, and the high-aluminium content, the Cerro del Almirez antigorites may become an important reference material in the study of the FMASH

system. As their order was achieved after a long metamorphic annealing at high-pressure and high-temperature conditions, they may be a proxy of the state of serpentinites at depth, such as in subduction zones. Finally, the extreme microstructural homogeneity may also explain the sharp antigorite-out reaction. In fact, only a few meters from the antigorite-out isograd, where antigorite transforms to olivine + enstatite + chlorite + water, antigorite shows limited microstructural variations. In this narrow zone, [001] stacking faults and (001) twins become evident, together with other disorder features and reaction rims. Disorder arises because of the antigorite recrystallization, accompanied by aluminium partitioning into chlorite. These processes may be locally evident, as resulting into pockets of recrystallized, large antigorite crystals associated with large, newly formed chlorites.

Acknowledgments

We wish to thank B. W. Evans and B. Wunder for their review of this manuscript. This work was supported by the Spanish "Ministerio de Educación y Ciencia" through research grant CGL2006-04440/BTE and by the Junta de Andalucía research groups RNM-131, RNM-145, RNM-148 and research proyect RNM-327. JAPN is supported by grant AP2005-060 from the "Programa de Formación del Profesorado Universitario". MM is grateful to the Secretaría de Estado de Universidades e Investigación del Ministerio de Educación y Ciencia de España for the invitation to spend a sabbatical term at Universidad de Granada (Grant SAB2005-0191). We thank M.A. Abad for technical assistance in the TEM facilities (U. Granada).

Lithos (2008) 156:679–688
DOI doi: 10.1016/j.lithos.2008.10.008
Received: 28 May 2008 / Accepted: 9 October 2008 / Published online: -

6 Breakdown mechanisms of titanclinohumite in antigorite serpentinite (Cerro del Almirez massif, S. Spain): A petrological and TEM study

López Sánchez-Vizcaíno, V[1*]· Gómez-Pugnaire MT[2,3]· Garrido CJ[3] · Padrón-Navarta, JA[2] · Mellini M[4]

Veins with titanclinohumite (Ti-Chu) and olivine occur close to clinopyroxenite layers scattered through the antigorite serpentinites from the Cerro del Almirez ultramafic massif (Sierra Nevada, Betic Cordillera, S. Spain). They formed at estimated maximum P-T conditions of 1.3 GPa and 475 °C, due to simultaneous breakdown of former Ti-rich clinopyroxene and brucite in the presence of 6 vol. % of free water. Breakdown of Ti-Chu single crystals to an olivine + ilmenite framework was gradual: small relict patches of Ti-Chu appear even at some distance from the reaction front and ilmenite grains coarsen and become less frequent away from the front. Detailed TEM data support this interpretation: olivine in equilibrium with Ti-Chu is structurally and chemically homogeneous, whereas Ti-Chu shows ubiquitous intermixed (001) olivine lamellae. Product olivine close to the front shows pervasive and continuous (001) Ti-Chu lamellar faults. These become less frequent away from the reaction front, due to the completion of the Ti-Chu breakdown. This textural sequence suggests both progressive transfer of Ti to ilmenite and progressive release of H_2O during the breakdown of Ti-Chu. A second hydration breakdown reaction can be observed very locally, in the contact between Ti-Chu and diopside, producing a symplectitic intergrowth of tremolite and ilmenite. Textural features of both reactions point to a very limited availability of water during Ti-Chu breakdown. This suggests that veins operated as closed systems. Complete obliteration of Ti-Chu owing to the antigorite dehydration breakdown can be observed in the Almirez massif rocks. This precludes OH-Ti-Chu from Atg-serpentinite as an efficient water or titanium carrier into deep mantle in hot subduction zones.

Keywords: Antigorite serpentinite, Titanclinohumite, Vein, Breakdown, Dehydration

1. Departamento de Geología, Universidad de Jaén Linares, Spain.
2. Departamento de Mineralogía y Petrología, Universidad de Granada, Spain.
3. Instituto Andaluz de Ciencias de la Tierra (IACT), Granada, Spain.
4. Dipartimento di Scienze della Terra, Universitá di Siena , Italy

6.1 Introduction

Incorporation and transport of water into the mantle has received great interest in the last years, as it is a relevant process for explaining the mantle's physical and chemical properties. Following the pioneer works of Kitamura et al. (1987) and Miller et al. (1987), recent studies have paid special attention to the incorporation mechanisms of OH planar and point defects into olivine, the main nominally anhydrous mineral of the upper mantle. Berry et al. (2005) experimentally correlated the OH incorporation in olivines from spinel peridotite with planar and point, Ti-associated defects. In fact, titanclinohumite, an OH and Ti-bearing phase, is believed to be the main carrier of water in upper mantle olivines (Berry et al., 2005). Further TEM studies carried on in experimental (synthetic lherzolite; Wirth et al., 2001) and natural systems (titanchondrodite and titanclinohumite bearing garnet-pyroxenite from Dabie Shan (China); Hermann et al., 2007) have demonstrated the occurrence in olivine of titanclinohumite lamellae, which allow the presence of H_2O and TiO_2 in this mineral.

Titanclinohumite (Ti-Chu after Kretz, 1983), $[4(M_2SiO_4)M_{1-x}Ti_x(OH,F)_{2-2x}O_{2x}]$ ($0<x<0.5$) is widespread as a common accessory mineral in several rock types (Trommsdorff and Evans, 1980). In metamorphic ultramafic rocks, Ti-Chu occurs from antigorite serpentinite to chlorite harzburgite and garnet peridotite (López Sánchez-Vizcaíno et al., 2005 and references therein). In these rocks Ti-Chu may play a significant role in the incorporation and release of titanium. In fact, oriented ilmenite rods within olivine from several garnet peridotite localities from the Eastern Alps have been interpreted as produced by dehydration of titanclinohumite defect layers at P~30 kbar and T~800 °C (Risold et al., 2001) due to continuous breakdown of this mineral to olivine plus ilmenite (Trommsdorff et al., 2001; Risold et al., 2003). Ilmenite in these rocks has been also attributed to exsolution of Ti incorporated to olivine at very high pressures (Dobrzhinetskaya et al., 1996; Green et al., 1997).

Another major interest of planar intergrowths of Ti-Chu within olivine is linked to their possible preservation beyond the total breakdown of the rock forming hydrous humite minerals (Hermann et al., 2007), thus acting as important reservoirs forwater and High Field Strength Elements (HFSE: Nb, Ta, Zr and Hf) in subduction zones, and for water in the subcontinentalmantle (Scambelluri et al., 2001; Berry et al., 2005; Garrido et al., 2005; López Sánchez-Vizcaíno et al., 2005; Hermann et al., 2007). In consequence, the study of the breakdown processes affecting Ti-bearing humite minerals – especially Ti-Chu – becomes a key point for the knowledge of the behavior of water and HFSE in subduction settings. The Cerro del Almirez ultramafic massif (Sierra Nevada, Betic Cordillera, SE Spain) provides a matchless example of antigorite serpentinite (Atg serpentinite) and chlorite-harzburgite (Chl-harzburgite; olivine + enstatite + chlorite + tremolite + magnetite) with spinifex-like texture separated from each other by a rather sharp boundary, interpreted as the antigorite-out dehydration isograd at highpressure (1.7–2.0 GPa) and temperature (640 °C) conditions (Trommsdorff et al., 1998; López Sánchez-Vizcaíno et al., 2005). This ultramafic massif is, thus, an important locality for the study of the Ti-Chu behaviour during subduction metamorphism at lower temperatures and pressures than those reported in the Alps (Risold et al., 2001) and Dabie Shan (Hermann et al., 2007).

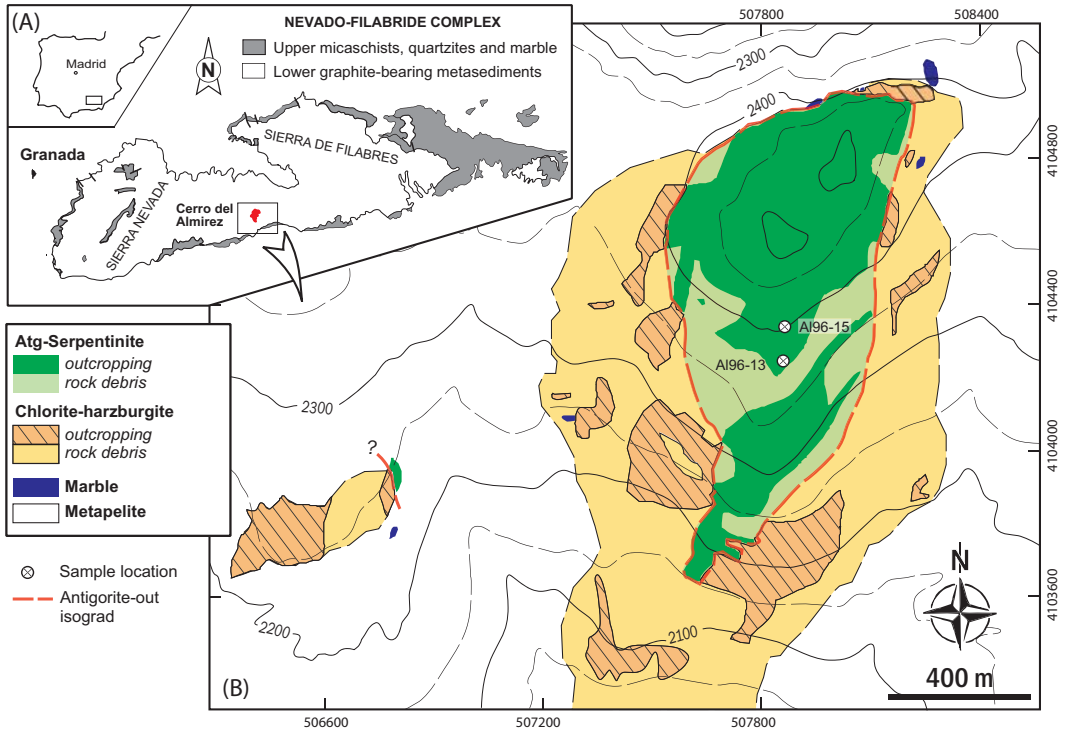

Figure 6-1. (a) Outline geological map of the Nevado-Filábride Complex of the Betic Cordilleras with location of the Cerro del Almirez outcrop. (b) Geological map of the Cerro del Almirez massif (modified after Schönbächler, 1999; Hürlimann, 1999) showing the distribution of the two main ultramafic rock types (antigorite serpentinite and chlorite harzburgite), the antigorite-out isograd and the location of the studied samples of Ti-Chu-olivine veins. Country rocks mainly consist of metapelites and small marble outcrops. Coordinate frame system is WGS (1984), UTM 30N.

In Cerro del Almirez, diverse Ti-Chu generations, with different textures, compositions, and breakdown mechanisms (Trommsdorff et al., 2001), occur both before and beyond the antigorite breakdown reaction isograd. OH titanclinohumite occurs in Atg-serpentinite as disseminated grains and veins, whereas F-OH-titanclinohumite occurs in Chl-harzburgite as porphyroblastic grains, in veins, and as irregular and lamellar intermixtures within prograde olivine.

The origin, evolution and breakdown processes in F-OH-Ti-Chu and their possible implications in subduction environments were investigated in a previous paper (López Sánchez-Vizcaíno et al., 2005). In this paper we focus on the breakdown reactions of OHtitanclinohumite (Ti-Chu hereinafter) from the Cerro del Almirez Atg-serpentinites, with special emphasis on the role of different Tibearing phases at the micro- and nano-scale. Petrographic and TEM observations of Ti-Chu-olivine veins demonstrate that the apparent sharp and discontinuous breakdown reaction occurred through several intermediate reaction stages, wherein titanium was first partly hosted in Ti-Chu lamellae in olivine before being totally transferred to ilmenite. Furthermore, we describe for the first time in this massif, the existence of another simultaneous Ti-Chu breakdown reaction, which occurs in contact with diopside to produce tremolite and ilmenite.

6.2 Field description and petrography

The Cerro del Almirez ultramafic massif (0.4 km thick, and 2 km wide) is the largest lens of ultramafic rocks within the upper sequence of the Nevado-Filábride Complex of the Betic Cordilleras (Fig.6-1a and b). Ultramafic rocks in the Nevado-Filábride Complex are surrounded by Paleozoic metasediments (Gómez-Pugnaire et al., 2000, 2004), with dominant pelitic rocks interbedded with quartzite and minor marble. The whole sequencewasmetamorphosed during the Miocene under eclogite facies conditions, recording peak metamorphic conditions of ~2 GPa and ~650 °C (Trommsdorff et al., 1998; Puga et al., 1999; López Sánchez-Vizcaíno et al., 2001, 2005).

The petrology and field relationships of the ultramafic lithologies cropping out in the Almirez massif (Atg-serpentinite and Chl-harzburgite) have been described elsewhere (Trommsdorff et al., 1998; Puga et al., 1999; Padrón-Navarta et al., 2008). The massif is composed of two lithological domains: an upper domain of strongly foliated antigorite serpentinite schists (Atg-serpentinite) overlying a lower domain of variably textured (spinifex-like to granular) enstatite + olivine + chlorite + tremolite rocks (Chl-harzburgite) (Fig. 6-1b). The Atg-serpentinite domain, which extends from the antigorite-out isograd up to the summit of the massif (Fig. 6-1b), is lithologically and structurally homogeneous, despite the local occurrence of cm to dm-scale clinopyroxenite layers and lenses, minor boudins of rodingite, and the titanclinohumite+olivine veins studied in this work. Oriented domains of antigorite define a low-dipping foliation, which locally contains a distinct stretching lineation defined by elongated magnetite-chlorite aggregates.

The sharp lithological boundary separating the Atg-serpentinite domain from the underlying Chl-harzburgite domain crosscuts the Atg-serpentinite foliation and constitutes the antigorite-out isograd (Trommsdorff et al., 1998). Within the Atg-serpentinites, Ti-Chu appears as three main textural types, usually associated to centimetric up to 1 m thick discontinuous clinopyroxenite layers (López Sánchez-Vizcaíno et al., 2005):

i) Rock-forming Ti-Chu in Atg-serpentinites occurring as small, mm-sized, granoblasts, associated with primary, titanium-rich, dusty clinopyroxene and, typically, close to the Ti-Chu-rich veins. Ti-Chu forms polygonal textures with antigorite, olivine and clear diopside. In some samples, Ti-Chu has also been found as microscopic lamellar intermixtures (3 to 60 μm in thickness and up to 0.5 mm in length) with olivine.

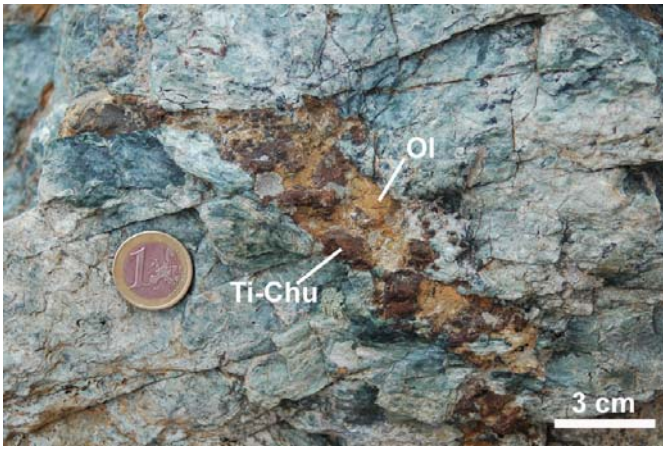

Figure 6-2. (a) Field occurrence of a representative Ti-Chu (dark red) – olivine (light brown) vein in Atg-serpentinite from the Cerro del Almirez massif. Mineral abbreviations after Kretz (1983).

ii) Deformed Ti-Chu and olivine veins (2–5 cm thick) (Fig. 6-2)

scattered through the upper part of the Cerro del Almirez massif (Fig. 1b) and, at places, associated with white, massive, aggregates of diopside fibres after former clinopyroxenite layers. This is the most common occurrence of Ti-Chu in Atg-serpentinite. Ti-Chu-rich veins are folded with axial planes parallel to the schistosity of Atg-serpentinites, indicating that their formation predates the last deformation event recorded in these rocks. In the veins, Ti-Chu forms up to 3 cm reddishbrown knob-like grains together with olivine of similar size and minor diopside, chlorite, and magnetite inclusions. At the microscope, perfect optical continuity can commonly be observed between Ti-Chu and olivine, indicating the simultaneous growth of both minerals (Trommsdorff and Evans, 1980). Olivine and Ti-Chu are locally stuffed with up to 0.5 mm long, needle-shaped inclusions of antigorite. This is the only textural type in which Ti-Chu grains can be found partially or totally replaced by breakdown reactions (1) and (2).

iii) Strings of small Ti-Chu grains in exsolution lamellae of dusty clinopyroxenes from the clinopyroxenites (see López Sánchez-Vizcaíno et al., 2005 for more details). Compositions of Ti-Chu in the three textural types (López Sánchez- Vizcaíno et al., 2005, their Fig. 6-3 and Table 6-3) are close to the maximal Ti saturation (X_{Ti}=0.5) at values of about X_{Ti}=0.42–0.47. F-contents are below detection limits. X_{Mg} ranges from 0.891 to 0.925 and is controlled by the bulk rock composition. Systematic compositional differences are not observed between Ti-Chu from different textural types, nor as compositional zoning within individual Ti-Chu grains. On the contrary, olivine in textural equilibrium with Ti-Chu shows some compositional variation (López Sánchez-Vizcaíno et al., 2005, Fig. 4, Table 6-4). The mean range of the Fo-content of olivine from Atg-serpentinite (90.4–93.5%) matches the values for Ti-Chu veins (89.5–92.1%).Mn and Ni contents are very similar in both olivine types (0.006–0.008 a.f.u. Mn and 0.003–0.006 a.f.u. Ni), although the highest contents of both elements always occur in Atg-serpentinite.

6.2.1 Ti-Chu breakdown reactions in veins

We observed two different Ti-Chu breakdown reactions. The first reaction is ubiquitous in all the studied veins samples, but is only rarely observed in the rock-forming Ti-Chu within Atg-serpentinite. Ti-Chu grains hosted in veins commonly appear partially or completely replaced by olivine (dusty olivine in the sense of Trommsdorff and Evans, 1980) choked with tiny ilmenite granules and scarcer magnetite (Fig. 6-3a), in accordance with equation

Ti-Chu → 8 olivine + ilmenite (+magnetite) + H_2O (1)
(Trommsdorff and Evans, 1980).

Perfect optical continuity is observed between Ti-Chu and the new dusty olivine, as well as between dusty olivine and clear, vein-forming olivine.

At the thin section scale, Ti-Chu grains (centimetric in size), completely transformed to dusty olivine, coexist with Ti-Chu grains lacking textural evidence of breakdown, or showing incipient or limited transformation to olivine and ilmenite. The onset of Ti-Chu

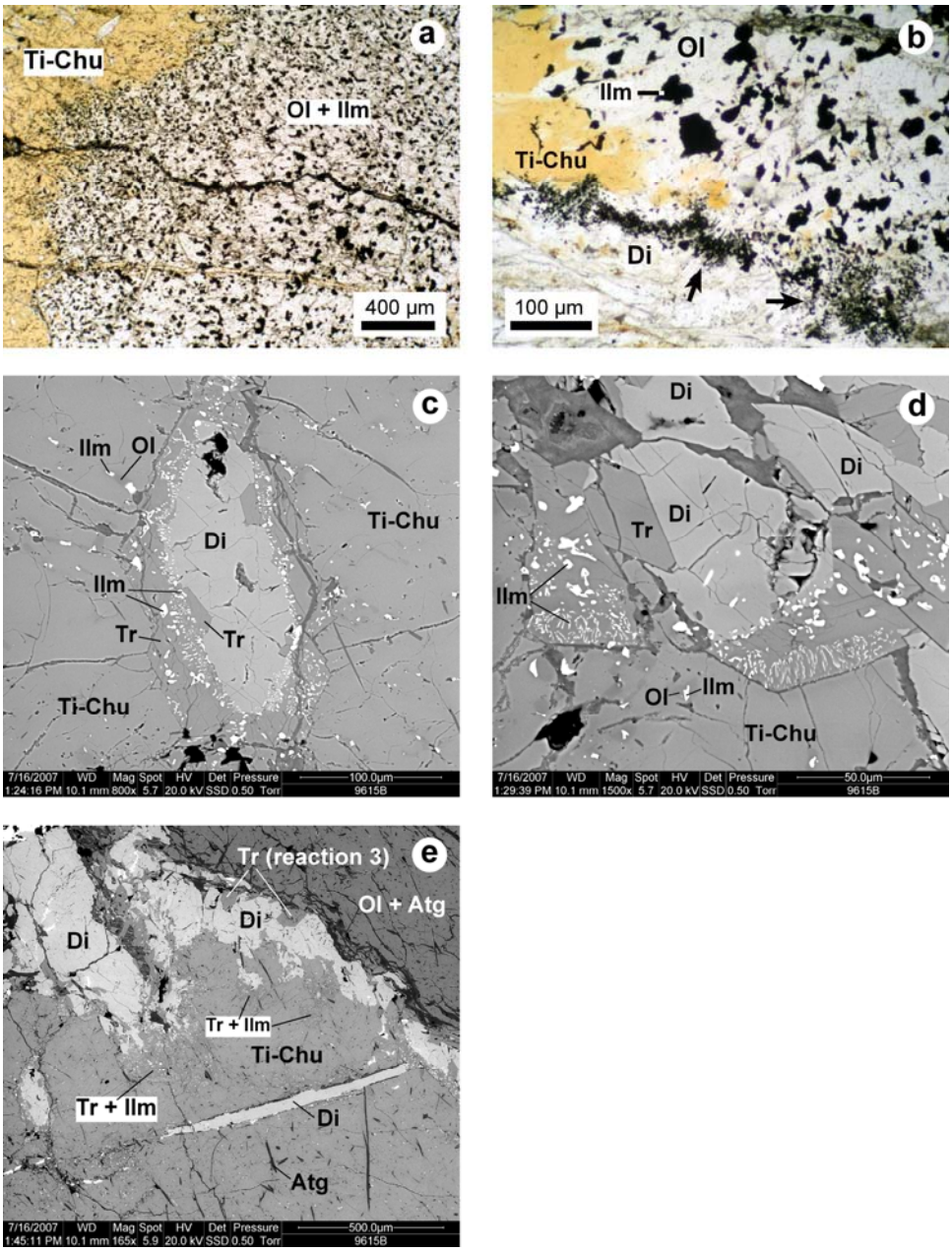

Figure 6-3. Microphotographs (one nicol) and scanning electron microscopy (SEM) images showing representative textures produced by Ti-Chu breakdown reactions (Sample Al96-15B). (a) Reactant (Ti-Chu) and products (olivine+ilmenite) of breakdown reaction (1) (see text). Note the irregular reaction front and the grain coarsening of ilmenite (black) with distance to the front. Both Ti-Chu and olivine are cut by late serpentinite veins. (b) Partially transformed Ti-Chu grain owing to breakdown reactions (1) and (2). The contact between product olivine-ilmenite and Ti-Chu is very curly in detail. Small relic patches of Ti-Chu (orange in color) remain within newly formed olivine. Products of reaction (2) appear as a dark rim (arrows) of symplectitic ilmenite and tremolite (not to be recognized in this photograph) in the contact with diopside. (c) Diopside inclusion within Ti-Chu and rimmed by the symplectitic intergrowth of ilmenite and tremolite due to reaction (2) (see text). Onset of Ti-Chu transformation producing granular olivine and ilmenite due to reaction (1) can be also observed in the upper left part of the image. (d) Details of the textural transformation of ilmenite (wormy to granular) within the newly formed tremolite. (e) Evidence of tremolite formation from diopside by different metamorphic reactions, (2) or (3) (see text for details), depending on the mineral in contact with diopside: Ti-Chu in the lower part of the image (reaction (2)) or antigorite and olivine in the upper right part of the image (reaction (3)). Mineral names abbreviations after Kretz (1983).

transformation is usually observed within Ti-Chu single grains in the form of granular ilmenite and magnetite associated with xenomorphic olivine patches in optical continuity with host Ti-Chu. The progress of the breakdown reaction produces a framework of olivine with granular ilmenite inclusions, both separated from the host Ti-Chu by a convoluted and very irregular reaction front (Fig. 6-3a and b). Product olivine is always a single crystal, most commonly in perfect optical continuity with reactant Ti-Chu. This possibly suggests that the replacement of Ti-Chu by olivine is topotactic and does not involve nucleation of new olivine but just of oxides.

Within the olivine-ilmenite framework, small orange, neat relic patches of Ti-Chu can be found, even at some distance from the reaction front (Fig. 6-3b). The Ti-Chu chemical composition remains almost constant in accordance with the univariant nature of the breakdown reaction (Trommsdorff et al., 2001). On the contrary, product olivine has higher Fo contents (92.5–94.0%) and lower Ni contents (below 0.015 a.f.u.) than olivine in equilibrium with Ti-Chu in the same sample. Mn spans from 0.004 to 0.009 a.f.u. (López Sánchez-Vizcaíno et al., 2005).

Ilmenite is nearly stoichiometric. In Ti-Chu grains preserving the breakdown reaction front, ilmenite grains typically coarsen with distance to the front, being more abundant and smaller (25–100 μm) near the front, and less abundant but bigger (100–225 μm) away from the front (Fig. 6-3a). Width of the transition zone is variable, attaining a thickness of up to 1.5 mm. The second Ti-Chu breakdown reaction is less common and has been locally observed, at the contact between Ti-Chu and diopside grains that rim Ti-Chu veins (Fig. 6-3b), or at the contact between isolated diopside within Ti-Chu knobs (Fig. 6-3c). Products occur as a thin (50–250 □m) and very irregular rim of wormy and granular ilmenite grains (submicroscopic up to 20 □m) intermixed with idiomorphic tremolite (Fig. 6-3d). Ilmenite grains less commonly occur included within diopside, but always close to the contact with tremolite. The distribution pattern of wormy and granular ilmenite grains is very irregular. In some places, wormy ilmenites appear at the contact between tremolite and Ti-Chu, changing to granular away fromthe contact (Fig. 3d). In other places, big granular ilmenites are found close to Ti-Chu, andwormy ilmenite grains occur near to or within diopside (Fig. 6-3c).

The reaction stoichiometry has been calibrated after mass-balance calculations from mineral analyses:

$$18.9\ \text{Ti-Chu} + 46.6\ \text{diopside} + 1.0\ H_2O \rightarrow 58.9\ \text{tremolite} + 2.5\ \text{ilmenite} \quad (2)$$

To our knowledge, reaction (2) has not been previously reported in the literature. Idiomorphic tremolite grains are also found at the rim between diopside and olivine (having abundant antigorite inclusions, Fig. 6-3e), formed according to the well-known tremolite-in reaction in serpentinites (Trommsdorff and Evans, 1974):

$$5\ \text{antigorite} + 2\ \text{diopside} \rightarrow \text{tremolite} + 6\ \text{olivine} + 9\ H_2O \quad (3)$$

Textural differences between isolated idiomorphic tremolite grains produced by reaction (3) (Fig. 6-3e) and the continuous tremolite rim around diopside due to reaction (2) (Fig. 6-3c and d) can be explained by the irregular distribution of the antigorite

grains within olivine in contact with diopside (Fig. 6-3e). Tremolite-producing reaction (3) would only take place where antigorite was abundant enough and in contact with diopside. Reaction (3) is also relevant as it determines minimum T conditions for reaction (2) (see Fig. 6-7).

6.3 TEM results for the different textural sites

6.3.1 Samples and methods

We have carried out the TEM study on selected, representative samples of Ti-Chu veins from the Cerro del Almirez Atg-serpentinites (specimen Al96-13 and two different thin sections from Al96-15d, identified as Al96-15d(1) and Al96-15d(2), respectively). TEM specimens have beenprepared following standard procedures, selecting study areas by gluing copper rings with 1000 μm hole over the thin sections. Each TEM grid is identified by a sub-label (e.g., G1) suffix after the sample label (e.g., Al96-13-G1). The detached sample grids have been ion-thinned by a Gatan DuoMill apparatus and finally carbon coated. The TEM data have been acquired with a Philips CM20 analytical TEM, equipped with microanalytical STEM-EDS, at the CIC facilities of the University of Granada. Microanalytical data were acquired in STEM modalities, alternatively using small or large scan windows (1000×200 Å and 10000×2000 Å), as most appropriate. Raw data were corrected by the Cliff and Lorimer (1975) method, using experimental proportionality factors, determined for each elements on mineral standards. Precision in the final, calculated atomic contents ranges from 1 to 5% relative, depending upon elemental abundances and window size.

In the selected samples, we have investigated by TEM the following textural features previously described in our petrographic study: i) Ti-Chu in textural equilibrium with clear olivine (grid: Al96-13-G1); ii) olivine formed by incipient breakdownwithin a Ti-Chu grain (grid:Al96-15d(2)-A3); iii) Ti-Chu together with product olivine and ilmenite at the reaction front (Al96-13-J2 and Al-96-13-J4); and (iv) product olivine and ilmenite after Ti-Chu, located severalmillimeters away from the reaction front, where Ti-Chu breakdown is complete or very advanced, and Ti-Chu remains only as tiny relic patches (Al96-15d(1)-I1 and Al96-13-J8).

6.3.2 Ti-Chu and olivine in textural equilibrium (Al96-13-G1)

TEM data (i.e., images, diffractions, STEM analyses) confirm that olivine is structurally and chemically homogeneous, as already pointed out by optical and chemical data (López Sánchez-Vizcaíno et al., 2005). Actually, even at the TEM scale olivine does not contain any significant fault or intermixed structure. The olivine grains show only normal imaging artefacts, such as bend and thickness contours, namely imaging features with no microstructuralmeaning. Conversely, the coexisting Ti-Chu grains systematically show ubiquitous lamellar faults, which correspond to intermixed (001) olivine lamellae (Fig. 6-4a). The mutual orientations of olivine and Ti-Chu are ruled by their polysomatic relationships; namely, $a_{ol}//a_{Ti\text{-}Chu}$, $b_{ol}//b_{Ti\text{-}Chu}$,$[001]_{ol}//[001]_{Ti\text{-}Chu}$. For this reason, during alignment of the TEM holder, we only searched for systematic 00l alignment conditions,

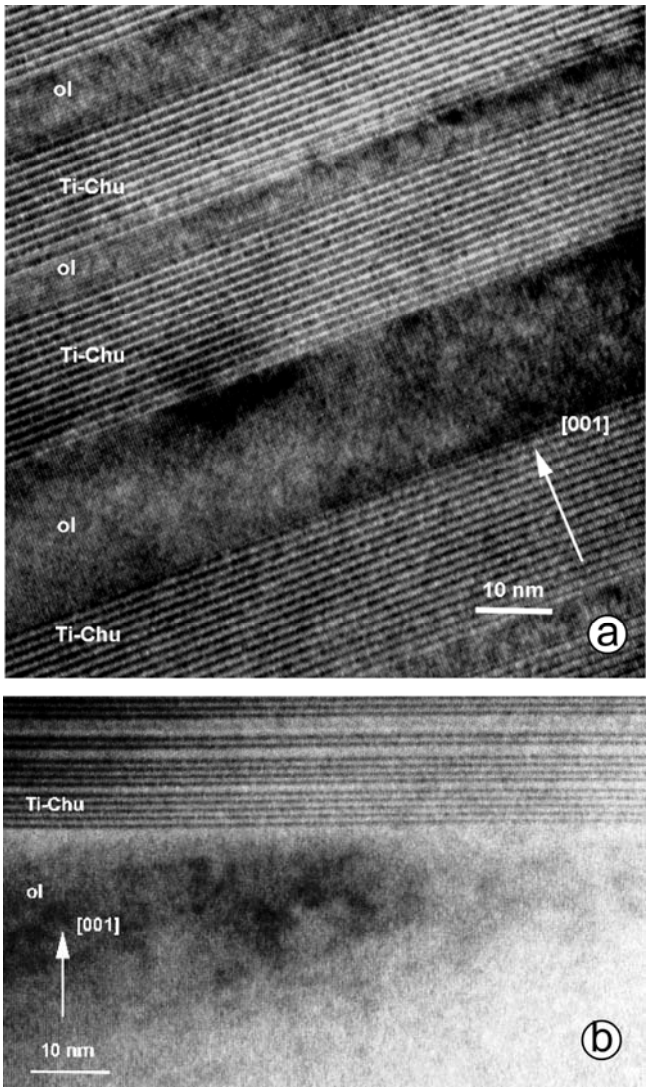

Figure 6-4. (a) (001) lamellar olivine faults (ol), intermixed within the titanclinohumite (Ti-Chu) grains (sample Al96-13-G1). (b) Sharp boundary between equilibrated olivine and Ti-Chu (bottom and top, respectively). Whereas olivine (ol) is completely homogeneous, Ti-Chu appears heavily faulted, by intermixed (001) ol lamellae (arrows). Sample Al96-13-G1.

without aligning the a or b axes. Accordingly, in Fig. 6-4 (as well as in Figs. 5 and 6), we only report the [001] direction.

The opposite microstructural patterns of equilibrated olivine and Ti-Chu are well evident in Fig. 6-4b. This image was taken at the olivine/Ti-Chu boundary; here, homogeneous olivine abruptly changes to a faulted intermixture of olivine lamellae within the Ti-Chu matrix. Sub-micrometrical chemical data have been acquired using a 0.2 μm wide scanning window, in the STEM mode. No anomalous chemical feature affects olivine, having the chemical composition

$$(Mg_{1.853}Fe_{0.160}Mn_{0.003}Ni_{0.002})_{\square=2.018}(Si_{0.970}Al_{0.007}Ti_{0.004})_{\square=0.981}O_{3.98}$$

Conversely, the Ti-Chu analyses only approximately match the expected, ideal values. Analytical data deviate from the ideal ones by amounts that depend on the relative proportion of intermixed olivine lamellae occurring within the relatively wide, 0.2 μm STEM scan window.

6.3.3 Incipient Ti-Chu breakdown (Al96-15d(2)-A3; Al96-13-J2/J4)

In contrast with the previous case, specimens with incipient Ti-Chu breakdown systematically show olivine that pervasively hosts several parallel, continuous (001) Ti-Chu lamellar faults (Fig. 6-5). The nature of the Ti-Chu faults has been determined by imaging the expected 13.4 Å periodicity, as well as by measuring locally the increase in Ti content. Owing to the occurrence of (001) Ti-Chu lamellar faults, olivine bulk analyses are characterized by higher titanium contents. Specifically, any chemical analysis performed over a lamellar intermixture area is expected to have Ti contents above the detection limit for this technique. Indeed, the titanium content measured by a 0.2 μm scan window over a faulted olivine (either in J2, J4 and A3 grids) indicated a mixed analyses (i.e., olivine plus Ti-Chu), where the Ti contents of olivine definitely increase, being typically 0.014 atoms per formula unit. By comparison, the Ti content of olivine was only 0.004 in the equilibrated sample Al96-13-G1.

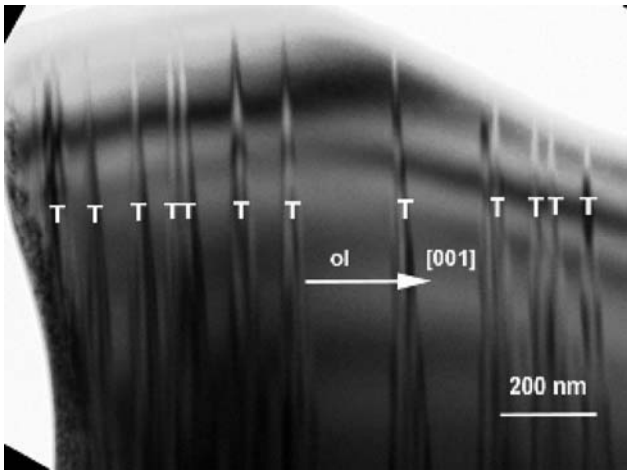

Figure 6-5. (001) Ti-Chu lamellar faults within olivine; sample Al96-13-J2. The lamellar faults are parallel and continuous throughout the whole field of observation.

6.3.4 Advanced Ti-Chu breakdown (Al96-13-J8; Al96-15d(1)-I1)

In the case of Al96-13-J8, the breakdown reaction is quite advanced, but not yet totally complete. The original Ti-Chu appears transformed to a patchy arrangement, where the dominant, newly formed olivine matrix hosts several residual Ti-Chu blebs (Fig. 6-6a).

When examined at higher magnification, the Ti-Chu blebs show pervasive intermixed (001) olivine lamellae (Fig. 6-6b), as indicated by the resolved lattice fringes thickness. Similarly, also product olivine pervasively hosts (001) Ti-Chu lamellae. In several cases, the lamellae are laterally terminated along the (001) plane, both within olivine (Fig. 6-6b) and within Ti-Chu. The lateral terminations of lamellae are marked by a strong black contrast. This contrast is indicative of local accumulation of elastic energy, deriving from the major structural deformations at the termination sites. By

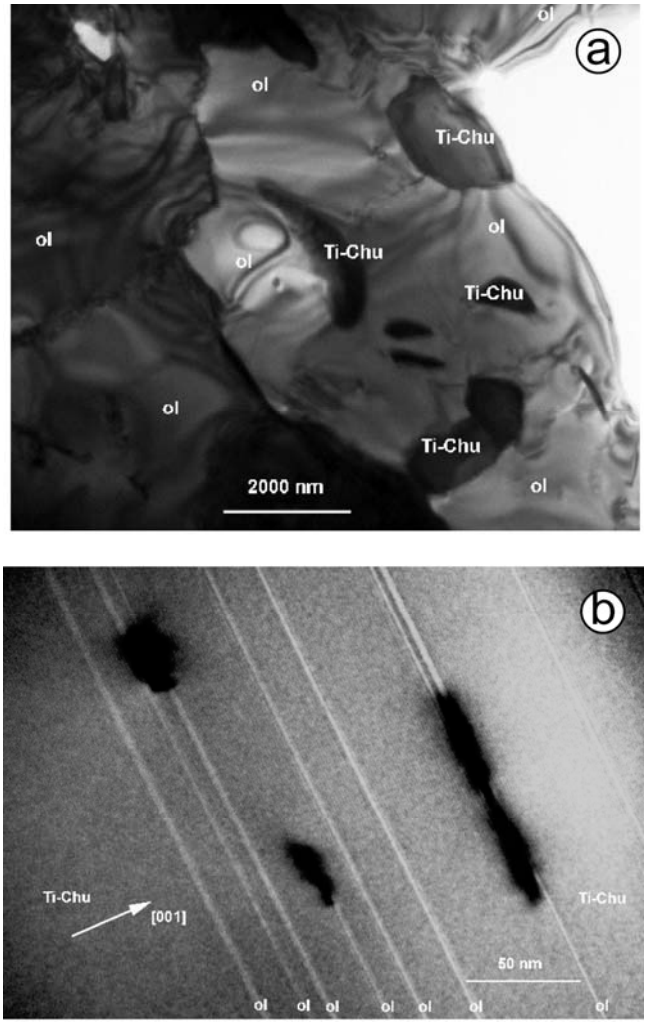

Figure 6-6. (a) Advanced destabilization of Ti-Chu, that breaks down to a patchy arrangement of more abundant, newly formed olivine and minor, residual Ti-Chu blebs (Al-96-13-J8). (b) Active olivine/Ti-Chu interfaces, occurring at the lateral terminations of olivine lamellae within the residual Ti-Chu blebs (Al-96-13-J8). Elastic deformation occurs at the termination and induces the evident, black image contrast.

performing observation under different directions, we concluded that no dislocation occurs. Therefore, we interpreted the blobs as due to strain contrast. Namely, the terminations at the olivine/Ti-Chu interface represent active reaction sites where Ti-Chu is reabsorbed by the breakdown reaction producing olivine+ilmenite.

In sample Al96-15d (1)-I1, the Ti-Chu breakdown was complete. This corresponds to total consumption of relic Ti-Chu lamellae that do not longer occur within olivine. As a consequence, the reaction products (olivine and ilmenite) do not show any anomalous chemical feature. In fact, their STEM chemical compositions are quite trivial:

Olivine:
$(Mg_{1.885}Fe_{0.135}Mn_{0.01})_{\sum=2.03}Si_{0.98}O_{3.99}$

Ilmenite:
$(Mg_{0.37}Fe_{0.61}Mn_{0.04})_{\sum=1.02}Ti_{0.96}O_{2.94}$

6.4 Discussion

6.4.1 Formation of Ti-Chu veins

In the Cerro del Almirez serpentinites, Ti mobility at different scales is evidenced by three occurrences of Ti-Chu:

1) Ti-Chu grains in the serpentinites, close to dusty clinopyroxene grains as well as in the clinopyroxenite layers. In this case, the length-scale of Ti mobility ranges up to several millimetres.

2) More or less continuous OH-Ti-Chu and olivine veins close to clinopyroxenite layers. In both cases, Ti-Chu results from the generalized reaction:

mantle-Cpx + Ol + Atg → Di + Chl + Ti-Chu + H_2O (4)
(Trommsdorff and Evans, 1980).

Even if some premetamorphic olivines can be locally preserved in the serpentinites (Trommsdorff et al., 1998), in most cases the lower temperature limit for reaction (4) is constrained by the following prograde olivine-producing reaction (Trommsdorff and Evans, 1974):

Atg + Brc → Ol + $3H_2O$ (5)

According to the phase diagram section (Fig. 6-7a), computed for a representative serpentinite (sample Al95-17) from the Cerro del Almirez massif (see López Sánchez-Vizcaíno et al., 2005 for calculation methods), brucite breakdown (equivalent to reaction (5)) took place at temperatures ranging from 465 to 500 °C and pressures of 1–2 GPa consistent with the regional metamorphic evolution.

Reaction (4) could not be modelled in the phase diagram section, because of the lack of appropriate solid solution models for Ti-bearing clinopyroxenes of mantle origin as those occurring in Almirez serpentinites. Independent estimates of the P-T conditions, on the basis of available experimental data (Weiss, 1997) for both the first occurrence of OH-Ti-Chu at low temperatures and the breakdown reaction of this mineral, are shown in Fig. 7 (see López Sánchez- Vizcaíno et al., 2005 for details). The estimated first appearance of Ti-Chu (equivalent to reaction (4)) almost coincides with the final breakdown of brucite (reaction (5)).

The calculated modal variations of olivine and "free" water (H_2O as an independent phase) in the phase diagram section (Fig. 6-7b and c) demonstrate that brucite breakdown was the first reaction, in which significant amounts of both olivine and water were produced during prograde metamorphism of the Cerro del Almirez serpentinites.

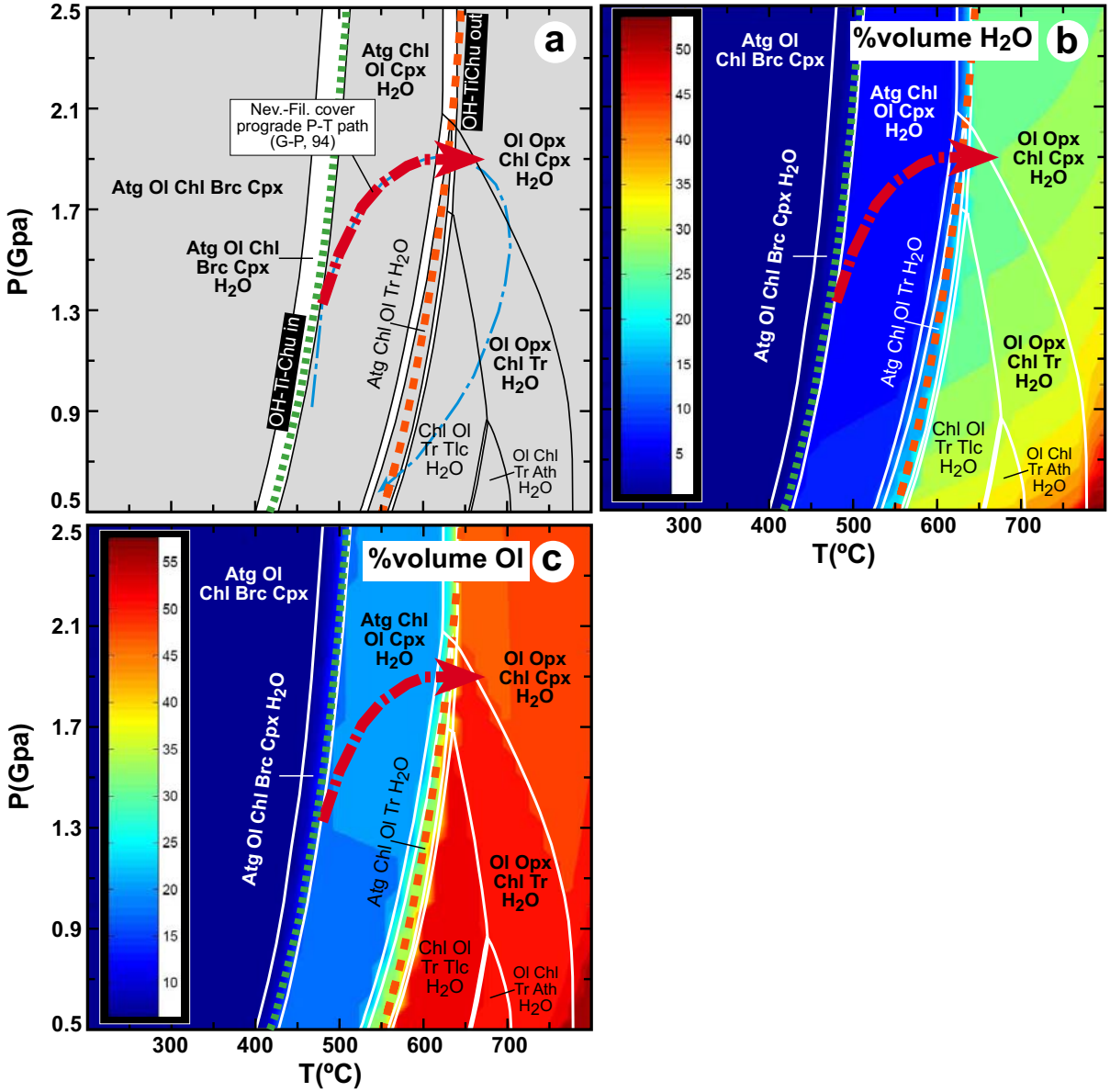

Figure 6-7. (a) Phase diagram section showing prograde metamorphic reactions in a representative serpentinite from the upper part of the Cerro del Almirez massif. Green and orange discontinuous lines show the stability limits for OH-Ti-Chu in the Almirez serpentinites. See López Sánchez Vizcaíno et al. (2005) for the computing methods and conditions for both phase diagram and Ti-Chu stability limits. The thick red arrow represents the prograde P-T path estimated by Gómez-Pugnaire et al. (1994) for metapelites from the upper sequence vol.%) of H_2O and olivine, respectively, calculated from the phase diagram section of (a). Calculations were made with the "werami" program of Perple_X computing package (www.perplex.ethz.ch/perplex.html). Outputwas contoured and coloured using a Matlab® script (www.perplex.ethz.ch/perplex_documentation.html#SCRIPTING).

Specifically, for every 6 vol.% of water released (Fig. 6-7b) (i.e., 2.5 wt.%), 19 vol.% of prograde olivine is generated ((Fig. 6-7c) i.e., 23 wt.%).

At increasing temperature conditions, the amounts of olivine and water in the rocks remained constant until the onset of antigorite breakdown to tremolite (T>615 °C for P>1.7 GPa). These reactions were very close to the onset of Ti-Chu breakdown (Fig. 6-7b and c).

In conclusion, reactions (4) and (5) were almost simultaneous and released an abundant aqueous fluid phase (composed of at least 6 vol.% H_2O), that favoured Ti mobility at metric scale and formation of Ti-Chu bearing veins. These results are in agreement with previous evidences indicating Ti mobility in certain metamorphic environments (Van Baalen, 1993). Specifically, transport of Ti by aqueous fluids on a meter scale in ultramafic rocks was already suggested by the occurrence of titanian andradite veins in the Val Malenco ultramafic rocks (Müntener and Hermann, 1994) or by the common observation of OH-Ti-Chu veins in antigorite serpentinites from the Alps (Trommsdorff and Evans, 1980 and references therein; Scambelluri et al., 1991). In our study, the estimated abundant fluid phase is testified also by olivine veins without Ti-Chu, widespreadly diffused through the Cerro del Almirez Atg-serpentinites. Phase relationships and modal abundances shown in Fig. 6-7 support suggestion by Hermann et al. (2000) that, in the presence of a fluid phase, continuous solution and precipitation of olivine may occur in serpentinites within the stability field of antigorite.

3) In a third occurrence, at grain scale, Ti-Chu grains in the veins appear intermixed with olivine lamellae (Fig. 4a and b). This texture reveals the restricted availability of Ti at small scale during the crystallization of Ti-Chu and olivine within the veins. As the Ti amount in the fluid was not buffered, but controlled by the limited amount of clinopyroxene dissolving after reaction (4), and olivine formation and water release were mainly controlled by independent reaction (5), olivine kept growing when Ti availability was low. An example of the abrupt change from Ti-Chu to olivine crystallization is given in Fig. 6-4b.

6.4.2 Breakdown reaction mechanisms

Our textural observations (Fig. 6-3) indicate that two nearly simultaneous Ti-Chu breakdown reactions (reactions (1) and (2)) operated in grains from Ti-Chu–olivine veins. Reaction (1) is the dominant breakdown reaction of Ti-Chu in our samples. Despite being a discontinuous reaction, our optical and TEM observations demonstrate that Ti-Chu does not transform directly to olivine + ilmenite. Instead, transition zones (up to 1.5 mm width) can be observed in the newly formed olivine, where Ti-Chu remains both as small orange relics (Fig. 6-3b) still preserving previous olivine lamellae (Fig. 6-4) and as Ti-Chu lamellae hosted in product olivine (Fig. 6-5). Away from the reaction front, a progressive decrease in the abundance of Ti-Chu relics occurs, together with a simultaneous decrease in the amount of Ti-Chu lamellae within the newly formed olivine. Once this transition zone is left, Ti-Chu has completely disappeared, both at optical and the TEM scale and, accordingly, all OH hosted in Ti-Chu has been released as free H_2O and all Ti has entered product ilmenite.

Rubie (1998) showed that dehydration reactions can be a very sluggish process, particularly when more than one phase has to nucleate and when the structural differences between the reactant and product phases are large. In the OH-Ti-Chu breakdown reaction, growth processes of product olivine and ilmenite are very different from each other. Product olivine replaced Ti-Chu topotactically, ruled by the very similar crystallographic structures of the two phases (e.g., Robinson et al., 1973; Veblen, 1991). As a consequence, new olivine grains grew with the same orientation as previous Ti-Chu. This kind of replacement mechanism, by which crystallographic orientations are preserved, is typical of limited fluid conditions (e.g., Le Gleuher et al., 1990). Actually, this seems to correspond to a negative feedback process: the scarcity of fluids would contribute to the slow Ti-Chu breakdown and the preservation of Ti-Chu lamellae within olivine. At the same time, the preservation of Ti-Chu lamellaewould contribute to the low availability of fluids (lower than that predicted by reaction (1)).

On the contrary, due to the completely different crystal structures of ilmenite and olivine, the ilmenite growth took place without any previous structural control. Nucleation required sharp separation of Ti and, to a lesser extent, Fe during diffusion through olivine and persisting Ti-Chu. However, well-defined chemical potential gradients of these elements are not possible until the ilmenite phase actually nucleates. Homogeneous nucleation of this phase owing to the development of the correct concentration of Ti and Fe is a chance event ruled by statistical probabilities (Rubie, 1998).

In the studied samples, the concentration of a larger amount of ilmenite grains close to the reaction front (Fig. 6-3a) points to an intense homogeneous ilmenite nucleation in this zone and to reaction supersaturation. In the earliest stages of the breakdown process, however, significant Ti and OH amounts remain in the abundant Ti-Chu lamellar faults hosted in product olivine (Fig. 6-5). This accounts for the relatively slow diffusion rate and the nucleation of abundant but small sized new ilmenite grains. Progress in the breakdown reaction resulted in total resorbtion of the Ti-Chu faults in olivine (Fig. 6-6b) and the complete release of water. Higher water availability promoted partial remobilisation of Ti and the growth of larger ilmenite grains (Ostwald ripening) away from the breakdown front (Fig. 6-3a).

Different textures of ilmenite in olivine, produced by Ti-Chu breakdown, are reported in literature. Granular or wormy ilmenite and rod shaped ilmenite are, theoretically, a consequence of discontinuous or continuous breakdown of OH-Ti-Chu and F-OH-Ti-Chu, respectively (Trommsdorff et al., 2001). Evidences reported in our study show that kinetic factors may induce divergences, at least at small (TEM or petrographic) scale, with the thermodynamically predicted development of the discontinuous, almost univariant breakdown of OH-Ti-Chu at constant P-T conditions (see Fig. 6-7). In other words, for a fixed temperature, variation in abundance and size of ilmenite may be explained by the changing water (and Ti) availability during the breakdown-growth process.

Despite the fact that the abundant fluid produced by reaction (3) should strongly enhance breakdown reactions (1) and (2), finegrained rock-forming Ti-Chu appears in

most Atg-serpentinite samples almost unreacted. As we lack TEM images of these Ti-Chu grains, we speculate that they might be poorer in olivine lamellae that would have enhanced the onset of the Ti-Chu to olivine transformation. Otherwise, because Ti-Chu in veins has a much larger crystal size than rock forming Ti-Chu, its wider crystal-fluid interface would favor the onset of the breakdown reaction relative to those in the serpentinites. On the other hand, López Sánchez-Vizcaíno et al. (2005) (their Table 6-5) have reported olivine/Ti-Chu partition coefficients (KD) for both Fe and Mg much closer to one in the case of olivine-Ti-Chu pairs in equilibrium within Atg-serpentinite (K_D^{Fe}=0.938, K_D^{Mg}=1.059) than in those analysed within the Ti- Chu-olivine veins (K_D^{Fe}=0.88, K_D^{Mg}=1.127). This would account for the higher stability of rock forming Ti-Chu in equilibrium with olivine within the Atg-serpentinite at equal P-T conditions).

Almirez breakdown textures of Ti-Chu at the TEM scales are rather similar to those described by Hermann et al. (2007) in garnet pyroxenites from Dabie Shan (China). These authors find olivine with oriented Ti-Chu lamellae owing to continuous breakdown reactions of OH-F-Ti humites taking place during the retrograde P-T path of the studied rocks. Lamellae formation precluded H_2O liberation in a single pulse and allowed the preservation of humite type defects beyond the stability fields of the humite minerals. The main difference with the lamellae studied in this paper is the significant F content of Ti-Chu (0.5 wt.%, their Table 1), which allowed the stabilization of Ti-Chu lamellae at higher temperatures (~720 °C at P ≈ 1.5 GPa; their Fig. 8) than those reached by (F-absent) OH-Ti-Chu in the Cerro del Almirez Atg-serpentinites. The compositions of Dabie Shan Ti-Chu lamellae are more comparable with those of OH-F-Ti-Chu occurring in Chl-harzburgite (i.e., beyond the antigorite-breakdown reaction) from the Cerro del Almirez massif (López Sánchez-Vizcaíno et al., 2005), which is not the object of the present study.

In Ti-Chu-bearing rocks from other localities, lamellar intergrowths of Ti-Chu with olivine are lacking. Instead, the breakdown products ilmenite+olivine occur as variably textured intergrowths, even in the same samples. Differences in reaction mechanisms and rates could, in fact, explain this textural variability. Risold (2001) shows wormy ilmenite close to ilmenite rods (her Fig. 5.4) in three different localities from the Central Alps; Muko et al. (2001) describe ilmenite with different textures produced by Ti-Chu breakdown in the same UHP rocks from Kokchetav; and, even in the Almirez Chlharzburgites, ilmenite rods and granular ilmenites can be found, both related to F-OH-Ti-Chu breakdown (compare for instance Fig. 2a with Fig. 2d, e and f in López Sánchez-Vizcaíno et al., 2005).

Reaction (2) is much more restricted, as requires highly specialized reaction sites, localized at the Ti-Chu–diopside interface. Therefore, its appearance is less evident than in the case of reaction (1). Furthermore, reaction (2) is a hydration reaction that requires availability of water released from another simultaneous dehydration reaction. Water is hosted in newly formed tremolite. Under these water consuming conditions, diffusion processes may be expected to be hampered, resulting into symplectitic ilmenite-tremolite growth. The observed irregular distribution of wormy and granular textured ilmenite might be also related to changes in the local supply of both water and Ti during the breakdown-growth process.

6.4.3 Metamorphic conditions and fluid availability

Based upon the calculated phase diagram and the conditions of the Ti-Chu-out reaction from Fig. 6-7a, we derive 620–640 °C at 1.7–2.0 GPa as probable conditions for reaction (1) and, according to textural relationships, also for reaction (2). These conditions are in good agreement with the phase relationships observed in the rocks, as remarked by López Sánchez-Vizcaíno et al. (2005). These conditions are also in agreement with the prograde segment (red thick arrow in Fig. 6-7) of the estimated P-T path for metapelites from the upper sequence of the Nevado-Filábride Complex (Gómez-Pugnaire et al., 1994; Fig. 12).

As mentioned by these authors, the lower temperature section of the path (blue, thin discontinuous line in Fig. 6-7a) was only inferred. Thus, and considering that the Ti-Chu bearing veins could only form after breakdown of brucite and clinopyroxene of mantle origin, we suggest that the onset of Ti-Chu formation in the Almirez serpentinites and veins occurred at maximum pressures and temperatures of 1.3 GPa and 475 °C.

Textures related to reactions (1) and (2) suggest a very limited fluid availability during Ti-Chu breakdown within the veins. On the contrary, at the estimated P-T conditions for reactions (1) and (2) (620–640 °C at 1.7–2.0 GPa), the total amount of a "free" water phase in the serpentinites reached ≈20 vol.% of bulk rock (Fig. 6-7b), equivalent to ≈5 wt.%. Water was mainly released through the prograde, antigorite consuming reaction (3), in which diopside transformed to tremolite. This reaction has only been very locally observed within the veins (Fig. 6-3d).

Hence, it can be inferred that, after vein formation due to circulation of water transporting Ti, the resulting Ti-Chu-olivine veins were sealed and acted as a closed system. In the veins, and despite higher temperature conditions, subsequent Ti-Chu breakdown reactions (i.e. 1 and 2) developed very slowly allowing intermediate stages of the breakdown process to be preserved, as demonstrated in this work.

The restricted location of hydration reaction (2), in spite of its very low water demand, can be also explained by the low water availability within the veins. Reaction (2) proceeded only locally, where water was released at the onset of dehydration reaction (1).

6.4.4 Fate of Ti-Chu and implications for subduction zones

The recycling of water in the deep mantle strongly relies on the stability of hydrous minerals during subduction and the water storage capability of nominally-anhydrous minerals (Bell and Rossman, 1992). Many authors have stressed the importance of the humite-group minerals for the storage of water in the mantle, mostly as defects of clinohumite or chondrodite-type structures (Kitamura et al., 1987; Berry et al., 2005). Humite-group minerals have stability fields>13 GPa and temperatures>1000 °C in hydrated model mantle assemblages (e.g. Kawamoto and Holloway, 1997). The recycling of water by Ti-Chu in olivine-bearing rocks, either as single grains, veins or as defects (planar lamellae) in olivine, depends on the stability of Ti-Chu during subduction, which

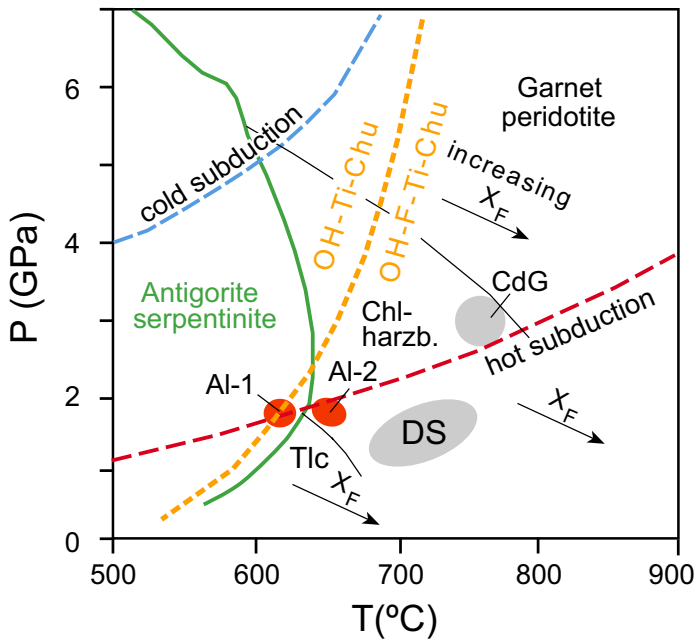

Figure 6-8. Summary of P-T conditions for the formation of Ti-Chu lamellae within olivine in several localities. Al-1: OH-Ti-Chu in Atg-serpentinite from Cerro del Almirez; Al-2: OHF- Ti-Chu in Chl-harzburgite from Cerro del Almirez (López Sánchez-Vizcaíno et al., 2005); DS: OH-F-Ti-Chu lamellae in olivine due to retrograde evolution of garnet pyroxenite from Dabie San (Hermann et al., 2007); CdG: oriented ilmenite rods after former Ti-Chu lamellae in Cima di Gagnone (Risold et al., 2001). The thick, orange dashed curve represents OH-Ti-Chu breakdown conditions. See Fig. 7 for calculations conditions. At higher temperatures only F-bearing Ti-Chu can be stable. XF in OH-F-Ti- Chu increases with temperature, as indicated by the thin black arrows (XF=F/2 a.p.f.u.). Stability conditions for Atg-serpentinite, Talc (Tlc), Chl-harzburgite (Chl-harzb.), and Garnet-peridotite were calculated from the same phase diagram section as in Fig. 7. P-T regimes for hot (red line) and cold subduction (blue line) are taken from Fig. 8 of Hermann et al. (2007).

in turn depends on the subduction thermal field (i.e., cold vs hot subduction regimes) and the F/OH ratio of this mineral, controlled by exchange vectors OHF_{-1} and $TiO_2Mg_{-1}F_{-2}$ (Evans and Trommsdorff, 1983). OH-Ti-Chu is restricted to relatively low temperatures (Fig. 6-8, where the thick orange, dashed curve, represents the breakdown curve of OH-Ti-Chu), but increasing F contents (thin arrows in Fig. 6-8) expand the stability of OH-F-Ti-Chu to maximum temperatures above 1300 °C (Weiss, 1997). Ti Chu is a common mineral in HP hydrated mantle rocks recording a history of subduction, but Ti-Chu lamellar intergrowths with olivine or their breakdown products (i.e. ilmenite rods) are reported only in a few localities (Cerro del Almirez massif, Dabie Shan, Eastern Alps, and Kokchetav) (Fig. 6-8).

In the Cerro del Almirez ultramafic massif, the presence of two Ti-Chu generations (OH-Ti-Chu and OH-F-Ti-Chu, corresponding to Al-1 and Al-2, respectively, in Fig. 8) with different F/OH ratios and in different rock types (Atg-serpentinite and Chl-harzburgite; Fig. 6-8 and López Sánchez-Vizcaíno et al., 2005) allows us to investigate their stability at intermediate-T in a hot subduction zone regime (Fig. 6-8). Aside, they

allow to check their possible contribution to the water and titanium recycling process in such environments.

In this paper we report a detailed study of the OH-Ti-Chu breakdown process at conditions corresponding to the Al-1 zone in Fig. 6-8. In the Almirez Atg-serpentinite, partially broken down OH-Ti-Chu remains in veins beyond the OH-Ti-Chu breakdown conditions (thick orange curve; Fig. 6-8). In the studied Ti-Chu grains, thin transition zones close to the reaction front contain Ti-Chu lamellae within product olivine. This could be interpreted as an example of preservation of Ti-Chu lamellae within olivine in subduction zones beyond the stability field of Ti-Chu. However, it should be noted that the antigorite dehydration breakdown reaction occurred in the Almirez at only 20 °C higher temperatures (thick grey curve, Fig. 6-8) and consumed every remaining OH-Ti-Chu grain beyond the antigorite- out isograd mapped in this ultramafic body (Fig. 1). No relics of OH-Ti-Chu can be found in the product Chl-harzburgite formed after Atg-serpentinite breakdown. In fact, Ti-Chu occurring in Chlharzburgite (Al-2 in Fig. 6-8) is a newly formed OH-F-Ti-Chu in equilibrium with the olivine + enstatite + chlorite + tremolite + magnetite assemblage typical of this rock type (López Sánchez-Vizcaíno et al., 2005). Hence, and according to the phase relations shown in Fig. 6-8, it can be concluded that preservation of OH-Ti-Chu in Atg-serpentinite either as mineral grains, veins, or lamellae within olivine, is highly improbable in subducted ultramafic bodies which underwent temperatures higher than ~640 °C, corresponding to the point where the breakdown curves for Ti-Chu and antigorite cross each other in Fig. 6-8. Theoretically, at pressures above ~2.4 GPa, OH-Ti-Chu formed and partially broken down in high pressure Chl-harzburgites or garnet peridotites could be preserved (as they do not cross any other dehydration breakdown reaction) in colder subduction regimes.

Ti-Chu reported in localities with a record of higher temperature and pressure, always contains fluorine. OH-F-Ti-Chu lamellae in olivine have been reported in the Almirez's Chl-harzburgites (López Sánchez-Vizcaíno et al., 2005) and in the Maowu ultramafic Complex of central Dabie Shan (Hermann et al., 2007). Oriented ilmenite rods formed after complete breakdown of previous OH-F-Ti-Chu lamellae also occur in several Central Alps localities, including Cima di Gagnone and Alpe Arami (Risold et al., 2001). Stability conditions for OH-F-TiChu in all these localities plot along the hot subduction geotherm (red dashed line in Fig. 6-8), thus suggesting that this is the most suitable thermal regime for the preservation of this mineral's lamellae within olivine and for the transfer of water and Ti at depth in subduction zones.

6.5 Conclusions

The petrographic and TEM study of Ti-Chu veins in Atgserpentinite from the Cerro del Almirez massif shows that these veins record different Ti-Chu breakdown reactions and mechanisms during prograde metamorphism at high P and T.

Formation of veins occurred by the simultaneous release in the serpentinites of Ti, owing to the breakdown of Ti-rich clinopyroxene of mantle origin, and of water and olivine produced by the brucite breakdown dehydration reaction. Our calculations

indicate that water release of the 6 vol.% of the serpentinites was enough to account for the Ti-Chu/Ol veins.

TEM images of abundant olivine lamellae intercalated within non transformed Ti-Chu knobs in the veins suggest that sharp variations in the supply of Ti to the veins took place in conditions in which olivine was always stable. According to phase diagram sections and the calculated P-T evolution for the upper Nevado-Filábride sequence, formation of the veins occurred at maximum conditions of 1.3 GPa and 475 °C.

The breakdown of Ti-Chu occurred in a probable P-T range of 1.7–2.0 GPa and 620–640 °C by two different reactions. Products of Ti-Chu breakdown reaction (1) (olivine + ilmenite) arewidespread, whereas the products of Ti-Chu breakdown reaction (2) (tremolite+ilmenite) are found very locally, in the contact between Ti-Chu and diopside. Detailed optical and TEMobservations of the reactants and products of reaction (1) show a gradual transformation of Ti-Chu to olivine+ilmenite. Ti-Chu lamellae are hosted in the newly formed olivine and they only disappear completely at a certain distance from the reaction front, where Ti and water are released. Textural variation in product ilmenite from the two reactions suggests that almost all the water available within the veins during Ti-Chu breakdownwas that released progressively by reaction (1). Thus, and despite the high amounts of free water (20 vol. %) in the enclosing serpentinites, we can conclude that the veins operated as a closed system during Ti-Chu breakdown.

At P<2.4 GPa and T conditions higher that those reported above, antigorite dehydration reaction took place giving place to the complete destruction of Ti-Chu in any textural position. Thus, OH-Ti-Chu from Atg-serpentinite can be precluded as an efficient water or titanium carrier into deep mantle in hot subduction zones.

Acknowledgements
This paper was highly improved by the critical suggestions of two anonymous reviewers. This work was supported by the Spanish “Ministerio de Ciencia e Innovación” through research grant CGL2006-04440/BTE and by the Junta de Andalucía research groups RNM-145 and RNM-131. MM is grateful to the “Secretaría de Estado de Universidades e Investigación” of the Spanish “Ministerio de Ciencia e Innovación” for the invitation to spend a sabbatical term at the Universidad de Granada (Grant SAB2005-0191). JAPN is supported by grant AP2005-060 from the “Programa de Formación del Profesorado Universitario”. We sincerely thank M.A. Abad and I. Guerra for the technical assistance at the TEM and SEM facilities of the University of Granada).

Contrib Mineral Petrol (2010) 159:25–42
DOI 10.1007/s00410-009-0414-5
Received: 13 February 2009 / Accepted: 29 May 2009 / Published online: 20 June 2009

7 An experimental investigation of antigorite dehydration in natural silica-enriched serpentinite

Padrón-Navarta, JA[1*]· Hermann J[2]· Garrido CJ[3]· López Sánchez-Vizcaíno, V[4]· Gómez-Pugnaire MT[1,3]

Piston cylinder experiments were performed to constrain the pressure and temperature conditions for two high-pressure antigorite dehydration reactions found in silica-enriched serpentinites from Cerro del Almirez (Nevado-Filábride Complex, Betic Cordillera, southern Spain). At 630–660ºC and pressures greater than 1.6 GPa, antigorite first reacts with talc to form orthopyroxene ± chlorite + fluid. We show that orthopyroxene + antigorite is restricted to high-pressure metamorphism of silica-enriched serpentinite. This uncommon assemblage is helpful in constraining metamorphic conditions in cold subduction environments, where antigorite serpentinites have no diagnostic assemblages over a large pressure and temperature range. The second dehydration reaction leads to the breakdown of antigorite to olivine + orthopyroxene + chlorite + fluid. The maximum stability of antigorite is found at 680 ºC at 1.9 GPa, which also corresponds to the maximum pressure limit for tremolite coexisting with olivine + orthopyroxene. The high aluminium (3.70 wt% Al_2O_3) and chromium contents (0.59 wt% Cr_2O_3) of antigorite in the investigated starting material is responsible for the expansion of the serpentinite stability to 60–70 ºC higher temperatures at 1.8 GPa than the antigorite stability calculated in the Al-free system. The antigorite from our study has the highest Al-Cr contents among all experimental studies and therefore likely constraints the maximum stability of antigorite in natural systems. Comparison of experimental results with olivine-orthopyroxene-chlorite-tremolite assemblages outcropping in Cerro del Almirez indicates that peak metamorphic conditions were 680–710ºC and 1.6–1.9 GPa.

Keywords: Antigorite dehydration · Silica metasomatism · Orthopyroxene-bearing serpentinite

1. Departamento de Mineralogía y Petrología, Universidad de Granada, Spain.
2. Research School of Earth Sciences, ANU, Canberra, Australia.
3. Instituto Andaluz de Ciencias de la Tierra (IACT), Granada, Spain.
4. Departamento de Geología, Universidad de Jaén Linares, Spain.

7.1 Introduction

Pioneering experimental work on the pressure-temperature stability of a serpentine mineral, antigorite, demonstrated the potential role of ultramafic rocks as H_2O-carrier to a depth of $\leq$200 km in subduction zones (for a comprehensive review see Ulmer and Trommsdorff 1999). The hydration of the upper mantle extensively occurs when oceanic lithosphere undergoes seafloor hydrothermal alteration at mid-ocean ridges (O'Hanley 1996; Bach et al. 2004, 2006), during submarine exhumation of subcontinental mantle rocks (Boillot et al. 1989; Lagabrielle and Bodinier 2008), during bending-related faulting of the slab across the ocean trench (Peacock 2001; Ranero et al. 2003) and when fluids released from the dehydration of the downgoing slab interact with cold parts of the mantle wedge (Tatsumi 1989; Bebout and Barton 1989; Guillot et al. 2000, 2001; Fumagalli and Poli 2005). A major area of interest is the link between the antigorite dehydration and the generation of arc volcanism (Tatsumi 1989; Ulmer and Trommsdorff 1995; Schmidt and Poli 1998). Observed P-wave velocities in active subduction zones and numerical modeling let Iwamori and Zhao (2000) to suggest that most of the H_2O released from the dehydration of the oceanic crust is incorporated back into the mantle wedge forming relatively thin (<7 km) "serpentinite channels" along the top surface of the subducting slab. More recently, the existence of these channels of hydrated mantle material has been suggested by detailed reflectivity profiles beneath northeastern Japan (Kawakatsu and Watada 2007). An exceptional locality to survey the high-pressure antigorite dehydration is the Cerro del Almirez ultramafic massif (Nevado–Filábride Complex, Betic Cordillera, southern Spain) (Trommsdorff et al. 1998; Puga et al. 1999; López Sánchez-Vizcaíno et al. 2005, 2009; Garrido et al. 2005). The antigorite breakdown took place during the Alpine collision in the Middle Miocene (López Sánchez-Vizcaíno et al. 2001) when serpentinites (antigorite + magnetite + olivine + tremolite/diopside) were subducted to depths of up to 70 km forming prograde chlorite harzburgite (olivine + orthopyroxene + chlorite + tremolite + magnetite) with spinifex-like textured olivine and orthopyroxene (Trommsdorff et al. 1998). This ultramafic massif has been used as a natural laboratory to investigate the composition of fluids during the high-P dehydration of serpentinites and the origin of the depletion of high-field-strength trace elements in subduction zone fluids (Scambelluri et al. 2001, 2004a, 2004b, 2007; Garrido et al. 2005). Close to the antigorite-out isograd metre-scale lenses occur consisting of antigorite + orthopyroxene + tremolite + magnetite ± olivine, referred to here as antigorite–orthopyroxene assemblage or simply orthopyroxene-bearing serpentinite. This unusual paragenesis could originate from an additional antigorite dehydration reaction in a Si-enriched serpentinite (Spandler et al. 2008). Previous experimental studies have demonstrated that the content of aluminium and chromium and the extent of polysomatic ordering have a great influence on the stability of antigorite (Bromiley and Pawley 2003; Wunder et al. 2001). Antigorite from Cerro del Almirez is highly ordered and has high iron, aluminium and chromium contents (Trommsdorff et al. 1998; Padrón-Navarta et al. 2008). Therefore, these samples represent a perfect starting material to experimentally investigate the stability of antigorite in natural systems in a subduction environment. In this paper we present an experimental approach to constrain the full grid in the natural $CaO–FeO–MgO–Al_2O_3–SiO_2–H_2O$ system (CFMASH) for a hydrated ultramafic composition using a Si-enriched (orthopyroxene-bearing) serpentinite from Cerro del Almirez. The experimental results

are compared to a calculated pseudosection for the same composition. This information is used to constrain the maximum thermal stability of antigorite at high-P in this ultramafic massif and to investigate the significance of the antigorite–orthopyroxene assemblage in subduction zones.

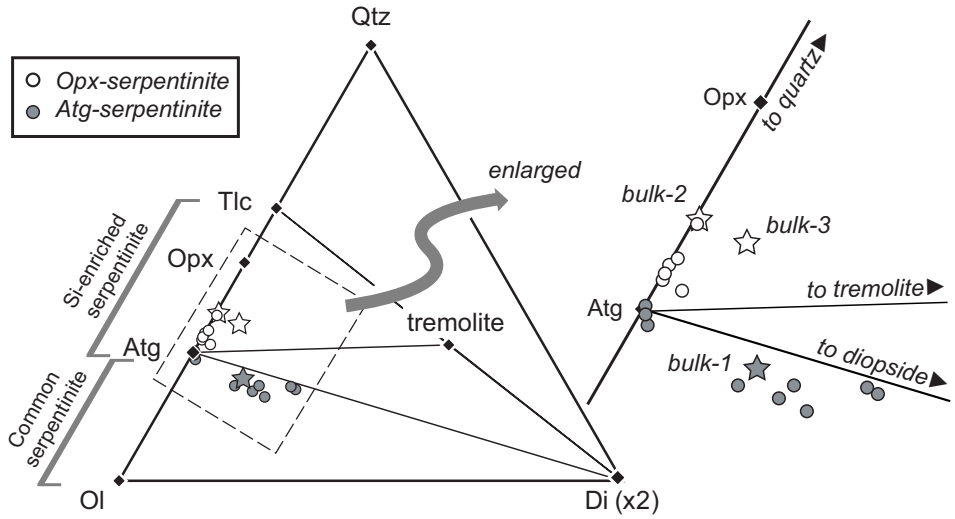

Figure 7-1 Definition of the terms ‘‘common serpentinite’’ (on the tie-line between olivine and antigorite, 1/2 <Si/Mg<34/48, in molar proportion) and ‘‘Si-enriched serpentinite’’ (on the tie-line between the antigorite and talc, 34/48<Si/Mg<4/3) in the quartz–forsterite– diopside ternary diagram projected from H2O. Compositions of the two types of serpentinite observed in Cerro del Almirez (antigorite–serpentinite and orthopyroxene-bearing serpentinite) plot in two different three-phase triangles. Bulk-1 to bulk-3 are different bulk compositions discussed in the text (see Tables 7-1, 7-2). Mineral abbreviations: Tlc talc, Opx orthopyroxene, Atg antigorite, Ol olivine, Di diopside, Tr tremolite, Qtz quartz. Other mineral abbreviations used in the text: Chl chlorite, L liquid phase, Mgt magnetite, Pn pentlandite. Diagram generated using the program CSpace, Torres-Roldán et al. 2000

7.2 Background and experimental strategy

Under water-saturated conditions and bulk compositions between antigorite and olivine (e.g. as the average of Cerro del Almirez serpentinite, bulk-1 in Fig. 7-1, Garrido et al. 2005) antigorite dehydrates above the invariant point [Di] (invariant points are labelled with the absent phase in brackets) exclusively through the reaction (see Fig. 2a for the loci of reactions, mineral abbreviations are given in Fig. 1):

$$\text{Atg} \rightarrow \text{Ol} + \text{Opx} + \text{L} \qquad (1)$$

However, in silica enriched bulk composition (Si-enriched bulk serpentinite composition is defined here as Si/Mg molar ratio higher than in the antigorite and lower than in the talc, i.e. 4/3>Si/Mg>34/48, e.g. bulk-2 and bulk-3 in Figs. 7-1, 7-2c) antigorite reacts with talc through the reaction (Fig. 7-2a):

$$\text{Atg} + \text{Tlc} \rightarrow \text{Opx} + \text{L} \qquad (2)$$

At lower pressures (i.e. below the invariant point [Di]) antigorite dehydrates in both bulk compositions through reaction (3):

$$Atg \rightarrow Ol + Tlc + L \qquad (3)$$

While there is a number of field evidence for the occurrence of reaction (3) in contact metamorphism of hydrated ultramafic rocks (Trommsdorff and Evans 1972, 1974; Springer 1974; Frost 1975; Arai 1975; Irving and Ashley 1976; Pinsent and Hirst 1977; Vance and Dungan 1977; Matthes and Knauer 1981; Worden et al. 1991; Nozaka and Shibata 1995), the occurrence of reaction (1) in natural rocks has been only reported in Cerro del Almirez (Trommsdorff et al. 1998). Reaction (2) is expected to be even more restricted in nature, as it requires a more specific serpentinite bulk composition.

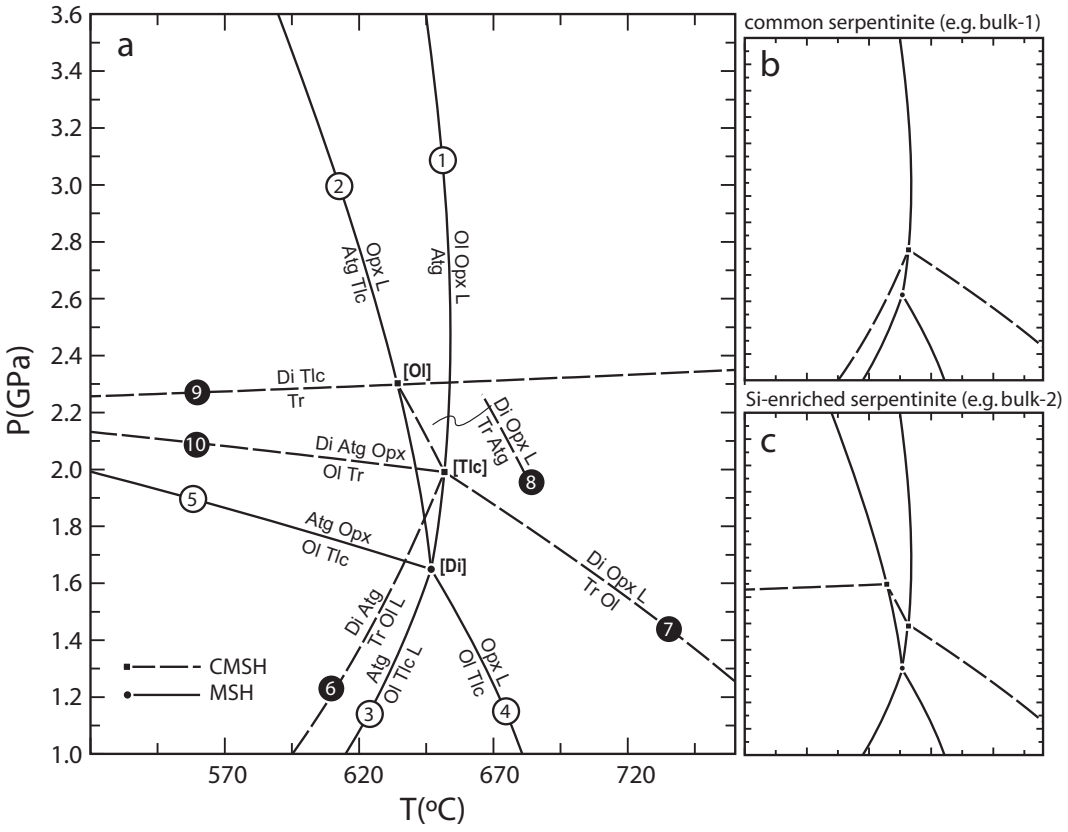

Figure 7-2 a Phase relations relative to hydrated mantle rocks in the simplified system CaO–MgO–SiO_2–H_2O (CMSH) computed with PerpleX package (Connolly 2005) and the updated Holland and Powell's (1998) database (hp02ver.dat) with reactions labelled like in the text. The CORK equation of state from Holland and Powell (1998) for H_2O (labelled as L) was chosen. The invariante points [Di], [Tlc] and [Ol] are labelled with the absent phase. See Fig. 7-1 for mineral abbreviation. **b** Relevant reactions for a water-saturated common serpentinite (bulk-1) and **c** for a water saturated Si-enriched serpentinite (bulk-2 and bulk-3)

When calcium is considered in the system, diopside and tremolite appear as two separated phases involved in five reactions (6, 7, 8, 9, 10, where reaction (9) is degenerated (Fig. 7-2a). The appearance of tremolite through reaction (6) occurs typically in normal serpentinite with increasing grade (e.g. Trommsdorff and Evans 1972). In contrast, for a Si-enriched composition tremolite is not a diagnostic mineral

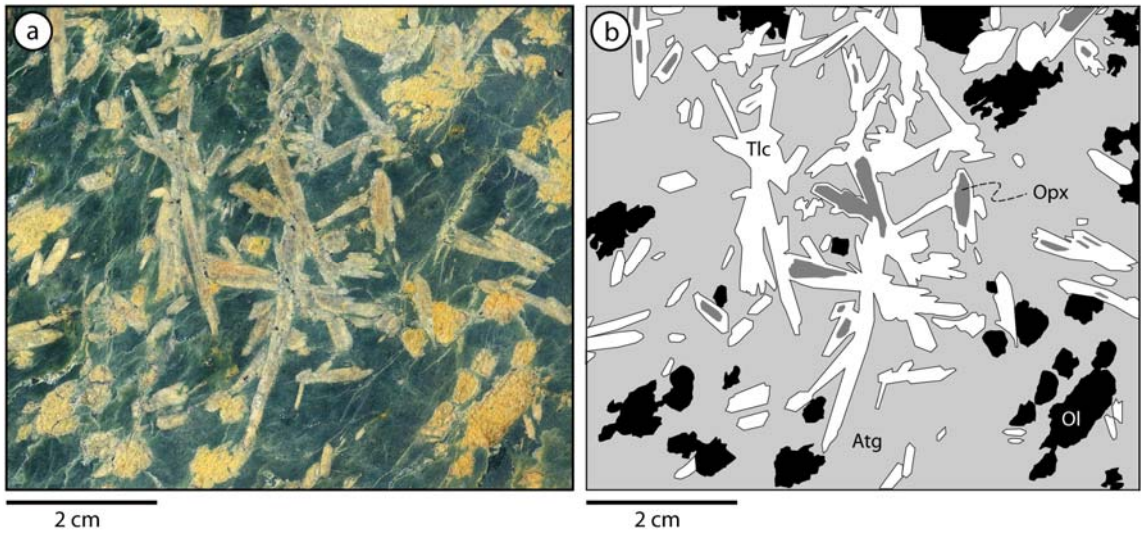

Figure 7-3 a Representative texture of a Si-enriched serpentinite (scanned polished-surface of sample Al06-37). The handsample was cut closely parallel to the rock foliation. **b** Sketch highlighting textural relationships between the elongated talc-pseudomorphs after enstatite (up to 2 cm in length) and olivine in the antigorite matrix. Mineral modes in Table 7-1 were estimated by image análisis using the whole area of this sketch (c. 8 x 7 cm)

because its stability field expands to lower temperature and higher pressure. In such a bulk composition the stability field of coexisting tremolite-antigorite is delimited by reactions (8) and (9) (Fig. 7-2c). Beyond the antigorite stability field, tremolite breaks down through reaction (7) for both bulk compositions, defining the boundary between the amphibolite facies and the granulite facies in ultramafic rocks (Evans 1977).

In contrast to calcium, iron can substitute for magnesium in all silicates considered above. So the addition of iron only increases the thermodynamic variance of the system without adding any new phase or new reactions. Moreover, the addition of iron to the system displaces all the reactions to lower temperatures (Worden et al. 1991; Bromiley and Pawley 2003). The addition of Al also increases the variance of reactions involving antigorite because it can be incorporated in it through tschermaks exchange. As tschermaks exchange is limited in the orthopyroxene at the temperature considered here and does not exist in the olivine, chlorite appears in the products from the antigorite dehydration reactions (1) (Bromiley and Pawley 2003) and (3) (Worden et al. 1991) and, although it has not yet been described, it is expected to occur also in reaction (2).

In this work we use a phase diagram approach in order to establish a more complete grid for natural serpentinite than previously reported. In this approach, the reactions are constrained by comparing runs with contrasting mineral assemblages. In natural systems a full reversal experimental approach is difficult to interpret as the reactions are not truly univariant. Although the relatively low temperature runs used in the experiments prevents the attainment of complete equilibrium, this approach has been found successful when reproducing the expected sequence of reactions with increasing temperature. A larger number of reactions can be determined using a Si-enriched composition instead of using a common serpentinite composition (Fig. 7-2b, c). Thus, a

natural Si-enriched bulk composition from the Cerro del Almirez locality was selected with the aim of constraining reactions (1) and (2). The assemblage of the selected starting material is composed of five (Opx + Atg + Tr + Tlc + Ol) solid phases and contains minerals of both the reactant and product sides of the investigated reactions. This enables us to use the starting material in a quasi-reversal experimental approach where the new growth of stable phases and the disappearance of unstable phases can be monitored.

7.3 Starting material

Most of the antigorite serpentinites outcropping in the Cerro del Almirez are quite homogeneous in composition (Trommsdorff et al. 1998; López Sánchez-Vizcaíno et al. 2005; Garrido et al. 2005) except for CaO. The extent of CaO variation in the bulk composition is directly related with the heterogeneous distribution of relic clinopyroxene in the protolith (Fig. 7-1, bulk-1). Antigorite from Cerro del Almirez is exceptionally ordered and consists of the polysome m = 17 (Padrón-Navarta et al. 2008), where m is the number of tetrahedra in a single chain defined by the antigorite wavelength. This high polysomatic ordering is distinctive of well-equilibrated antigorite in high-grade terrains (Mellini et al. 1987; Capitani and Mellini 2004).

Sample Al06-37 (bulk-2) is an antigorite serpentinite with centimetre-sized orthopyroxene porphyroblasts partially or completely replaced by retrograde talc (Fig. 7-3). Orthopyroxene is commonly elongated with aspect ratios (length/with ratio) of 2.75 ± 0.55. This sample has a remarkably higher silica (Fig. 7-1, bulk-2) content with respect to other Almirez serpentinites (Fig. 7-1, bulk-1). To our knowledge, this is the first report of high-pressure orthopyroxene-bearing serpentinite. Antigorite from sample Al06-37 has high aluminium (3.70 ± 0.34 wt% Al_2O_3; Table 7-1) and chromium contents (0.59 ± 0.08 wt% Cr_2O_3), and is also highly ordered, polysome ranging from m = 15 to m = 16 (M. Mellini, personal communication, 2009). Tremolite is scarce and spatially associated with orthopyroxene. Olivine occurs in the matrix (Table 7-1; Fig. 7-3) and rarely as centimetre-sized veins cutting the foliation. Magnetite (chromium-magnetite and titaniferous magnetite) and pentlandite are also present as accessory minerals.

Large blocks of Si-enriched serpentinite (six samples, usually > 2 kg) were cleaned and cut in parallelepipeds (4–6 cm in length) with a diamond saw. Final parallelepipeds (0.5–1 kg) where crushed in a steel jaw crusher and quartered several times in a riffle-splitter. The resulting aliquots were pulverised in an agate ring mill. Whole rock major elements were analysed using standard X-ray fluorescence procedure (XRF) in the Geoscience Laboratories (GeoLabs), Ontario Geological Survey, Sudbury, Canada. The samples were first run for loss on ignition and then fused with borate flux to produce a glass bead. Ferrous iron was determined in the same laboratory by potentiometric analysis using potassium permanganate as oxidation agent. Ferric iron was calculated from the difference of the total iron measured by XRF and the measured ferrous iron. The composition of the sample Al06-37 (bulk-2; Table 7-1), together with other Si-enriched serpentinite samples, is plotted in Fig. 7-1.

Except for one exploratory run (C-2967; Table 7-2), the experiments were performed using a slightly modified composition from sample Al06-37 (referred to here as bulk-3; Fig. 7-1). Fresh pieces of sample Al06-37 (bulk-2) were crushed and ground in an agate mortar under acetone. We added 2.29 wt% of synthetic wollastonite ($CaSiO_3$) and 1.53 wt% of aluminium hydroxide $Al(OH)_3$ to this composition in order to increase the modal amount of tremolite and diopside that could form and slightly increase the Al_2O_3 and H_2O by 1.0 and 0.5 wt%, respectively (bulk-3; Table 7-1, Fig. 7-1). The final grain size distribution of the starting material used in the experiments was measured by soft X-ray monitored gravity sedimentation (SediGraph 5100, Micromeritics® at the University of Granada). More than 80% of the starting material was normally distributed below 10 μm (with a mean value ca. 5 μm), and the rest of the population clustered around 12–18 μm. Both bulk compositions (bulk-2 and bulk-3, Fig. 7-1) plot inside the antigorite–orthopyroxene–tremolite triangle and, thus, both of them result in the same phase relations.

7.4 Experimental and analytical techniques

The experiments reported here are conventional quenching experiments conducted in a range of 1.6–2.5 GPa and 600–700 ºC. Experiments were performed in 0.5-inch (12.7 mm) end-loaded piston cylinder apparatuses at the Research School of Earth Science (The Australian National University) using a vessel with a 32-mm length bore, employing pure NaCl, low friction assemblies. Sample containers were Au-capsules with an outer diameter of 2.3 and 6–7 mm in outer length resulting in cylindrical samples of 4–6 mm in length. Temperature gradients within the capsule depend, among other factors, on the temperature, pressure, capsule material, assembly design, heater shape and type of solid pressure transmitting media (Schilling and Wunder 2004). This Complex interrelation of factors and the additionally observed off-centre hotspot effect (Pickering et al. 1998) prevent an accurate determination of the temperature gradient in the actual runs. Watson et al. (2002), however, measured at 1,400 ºC, a decrease in temperature of 10–25ºC, at distances of 2–3 mm from the hotspot using a reaction-progress thermometer. For lower temperatures, as those employed in our experiments, the temperature gradient is expected to be much smaller (Schilling and Wunder 2004), in the range of the thermocouple accuracy. Gold capsules were placed in a MgO tube, inside a Teflon coated NaCl-graphite assembly. The use of gold capsule and the "dry" furnace assembly produces conditions close to the Ni–NiO transition (Hermann and Spandler 2008), which is similar to the FMQ buffer in the investigated temperature range. Capsules were welded shut and tested for leakage prior to the experiment. A disk of 1-mm MgO was placed between the thermocouple end-point and the capsule to avoid reaction between them. Pressure was measured directly, converting the load in the cell to pressure for a low friction assembly and was kept constant during the experiments. No pressure corrections were applied because of the low friction behaviour of the NaCl cells and the relatively long run durations. Measurements on piston travel have shown that in such an assembly and given run temperatures, friction dissipates within the first 24–36 h. From this we estimate that pressure is accurate within ±0.1 GPa. Temperatures were measured using type B thermocouples ($Pt_{94}Rh_6$–$Pt_{70}Rh_{30}$), protected by two bore mullite tubes. The thermocouple precision is better than ± 2 ºC and accuracy is ±10 ºC. The samples were quenched at the end of the runs by turning off the power of

Table 7-1. Mode and composition (average and 1σ) of the starting material (sample Al06-37, bulk-2). [X_{Mg} is Mg atoms/(Mg + Fe + Mn + Ni) atoms] and other bulk compositions described in the text.

Weight %	Atg (*n* = 16)	Opx (*n* = 43)	Tremolite (*n* = 10	Olivine (*n* = 52)	Talc (*n* = 38)	Mag (*n* = 4)		[1]bulk-1 *(n = 9)*	bulk-2	bulk-3
mode†	66.8	3.5	-	9.9	19.8	-				
SiO_2	42.38 (0.61)	58.22 (0.66)	59.14 (0.62)	41.29 (0.40)	62.85 (1.71)	0.16 (0.25)	SiO_2	40.54 (0.69)	45.07	44.90
TiO_2	0.02 (0.01)	0.02 (0.01)	0.02 (0.01)	b.d.l.	0.02 (0.01)	0.29 (0.03)	TiO_2	0.17 (0.21)	0.08	0.08
Al_2O_3	3.70 (0.34)	0.03 (0.06)	0.21 (0.12)	b.d.l.	0.09 (0.06)	0.05 (0.02)	Al_2O_3	2.75 (0.46)	2.19	3.10
Cr_2O_3	0.59 (0.08)	0.02 (0.01)	0.02 (0.01)	b.d.l.	b.d.l.	1.71 (0.35)	Fe_2O_3	8.06 (0.45)	3.08	2.99
Fe_2O_3[a]						66.05 (1.86)	FeO*	- -	3.78	3.67
FeO	4.05 (0.16)	8.04 (0.20)	1.87 (0.16)	11.19 (0.52)	1.24 (0.34)	30.62 (0.19)	MgO	36.35 (1.71)	36.98	35.90
NiO	0.09 (0.03)	0.04 (0.01)	0.05 (0.01)	0.26 (0.03)	0.07 (0.02)	0.23 (0.02)	MnO	0.11 (0.02)	0.09	0.09
MgO	38.44 (0.39)	34.82 (0.42)	24.42 (0.40)	49.14 (1.02)	31.41 (1.19)	0.52 (0.11)	CaO	2.45 (1.88)	0.16	1.23
MnO	0.04 (0.01)	0.39 (0.03)	0.12 (0.05)	0.17 (0.04)	b.d.l.	0.06 (0.00)	Na_2O	b.d.l. -	0.05	0.05
CaO	0.02 (0.01)	0.12 (0.03)	13.12 (0.29)	0.02 (0.02)	0.05 (0.09)	0.02 (0.00)	L.O.I.	10.07 (1.15)	7.71	8.00
Na_2O	b.d.l.	0.01 (0.02)	0.23 (0.17)	b.d.l.	0.06 (0.05)		Total	100.51 (0.44)	99.19	100.00
H_2O calc	12.25 (0.13)		2.23 (0.02)		4.74 (0.08)					
Total	101.57 (1.78)	101.72 (1.48)	101.42 (1.95)	102.07 (2.15)	100.53 (3.61)	99.72 (2.86)				
Ions calculated on the basis of 4 oxygens (olivine), 6 oxygens (orthopyroxene), 11 oxygens (talc), 23 oxygens and Fe^{3+}/Fe_{tot} = 0 (amphibole), 6.823 oxygens and Fe^{3+}/Fe_{tot} = 0 (antigorite, *m* =17) and 3 cations (magnetite)										
Si	1.892 (0.016)	1.988 (0.011)	7.948 (0.037)	0.997 (0.010)	3.974 (0.064)	0.006 (0.010)				
Ti	0.001 (0.000)	0.000 (0.000)	0.002 (0.001)		0.001 (0.001)	0.008 (0.001)				
Al	0.194 (0.018)	0.001 (0.002)	0.033 (0.019)		0.007 (0.004)	0.002 (0.001)				
Cr	0.021 (0.003)	0.000 (0.000)	0.002 (0.001)			0.051 (0.010)				
Fe^{3+}						1.918 (0.013)				
Fe^{2+}	0.151 (0.006)	0.230 (0.005)	0.210 (0.018)	0.226 (0.010)	0.065 (0.019)	0.973 (0.005)				
Ni	0.003 (0.001)	0.001 (0.000)	0.005 (0.001)	0.005 (0.001)	0.004 (0.001)	0.007 (0.001)				
Mn	0.002 (0.000)	0.011 (0.001)	0.013 (0.006)	0.004 (0.001)		0.002 (0.000)				
Mg	2.558 (0.013)	1.773 (0.024)	4.894 (0.075)	1.769 (0.027)	2.961 (0.118)	0.029 (0.006)				
Ca	0.001 (0.000)	0.004 (0.001)	1.890 (0.045)		0.003 (0.006)	0.001 (0.000)				
Na			0.059 (0.044)		0.007 (0.006)					
Sum cations	4.823 (0.008)	4.011 (0.011)	15.062 (0.040)	3.003 (0.010)	7.025 (0.064)	3.000				
OH	3.647		2.000		2.000					
X_{Mg}	0.942 (0.002)	0.880 (0.003)	0.955 (0.004)	0.883 (0.008)	0.977 (0.006)	0.029 (0.006)				

† Calculated using image analyses on the polished surface of hand sample Al06-37 (Fig. 3) neglecting tremolite and magnetite , not visible at this scale.

[a] Calculated assuming stoichiometry. L.O.I., Loss On Ignition; b.d.l., below detection limit

[1]bulk-1: Almirez serpentinite average (Garrido et al. 2005); bulk-2: Si-enriched serpentinite (sample Al06-37); bulk-3: the same as bulk-2 but with 2.29 wt.% wollastonite and 1.53 wt.% $Al(OH)_3$ added.

* Ferrous iron was determined by potentiometric analysis in bulk-2 (sample Al06-37). In bulk-1 ferrous iron was not determinated and Fe_{tot} is expresed as Fe_2O_3.
The detection limit for the XRF analyses is 0.01 wt.% except for L.O.I. 0.05 wt.%

the furnace. Afterwards the experiments capsules were pinched and dried in the oven for 4 h. They were mounted in epoxy and ground down until a representative section was exposed.

Mineral analyses of the natural sample used as starting material in the experiments (Al06-37) were performed using a Cameca SX100 electron microprobe at the RSES (Australian National University) with operating conditions of 15-kV acceleration voltage, and 20-nA beam current (Table 7-1). Natural and synthetic mineral and glasses were used as standards. The resulting phases from the experiments were observed in polished mounts under backscattered electron images and analysed using a JEOL JSM 6400 scanning electron microscope (SEM) (Electron Microscopy Unit, ANU), equipped with a LINK-ISIS energy dispersive spectrometer (EDS), operated at 15-kV accelerating voltage, 1-nA beam current and a working distance of 39 mm, with counting time of 100 s. No differences were observed using a spot or defocused beam due to the low alkalis concentration in the hydrous phases (Appendix 14.3).

Table 7-2. Starting material, experimental conditions and assemblages. See Fig.7-1 for mineral abbreviations.

Label	Notes					Major Phases	Minor phases
bulk-2	Si-enriched serpentinite (sample Al06-37)					Atg, Tr, Tlc, Opx, Ol	Mgt, Pn
bulk-3	bulk-2 modified for the experiments					the same as above plus wollastonite and $Al(OH)_3$	
Run no.	Start mat	P (kbar)	T (ºC)	Time (h)	Weight loss (%)*	Major Phases	Minor phases
C-2990	bulk-3	16.0	640	168	0.2	Atg, **Tr**, Tlc, *Ol*	Mgt, Pn
C-2989	bulk-3	16.0	660	168	1.0	Atg, **Tr**, Tlc, *Opx, Ol*	Mgt, Pn
C-3004	bulk-3	16.0	680	168	7.4	**Tr, Opx, Ol, Chl**	Mgt, Pn
C-3044	bulk-3	18.0	680	168	6.0	Atg, **Tr, Opx, Ol, Chl**	Mgt, Pn
C-3012	bulk-3	18.0	700	168	NA	**Opx, Ol, Chl,** (Di)	Pn
D-912	bulk-3	20.0	600	168	0.0	Atg, **Tr**, Tlc, *Ol*	Mgt, Pn
C-2978	bulk-3	20.0	650	168	NA	Atg, **Tr**, Tlc, *Opx* , *Ol*	Mgt, Pn
C-3003	bulk-3	20.0	670	168	1.8	Atg, **Tr, Opx, Ol, Chl**	Mgt, Pn
C-3011	bulk-3	20.0	700	168	NA	**Opx, Ol, Chl,** (Di)	Pn
C-3219	bulk-3	22.5	625	168	1.8	Atg**, Tr,** Tlc**, Opx,** *Ol* **, Chl**	Pn
C-3220	bulk-3	22.5	665	168	2.2	Atg**, Opx, Ol, Chl,** (Di)	Pn
D-756	bulk-3	22.5	680	168	6.5	**Opx, Ol, Chl,** (Di)	Mgt, Pn
C-2967	bulk-2	25.0	670	120	NA	**Opx, Ol, Chl**	Pn

Cleary growing new phases in bold, not growing and relic phases from the starting material in roman and italics, respectively. (Di) diopside is not in textural nor chemical in equilibirum.
*loss of weight of the experimental capsule after its piercing and drying in the oven. NA not available

7.5 Results

7.5.1 Phase relations

Mineral assemblages at different pressure and temperature conditions are presented in Table 7-2 and plotted in Fig. 7-4. The appearance or disappearance curves of key phases were obtained by detailed textural studies of the run assemblages and comparison with the starting material. Lower temperatures runs (D-912, C-2990) show little textural evidences of reaction except for the disappearance of orthopyroxene and growth of tremolite. Olivine grain shapes in these runs are anhedral and sharp indicating they are relicts (Fig. 7-5a). This suggests that water saturated conditions were not attained and

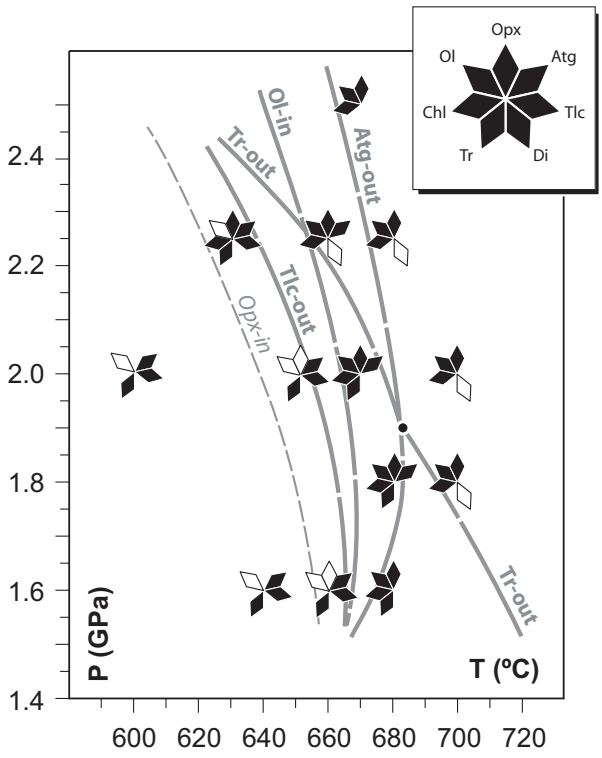

Figure 7-4 Experimental results in the P–T space. Phases in textural equilibrium are shown in black. Empty diamonds indicate relic phases and diopside (always in textural and chemical disequilibrium). Opx-in curve (dashed line) is poorly constrained. See Fig. 7-1 for mineral abbreviations

that the water was first consumed to form tremolite and talc + antigorite at the expense of wollastonite and orthopyroxene, respectively, before olivine completely reacted out.

Opx-in reaction

Minor orthopyroxene observed in runs C-3219, C-2978 and C-2989 is anhedral and, at least in part, is a relict phase from the starting material based on the average grain size (16.0 ± 8.3 lm) and low aspect ratio (1.7 ± 0.5). Nevertheless, no textural evidences of its breakdown were found indicating that either it is in equilibrium with the assemblage or the kinetic barrier of the reaction was not attained. Small amounts of chlorite were detected in one of these runs (C-3219) together with small (2.9 ± 1.4 lm) but euhedral and prismatic orthopyroxene (3.0 ± 1.3 aspect ratio). Because of the high Al-content of the reactant antigorite and the low Al-content of the produced orthopyroxene, we interpret that this chlorite is formed by the reaction between antigorite and talc to produce orthopyroxene [reaction (2)]. This allows us to tentatively trace the Opx-in curve from 650 ºC at 1.5 GPa to c. 600 ºC at 2.5 GPa (Fig. 7-4). More interestingly, talc, occurring as irregular patches in the matrix, is still stable in all these runs (C-3219, C-2978 and C-2989) indicating that Tlc-out and Opx-in curves are not coincident.

Tlc-out and Ol-in reactions

With increasing temperature talc completely disappears and new idiomorphic orthopyroxene and olivine are observed (C-3044, C-3003 and C-3220). These reactions were easily detected by SEM observations because of the growth of large euhedral orthopyroxene and minor olivine. There is a remarkable change in texture beyond the Tlc-out and Ol-in reactions where the assemblage Opx + Atg + Ol + Chl + Tr/Di is stable (compare Fig. 7-5a with Fig. 7-5b, c). The modal amount of olivine is lower than that of orthopyroxene. Olivine overgrowths relict grains from the starting material or occurs as small grain-sized euhedral crystals (usually 2–5 μm, Fig. 7-5c). Widespread needles of prismatic orthopyroxene (up to 30 m in length) with nice crystal shapes grow in a matrix of antigorite and minor chlorite (Fig. 7-5b, c). The size of such needles is considerably larger than in the finely ground starting material, providing additional evidence for growth of orthopyroxene. Moreover, their aspect ratio is also high (3.1 ± 1.3, Fig. 7-5e). From thermodynamic analysis (Fig. 7-2, reaction 2), the Tlc-out curve must occur at lower temperatures than the Ol-in, reaction, although this could not be experimentally resolved with the temperature resolution used in the experiments. Tlc-out, Ol-in and Atg-out reactions converge at 1.5 GPa and 650–670 ºC (Fig. 7-4).

Atg-out reaction

At temperatures higher than 670–680 ºC, the disappearance of antigorite is easily detected by the increase of the modal amount of small olivine crystals (usually 2–4 lm), abundant orthopyroxene needles and chlorite flakes in the matrix (Fig. 7-5d–f). Moreover, water released from the complete antigorite dehydration (c. 8 wt. % for this bulk composition) is evidenced by the high porosity developed in the resulting assemblage Ol + Opx + Chl + Tr/Di (e.g. Fig. 7-5f) and by the loss of weight of the experimental capsule after its piercing and drying in the oven (Table 7-2). Newly formed orthopyroxene and olivine are commonly free of inclusions (Fig. 7-5e). The antigorite-out reaction has a small pressure dependency in the pressure range investigated (1.6–2.5 GPa) increasing from 670ºC and 1.6 GPa to 680ºC at 1.9 GPa. At higher pressure ([1.9 GPa), it slightly bends back (c. 665ºC at 2.5 GPa; Fig. 7-4).

Tr-out reaction

Tremolite is euhedral even at low temperatures. Nevertheless, the reactions involving tremolite and diopside are more sluggish compared with those involving antigorite owing to the different amount of water released. Newly formed diopside shows evidence of textural (Fig. 7-5d) and chemical disequilibrium (see below). In addition, very porous aggregates of relic wollastonite (added to the bulk composition) intermixed with diopside/tremolite (hard to analyse due to the small grain size) were common in some of the investigated runs (e.g. Fig. 7-5a). Therefore, the lack of tremolite was used to constrain the tremolite out curve (Fig. 7-4) instead of the appearance of diopside. With increasing temperature at pressures higher than 1.9-GPa tremolite disappears before the dehydration of antigorite. The Tr-out curves below and above the Atg-out curve (Fig. 7-4) correspond to reactions (7) and (8), respectively (Fig. 7-2).

7.5.2 Phase composition

Average major-element compositions of all phases analysed by EDS–SEM are available through electronic supplementary material (Appendix 14.3).

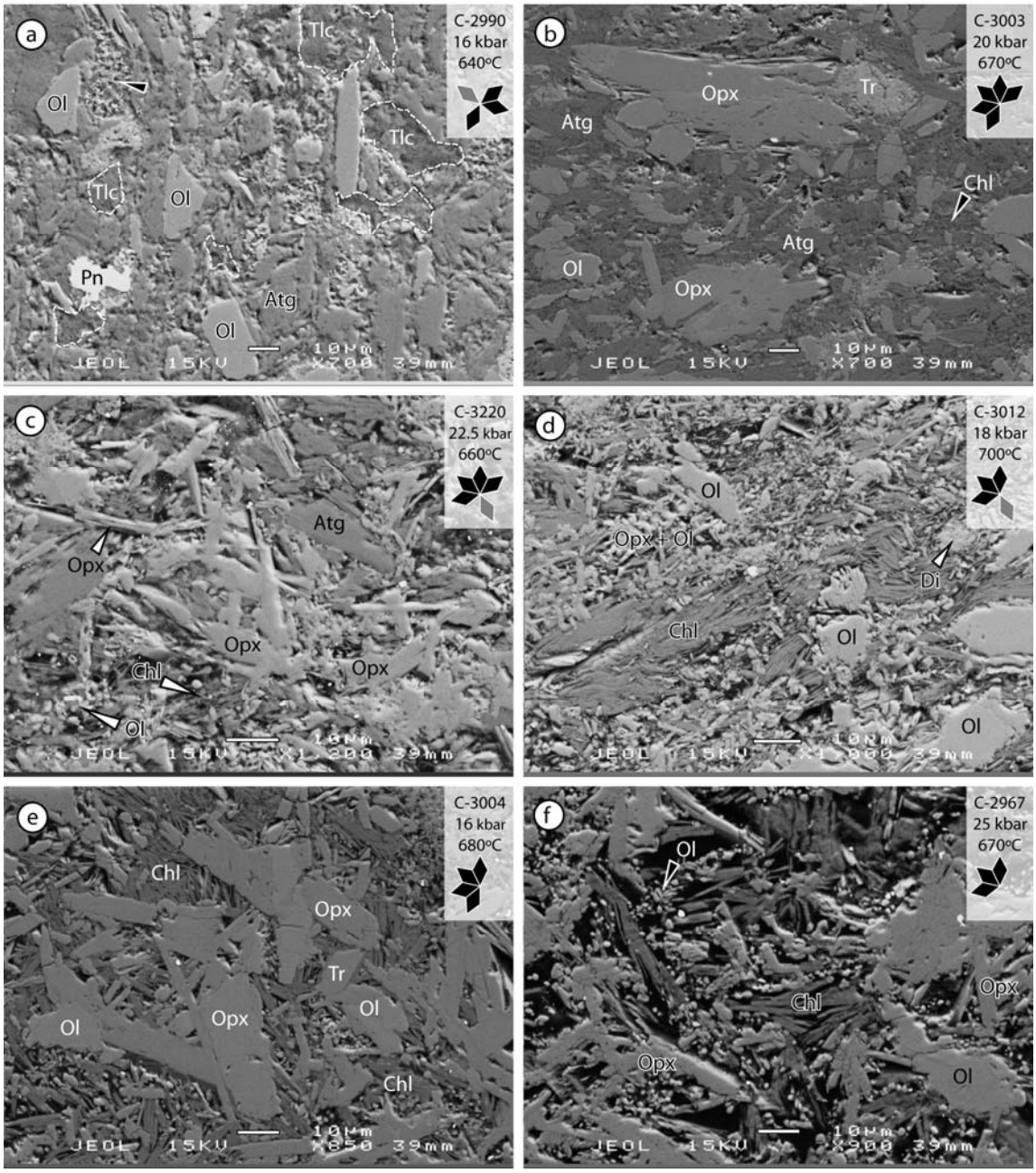

Figure 7-5 Back-scatter electron images showing representative texturas and assemblages of runs products. Scale bars represent 10 µm **a** Antigorite, talc and tremolite (not seen) coexist at 640ºC and 1.6 GPa, olivine is relic from the starting material. Relics of added wollastonite forms porous aggregates intermixed with tremolite (*arrow*) **b** Texture after the talc breakdown and ol-in reaction where antigorite is stable with large prismatic orthopyroxene, anhedral olivine grains (>10 µm) and minor chlorite. **c** Same as b but with orthopyroxene needle crystals and small idiomorphic olivine grains (<5 µm). Chlorite flakes are interstitial and diopside occurs as irregular aggregates. **d** Texture after the antigorite breakdown. Chlorite is the only phase in the matrix where small idiomorphic olivine and orthopyroxene nucleate. Large olivine overgrowths occur on olivine seeds from the starting material. **e** Large olivine and prismatic orthopyroxene (>30 lm) growth in chlorite matrix. Tremolite is stable. **f** Elongated orthopyroxene and two olivine generations (small grain-sized and large overgrowths) are in equilibrium with chlorite in a highly porous texture

Olivine

The main range of Fo-content [expressed as X_{Mg} = Mg/ (Mg + Fe + Ni + Mn), in atoms] is 0.879–0.891 matching the range observed in olivine from the starting material (Table 7-1). No compositional variation among olivines in the various textures was observed. Also no systematic increase in X_{Mg} with temperature is present.

Antigorite

At temperatures higher than the Ol-in and Tlc-out curves antigorite is stable with chlorite and has a mean Al-content slightly lower than in the starting material (3.40–3.63 wt% Al_2O_3; Appendix 14.3). At lower temperatures the amount of chlorite is minor or lacking, so the Al-content in antigorite is not buffered by the assemblage. The highest value (3.75 ± 0.33 wt% Al_2O_3) was found at 640ºC and 1.6 GPa where no evidence of reaction was observed. The Cr_2O_3 content is also high (0.51–0.67 wt. %) and similar to that of the starting material.

Chlorite and orthopyroxene

Chlorite displays a variation in aluminium with pressure. This variation can be explained through a series of substitutions: $^{IV}Al^{VI}AlSi_{-1}Mg_{-1}$ (tschermaks exchange), $^{IV}AlCr^{3+}Si_{-1}Mg_{-1}$ (Cr-tschermaks exchange) and, to a lesser extent, $^{IV}Al_2Ti^{4+}Si_{-2}Mg_{-1}$ (Ti-tschermaks exchange). Chromium content is high (1–2 wt. % Cr_2O_3). A correlation between ^{IV}Al and $^{VI}Al + 2 \cdot Ti + Cr$ exists and is fairly dependent on pressure (Fig. 7-6a).

Orthopyroxene in the starting material, as well as in the low temperature assemblages, is almost aluminium-free (Table 7-1; Appendix 14.3), whereas orthopyroxene in equilibrium with chlorite displays a significant increase in aluminium (0.45–1.13 wt. % Al_2O_3). Similar to chlorite, orthopyroxene displays a good correlation of tetrahedraland octahedral-coordinated aluminium. Tschermaks exchange in the orthopyroxene strongly increases with increasing pressure (Fig. 7-6b).

Other phases

Talc analyses show little chemical variation (Appendix 14.3). Talc is low in Fe and Al and has a narrow X_{Mg} ratio of 0.972–0.977. No significant tschermaks substitution has been detected in tremolite with Al_2O_3 content within the range of the starting material (0.21 ± 0.12 wt. %). Porous aggregates of diopside (Fig. 7-3f) were hard to analyse with systematic low totals and a wide range in X_{Mg} = 0.786–0.857 (Appendix 14.3). Pentlandite is ubiquitous and occurs in all runs, whereas magnetite is lacking in some of them (Table 7-2). Magnetite is also chromium rich like in the starting material.

Mg partitioning

The order of preference for Mg expressed as X_{Mg} in the experiments is: talc>tremolite>chlorite>antigorite>orthopyroxene (Fig. 7-7). The observed sequence of Mg partitioning between olivine and other phases is similar to those reported for other lower-P prograde serpentinite (Trommsdorff and Evans 1972, 1974; Springer 1974; Frost 1975) and high-P prograde serpentinite (Trommsdorff et al. 1998). One exception is diopside, not shown in Fig. 7-7, with a range in X_{Mg} of 0.786–0.857, far from the expected (X_{Mg} = 0.965–0.975) as observed in natural assemblages (cf. Trommsdorff and Evans 1972). Orthopyroxene also deviates slightly from the Kd = 1.0 line when chlorite is

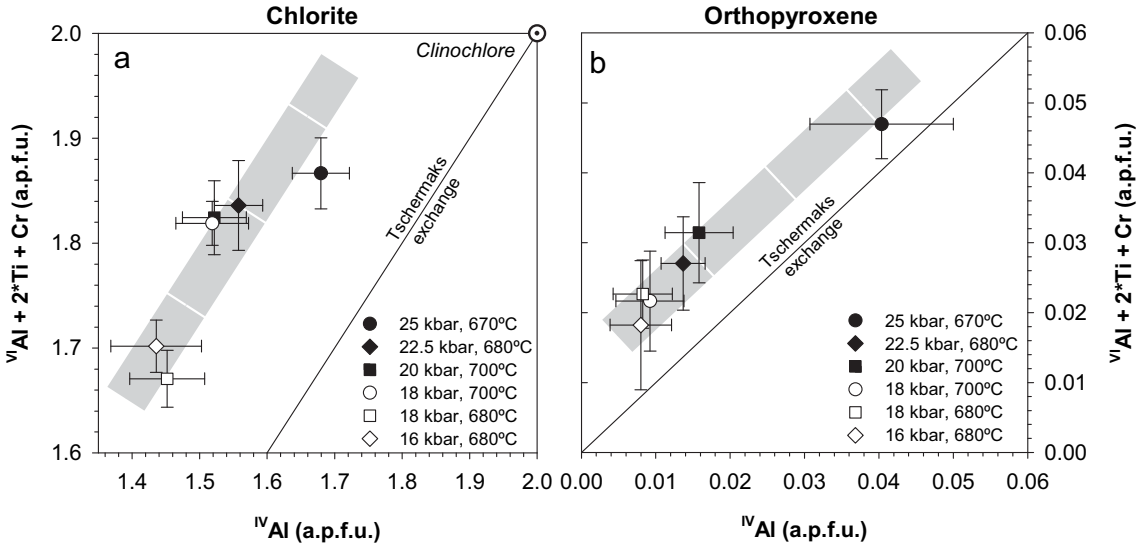

Figure 7-6 Composition in atoms per formula unit (apfu) of experimentally determined chlorite and orthopyroxene in equilibrium with olivine. *Black* and *white symbols* represent high (>18 kbar) and low pressure runs (≤18 kbar), respectively. Run C-2967 performed on bulk-2 is indicated with grey symbol. **a** The tschermaks content in chlorite (normalised on 28 oxygens) increases with pressure but never reaches the clinochlore end-member in the PT range investigated. All analyses plot above the tschermaks exchange line indicating some extent of vacancies in the octahedral site. **b** Orthopyroxene (normalised to six oxygens) follows the same pattern. *Error bars* in a and b refer to 1σ errors of typically ≥5 analyses per run.

present at the highest temperature range investigated (670–700ºC) reaching a maximum value of 0.909 ± 0.004 for a 0.886 ± 0.008 olivine (700ºC and 2.0 GPa, run C-3011).

7.6 Discussion

7.6.1 Attainment of equilibrium

In the experiments reported here, the higher temperature runs show well-equilibrated textures where prismatic orthopyroxene and idiomorphic olivine grow in a chlorite matrix. (Fig. 7-5d–f). Moreover, the assemblage orthopyroxene–antigorite–olivine (Fig. 7-5b) is also texturally well equilibrated reproducing nicely the observed texture in the natural rocks (Fig. 7-3). However, lower temperature runs preserve olivine relics from the starting material suggesting only a partial equilibrium. Nevertheless, because the starting material contained minerals on the reactant and product side, reactions could be traced by the new growth and disappearance of phases. Additionally, the comparison of size and shape of minerals in the starting material with run products provides information on mineral growth. One interesting aspect of our study is that the appearance of a new product phase (for example Opx) does not coincide with the complete disappearance of a reactant phase (for example talc). This could be interpreted at first sight as a "sluggish reaction." Instead, as shown in the next section, this is a direct consequence of the studied natural system, where reactions are continuous rather than discontinuous. The calculated temperature range of 20 ºC of fields between

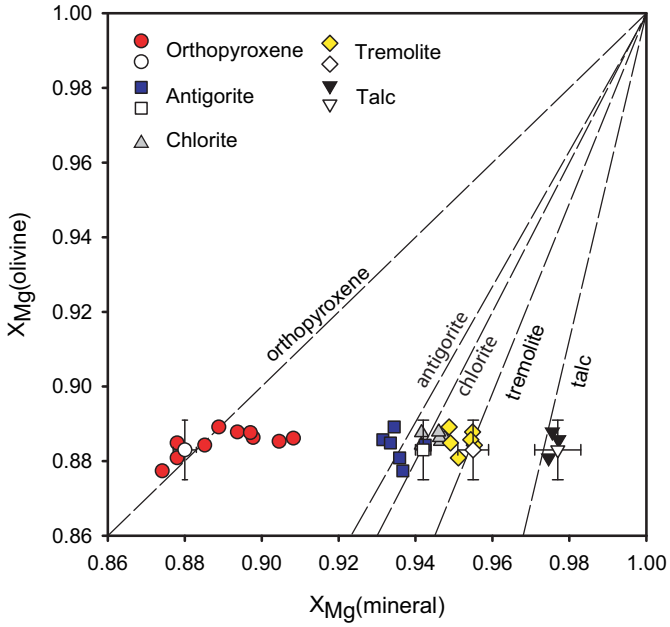

Figure 7-7 Partitioning of Mg between olivine and other silicates [X_{Mg} is Mg atoms/(Mg + Fe + Mn + Ni) atoms]. Solid lines are taken from Trommsdorff and Evans (1972) except for chlorite and antigorite which are eye-ball fits. *Empty symbols with error bars* indicate the composition of the starting material showed in Table 7-1

orthopyroxene-in and talc-out as well as olivine-in and antigorite-out (Fig. 7-8) is in very good agreement with the experimental data (Fig. 7-4). This suggests that no significant overstepping (not more than 10 ºC) is required for a reaction to progress.

Except for diopside, the order of Mg-partitioning in the experiments (Fig. 7-7) is the same as that observed in equivalent natural assemblages, indicating attainment of local chemical equilibrium. Also, there is no evidence for Fe-loss to the gold capsule. Departure from the equilibrium in the Mg partitioning may occur if the oxygen conditions change owing to hydrogen diffusion to the gold capsule. However, the presence of magnetite in equilibrium with the assemblage in most of the runs and the systematic occurrence of pentlandite point to constant oxygen and sulphur fugacity in the pressure and temperature range investigated. The magnesium enrichment in the orthopyroxene is most likely due to the tschermaks exchange ($Fe^{-1}Si^{-1}{}^{VI}Al^{IV}Al$) in equilibrium with chlorite. Indeed, if tschermaks is subtracted from the orthopyroxene composition, its X_{Mg} shifts to values closer to those of olivine (e.g. 0.898 ± 0.005 in C-3011). All these observations, suggest that the experiments partially approached equilibrium during the relatively long run durations.

7.6.2 Variables controlling the position of the antigorite dehydration

The antigorite composition in natural systems is Complex and thus there are several variables influencing the position of the antigorite breakdown reaction (e.g. Ulmer and

Trommsdorff 1999 and references therein). The effect of these additional components in antigorite must be evaluated before the experimental results from simplified systems can be applied to nature.

Iron is a major component that must be considered in natural serpentinite. A significant part of the iron in serpentinite occurs as magnetite as a result of Complex reactions during the onset of serpentinization (e.g. Bach et al. 2006; Evans 2008; and reference therein) that increase the X_{Mg} in the minerals relative to their protolith. The role of magnetite during the antigorite dehydration has not yet been addressed but it is believed to behave as a passive phase. Moreover, magnetite occurs independently of the assemblage stable in the PT range investigated here (Table 7-2). The iron addition to the CMSH system can be evaluated by computing a fixed bulk composition, phase diagram section ("pseudosection"). Phase relations for the Si-enriched serpentinite bulk composition used in the experiments (bulk-3 in Table 1) were computed using Perple_X software (Connolly 2005) in the CFMSH system under water saturated conditions (Fig. 7-8a). Ferric iron content (see the analytical techniques section) was subtracted from the bulk composition resulting in a X_{Mg} = 0.946 [X_{Mg} = Mg/(Mg + Fe), in molar proportion]. Considering that all ferric iron is forming magnetite the bulk composition would shift to a higher magnesium number (X_{Mg} = 0.965). Nevertheless the value of X_{Mg} = 0.946 was preferred because of the low modal amount of magnetite in Al06-37 (<3 vol%) supporting that most of the ferric iron from the bulk rock is hosted in antigorite.

Comparing the CMSH phase diagram (Fig. 7-2a) with the pseudosection computation (Fig. 7-8a) three main differences stand out: (1) the univariant reactions are now divariant fields in the CFMSH system; (2) invariant points are now transformed into univariant reactions, and (3) the terminal reactions (e.g. Atg-out) are displaced to lower temperatures relative to the CMSH system. The magnitude of the displacement and the extent of the divariant fields are directly related with the Fe–Mg partitioning of the different phases (Fig. 7-7). For instance, the iron effect on the extent of the divariant field equivalent to reaction (4) (Ol + Tlc → Opx + L, Fig. 2) is very minor (<5 ºC) in the CFMSH pseudosection (Fig. 8), because olivine and orthopyroxene (with a $K_D^{Mg–Fe}$ ~ 1.0) occur on both sides of the reaction and because the talc composition is close to the Mg-endmember. This is not the case for the divariant fields equivalent to reactions (1) (Ol–Di–Atg–Opx field) and (2) (Tlc–Tr–Atg–Opx) in the CFMSH system, resulting in a considerable enlargement of the divariant fields and displacement of reactions to lower temperatures. The width of the divariant fields equivalent to reaction (1) and (2) is c. 20 ºC and c. 30 ºC at 1.8 GPa, respectively (Fig. 7-8a, b). Therefore, these fields can be detected with the experimental resolution used in this work. From the experimental results we conclude that the Opx-in and Tlc-out curves, as well as the Ol-in and Atg-out curves, are not coincident (Fig. 7-4). The temperature interval between the appearance and disappearance of these phases as calculated in the pseudosection is in good agreement with those experimentally observed (Fig. 7-8a).

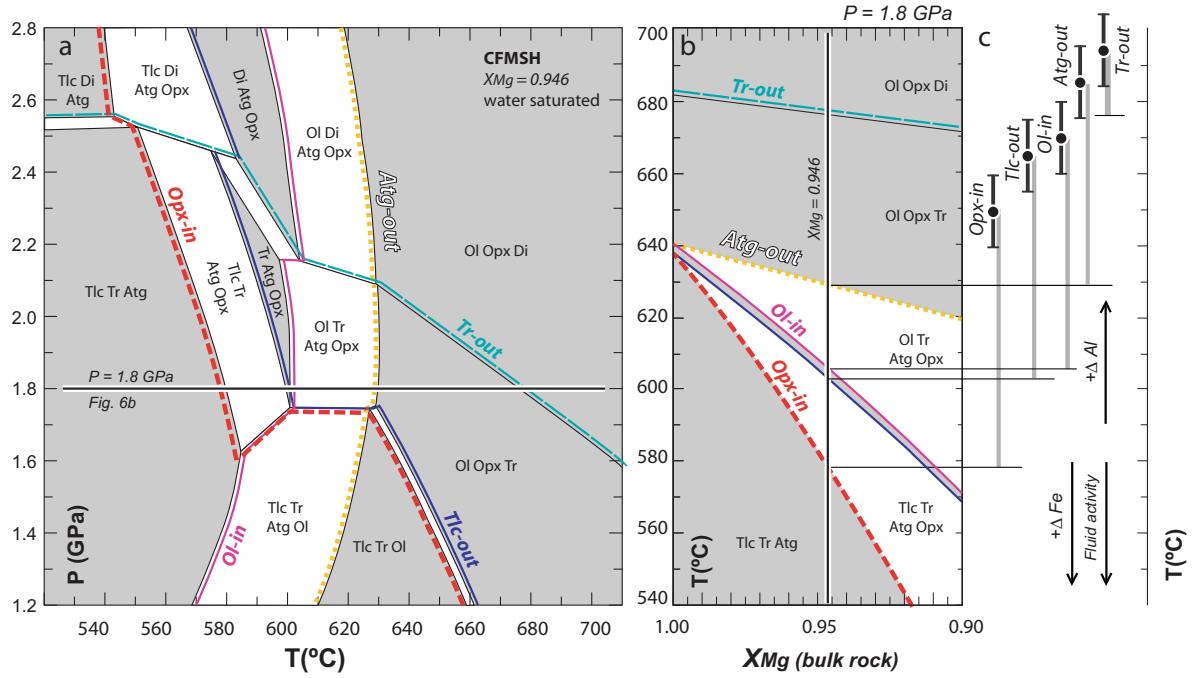

Figure 7-8 a Pressure–temperature phase diagram section for a Si-enriched bulk composition (Al06-37, Table 7-1, bulk-3) in the CFMSH system computed with PerpleX (Connolly 2005). Solid Solutions considered here are the same as in López Sánchez-Vizcaíno et al. 2005 (see their Table 6 for details). Thermodynamic data were taken from the internally consisted database of Holland and Powell (1998, revised 2002), except for the antigorite bulk modulus (Hilairet et al. 2006a). White and grey fields are divariant and trivariant fields, respectively. Lines dividing fields with the same variance are univariant reactions. Key reactions discussed in the text are labelled and highlighted with different line symbols (e.g. red dashed line for Opx-in) **b** Isobaric (P = 1.8 GPa) XMg-temperature pseudosection showing the temperature dependency of the fields from a. Vertical line is the XMg in Al06-37. **c** Temperature differences (grey vertical lines) between the experimentally determined (Fig. 4) and the computed curves of b. Temperature accuracy of thermocouples are depicted as thick black brackets (temperature gradient in the capsule and temperature hysteresis of the reactions are not considered here). These differences are attributed to aluminium in antigorite. The effect of iron and decrease of the fluid activity are also schematically showed with arrows.

The dependency of the antigorite breakdown reaction with decreasing bulk X_{Mg} can be inspected at a constant pressure in Fig. 7-8b. The position of the antigorite dehydration curve for X_{Mg} = 0.946 in the bulk rock (Atg-out in Fig. 7-8b) shrinks only 10 ºC relative to that of the CMSH system. The effect of bulk rock X_{Mg} is, however, much more pronounced for the appearance of orthopyroxene, which appears at 60 ºC lower than in the pure CMSH system (Fig. 7-8b). Other components that must be addressed are aluminium and other trivalent cations like Fe^{3+} and Cr^{3+}. The pseudosection approach cannot be used in this case because there are no thermodynamic solid solution models for these cations in antigorite. Their effect in the terminal reactions can be, however, qualitatively assessed by comparing the positions of the experimentally determined curves (Fig. 7-4) with those calculated in the CFMSH system (Fig. 7-8b, c). The discrepancies in temperature between the calculated and observed curves are c. 60–70ºC at 1.8 GPa. We interpreted these differences as due to the incorporation of Al and minor Cr and Fe^{3+} in the antigorite structure. Bromiley and Pawley (2003) reported a

temperature difference between the antigorite dehydration curve in the MSH and MASH systems of about 50 ºC below 2.5 GPa, in good agreement with our results. Interestingly, the experimentally determined Tr-out curve almost matches that calculated in the pseudosection (Fig. 7-8b, c), because of the low Al solubility in clinopyroxene and tremolite for this pressure–temperature range.

The water activity of the fluid is also an important variable controlling the position of the antigorite dehydration equilibria in a P–T phase diagram. Although unknown, the water activity in our experimental runs is constrained by the assemblage and thus should correspond closely to that occurring in the nature. Lowering the water activity shifts the reaction to lower temperatures. Perrillat et al. (2005) reported a decrease of the water activity (aH_2O = 0.5–0.8) during experimental dehydration of Al-bearing antigorite at very low temperatures (570ºC at 1.8 GPa). The lower water activity in their experiment was imposed by the type of containers (hexagonal boron nitride) required for the time-resolve X-ray diffraction measurement (Perrillat et al. 2005). Such a great reduction of water activity is unlikely to occur in nature. The composition of the fluid released during the antigorite dehydration is difficult to be constrained from fluid inclusions studies because fluid compositions are re-equilibrated with their host minerals (Scambelluri et al. 2001). At 750ºC and 3.0 GPa antigorite dehydration fluids dissolve c. 6 wt% SiO_2, c. 2 wt% MgO and only minor amounts of CaO and Al_2O_3 (Tenthorey and Hermann 2004), and are thus essentially aqueous fluids.

7.6.3 Comparison to other studies

Since the pioneering work of Bowen and Tuttle (1949), the phase relations involving serpentine minerals (antigorite, crysotile and lizardite) have been intensively surveyed from the experimental point of view (Bromiley and Pawley 2003; Ulmer and Trommsdorff 1999 and references therein). Excluding studies at very high pressures ([5 GPa) (Bose and Navrotsky 1998), antigorite breakdown through reaction (1) (antigorite = forsterite + orthopyroxene + water) has been bracketed by many authors (Ulmer and Trommsdorff 1995; Wunder and Schreyer 1997; Bromiley and Pawley 2003; Komabayashi et al. 2005), and, at lower pressure, through reaction (4) (antigorite = forsterite + talc + water) by Johannes (1975) and Evans et al. (1976).

The iron effect on the position of the antigorite dehydration curve is minor, as discussed before, but has to be taken into account when comparing the results obtained here with previous works. Although all the previous experimental studies were addressed to establish the antigorite stability in the MSH or MASH systems, they used natural antigorite that invariably contained appreciable amounts of FeO (specially in the case of Ulmer and Trommsdorff 1995 and sample BM1913,87 from Bromiley and Pawley 2003).

Figure 7-9a and b shows the positions of the antigorite terminal reaction as determined in the present study compared to previous work. Ulmer and Trommsdorff (1999) reported higher temperature stability for antigorite (~20ºC) compared to the antigorite breakdown reaction observed here (Atg-out, Fig. 9). The same reaction, when reported by Wunder and Schreyer (1997), occurs at c. 40ºC lower temperatures. The significant discrepancy between the position of reaction (1) by Ulmer and Trommsdorff (1995) and

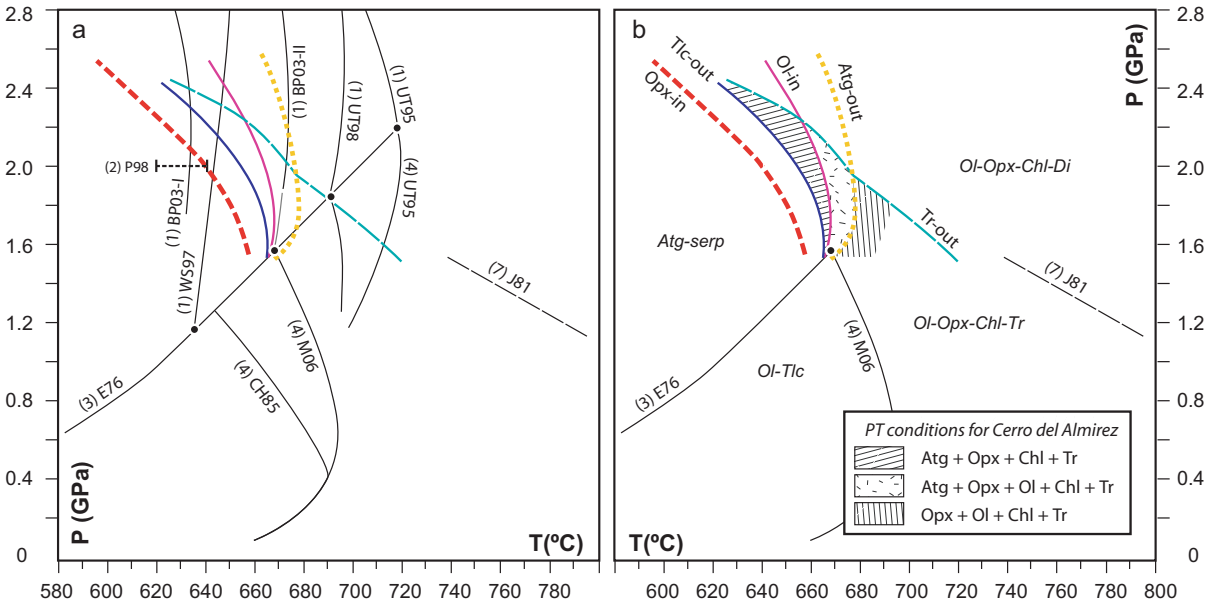

Figure 7-9 a Summary of selected experimental curves involving the antigorite breakdown. The numbers in brackets indicate the reactions as showed in Fig. 2. Experimental fits are by E76—Evans et al. (1976); J81—Jenkins (1981); CH85—Chernosky et al. (1985); WS97—Wunder and Schreyer (1997); UT99 Ulmer and Trommsdorff (1999); BP03-I and BP03-II- Bromiley and Pawley (2003) for free-Al (0.01 wt% Al_2O_3) and Al-bearing antigorite (3.06 wt% Al_2O_3), respectively; M06—Melekhova et al. (2006). The bracket of reaction (2) P98 from Pawley (1998) is also showed. Superimposed are the experimentally determined curves from this study (curve patterns as in Figs 8, 9b). Also shown are the invariant points [Di] (filled black dots) at the intersection of reaction (3) E76 and reactions (1) and (4) from previous works. **b** Preferred experimentally-based petrogenetic grid for Si-enriched bulk composition from Cerro del Almirez. PT-conditions inferred for the antigorite + orthopyroxene + chlorite + tremolite assemblage, antigorite + orthopyroxene + olivine + chlorite + tremolite and olivine + orthopyroxene + chlorite + tremolite assemblage (prograde harzburguite) in Cerro del Almirez are depicted with different patterns.

Wunder and Schreyer (1997) has been already discussed by Wunder and Schreyer (1997), Mysen et al. (1998) and Bromiley and Pawley (2003). They concluded that the most likely explanation is the contrasting Al-content of the antigorite used in these studies and, to a lesser extent, other trivalent cations such as Cr^{3+} and Fe^{3+}. However, in this discrepancy the higher Fe-content of the natural antigorite (with a X_{Mg} = 0.965) used by Ulmer and Trommsdorff (1995) compared to the almost Fe-free antigorite (X_{Mg} = 0.991) from Wunder and Schreyer (1997) must also be taken into account. The X_{Mg} of our starting material is similar to the X_{Mg} of the natural antigorite from sample Mg159 chosen by Ulmer and Trommsdorff (1999), but their sample contains less trivalent cations (Mellini et al. 1987). Thus, the reason for the higher temperature of antigorite breakdown reported by Ulmer and Trommsdorff (1999) is not fully clear. We expect that the antigorite-out reaction determined here is located close to the maximum temperature for natural systems as the antigorite from our study has the highest Al-content among all experimental studies.

Bromiley and Pawley (2003) conducted a series of experiments of antigorite dehydration in the MSH and (F)MASH systems in order to demonstrate the stabilization of antigorite to considerably higher temperatures and pressures in the presence of Al. They found

that at 2 GPa the antigorite stability field expands by c. 40 ºC from about 630 ºC for Al-free antigorite to 670 ºC for Al-bearing antigorite (3.06 wt% Al_2O_3) [curves (1)BP03-I and (1)BP03-II, respectively in Fig. 9a]. At higher pressure the thermal difference is even larger (90 ºC at 5 GPa). The Al-bearing antigorite dehydration curve experimentally determined by Bromiley and Pawley (2003) is in excellent agreement with the results presented here for an antigorite with 3.70 wt% Al_2O_3 and 0.59 wt% Cr_2O_3. Moreover, their natural antigorite BM1913,87 (X_{Mg} = 0.916) and the antigorite used in this study (X_{Mg} = 0.942) share a relatively high iron content. Therefore, it is expected that the Al-effect would be even greater (>40 ºC) for Fe-poor antigorite. The antigorite used in the starting material for this study contains high amounts of aluminium and chromium and derives from rocks that were formed in a high pressure environment. Hence, the experimentally determined breakdown of antigorite reported here should closely match the one expected in natural subducted serpentinites between 1.6 and 2.5 GPa.

In silica-rich bulk compositions (Fig. 7-1), a first antigorite dehydration reaction (2) occurs at considerably lower temperature (Fig. 7-2). This reaction has only been experimentally investigated by Pawley (1998) in the MSH system. She determined the position of the reaction at 2 GPa to be situated between 620 and 640ºC [bracket (2) P98 in Fig. 7-9a], which is in agreement with our results for the Opx-in curve (Fig. 7-9a, b). The invariant point [Di] in MSH (Fig. 7-2a) arises at the intersection of reactions (1) and (2). Considering the divariant fields, this corresponds with a narrow temperature range of 660–670ºC at c. 1.6 GPa, where all the terminal reactions corresponding with reactions (1) and (2) converge (Fig. 4). This is in good agreement with the intersection of reaction (1) from Bromiley and Pawley (2003), reaction (3) (Atg → Ol + Tlc + L) from Evans et al. (1976) and reaction (4) (Ol + Tlc = Opx + L) from Melekhova et al. (2006) at 670ºC and 1.6 GPa (Fig. 7-9a, b). Reaction (4) is independent of the antigorite Al-content and rather insensitive to the Fe-effect and thus can be used independently to constrain the position of the invariant point [Di]. Reaction (4) (Melekhova et al. 2006) intersects with the Atg-out curve from this study and from Bromiley and Pawley (2003) in their (F)MASH system at about 1.6 GPa. As outlined in the previous section, the invariant point [Di] in MSH will translate into a univariant line in FMSH (Fig. 7-8a) that terminates the Atg + Opx assemblage at 1.8 GPa. Due to the negative slope of the reaction (4), the termination of Atg + Opx will be displaced to lower pressure of 1.6 GPa and slightly higher temperature with the increasing of Al-content in the antigorite.

The tremolite-out reactions [reactions (7) and (8)] have been poorly constrained experimentally. Jenkins (1981) reported experiments up to 1.4 GPa in the CMASH system of the reaction (7) (Tr + Ol = Di + Opx). The slope of this reaction is in agreement with the results reported here (Fig. 7-4). It is worth noting that the reaction (6) could not be determined using the starting material of this study but its intersection with reaction (1) must occur at 680ºC and 1.9 GPa at the invariant point [Tlc] in the CMSH system (Fig. 7-2).

7.6.4 PT conditions of Cerro del Almirez

The experimental approach used here permits to constrain the pressure and temperature conditions for the Ol + Opx + Chl + Tr assemblage (termed chlorite

harzburgite by Garrido et al. 2005) extensively outcropping in Cerro del Almirez, as well as for the Atg + Opx + Ol + Tr assemblage outcropping only as metre-sized lenses close to the antigorite isograd. The antigorite stability field found in this study constrains the minimum temperature for the chlorite harzburgite between 660 and 680 ºC at temperatures between 1.6 and 2.5 GPa, (Fig. 7-9b). The occurrence of tremolite in the Ol + Opx + Chl rocks limits the pressure below 1.9 GPa. The Tr-out reaction also constrains the maximum temperature, which ranges from 680 to 710ºC for 1.9 and 1.6 GPa, respectively.

The PT conditions for the antigorite dehydration in Cerro del Almirez has been previously constrained (1.7–2.0 GPa and 635–640 ºC) combining thermodynamic modeling (pseudosections) of selected Cerro del Almirez bulk composition (López Sánchez-Vizcaíno et al. 2005, 2009) with the PT conditions for the equilibrium between OH-titanclinohumite and ilmenite + olivine fitting the experimentally determined reaction by Weiss (1997) (see also Ulmer and Trommsdorff 1999). López Sánchez-Vizcaíno et al. (2005) estimated a minimum temperature of about 650ºC for the prograde assemblage at P = 1.70–2.05 GPa. The uncertainty on the FeO/Fe_2O_3 ratio was overcome by subtracting different modal amounts of magnetite occurring in the Almirez serpentinites (López Sánchez-Vizcaíno et al. 2005). The thermodynamic data for the antigorite iron endmember was taken from Rupke et al. (2004) and an ideal mixing model was considered. The large aluminium content in the Cerro del Almirez antigorite (up to 4 wt% Al_2O_3, Trommsdorff et al. 1998; Padrón-Navarta et al. 2008) is a common feature of serpentinites from high-grade terranes (Uehara and Kamata 1994; Auzende et al. 2002, 2006). However a solution model for Al in the antigorite is not yet available. Moreover, a new experimentally determined equation of state for the antigorite indicates that the isothermal bulk modulus (K_0) was underestimated in the Holland and Powell's (1998) database. The updated bulk modulus shrinks the stability of the antigorite to lower temperature and pressures (c. 10ºC at 1.8 GPa, Hilairet et al. 2006a, 2006b; Nestola, personal communication, 2009). The lack of a solid solution model for a chloritecomponent in antigorite and the underestimated bulk modulus for the antigorite in the thermodynamic dataset (Holland and Powell 1998, revised 2002) used by López Sánchez-Vizcaíno et al. (2005) explain the slightly lower temperatures previously reported for the minimum temperature for the chlorite harzburgite.

The pressure conditions for the chlorite harzburgite reported here are consistent with those estimated for the metamorphic peak in the upper series of the Nevado– Filábride Complex. Puga et al. (1999, 2002) found a temperature range from 650 to 725ºC at 1.8 GPa using the Grt–Cpx geothermometer of Ellis and Green (1979) in eclogitized dykes preserved in metarodingites from the Cerro Blanco-Montenegro outcrop (20 km eastwards from Cerro del Almirez), in agreement with our results. However, their pressure constraints are based on the experimental curves from Ulmer and Trommsdorff (1995) and Wunder and Schreyer (1997) and, as discussed before, cannot be directly applied to the Cerro del Almirez. Eclogites studied in other areas of the Nevado–Filábride Complex indicated pressures of 1.2–1.3 GPa and 500–540ºC (Gómez-Pugnaire and Fernández-Soler 1987) and near 1.5 GPa and 700ºC (Puga et al. 1989). Other lithologies (scapolite-bearing metaevaporites) point to a minimum pressure of 1.8 GPa at 500–650ºC (Gómez-Pugnaire et al. 1994). The maximum pressure recorded in the metapelites from the upper series are deduced by the assemblage of chloritoid +

staurolite + almandine + kyanite, suggesting pressure values of 1.5–1.7 GPa for 600ºC (Puga et al. 2002). In any case the chlorite harzburgite from Cerro del Almirez preserves the highest temperatures recorded by the Nevado–Filábride Complex rocks.

7.6.5 New antigorite dehydration in silica enriched serpentinite

The present study constrains the pressure-temperature conditions for the assemblage Atg + Opx and Atg + Opx + Ol in equilibrium with tremolite and minor chlorite under water saturated conditions (Fig. 7-9b). Opx-bearing serpentinite with or without olivine is stable between 640 and 680ºC and pressure higher than 1.6 GPa. The bulk chemistry of these rocks indicates an enrichment of silica relative to other common serpentinites (Fig. 7-1). The resulting assemblage is diagnostic of metaperidotites that experienced silica metasomatism (Manning 1994, 1995, 2004; Peacock and Hyndman 1999). Si-rich serpentinite may be a common lithology in mid-ocean ridge and subduction settings. At the basement of slow-spreading mid-ocean ridges, peridotite is heavily veined, with talc and talc-oxide-sulphide veins (Bach et al. 2006). Earlier serpentinized peridotite undergoes massive replacement by talc, forming amphibole-chlorite-talc schists (Bach et al. 2004). These metasomatic reactions require either removal of Mg or addition of Si to the system. In the mid-Atlantic ridge, talc altered rocks are formed by silica metasomatism, where silica is mobilised from gabbros and harzburgite undergoing high-temperature (>350ºC) fluid–rock interactions (Bach et al. 2006; Paulick et al. 2006; Alt et al. 2007). Seawater-alteration coupled with Mg-removal generates serpentinites with anomalously high SiO_2/MgO ratios, which are reported in ophiolites (Marchesi et al. 2006) and abyssal peridotites (Snow and Dick 1995). Hence, Si-rich serpentinites produced either by Si-metasomatism or Mg loss during mid-ocean ridge processes may be a common input in subduction zones.

Antigorite-talc schist may also form during prograde metamorphism in subduction settings as a result of chaotically intermixing of ultramafic rocks with metasediments and metabasites in a mélange zone (Moore and Lockner 2007; King et al. 2003; King and Bebout 2006; Spandler et al. 2008). Si-enriched ultramafic rocks such as talc-schist and talc-bearing serpentinite have been observed in several HP rock suites (Sorensen and Grossman 1989, 1993; Bebout and Barton 2002; Spandler et al. 2008). These hybrid rocks are interpreted as the result of the interaction of ultramafic rocks with Si-rich fluid (Spandler et al. 2008). Si-rich fluids can be provided by the dehydration of mafic and metasedimentary rocks in the blueschist/eclogite-facies transition (Clarke et al. 1997; Spandler et al. 2003, 2008) and hence it is expected that Si-enriched ultramafic rocks are common in the serpentinized mantle wedge above subduction zones.

Talc-schist and talc-bearing serpentinite may hence be common lithologies in subduction settings and will undergo different dehydration reactions. Antigorite and talc will react at lower temperature than the terminal antigorite dehydration. Although this reaction is not expected to be as important in the transfer of water to mantle depth as the breakdown of antigorite, it represents nevertheless a dehydration event in subduction zones that has not been considered so far. We anticipate that this reaction might be particularly important for the fore-arc mantle wedge. The amount of water released would depend on the modal proportion of these two phases that is ultimately related

with the degree of interaction of the ultramafic rocks with the metasomatic fluid. The appearance of orthopyroxene in talc-bearing serpentinite is restricted to pressures higher than 1.6 GPa inside the antigorite stability field. Moreover, the transition from tremolite to diopside at 2.3–2.5 GPa is an additional excellent barometer in silica enriched serpentinites (Figs. 2, 8). The Opx-serpentinite facies is thus helpful in the reconstruction of PT conditions of subducted ultramafic rocks where common serpentinites have no diagnostic assemblage over a large range in PT space (Scambelluri et al. 1995; Hermann et al. 2000).

7.7 Conclusions

Piston cylinder experiments on silica enriched serpentinites from the Cerro del Almirez ultramafic Complex constrain the maximum temperature stability for highly polysomatic ordered (m = 15–16) antigorite with high-Al and Cr contents to 680ºC at 1.9 GPa. This is also the maximum pressure stability of tremolite in an olivine + orthopyroxene + chlorite assemblage. In this bulk composition, the olivine-in reaction occurs 20–30ºC below the antigorite out reaction. At 1.8 GPa, Al and other trivalent cations in antigorite expand its stability 60–70ºC when compared with the Al-free system. The maximum temperature for antigorite stability is bracketed between 680 and 660ºC at 1.6 and 2.5 GPa. The Tr-out reaction also constrains the maximum temperature for chlorite harzburgite from Cerro del Almirez, which ranges from 680 to 710ºC for 1.9 and 1.6 GPa. These data are in reasonable agreement with peak P–T conditions estimated for the Nevado–Filábride Complex upper series. Orthopyroxene + antigorite assemblage is restricted to high-pressure metamorphic conditions of silica enriched serpentinite, and constraints P–T conditions in cold to intermediate temperature subduction environments, where antigorite serpentinite has no diagnostic assemblages over a large pressure and temperature range.

In silica enriched serpentinites, antigorite and talc dehydrate at lower temperature than the final breakdown of antigorite. This dehydration reaction releases a variable amount of water depending on the relative proportion of talc and antigorite, and represents therefore a lower temperature dehydration event in Si-metasomatized, subducted ultramafic rocks.

Acknowledgments

Three anonymous reviewers are thanked for their insightful and helpful reviews. We thank D. Scott, W.O. Hibberson and D. Clark for their technical support in the running of the high-pressure experiments at the RSES (ANU) and Frank Brink for his technical assistance in the Electron Microscopy Unit (ANU). We also thank Prof. Marcello Mellini for his comments on an early draft of the paper. This work was supported by the Spanish "Ministerio de Ciencia e Innovación (MICINN)" through research grants CGL2006-04440, CGL2007-61205/BTE, and ACI2006-A9-0580, the Spanish Council for Research (CSIC) through grant 2008-30I014, and by the "Junta de Andalucía" research groups RNM-145 and RNM-131. J.A. Padrón-Navarta is supported by fellowship AP2005-060 from the "Programa de Formación del Profesorado Universitario". J. Hermann acknowledges financial support by the Australian Research Council. We are grateful for the editorial help and support provided by J. Hoefs.

Submitted to Earth and Planetary Science Letters

8 Fluid transfer into the wedge controlled by high-pressure hydrofracturing in the cold top-slab mantle

Padrón-Navarta, JA[1*] · Tommasi, A[2] · Garrido CJ[3] · López Sánchez-Vizcaíno, V[4*]· Gómez-Pugnaire MT[1,3]· Jabaloy, A[4] · Vauchez, A[2]

Before attaining the mantle wedge, where they trigger partial melting, volatiles released from dehydration reactions in the slab have to migrate across a relatively cold (<750ºC), peridotite-layer above the incoming slab. To unravel the mechanisms allowing for this initial stage of fluid transport, we performed a detailed field and microstructural study of prograde peridotites in the Cerro del Almirez ultramafic massif (Betic Cordillera, Spain), where one of the most important dehydration reactions in subduction zones, the high-pressure antigorite breakdown (P = 1.6-1.9 GPa and T ≈ 680ºC), can be mapped in the field. This reaction led to arborescent growth of centimeter-size olivine and orthopyroxene, producing a chlorite-harzburgite with a spinifex-like texture. Microstructural observations and crystal preferred orientations (CPO) mapping show no evidences of solid-state deformation during the prograde growth of olivine and orthopyroxene at the expenses of antigorite. However, a few tens to a hundred meters away from the reaction front, the metamorphic texture is partially obliterated by grain-size reduction zones (GSRZ), a few mm to meters wide, which form roughly planar conjugate structures. GSRZ are characterized by (1) sharp contacts with undeformed spinifex-like texture domains, (2) an important reduction of the olivine grain size (60-250 μm), (3) olivine color change (from brownish to colorless), (4) decrease in the modal amount of orthopyroxene, and (5) at the mm- to cm-scale, irregular shapes and abrupt terminations. Field and microstructural observations rule out relative displacement across these GSRZ. Changes in modal composition imply reactions with fluids undersaturated in silica. Analysis of olivine crystal-preferred orientations (CPO) in GSRZ shows similar patterns, but a higher dispersion than in neighboring spinifex-like domains. It also reveals mm- to cm-scale discrete domains with rather homogeneous crystallographic orientations suggesting inheritance from the preexisting spinifex-like olivines in the host peridotite. Misorientation angles between neighboring grains in the GSRZ show peaks at ~5-10º and ~20º, but the rotations are not crystallographically controlled. Based on these observations, we rule out the formation of the GSRZ by dynamic recrystallization during dislocation creep and propose that they record brittle deformation (microcraking) of the spinifex-like chlorite-harzburgites, probably induced by hydrofracturing at high pressure and relative low temperature conditions (680-710ºC). High-pressure hydrofracturing can, thus, be invoked an efficient mechanism for fluid flow across the cold top-slab mantle layer, allowing the slab-derived fluids to ingress in the wedge.

Keywords: subduction, fluid flow, hydrofracturing, high-pressure, deformation, chlorite-harzburgite, olivine, crystal preferred orientations, grain size reduction, recrystallisation

1. Departamento de Mineralogía y Petrología, Universidad de Granada, Spain.
2. Géosciences Montpellier, CNRS & Université Montpellier 2, France
3. Instituto Andaluz de Ciencias de la Tierra (IACT), Granada, Spain.
4. Departamento de Geología, Universidad de Jaén Linares, Spain.
5. Departamento de Geodinámica, Universidad de Granada, Spain.

8.1 Introduction

Transfer of fluids from the subducting slab to the mantle wedge is an essential process in the subduction dynamics, controlling the onset of the partial melting process and, hence, the location and the chemical characteristics of the arc magmatism. Release and fluid motion from different parts of the subducting slab has been proposed as one of the possible explanations for seismic tremor (e.g. Brown et al., 2005). Moreover, hydration-induced rheological weakening in the mantle wedge (Mackwell et al., 1985, Mei et al., 2002, Arcay et al., 2005) has been considered to change the subduction dynamics, producing extensive thinning of the upper plate (Arcay et al., 2006) or development of cold diapirs in the wedge (Gerya and Yuen, 2003). Furthermore, the release of fluid from the downgoing slab has been recently suggested as the driving force controlling the style of subduction itself (Gerya et al., 2008). Fluid migration linked to devolatilization reactions is, thus, required in order to explain all these processes involved in the subduction machinery. Nevertheless, the mechanisms allowing the extraction of aqueous fluids (or hydrous melts, see Hermann et al., 2006 for a comprehensive review of this terminology) from the slab and cold supra-slab mantle, where devolatilization reactions take place, are still a matter of debate. Estimated dehydration fluxes (e.g., Hacker, 2008) depart significantly from low fluid–rock interaction and limited fluid flow proposed at high-P low-T conditions in some fossil subduction zone suites based on stable isotope systematics and petrologic constrains (e.g., Ague, 2003, Hermann et al., 2006 and references therein), pointing to channeling of fluids into high permeability pathways, such as fractures or lithologic contacts.

In the last decades high attention has been paid to the dehydration of serpentinite (hydrated ultramafic rocks) in subduction zones because of its potential ability to produce large amounts of fluids at high pressure conditions through a series of discontinuous reactions (Ulmer and Trommsdorff, 1995; Scambelluri et al., 1995; Schmidt and Poli, 1998; Scambelluri and Philippot, 2001; Padrón-Navarta et al., 2010). Chlorite-harzburgite produced by the serpentinite dehydration at high pressure (~1.5-5.5 GPa) is an important lithology expected in both the downgoing slab mantle and in the cold mantle wedge above the slab that was hydrated in earlier stages of subduction (Fig. 8-1) (Hacker et al., 2003; Garrido et al., 2005). Fluids released from the slab, and wedge serpentinite, dehydration in the range of 50-150 km depth certainly have to cross this cold (680-750ºC), 5-10 km thick layer of chlorite-harzburgite before attaining the hotter inner parts of the mantle wedge, where ductile deformation and fluid-rock reactions enhance the permeability and allow porous flow (e.g., Stevenson, 1989; Aharonov et al., 1995; Rosenberg and Handy, 2000; Holtzman et al., 2003; Takei, 2005; Le Roux et al., 2008; Soustelle et al., 2010). Yet, the processes allowing transport of the dehydration-related fluids from the downgoing slab across the high-viscosity low permeability chlorite-harzburgite layer have not been investigated so far, despite their implications for the fluid chemical signature and for the mechanical behavior of the slab-mantle interface.

In this paper we present a combined field and microstructural study of chlorite-harzburgite from the km-scale Cerro del Almirez ultramafic massif, Betic Cordillera, SE

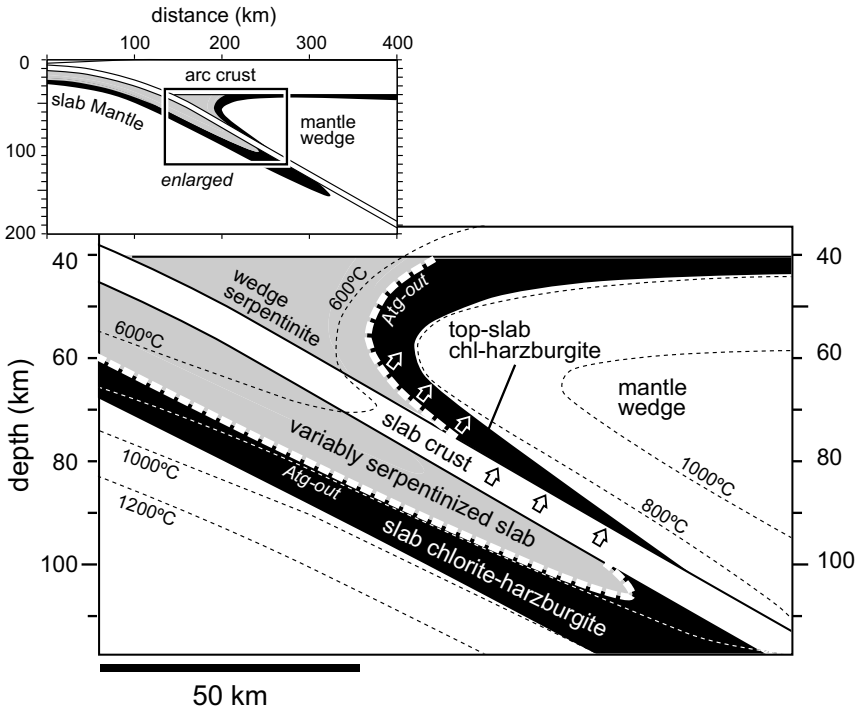

Figure 8-1. Ultramafic rocks metamorphic facies distribution in an intermediate age subduction zone setting (Nankai, SW Japan, modified from Hacker et al., 2003), highlighting the antigorite-out isograd (dashed white line) and the loci of chlorite-harzburgite (black) affected by fluid flow derived from the antigorite dehydration (black arrows).

Spain, where the antigorite-out isograd produced by high-pressure serpentinite dehydration, the most important devolatilization reaction in subduction zones, can be mapped at the outcrop scale (Trommsdorff et al., 1998; Garrido et al., 2005; Padrón-Navarta et al., 2008). Analysis of the microstructures, crystal preferred orientations, and compositional changes in localized, grain-size reduction bands crosscutting the prograde chlorite-harzburgite, suggest that brittle deformation took place under high-pressure conditions, probably owing to hydrofracturing. We discuss the connection between this deformation mechanism and the transport of hydrous fluids, produced at the antigorite dehydration front, into the mantle wedge and the potential implications of this process for subduction.

8.2 The Cerro del Almirez ultramafic massif (Betic Cordillera, S Spain)

The Cerro del Almirez ultramafic massif is the largest (~2.3 km^2) of several small and discontinuous ultramafic bodies outcropping in the Nevado-Filábride Complex, the lowermost unit of the Internal Zones of the Betic Cordillera (Southern Spain, Fig. 8-2a and b). The Betic Cordillera is part of the Betic-Rifean orogenic system (or peri-Alborán orogenic system), the westernmost segment of the Alpine belt in Europe. These ultramafic rocks are intercalated with metapelites, marbles and locally with orthogneisses, in the upper part of the Nevado-Filábride sequence.

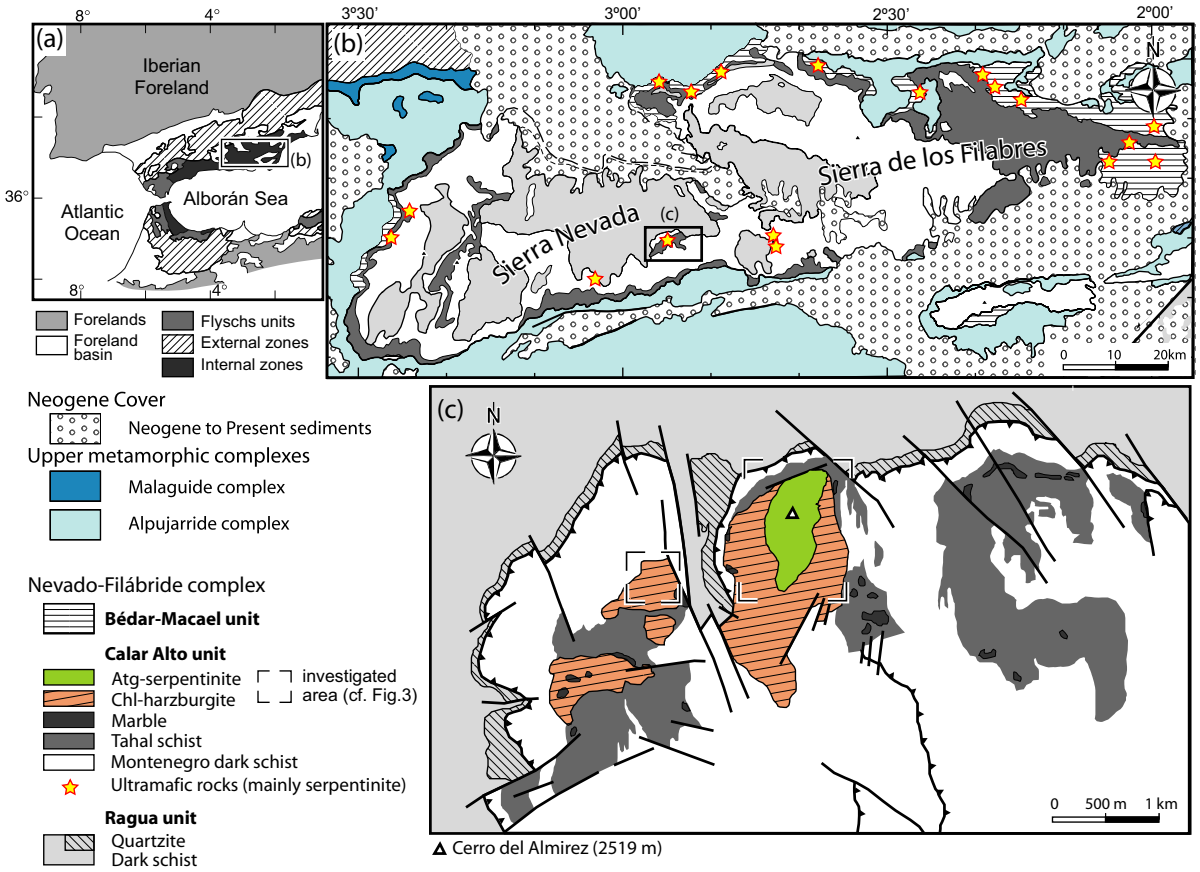

Figure 8-2. (a) Simplified geological map showing the main tectono-metamorphic domains of the Betic-Rif orogen; (b) Location of the Cerro del Almirez ultramafic massif (inset) together with other ultramafic rocks (mainly serpentinite, stars) outcropping in the Nevado-Filábride Complex (modified from Martínez-Martínez et al., 2002); (c) Geological map showing the distribution of the two main ultramafic rock types (antigorite serpentinite and chlorite-harzburgite) in the Cerro del Almirez (modified from IGME, 1981, Schönbächer, 1999, Hürlimann, 1999 based on our own field observations).

The Cerro del Almirez massif is the main ultramafic body of the Nevado-Filábride sequence. It is mainly composed of two rock types: foliated antigorite serpentinite in the upper part and more massive chlorite-harzburgite in the lower part of the body (Figs. 8-2c and 8.4, Trommsdorff et al., 1998). Three minor ultramafic bodies west of the Cerro del Almirez complete the sequence; they are composed essentially of chlorite-harzburgite (Fig. 8-2c). Detailed petrographic and mineral chemistry studies, as well as thermodynamic calculations, lead Trommsdorff and coworkers (1998) to interpret the chlorite-harzburgite as a result of the high-pressure dehydration of the antigorite serpentinite during the Alpine metamorphism of the Nevado-Filábride Complex. This event occurred during the Middle Miocene, as revealed by SHRIMP U-Pb analysis of zircon resulting in an age of 15.0 ± 0.6 Ma (95 % c.l.) (López Sánchez-Vizcaíno et al., 2001). Analysis of metabasites of the upper Nevado-Filábride sequence indicates pressures and temperatures of 1.2-1.4 GPa and 550-600ºC for this early alpine event (Gómez-Pugnaire and Fernández-Soler, 1987). Higher pressures and temperatures, however, have been determined locally in several different rock types (>1.8 GPa and

650-700ºC, Gómez-Pugnaire et al., 1994; Trommsdorff et al., 1998; Puga et al., 2002). Experiments (Padrón-Navarta et al., 2010) further constrain the maximum stability of antigorite (680ºC at 1.9 GPa) and the peak metamorphic conditions of the chlorite-harzburgite to 680–710ºC and 1.6–1.9 GPa.

One of the most striking features of the prograde chlorite-harzburgite is its spinifex-like texture (Fig. 8-3a, Trommsdorff et al., 1998), owing to the growth of large arborescent olivine crystals (up to 10 cm in length) in a matrix composed of radial aggregates of acicular orthopyroxene crystals (50-100 μm wide and 0.5-2 mm long), long chlorite flakes (<1mm), aggregates of magnetite, and rare idiomorphic tremolite. Both the grain size and the preferred orientation of olivine and orthopyroxene crystals in the spinifex-like chlorite-harzburgite vary at the centimeter to meter scale. Strong shape preferred orientation of olivine crystals producing a typical fish-tail texture (Fig. 8-3a) is usually observed in rocks with large and highly anisomorphic olivine crystals (up to 10 cm in length and aspect ratios of 50:1), whereas more radial/arborescent or even random oriented textures tend to correspond with smaller grain size (5-10 mm) and lower aspect ratio (~6:1) olivine crystals. The ol:opx modal proportion is similar (~1:1) in both textures (strongly and randomly oriented). Although very strong shape preferred orientations exist locally, there is not a general orientation pattern of the spinifex texture at the scale of the massif. Moreover, not every chlorite-harzburgite outcrop displays a spinifex-like texture; chlorite-harzburgite characterized by coarse granular olivine occurs intercalated with the spinifex-like one at the meter to tens of meters scale over the entire massif. In the present paper we focus on the study of recrystallization structures that overprint these primary metamorphic textures.

8.3 Macro- and meso-scale observations

Primary, metamorphic textures of prograde chlorite-harzburgite are locally transected by zones where important grain size reduction (GSR) of the olivine crystals occurs, being more patent where it affects the spinifex-like chl-harzburgite. At the outcrop and thin section scales, GSR zones (GSRZ) are characterized by a conspicuous color change of olivine. Spinifex-like olivine is brown (Fig. 8-3a and b) due to the large amount of solid and fluid inclusions (Trommsdorff et al. 1998), while fine-grained olivine in the GSRZ is pale green and lacks impurities at submicroscopic scale.

Grain size reduction usually occurs in irregular bands with roughly planar shapes that are commonly a few mm to several cm wide and cm to m in length. More rarely, they occur as small irregular pockets a few mm to cm wide (Figs. 8-3b and c). The abundance of the GSR bands and the spacing between them are highly variable across the massif. In the Cerro del Almirez largest body, GSR mostly affects small (mm^3 to cm^3) volumes of the chlorite-harzburgite. In the smaller chlorite-harzburgite massif to the west of the main body (Figs. 8-2c and 8-4b), GSR affects larger volumes (cm^3 to m^3) of the chlorite-harzburgite. In these areas, GSR occurs as closely-spaced (2-3 cm apart) bands, approximately parallel to each other and show sharp contacts with the host spinifex-like harzburgite. At larger scales, smaller GSRZ occasionally join larger planar grain-size reduction zones (GSRZ) up to 1-2 meter wide, where the primary spinifex-like texture of chl-harzburgite vanishes (Fig. 8-3d).

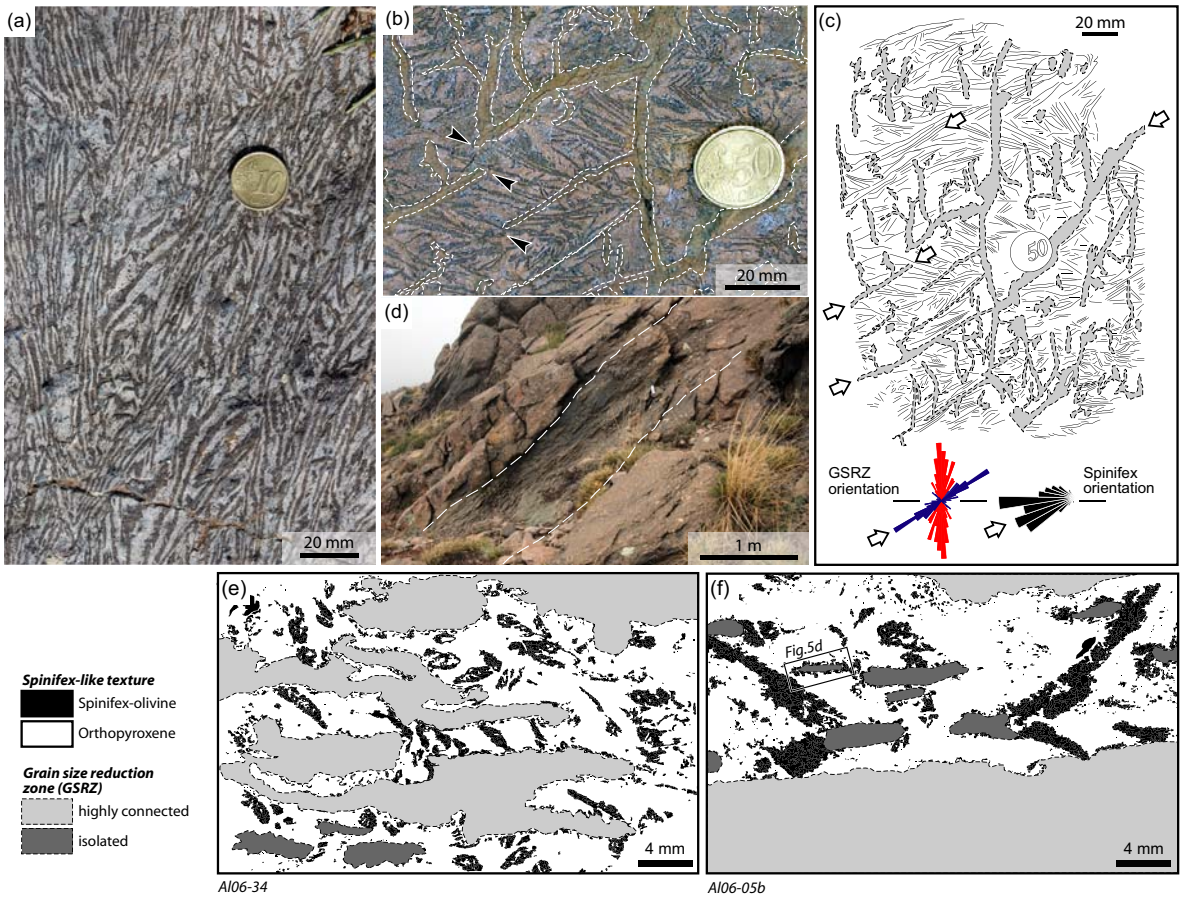

Figure 8-3. (a) Undeformed spinifex-like texture in chlorite-harzburgite showing centimeter-size brown olivine (dark areas) and aggregates of acicular enstatite weathered to talc (light areas) (see also Fig. 5a); (b) Cm-wide grain size reduction zones (GSRZ) (limits highlighted with white dashed lines) cutting a spinifex-like texture. Note that GSRZ have sharp contacts at this scale and are mostly discontinuous. Spinifex olivines are preserved without evidences of deformation or displacement by the GSRZ; black arrows mark abrupt terminations of GSRZ (see also Fig. 5b and c); (c) Sketch of a wider view of the same rock as in (b) highlighting the relationship of two family planes of GSRZ and the orientation of the apparent maximum spinifex olivine elongation; (d) View of an outcrop where GSRZ affect a larger rock volume (ca. 1 m thick) and define rough planar structures; (e) and (f) Thin section sketches showing in detail the irregular, almost sinuous contacts between GSRZ and the host rock. Both connected (light gray) and isolated (dark grey) GSRZ are observed in these two samples.

Careful observation at the outcrop scale using the spinifex-like olivine as strain markers (arrows in Fig. 8-3b) reveals no relative displacement (shearing or opening) associated with the grain size reduction process. In figure 8-3c, we show both the orientation of mm-wide GSR bands and the trace of the maximum elongation of the spinifex-like olivine in the outcrop (see also Fig. 8-3b). At first sight, these bands indicate an apparent non-isotropic orientation pattern, characterized by two families of planes intersecting at high angles (ca. 60º), but with no clear relationship with the average spinifex olivine orientation (horizontal in Fig. 8-3c). However, a closer analysis shows

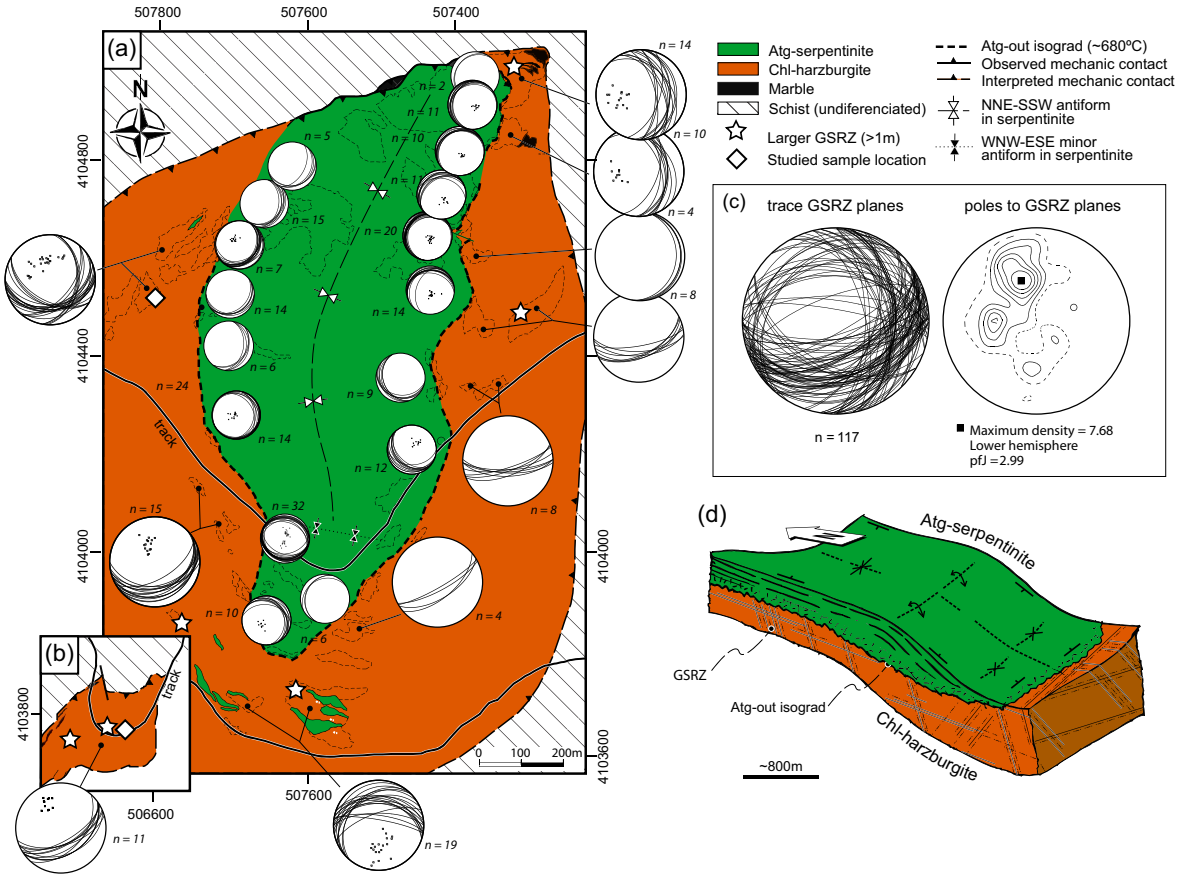

Figure 8-4. (a) and (b) Enlarged geological maps of the two ultramafic bodies from the Cerro del Almirez area (location is indicated by squares in Fig. 8-2c). Large stereonets (geographic reference frame, north on the top) show the orientation of large GSRZ measured in well exposed outcrops (highlighted by dashed lines) and small ones display the orientation of serpentinite foliation, n = number of measurements. Coordinate frame system is WGS (1984), UTM 30 N; (c) GSRZ traces and poles to planes for the whole data set highliting the average 40-50° angle between the two families of GSRZ orientations; (d) Block sketch summarizing the structural relations between the reaction front, serpentinite foliation, and GSRZ. Note that the GSRZ cut at different angles the antigorite out isograd.

that one of the two GSRZ follows a locally well-developed shape preferred orientation of the spinifex olivine (white arrows in Fig. 8-3c).

At thin section scale, although a roughly planar structure is still observed, GSRZ show more irregular, lobate shapes, but remarkably sharp contacts (Fig. 8-3e and f). These irregular GSR bands are usually interconnected (light grey domains in Fig. 8-3e and f). However, recrystallization of single spinifex-olivine crystals is also observed producing isolated GSR pockets in an, otherwise pristine, spinifex-like texture (dark grey domains in Fig. 8-3e and f, see also Fig. 8-5d). Similarly to the outcrop scale, analysis of the spinifex structure on both sides of a GSRZ shows no relative displacement across it.

When the reduction of the grain size affects larger volumes of rocks, one of the GSRZ orientations tends to dominate with respect to the others, resulting in thick (typically 50 cm – 1m), usually meter-spaced (2 m or more), dark green, planar zones (Fig. 8-3d).

Neither olivine stretching nor magnetite lineation were observed in these thicker bands, pointing also to an absence of displacement across them. The contact with the host spinifex-textured harzburgites keeps always as sharp as in the thinner GSRZ (Fig. 8-3b and c). Their distribution is heterogeneous at the scale of the ultramafic bodies (stars in Fig. 8-4a) irrespective of their distance to the antigorite-out isograd. Wide GSRZ occur both close to the reaction front in the eastern part of the main ultramafic body, but also further away from it (Fig. 8-4a), as well as in the smaller ultramafic body located to the west (Fig. 8-4b).

Figures 8-4a and b (large stereonets) show the measured orientation of the GSRZ bands in well-exposed outcrops. Only the larger bands that define a rough planar fabric are plotted, but another orientation at ~40-50º from the main one (Fig. 8-4b and c) occurs systematically in most of the outcrops. For reference, the serpentinite foliation, marked by the orientation of antigorite, is also shown (small stereonets in Fig. 8-4a). This shallowly dipping foliation (20-30º) defines an open NNE-SSW trending synclinal. Minor, WNW-ESE trending folds with rare crenulation cleavage are superimposed. In contrast, large GSRZ have more steeply-dipping orientations (30-60º) with one or more directions. As in the smaller mm- to cm-wide GSRZ (Fig. 8-3b and c), analysis of the orientation data for all the larger bands suggests that they group around two conjugated planes at ca. 55º to each other, oriented E-W and N-S in average, respectively (Fig. 8-4c). The three-dimensional block in Fig. 8-4c schematically depicts the relative orientation of the structure of antigorite-serpentinite, the GSRZ in chl-harzburgite and the Atg-out isograd in Cerro del Almirez main body.It can be noted that the atg-out isograd is fairly subhorizontal and most GSRZ (especially in the eastern and southern areas of the body) crosscut it at high angles, and that the orientation of the GSRZ network is oblique to the foliation of atg-serpentinite.

8.4 Microstructures

8.4.1 Spinifex-like texture

Olivine in the spinifex-like texture is very coarse (typically from 5 mm to up to 10 cm in length) and commonly encloses randomly oriented chlorite flakes (200-400 μm, Fig. 8-5a). Spinifex olivine crystals are straight or, more commonly, slightly curved (sheath shapes). Grain boundaries are straight and commonly underlined by chlorite flakes. Spinifex olivine has a typical brownish pleochroism and is crowded with Fe-Cr-Ti-oxides, fluid inclusions (Scambelluri et al., 2001a), and silica-rich mineral inclusions (orthopyroxene and talc) parallel to (100) olivine planes (Ruiz Cruz et al., 1999). Microscopic lamellae of titanclinohumite parallel to (001) have been also reported (López Sánchez-Vizcaíno et al., 2005). Orthopyroxene occurs in fan-like aggregates (up to 8 cm wide) composed of fine acicular crystals with similar crystallographic orientations (200-300 μm in length) and randomly-oriented chlorite flakes (Fig. 8-5a).

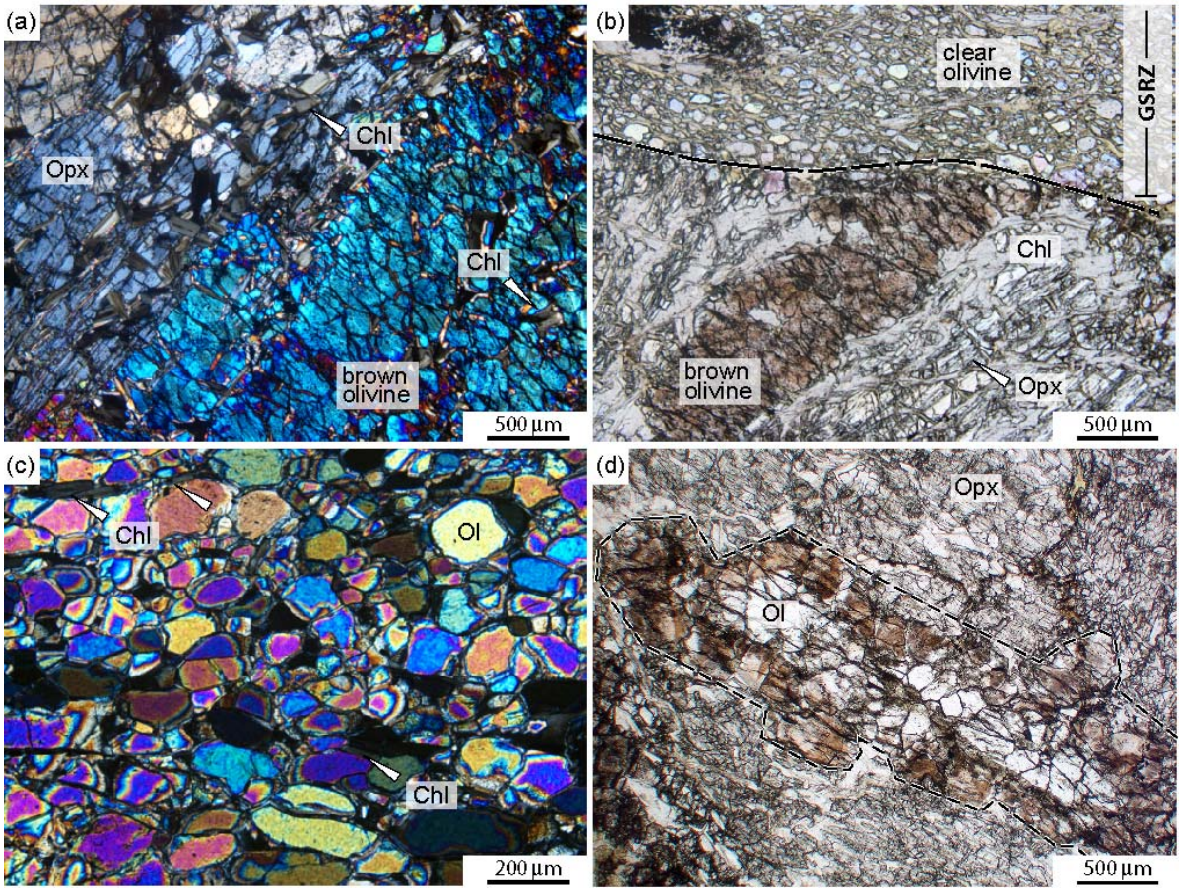

Figure 8-5. (a) Undeformed spinifex-like texture with coarse enstatite and brown olivine (> 10 mm). Straight grain contacts suggest growth in equilibrium.. Chlorite (arrow) and tremolite commonly occur as inclusions in both olivine and enstatite or in the matrix (crossed nicols); (b) Sharp contact between a GSRZ (upper half) composed mainly by fine-grained olivine and an undeformed zone (lower half) composed by coarse brown olivine, orthopyroxene (Opx), and chlorite (Chl). Note the abrupt color change of olivine between the two zones; (c) Detail of a GSRZ where the grain size of olivine ranges from 100 to 200 µm. Note the lack of orthopyroxene and the presence of small chlorite grains (white arrows) along olivine grain boundaries; (d) Isolated fine-grained olivine pockets in an otherwise well preserved spinifex-like texture domain. Note that inner parts of the aggregate are colorless, whereas the rims conserve the original brownish color. Orthopyroxene is well preserved and not recrystallized.

8.4.2 Grain size reduction zones (GSRZ)

At thin section scale (Figs. 8-5b and c), GSRZ are easily distinguished by (1) reduction of the olivine grain size from mm-scale to 60-250 µm (leading to average areas of 15,000-26,000 µm², Table 1) and (2) an abrupt change in color of olivine from brownish in the spinifex-like domains to colorless in the recrystallized domains due to a lower content of inclusions (Fig. 8-5b). GSRZ have very sharp contacts with undeformed spinifex-like texture domains (Figs. 8-3e, f, and 8-5b). They are mostly composed of olivine, chlorite, magnetite, and minor tremolite (Fig. 5c). Chlorite flakes are smaller (100-150 µm in length, Fig. 8-5c) and locally tend to align parallel to the elongation of the GSRZ. Olivine is equigranular with 5-6 faceted polygonal shapes (Fig. 8-5c), resulting in a well developed granoblastic texture. Olivine crystals are deformation-free, without subgrains or wavy extinction, and free of inclusions. Grain boundaries are usually masked by low-

temperature serpentine due to late weathering. Orthopyroxene is also observed locally in GSRZ, forming isolated aggregates with irregular, highly lobate shapes, but its proportion is much lower than in the spinifex-like texture domains (Table 8-1). Scarce orthopyroxene aggregates in GSRZ are acicular with fan-like distribution in the same way as those observed in the spinifex-like texture domains. In places, talc replaces orthopyroxene due to late weathering.

Recrystallization of isolated single spinifex olivine (Fig. 8-5d) also occurs outside the main GSRZ (see also Fig. 8-3e and f). In these cases, the grain size reduction is less severe (300-400 μm). Both the external shape of the original spinifex olivine crystal and brownish color, in particular at the rims, are preserved. Misorientation is weak between the recrystallized fragments derived from a single former spinifex olivine, as indicated by the preservation of similar polarization colors and extinction angles. Orthopyroxene enclosing these isolated GSRZ is not recrystallized. Furthermore, these isolated recrystallized domains within an otherwise undeformed spinifex-like harzburgite are less weathered and late serpentine along olivine grain boundaries is lacking (Fig. 8-5d).

8.4.3 Dislocations

We used the decoration technique (Kohlstedt et al., 1976) to investigate the dislocation density and arrangement in samples where both the spinifex-like texture and GSRZ were present. This method consists in annealing a polished sample slab during 30 minutes in air at 900°C (oxidizing conditions). A standard 30-μm thin section is prepared with the previously polished face in contact with the glass slide. Observations were made using an optical microscope in natural light (Fig. 8-6). This technique is especially suitable when the dislocation density is expected to be heterogeneous, but rather low at the thin section scale.

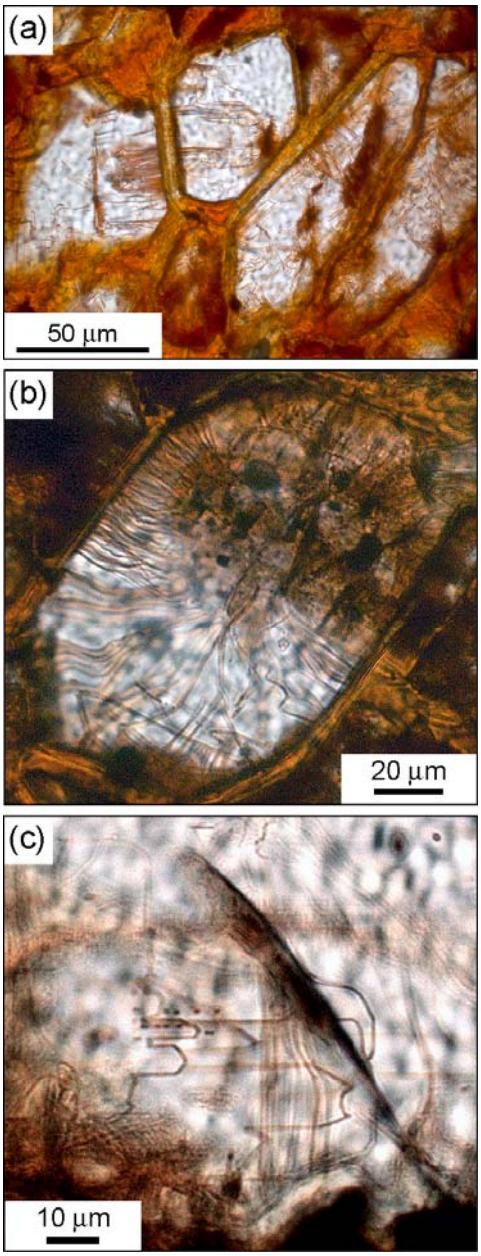

Figure 8-6. Examples of decorated dislocations in olivine from GSRZ. Different observation scales showing: (a) the general low dislocation density (sample Al06-05b); (b) common radial dislocations normal to the crystals polygonal faces (sample Al06-05a); and (c) rare dislocations in glide morphologies in an olivine core (sample Al06-05b).

The strong oxidation of the spinifex-like olivine, probably due to the high content of inclusions, prevents a clear observation of their internal microstructure. Nevertheless, spinifex-like olivine is essentially characterized by closely-spaced inclusions, preferentially arranged in two crystallographic exsolution directions. These crystallographic-controlled inclusion trails may correspond to the microscopic and submicroscopic solid inclusions of magnetite, Cr-bearing spinel, ilmenite and other Ti-rich particles observed by transmission electron microscopy (Ruiz Cruz et al., 1999), part of them interpreted by López Sánchez-Vizcaíno et al. (2005) as the destabilization product of lamellar intergrowths of titanclinohumite in the brown spinifex-like olivine. Most important, dislocations are very rarely observed in these crystals. When present, they tend to be normal to the grain boundaries.

Olivine crystals in the GSRZ display easy-recognizable dislocations, but their density is extremely low. Most crystals show large volumes completely devoid of dislocations (Fig. 8-6a). The most common feature, displayed by the majority of olivine crystals in GSRZ, are rather straight dislocation lines concentrated at the crystal rims and running normal to the polygonal olivine crystal faces (Fig. 8-6b). Local dislocation concentrations are also observed around inclusions. A few isolated crystals within GSRZ display a low density of dislocation loops with polygonal shapes due to the predominance of straight dislocation segments (Fig. 8-6c), suggesting incipient plasticity. Subgrain boundaries were never observed.

8.5 CPO in the grain-size reduction zones

8.5.1 Sample selection and analytical methods

A subset of 5 fresh samples was selected for crystal preferred orientation measurements from a total of 31 samples where GSRZ were clearly identified at hand and thin section scale. We also analysed the crystal preferred orientation of a spinifex-like textured chlorite-harzburgite with a strong olivine shape-preferred orientation (fish-tail texture, sample Al06-42). This sample selection ensures that the whole range of recrystallization degrees (2-100 %, area fraction at the thin section scale) is covered (see Table 8-1 for details).

Table 8-1. Proportion of grain size reduction zones (GSRZ), Opx:Ol modal ratio and average grain size in the investigated samples.

		Opx:Ol modal ratio		Average olivine grain size (μm^2)[1].		
Sample	% GSRZ	spinifex-like texture	GSRZ	spinifex-like texture	number of grains	GSRZ
Al06-42	2	1.00	-	3400044	65	-
Al06-05a	36	1.03	0.14	684653	38	15100
Al06-34	38	1.16	0.17	1845159	37	26471
Al06-05b	39	1.01	0.15	4637244	14	25481
Al06-35	46	1.22	0.10	1024691	18	25272
Al07-07	100	-	0.30	-	-	15847

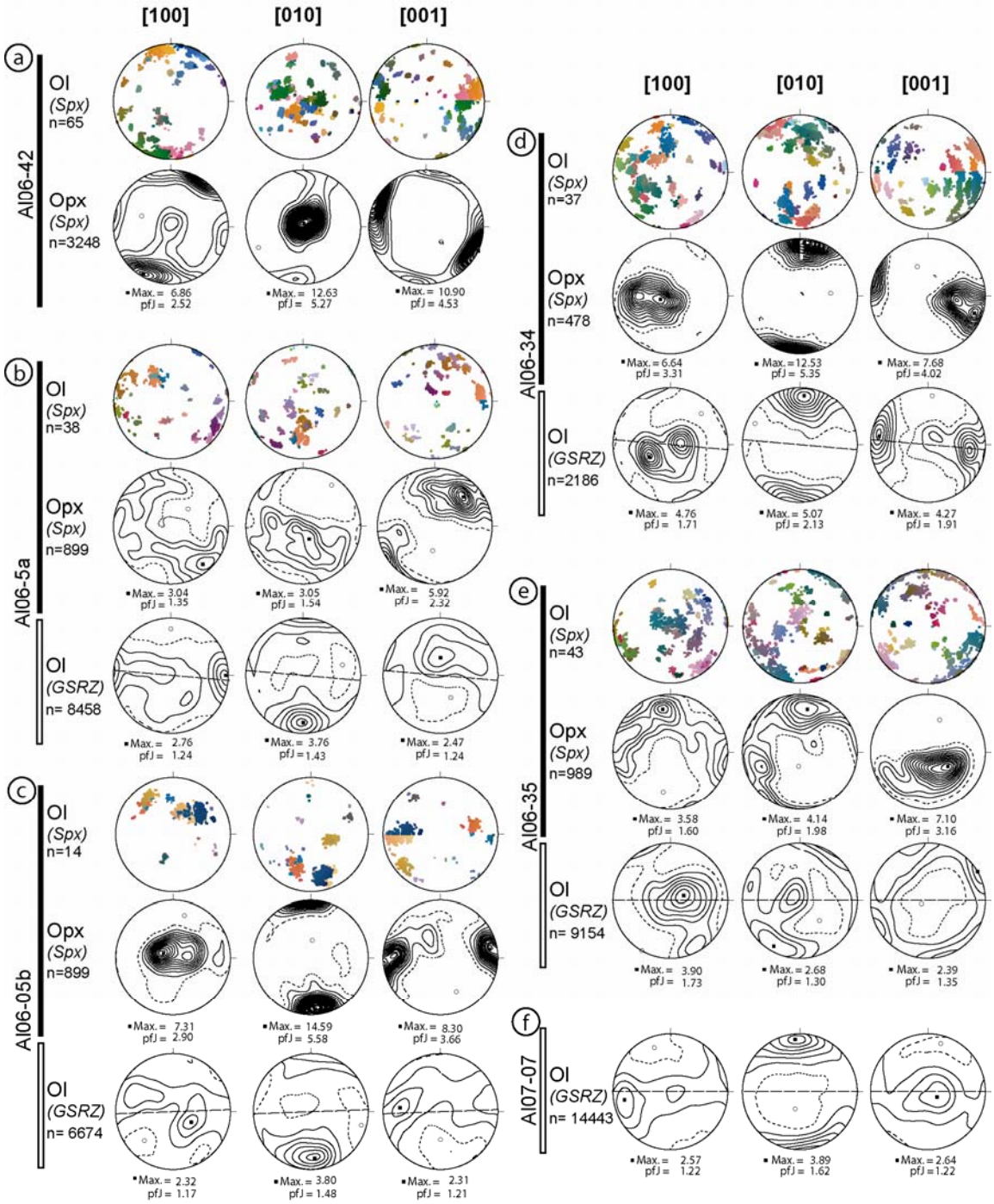

Figure 8-7. Crystal-preferred orientations (CPO) of olivine (Ol) and orthopyroxene (Opx) in the spinifex-like texture domains (Spx, black vertical bar) and in the grain-size reduction zones (GSRZ, empty vertical bar) of six chlorite-harzburgites presenting: **(a)** 100% vol. spinifex-like texture (Al06-42); **(b)** 36% vol. GSRZ (Al06-05a); **(c)** 39% vol. GSRZ (Al06-05a); **(d)** 38% vol. GSRZ (Al06-34); **(e)** 46% vol. GSRZ (Al06-35); **(f)** 100% vol. GSRZ (Al07-07). Equal area lower hemisphere projections in the thin-section reference frame (insert, see text for details). The straight dashed line in the stereonets for the GSRZ marks the orientation of the best-developed GSRZ. Pole figures are represented using average Euler angles for each grain except for spinifex-like olivine, where each grain is represented by a set of orientations; variations in crystallographic orientation within a spinifex grain are due to the curved shape of the olivine laths, not to intracrystalline deformation, [001] is always parallel to the main crystal elongation. Contours at 0.5 of multiple of a uniform distribution intervals. n = Number of grains measured; pfJ = fabric strength for each crystallographic axis.

In Table 8-1, the amount of GSRZ and the orthopyroxene:olivine ratio within and outside of the GSRZ were estimated based on the analysis (Fovea Pro 4.0 toolbox for Adobe Photoshop® software) of high-quality double-polarized images of thin sections. Samples were cut perpendicular to the dominant plane of GSR. Additional slices were cut parallel to this plane. Etching by dilute clorhidric acid of these plane-parallel sections did not reveal neither macroscopic nor microscopic (at thin section scale) lineation. Therefore, final thin sections were prepared normal to the dominant GSR plane (Z direction) and parallel to the geographic North (X direction). The spinifex-like sample used for reference (Al06-42) was cut in a plane containing the average maximum and minimum elongation axes of the olivine crystals.

Crystal-preferred orientations (CPO) of olivine and orthopyroxene were measured by indexing of Electron Back Scattered Diffraction (EBSD) patterns using the SEM-EBSD systems at Geosciences Montpellier (CNRS-Université de Montpellier 2, France). Indexing was performed by automatic EBSD mapping of whole thin sections on a JEOL JSM 5600 using a regular grid step of 30-35 μm. Detailed mapping of selected areas in sample Al06-05b was performed using the CamScan X5000FE CrystalProbe in a low vacuum mode and a grid step of 12 μm. The selected regular grid step of 30-35 μm is in average 2-3 times smaller than the smallest observed grains over the entire thin section. EBSD patterns were indexed automatically using CHANNEL 5 software package from HKL Technology. Raw maps are characterized by 40–50% indexed surface. Non-indexed pixels are linked to serpentinization, polishing defects and grain boundaries. Orthopyroxene was particularly ill-indexed in most samples; because of the fine-grain size of the individual acicular crystals that compose the aggregates and their poorer polishing (they form low relief domains compared to olivine during sample preparation). In order to increase the indexing rate, a post-acquisition data treatment using CHANNEL 5 software, described in detail by Tommasi et al. (2008), was performed.

Pole figures are represented using average Euler angles for each grain, instead of individual measurements, to avoid over-representation of larger grains on the thin section. In addition, we set up a minimum grain area of 4,500-6,125 μm² (5 contiguous measurement points for step 30-35 μm, respectively) to avoid over-representing poorly indexed grains. This minimum area is small enough not to loose information on the orientation of the smaller grains, which are on average 100 μm-wide. The number of indexed grains is highly variable between thin sections due to different recrystallization degrees, but usually ranges from 2,000 to 14,000 grains in the GSRZ. When GSR and spinifex-like texture zones occur in the same mapped thin section a subset was created in CHANNEL 5 by manually selecting large spinifex olivine grains (> 700,000 μm²), this selection was verified by comparing the olivine orientation map with the scanned thin section image where brown spinifex olivine is easily identified. The remaining data

⇒ **Figure 8-8.** Crystallographic orientation maps for olivine in samples showing different obliteration degrees of the initial spinifex-like texture; colors represent the orientation of an orthorhombic symmetry crystal relative to the direction X (see insert): (a) spinifex-like texture (Al06-42); (b) mm-wide irregular GSRZ (Al06-05a); (c) mm- to cm-wide planar GSRZ (Al06-35); (d) both isolated GSR pockets and a cm-wide well-developed GSRZ (Al06-05b). White dashed line sets the boundary between GSRZ and the spinifex-like texture zones. Grey background is the band orientation contrast for orthopyroxene, whereas black areas correspond to chlorite, magnetite, and non-indexed areas.

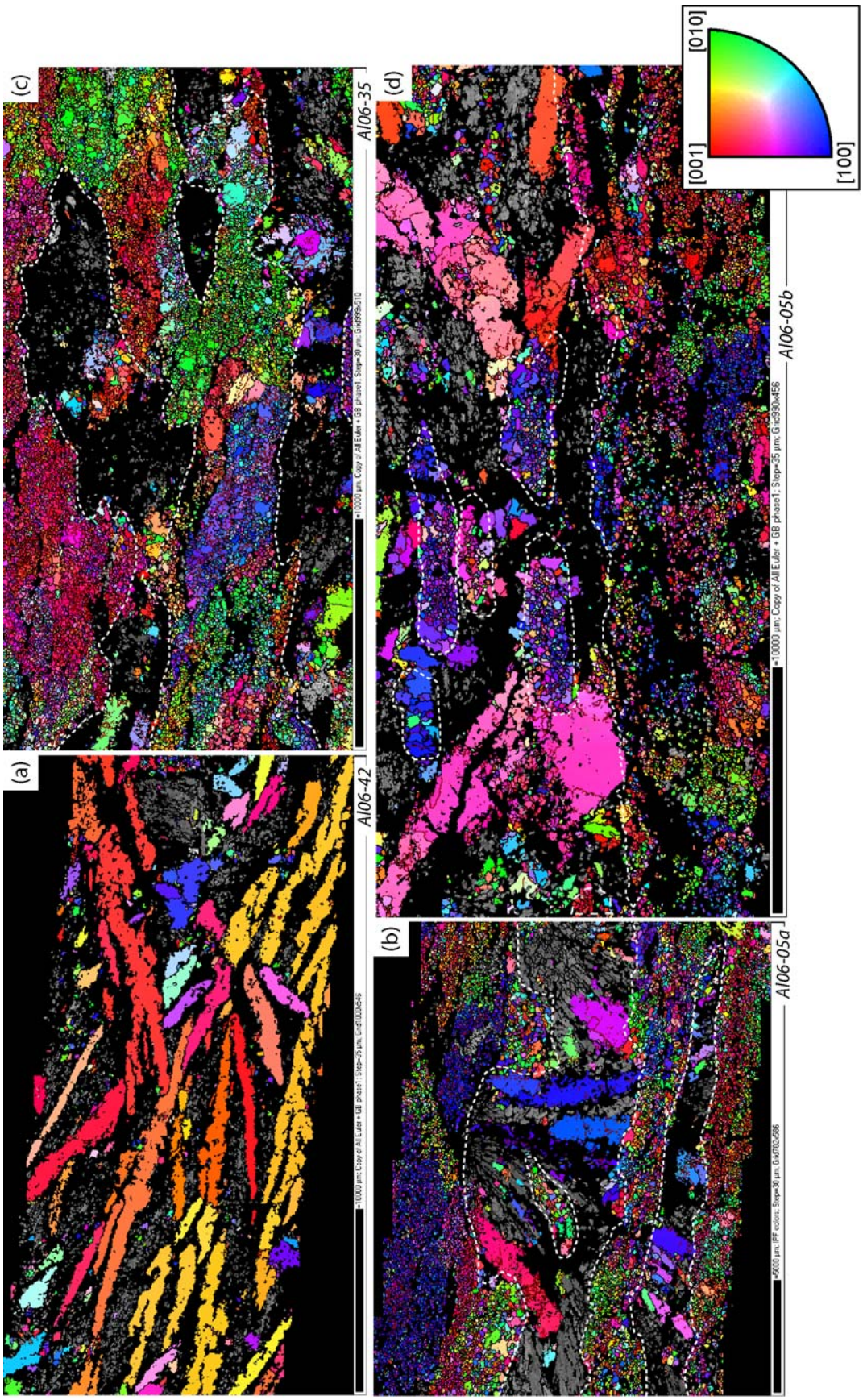
(a)
AI06-42
(b)
AI06-05a
(c)
AI06-35
(d)
AI06-05b
[010]
[001]
[100]

correspond to the olivine orientation in the GSRZ. All EBSD data were processed and contoured as conventional pole figures using the software PFCH5 (Mainprice, 1990).

8.5.2 Spinifex-like texture

A striking characteristic of the chlorite-harzburgite with a spinifex-like texture is the strong correlation between olivine and orthopyroxene crystal preferred orientations: olivine [100] axes are roughly parallel to the orthopyroxene [100] ones and the same is true for the other crystallographic axes (Fig. 8-7). This orientation relation is rather unusual and does not correspond to the one normally observed in naturally deformed peridotites, where olivine [100] axes tend to align at low angle with the orthopyroxene [001] ones (e.g., Tommasi et al., 2004; Tommasi et al., 2006; Soustelle et al., 2010). Moreover, orthopyroxene CPO in spinifex-like chlorite-harzburgite clearly differs from those in naturally deformed peridotites as it often shows a stronger orientation of [010] relative to [001] and [100] (Fig. 8-7).

There is also a strong correlation between the crystal-preferred orientations (CPO) of olivine and orthopyroxene and their shape preferred orientation (SPO). The maximum elongation of both large spinifex-like olivine and acicular orthopyroxene crystals forming aggregates is parallel to their [001] axis. The minimum elongation of spinifex olivine is parallel to the [100] axis (Figs. 7a and 8a). Sample Al06-42, characterized by a strong SPO of olivine (Fig. 3a and 8a) and almost lack of GSRZ, shows a very strong olivine CPO with two maxima of the three main crystallographic axes forming an angle of ca. 30°. Within a single olivine crystal, crystallographic orientations are remarkably homogeneous and subgrains are absent (Fig. 8-7a). However, the slight curvature of some olivine grains, probably formed during growth, results in a gradual orientation change; in these cases the total misorientation within a single crystal may attain 15-20º (Fig. 8-7a).

Samples that show weaker SPO have more dispersed CPO. The spinifex-like olivine orientation varies, therefore, from rather strong (Fig. 8-7a, c, and d) to more scattered (Fig. 8-7e), depending on the SPO strength, but it is never random. At the thin section scale, two or more orientation families intersecting at 30-40º are usually observed (Figs. 8-7 and 8-8).

8.5.3 Grain size reduction zones (GSRZ)

Although there is a clear correlation between the olivine CPO in the GSRZ and the orientation of the neighboring spinifex crystals, CPO in the GSRZ are more dispersed (Fig. 8-7b and e). This dispersion affects all three main crystallographic axes, but it is stronger for [100] and [001]. This results in a [010]-fiber olivine CPO, where [010] forms a weak point maximum ($pfJ_{[010]}$=1.43-2.13) roughly normal to the dominant orientation of the GSRZ (Fig. 8-7). The two other axes are dispersed in a wide girdle subparallel to this plane. Sample Al06-35 departs from this trend by showing a stronger concentration of [100] and a higher obliquity between the CPO and the average orientation of the GSRZ, but the clear correlation between the olivine CPO in the spinifex-like and GSR domain is always observed (Fig. 8-7e). Finally, there is no relation between the CPO

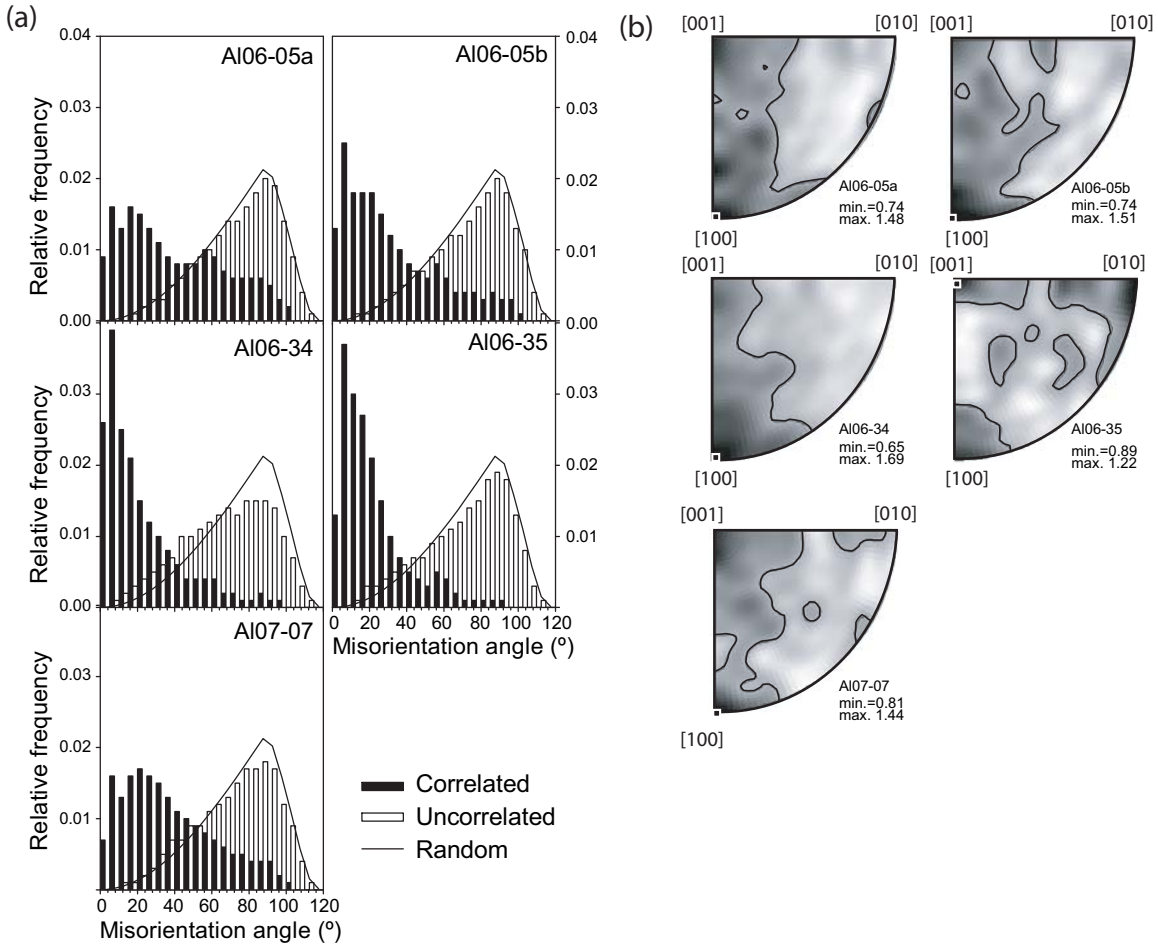

Figure 8-9. (a) Misorientation frequency distribution in the GSRZ for all samples except Al06-42. Correlated are misorientations between neighboring points, uncorrelated are misorientations between non-neighboring points selected randomly, and random indicates the theoretical distribution for an olivine random crystallographic orientation; **(b)** Inverse pole figure (IPF) of the rotation axes accommodating misorientations within grains and across subgrain boundaries in the crystal reference frame for the same samples. Because of the almost random distribution data has been only contoured at 1 multiple of uniform distribution (m.u.d.).

intensity and the surface area fraction of the sample affected by GSRZ. The completely recrystallized sample Al07-07 displays the same fabric features as the mm-wide GSR band in sample Al06-05a (Fig. 8-7f).

Inspection of crystal orientation maps (Fig. 8-8) reveals that all GSRZ, independently of their thickness, are composed by discrete domains with similar orientations. The size and shape of these domains (up to 1 cm in length) is comparable to those of the neighboring spinifex-like olivine crystals. This preservation of the original spinifex-like shape is even clearer in isolated GSRZ (Figs. 8-3f, 8-5d, and 8-8d), where GSR is less pronounced. Some partially recrystallized crystals even preserve their original brownish color at the rims (Fig. 8-5d). These observations corroborate the conclusions drawn from the structural observations at the outcrop and thin-section scales, notably: (i) the GSRZ formed at the expenses of the previous metamorphic crystallization textures; and (ii) the

process (or processes) responsible for the grain size reduction does not involve significant displacement gradients across the GSRZ.

To further characterize the changes in olivine CPO associated with the GSR, we analyze the distributions of correlated and uncorrelated misorientation angles, that is, the variations in the crystallographic orientation between neighboring or randomly chosen measurement points or pixels in the crystallographic orientation map, respectively. The correlated distribution departs notably from the misorientation distribution of a random aggregate of orthorhombic crystals (solid line in Fig. 8-9a). In all the samples the correlated distribution is highly asymmetric, with a maximum at 5-10º. A secondary maximum, located around 20º, is observed for samples Al06-05a, Al06-05b and Al07-07 (Fig. 8-9a). In contrast, the uncorrelated misorientation distribution of olivine in most samples matches closely the random distribution, except for samples Al06-34 and Al06-35 that show a higher proportion of low angle misorientations < 40°. These uncorrelated misorientation distributions are consistent with the measured olivine CPO in the GSRZ, which are slightly stronger for the two latter samples (Fig. 8-7). This difference between correlated and uncorrelated misorientation distributions points to a short range control on the crystal preferred orientations (mm scale domains, corresponding to the original spinifex-like olivine crystals).

Analysis of the lattice rotations across all low-angle olivine-olivine boundaries (2-12º) in the GSRZ, represented as inverse pole figures in the crystal reference frame (Fig. 8-8b), shows that the rotations producing these misorientations are not crystallographically controlled: the inverse pole figures show almost homogeneous distributions (the minima are >0.65 and the maxima are <1.69 m.u.d. multiples uniform distribution). This observation is at odds with the rotation axes distributions for low-angle misorientations usually measured in naturally-deformed peridotites, where a predominance of [0vw] rotation axes, mainly [001] and [010], is consistent with deformation by dislocation creep with dominant activation of [100] glide (Tommasi et al., 2008; Soustelle et al., 2010).

8.6 Discussion

8.6.1 Processes responsible for the formation of the grain size reduction zones

GSRZ display characteristic features: (i) dominant planar shapes with two conjugated orientations intersecting at 40-60°, (ii) irregular, but sharp contacts with the host spinifex-like chlorite-harzburgite, and (iii) absence of displacement (neither shearing nor stretching) across them (Fig. 8-2). These features are the same irrespectively of the rock volume affected by the grain reduction size process (i.e., in large, meter-wide and in small, mm-wide GSRZ). Furthermore, the final grain size is remarkably homogeneous (Table 8-1) and does not depend neither on the initial spinifex olivine grain size, which is strongly variable, nor on the spinifex orientation which varies from strong to highly scattered. The sharp contacts, irregular shapes, and abrupt terminations of the GSRZ at both outcrop and microscopic scales (Figs. 8-3 and 8-5) are not consistent with the formation of the GSRZ in response to dynamic recrystallization. Together with the self-

similarity of the structures at macroscopic and microscopic scales and with the conjugate orientations of the planar GSRZ, these observations rather point to brittle deformation (cataclasis). The absence of displacement across the GSRZ, independently of their thickness, is nevertheless inconsistent with tectonic faulting and rather points to cataclasis induced by hydrofracturing.

The orientation of the recrystallized bands observed at cm-scale (Fig. 8-3b and c) and at the scale of the massif shows indeed a strong, but not random, dispersion (Fig. 8-4). Although the dominant direction varies between different sections of the massif (Fig. 8-4a), analysis of the orientation data for wide GSRZ at the scale of the massif highlights two main shallowly-dipping conjugated planes at ca. 55º to each other, oriented in average ENE and N-S (Fig. 8-4c). This points to the contribution of a large-scale, regional stress field in the geometric distribution of the brittle deformation.

Self-similar patterns and non-random distributions of geometric frameworks are distinctive features of brittle deformation by hydrofracturing in metamorphic terrains (e.g., Manning, 1994a; Toriumi and Hara, 1995) and can be produced during mineral replacement processes (e.g., Jamtveit et al., 2008, 2009). Planar fractures would represent pathways for overpressured fluids inducing high permeability zones. Similar Complex fracture networks occur in the high pressure ultramafic terrain of Almklovdalen (western Norway). Kostenko et al., (2002) interpreted these fracture networks in the Almklovdalen terrain as hydrofractures produced during 'forcefully' introduced external fluids.

The observed sharp contacts between GSRZ and the host spinifex-like peridotites in the Cerro del Almirez ultramafic massif are also in agreement with the sharp front separating domains where grain boundaries were pervasively infiltrated by fluids produced by prograde metamorphic reactions as described in the Almklovdalen massif (Kostenko et al., 2002) and in contact metamorphic terrains (Holness and Watt, 2001, 2002). We propose that hydrofracturing is also the most likely mechanism for the formation of GSRZ in the Cerro del Almirez ultramafic massif.

8.6.2 Olivine microstructures and CPO in GSRZ

Analysis of the olivine microstructures further supports a brittle rather than a ductile mechanism (i.e., grain size reduction by dynamic recrystallization during dislocation creep) for the formation of GSRZ. The most striking observations corroborating this interpretation at the microscopic scale are (i) the presence of isolated GSR pockets (Figs. 8-3d, f, and 8-5d), the abrupt termination of irregular GSRZ and their lack of lateral continuity (Fig. 8-3d), (ii) the lack of displacement across the GSRZ, and (iii) the preservation of the original spinifex-like shape in partially (Fig. 5d) or completely recrystallized crystals (Fig. 8-8b, c, and d). All these features imply that the process responsible for the grain size reduction in the Cerro del Almirez chlorite harzburgite is not associated with ductile strain (i.e. a change of shape) of the olivine crystals. This rules out recrystallization owing to ductile deformation, since the latter occurs in response to the accumulation of dislocations in the crystals and is a strain-dependent process.

The presence of a well-developed CPO is usually a diagnostic feature of deformation by dislocation creep. However, the high correlation between olivine and orthopyroxene CPOs in the spinifex-like texture domains and in neighboring GSRZ (Fig. 8-7b, c, d, and e) suggests that the crystallographic orientation in GSRZ is mainly inherited from the preexisting CPO in the host peridotite. Indeed, well–defined olivine CPO in GSRZ pattern are observed in samples with a strong coherent orientation of both olivine and orthopyroxene in the relict spinifex-like textured zone (Fig. 8-7b, c and d), whereas the sample with the least oriented spinifex-like texture shows a weak olivine CPO in the adjacent GSRZ (Fig. 8-7e). The systematically weaker CPO in the GSRZ relatively to the adjacent spinifex-like texture domains indicates, nevertheless, that the grain size reduction process results in a dispersion of the original orientation.

Analysis of the misorientation angle distribution enables further discrimination between ductile or brittle deformation mechanisms. Dynamic recrystallization by subgrain rotation results in a predominance of low-angle misorientations and in characteristic rotation axes in the crystal reference frame, since both the orientation of the subgrain boundary and the misorientation across it are directly related to the dislocations forming the boundary (Amelinckx and Dekeyser, 1959). The analysis of the rotation axes accommodating low-angle misorientations may thus be used to infer active slip systems. For instance, deformation by dislocation creep with dominant activation of high-temperature, low-stress (0kl)[100] slip systems would result in rotation axes parallel to [001] and [010] (Tommasi et al., 2000); this pattern can be observed even in strongly annealed peridotites (Tommasi et al., 2008; Soustelle et al., 2010). Brittle deformation, on the other hand, leads to random rotation axes.

Orientation maps (Fig. 8-8b, c, and d) show that GSRZ are formed by relatively large discrete domains (up to 1cm) with roughly similar orientation, supporting a strong inheritance from preexisting large grains. Furthermore, the correlated misorientation distribution for olivine (that is, between neighboring measurement points in the map) is characterized by maxima at relatively high misorientation angles (at ~5-10º and ~20º, Fig. 8-9a) that significantly differ from those observed in olivine-rich rocks deformed by dislocation creep (<5º). Moreover, the rotation axes accommodating low-angle misorientations in the GSRZ do not display any clear crystallographic control; they are randomly distributed (Fig. 8-9b), implying that dislocation creep was not involved in the grain size reduction process.

The extremely low dislocation densities (Fig. 8-6a) and of the rare occurrence of dislocations with glide morphologies (Fig. 8-6c) corroborate that, during the grain size reduction process, dislocation creep was not involved. The observed radial dislocations in olivine from GSRZ are indicative of fast growth. Grain boundary migration is also suggested by the polygonal grain shapes of olivine in the GSRZ (Fig. 8-6). Although PT conditions during the formation of the GSRZ cannot be accurately constrained by thermobarometry, the similarity of mineral assemblages in the GSRZ and spinifex-like chlorite harzburgites suggests that deformation took place close to the metamorphic peak of the latter. Occurrence of tremolite constrains a maximum temperature of 680-710 ºC for the pressure range of 1.6-1.9 GPa (López Sánchez-Vizcaíno et al., 2005; Padrón-Navarta et al., 2010). Under dry conditions, these low-temperature conditions

would imply very slow diffusion rates and should prevent grain growth. A fluid-rich environment might, however, allow a fast grain growth, even under low-temperature conditions, by a mechanism akin to pressure-solution.

The association of hydrofracturing and grain growth in presence of fluids can, therefore, account for the release of the solid and fluid inclusions from the preexisting brownish spinifex-like olivine and for the related color change. Static grain growth simulations (Jessell et al., 2003) show that microstructural defects are easily swept by grain boundaries migration. Hydrofracturing followed by static grain growth has already been proposed to account for local grain coarsening and decrease in the inclusions density at the olivine rims in the Almklovdalen peridotite in west Norway (Kostenko et al., 2002; Jessell et al., 2003). Recrystallized grain sizes of olivine in the Cerro del Almirez are smaller than those from the Almklovdalen peridotite, what it is consistent with the lower temperature conditions of formation of GSRZ in Almirez.

8.6.3 Orthopyroxene dissolution

A striking feature of the GSRZ is the substantial reduction of the orthopyroxene modal content compared to the spinifex-like textured domains (Table 8-1, Fig. 8-8). The similarity between orthopyroxene CPO in undeformed domains and that of olivine in the GSRZ (parallelism of main crystallographic axes, Fig. 8-7) suggests that crystallization of olivine at the expense of orthopyroxene might have occurred during the grain size reduction process. This reaction implies an open system for an externally derived silica undersaturated fluid. Thus, a reactive and interconnected fluid phase might have been present during the formation of the GSRZ, consistently with the microstructural observations that point to hydrofracturing.

The composition and source of this fluid cannot be assessed unambiguously. One major possible source is the antigorite dehydration reaction, since the GSRZ can be observed only a few hundred meters away from the reaction front (Fig. 8-3). It has been experimentally showed (Tenthorey and Hermann, 2004) that the fluids produced by this reaction are water-rich and contain ~6 wt. % SiO_2, ~2 wt. % MgO, ~1 wt. % CaO, and ~1 wt. % Al_2O_3. Calculated curves for silica solubility (Manning, 1994b) indicate a maximum SiO_2 solubility of 4-6 wt. % at 650-700ºC and 1.5-2.0 GPa. The ability of the fluids produced by the antigorite dehydration to dissolve orthopyroxene under the conditions inferred for the formation of the GSRZ is therefore rather low. One possible explanation allowing to reconcile the observed reduction in the orthopyroxene content in the GSRZ and the experimental data would be an increase of the silica solubility in the fluid during the hydrofracturing process because of the more reactive character of overpressure fluids (Manning, 1994).

8.6.4 Relation between GSRZ and the antigorite dehydration front

Embrittlement and weakening owing to dehydration reactions has been recognized since the earliest experimental works on serpentinite deformation (Raleigh and Paterson,

1965). The two processes were attributed to a transient reduction of the effective confining pressure due to an increase of the fluid pressure. This effect has been commonly invoked to explain both intermediate- and deep-focus earthquakes in subduction zones (Nishiyama, 1989; Peacock, 2001; Dobson et al., 2002; Tenthorey and Cox, 2003; Hacker et al., 2003; Seno and Yamasaki, 2003; Jung et al., 2004). Conventional petrological wisdom is also in agreement with this dehydration-related deformation model, as it has been invoked to account for the ubiquitous occurrence of olivine veins with prograde assemblages in serpentinites from high grade terrains (Strating and Vissers, 1991; Scambelluri et al., 1991b; Healy et al., 2009; López Sánchez-Vizcaíno et al., 2009). All these field observations are, nevertheless, only relevant for partial dehydration reactions (related to the brucite breakdown), but not for the complete antigorite dehydration (Trommsdorff et al., 1998). The scarcity of exposures of arrested dehydration fronts of atg-serpeninites has prevented so far adetailed investigation of the dehydration-related deformation in prograde peridotites. In fact, field observations and experimental studies suggest that macroscopic, ductile structures, instead of brittle ones, may also be produced owing to dehydration reactions like the transformation of diaspore into corundum (Urai and Feenstra, 2001; Feenstra and Wunder, 2002).

These apparently contradictory observations can be explained by the time-dependent feedback between the evolution of the fluid pressure and deformation during dehydration. At the temperatures and confining pressures prevailing in the lower crust and upper mantle, metamorphic fluid flow is mainly controlled by permeability gradients produced during devolatilization reactions (Thompson and Connolly, 1990). Coupled metamorphic-rheological numerical simulations (Connolly, 1997; Connolly and Podladchikov, 1998) have shown that positive fluid pressure anomalies produced at the dehydration reaction front can be propagated by creep mechanisms over large distances, hindering hydrofracturing if viscous relaxation times are short enough. Alternatively, microcraking by inter- and intragrain hydrofracturing will occur when viscous relaxation times are long and the fluid pressure exceeds the minimum principal stress and the tensile strength of the rock (Nishiyama, 1989).

There is an increasing body of evidence for the role of microcracks as an effective mechanism to enhance fluid flow during dehydration (Miller et al., 2003; Ko et al., 1997). Experiments confirm that reaction-induced microcraking is an efficient mechanism to enhance anatectic melt extraction, for instance, but extraordinarily fast reaction rates are required (Connolly, 1997; Watt et al., 2000). Therefore, transient fluid flow will depend on the interplay between the rheology and permeability of the rock matrix and the fluid production rate. Perrillat et al., (2005) estimated that water production rates for the antigorite dehydration (3×10^{-6} to 3×10^{-8} m^3_{fluid} m^{-3}_{rock} s^{-1}) largely exceed the strain rates inferred for viscous relaxation in serpentinites, allowing for reaction-induced embrittlement. As pointed by the same authors, these values are strongly dependent on the grain size. Their fluid production rate should be taken as an upper bound as it was calculated from experimental powder grain size (1-10 μm), which significantly departs from those observed in natural high-grade serpentinites (10-50 μm, e.g., Fig. 5-2 in Padrón-Navarta et al., 2008).

In the Cerro del Almirez ultramafics, micro- and macrostructures that can be attributed to hydrofracturing related to the antigorite dehydration are only observed in the prograde chlorite-harzburgite. This is a logical consequence of the highly contrasting rheological behavior of serpentinites and peridotites. Recent deformation experiments (Hilairet et al., 2007) suggest that viscous relaxation times for antigorite at high pressure conditions are at least 10 orders of magnitude shorter than those for olivine. Thus, plastic deformation in serpentinites may probably allow the propagation of the reaction-induced porosity anomaly reducing the fluid pressure at the reaction front (Connolly et al., 1997; Connolly and Podladchikov, 1998). In contrast, due to the higher viscosity peridotites at low temperature, chl-harzburgite will lead to fluid release by hydrofracture. This is consistent with the occurrence of veins and cracks in peridotite wall-rocks adjacent to serpentinite mylonites during the high pressure metamorphism of the Voltri Massif (Strating and Vissers, 1991) that suggest brittle deformation due to transient fluid overpressures in the peridotites.

In order to estimate the porosity production and the overpressure (related with the positive volume change of the reaction, ΔVrxn) linked to the antigorite dehydration, we computed the solid and reaction volume changes for the following balanced reaction:

$Mg_{46.5}Al_3Si_{32.5}O_{85}(OH)_{62} \rightarrow 11\ Mg_2SiO_4 + 8.5\ Mg_2Si_2O_6 + 1.5\ Mg_5Al_2Si_3O_{10}(OH)_8 + 25\ H_2O.$
antigorite (3.4 wt.% Al_2O_3) forsterite enstatite clinochlore

We used Perple_X (Connolly, 2005), the updated version of the mineral database from Holland and Powell (1998), the CORK fluid equation of the state (Holland and Powell, 1991; Holland and Powell, 1998), a representative antigorite composition in terms of Al_2O_3 content (e.g. Padrón-Navarta et al., 2008) and the new compressibility data for antigorite fitted by a third-order Birch–Murnaghan equation of state (Nestola et al., in press) at the pressure and temperature conditions relevant for the Cerro del Almirez (1.7-1.9 GPa and 680ºC). Results show a significant porosity production due to solid volume decrease (ΔVsolids ~ – 21.5 vol. %) and a moderate positive increase of the total volume of the reaction (ΔVrxn = + 2.3-2.7 vol. %). The extent of water release is bulk-composition dependent as Al_2O_3 stabilizes chlorite in the prograde assemblages. Common Al2O3 contents in serpentinite from Cerro del Almirez (1.7-3.4 wt. %, Garrido et al., 2005, Padrón-Navarta et al., 2008) result in an upper bond of fluid release of ~9-10 wt. % (the common occurrence of minor phases in natural serpentinite slightly reduces this value) over a 20-30 ºC interval starting at ~660ºC (Padrón-Navarta et al., 2010). Accordingly, we propose that fluid released during the antigorite dehydration can be drained through porosity propagation by viscous creep in the serpentinites and/or hydrofracturing in the chlorite-harzburgite promoted by microcracking. In this scenario, GSRZ would be the relic evidences of such fluid propagation waves through microcraking mechanisms. On the other hand, the systematic orientation of the larger GSRZ at the outcrop scale (Fig. 8-3) does not rule out a possible role of changes in the large-scale stress field, due to large intermediate depth earthquakes, for instance (Abers et al., 2009), that may enhance reaction rates, favoring the formation of overpressures.

8.6.5 Hydrofracturing at mantle conditions and implications for subduction zones

Field evidences suggest that hydrofracturing is a common process at high- (Toriumi and Hara, 1995; Pennacchioni, 1996; Cesare et al., 2001) and ultra-high pressure conditions (Vrijmoed et al., 2006; Vrijmoed et al., 2008; Malaspina et al., 2009). Hydrofracturing has also been proposed to account for deep-crustal seismicity (Lund and Austrheim, 2003; Andersen et al., 2008). A large body of evidence also attests for the importance of brittle deformation in subduction zones; i.e. field observations of brittle failure in exhumed subducted rocks (Hermann et al., 2000; John et al., 2004; Healy et al., 2009), evidences for hydraulic fracturing during hydrous metasomatism of mantle wedge xenoliths (Wilshire and Kirby, 1989; Schneider and Eggler, 1986; McInnes et al., 2001; Soustelle et al. 2010), dehydration experiments (Miller et al., 2003; Tenthorey and Cox, 2003; Perrillat et al., 2005), seismicity, including episodic tremor and slip and regular intermediate-depth earthquakes (Kirby et al., 1996; Obara, 2002; Rogers and Dragert, 2003; Shelly et al., 2006; Abers et al., 2009), and numerical models (Furukawa, 2009).

Based on field and microstructural observations presented above, we suggest that hydrofracturing is a plausible mechanism, allowing the migration of fluids produced by dehydration reactions across an otherwise almost impermeable cold, top-slab mantle wedge. Our observations are consistent with a scenario where the migration of the fluids produced by dehydration reactions in the slab and in the serpentine-rich channel above the slab, is slowed down when they reach the cold and, hence, high viscous peridotites in contact with the upper part of the slab, promoting the required overpressure for hydrofracturing. This process, which results in the formation of the GSRZ, enhances the permeability, allowing the fluids to attain the hotter parts of the mantle wedge.

This high-pressure hydrofracturing, however, would result in a minor seismological signal (low magnitude events, more akin to seismic tremors) due to minor or null displacement associated with the GSRZ. Intermediate-depth (50-70km), low-magnitude events are nevertheless very difficult to observe. Indeed, in the Cascadia and Nankai subduction zones, episodic tremor and slip (ETS) nucleates near to the slab interface (La Rocca et al., 2009), as expected for the hydrofracturing mechanism proposed here, but it is usually restricted to < 40 km depth (Shelly et al., 2006; Abers et al., 2009). The described porosity enhancement and near-lithostatic fluid pressures should, nevertheless, produce transient low seismic velocities, high Poisson ratios, and high attenuation zones, similar to those associated with ETS in the Nankai and Cascadia subduction zones (Kodaira et al., 2004; Abers et al., 2009; Audet et al., 2009).

8.7 Conclusions

Chlorite-harzburgite is the expected lithology in the cold, top-slab mantle wedge, a key setting with large amounts of fluids released from the slab dehydration. Based on detailed field and microstructural observations of this lithology in the high pressure Cerro del Almirez ultramafic massif (Betic Cordillera, Spain) we reach the following conclusions:

(a) Anisomorphic growth of olivine and orthopyroxene in the spinifex-textured chlorite-harzburgite represents a primary metamorphic crystallization texture, characterized by a strong correlation between the crystal-preferred orientations (CPO) of olivine and orthopyroxene and their shape preferred orientation (SPO).

(b) This primary metamorphic texture was affected by localized grain-size, reduction zones (GSRZ) along irregular and roughly planar structures with two conjugated orientations, intersecting at 40-60º. GSRZ display a series of distinctive features: (1) irregular sharp contact with the host undeformed peridotite, (2) non-random distribution and self-similarity at different scales, (3) lack of displacement (neither shearing nor stretching) across them, (4) remarkable homogeneity of the olivine grain size irrespective of the rock volume affected by recrystallization, and (5) extremely low dislocation densities in the recrystallized olivine. All these features rule out formation of the GSRZ by dislocation creep and are consistent with brittle deformation.

(c) Brittle deformation results in some dispersion of the olivine crystals orientation in the GSRZ, but a strong inheritance from the precursor spinifex-like texture in the chl-harzburgite can still be recognized. Large discrete domains (up to 1cm long) with low misorientations are preserved in the GSRZ; they correspond to former spinifex-like olivine crystals. These domains result in a short range control on the crystal preferred orientations causing differences between the correlated and uncorrelated olivine misorientation distribution. The almost random distribution of the rotation axes accommodating low-angle misorientations in the GSRZ is a further evidence for brittle deformation.

(d) Based on these observations we propose that hydrofracturing is the main mechanism accounting for grain size reduction in the Cerro del Almirez chlorite-harzburgites. The flux of an overpressure fluid through the GSRZ is also supported by substantial reduction of the orthopyroxene modal content compared with the spinifex textured domains.

(e) Development of the GSRZ network was probably linked to the fluid release during the antigorite dehydration. Microcraking may allow for the formation of high permeability channelways for overpressured fluids in an otherwise almost impermeable and cold (680-710ºC) peridotite. We suggest that this high-pressure hydrofracturing may be an essential mechanism in the first stages of fluid flow through the coldest parts of top-slab mantle in subduction zones, before the fluids attain the hotter parts of the mantle wedge where their migration may be assisted by viscoplastic deformation processes. The near-lithostatic pressures associated with this process will produce transient low seismic velocities, high Poisson ratios, and high attenuation zones, similar to those associated with episodic tremor and slip attenuation zones, similar to those associated with episodic tremor and slip.

Acknowledgements
D. Mainprice is thanked for discussions on the olivine CPO and dislocation structures and for providing software for analyzing and plotting CPO data. C. Nevado supplied high quality polished thin sections for EBSD measurements. We also thank F. Barou for

his technical assistance in the EBSD facilities at Geosciences Montpellier. This work was supported by the Spanish "Ministerio de Ciencia e Innovación (MICINN)" through research grants CGL2006-04440, CGL2007-61205/BTE, and ACI2006-A9-0580, the Spanish Council for Research (CSIC) through grant 2008-30I014, and by the "Junta de Andalucía" research groups RNM-145 and RNM-131. J.A. Padrón-Navarta is supported by fellowship AP2005-060 from the "Programa de Formación del Profesorado Universitario".

PART THREE

9 The Arrested Metamorphic Transition of Metastable Hornblende Gabbronorite to Mafic Opx-Free, Garnet Granulite in the lower Crust of a Paleo-Island Arc (Jijal Complex, Kohistan, north Pakistan)

10 Oriented Growth of Garnet by Topotactic Reactions and Epitaxy in High-Pressure, Mafic Garnet Granulite formed by Dehydration Melting of Metastable Hornblende-Gabbronorite (Jijal Complex, Kohistan Complex, north Pakistan)

Submitted to Journal of Petrology

9 The Arrested Metamorphic Transition of Metastable Hornblende Gabbronorite to Mafic Opx-Free, Garnet Granulite in the lower Crust of a Paleo-Island Arc (Jijal Complex, Kohistan, north Pakistan)

Padrón-Navarta, JA[1*] · Garrido CJ[2]. · López Sánchez-Vizcaíno, V[3] · Bodinier J[4] · Gómez-Pugnaire MT[1,2] · Hussain SS[5] · Dawood H[5]

The upper part of the Jijal Granulitic Gabbro Unit (GGU) records the arrested transformation of hornblende gabbronorite to garnet granulite, involving the coeval breakdown of amphibole and orthopyroxene, and the formation of garnet and quartz. Close to the transformation front (2-3 cm), clinopyroxene from the granulite displays a strong Ca-tschermark zoning with lower Al-contents at rims. REE zoning of clinopyroxene and pseudosection diagrams indicate that only clinopyroxene rims reflect chemical equilibrium with garnet in the reaction front (P = 1.1 ± 0.1 GPa, T = 800 ± 50ºC), whereas the cores retained high-Al contents inherited from precursor gabbronorite clinopyroxene and remained in chemical disequilibrium only in a few centimeters with the garnet granulite assemblage. Clinopyroxene of garnet granulites from the Jijal lower GGU are completely re-equilibrated with garnet (P = 1.5 ± 0.1 GPa, T = 800 ± 50ºC). If ferric iron corrections are disregarded, equilibration pressure and temperature are highly overestimated yielding exceedingly high pressures for an island arc setting. The pressure difference between the upper and lower Jijal GGU granulites (~0.4 GPa) and its current thickness (<5 km) implies delamination of the denser parts of Jijal crust. Thermodynamically computed phase diagram sections for upper GGU bulk compositions show that, at the equilibration conditions of Jijal garnet granulite, the equilibrium assemblage is orthopyroxene-free and amphibole-free garnet granulite coexisting with melt or a fluid phase, depending on the water activity at the onset of amphibole breakdown. Pseudosections indicate that hornblende gabbronorite assemblages are highly metastable at lower arc crust depths. The transformation to garnet granulite was therefore substantially overstepped in terms of pressure and temperature. Only with substantial compression from 0.5 GPa to 1.1 GPa would the hornblende gabbronorite assemblage be transformed to high-pressure garnet granulite. This is consistent with a top-to-bottom growth of the island arc crust where shallower intrusions are sequentially foundered into the deeper levels of the arc crust. Isothermal P-M(H_2O) pseudosections show that the compression paths walk through fluid-absent fields until the attainment of melt- or fluid-present amphibole-free, garnet granulite. Altogether this suggests that burial and partial melting at the island root conditions are the key factors accounting for the transformation of hornblende gabbronorite to high-pressure granulite observed in Jijal. If common, such processes may have important geochemical and geophysical implications for the stability and intracrustal differentiation of the island arc crust.

Keywords: Amphibole dehydration-melting; hornblende-gabbronorite; metastability; Kohistan island arc; Opx-free garnet granulite

1. Departamento de Mineralogía y Petrología, Universidad de Granada, Spain.
2. Instituto Andaluz de Ciencias de la Tierra (IACT), Granada, Spain.
3. Departamento de Geología, Universidad de Jaén Linares, Spain.
4. Géosciences Montpellier, CNRS & Université de Montpellier II, France.
5. Pakistan Museum of Natural History, Garden Islamabad, Pakistan.

9.1 Introduction

It has been long recognized that garnet granulite terrains somehow record processes of differentiation and maturation of the Earth's Continental Crust (Fyfe, 1973b; Harley, 1987; Rudnick, 1992; Taylor & McLennan, 1995; Windley, 1981). Granulite metamorphism and related granitic magmatism, concurrent or not with basaltic magmatic underplating, may be one of the recipes to account for the evolved composition of the continental crust from basaltic to its current andesitic composition (Garrido *et al.*, 2006; Kelemen, 1995; Rudnick & Presper, 1990; Springer & Seck, 1997; Vielzeuf *et al.*, 1990). High- to intermediate-pressure orthopyroxene-free, mafic granulites are volumetrically and regionally underrepresented in the geological record relative to their more evolved, intermediate to acid, counterparts. However, the prominent basaltic composition of the lower continental and arc crust, evidenced by its seismic properties (Christensen & Fountain, 1975), indicates that high- to intermediate-pressure mafic granulite terrains may provide a unique window into common metamorphic and igneous processes occurring at depths of the lowermost crust of continents and magmatic arcs.

Detailed metamorphic studies of mafic opx-free, garnet granulites are yet scarce in the literature compared with other granulite types (Hartel & Pattison, 1996; Indares, 2003; Indares & Martignole, 2003; Kelsey *et al.*, 2003a; O'Brien, 2006; O'Brien & Rotzler, 2003; Pattison, 2003). From a metamorphic perspective, it is well established that they can be formed under intermediate to high-pressure conditions (Pattison, 2003). But beyond their metamorphic significance, high-pressure granulites are of outstanding relevance for our understanding of the machinery of magmatic arcs. Increasing geological and numerical modeling evidence indicate that the lower crust of arcs is much hotter than previously anticipated (Arcay *et al.*, 2006; Behn & Kelemen, 2006; Garrido *et al.*, 2006; Jull & Kelemen, 2001; Kelemen *et al.*, 2003; Yoshino & Okudaira, 2004). Thus, the prevalence of steady or non-steady high geothermal gradients at lower crust conditions represent a favorable scenario for the formation of high-pressure garnet granulites in these tectonic settings. This has noteworthy consequences for the stability (Behn & Kelemen, 2006; Jull & Kelemen, 2001) and the intracrustal differentiation (Garrido *et al.*, 2006) of the lower crust of magmatic arcs. Transient, low geothermal gradient and/or sudden magmatic (Brown, 1996; Brown & McClelland, 2000) loading may favour the persistence of metastable, low-P assemblages until attaing melt/fluid present conditions at the hot roots of island arcs (Padrón-Navarta et al., 2008; Dazcko *et al.* 2009; Dazcko & Halpin, 2009; Allibone *et al.* 2009).

The Jijal Complex (Kohistan paleo-island arc Complex, NW Pakistan), as well as the Pembroke granulite (Mildford Sound, Fiordland, New Zealand), is an exceptional occurrence of high-pressure (HP), mafic, opx-free, garnet granulite formed in the lower crust of a magmatic arc. Of particular interest in these two granulite terrains is the preservation of the arrested transformation of low-pressure, mafic two-pyroxene, hornblende-bearing granulite (referred to here as hornblende (hbl-) gabbronorite owing to its primary igneous origin, cf. Garrido *et al.*, 2006) to opx-free, grt-granulite. In Fiordland, Palaeozoic to Early Cretaceous two-pyroxene metadiorite and metagabbro were transformed into HP, opx-free grt-granulite along the wall-rock of veins at 1.4 GPa and c. 750 ^{o}C (Blattner, 1976, 2005; Clarke *et al.*, 2000; Daczko *et al.*, 2001a, 2002, 2009),

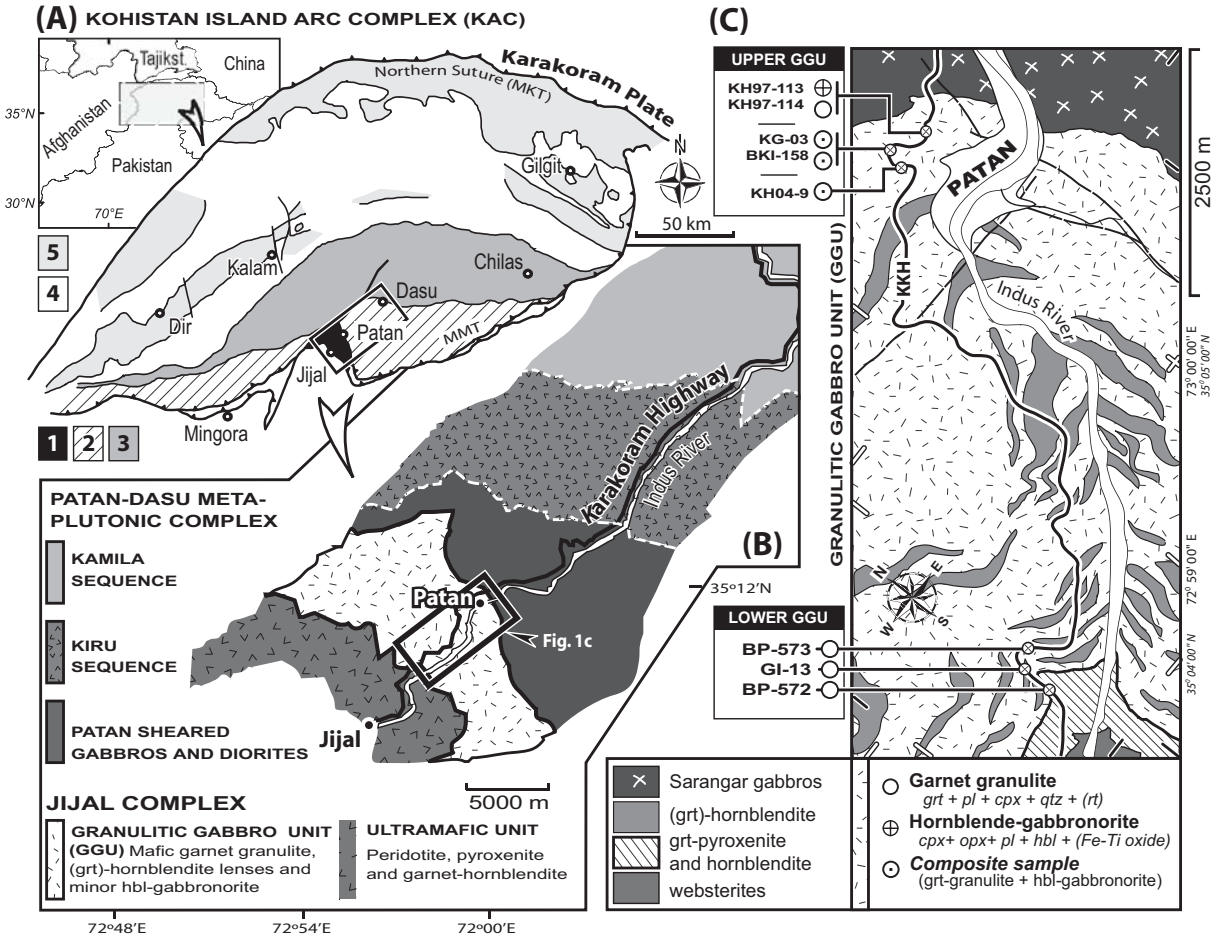

Figure 9-1 (a) Simplified geological map of the Kohistan Island Arc Complex (KAC, Northern Pakistan) (modified after Burg *et al.*, 1998). From south to north, the main petrological and structural units of the KAC are: (1) the Jijal ultramafic-mafic Complex; (2) the Kamila amphibolite belt or, along the Indus River, the Patan-Dasu metaplutonic Complex; (3) the Chilas ultramafic-mafic Complex; (4) the Kohistan batholith; (5) the Jaglot, Yasin-Chalt and other volcanics series (undifferentiated). The rectangle indicates the location of the Jijal Complex section shown in Fig. 1b. **(b)** Simplified geological map of the Jijal-Dasu transect of the Kohistan arc along the Indus Valley showing the main units of the Jijal and metaplutonic Complexes (modified after Zeilinger, 2000 and Garrido *et al.*, 2006) **(c)** Geological map of the Granulitic Gabbro Unit (GGU) of the Jijal Complex (after Zeilinger, 2002 and Garrido *et al.*, 2006) showing the location of the studied samples from the upper GGU, where minor hornblende gabbronorite patches occur, and from the lower GGU.

during thickening related to a short-lived subduction (Clarke *et al.*, 2000; Daczko *et al.*, 2001b) or magma loading in the middle crust (Brown, 1996). In the Jijal Complex, mafic opx-free, grt-granulite occurs in the crustal section above the mantle-crust transition of the Cretaceous Kohistan island arc Complex (Fig. 9-1a) (Bard, 1983a; Bard, 1983b; Dhuime *et al.*, 2007, 2009; Garrido *et al.*, 2006, 2007; Yamamoto & Yoshino, 1998), which was exhumed as the result of the collision of the Indian and the Karakoram plates in the Tertiary. The upper part of the Jijal crustal section preserves a well-exposed example of the transformation of low-pressure, hbl-gabbronorite into HP opx-free, grt-granulite (Yamamoto *et al.*, 2005; Yamamoto & Nakamura, 2000; Yamamoto & Yoshino, 1998; Yoshino & Okudaira, 2004). P-T conditions of grt-granulite ranges from 0.8–1.1 GPa and 800 °C (Yoshino & Okudaira, 2004; Yoshino *et al.*, 1998), although higher pressure (c. 2.0

GPa) and ultra-high temperatures (> 1000 ºC) have also been reported in granulites from Jijal (Ringuette *et al.*, 1999). Recent experimental works on high-*P* crystal fractionation of hydrous basaltic andesite to andesite liquids (4-8 wt.% H_2O) at *P*=0.8-1.2 GPa and *T*=800-1000 ºC (Alonso-Pérez *et al.* 2009; Müntener & Ulmer, 2006), refer to the mafic-ultramafic Jijal sequence as a natural example of this process. However, the lack of trace-element and isotopic cogenetic relationships between mafic and ultramafic rocks of the Jijal Complex rules out this simple scenario (Garrido *et al.*, 2007; Dhuime et al., 2007, 2009).

In this paper, we present a detailed metamorphic study of the transformation of hbl-gabbronorite to HP, opx-free, grt-granulite in the Jijal Complex. Our study aims to constrain the *P-T* conditions and the fluid/melt regime of this transformation by combining detailed petrography and mineral chemistry with conventional geothermobarometry and fixed-composition phase diagrams (pseudosections) in the presence of melt. We show that the observed assemblages and mineral compositions in HP, opx-free garnet granulite of the Jijal Complex are consistent with dehydration melting after metastable low-P assemblages at the root of a thick island arc.

9.2 Geological Setting: The Jijal Complex

The Kohistan arc Complex (Himalaya, Pakistan) is an exhumed section of a Cretaceous island arc formed during northward subduction of the neo-Tethys ocean beneath the Karakoram plate (Bard, 1983a; Bard, 1983b; Burg *et al.*, 1998; Tahirkheli, 1979). The Kohistan Complex is sandwiched between the collided Indian and Karakoram plates and separated from these blocks by two major sutures: the Main Karakorum Thrust (MKT) to the north, and the Main Mantle Thrust (MMT) to the south. The studied samples come from the Jijal Complex, which is located in the hanging wall of the MMT and constitutes the structurally lowermost unit, representing the lower arc crust of the Kohistan Complex (Fig. 9-1a and b).

The Jijal Complex consists of an upper unit dominated by granulite-facies gabbroic rocks (granulitic gabbro unit, GGU) (Dhuime *et al.*, 2007, 2009; Garrido *et al.*, 2006, 2007; Jan & Howie, 1981; Jan & Windley, 1990;Yamamoto & Yoshino, 1998) overlying a thick unit of layered peridotite-pyroxenite representing the mantle-crust transition of the Kohistan arc (Bard, 1983b; Burg *et al.*, 1998; Garrido *et al.*, 2007) (Fig. 9-1a & b). Several investigators have provided comprehensive descriptions of the field and petrographic relations of the Jijal GGU (Bard, 1983b; Burg *et al.*, 1998; Garrido *et al.*, 2006; Jan & Howie, 1981; Yamamoto & Yoshino, 1998; Zeilinger, 2002). Along the Karakoram highway (KKH) in the Indus valley the GGU is exposed SW of the village of Patan (Fig. 9-1b). Here it is dominated by mafic opx-free, grt-granulite including ultramafic lenses of garnet hornblendite, subordinate hornblendite and plagioclase-bearing hornblendite, and rare dunite (Fig. 9-1b). North of Patan, in the uppermost part of the GGU (upper GGU; Fig. 1c), relic hbl-gabbronorite bodies occur (Bard, 1983a; Yamamoto & Yoshino, 1998; Garrido et al., 2006). The transition between hbl-gabbronorite and grt-granulite can be only observed at outcrop scale and cannot be mapped at the regional scale. Smaller patches of hbl-gabbronorite sporadically occur in grt-granulite in the middle section of the GGU (e.g., sample KG-02 of Garrido et al., 2006).

9.3 The Transition of Hbl-gabbronorite to Grt-granulite

Several authors have presented compelling field and petrological evidence for the transformation of meta-igneous, hbl-gabbronorite to opx-free, grt-granulite in the Jijal upper GGU (Bard, 1983a, Bard, 1983b, Garrido *et al.*, 2006, Yamamoto & Nakamura, 2000, Yamamoto & Yoshino, 1998) (Figs 9-1c & 9-2). In this unit, modal variations in hbl-gabbronorite indicate the breakdown of precursor amphibole and orthopyroxene into the anhydrous, opx-free, grt-granulite assemblages (Yamamoto & Yoshino, 1998). Hbl-gabbronorite occurs as very variable sized (decimetric to several meters) elongated patches (Fig. 9-2a), lenses (Fig. 9-2b) or tabular bodies hosted in grt-granulite. Locally, planar garnet-bearing veins are surrounded by thin, grt-granulite reaction zones within hbl-gabbronorite (Fig. 9-2c). In the same outcrop, the transition from hbl-gabbronorite to grt-granulite is convoluted in shape and cross-cut by garnet-rich veins (Garrido *et al.*, 2006; their Fig. 3c). These veins are reminiscent of garnet reaction zones similar to those described in the Pembroke grt-granulite (Blattner, 1976, Blattner 2005, Daczko *et al.*, 2001a). Additionally, thin leucocratic veins cross cut garnet granulite and hbl-gabbronorite inducing retrogression (amphibolitization) along vein walls (Yamamoto &

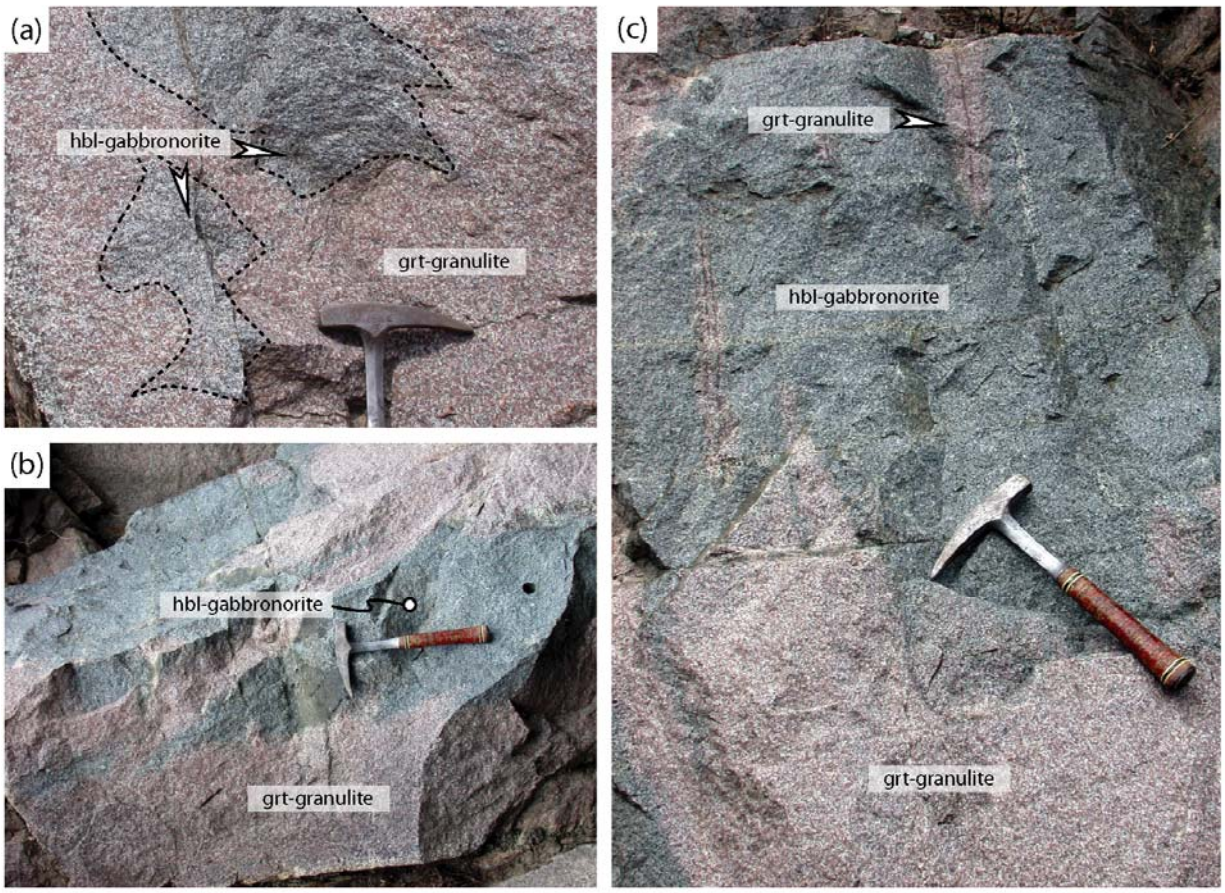

Figure 9-2: (a) Contact between hornblende gabbronorite and garnet granulite (dashed lined) in the upper part of Jijal Complex (Fig. 1c) showing a convolute almost sharp transition. Note relic patches of hbl-gabbronorite. **(b)** Irregular lenses of hbl-gabbronorite in the grt-granulite host. **(c)** Minor lenses of garnet granulite occurring near the hbl-gabbronorite transition to grt-granulite. Lenses are centred on one (right) or more (left) 1-cm wide garnet-rich bands.

Yoshino, 1998; Garrido *et al.*, 2006, their Fig. 3a). Sm-Nd radiometric ages constrain the transformation of hbl-gabbronorite to HP grt-granulite between *c.* 91 and 97 Ma during the intra-oceanic building stage of the Kohistan arc (Anczkiewicz *et al.*, 2000, Yamamoto & Nakamura, 2000).

9.4 Sample Selection and Analytical Methods

A first set of samples for the present study come from the upper GGU along the KKH (Fig. 9-1c). This sampling encompasses three representative, composite samples (KG-03, BK1-158 and KH04-9) preserving the transition of hbl-gabbronorite to grt-granulite (Figs 9-2 & 9-3a). In addition, we selected one hbl-gabbronorite (sample KH97-113) and one grt-granulite (sample KH97-114) from the upper GGU, both of them distant from the other outcrops. For comparative purposes, we have studied a second set of grt-granulite samples from the Jijal lower GGU, close to the mantle-crust transition (BP-572, BP-573 and GI-13) (Fig. 9-1c). These samples come from Prof. J.P. Bard's collection and have been investigated previously for geothermobarometry by Ringuette *et al.* (1999) (samples P572, P573 and GI-13; cf. Table 1 of Riguette *et al.*, 1999).

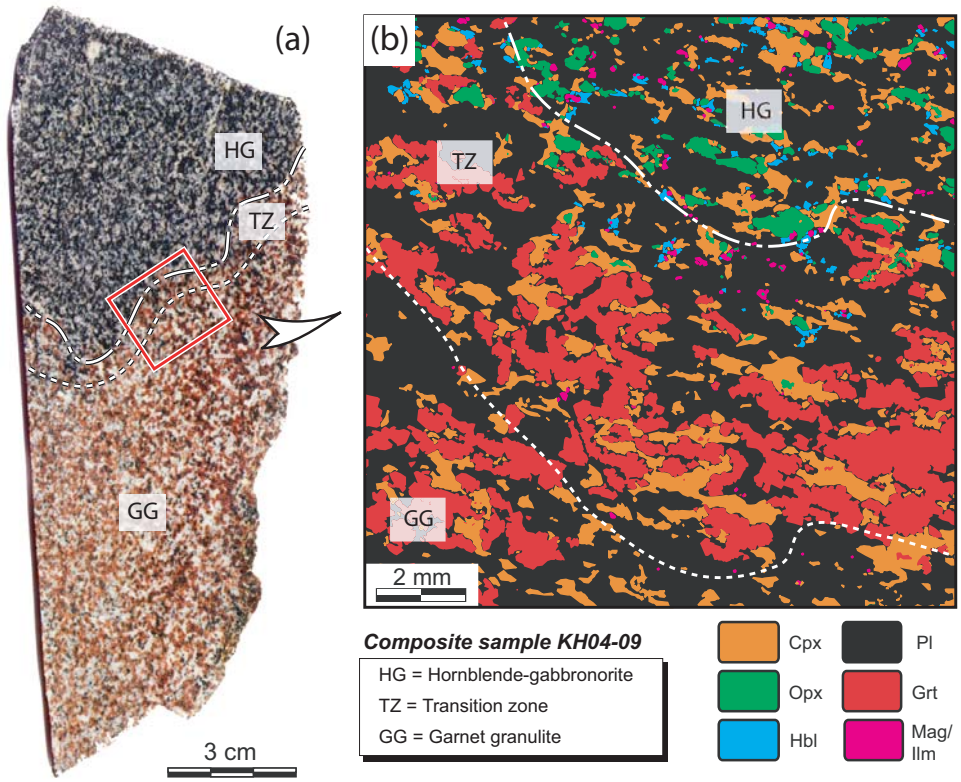

Figure 9-3: (**a)** Photograph of a hand-specimen slice of composite sample KH04-09 showing the transition zone (TZ) between hbl-gabbronorite (HG) and grt-granulite (GG). The red square outlines the area shown in Fig. 3b. (**b)** Modal mapping, obtained by combining different X-ray maps, of the transition zone shown in sample KH04-09. White lines outline the width of the TZ in this area. The dotted-dashed, white line delineates the transition between the HG and the TZ, while the dotted, white line delineates the approximate transition from the TZ to the GG.

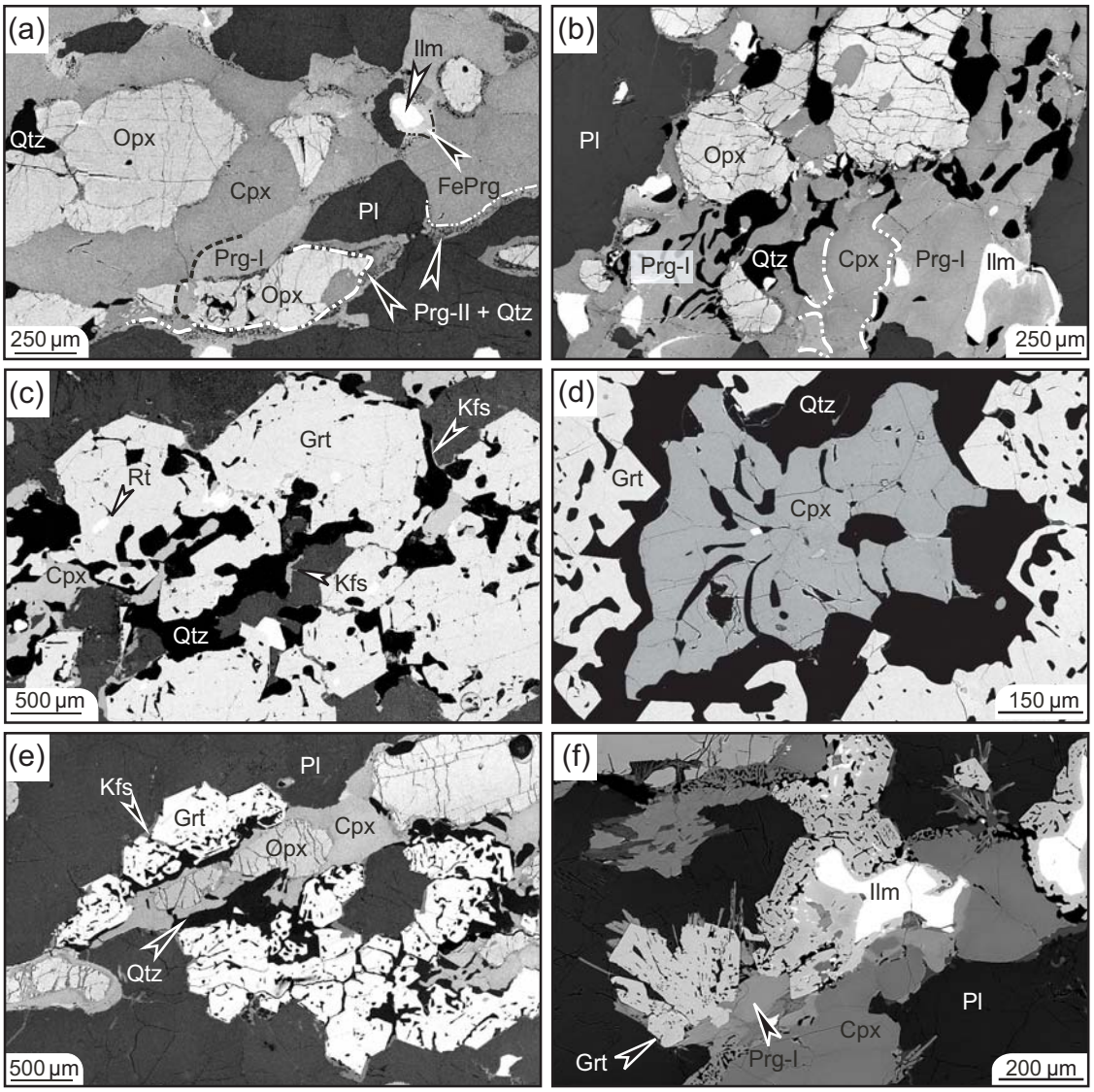

Figure 9-4: Backscattered, Scanning Electron Microscope images showing representative mineral textures in composite samples. (**a)** Mafic cluster (hbl-gabbronorite; sample KG03) displaying an orthopyroxene (Opx) core surrounded by clinopyroxene (Cpx) and pargasite (Prg-I), associated with quartz (Qtz) and hemato-ilmentite (Ilm) rimmed by Fe-rich pargasite (FePrg). Double-dotted white lines depict pargasite and quartz intergrowths (Prg-II + Qtz) between mafic minerals and the plagioclase matrix (Pl). (**b)** Mafic cluster (hbl-gabbronorite; sample KH97-113) with abundant inclusions of quartz and hemato-ilmenite. **(c)** Large subhedral garnet (Grt) (grt-granulite; sample KG-03-B) with inclusions of quartz (Qtz) and minor rutile (Rt). Films and blebs of K-feldspar (Kfs) and quartz occur between garnet and plagioclase grain boundaries. **(d)** Detail of garnet-quartz aggregates (grt-granulite; sample BKI-168) and newly formed clinopyroxene-quartz intergrowths with a rim of quartz between them. **(e)** Representative textures from Transition Zone (TZ) in composite sample KG-03. Garnet corona overgrowing orthopyroxene (Opx) and clinopyroxene (Cpx) mafic clusters. Quartz (Qtz) is more abundant towards the contact with clinopyroxene. A thin K-feldspar (Kfs) rim occurs along grain boundaries between garnet and plagioclase (Pl). **(f)** Other garnet corona textures from TZ (sample KG-03) can be observed in the central part of the image, with garnet (Grt) growing around ilmenite (Ilm); note the Qtz inclusion-poor part of garnet core (lower left) in contact with Ilm. Subhedral garnet replacing pargasite (Prg-I). Grt grows through an intermediate aggregate of prismatic biotite-like phyllosilicate.

Mineral analyses were performed using a Cameca SX50 electron microprobe at the CIC (Universidad de Granada, Spain) with operating conditions of 15 kV accelerating voltage, and 20 nA beam current and a range of 20-50 seconds peak counting time depending of the analyzed element. X-rays maps of samples KG-03 and BKI-158 were performed in a Cameca SX100 Superprobe at Géosciences Montpellier (CNRS-Université de Montpellier II, Montpellier, France). The counting time per point for Ca, Na, K, Fe, Mg, Al and Si cations was of 20 milliseconds. Additional X-ray mapping for K, Na Mg, Fe, Ca, Si, Ti, and O were made at CIC by EDS-SEM in a LEO 1430-VP instrument under an acceleration voltage of 20 kV, a beam current of 20 nA, and a beam diameter of 2 μm. Time counting for a frame was 105.8 seconds for a 1024x1024 pixel images.

Trace element analyses on clinopyroxene were carried out by LA-ICP-MS in an Agilent-7500a ICP-MS coupled to a 213 nm wavelength Nd-YAG Mercantek® laser at the CIC (University of Granada, Spain). Laser ablation analyses were done on thick sections (~ 80 μm) using laser spots of c. 60 μm. Ablation was done in a He atmosphere, data were acquired for 60 s, and the laser repetition rate was 10 Hz. As internal standard we used Si, determined by EPMA, and glass NIST-610 as external standard. Data were reduced using procedure described by Bea *et al.* (2006).

9.5 Petrography

9.5.1 Hornblende gabbronorite

Hbl-gabbronorite from composite samples is similar in terms of modal compositionand textures to hbl-gabbronorite from rocks distant to the transition zone (e.g. KH97-113). It is composed of plagioclase (51-60 vol.%), clinopyroxene (15-20 vol.%), orthopyroxene (10-15 vol. %), amphibole (10-15 vol.%), Fe-Ti oxides (3-8 vol.%), and minor quartz (3-6 vol.%) and apatite (< 2 vol.%) (Fig. 9-3b). Mafic minerals occur as clusters in a matrix of plagioclase (1-2 mm). Although recrystallized during metamorphism, the rock displays a magmatic foliation defined by alternating mafic- and plagioclase-rich layers with a well preserved lattice preferred orientation (Padrón-Navarta *et al.*, 2008). On the foliation plane, there is a distinct lineation defined by the shape preferred orientation of mafic clusters (Zeilinger, 2002; Padrón-Navarta *et al.*, 2008). The mafic clusters (3-5 mm long) are composed of subhedral to anhedral orthopyroxene surrounded by clinopyroxene (1-2 mm), each showing exsolution lamellae of the counterpart pyroxene and Fe-Ti oxides. Pyroxene is armoured by anhedral, brown pargasite (pargasite-I) with abundant inclusions of Fe-Ti oxides (Fig. 9-4a). Quartz is associated with mafic aggregates as anhedral (<250 μm) inclusions in orthopyroxene or with intergrowths of amphibole and clinopyroxene (Fig. 9-4b). In the plagioclase matrix, quartz occurs as single anhedral grains. Apatite (200-300 μm) occurs as hexagonal to subhedral grains with fine aligned opaque inclusions dispersed in the plagioclase matrix. Fe-Ti oxides, occurring as subhedral grains (< 500 μm), associated to mafic clusters or, less commonly, dispersed in the plagioclase matrix, are haemo-ilmenite or ilmeno-haematite with inclusions of magnetite and rare baddeleyite. Secondary minerals comprise fine-grained symplectitic intergrowth of amphibole (pargasite-II) and quartz (Fig. 9-4a), and rare epidote. Pargasite-II is rare or absent in hbl-gabbronorite away from the transition to grt-granulite.

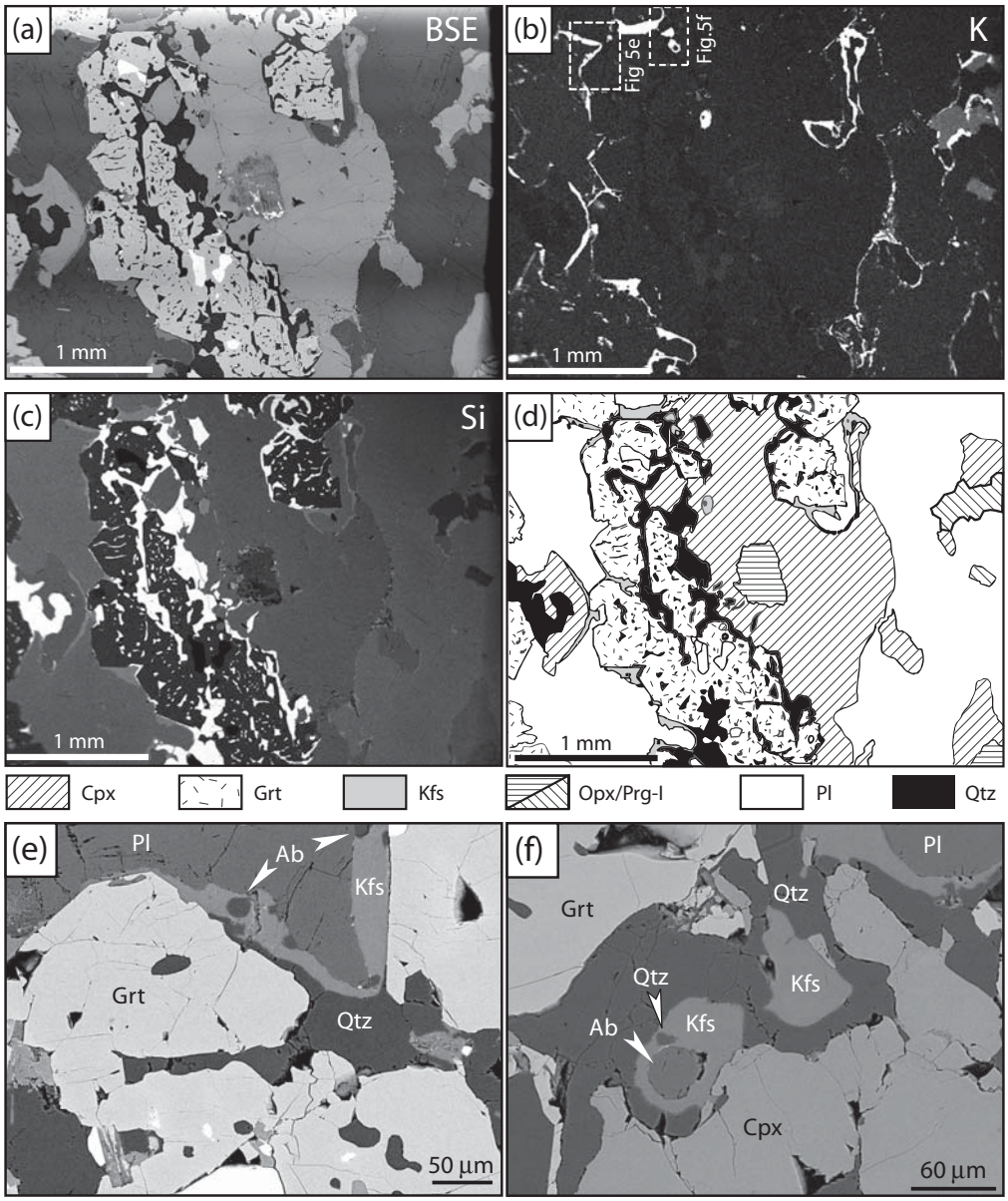

Figure 9-5: Representative K-feldspar-quartz films at the beginning of TZ from composite sample KG03 (amphibole from the right of the image belongs to the hbl-gabbronorite) **(a)** BSE image of a typical orthopyroxene-clinopyroxene mafic cluster surrounded by garnet with inclusions of quartz (black grains) and minor rutile (white grains). Clinopyroxene inclusions (not showed at this scale) are also present **(b)** EDS-SEM map for K for the same areas as Fig. 5a where K-feldspar stands up as white films along clinopyroxene-plagioclase and garnet-plagioclase grain boundaries. Medium grey to the right is amphibole, which is also partially surrounded by K-feldspar films. Dashed line box insets depict the location of detail figures 5e and f. **(c)** EDS-SEM map for Si where quartz appears in white colour. **(d)** Schematic cartoon showing the textural relationships between K-feldspar films and blebs and other garnet granulite minerals. **(e)** BSE-SEM image showing K-feldspar (Kfs) films and patches along garnet-plagioclase and quartz-plagioclase interfaces. Albite (dark inclusions within Kfs patches) occurs as round inclusions near the rims of plagioclase. K-feldspar can be partially included in the garnet (upper left). **(f)** BSE-SEM image of a round K-feldspar (Kfs) included in quartz along a clinopyroxene-garnet grain boundary. Large albite (Ab) and small quartz (Qtz) inclusions occur within Kfs (left).

9.5.2 Garnet granulite

Mafic garnet granulite from the upper GGU displays tipically a granoblastic texture (1-2 mm-sized grains), but in composite samples close to the transition zone it preserves a relic foliation, defined by garnet-bearing, mafic clusters, parallel to that of hbl-gabbronorite. The characteristic mineral assemblage consists of plagioclase (40-45 vol. %), garnet (35-40 vol. %), clinopyroxene (15-20 vol. %), quartz (5-7 vol. %), and rutile (3-5 vol. %) with minor apatite. Orthopyroxene and amphibole are scarce close to the TZ and absent (but in the case of minor orthopyroxene relics) away for it (Fig. 9-3b). Coarse garnet and garnet with coronitic textures surround quartz and granoblastic clinopyroxene, both embedded in an undeformed matrix of plagioclase. In composite samples garnet is spatially associated with mafic minerals and occurs as subhedral aggregates with inclusions of quartz, minor clinopyroxene, rutile and apatite. Quartz is mostly irregular and lobated and occurs in the inner part of the garnet aggregates (Fig. 9-4c), as coronas (up to 100 μm thick) surrounding anhedral clinopyroxene, and as vermicular inclusions within this latter mineral (Fig. 9-4d). Recrystallized clinopyroxene is granoblastic and smaller in size than that from hbl-gabbronorite. Garnet aggregates are rimmed by films and blebs of K-feldspar (arrows in Fig. 9-4c). Rutile is the main oxide in the grt-granulite. It occurs as subhedral inclusions in garnet and rare, oriented needles in garnet. Baddeleyite is rare and occurs in contact with rutile. Apatite grains are similar in size, shape and textural location as those from the hbl-gabbronorite.

Grt-granulite from Jijal lower GGU has the same mineral assemblage as that of the upper GGU. Texturally it differs in the occurrence of centimetric clinopyroxene-rich and plagioclase-poor (< 10% plagioclase) bands (sample BP-572). Plagioclase is commonly saussuritized and replaced by cauliflower-like symplectitic intergrowths of epidote (3 vol.%).

9.5.3 The transition zone (TZ)

In composite samples, the transition between hbl-gabbronorite and grt-granulite is characterized by an irregular, up to 2-3 cm thick, front made up of garnet, clinopyroxene, orthopyroxene, plagioclase, Fe-Ti oxides, rutile, quartz, and minor amphibole, apatite and K-feldspar (Figs 9-3 & 9-4). It is characterized by: (i) garnet coronas around the pyroxene clusters and oxides; (ii) a sharp decrease of the modal content of orthopyroxene and amphibole relative to the hbl-gabbronorite; and (iii) the transformation of Fe-Ti oxides characteristic of hbl-gabbronorite to rutile. Rutile is found as reddish brown anhedral to subhedral grains (up to 100 μm thick) commonly associated with magnetite-poor Fe-Ti oxides. The transformation of Fe-Ti oxides to rutile is observed even in single grains, where the boundary between rutile and ilmenite-haematite is sharp. Very fine-grained intergrowths of titanite and rare baddeleyite occur in Fe-Ti oxides. One of the most prominent features of the TZ is the sharp appearance of K-feldspar films and blebs that are pervasive along grain boundaries of minerals, being more common and thicker in plagioclase-garnet grain boundaries (Fig. 9-5). The preservation of the mafic layering in the grt granulite from the hbl gabbronorite, infered by the strong lattice-preferred orientation relationship between pyroxene clusters and garnet in the TZ (Padrón-Navarta et al., 2008), rules out the xenolithic origin of the hbl gabbronorite and strongly supports that the transition represents a replacement front.

9.5.4 Distribution of intergranular K-feldspar

Detailed BSE-SEM observations (Fig. 9-5a) and X-ray mapping (Fig. 9-5b & c) in composite samples reveals the presence of intergranular thin films, blebs and micro-veins (up to 60μm thick) of K-feldspar associated with minor albite and quartz. These films are pervasive along grains boundaries in the TZ and in the grt-granulite close to the TZ, but are absent in the hbl-gabbronorite, where amphibole is the only K-bearing phase. The abrupt appearance of intergranular K-feldspar at the TZ is spatially associated with the onset of amphibole breakdown (Fig. 9-5b).

K-feldspar in the TZ and grt-granulite occurs as K-feldspar-quartz-albite films along garnet-plagioclase grain boundaries (Fig. 9-5b, c & e), as blebs at clinopyroxene-plagioclase and plagioclase-plagioclase grain boundaries, and as rare inclusions in garnet. K-feldspar films with quartz occur at the garnet-clinopyroxene interfaces (Fig. 9-5e), whereas those at the clinopyroxene-plagioclase interfaces are quartz lacking (Fig. 9-5b & c). K-feldspar blebs and films contain spherical inclusions of albite (10-50 μm in diameter, Fig. 9-5f). We have not observed myrmekite albite intergrowths that are often reported in other mafic granulites.

Table 9-1. Representative analyses of feldspar

	Hbl-gabbronorite				Grt-granulite							
sample	KH97-113		KH04-9-1		KG-03/TZ						BKI-158/GG	BP-573
ID	981 core	957 rim	631 core	620 rim	734 core	748 rim	micro-veins[a]		micro-inclusion[b]		907 rim	916 rim
mineral	Plg	Plg	Plg	Plg	Plg	Plg	Albite	Kfs	Albite	Kfs	Plg	Plg
(wt. %)												
SiO_2	54.21	57.51	53.81	57.87	57.71	58.88	66.33	64.42	66.45	63.27	56.72	56.67
Al_2O_3	29.21	26.9	28.96	26.44	26.29	25.38	21.2	18.72	19.56	19.21	27.02	27.05
Fe_2O_3*	0.05	0.16	0.02	0.10	0.12	0.08	0.11	0.24	0.72	0.27	0.29	0.06
CaO	11.11	8.61	11.91	8.77	8.75	7.27	0.53	0.08	0.64	-	8.93	8.63
BaO	-	-	-	-	-	-	0.15	1.12	0.13	1.63	-	-
Na_2O	5.54	6.82	4.87	6.68	6.62	7.55	11.39	0.8	12.36	0.96	6.55	6.88
K_2O	0.16	0.18	0.12	0.17	0.29	0.22	0.29	14.61	0.14	14.74	0.37	0.14
Total	100.3	100.2	99.7	100.0	99.8	99.4	100[c]	100[c]	100[c]	100[c]	99.9	99.4
O†	8	8	8	8	8	8	8	8	8	8	8	8
Si	2.44	2.58	2.44	2.59	2.59	2.65	2.91	2.98	2.94	2.95	2.55	2.56
Al	1.55	1.42	1.55	1.40	1.39	1.34	1.10	1.02	1.02	1.05	1.43	1.44
Fe^{3+}	0.00	0.01	0.00	0.00	0.00	0.00	0.00	0.01	0.02	0.01	0.01	0.00
Ca	0.54	0.41	0.58	0.42	0.42	0.35	0.03	0.00	0.03	-	0.43	0.42
Ba	-	-	-	-	-	-	0.00	0.02	0.00	0.03	-	-
Na	0.48	0.59	0.43	0.58	0.58	0.66	0.97	0.07	1.06	0.09	0.57	0.60
K	0.01	0.01	0.01	0.01	0.02	0.01	0.02	0.86	0.01	0.88	0.02	0.01
Total	5.03	5.01	5.00	5.00	5.01	5.02	5.03	4.97	5.08	5.01	5.02	5.03
X_{An}	0.52	0.41	0.57	0.42	0.42	0.34	0.02	0.00	0.03	-	0.42	0.41
[d]X_{Ce}	-	-	-	-	-	-	0.00	0.02	0.00	0.03	-	-
X_{Ab}	0.47	0.58	0.42	0.57	0.57	0.65	0.96	0.08	0.96	0.09	0.56	0.59
X_{Or}	0.01	0.01	0.01	0.01	0.02	0.01	0.02	0.90	0.01	0.88	0.02	0.01

TZ= transition zone, GG = garnet granulite part of composite sample.

[a,b] Integrated spectra using quantitative SEM image shown in Fig. 5b. and Fig.6c respectively.[c] Oxygen by [d] Celsian - $BaAl_2Si_2O_8$ *Fe_2O_3 was calculated as total iron. † Cations calculated on the basis of 8 oxygens

9.6 Mineral Chemistry

9.6.1 Feldspar

Plagioclase of hbl-gabbronorite in single and composite samples displays a rimward increase of the albite (Ab) contents towards clinopyroxene and plagioclase respectively (Table 9-1). The orthoclase (Or) content of plagioclase is negligible. Plagioclase of grt-granulite in single and composite samples displays a similar zoning to that of hbl-gabbronorite plagioclase but, on average, has lower An and higher Or contents (Table 9-1). Larger variation of the anorthite content (An_{27}-An_{50}) is found in plagioclase of composite samples. Alkali feldspar, widespread in grt-granulite samples, has a constant composition irrespective of its textural location (Table 9-1). As noted by Yoshino *et al.* (1998), plagioclase of grt-granulites from the lower GGU has low anorthite content (An_{35}-An_{40}).

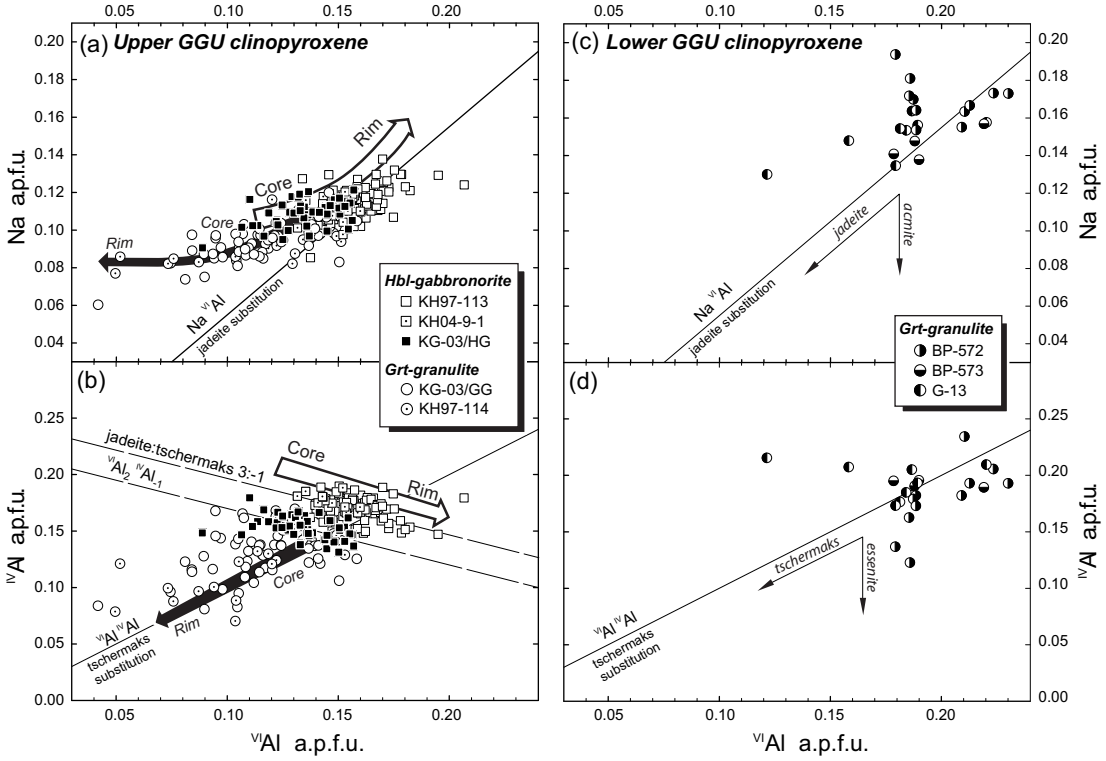

Figure 9-6: (a) Na vs. ^{VI}Al in a.p.f.u (6 oxygens) for clinopyroxenes from the studied samples of the transition between hbl-gabbronorite (squares) and mafic garnet granulite (circles). Clinopyroxene from mafic garnet granulite near the transition (i.e. KG-03 and KH97-114) plot off the jadeite substitution line due to the low variation in sodium related to a major range in ^{VI}Al. **(b)** ^{IV}Al vs. ^{VI}Al in a.p.f.u. for clinopyroxene [same symbols as (a)]. Note that in contrast to clinopyroxene from hbl-gabbronorite the ^{VI}Al variations in garnet granulite clinopyroxene are positively correlated with ^{IV}Al due to a Tschermaks like substitution. **(c)** and **(d)** Na vs. ^{VI}Al and ^{IV}Al vs. ^{VI}Al, respectively, for clinopyroxene from the lower part of the GGU (i.e. samples BP-572, BP-573 and G-13). Note that this clinopyroxene shows variable and Complex trends due to the interaction of acmite and essenite exchanges.

9.6.2 Pyroxene

Clinopyroxene from single (KH97-113) and composite samples (KH04-9-1/HZ and KG03/HZ) of hbl-gabbronorite has a similar composition being diopside with minor amounts of augite component. Hbl-gabbronorite clinopyroxene is characterized by high Al (up to 0.21 ^{VI}Al and 0.19 ^{IV}Al, atoms per formula unit [a.p.f.u.], calculated on the basis of 6 oxygens) and Na contents (up to 0.14 Na, a.p.f.u) (Table 9-2, Fig. 9-6). The X_{Mg} (=Mg/[Fe+Mg]; a.p.f.u) of clinopyroxene rims increases in contact with orthopyroxene, pointing to Fe-Mg exchange between both pyroxenes. Clinopyroxene in hbl-gabbronorite KH97-113 shows a rimward increase of ^{VI}Al (from 0.14 to 0.18 a.p.f.u) and Na (from 0.10 to 0.12) contents, and a decrease of ^{IV}Al content (0.17 to 0.15 a.p.f.u). The rimward increase of the ^{VI}Al/^{IV}Al ratio and Na content of clinopyroxene are consistent with an increase of the jadeite component (Fig 9-6). Orthopyroxene in hbl-gabbronorite is aluminian enstatite (Morimoto *et al.*, 1988) containing 0.13-0.25 Al_{total} a.p.f.u.

Table 9-2. Representative analyses of pyroxenes.

	Hbl-gabbronorite				Grt-granulite				TZ
sample	KH97-113	KH97-113	KH97-113	KH97-113	KG-03/TZ	KG-03/TZ	GI-13	BP572	KG-03/TZ
mineral	Cpx	Cpx	Opx	Opx	Cpx	Cpx	Cpx	Cpx	Opx
ID	198core	213rim	486core	479rim	225core	241rim	1057rim	922rim	535core
SiO_2 (wt. %)	48.83	48.81	49.45	49.23	50.66	51.97	48.77	48.30	52.66
TiO_2	0.44	0.35	-	-	0.47	0.41	0.79	0.80	-
Al_2O_3	7.13	7.53	5.20	5.64	5.93	4.31	9.34	8.95	2.59
Cr_2O_3	-	-	-	-	-	-	-	-	-
FeO*	11.10	10.34	24.61	24.33	8.40	7.23	7.09	7.71	20.67
MnO	0.36	0.29	0.78	0.75	0.06	0.11	-	-	0.17
MgO	10.11	9.93	19.43	19.51	12.11	13.15	10.08	9.99	24.09
CaO	20.48	19.47	0.44	0.35	20.71	21.59	20.69	20.91	0.49
Na_2O	1.44	1.65	-	-	1.33	1.13	2.18	2.27	-
Total	99.91	98.41	100.01	99.88	99.70	99.90	98.97	98.98	100.83
O†	6	6	6	6	6	6	6	6	6
Si	1.826	1.847	1.859	1.851	1.878	1.917	1.811	1.795	1.933
Ti	0.012	0.010	-	-	0.013	0.011	0.022	0.022	-
^{IV}Al	0.174	0.153	0.141	0.149	0.122	0.083	0.189	0.205	0.067
^{VI}Al	0.140	0.182	0.090	0.101	0.137	0.105	0.219	0.187	0.020
Al_{tot}	0.314	0.336	0.231	0.250	0.259	0.187	0.408	0.392	0.087
Fe^{3+} ‡	0.114	0.071	0.050	0.049	0.054	0.036	0.083	0.137	0.045
Fe^{2+} ‡	0.233	0.256	0.724	0.716	0.207	0.187	0.137	0.103	0.582
Mn	0.012	0.009	0.025	0.024	0.002	0.004	-	-	0.007
Mg	0.564	0.560	1.089	1.093	0.669	0.723	0.558	0.553	1.327
Ca	0.820	0.789	0.018	0.014	0.822	0.853	0.823	0.832	0.016
Na	0.104	0.121	-	-	0.096	0.084	0.157	0.164	-
Total	4	4	4	4	4	4	4	4	4
CaTs	0.063	0.082			0.058	0.036	0.088	0.065	
Jd	0.077	0.100			0.079	0.070	0.130	0.121	
CaTiTs	0.025	0.020			0.026	0.023	0.044	0.045	
Es	0.086	0.050			0.037	0.023	0.056	0.095	
Acm	0.028	0.021			0.016	0.014	0.026	0.042	
MgTs			0.089	0.099					0.019
MgTiTs			0.003	0.002					0.003
X_{Mg} §	0.707	0.686	0.601	0.604	0.764	0.795	0.803	0.844	0.695

TZ= transition zone, GG = garnet granulite part of composite sample. - below detection limit (typically 0.05 wt.% in WDS)

* FeO was calculated as total iron. † Cations calculated on the basis of 6 oxygens ‡ Fe^{2+} and Fe^{3+} were calculated based on pyroxene stoichiometry. CaTs = (Al-Jd-CaTiTs-Cr-Es)/2; Jd = Na·{Al/(Al+Fe^{3+})}; CaTiTs = 2Ti; Es = Fe^{3+}-Acm; Acm = Na·{Fe^{3+}/(Al+Fe^{3+})}. MgTs = (Al-MgTiTs-Cr-Fe^{3+})/2; MgTiTs = 2Ti. § X_{Mg} = Mg/(Mg+Fe^{2+}).

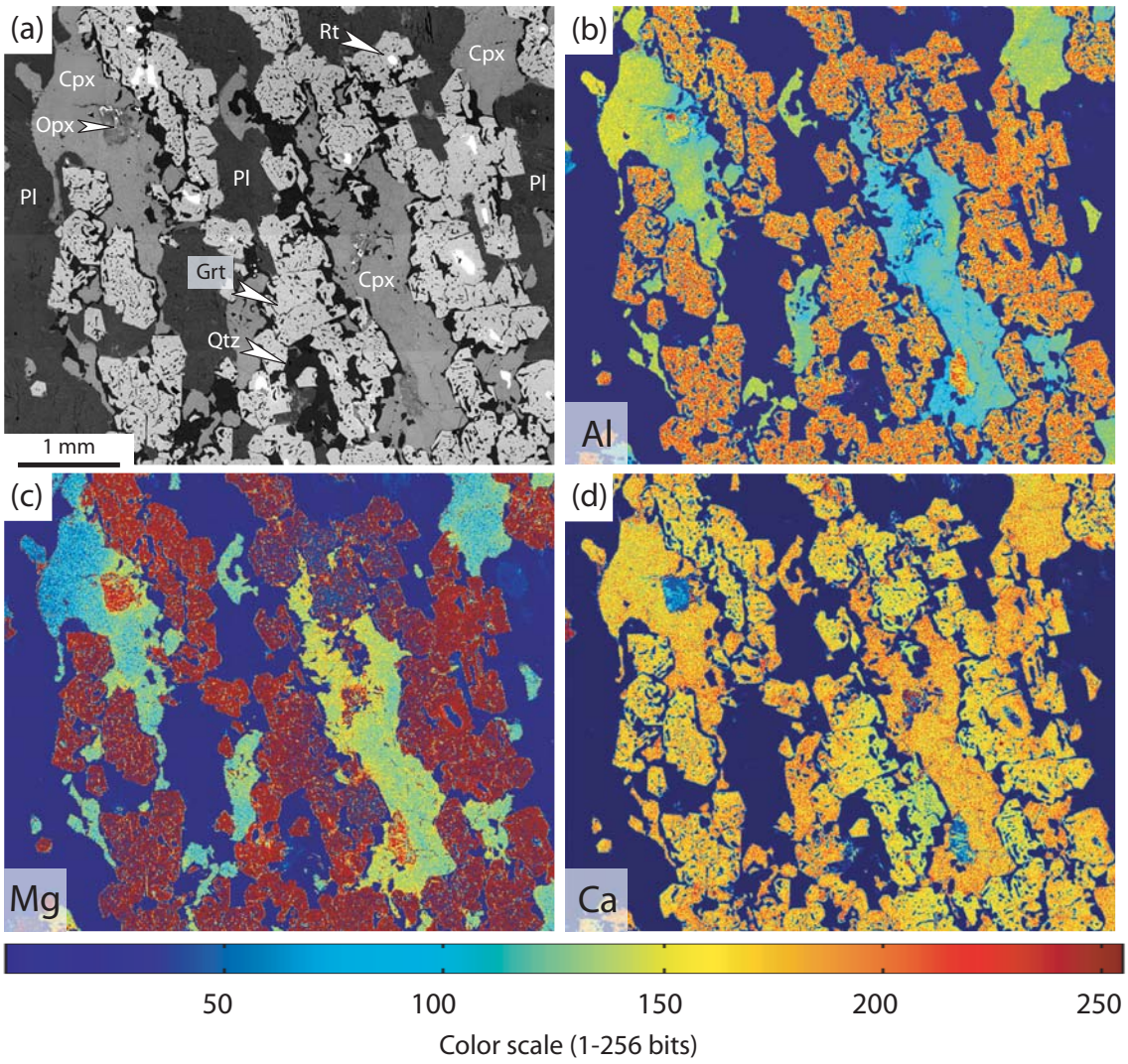

Figure 9-7: (a) Backscattered image of a selected area from the Transition Zone (sample KG03/TZ) showing two mafic clusters surrounded partially (left) and completely (right) by garnet that controls the main zoning in clinopyroxene. **(b)**, **(c)** and **(d)** X-ray compositional maps (EPMA) of the same area as (a) for aluminium, magnesium and calcium, respectively. See text for details. Maps were elaborated using Matlab image toolbox® (relative color scale from 1 to 256 bits, high contents of the element are represented by warm color and low contents by cold). Plagioclase was omitted in the maps for clarity.

Orthopyroxene from TZ of composite samples has higher X_{Mg} (= 0.70) relative to that of hbl-gabbronorite (X_{Mg} = 0.60).

Clinopyroxene from the TZ and from grt-granulite has lower contents of non-quadrilateral components relative to that of hbl-gabbronorite. The $^{VI}Al/^{IV}Al$ correlation follows a distinct tschermaks substitution trend (Fig. 9-6b), which markedly differs from the jadeite:tschermaks substitution (3:-1) trend characteristic of hbl-gabbronorite clinopyroxene (Fig. 9-6a & b). X-ray mapping of the TZ shows that clinopyroxene in contact with garnet has strong rimward depletion in Al and Mg, which is not observed in the hbl-gabbronorite clinopyroxene or in TZ clinopyroxene which is not in contact with garnet (Fig. 9-7a & b). Therefore the rimward depletion of Al and Mg in TZ

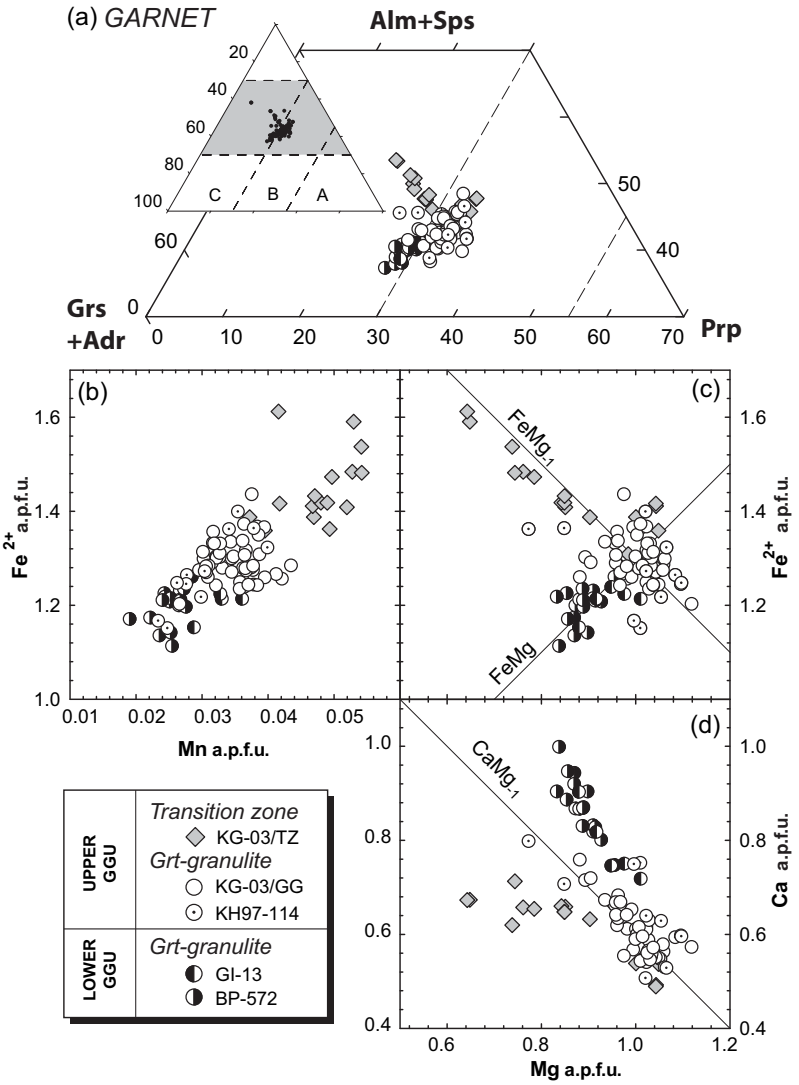

Figure 9-8: Compositional variation of garnet from garnet granulite near the transition zone (samples KG-03/GG and KH97-114) and from other granulites from the lower part of the Jijal Complex (GI-13 and BP-572). Garnet from the transition zone (sample KG-03/TZ) was also distinguished and corresponds mainly to rare pargasite-I/garnet contacts. **(a)** Enlarged triangular plot in terms of normalized grossular+andradite (Grss+Adr), pyrope (Py) and almandine+spessartine (Alm+Sps) components. A, B and C regions following Coleman *et al.* (1965). **(b)** Fe^{2+} vs Mn in a.p.f.u. plot (24 oxygens) showing that Mn is subordinate to ferrous iron in all the rock types, but shows higher amounts in cluster garnets from TZ **(c)** Fe^{2+} vs Mg in a.p.f.u. plot. Garnet from garnet granulites shows a positive correlation between Fe and Mg in contrast to garnet from TZ. **(d)** Ca vs Mg in a.p.f.u. plot. Note that garnet from TZ and from lower structural levels of the granulite unit plots off the $CaMg_{-1}$ vector and shows very different correlation trends.

clinopyroxene is due to tschermaks coupled substitutions with garnet associated with garnet-forming reactions. TZ clinopyroxene shows a rimward increase of the X_{Mg} ratio and the Ca content (Fig. 9-7c & d) towards adjacent garnet. In contrast, clinopyroxene of grt-granulite from the lower GGU shows substantially higher Al and Na contents (up to 0.23 ^{VI}Al and 0.24 ^{IV}Al, and up to 0.20 Na, a.p.f.u.). Na and ^{IV}Al variations are

Table 9-3. Representative analyses of garnet.

	Transition Zone				Grt-granulite			
sample	KG-03/TZ				KG-03/TZ		BKI-158/GG	BP-573
ID	363 rim	347 rim	323 core	331 rim	329 core	330 rim	901 core	918 rim
Neighbor Phase	Prg-I	Fe-Ti oxide	Opx	Opx	Cpx	Cpx	Cpx	Cpx
SiO_2 (wt. %)	37.85	39.22	39.26	39.60	39.57	39.58	39.17	39.41
TiO_2	0.09	-	-	-	0.05	0.09	-	0.06
Al_2O_3	21.22	21.95	22.22	22.11	21.91	21.91	21.89	21.95
Cr_2O_3	-	-	-	-	-	-	-	-
FeO*	26.06	23.98	21.89	22.70	22.46	23.26	22.68	20.47
MnO	0.80	0.73	0.50	0.62	0.60	0.59	0.63	0.42
MgO	5.56	7.51	8.73	9.34	8.91	8.63	8.33	8.44
CaO	8.04	7.97	7.97	6.66	7.42	6.83	7.89	9.85
Total	99.64	101.42	100.60	101.07	100.92	100.89	100.65	100.60
O	12	12	12	12	12	12	12	12
Si	2.960	2.973	2.970	2.982	2.988	2.998	2.974	2.976
Ti	0.005	-	-	-	0.003	0.005	-	0.003
Al	1.956	1.961	1.981	1.962	1.950	1.956	1.959	1.954
Fe^{3+} †	0.114	0.087	0.076	0.070	0.068	0.037	0.089	0.087
Fe^{2+} †	1.590	1.432	1.309	1.359	1.350	1.436	1.351	1.206
Mn	0.053	0.047	0.032	0.040	0.039	0.038	0.041	0.027
Mg	0.648	0.849	0.984	1.048	1.003	0.975	0.943	0.950
Ca	0.674	0.647	0.646	0.537	0.600	0.555	0.642	0.797
Total	8	8	8	8	8	8	8	8
X_{Py}	*0.211*	*0.277*	*0.323*	*0.343*	*0.328*	*0.321*	*0.308*	*0.310*
X_{Alm}	*0.517*	*0.468*	*0.429*	*0.445*	*0.441*	*0.472*	*0.441*	*0.393*
X_{Sps}	*0.017*	*0.015*	*0.011*	*0.013*	*0.013*	*0.012*	*0.013*	*0.009*
X_{Grs}	*0.219*	*0.211*	*0.212*	*0.176*	*0.196*	*0.182*	*0.209*	*0.260*
X_{Adr}	*0.037*	*0.029*	*0.025*	*0.023*	*0.022*	*0.012*	*0.029*	*0.028*
X_{Mg} ††	0.290	0.372	0.429	0.436	0.426	0.404	0.411	0.441

TZ= transition zone, GG = garnet granulite part of composite sample. - below detection limit (typically 0.05 wt.% in WDS)
*FeO was calculated as total iron. † Fe^{2+} and Fe^{3+} were calculated based on garnet stoichiometry. †† X_{Mg} = Mg/(Mg+Fe^{2+}).

uncorrelated with ^{VI}Al (Fig. 9-6a & b) indicating that acmite and essenite are important components of clinopyroxene in lower GGU grt-granulites.

9.6.3 Garnet

Garnet from the upper GGU is almandine-rich (Alm_{36-58}, Prp_{6-10}, Grs_{16-33}, symbols after Kretz, 1983) with minor spessartine (Sps) and andradite (Adr) components (Sps_{1-2}, Adr_{1-4}) (Fig. 9-8a). In all samples garnet has a limited compositional zoning, except in the TZ, where it shows a rimward decrease of grossular content coupled with Fe-Mg exchange with clinopyroxene and, to a lesser extent, with orthopyroxene (Table 9-3, Fig. 9-8c), and an increase of almandine content where in contact with oxides. Thus, in the TZ, garnet coronas around Fe-Ti oxides (Table 9-3) have lower X_{Mg} (0.37-0.39) than those around orthopyroxene (0.42-44). Garnet adjacent to amphibole has relatively lower X_{Mg} (0.14-0.38), and higher Mn (up to 0.07 a.p.f.u., calculated on the basis of 12 oxygens, Fig. 8b).

Garnet from the lower GGU grt-granulites has higher grossular contents (24-33 mol %, Fig. 9-8d) relative to those of upper GGU (16-26 mol %). The andradite content is also

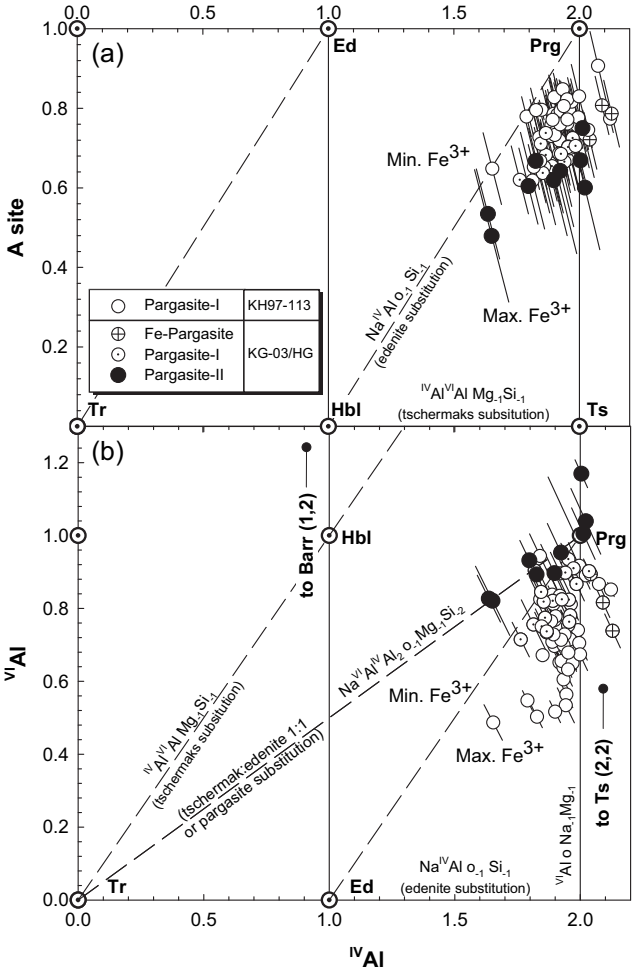

FIGURE 9-9: (a) Plot of A-site occupancy versus ^{IV}Al in amphibole from hornblende gabbronorite samples. Tr: tremolite, Hbl: hornblende, Ed: edenite, Prg, pargasite, Ts: tschermakite. **(b)** Plot of ^{IV}Al vs. ^{IV}Al. Main variations correspond to tschermakite-type substitution. Tschermakite end member plots off the diagrams. The optimal range of possible amphibole formulae that is caused by uncertainties on the estimation of Fe^{3+} is computed following Schumacher's method (Leake *et al.* (1997); see Table 9-4 for details). Solid gray lines in both diagrams depict the maximum uncertainty estimated from calculated stoichiometric limits of Fe^{3+}. Amphibole analyses are plotted as the mean value between these two extremes.

different in garnet from the upper (1-10 mol %) and lower (2-4 mol %) GGU and does not correlate with the grossular content.

9.6.4 Amphibole

Primary amphibole of likely igneous origin (Prg-I) in hbl-gabbronorite is potassian pargasite and potassian, ferroan-pargasite (after Leake *et al.* 1997), containing 0.40 and 0.44 a.p.f.u. of K, respectively (see Table 9-4 for details of the cation calculation method). Prg-I is similar in composition to amphibole in plutonic xenoliths and phenocrysts from island arc basalts (Arculus *et al.*, 1983, Fichaut *et al.*, 1989), and to that in Pembroke two-pyroxene granulite (Mildford Sound, New Zealand) (Blattner, 1976, Clarke *et al.*, 2000, Daczko *et al.*, 2001a).

Table 9-4. Representative analyses of amphibole.

	Pargasite-I		FePrg	Pargsite-II			Pargasite-I		FePrg	Pargsite-II	
sample ID	KG03/HG 13 core	KG03/HG 36 rim	KG03/HG 48	KG03/HG 41 core	KH04-9 2 rim		KG03/HG 13 core	KG03/HG 36 rim	KG03/HG 48	KG03/HG 41 core	KH04-9 2 rim
						O	23	23	23	23	23
SiO_2 (wt. %)	39.77	40.24	39.96	41.07	40.95	Si	6.057	6.053	6.068	6.077	6.076
TiO_2	1.55	1.95	1.51	-	-	Ti	0.178	0.220	0.173	-	-
Al_2O_3	14.12	15.01	14.32	16.49	17.19	^{IV}Al	1.943	1.947	1.932	1.923	1.924
Cr_2O_3	-	-	-	-	-	^{VI}Al	0.592	0.715	0.631	0.953	1.082
FeO	15.63	14.42	16.89	15.66	14.84	Al_{tot}	2.534	2.662	2.562	2.876	3.007
MnO	0.18	-	0.06	0.30	0.40	Fe^{3+} †	0.296	0.101	0.280	0.452	0.429
MgO	9.99	10.03	9.21	9.90	9.79	Fe^{2+}-C^{site}	1.666	1.713	1.832	1.406	1.321
CaO	11.30	11.51	11.08	11.04	10.69	Fe^{2+}-B^{site}	0.028	0.000	0.032	0.080	0.091
Na_2O	1.73	1.45	1.56	1.66	1.96	Mn	0.045	-	0.048	0.037	0.032
K_2O	1.83	2.61	2.33	1.58	1.05	Mg	2.268	2.250	2.084	2.185	2.165
F	0.12	0.11	0.14	0.14	0.14	Ca	1.844	1.854	1.802	1.750	1.699
Total	96.24	97.39	97.08	97.89	97.04	Na-B^{site}	0.083	0.117	0.118	0.133	0.178
O=F	0.05	0.05	0.06	0.06	0.06	Na-A^{site}	0.428	0.306	0.340	0.344	0.385
Total	96.19	97.34	97.02	97.83	96.98	K	0.356	0.501	0.452	0.299	0.199
						Total	15.780	15.810	15.790	15.640	15.580
						*Xgln**	0.042	0.059	0.059	0.066	0.089
						Xprg	0.783	0.807	0.792	0.643	0.585
						Xts	0.100	0.056	0.087	0.317	0.376
						Xtr	0.076	0.078	0.062	-0.026	-0.050
						Stoichiometric and chemical limits on ferric-Fe estimates used in average formulae.††					
						lower Fe^{3+} limit	15eNK	all ferrous	all ferrous	15eNK	all ferrous
						upper Fe^{3+} limit	13eCNK	13eCNK	13eCNK	13eCNK	13eCNK

HG= hbl-gabbronorite part of composite sample. - below detection limit

† Cations calculated on the basis of average between upper and lower limits on ferric-Fe estimates.

†† 15eNK = all cations exclusive Na and K normalized to 15; 13eCNK = 13 cations exclusive Ca, Na and K normalized to 13.

*Xgln=Na-Bsite/2; Xprg=Asite; Xts=(VIAl+Ti+Fe3+Na-Asite-Na-Bsite)/2

Secondary amphibole (Prg-II) is potassian pargasite richer in Fe^{3+} than Prg-I (0.45 vs. 0.30 a.p.f.u., calculated on the basis of 23 oxygens; Table 9-4). Although primary (Prg-I) and secondary (Prg-II) pargasite display some compositional overlaps (Fig. 9-9a & b), Prg-II has lower A-site occupancy, which is due to its lower K contents (Fig. 9-9a). Moreover, Prg-I and Prg-II follow distinct $^{IV}Al/^{VI}Al$ trends. While Prg-I has a rather constant ^{IV}Al content relative to ^{VI}Al (Fig. 9-9b), Prg-II follows a well-defined trend with a 2:1 ratio of $^{IV}Al/^{VI}Al$ following a pargasite substitution (tschermakite:edenite 1:1). The tshermakite (X_{ts}) and pargasite (X_{prg}) component increase and decrease, respectively, from primary to secondary amphibole (Table 9-4; Prg-I: X_{ts} =0.100; X_{prg}=0.783; and Prg-II, X_{ts} =0.317; X_{prg}=0.643). Prg-II is also characterized by lower Ti content (>0.01 contrasting with 0.18-0.22 from igneous pargasite, a.p.f.u.).

9.6.5 Oxides

Hbl-gabbronorite contains Ti-poor magnetite, ilmenite and haematite. Ilmenite and haematite have fine exolution lamellii of haematite and ilmenite, respectively. Magnetite, containing very low ulvöspinel content (0.76-3.02 mol. %), is rare in the TZ. Magnetite from island arc gabbroic cumulates has comparatively higher ulvöespinel content (e.g. Fichaut *et al.*, 1989). This difference can be due to the loss of Ti during re-equilibration of magnetite on cooling in Jijal samples. Rutile in grt-granulite has a very homogeneous, almost pure stoichiometric composition.

9.7 Sequence of Garnet-forming Reactions

Textures related to garnet-forming reactions are well preserved in the TZ of composite samples, where relics of reactant orthopyroxene, hornblende and Fe-Ti oxides provide a snapshot of the sequence of garnet-forming reactions after hbl-gabbronorite parageneses (Padrón-Navarta *et al.*, 2008). Textural observations and modal variations in composite samples indicate that garnet formed via three main reactions:

(i) *Garnet-forming reaction after amphibole:* This reaction would account for the garnet rims (250-500 μm thick) with vermicular quartz inclusions overgrowing amphibole that occur between mafic clusters and plagioclase (Fig. 9-4e). The exact nature of the amphibole breakdown reaction (i.e., dehydration *versus* dehydration-melting reaction) in HP mafic grt-granulite cannot be unambiguously constrained by textural observations (e.g., Hartel & Pattison, 1996). Amphibole breakdown can take place through the following balanced subsolidus dehydration reaction:

$$2NaCa_2Mg_4Al_3Si_6O_{22}(OH)_2 + 2SiO_2 = Ca(Fe,Mg)_5Al_4Si_6O_{24} + 3Ca(Fe,Mg)Si_2O_6 + 2NaAlSi_3O_8 + 2H_2O \quad (1a)$$

pargasite — quartz — garnet — clinopyroxene — albite

However, trace element variations in composite samples (Garrido *et al.,* 2006) and affinity of garnet-producing reactions (Padrón-Navarta et al., 2008) point to melt-present reactions. Although the nature of the breakdown reaction will be discussed below, we anticipate an overall dehydration-melting reaction analogous to that proposed for other HP mafic grt-granulites (Hartel & Pattison, 1996; Pattison, 2003):

$$NaCa_2Mg_4Al_3Si_6O_{22}(OH)_2 + CaAl_2Si_2O_8 + SiO_2 = Ca(Fe,Mg)_5Al_4Si_6O_{24} + Ca(Fe,Mg)Si_2O_6 + melt \quad (1b)$$

pargasite — anorthite — quartz — garnet — clinopyroxene

(ii) *Garnet-forming reaction after orthopyroxene:* A second garnet-forming reaction involved the breakdown of orthopyroxene and accounts for most of the garnet present in the grt-granulite. In the TZ, orthopyroxene and garnet are separated by skeletal intergrowths of quartz and clinopyroxene similar to those observed in garnet porphyroblasts of the grt-granulite (Fig. 9-4c & d). Textural and modal variations point to garnet formation after orthopyroxene by a solid-state reaction similar to that proposed for other mafic granulites (Waard, 1965):

$$6(Fe,Mg)SiO_3 + 2CaAl_2Si_2O_8 = Ca(Fe,Mg)_5Al_4Si_6O_{24} + Ca(Fe,Mg)Si_2O_6 + 2SiO_2 \quad (2)$$

orthopyroxene — anorthite — garnet — clinopyroxene — quartz

Microstructural EBSD-SEM and HRTEM observations in the transition zone revealed a topotaxial relationship between orthopyroxene, amphibole and garnet ($<111>_{Grt} // [001]_{Opx,Amp}$, Padrón-Navarta *et al.*, 2008) strongly supporting that reaction 1 (a or b) and 2 took place simultaneously. Furthermore, the orientation of mafic precursor phases in the hbl-gabbronorite fully conditioned the nucleation site and the crystallographic orientation of garnet because of topotaxial transformation reactions and homoepitaxial growth of garnet.

(iii) *Garnet formation after Fe-Ti oxides:* A third type of garnet-forming reaction would account for garnet surrounding Fe-Ti oxides either in isolated porphyroblasts in

the plagioclase matrix or, more commonly, in inclusions within mafic clusters (Fig. 9-4f). Textural and modal variations indicate that garnet growth after oxides occurred by breakdown of Fe-Ti oxides and orthopyroxene *via* a reaction similar to that proposed by McLelland & Whitney (1977):

$$(6-\beta)(Fe,Mg)SiO_3 + 2CaAl_2Si_2O_8 + \alpha Fe\text{-}Oxide + (\beta-2)SiO_2 = Ca(Fe,Mg)_5Al_4Si_6O_{24} + Ca(Fe,Mg)Si_2O_6 \quad (3)$$

orthopyroxene anorthite quartz garnet clinopyroxene

Depending on the value of the α coefficient, which is controlled by the X_{Mg} ($X_{Mg}=Mg/[Mg+Fe^{2+}]$) of reactants and products, quartz may be either a reactant or a product of the reaction. In our sample, local variations of the X_{Mg} and/or disequilibrium (McLelland & Whitney, 1977) would account for vermicular intergrowth of garnet surrounding oxides, and quartz-free garnet coronas around oxides (Fig. 9-4f).

The abrupt appearance of rutile coupled with the consumption of Fe-Ti oxide in the TZ of composite samples indicates that rutile was formed coevally with garnet after Fe-Ti oxide- and orthopyroxene-consuming reactions. Because reaction (3) does not consider Ti, it does not account for the formation of rutile after Fe-Ti oxides. Using the average X_{Mg} of the cores of orthopyroxene and clinopyroxene from the hbl-gabbronorite (0.60 ± 0.03 and 0.78 ± 0.03, respectively) and that of garnet rims from the TZ (0.44 ± 0.02), the following overall, mass-balance reaction would account for the formation of garnet and rutile in the grt-granulite after orthopyroxene and Fe-Ti oxides:

$$5(Fe_{0.40}Mg_{0.60})SiO_3 + 2CaAl_2Si_2O_8 + FeTiO_3 = Ca(Fe_{0.56}Mg_{0.44})_5Al_4Si_6O_{24} +$$

orthopyroxene anorthite ilmenite garnet

$$Ca(Fe_{0.22}Mg_{0.78})Si_2O_6 + SiO_2 + TiO_2 \quad (4)$$

clinopyroxene quartz rutile

9.8 Geothermobarometry

Conventional thermobarometry using several calibrations of barometers involving garnet-clinopyroxene-plagioclase-quartz were determined with the GTB software (Spear & Kohn, 2001) for the Jijal opx-free, grt-granulites. Results are provided in Table 9-5 (see table caption for details of the selected geobarometers and geothermometers). Two main issues arise when trying to calculate the peak-metamorphic P-T conditions in Jijal opx-free, grt-granulites: (i) the extent to which core and/or rims of garnet, pyroxene and plagioclase composition reflect peak equilibrium compositions (e.g., O'Brien & Rotzler, 2003); and (ii) the effect of ferric iron content of clinopyroxene on the temperature estimates and its propagation to pressure estimates (e.g., Stipska & Powell, 2005). The first issue can be investigated in composite samples where grt-granulite replaced a lower-pressure protolith. Whereas garnet in the grt-granulite of composite samples is compositionally homogeneous, clinopyroxene preserves a strong Al-zoning characterized by Al-rich cores similar to those from the hbl-gabbronorite of the same sample (Fig 9-6; Table 9-2). Clinopyroxene rims and smaller neoblasts are relatively depleted in Al. These Al variations in clinopyroxene can be due either to disequilibrium, whereby the high-Al content is inherited from the hbl-gabbronorite clinopyroxene owing to the slow diffusion of Al in this mineral (e.g., Carlson, 2002), or to peak conditions of the grt-granulite assemblage. The extent of preservation of disequilibrium in the high-Al cores

Table 9-5. Estimates of garnet granulite equilibration pressure and temperature.

Sample	Assemblage	Assumptions		Results		Method*
				T (ºC)	*P* (GPa)	
KG-03/TZ	Grt_{329}+ Cpx_{241}+Pl_{748}+Qtz	T= 800ºC	$Fe_{total} = Fe^{2+}$		1.09, 1.03, 1.19, 1.18, 1.24, 1.11	1,2,3, 4,5,6
			Fe^{3+} corrected		0.98, 0.91, 1.07, 1.06, 1.22, 0.97	1,2,3, 4,5,6
		P = 1.10 GPa	$Fe^{2+} = Fe_{total}$	824, 806, 640		7,8,9
			Fe^{3+} corrected	757, 737, 571		7,8,9
	Grt_{329}+Rt+Ilm+Pl+Qtz (GRIPS)	T= 800ºC	$Fe^{2+} = Fe_{total}$		1.11, 0.98	10,11
			Fe^{3+} corrected		1.15, 1.01	10,11
BP-573 Garnet granulite	Grt_{918}+ Cpx_{917}+Pl_{916}+Qtz	T= 900ºC	$Fe_{total} = Fe^{2+}$		1.43, 1.38, 1.53, 1.51, 1.45, 1.45	1,2,3, 4,5,6
			Fe^{3+} corrected		1.27, 1.27, 1.40, 1.39, 1.46, 1.33	1,2,3, 4,5,6
		P = 1.40 GPa	$Fe^{2+} = Fe_{total}$	996, 986, 873		7,8,9
			Fe^{3+} corrected	815, 798, 644		7,8,9
BP-572 Garnet & Garnet pyroxenite	Grt+Cpx+Pl+Qtz	T= 900ºC	$Fe^{2+} = Fe_{total}$		1.63, 1.60, 1.74, 1.71, 1.54, 1.67	1,2,3, 4,5,6
			Fe^{3+} corrected		1.57, 1.53, 1.67, 1.64, 1.74, 1.58	1,2,3, 4,5,6
		P = 1.60 GPa	$Fe^{2+} = Fe_{total}$	1109, 1106, 1041		7,8,9
			Fe^{3+} corrected	874, 859, 709		7,8,9
GI-13 Garnet granulite	Grt+ Cpx+Pl+Qtz	T= 900ºC	$Fe^{2+} = Fe_{total}$		1.43, 1.39, 1.52, 1.52, 1.39, 1.44	1,2,3, 4,5,6
			Fe^{3+} corrected		1.32, 1.27, 1.39, 1.40, 1.65, 1.32	1,2,3, 4,5,6
		P = 1.40 GPa	$Fe^{2+} = Fe_{total}$	1050, 1037, 942		7,8,9
			Fe^{3+} corrected	724, 703, 509		7,8,9

(*) = (1) Newton & Perkins (1982); (2) Powell & Holland (1988) using Hodges & Spear's garnet model; (3) Powell & Holland (1988) using Ganguly & Saxena's garnet model (1984); (4) Moecher et al. (1988) Mg end-member; (5) Moecher et al. (1988) Fe end-member; (6) Eckert et al. (1991), (7) Ellis & Green (1979); (8) Powell (1985); (9) Pattison & Newton (1989); (10) Bohlen & Liotta (1986); (11) using Hodges &

of clinopyroxene in the grt-granulite can be assessed in the TZ of composite samples by comparing rim-core analyses of Rare Earth Elements (REE) patterns in precursor hbl-gabbronorite and grt-granulite pyroxenes (Fig. 9-10). Because garnet highly partitions Heavy-REE (HREE) relative to Light-REE (LREE) during metamorphic reactions, clinopyroxene equilibrated with garnet shows a humped-shape REE pattern characterized by a strong HREE depletion relative to LREE.

In composite samples, cores and rims of clinopyroxene from the hbl-gabbronorite show LREE-depleted patterns (Fig. 9-10a) similar to those of the whole rock (Garrido *et al.*, 2006), in agreement with their igneous origin and the lack of equilibration with garnet. Clinopyroxene cores from the TZ show REE patterns similar to those from hbl-gabbronorite clinopyroxene, implying their lack of reequilibration with garnet and their inheritance from hbl-gabbronorite clinopyroxene (Fig. 9-10b). In contrast, clinopyroxene rims display convex-upward, REE patterns strongly depleted in HREE relative to LREE indicative of equilibration with garnet (Fig. 9-10b). In clinopyroxene from the garnet granulite away from the TZ neither relics of Al-rich cores nor non-convex-upward, REE patterns occur. As REE elements likely diffuse slower than Al (Carlson, 2002), the

sympathetic variations of Al and HREE indicate that Al-rich and HREE-enriched clinopyroxene cores are in disequilibrium with garnet, whereas the low-Al and HREE-depleted rims of pyroxenes record the peak conditions of grt-granulites.

Assuming a temperature of 800 ºC and all Fe as Fe^{2+}, the composition of coexisting plagioclase, garnet rims and clinopyroxene from composite sample KG-03 yields pressures ranging from 1.03-1.24 GPa. For Fe^{3+} corrected analyses P = 0.91-1.22 GPa (Table 9-5). On the other hand, GRIPS barometry seems barely affected by Fe^{3+} corrections yielding equilibration pressures of 0.98-1.11 GPa and 1.01-1.15 GPa, respectively. For Fe^{3+} uncorrected and corrected estimates temperatures calculated for pressure of 1.1 GPa yield 806-824 ºC and 737-757 ºC, respectively. We found anomalously low temperatures (T=571-640 ºC) with Pattison & Newton's (1989) calibration that will not be further considered in the following.

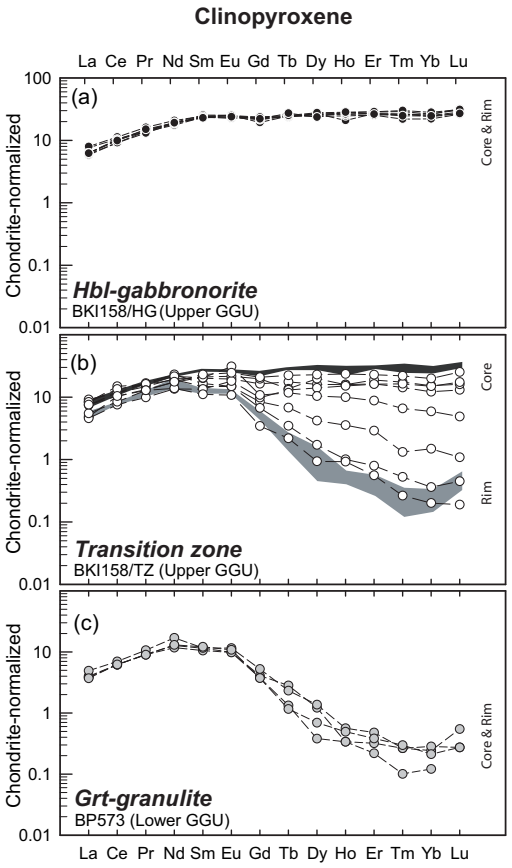

Figure 9-10: Chondrite-normalized REE patterns of clinopyroxene from composite samples and grt-granulite. Normalizing values after Sun & McDonough (1989). **(a)** REE patterns of core and rim analyses of clinopyroxene in the hbl-gabbronorite of composite sample BKI158. **(b)** REE pattern of core (C) and rim (R) analyses of clinopyroxenes from the TZ of composite sample BK158 Also shown are the fields of REE patterns from the hbl-gabbronorite (black), and from grt-granulite samples (dark-gray). **(c)** REE pattern of core and rims analyses of clinopyroxene of grt-granulite sample BP573.

In grt-granulites from Jijal lower GGU, both cores and rims of clinopyroxene from sample BP573 display convex-upward, HREE-depleted patterns (Fig. 9-10c), symptomatic of REE equilibration of clinopyroxene with garnet. Thermobarometric results for lower GGU samples (BP573 and GI13) point to a dramatic effect of the ferric iron correction on temperature and, to a much lesser extent, on pressure: for an equilibration temperature of 900 ºC, we obtain pressures of 1.27-1.65 and 1.38-1.43 GPa, respectively (Table 9-5). Higher pressures obtained in garnet clinopyroxenite patches from sample BP-572 (1.53-1.74 GPa) probably reflect lack of equilibration with plagioclase (Table 9-5).

Our P and T estimates for Jijal lower GGU grt-granulites are substantially lower than those obtained for the same samples by Ringuette *et al.* (1999): P and T ranges of 1.70-2.10 GPa and 856-1093 ºC, respectively. These discrepancies are due to the fact that Ringuette *et al.* (1999) overestimated equilibration temperatures of granulite as they used high-Al clinopyroxene cores in chemical disequilibrium with garnet (in the case of

sample BKI-158) and, more importantly, to the lack of consideration of the acmite ($NaFe^{3+}R^{2+}_{-2}$) and essenite ($AlFe^{3+}R^{2+}_{-1}Si_{-1}$) components in clinopyroxene. In Jijal lower GGU grt-granulites, Na and ^{IV}Al in clinopyroxene are uncorrelated with ^{VI}Al (Fig. 9-6a & b), demonstrating that acmite and essenite are important components. An increasing $Fe_2O_3/(FeO + Fe_2O_3)$ ratio of clinopyroxene results in a systematic decrease in analytical temperature (Stipska & Powell, 2005), biasing Fe^{3+}-uncorrected temperature towards high-temperature and high-pressure estimates.

9.9 Discussion

9.9.1 The transformation of hbl-gabbronorite to opx-free, grt-granulite: metastability, reaction inhibition and the role of amphibole breakdown

Understanding the origin of the transformation of hbl-gabbronorite to opx-free, grt-granulite in Jijal requires consideration of the sequence of prograde assemblages in quartz-saturated, metabasic bulk compositions (Pattison, 2003), which depends upon the fluid regime (i.e., fluid saturated or undersaturated conditions) during their metamorphic path (e.g., Carson *et al.*, 1999; Stipska & Powell, 2005, Wei *et al.* 2009). Figure 9-11 shows two schematic phase diagrams for Ca-poor, quartz-saturated metabasic bulk compositions under water-saturated (Fig. 9-11a; modified after Pattison,

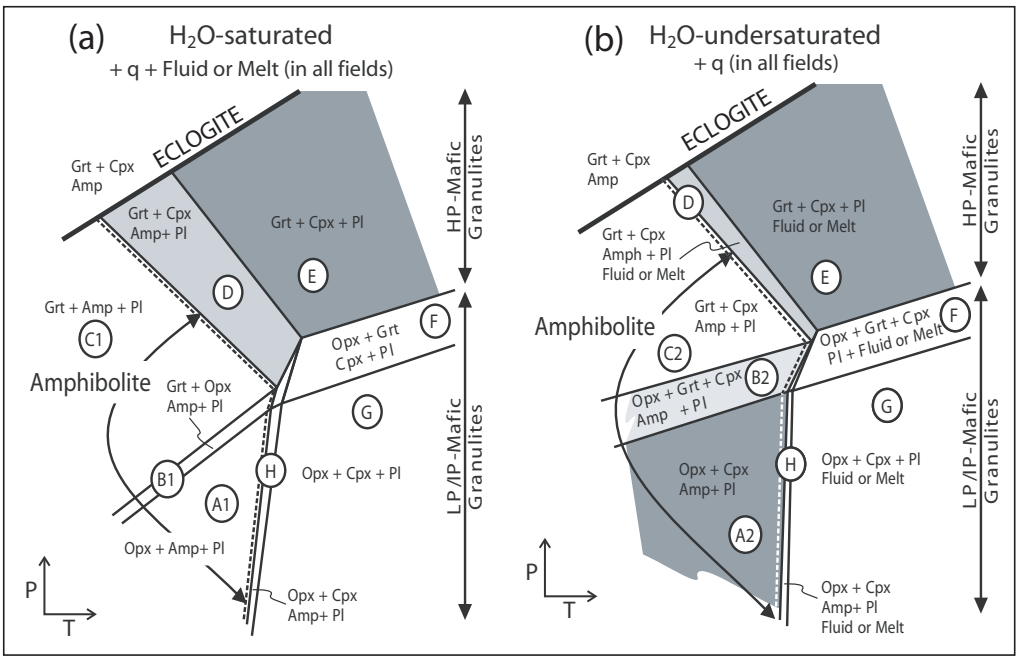

Figure 9-11: Schematic P-T diagrams for a relatively Si-rich metabasic bulk composition at H_2O-saturated (cf. Pattison, 2003) **(a)** and H_2O-undersaturated condtions **(b),** both showing key assemblages in Opx-free HP-mafic granulites (Grt+Cpx+Pl+Fluid/Melt) stable at similar conditions (E fields). Hbl-gabbronorite assemblage (A2) is only stable in undersaturated conditions (b) and three phase fields must be crossed to reach the field E (i.e. B2, C2 and D, or H, G and F). Dashed line depicts the amphibole dehydration melting reaction at fluid present (a) or fluid absent (b) conditions. Note the different extension of field D between (a) and (b).

2003) and water–undersaturated conditions for low temperature assemblages (Fig. 9-11b; this work). Apart from differences at the amphibolite facies conditions, these phase diagrams show that mineral assemblages at low- to intermediate- P and HT (phase fields H, G, and F) and HP and HT (phase fields D and E), characteristic of granulite facies, are analogous irrespective of the fluid/melt saturation conditions. Therefore, if the protolith and/or prograde sequence of assemblages are unknown, the opx-free, garnet granulite mineral assemblage is little revealing of the fluid regime during the prograde path.

Field and textural relationships in Jijal composite samples indicate that the precursor assemblage of opx-free, grt-granulite was that of hbl-gabbronorite (Pl+Cpx+Opx+Amp+Qtz). The presence of hornblende and clinopyroxene, along as the lack of garnet, bounds the P-T equilibration conditions of hbl-gabbronorite to the amphibolite facies under water-undersaturated conditions (low-T and intermediate-P; phase field A2 in Fig. 9-11b). The transformation of this precursor assemblage (phase field A2) to the opx-free, grt-granulite assemblage (phase field E) might have taken place along two main prograde P-T paths: (i) a clockwise path through the high-variance phase fields B2, C2, and D, where the onset of Grt growth (B2) and Opx breakdown (C2) would occur prior to amphibole breakdown to a melt or fluid phase (D); or (ii) a counter clockwise path through the high-variance phase fields (H, G, F), where amphibole breakdown (H) would occur prior to the onset of Grt growth and Opx breakdown (F) (Fig. 9-12b). Mineral assemblages and textural relationships in the composite samples (Figs 3 & 4) show the transformation of a precursor low-P assemblage (Pl+Cpx+Opx+Amp+Qtz; phase field A2 in Fig. 9-11b) to a HP opx-free, grt-granulite assemblage (Grt+Pl+Cpx+Qtz; phase field E in Fig. 9-11). The textural relationships (Figs. 9.3 & 9.4) and the sequence of garnet-forming reactions in the TZ of composite samples are more consistent with metamorphic path (i) to account for the nearly direct transformation of hbl-gabbronorite to opx-free, grt granulite. Because this transformation occurs across a tiny transition zone (2-3 cm thick), it most likely reflects thermodynamic disequilibrium whereby the precursor, hbl-gabbronorite assemblage was metastable and prograde reactions were kinetically inhibited until attaining HP granulite facies conditions (phase field E: Fig. 9-11b).

Preservation of prograde and/or peak metamorphic assemblages in regional metamorphism is commonly ascribed to the absence of a free fluid or melt phase along the prograde or retrograde metamorphic path (Rubie, 1998; Stipska & Powell, 2005; Wain *et al.*, 2001), and favored by static conditions (Baxter & DePaolo, 2004). In Jijal, the protracted metastability of the precursor meta-gabbronorite assemblage until P-T conditions of the lower arc crust indicates the kinetic inhibition of prograde reactions owing to the absence of a free fluid- or melt- phase along the prograde clockwise path through phase fields B2 and C2 until attaining phase fields D and E (Fig. 9-11b). The cease of the metastability at HP granulite facies conditions may have been triggered either by infiltration of a fluid/melt phase prior to attaining phase field D (e.g., Blattner, 2005; Harlov & Forster, 2002), or by the onset of amphibole breakdown due to dehydration (-melting) reactions (Waters & Whales, 1984; Waters & Lovegrove, 2002; Wilbur & Ague, 2006; Zeh & Holness, 2003).

In Jijal composite samples, the systematic spatial relationships of K-feldspar films in grt-granulite are suggestive of a cause-effect link between the transformation of hbl-gabbronorite to grt-granulite and the potential presence of a melt/fluid phase. K-feldspar films and blebs in grt-granulites are interpreted either as evidence of fluid-driven metasomatism by CO_2-rich fluids and/or alkalic supercritical brines, or of dehydration melting of amphibole (Franz & Harlov, 1998; Harlov & Forster, 2002; Harlov *et al.*, 1998; Harlov & Wirth, 2000; Perchuk & Gerya, 1993; Perchuk *et al.*, 2000). The abrupt appearance of garnet futher supports that a free-fluid/melt phase mediated in the abrupt equilibration of metastable hb-gabbronrite under HP grt-granulite conditions (phase field E; Fig. 9-11b). Fast nucleation and growth rates of garnet in composite samples are consistent with the high-affinity of the overstepped, metastable garnet-forming reactions for the P-T conditions of Jijal grt-granulites (Padrón-Navarta *et al.*, 2008), which are otherwise similar to the affinities estimated for the formation of garnet coronas in mafic granulites (Ashworth *et al.*, 1998) and those derived from experimental studies (Wilbur & Ague, 2006; Zeh & Holness, 2003).,

Geochemical variations of trace elements in Jijal composite samples and grt-granulites are more consistent with the formation of gr-granulite by dehydration melting of hbl-gabbronorite (Garrido et al., 2006). The estimated metamorphic conditions for Jijal granulites also support an amphibole dehydration melting scenario. Previous P-T estimations (Yoshino & Okudaira, 2004), along our pseudosection computations and P-T estimates (Fig. 9-12), indicate that upper and lower Jijal GGU grt-granulite equilibrated at P-T conditions in melt-present conditions for metabasic bulk compositions of hbl-gabbronorite. The large regional extension of grt-granulites and the rare occurrence of relic bodies of metastable hbl-gabbronorite, where the arrested transition can be only observed, indicate a pervasive equilibration, more consistent with a regional metamorphic transformation. However the preservation of the reaction front and the metastable hbl-gabbronorite bodies in the upper GGU remains unclear. Local temperature or pressure gradients produced during dehydration reactions (e.g. Connolly 1997; Miller *et al.*, 2003) can affect the reaction kinetics promoting the quenching of the transformation.

9.9.2 Pseudosections and isopleths thermobarometry

Figure 9-12a shows the fixed-composition phase diagram section ("pseudosection") computed with Perple_X software (Connolly, 1990, 2005) for composite sample KG03 and the model system Na_2O-CaO-K_2O-FeO-MgO-Al_2O_3-SiO_2-H_2O (NCKFMASH), which ensures that most minerals of the Jijal grt-granulite and hbl-gabbronorite are considered. The source of thermodynamic data and the mineral solution models are provided in Table 9-6. Solid solution models include haplogranitic melts in the system NCFKMASH (White *et al.*, 2001, Holland & Powell, 2001), which allow the computation of partial melting equilibria and the investigation of the relationships between the common minerals in our samples and silicate melts. Bulk rock composition employed in the calculated pseudosection was corrected with the determination of the bulk FeO/Fe_2O_3 ratio, as reported in Table 9-7. The use of the haplogranitic melt solution model (White *et al.*, 2001: Holland & Powell, 2001) for mafic bulk compositions deserves further comments and assessment. The melt model has been applied mostly to metapelitic bulk compositions (but see Diener *et al.,* 2008) and its applicability to mafic

Table 9-6. Solution model, phases including for pseudosection compunting and thermodynamic data sources.

Solution	Symbol	Formula[1]	Endmembers	Source
Clinopyroxene	Cpx	$Na_{1-y}Ca_yMg_{xy}Fe_{(1-x)y}Al_ySi_2O_6$	cats, jd, hed, di	Holland & Powell (1996), modify for non-ideal cats after Zeh et al. (2005)
Garnet	Grt	$Fe_{3x}Ca_{3y}Mg_{3z}Mn_{3(1-x-y-z)}Al_2Si_3O_{12}$ †	spss, alm, py, gr	Holland & Powell (1996)
Melt	Melt	Na-Mg-Al-Si-K-Ca-Fe hydrous silicate melt	h2oL, fo8L, fa8L, abL, sil8L, anL, q8, KspL	Holland & Powell (2001); White et al. (2001)
Ortopyroxene	Opx	$[Mg_xFe_{1-x}]_{2-y}Al_{2y}Si_{2-y}O_6$	mgts, fets, en, fs	Powell & Holland (1999)
Plagioclase	Pl	$K_yNa_xCa_{1-x-y}Al_{2-x-y}Si_{2+x+y}O_8$ ‡	ab, an, or	Furman & Lindsley 1988
Clinoamphibole	Amp	$Ca_2Na_z[Mg_xFe_{1-x}]_{3+2y+z}Al_{3-3y}Si_{7+y}O_{22}(OH)_2$ §	tr, ftr, parg, fparg, ts , fts	Dale et al. (2005)
Quartz	qtz	SiO_2		
Kyanite	ky	Al_2SiO_5		
Muscovite	mu	$KAl_3Si_3O_{10}(OH)_2$		
Zoisite	zo	$Ca_2Al_3Si_3O_{12}(OH)$		

[1]compositions (w, x, y and z are fractions varying between zero and unity and are determined as a function of pressure and temperature by free energy minimization), †$x+y+z \leq 1$, ‡$x+y \leq 1$, §$y+z \leq 1$.

bulk compositions, richer in CaO, FeO and MgO, must be considered with great caution. Although the model properly accounts for CaO (Holland & Powell, 2001), it may encounter some limitations in its applicability to FeO and MgO–rich compositions (e.g. Grant, 2009; Powell, pers. comm., 2009). As we show below, the succesful application of the melt model to our mafic bulk composition is endorsed partly by the excellent agreement of the calculated PT conditions, melt fractions and mineral assemblages from the computed pseudosection, with those independently derived from conventional geothermobarometry, geochemistry and petrography, respectively.

The computed pseudosection (Fig. 12a) shows that the hbl-gabbronorite assemblage (Pl+Cpx+Opx+Amp+Qtz) without a free fluid phase is stable only at low pressure (0.2-0.8 GPa) and temperatures below c. 800 ºC (Fig. 9-12a). The opx-free, grt-granulite assemblage is stable at temperatures above c. 800 ºC and pressures greater than 1.0 GPa, where it coexists with a melt phase. A simple approach to assess the accuracy of pseudosections is to compare the observed, actual mineral assemblages, modes, and mineral compositions of the studied rocks with those calculated from the equilibrium pseudosection for the same samples (e.g., Gaidies *et al.*, 2006; Kelsey *et al.*, 2003a; Kelsey *et al.*, 2003b; Stipska & Powell, 2005). Forward P-T estimates and assessment of equilibrium conditions in the studied sample of grt-granulite (KG-03) can be obtained by comparing the computed composition of garnet and clinopyroxene (displayed as isopleths showing the variation of their main components; Fig 9-12b-d) with the actual compositions of these phases in the rock. For this purpose, we consider the same analyses we have used for conventional garnet-clinopyroxene barometry (Table 9-5). We consider ferrous iron as total iron and a 1σ uncertainty of 0.02 in the mole fraction of Cpx and Grt components.

The high X_{CaTs} and X_{Jd} values, and the low X_{Mg} value of clinopyroxene cores in the transition zone (Cpx-core225, Table 9-5; see also Fig. 9-7), yielding high P ≈ 1.4 GPa

Table 9-7. Averaged mineral analyses and whole-rock analyses from a representative hbl-gabbronorite (sample KH97-113) and a mafic garnet granulite (sample KG03). Modal proportions were calculated by least-squares (NKTCFMASH system) using the measured composition of minerals and the rock bulk compositions, where all iron was ferrous iron. Model bulk compositions were then recalculated using Fe^{2+}/Fe^{3+} ratio in minerals from stoichiometry and the calculated modal composition. The L.O.I of the hbl-gabbronorite sample was assumed as the initial water content for the pseudosections calculations.

Hornblende gabbronorite (sample KH97-113)

mineral	Opx	Cpx	Pl	Prg-I	Mag	Ilm	Qtz	Bulk	Model
SiO_2 (wt. %)	49.50	48.95	54.21	39.93	0.37	-	100.00	51.35	51.24
TiO_2	0.05	0.36	-	1.46	0.43	46.30		0.73	0.66
Al_2O_3	4.17	6.51	29.21	14.81	0.84	0.07		17.67	17.56
Fe_2O_3	2.47	3.77	0.10	1.94	66.14	11.90		0.00	2.74
FeO	22.92	7.26	-	14.24	31.78	41.13		9.55	6.81
MnO	0.64	0.26	-	0.14	0.00	0.33		0.20	0.15
MgO	19.54	10.57	-	9.41	0.11	0.10		5.35	5.27
CaO	0.51	19.97	11.11	11.12	-	-		9.83	9.73
Na_2O	-	1.49	5.54	1.53	-	-		2.73	3.14
K_2O	-	-	0.29	2.23				0.28	0.36
H_2O				2.00				0.13	0.19
Total	99.84	99.13	100.48	98.82	99.68	99.92	100.00	97.82	97.86
modal (%)	14.52	15.37	50.92	9.74	2.27	0.99	6.13		
Sum R-square	0.222								

Mafic garnet granulite (sample KG03)

mineral	Grt	Cpx	Pl	Rt	Kfs	Qtz		Bulk	Model
SiO_2 (wt. %)	38.16	50.14	56.43	-	64.42	100.00		52.100	51.990
TiO_2	0.11	0.53	-	98.99	18.72			0.810	0.800
Al_2O_3	21.56	5.52	26.16	0.05	0.24			17.500	17.420
Fe_2O_3	3.12	2.69	0.07	-	0.08			0.000	1.550
FeO	20.26	5.70	-	0.25	-			8.930	7.590
MnO	0.54	0.07	-	-	-			0.180	0.190
MgO	8.76	12.14	-	-	-			5.220	5.170
CaO	7.28	21.10	8.62	-	-			9.640	9.620
Na_2O	-	1.29	6.55	-	0.80			2.580	2.630
K_2O	-	-	0.26	-	14.61			0.390	0.370
H_2O									
Total	99.78	99.18	98.11	99.40	98.87	100.00		97.3	97.34
modal (%)	32.51	19.88	36.71	0.31	1.94	8.53			
Sum R-square	0.013								

- below detection limit

and T > 950ºC (not shown in figure), are not in chemical equilibrium with any garnet composition for the same sample. This discrepancy confirms our earlier inference that clinopyroxene cores in the transition zone with high-Al and HREE contents are metastable compositions inherited from the precursor clinopyroxene. On the contrary, garnet core isopleths (Grt-329core, X_{Grs} = 0.20±0.02, X_{Mg}=0.41 ± 0.02; Table 9-5, Fig. 9-12b) overlap the isopleths corresponding to the clinopyroxene rim compositions (Cpx-rim241, X_{Jd} = 0.07±0.02, X_{CaTs} = 0.05±0.02, Fig. 9-12c) yielding equilibration pressures of 1.1-1.2 GPa and temperatures of 800-840ºC (Fig. 9-12d). These equilibration P and T conditionsmost likely record the peak metamorphic condition of the transition zone for sample KG-03. Thus, forward P-T estimates by means of Grt-Cpx isopleths (Fig. 9-12d) are in good agreement with our estimates using conventional thermobarometry for the same sample (Table 9-5) and also with previous P-T estimates (Yoshino & Okudaira, 2004).

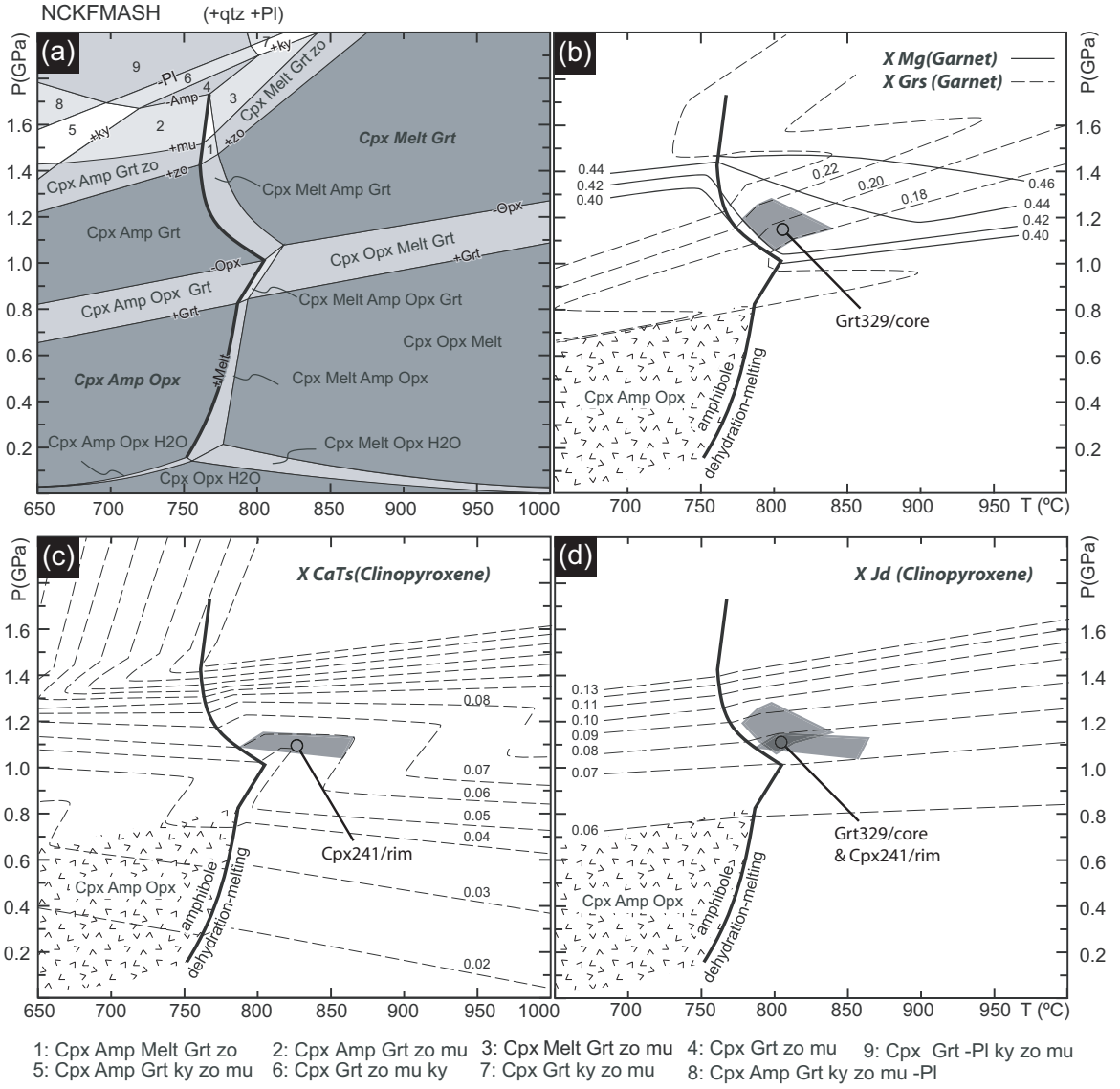

Figure 9-12: (a) P-T pseudosection in NCKFMASH (+Qtz +Pl; absent plagioclase is denoted as -Pl), computed for the bulk rock composition of garnet granulite KG03B in the model system Na_2O:CaO:K_2O:FeO:MgO:Al_2O_3:H_2O = 6.63:27.47:0.64:16.63:20.71:27.44:0.47 (mol.%). Divariant, six-phase fields are white and higher variance fields display progressively darker shading. Computations were performed with PERPLEX software (Connolly, 1990, Connolly & Petrini, 2002) and the updated mineral thermodynamic database of Holland and Powell (1998) implementing a gridded Gibbs free-energy minimization algorithm (Connolly, 2005). Endmembers and solid solution models used in the pseudosection are given in Table 6. Isopleths were calculated with WERAMI, a program part of the PERPLEX software. The predicted compositions for the different minerals are represented as contour plots of the mole fractions of: **(b)** grossular (X_{Grs}), and X_{Mg} in garnet; **(c)** Ca-tschermaks (X_{CaTs}) in clinopyroxene; and **(d)** jadeite (X_{Jd}) in clinopyroxene. In the isopleth plots (b-d), the thick, solid line is the amphibole dehydration melting curve. The stability field of the equilibrium assemblage corresponding to hornblende gabbronorite is also highlighted (pattern-filled). Light grey fields correspond to the predicted P-T conditions for the observed compositions of Grt 329 core (b and d) and Cpx 241 rim, which overlap in the dark grey field of (d).

9.9.3 The role of water activity on the type of amphibole breakdown reaction

Pseudosections and forward and inverse geothermobarometry demonstrate that Jijal grt-granulite formed at high-P and intermediate T conditions after metastable hbl-gabbronorite. Whether grt-granulite formation resulted from dehydration (i.e., coexistence with a fluid phase) or partial melting (i.e., coexistence with a water-undersaturated, melt phase) depends on the type of amphibole breakdown reaction. Possible amphibole breakdown reactions under fluid-absent conditions are (Clemens & Watkins, 2001; Fyfe, 1973a; Thompson, 1990; Vielzeuf & Schmidt, 2001):

Amp = Anhydrous phases + Fluid [Melt] "subsolidus dehydration" (5a)
Amp = Anhydrous phases + Melt [Fluid] "dehydration or fluid-absent melting" (5b)

And under fluid-present conditions:

Amp + Fluid = Melt [Anhydrous phases] "wet or fluid-present melting" (5c)

Another key melt-producing reaction not involving Amp is:

Anhydrous phases + Fluid = Melt [Amp] (5d)

In these reactions, the absent phase is enclosed in brackets.

The activity of water, $a(H_2O)$, is one of the key factors determining the type of amphibole breakdown reaction in fluid-absent conditions (e.g., Clemens & Watkins, 2001; Thompson, 1990; Vielzeuf & Schmidt, 2001). Figure 9-13 shows three schematic P-T pseudosections for Jijal grt-granulite KG-03 at $a(H_2O)$ of 1, 0.9 and 0.5, respectively, for water-undersaturated conditions and aimed at illustrating the effect of variations of the $a(H_2O)$, caused by the presence of additional internally derived fluid components (e.g., CO_2, F and Cl), on the type of amphibole breakdown reaction in a closed system.

For $a(H_2O) = 1.0$ (Fig. 9-13a), the amphibole subsolidus dehydration (reaction 9-5a, [Melt]) and reaction 9-5d [Amp] (dashed-dotted and dashed curves, respectively, in Fig. 9-13a) are located at $P < 0.4$ GPa. At higher pressure, amphibole breakdown occurs under fluid-absent melting conditions ([Fluid], reaction 9-5b; thick solid line in Fig. 9-13a) generating a water-undersaturated silicate melt. A slight decrease of $a(H_2O)$ from 1 to 0.9 (Fig. 9-13b) shifts reactions (5a) and (5d) towards lower and higher temperature, respectively; accordingly, their joint shifts towards higher pressure (c. 0.8 GPa; Fig. 9-13b). Fluid-absent melting of amphibole is restrained to the pressure interval between 0.8-1.1 GPa (Fig. 9-13b; solid curve). For substantially lower $a(H_2O)$ of 0.5 (Fig. 9-13c), the subsolidus dehydration [Melt] curve shifts to lower temperatures, and the [Amp] reaction shifts to temperatures of c. 950 °C and becomes nearly isothermal (Fig. 9-13c) resembling that for dry melting. This shifting of reactions would dehydrate the amphibole before the peak conditions of Jijal grt-granulites were attained.

The above considerations bound the $a(H_2O)$ above c. 0.9 with the formation of Jijal grt-granulite by dehydration (fluid-absent) melting of amphibole; otherwise, amphibole

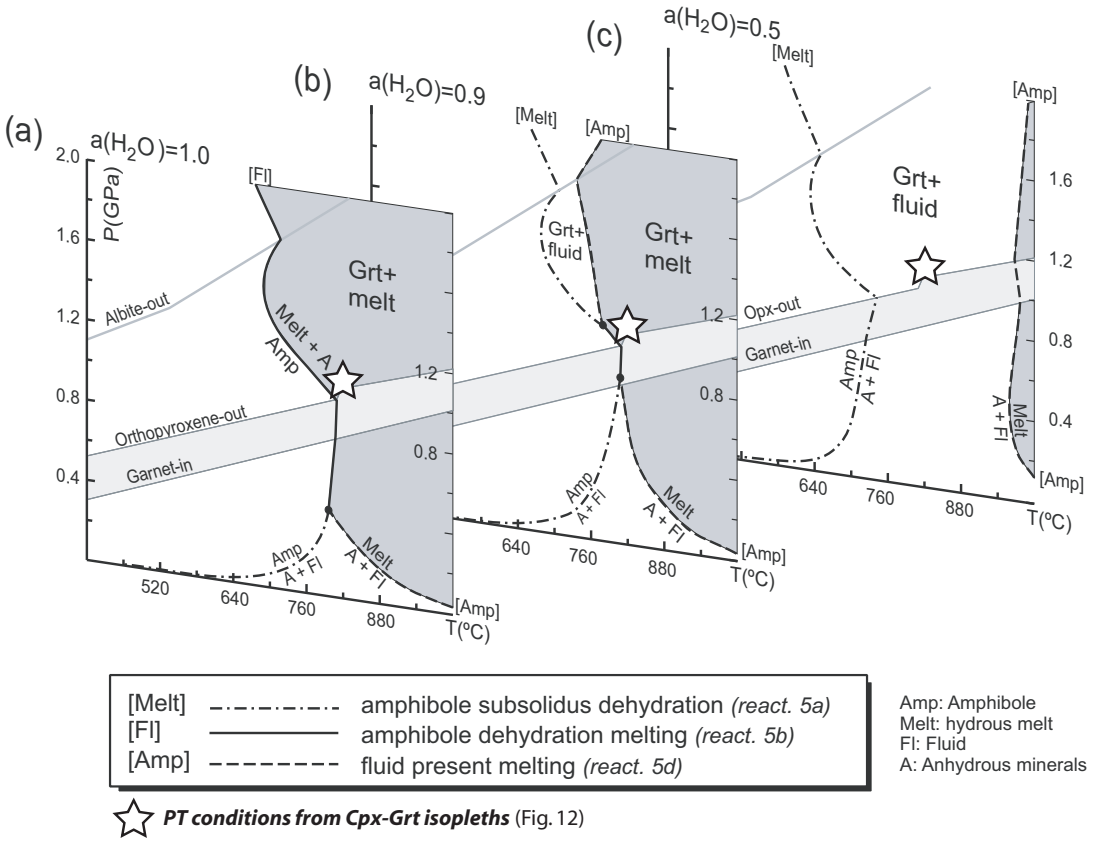

Figure 9-13: Simplified P-T pseudosections for sample KG03 for different values of the activity of water, a(H_2O) **(a)** a(H_2O)=1.0; **(b)** a(H_2O)=0.9; and **(c)** a(H_2O)=0.5**.** The P-T pseudosections illustrate the effect of a(H_2O) on the displacement of the two kinds of amphibole breakdown reactions: "subsolidus dehydration" (fluid-absent conditions, Amp= Anhydrous phases + Fluid [Melt]), and dehydration melting (fluid-absent conditions, Amp = Anhydrous phases + Melt [Fl]). They also show the position of the fluid present solidus (wet solidus, Anhydrous phases + Fluid = Melt [Amp]).

dehydration would have occurred before melting (Fig. 9-13). An extreme reduction of the fluid activity in a closed system (i.e. a(H_2O) = 0.5, Fig. 9-13c) can be excluded because the amphibole breakdown would occur at much lower temperatures (<700ºC), precluding the preservation of hbl-gabbronorite metastability at the PT conditions recorded in the transition zone (stars in Fig. 9-13).

9.9.4 Constrains for the preservation of metastability of hbl-gabbronorite

P-M(H_2O) and *T-M*(H_2O) pseudosections are particularly suitable for investigating the fluid-regime and a(H_2O) required for the preservation of metastable metamorphic assemblages along a given metamorphic path (Carson *et al.*, 1999; 2000; Clarke *et al.*, 2000; Guiraud, 1996; Holland & Powell, 2001; Stipka & Powell 2005; White *et al.*, 2001). Figure 9-14 shows two isothermal *P-M*(H_2O) pseudosections (where *M*(H_2O) is the mole fraction of water in system) showing the possible partial melting and dehydration equilibria of Jijal composite sample KG03 computed for a(H_2O) of 1.00 (Fig. 9-14a & b)

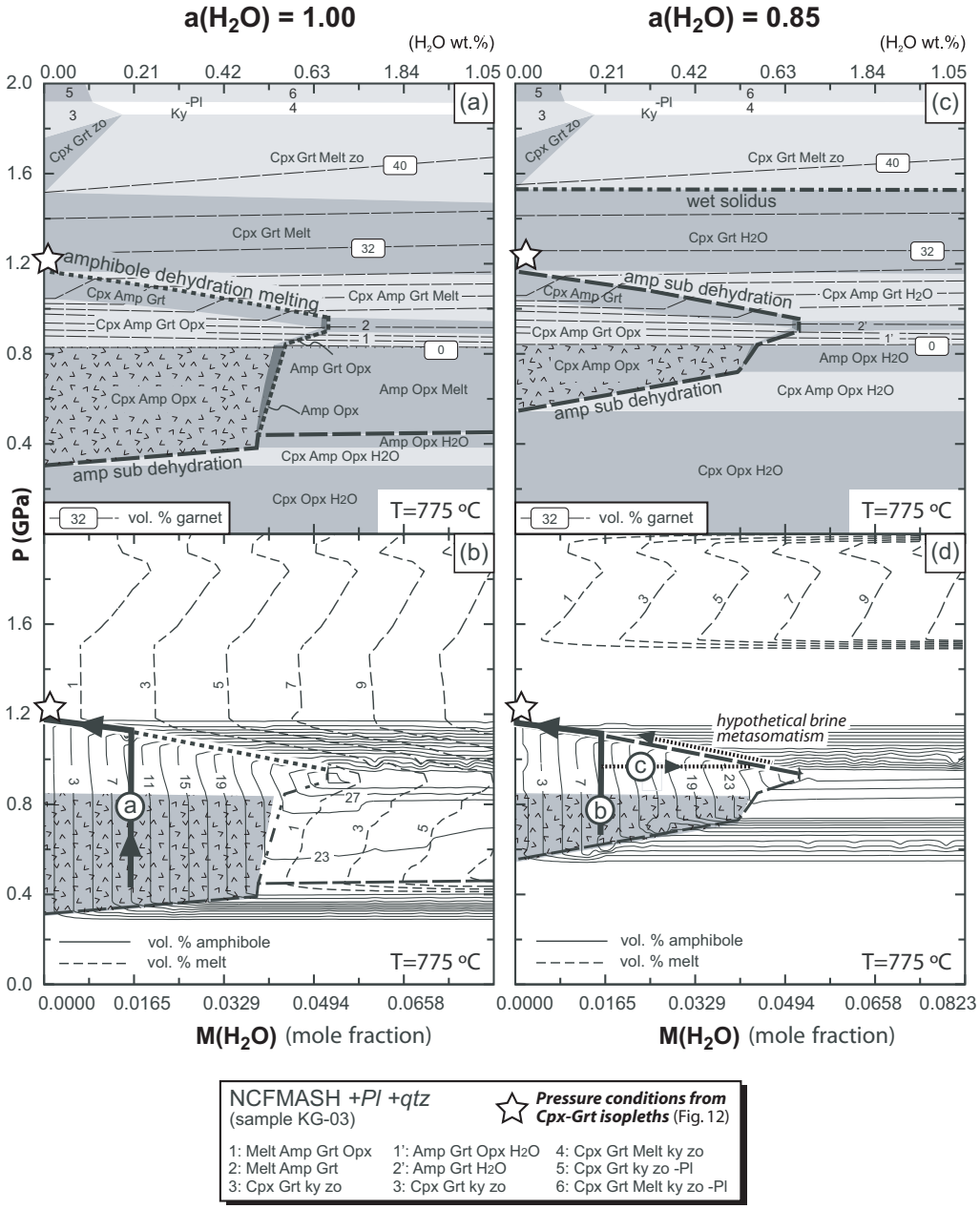

Figure 9-14: *P*-*M*(H_2O) pseudosections at T=775ºC for garnet-granulite (sample KG-03) in the simplified system Na_2O-CaO-FeO-MgO-Al_2O_3-SiO_2-H_2O, where *M*(H_2O) represents the molar proportion of H_2O in the bulk composition. For an anhydrous system (*M*(H_2O) =0.0) the bulk composition (mol.%) is Na_2O:CaO:FeO:MgO:Al_2O_3:H_2O= 6.87:27.72:17.07:20.74:27.60:0.00 and for *M*(H_2O)=0.0823 the bulk composition is 6.30:25.44:15.67:19.04:25.33:8.23 (1.05 H_2O wt.%). Small fields are labelled from 1 to 6. Plagioclase (Pl) and quartz (qtz) are stable in all the assemblages, except for high-pressure fields (>1.9 GPa), where plagioclase is not stable (denoted as -Pl in the labels 5 and 6). Garnet is stable at pressures above 0.8 GPa. Garnet modal amounts are indicated (dashed lines, spacing 5 vol. %). The observed amount of garnet in the granulites is 32 vol.%. Amphibole subsolidus dehydration and amphibole dehydration melting curves are also shown. **(a)** *P*-*M*(H_2O) pseudosection for a(H_2O)=1.00, where amphibole dehydration melting can occur when pressure increases. **(c)** *P*-*M*(H_2O) pseudosection for a(H_2O)=0.85, where amphibole dehydration does not involve the release of a melt phase at any pressure or *M*(H_2O) value. Wet solidus can be reached at ca. 1.5 GPa at 800ºC. **(b)** and **(d)** show the *P*-*M*(H_2O) pseudosections of (a) and (c), respectively, contoured for amphibole and melt modal amounts. The stability conditions of the hbl-gabbronorite assemblage (Cpx+Amp+Opx+Pl+Qtz) are highlighted in the grey pattern-filled field. Two possible P-T paths are depicted in each case: paths a (b) and b (d) correspond to metamorphic compressive conditions in a closed-system scenario. In (d) a hyphotetical brine metasomatic path c is also shown. See text for details and discussion.

and of 0.85 (Fig. 9-14c & d) at 775 °C. This temperature is an approximate upper bound that ensures that the *P-M*(H_2O) pseudosection contains fluid/melt-absent phase fields at intermediate-pressures up to the amphibole breakdown at the P and T of equilibration of the Jijal grt-granulite (P = 1.1 ± 0.1 GPa; T = 800 ± 50°C; Fig. 9-12d and white star in Fig. 9-14). At higher temperature, no fluid/melt-absent phase field would be present in any isothermal *P-M*(H_2O) pseudosection of this sample, whereas at lower temperature no breakdown of amphibole to grt-granulite would occur at the pressure of equilibration of Jijal grt-granulite.

In the *P-M*(H_2O) pseudosection for a(H_2O)= 1.00 (Fig. 9-14a & b), the phase field of hbl-gabbronorite (pattern-filled) occurs at pressures in the range of 0.35 to 0.82 GPa for a maximum H_2O content of 0.45 and 0.48 wt.%, respectively. Metastable preservation of this assemblage in Jijal composite samples requires that any compressive path departing from this phase field runs through fluid/melt absent, phase fields until the Cpx+Grt+ Pl+Fluid/Melt phase field. This requirement highly constrains potential variations in the bulk water content for a fixed a(H_2O) along their metamorphic path. Below we explore two potential isothermal scenarios that might account for transformation of metastable hbl-gabbronorite to opx-free, grt-granulite: i) bulk water conservative paths; and ii) infiltration of low a(H_2O) fluids due to brine metasomatism.

Conservative water budget during compression

A first scenario is a bulk water-conservative compressive path with a bulk water content similar to those of Jijal hbl-gabbronorite (*M*(H_2O) = 0.0165 mole fraction; paths *a* and *b* in Fig. 9-14b & d). For a(H_2O)= 1 (path *a* in Fig. 9-14b), fluid-absent assemblages would prevail until the onset of dehydration melting of amphibole at c. 1.1 GPa (short dashed line in Fig. 9-14a & b), where 2.4 vol. % of granitic melt is generated (Fig. 9-14b). For a similar path but for a(H_2O)= 0.85 (path *b* in Fig. 14d), fluid-absent conditions also would prevail until 1.1 GPa, but at this pressure amphibole subsolidus dehydration (long dashed line in Fig. 9-14c & d) would occur instead of amphibole fluid-absent melting. Starting at the Cpx+Amp+Opx phase field, the sequence of fluid-absent assemblage fields is similar for both compressive paths, with the income of Grt at 0.8 GPa, the consumption of Opx at 1.0 GPa, and the breakdown of amphibole at about 1.2 GPa (Fig. 9-14a & b).

Our petrographic observations show that amphibole breakdown was coeval with the appearance of garnet at c. 1.2 GPa. For a bulk water content similar to that of hbl-gabbronorite, the extent of the field where amphibole and garnet coexist at high pressure (Cpx+Amp+Grt+Melt/Fluid; Fig. 9-14a & b) with a melt/fluid, is highly restrained for water conservative paths *a* and *b* (Fig. 9-14a & c). Moreover, this phase field becomes narrower with decreasing *M*(H_2O) owing to segregation of the melt/fluid phase during melting or dehydration. This decrease of the bulk water content shifts path *a* and *b* towards lower *M*(H_2O) along either the amphibole dehydration melting (short dashed line in Fig. 9-14b) for a(H_2O)=1, or the amphibole dehydration boundary (long dashed line Fig. 9-14 d) for a(H_2O)=0.85. Both paths would lead to the direct transformation of the metastable hbl-gabbronorite to the high-pressure grt-granulite assemblage, and would also account for the limited retrogression of grt-granulite in Jijal composite samples. Furthermore, these paths are consistent with modal proportions of

amphibole (~ 10 vol. %) and garnet (~32 vol. %) observed in precursor, metastable hbl-gabbronorite and the final grt-granulite, respectively.

Infiltration of low a(H_2O) fluids due to brine metasomatism

Subsolidus dehydration of amphibole driven by brine metasomatism is often invoked for the generation of granulites. It could be argued that isobaric and isothermal, infiltration-driven subsolidus dehydration caused the transformation of metastable hbl-gabbronorite to grt- granulite in Jijal. Such scenario would require that, at the P and T equilibration conditions of grt-granulite, fluid-absent or melt-absent conditions prevailed at high-a(H_2O) to sustain the metastability of the hbl-gabbronorite assemblage. However, at these P and T conditions, melt-present or fluid present conditions already prevailed for both high and low a(H_2O) (stars in Fig. 9-14). Therefore, isothermal and/or isobaric infiltration metasomatism cannot be realistically invoked for the shifting from fluid-absent to fluid-present conditions in the studied rocks. Infiltration of brine at P lower than that of equilibrium of grt-granulite (e.g. the horizontal part of path c in Fig. 14d) would produce an increasing amount of amphibole (up to 30 vol. %) until the amphibole subsolidus dehydration was attained. A subsequent increase of pressure (part of path c toward lower $M(H_2O)$ values; Fig. 9-14d) would be required in order to produce garnet from the amphibole subsolidus dehydration (see lines indicating vol % of garnet in Fig. 9-14c). However, this would occur during a large pressure interval coexisting with a free fluid phase, incompatible with the preservation of the hbl-gabbronorite stability and would be also in disagreement with the observed modal amount of amphibole before the garnet nucleation.

9.10 Geodynamic Implications

The transformation of hbl-gabbronorite to grt-granulite in Jijal demonstrates that granulite metamorphism of shallow, metaestable protoliths occurred at the deep roots of an island arc, indicating that the island arc crust grew from top-to-bottom. Fast burial would explain the protracted metastability of low pressure, precursor hbl-gabbronorite due to the inhibition of prograde reactions under fluid-absent conditions until the onset of grt-granulite formation by amphibole dehydration melting. As proposed for the Fiorland grt-granulite arc terrain, a possible geodynamic scenario for such growing mechanism of the island crust is magmatic intra-plating or magma loading in the middle crust (e.g., Brown, 1996; Brown & McClelland, 2000, Clarke *et al*. 2000; Dhuime *et al*., 2009; Daczko *et al*. 2001b, 2009; Garrido *et al.*, 2006) coupled with hot mantle upwelling at the island arc mantle-crust transition (Garrido *et al.*, 2006; 2007; Arcay *et al.,* 2007; Dhuime *et al.*, 2007; 2009). The constrasted volumen preservation of metaestable assemblage in lower crust of Fiorland (>90 %, Dazcko *et al.* 2009; Dazcko & Halpin, 2009; Allibone *et al.* 2009), compared with those described here for Kohistan (<95 %), can be adscribed to different thermal histories of these two arc roots.

Our pressure estimates for Jijal upper GGU (P = 1.1 ± 0.1 GPa) are consistent with the expected depths of the lower crust in a mature island arc (c. 30-35 km). The high temperature recorded in grt-granulite (ca. 800 ± 50ºC) confirms the existence of hot geotherms in island arc terrains (Garrido *et al.*, 2006; Arcay *et al.*, 2006; 2007; Hacker *et al.*, 2008). Our P-T estimate for Jijal lower GGU (P = 1.5 ± 0.1 GPa, T = 800 ± 50ºC) yields significantly lower pressures and temperatures than previously reported by

Ringuette *et al.* (1999) for the same samples, suggesting that pressure was overestimated by these authors as they disregarded Fe^{3+} corrections in clinopyroxene. Our pressure estimate is more consistent with the thickness expected in a mature arc. Pressures over 2 GPa (Ringuette *et al.*, 1999) could be hardly accounted for a simple scenario for an island arc. Yet, the pressure difference between Jijal upper and lower GGU granulites (c. 0.4 GPa; c. 12-14 km) implies that the GGU was at least twice thicker than its current thickness (<5 km; Fig. 9-1). Although shearing may have been responsible for part of the thinning of the Jijal GGU section (e.g., Burg *et al.*, 2005), this pressure gap may also witness for delamination and foundering of part of the grt-granulite and allied ultramafic lithologies into the underlying mantle wedge (Garrido *et al.*, 2006; Garrido *et al.*, 2007).

9.11 Conclusions

Outcrops of hbl-gabbronorite and grt-granulite in the Jijal Complex evidence the prograde origin of opx-free, grt-granulite (see also Bard, 1983b; Yamamoto and Yoshino, 1998; Yoshino and Okudaira, 2004) after metastable low-P hbl-gabbronorite (Padrón-Navarta *et al.*, 2008) in this lower arc crust section. The study of composite samples of hbl-gabbronorite and grt-granulite shows that the arrested transformation of hbl-gabbronoite to grt-granulite occurs along a narrow transition zone (2-3 cm) where relic mineral compositions from the precursor assemblage are preserved. In these zones - interpreted as reaction fronts- the variations of the HREE contents and of the tschermaks and jadeite components in clinopyroxene armoured by garnet coronas indicate the abrupt clinopyroxene-garnet equilibration under high-*P*, lower arc crust conditions. Among other observations, the presence of non-equilibrated clinopyroxene cores in these transition zones, the topotactic relationships of garnet in grt-granulite with the precursor mafic assemblages, and the similarity of crystal preferred orientation of between the hbl-gabbronorite and grt-granulite (Padrón-Navarta *et al.,* 2008) strongly support the metamorphic prograde origin of Jijal opx-free, grt-granulite.

Isopleths thermobarometry from a melt-present pseudosection is consistent with conventional thermobarometry, yielding equilibration pressures of $P \approx 1.1$-1.2 GPa and $T \approx 800$-850 ºC for the Jijal upper GGU grt-granulite. These PT conditions imply differences in depth of ≥ 12 km between the precursor hbl-gabbronorite and the attainment of the high-P equilibration conditions of the grt-granulite part. These PT estimates, together with phase diagram considerations, indicate that low-P hbl-gabbronorite remained metastable, due most likely to the persistence of fluid/melt-absent conditions during burial until attaining PT conditions of the lower arc crust. At these depths, amphibole dehydration (fluid-absent) melting occurred, enhancing kinetics and triggering the transformation of metastable, low-P assemblages to high-P, opx-free, grt-granulite. Phase diagram considerations indicate that the $a(H_2O)$ was high (e.g. 0.85), preventing the breakdown of amphibole by subsolidus dehydration at lower pressures. Reduction of the fluid activity by external components of metasomatic brines is also ruled out, because it would preclude the metastability of the hbl-grabbronorite until the attainment of the *P-T* condition of grt-granulite in the lower arc crust. High $a(H_2O)$ and water conservative compressive paths leading to amphibole, fluid-absent, dehydration melting reactions with melt fractions of 2-3 vol. % are consistent with the

reported field and petrographic variations in upper Jijal GGU rocks and with geochemical estimates (Garrido *et al.*, 2006).

Our work indicates that the protracted metastability of low-P, hydrated, mafic compositions until partial melting conditions in the lower arc crust leads to the suddend equilibration of dense, high-P granulite. These results add up to increasing evidence in arc settings for the protracted metastability of low-P assemblages in mafic, intermediate, and felsic bulk compositions until attaing melt/fluid present conditions at the hot roots of island arcs (Padron-Navarta et al., 2008; Daczko *et al.* 2009; Daczko & Halpin, 2009; Allibone *et al.* 2009). The abrupt transformation of low-P metastable assemblages to denser, high-P, granulitic assemblages in the lower arc crust has important implications for the mechanical stability of the lower arc crust as it may trigger delamination of the lower arc crust (Behn & Kelemen, 2006) and lead to intra-crustal differentiation of the island arcs (Garrido *et al.*, 2006; Garrido *et al.*, 2007; and references therein).

Acknowledgements

We thank Prof. Jean-Pierre Bard for kindly providing samples and field notes on his early expeditions to Pakistan, and the Pakistan National Museum of Natural History for providing infrastructure for sampling of the Jijal Complex. We also thank James Connolly and Roger Powell for their comments on the computation of pseudosection and the limitations of melt solution models in mafic systems. This work was supported by the Spanish "Ministerio de Ciencia e Innovación (MICINN)" through research grants CGL2006-04440, CGL2007-61205/BTE, and ACI2006-A9-0580, the Spanish Council for Research (CSIC) through grant 2008-30I014, and by the "Junta de Andalucía" research groups RNM-145 and RNM-131. J.A. Padrón-Navarta is supported by fellowship AP2005-060 from the "Programa de Formación del Profesorado Universitario". We are very grateful to Geoffrey Clarke for his diligent editorial handling and support.

Journal of Metamorphic Geology (2008) 26:855-870
DOI 10.1111/j.1525-1314.2008.00789.x
Received: 8 April 2008 / Accepted: 7 July 2008 / Published online: 26 August 2008

10 Oriented growth of garnet by topotactic reactions and epitaxy in high-pressure, mafic garnet granulite formed by dehydration melting of metastable hornblende-gabbronorite (Jijal Complex, Kohistan Complex, north Pakistan)

Padrón-Navarta, JA[1*] · Garrido, CJ[2] · Sánchez-Navas, A[1,2] · Tommasi, A[3] · López Sánchez-Vizcaíno, V[4] · Gómez-Pugnaire MT[1,2] · Hussain SS[5]

Garnet growth in high-pressure, mafic garnet granulites formed by dehydration melting of hornblendegabbronorite protoliths in the Jijal Complex (Kohistan palaeo-island arc Complex, north Pakistan) was investigated through a microstructural EBSD-SEM and HRTEM study. Composite samples preserve a sharp transition in which the low-pressure precursor is replaced by garnet through a millimetre-sized reaction front. A magmatic foliation in the gabbronorite is defined by mafic-rich layering, with an associated magmatic lineation defined by the shape-preferred orientation (SPO) of mafic clusters composed of orthopyroxene (Opx), clinopyroxene (Cpx), amphibole (Amp) and oxides. The shape of the reaction front is convoluted and oblique to the magmatic layering. Opx, Amp and, to a lesser extent, Cpx show a strong lattice-preferred orientation (LPO) characterized by an alignment of [001] axes parallel to the magmatic lineation in the precursor hornblende-gabbronorite. Product garnet (Grt) also displays a strong LPO. Two of the four <111> axes are within the magmatic foliation plane and the density maximum is subparallel to the precursor magmatic lineation. The crystallographic relationship $<111>_{Grt}$// $[001]_{Opx,Cpx,Amp}$ deduced from the LPO was confirmed by TEM observations. The sharp and discontinuous modal and compositional variations observed at the reaction front attest to the kinetic inhibition of prograde solid-state reactions predicted by equilibrium-phase diagrams. The P–T field for the equilibration of Jijal garnet granulites shows that the reaction affinities are 5–10 kJ $mol.^{-1}$ for the Grt-in reaction and 0–5 kJ $mol.^{-1}$ for the Opx-out reaction. Petrographic and textural observations indicate that garnet first nucleated on amphibole at the rims of mafic clusters; this topotactic replacement resulted in a strong LPO of garnet. Once the amphibole was consumed in the reaction, the parallelism of [001] axes of the mafic-phase reactants favoured the growth of garnet crystals with similar orientations over a pyroxene substrate. These aggregates eventually sintered into singlecrystal garnet. In the absence of deformation, the orientation of mafic precursor phases conditioned the nucleation site and the crystallographic orientation of garnet because of topotaxial transformation reactions and homoepitaxial growth of garnet during the formation of high-pressure, mafic garnetgranulite after low-pressure mafic protoliths.

1. Departamento de Mineralogía y Petrología, Universidad de Granada, Spain.
2. Instituto Andaluz de Ciencias de la Tierra (IACT), Granada, Spain.
3. Géosciences Montpellier, CNRS & Université de Montpellier II, France.
4. Departamento de Geología, Universidad de Jaén Linares, Spain.
5. Pakistan Museum of Natural History, Garden Islamabad, Pakistan.

10.1 Introduction

The knowledge of the mechanisms of garnet growth during metamorphic reactions is necessary for estimating the rate of metamorphic reactions and, hence, for using metamorphic textures and metamorphic P–T–t paths to unravel tectonic and geodynamic processes. The kinetics of garnet growth and nucleation during metamorphic reactions has been investigated through the analysis of 2D and 3D compositional zoning of garnet, crystal sizes and spatial distribution, by combining X-ray tomography and statistical analysis of the microstructure, numerical modelling of crystal habits and textures, and measurements of lattice-preferred orientation (LPO) of precursor phases and garnet by electron backscatter diffraction, scanning electron microscopy (EBSD-SEM) (Carlson,1989, 1991; Spiess & Bell, 1996; Denison & Carlson, 1997; Denison et al., 1997; Spiess et al., 2001; Prior et al., 2002; Hirsch et al., 2003; Ketcham, 2005).

Several nucleation and growth models are proponed in the literature to account for the compositional zoning, crystal sizes and spatial distribution of garnet in metamorphic rocks derived from different sedimentary and igneous protoliths. Based on classical studies of garnet size and spatial distribution, Kretz (1969) and Carlson (1989, 1991) proposed that the rate-limiting step for garnet porphyroblast growth is the intergranular diffusion of the necessary chemical components. In such a model, the spatial distribution of garnet nuclei and the final size of porphyroblasts are controlled by competitive growth of nuclei that limits the availability of components, inhibiting further nucleation of nearby porphyroblasts. Other authors have emphasized the role of other factors, such as a potential microstructural control on the site of porphyroblast nucleation and growth due, among other factors, to partitioning of deformation (Spiess & Bell, 1996), and/or preferential nucleation and growth on reactant precursor phases (Spiess et al., 2007).

Electron backscatter diffraction has proved to be an extremely useful tool to survey garnet microstructures in metamorphic rocks (Whitney et al., 2008 and references therein). Polygonal textures and low- and high-angle boundaries in metamorphic garnet can easily be detected in EBSD maps of crystallographic orientation. Although more attention has been paid to the influence of P–T conditions on the deformation mechanisms of garnet (Kleinschrodt & McGrew, 2000; Prior et al., 2000, 2002; Kleinschrodt & Duyster, 2002; Mainprice et al., 2004; Storey & Prior, 2005), several recent studies focused on garnet growth mechanisms using orientation distribution data (Spiess et al., 2001, 2007; Hirsch et al., 2003; Storey & Prior, 2005; Whitney et al., 2008).

This paper presents a microstructural EBSD-SEM and TEM study of garnet growth in high-pressure mafic garnet granulites formed by dehydration meeting of hornblende-gabbronorite protoliths in the Jijal Complex (Kohistan palaeo-island arc Complex, north Pakistan) (Jan, 1979; Jan & Howie, 1981; Yamamoto, 1993; Yamamoto & Yoshino, 1998; Yoshino et al., 1998; Yoshino & Okudaira, 2004; Garrido et al., 2006, 2007; Dhuime et al., 2007). High-pressure garnet granulites developed after a low-pressure hornblende gabbronorite protolith through a sharp reaction front at both outcrop and thin-section scales. This sharp transformation boundary provides a unique opportunity to study, at the thin-section scale, the role of precursor phases on the nucleation and growth of

garnet, as well as to constrain the factors controlling the growth of garnet porphyroblasts and their habit variations. In concordance with recent studies (Spiess et al., 2007), in the absence of deformation, the orientation of mafic precursor phases conditioned the nucleation site and led to the oriented growth of garnet due to topotaxial transformation reactions (i.e. reactions where a crystallographic relationship exists between reactant and product phases across interfaces) and to homoepitaxial growth (overgrowth of the same phase without lattice mismatch) of garnet. As a consequence, the orientation and texture of precursor phases fully determined the nucleation sites and the orientation of garnet during the formation of highpressure, mafic garnet granulite after low-pressure mafic protoliths.

10.2 Sample selection and metamorphic conditions

A composite sample (KG-03) was selected from the Jijal Complex (north Pakistan) that preserves the transition from precursor hornblende-gabbronorite to garnet granulite (Garrido et al., 2006). The thin section shows a sharp, millimetre-scale transition (dotted line in Fig. 10-1) between the low-pressure precursor hornblende-gabbronorite and the garnet granulite product assemblage, which covers about 40% of the investigated thin section (Fig. 10-1a,b). A magmatic foliation in the hornblende-gabbronorite is defined by mafic-rich layering (dashed line *L in Fig. 10-1); the associated magmatic lineation is defined by the shape-preferred orientation (SPO) of mafic clusters composed of Opx + Cpx + Amp + oxides (Zeilinger, 2002). The shape of the reaction front is convoluted and oblique to the magmatic layering (RF in Fig. 10-1). The thin section was cut to ensure that precursor and reactant phases were both present in the same thin section, so the XY reference frame is arbitrarily set.The intensity of the magmatic fabric is weak in the studied area. The foliation is on average 40º NW-dipping and the lineation plunges 35º NW (Zeilinger, 2002). The magmatic foliation is replaced locally by a higher intensity, regional tectonic fabric that is not observed in this sampling locality (Zeilinger, 2002).

Conventional thermobarometry, based upon selected exchange and net-transfer reactions involving garnet-clinopyroxene-plagioclase-quartz and Fe-Mg exchange thermometers and implemented with the GTB software (Spear & Kohn, 2001), yields equilibration pressures of 1.0–1.2 GPa and temperatures in the range of 810–825 ºC for the formation of garnet granulite. If Fe^{3+} in clinopyroxene is taken into account, slightly lower equilibration pressures and temperatures are obtained ($1.0 < P < 1.1$ GPa; $735 < T < 750$ ºC). These P–T estimates are in good agreement with previous studies (Yamamoto, 1993; Yoshino et al., 1998; Yoshino & Okudaira, 2004) and with pseudosection thermodynamic calculations (PERPLE_X software; Connolly, 1990; Connolly & Petrini, 2002; and the updated version of the internally consistent thermodynamic database of Holland & Powell, 1998) of mineral composition isopleths for this sample (1.1–1.2 GPa; 825–875 ºC) (J. A. Padrón-Navarta et al., unpublished data, cf. Chapter 9).

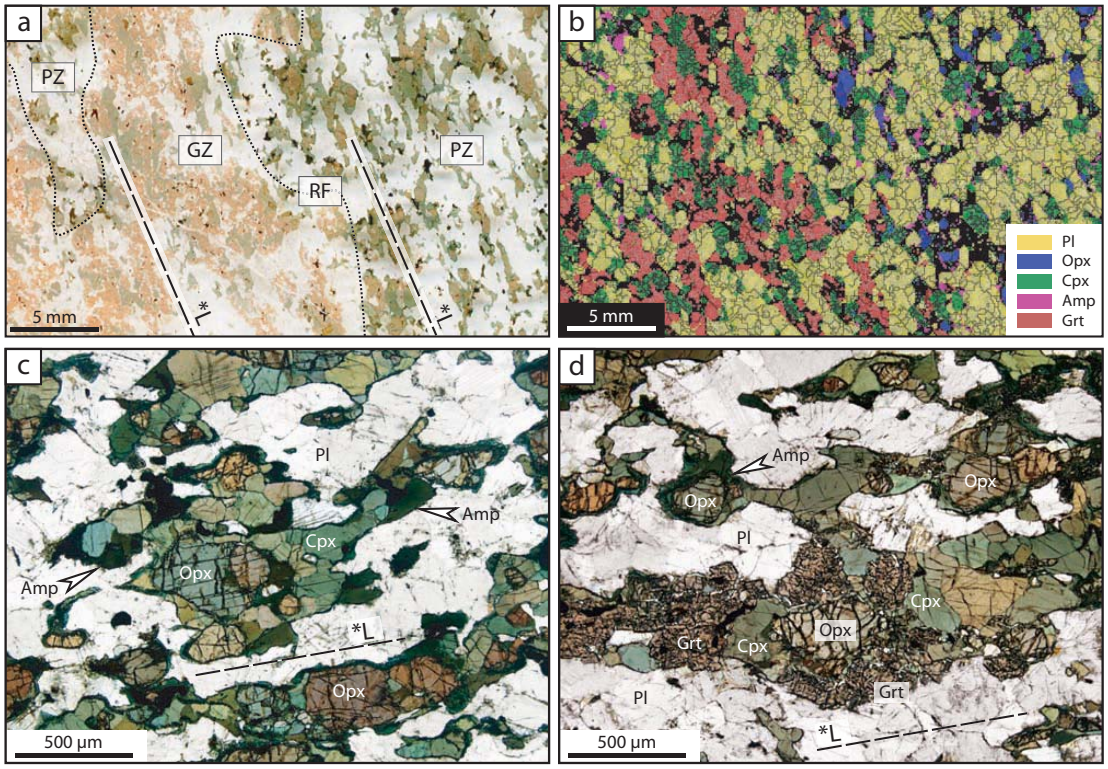

Figure 10-1: (a) Scanned thin section of composite sample KG-03 showing the sharp and convolute reaction front (RF, dotted lined) between the zone with hornblende-gabbronorite (PZ, precursor protolith zone) and the high-pressure garnet granulite zone (GZ). Also shown is the trace of the foliation defined by the magmatic layering (*L) in the precursor hornblende-gabbronorite (PZ) that is cut by the PZ. Note that the trace of the foliation (*L) is still recognized in the garnet granulite zone (GZ). Compare with (b) for phase identification in the two zones. (b) Phase map of the same thin section shown in (a). The colour phase map was obtained by EBSDSEM automated mapping and indexing in a 100 lm mesh, rectangular grid. (c) Micrograph of the PZ showing the aligned mafic clusters characteristics of the precursor, hornblende-gabbronorite. The cluster are composed of cores of orthopyroxene (Opx) surrounded by clinopyroxene (Cpx) and amphibole-oxides (plane-polarized light). (d) Micrograph showing the RF where garnet corona overgrows mafic clusters. The elongated shape of former mafic cluster can be still recognized. *L is shown in (a,b) as dashed line.

10.3 Analytical methods

10.3.1 Scanning electron microscopy

Scanning electron microscope (SEM) observations were performed by secondary and back-scattered electron imaging in carbon-coated polished thin sections using a Zeiss DMS instrument at the Centro de Instrumentación Científica (CIC) of the Universidad de Granada (Spain). The SEM was operated at an acceleration voltage of 20 kV. To carry out 3D SEM observations of garnet aggregates, the sample was crushed in an agate mortar and plagioclase-garnet aggregates concentrated by means of a Frantz magnetic separator. Aggregates were then leached several minutes with cold 5 N nitric acid to selectively remove plagioclase. Leached garnet aggregates were handpicked under a

binocular microscope, mounted on a sample holder and carbon-coated for SEM observation.

10.3.2 Electron backscatter diffraction-scanning electron microscopy

Mapping of the LPO of garnet, clinoamphibole (pargasite), orthopyroxene, clinopyroxene and plagioclase was performed by indexation of EBSD patterns. To improve the quality of Kikuchi diffraction patterns, standard diamond-polished (0.25 lm grain size) thin sections were further polished for 5 min with a chemical–mechanical procedure using colloidal silica suspension (Buehler™ Mastermet™). EBSD measurements were performed on a JEOL JSM 5600 SEM at Géosciences Montpellier (CNRS-Université de Montpellier 2, Montpellier, France) using a ~17 kV accelerating voltage and a working distance of 25 mm. EBSD patterns were collected in the uncoated thin section, tilted at 20º to the vertically incoming electron beam and taped on the sample holder with conductive adhesive carbon tape. Automated EBSD mapping ofthe whole thin sections was acquired in a 100-lm mesh, rectangular grid. EBSD patterns were indexed automatically using CHANNEL 5 software package from HKL Technology. Lattice orientation by CHANNEL 5 software is achieved by automatic indexation of Kikuchi patterns using the Hough transform and six to nine detected band edges and their zones axis in the diffraction pattern. To index diffraction patterns of garnet, a pyrope end-member reflector file was used (Meagher, 1975). The other minerals were indexed using the standard Channel reflector file database. The EBSD data were processed and contoured as conventional CPO pole figures for selected crystallographic planes and directions using the software PFCH5 (Mainprice, 1990, 2007; Mainprice & Humbert, 1994).

10.3.3 Transmission electron microscopy

Selected areas of thin sections were detached from thin sections in copper grids, ion-milled and carbon coated for transmission electron microscopy (TEM) observation. Samples were examined using a Philips™ CM20 instrument at the CIC of the Universidad de Granada, operated at 200 kV and equipped with an energy dispersive X-ray (EDX) model EDAX system for analytical electron microscopy applications. Reflections with d-values <0.4 nm on selected-area electron diffraction patterns (SAED) were used to obtain crystal lattice images. STEM microanalyses were carried out using a 5-nm beam diameter and a scanning area of 1000 nm x 20 nm.

10.4 Petrography

For descriptive purposes, the studied thin section can be subdivided into three zones: a precursor zone (PZ), the reaction front (RF) and the garnet granulite zone (GZ) (Fig. 1a). The PZ shows the reactant magmatic assemblage consisting of Pl + Cpx + Opx + Amp + Qtz + oxides (hornblende gabbronorite) (Fig. 1c). The GZ contains only the product assemblage that is composed of Pl + Cpx + Grt + Qtz + Rt (garnet granulite). Both areas are separated by a thin RF where product and reactant phases coexist.

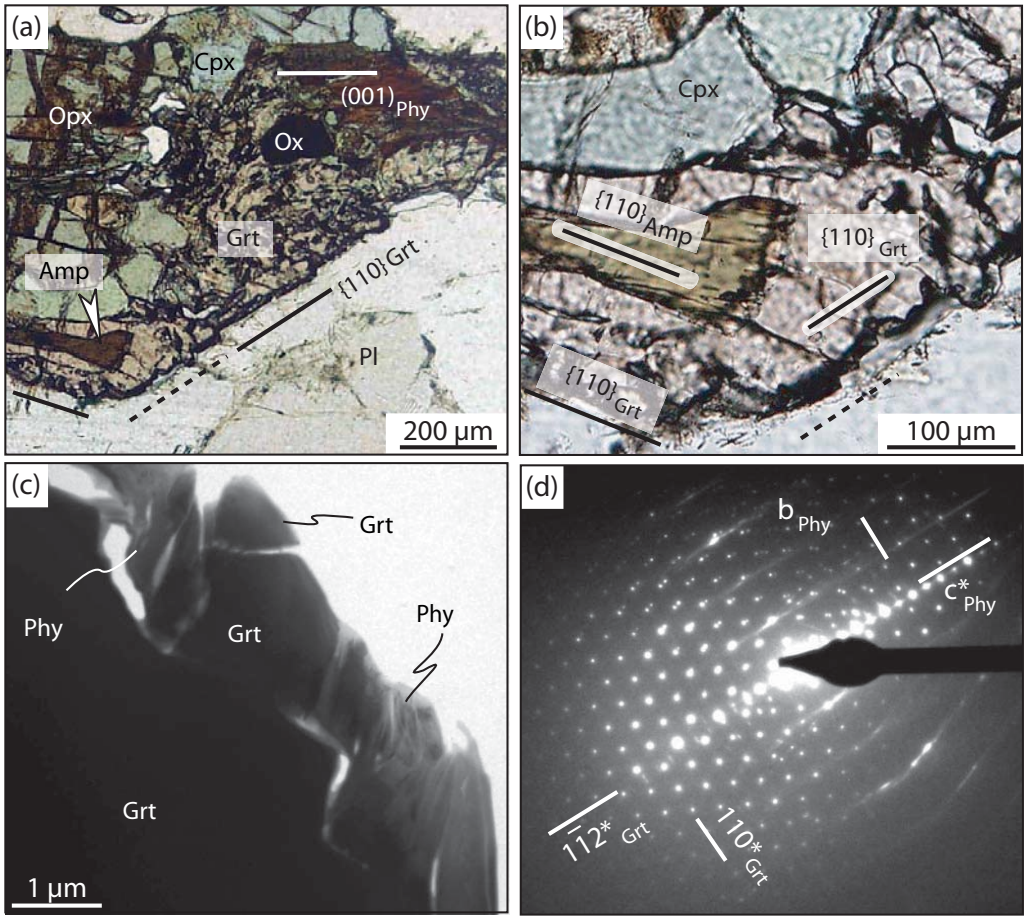

Figure 10-2: (a) Micrograph of a partly transformed mafic cluster at the reaction front of sample KG-03. he mafic cluster is composed of a core of orthopyroxene (Opx) rimmed by clinopyroxene (Cpx), hemato-ilmenite (Ox) and amphibole (Amp) that is partly transformed to phyllosilicate (Phy). The cluster is overgrown by garnet (with quartz inclusions) showing a sharp interface (trace of rhombic dodecahedral faces) with plagioclase (Pl). Garnet preserves inclusions of precursor amphibole (parallel nicols); (b) Zoom of (a) showing the amphibole inclusion in garnet and the inferred orientation relationships between amphibole cleavage {110} and rhombic dodecahedral {110} faces of garnet; (c) TEM image of the garnet-phyllosilicate interfaces. Phyllosilicate spacing is consistent with a chlorite/smectite intergrown. (d) SAED of the garnet-phyllosilicate interface shown in (c). The SAED shows that phyllosilicate (001) planes are parallel to (112) garnet planes.

Garnet first occurs at the RF as films grown (~200 µm thick) over precursor mafic clusters (aggregates of subhedral to anhedral orthopyroxene surrounded by clinopyroxene and amphibole) (Figs 1d & 2). Inclusions of precursor amphibole in garnet show their Garr cleavage planes subparallel to one of the rhombic dodecahedral {110} faces of garnet (Fig. 2a,b). Because of the preferential ion milling of amphibole relative to garnet, it has not been possible to inspect by TEM the garnet–amphibole interfaces to infer the relative crystallographic orientation between amphibole and garnet interface. However, the relative crystallographic orientation of garnet with secondary phyllosilicate after amphibole (altered to chlorite/smectite as confirmed by TEM and AEM observations) was successfully inferred, which allows retrieving the original

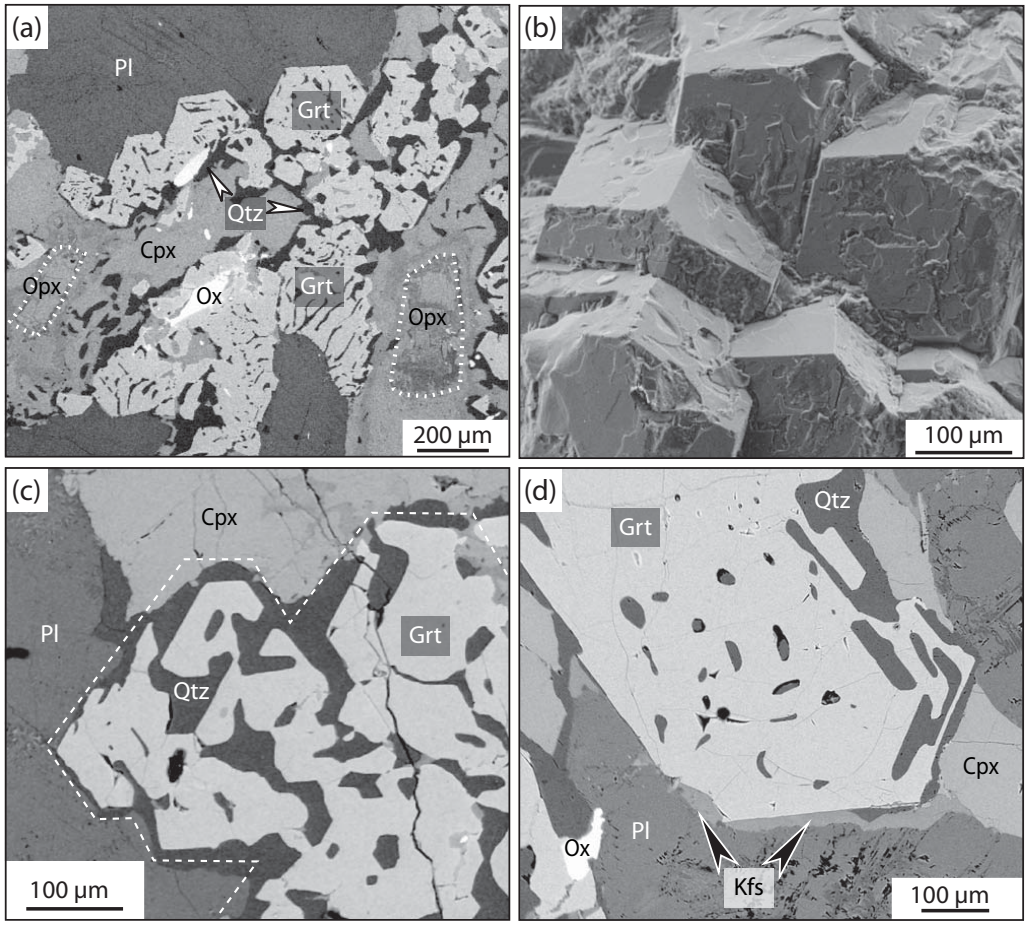

Figure 10-3: (a) Garnet corona overgrowing previous orthopyroxene (Opx, dashed lines) – clinopyroxene (Cpx) mafic clusters. Quartz (black zones) is more abundant towards the contact with clinopyroxene. (b) SE-SEM 3D image of garnet coronitic structures around mafic clusters, showing that they are composed of parallel aggregates of rhombic dodecahedra. (c) Detail of the garnet-clinopyroxene contact showing hopper morphologies in the garnet crowded with quartz inclusions. Note that garnet is a single crystal (grain boundaries are shown by white dashed lines) and the re-entrants are filled by quartz. (d) K-feldspar (Kfs, arrowed) film in the garnet–plagioclase boundary grain where garnet shows euhedral faces. In contrast garnet and clinopyroxene are divided by skeletal quartz inclusions subparallel to incipient/starting rhombic dodecahedral garnet faces.

crystallographic orientation between amphibole and garnet (Fig. 10-2a,c). The SAED pattern shows that phyllosilicate (001) planes are parallel to (112) garnet planes (trapezohedron faces) (Fig. 10-2d). The garnet habit and its interface shape with mafic minerals and plagioclase show gradual variations from the RF to the GZ. At the RF, garnet shows coronitic textures around mafic minerals showing sharp, planar interfaces with plagioclase (Fig. 10-3a). K-feldspar and quartz films are present in many of the plagioclase–garnet interfaces. Garnet coronitic aggregates around a given mafic cluster are composed of euhedral garnet aggregates with sub-parallel crystal faces (Fig. 10-3b). Three-dimensional, secondary electron SEM images of these garnet aggregates confirm that they are constituted by crystal aggregates of garnet with rhombic dodecahedral {110} habits (Fig. 10-3b).

Towards the mafic minerals, the garnet coronitic aggregates display a graphic texture consisting of garnet intergrowths with quartz, evolving inwards to quartz aggregates surrounding cores with relict hornblende and/or orthopyroxene, or secondary clinopyroxene and/or oxides (Fig. 10-3a). The skeletal garnet intergrowth shows hopper and skeletal morphologies with quartz inclusions (Fig. 10-3c,d), which, in places, are subparallel to garnet rhombic dodecahedral faces (Fig. 10-3d). The hopper and skeletal garnet morphologies are indicative of enhanced garnet growth at rhombic dodecahedral corners (Fig. 10-3c,d). This is confirmed by TEM imaging of the inner aggregates that shows how garnet skeletal and hopper morphologies with quartz develop at the nano-scale (Fig. 10-4), indicating that the rate of growth normal to the rhombic dodecahedral garnet faces was higher at the crystal corners than at the crystal faces (Fig. 10-4). In the GZ, the coronitic garnet intergrowths tend to be less common. In this zone, garnet aggregates are somehow transformed in large single crystals with few quartz inclusions and irregular shapes with embayments filled by coarse quartz aggregates.

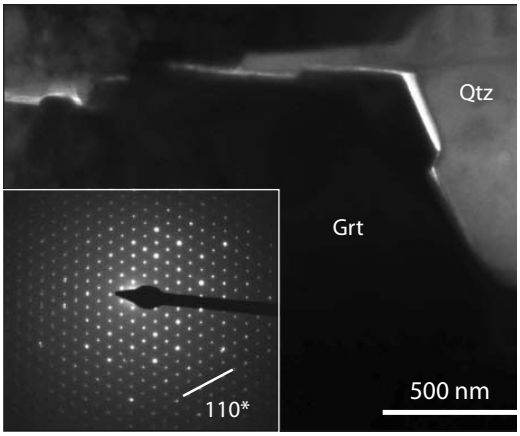

Figure 10-4: TEM image of a garnet–quartz interface of graphitic intergrowth of garnet showing skeletal garnet morphologies demonstrating enhanced garnet growth at the crystal corners of rhombic dodecahedral garnet faces. Inset (lower left): SAED showing the garnet orientation.

10.5 Lattice-preferred orientation

The LPO of reactant and product mafic minerals (Opx, Amp, Cpx and Grt) in the composite sample KG-03 was investigated by means of EBSD-SEM (Fig. 10-1a). This technique allows the characterization of thecrystallographic orientation of precursor and product minerals at the scale of the thin section, providing a statistically significant investigation of the LPO relationships among reactant and product assemblages at larger length-scales than those permitted by TEM observations (Prior et al., 2002; Spiess et al., 2007).

Figure 10-5 shows contoured pole figures of the LPO of mafic silicates in the composite sample KG-03. As the sample was cut to ensure that both precursor and reactant phases were present in the same thin section (Fig. 10-1a), the XY reference frame of pole figures does not correspond to the foliation and lineation plane. The magmatic foliation and lineation, which are defined by the alignment of mafic clusters and their SPO in the precursor hornblende gabbronorite (Fig. 10-1a), are depicted as a great circle (white continuous line) and a red star, respectively, in the pole figures (Fig. 10-5). The strength of the orientation of each crystallographic axis or sharpness of the pole figure is quantified by the pfJ index (Fig. 10-5). The pfJ index is related to the J index (Mainprice & Silver, 1993; Michibayashi & Mainprice, 2004) that is calculated using the orientation distribution function from the triplet of Euler angles (Bunge,

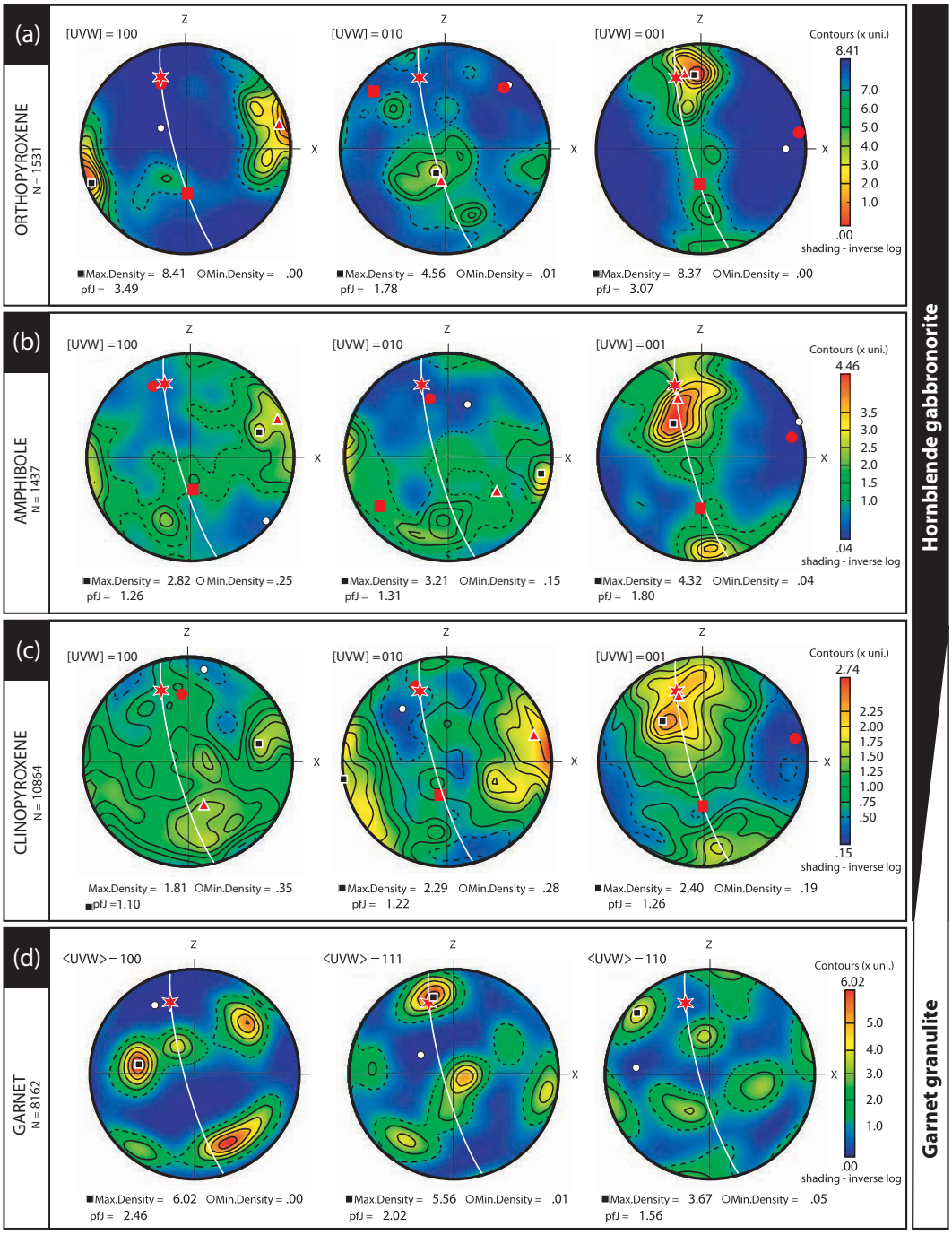

Figure 10-5: Pole figures showing the LPO of orthopyroxene (a), amphibole (b), clinopyroxene (c), and garnet (d) in the composite sample KG-03. Pole figures are represented on lower hemisphere equal area projections. Foliation is represented by a continuous white line (pole to foliation plane, 75º / 10º) and lineation of elongated mafic cluster by a red star. Filled contour in multiples of a uniform distribution (m.u.d.). N = number of patterns indexed used for plotting. Only clinopyroxene occurs in hornblende gabbronorite and garnet granulite zone. Amphibole and orthopyroxene are absent in the garnet granulite assemblages zone of sample KG-03. Maximum and minimum density values and the pole figure J index (pfJ) are also indicated. The three eigenvectors S1, S2, S3 are plotted as red triangles, squares and dots respectively (for eigenvalues and their orientation, see Table 1).

1982). However, the pfJ index for a given crystal direction cannot be compared among different minerals as it depends on the crystal symmetry (Michibayashi & Mainprice, 2004). Orthopyroxene and amphibole, the main mafic precursor phases of garnet, are only present in the gabbronorite zone and at the reaction front (PZ and RF, respectively, in Fig. 10-1a). Orthopyroxene, amphibole and, to a lesser extent, clinopyroxene, show a strong LPO that is intimately related to the magmatic foliation and lineation in the precursor hornblende gabbronorite. Their [001] axes are largely contained in the foliation plane with a maximum subparallel to the lineation (Fig. 10-5a–c). Orthopyroxene displays the strongest LPO (pfJ[100] = 3.49 and pfJ[001] = 3.07; Fig. 10-5a) characterized by the alignment of [100] axes normal to the foliation and a girdle distribution of [001] axes in the foliation plane with a strong maximum subparallel to the lineation (Fig. 10-5a). Garnet aggregates also display a strong LPO (Fig. 10-5d). The lower pfJ index for <111> and <110> axes relative to the <100> axis in garnet pole figures is due to symmetry effects. Garnet LPOs show a maximum density distribution resembling that of a single-crystal of garnet with two of the four <111> axes within the magmatic foliation plane, one of them subparallel to the magmatic lineation (Fig. 10-5d).

The strength and the symmetry of the crystals' orientation distribution (i.e. random, point or girdle distribution) can be quantified by eigenvector analysis of the poles to (hkl) planes and [uvw] directions (Woodcock & Naylor, 1983; Vollmer, 1990). The eigenvalues of these orientations for KG-03 mafic minerals are given in Table 10-1 and the three eigenvectors (S_1, S_2 & S_3) for each mineral are plotted on the pole figures (Fig. 10-5). The strongest concentration is given by the eigenvector with the greatest eigenvalue and the pole to the best plane by the smallest eigenvalue for each crystallographic direction. The shape of the orientation distribution and its strength can be quantified by the ratios of eigenvalues and by the shape parameter, K [$K = \ln(S_1 / S_2) / \ln(S_2 / S_3)$] (Woodcock & Naylor, 1983). A cluster distribution of orientation data is characterized by $S_1 > S_2 \approx S_3$ and $K > 1.0$, with a $K = \infty$ for a uniaxial cluster distribution, whereas a girdle

Table 10.1. Summary of EBSD data for sample KG-03 processed using software PFch5 (Mainprice, 1990; Mainprice & Humbert, 1994; Mainprice, 2007).

Phase	*n*	Type		S_1	Dec	Inc	S_2	Dec	Inc	S_3	Dec	Inc	K	C
		a-axis		0.7161	75.16	8.57	0.1909	177.47	54.74	0.0930	339.34	33.90	1.84	7.70
Opx	1531	b-axis		0.4968	186.75	65.27	0.3178	308.86	13.76	0.1854	44.01	20.13	0.83	2.68
		c-axis		0.6308	347.60	27.06	0.3140	181.79	62.22	0.0552	80.59	5.84	0.40	11.43
		a-axis		0.3811	158.78	54.50	0.3422	259.63	7.65	0.2767	354.92	34.42	0.51	1.38
			[100]	0.3932	179.98	49.10	0.3287	274.06	3.53	0.2781	7.10	40.68	1.07	1.41
Cpx	10864	b-axis		0.4672	73.45	13.04	0.2902	190.30	62.85	0.2427	337.70	23.37	2.66	1.93
		c-axis		0.4690	339.91	34.04	0.3184	179.81	54.31	0.2126	76.38	9.47	0.96	2.21
			[001]	0.4754	340.19	30.55	0.3324	189.90	55.80	0.1923	78.58	13.88	0.65	2.47
		a-axis		0.4425	66.33	8.91	0.3148	175.39	64.37	0.2427	332.36	23.82	1.31	1.82
			[100]	0.4725	72.70	9.71	0.3024	176.38	54.13	0.2251	336.04	34.14	1.51	2.10
Amp	1437	b-axis		0.4021	124.96	42.54	0.3734	234.40	19.94	0.2245	342.64	40.78	0.15	1.79
		c-axis		0.5484	338.08	38.38	0.3058	181.46	49.21	0.1457	77.54	11.72	0.79	3.76
			[001]	0.5258	335.84	35.91	0.2951	176.45	52.27	0.1791	73.21	10.05	1.16	2.94
					Max. Density									
Grt	8162		<111>		345.00	25.00								

S_1, S_2 and S_3 are maximun, intermediate and minumun normalized eigenvalues respectively. Dec: declination. Inc: inclination. Shape parameter, $K=\ln(S_1/S_2)/\ln(S_2/S_3)$ and strength parameter $C=S_1/S_2$ (Woodcock & Naylor, 1983).

distribution is characterized by a $S_1 \approx S_2 > S_3$ and $K < 1.0$, with $K = 0$ for a perfect uniaxial girdle distribution. On the other hand, the randomness of the distributions may be expressed by the strength or critical parameter, C ($C = S_1 / S_3$). The eigenvalues of a perfect uniform distribution are equal and hence C = 1, whereas a strong fabric has high C values. Table 10-1 gives the computed K, C and eigenvalues of the poles to selected (hkl) planes and [uvw] directions for KG-03 mafic minerals. The three eigenvectors (S1, S_2 & S_3) for each mineral are also plotted on their corresponding pole figure (Fig. 10-5). Eigenvector analysis is strictly valid for non-orthorhombic symmetries, but it used here, along with the pfJ index, to explore quantitatively the strength of the correlation and type of orientation distribution of crystallographic axes and planes of orthopyroxene, clinopyroxene, amphibole and garnet. Orthopyroxene is characterized by a strong cluster distribution (K = 1.84, C = 7.70) of [100] axes and a strong girdle distribution of [001] axes (K = 0.40, C = 11.43) with a maximum concentration, marked by the S1 eigenvector (347.6º/27.1º), that is subparallel to the magmatic lineation (Fig. 10-5a). For amphibole, the eigenvector of the poles to (100) is normal to the foliation plane (72.7º / 9.7º) and, similarly to orthopyroxene, the poles to (001) and of the [001] axes show a girdle distribution around it on the foliation plane (K = 0.79, C = 3.76) with a maximum concentration (335.8º/35.91º and 338.1º/38.4º, respectively) subparallel to the lineation (Fig. 10-5b). The LPO of clinopyroxene is more scattered and, in contrast to what is observed for orthopyroxene and amphibole, clinopyroxene [010] axes are strongly clustered almost normal to the foliation (73.5º / 13.0º; K = 2.66; cf. K[010] of other minerals in Table 10-1). Clinopyroxene poles to (001) and [001] axes have a girdle distribution in the foliation plane (K = 0.65 and 0.96, respectively) with a weak maximum close to the lineation (Fig. 10-5c). Summing up, the EBSD study shows that both precursors and product minerals have a strong LPO that is intimately related to the magmatic lineation and foliation, which are defined by the SPO of mafic clusters. Precursor amphibole and orthopyroxene show poles to (001) and [001] axes clustered within the magmatic foliation, with a strong concentration subparallel to the lineation. A weaker, but similar crystallographic fabric is observed for clinopyroxene. On the other hand, garnet aggregates in the RF and the GF display a surprisingly strong orientation characterized by alignment of two of the <111> on the foliation plane, with one of them parallel to the magmatic lineation of the precursor hornblende gabbronorite zone. These orientation relationships suggest that the orientation of precursor, magmatic phases exerted a strong crystallographic control on the growth of garnet.

10.6 Discussion

10.6.1 Origin of the LPO of precursor phases

An important finding of this study is the strong control that the LPOs of precursor, hornblende-gabbronorite minerals exerted on the oriented growth of garnet during high-pressure granulite metamorphism. Hence, the first requirement is to understand the origin of the observed LPO in hornblende gabbronorite precursor minerals and its close orientational relationships with magmatic layering and lineation. Although crystal-plastic deformation by dislocation creep with dominant activation of the high-temperature (100)[001] system for orthopyroxene (Coe & Kirby, 1975; McLaren & Etheridge, 1976; Mercier, 1985; Dornbush et al., 1994) and (010)[001] system for

clinopyroxene (Bascou et al., 2002; Terry & Heidelbach, 2006) may account for the observed LPO of pyroxene in the hornblende gabbronorite zone, at the petrographic and TEM scales there is no microstructural evidence for subsolidus crystal-plastic deformation (i.e. dynamic recrystallization, ribbon grains, undulose extinction, kink bands or subgrain boundaries) in precursor minerals.

Rigid-body rotation of elongated mafic minerals or clusters during magmatic flow at supersolidus conditions (Nicolas & Ildefonse, 1996; Lamoureux et al., 1999; Yoshinobu & Harper, 2004) is the most plausible mechanism, accounting for the LPO of Opx and its strong correlation with the SPO of mafic clusters in the hornblende gabbronorite. Textural observations show that crystallization of orthopyroxene occurred first, followed by clinopyroxene, amphibole and oxides, and that the two later phases formed at the waning stages of crystallization (Fig. 10-1a). The similarity between ortho-pyroxene and clinopyroxene LPO can be accounted for by either topotactic growth of magmatic clinopyroxene on earlier crystallized orthopyroxene or by rigid rotation of clinopyroxene crystals during magmatic flow. Amphibole and oxides tend to rim mafic clusters, replacing earlier clinopyroxene and orthopyroxene (Fig. 10-1c). These replacement textures are common in arc-derived hornblende-gabbronorite. They are formed due to peritectic reactions between amphibole and pyroxene on cooling in closed-system crystallization or in situ crystallization, or to late replacement by evolved melt/fluids (Arculus & Wills, 1980; Conrad & Kay, 1984; Fichaut et al., 1989; Costa et al., 2002). As crystallization of amphibole occurs at small melt fractions when magmatic flow is unlikely (Nicolas & Ildefonse, 1996), the similarity between amphibole and pyroxene LPO is better explained by the well-known topotactic relation between amphibole and pyroxene during near-solidus peritectic reactions (Thompson, 1978).

10.6.2 Crystallographic relationships between garnet and precursor phases

This textural study indicates that the LPO of precursor magmatic phases controlled the oriented growth of garnet during high-pressure garnet granulite metamorphism. The [001] axes of precursor pyroxene and amphibole are contained within the magmatic layering plane and are subparallel to the magmatic lineation (Fig. 10-5c). The garnet-in reaction was a reconstructive topotatic reaction in the sense of Figlarz et al. (1990), because garnet took advantage of the crystal lattices of precursor phases as substrates for its oriented growth.

Petrographic and textural observations indicate that garnet first nucleated on precursor amphibole surrounding mafic clusters (Figs 10-1b,d & 10-2). TEM observations (Fig. 10-2) show that retrograde phyllosilicates (Phy) in contact with garnet display the following crystallographic relationships (Fig. 10-2b,d):

$$[110]_{Grt}//b_{Phy}, \qquad [1\underline{1}2]_{Grt}//c^*_{Phy}, \qquad [\underline{1}11]_{Grt}//a_{Phy} \tag{1}$$

where c^*_{Phy} denotes the direction normal to the $(001)_{Phy}$ planes (see Putnis, 1992 for the crystallographic notation used here; note that for clinopyroxene and amphibole c*- and c-axes are not coincident). Phyllosilicate results from the well-known topotactic reaction

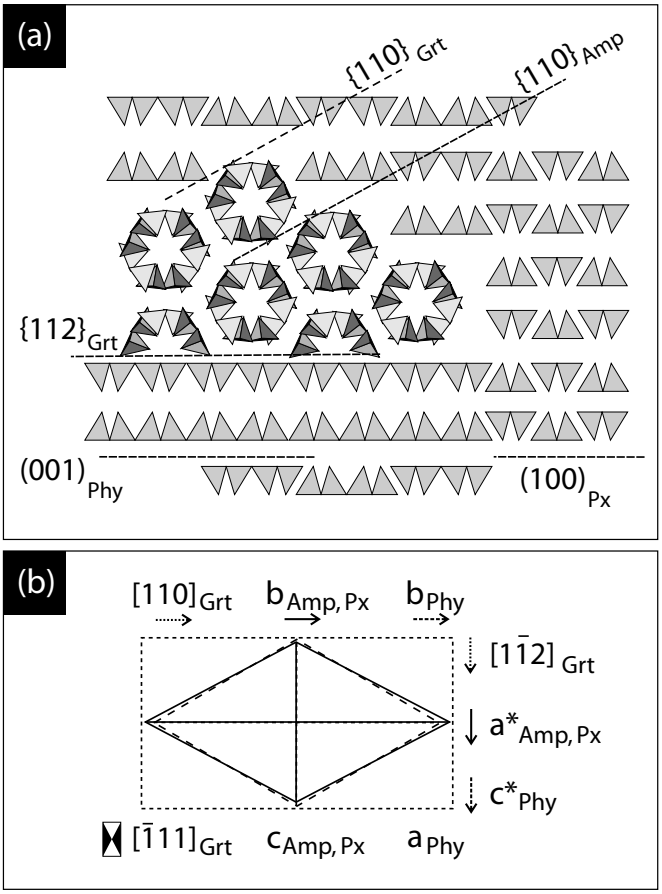

Figure 10-6: (a) Projections of the polyhedral representation of the crystal lattice of garnet (Grt), amphibole (Amp), pyroxene (Px) and phyllosilicate (Phy) showing the orientational and dimensional relationships between the crystal lattices of these minerals inferred by TEM and EBSD orientation data and best explaining the topotactic reactions of garnet on amphibole substrates. The garnet lattice is projected down the ternary axis, that of amphibole down the [001] axis, and that of phyllosilicate down the a-axis. Only tetrahedra are shown for simplicity. The traces of mineral interfaces have also been drawn (cf. Fig. 10-2). Match among amphibole and garnet lattices (the solid, dashed and dotted lines correspond to amphibole, garnet and phyllosilicate lattices, respectively). Note that the topotaxial relationship between garnet and amphibole is $(110)_{Grt}$ // $(110)_{Amp}$ and $[\underline{1}11]_{Grt}$ // $[001]_{Amp}$ when is expressed as common plane and parallel direction respectively.

after amphibole characterized by parallelism between [010] axes of amphibole and phyllosilicate, as well as parallelism between [001] axis of amphibole and [100] axes of phyllosilicates (Veblen, 1991, 1992):

$$b_{Amp} // b_{Phy},\ a^*_{Amp} // c^*_{Phy}; c_{Amp} // a_{Phy} \qquad (2)$$

This topotactic reaction, along with the crystallographic relations observed between garnet and phyllosilicate (Eq. 1), suggests a topotactic replacement of garnet by amphibole characterized by:

$$[110]_{Grt} // b_{Amp},\ [112]_{Grt} // a^*_{Amp},\ [\underline{1}11]_{Grt} // c_{Amp} \qquad (3)$$

This topotactic replacement is consistent with the petrographic observation showing that {110} garnet faces are parallel to the {110} amphibole cleavage (Fig. 10-2a,b). As the [001] axis of amphibole is subparallel to the magmatic lineation (Fig. 10-5b), the garnet topotactic reaction after amphibole (Eq. 3) caused garnet growth with two of its four <111> directions within the magmatic foliation, one of them subparallel to the magmatic lineation (Fig. 10-5d). This strong orientational relationship between reactant (amphibole, pyroxene and orthopyroxene) and product phases (garnet) implies that nucleation and growth of garnet were conditioned by the orientation of its precursor phases.

Figure 10-6 shows a cartoon of the lattice projections of garnet, amphibole, pyroxene and phyllosilicate, showing the above-inferred orientational relationships. These structural relationships minimize the mismatch between garnet and amphibole crystal lattices. Using published lattice parameters of amphibole and garnet, the lattice misfit at ambient temperature is ~9.5% along $[110]_{Grt}$ // b_{Amp} and 1% along $[112]_{Grt}$ // a_{Amp} (Fig. 10-3). A higher mismatch of ~20% is estimated along $[\underline{1}11]_{Grt}$ // c_{Amp}. The good orientational relationships of precursor amphibole and pyroxene in mafic clusters, which are in accordance with the well-known topotactic relationships in biopyroboles (Thompson, 1978), allow us to infer the overall crystallographic relationship between precursor, reactant phases (Opx, Cpx and Amp) and garnet as:

$$<111>_{Grt} // [001]_{Opx,Cpx,Amp} \qquad (4)$$

Although all the relative orientational relationships implied by this topotactic law have not been confirmed by TEM observations, this crystallographic relationship between mafic precursors and garnet accounts for the LPOs of garnet and its inheritance of the precursor magmatic fabric. Once amphibole was consumed in the reaction, the strong orientational relationship between mafic-phase reactants allowed the growth of garnet with the same orientation over a pyroxene substrate, eventually sintering into single-crystal garnet. Finally, it is worth noting that, within the framework of the ionic model of crystal lattice, oriented growth of product phases on precursor minerals during topotactic reaction is customarily accounted for by the parallelism of their interfaces to planes with the highest density of framework oxygen closed-packing (Spry, 1969; Worden et al., 1987). In the present case, the garnet and amphibole interfaces of the topotactic reaction of garnet after amphibole ($\{110\}_{Grt}$//$\{110\}_{Amp}$; Fig. 10-6) are inconsistent with this model. Garnet–amphibole interfaces (dotted line in Fig. 6; see also Fig. 2) are parallel to the periodic bond chains (PBC) (Hartman & Perdok, 1955), which are crystallographic directions with strong (i.e. more covalent) chemical bonds. Consequently, the attachment of amphibole-garnet tetrahedra across these interfaces corresponds to weak bonds involving cations other than Si.

10.6.3 Overstepping of garnet-forming reactions

From phase diagram constraints and P–T estimates, the precursor, hornblende gabbronorite assemblage remained metastable until the prograde amphibole breakdown reaction occurred. The sharp discontinuous modal and compositional variations observed at the reaction front attest to the role of kinetic inhibition of earlier prograde, solid-state

reactions predicted by equilibrium-phase diagrams. In particular, the non-preservation of the predicted intermediate stages of replacement of orthopyroxene by garnet in the presence of stable amphibole is remarkable, considering the large P–T field (P > 2 kbar, Fig. 10-7) along the prograde path wherein this assemblage is stable. As the nucleation step is the main limiting step for the departure from equilibrium of metamorphic reactions (Rubie, 1998; Waters & Lovegrove, 2002), the metastability of the hornblende-gabbronorite assemblage indicates that garnet nucleation after orthopyroxene never overcame the kinetic barriers until the dehydration-melting breakdown reaction of amphibole occurred. The calculated phase diagrams indicate that melt released (2–4%) by amphibole breakdown drove the system towards equilibrium by plagioclase dissolution, leading to the rapid exhaustion of metastable orthopyroxene. The most plausible explanation for reaction inhibition is the sluggish plagioclase dissolution under fluid-absent conditions, as is observed in experimental dehydration melting of a hornblende-plagioclase mixture of amphibolitic composition at 1000 C and at 8 and 12 kbar (Johannes & Koepke, 2001).

Classical nucleation theory predicts that the nucleation probability is virtually zero until a threshold overstep of the reaction free energy is overcome (Ridley & Thompson, 1986; Lasaga, 1998; Rubie, 1998). The value of the critical overstep for nucleation is poorly constrained and there are important discrepancies between experimentally and naturally derived quantities. The relative amount of the reaction overstep can however be examined in terms of the amount of free energy relative to the target equilibrium reaction as a function of pressure and temperature ($\Delta G_{P,T}$), also known as the reaction affinity (A) (Ashworth & Sheplev, 1997; Ashworth et al., 1998; Waters & Lovegrove, 2002). The affinity for a reaction ($-\Delta G_{P,T}$)(eq. 5) involving a Θ total number of phases at constant P–T is the difference of molar free energy (G_k) among k-phases reactants and products balanced by their stoichiometry coefficients (υ_k) (Prigogine & Defay, 1954; Ashworth & Sheplev, 1997; Ashworth et al., 1998):

$$(-\Delta G_{P,T}) = \sum_{k=1}^{\Phi} \upsilon_k G_k$$

The first nucleation of garnet after orthopyroxene (Grt-in reaction) and the orthopyroxene exhaustion (Opx-out reaction) reactions in the simplified CFMAS system are (end-member abbreviation after Kretz, 1983):

$$2\ En_{48}Fs_{52} + An = Prp_{48}Alm_{52} + Di_{48}Hd_{52} + Qtz \quad (6)$$

$$2\ En_{63}Fs_{37} + An = Prp_{63}Alm_{37} + Di_{63}Hd_{37} + Qtz \quad (7)$$

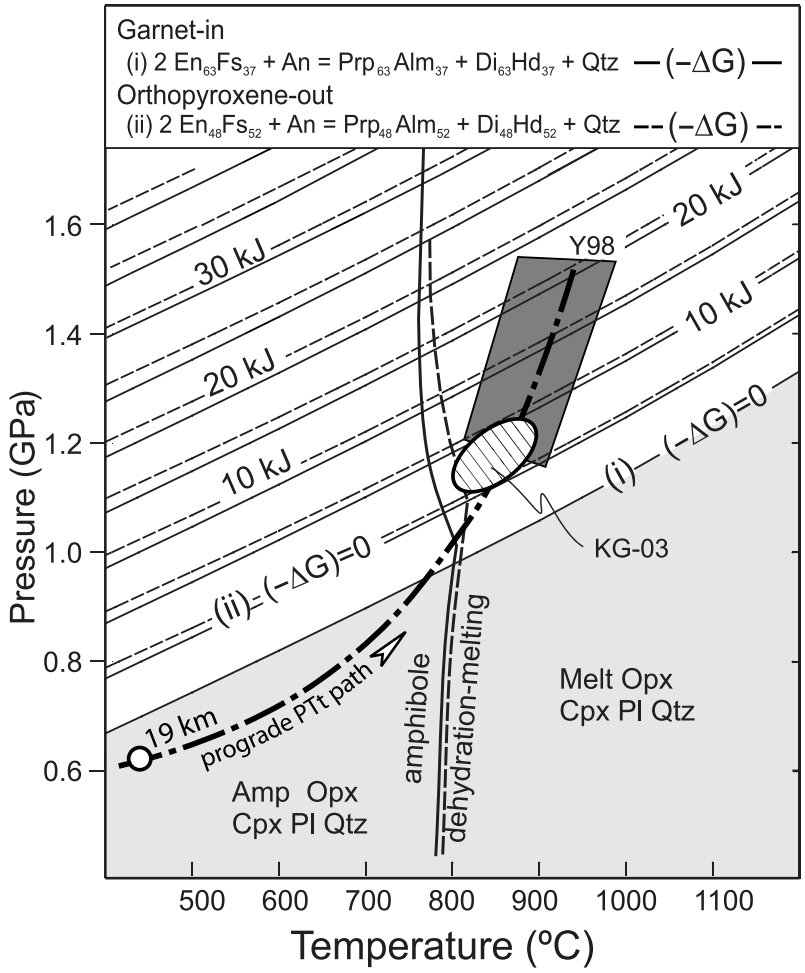

Figure 10-7: Contours of the reaction overstep for garnet-in and orthopyroxene-out overall reaction (Eqs 6 and 7 respectively) in the CFMAS system in kJ per mol. of garnet produced. Computations were carried out using FRENDLY, a FORTRAN program included in the thermodynamic software package PERPLE_X (vs. 2007) (Connolly, 1990) using the internally consistent thermodynamic dataset of Holland & Powell (1998). Also, shown are the P–T conditions estimates for garnet granulite for the sample KG-03 (hatched) and those derived by Yoshino et al. (1998) and Yoshino & Okudaira (2004) (Y98). The grey field at low pressure shows the equilibrium assemblage without garnet in the hornblende gabbronorite assemblage. Amphibole dehydrationmelting curve (solid line) and amphibole-out curve (dashed line) for KG-03 are those derived by (J. A. Padrón-Navarta et al., unpublished data, Chapter 9). P–T–t path inferred by thermal modeling and proposed for the evolution of the Kohistan lower crust for the case of intrusions intruded at initial depth of 19 km (white dot) in the double-plate model of Yoshino & Okudaira (2004).

In these reactions, the compositions of garnet and orthopyroxene in the CFMAS system are obtained from pseudosection phase diagrams. Figure 10-7 shows the contours of the affinity in the P–T space calculated from thermochemical data for the foregoing reactions. The P–T field for the equilibration of Jijal garnet granulites establishes reaction affinities of 5– 10 kJ mol.$^{-1}$ for the Grt-in reaction (Eq. 6), and 0–5 kJ mol.$^{-1}$ for the Opx-out reaction (Eq. 7). These overstepping quantities are similar to those estimated for the formation of garnet coronas in mafic granulites (6.9 ± 1.8 kJ mol.$^{-1}$, Ashworth et al., 1998), and those estimated for other metamorphic reactions (e.g. 5.0 kJ

mol.$^{-1}$, Waters & Lovegrove, 2002; 5.6 ± 2.4 kJ mol.$^{-1}$; Baxter & DePaolo, 2002) and experimental studies (1.2–8.0 kJ mol.$^{-1}$; Ridley & Thompson, 1986; Ague, 2003 and references therein). Based on Monte Carlo simulation of natural garnet growth morphologies, Wilbur & Ague (2006) estimated an overstep of at least ~ 2 kJ mol.$^{-1}$ for garnet produced by muscovite and chlorite dehydration during Barrovian metamorphism. Thus, it can be concluded that for the Jijal Complex the garnet-forming reaction after orthopyroxene had a high affinity at the peak P–T equilibration conditions of the granulite assemblage. The very sharp dependence of the nucleation and growth rate on the reaction affinity entails very high nucleation and growth rates of garnet after metastable orthopyroxene.

10.6.4 Garnet nucleation and growth mechanisms

The spatial textural variation of garnet observed can be used to infer the temporal sequence of garnet nucleation and growth, as well as the different garnet growth mechanisms that operated during the transformation of hornblende-gabbronorite to garnet granulite. Textural observations indicate that the onset of garnet nucleation and growth occurred along plagioclase–amphibole interfaces. This is evidenced by rough interfaces composed of garnet films coating amphibole and by relatively flat interfaces with plagioclase (Figs 10-1d & 10-2a,b). This texture suggests that the first stage of the amphibole-breakdown reaction produced a fluid/melt film between amphibole and plagioclase, where garnet nucleated preferentially on amphibole interfaces.

The topotaxial orientational relationships inferred between garnet and amphibole suggests that oriented nucleation of garnet on the reactant amphibole substrate may have played a key role in overcoming the critical overstep for the amphibole-breakdown reaction. A topotaxial reaction equally accounts for heterogeneous nucleation of garnet on mafic clusters, which determined the spatial distribution of garnet porphyroblast in the GZ, and the inheritance of the hornblende-gabbronorite fabric. Topotaxial reactions in material science and mineralogy are commonly ascribed to solid-state transformation and reactions (Putnis, 1992). The onset of garnet growth most likely was a fluid/melt-present, interface-coupled dissolution–precipitation reaction, where garnet nucleation took place at the surface of amphibole. Variations of trace element contents and ratios in Jijal composite samples are more consistent with partial melting and segregation of low fractions of granitic melts (Garrido et al., 2006). Oriented growth of the product phase because of dissolution–precipitation reactions can take place if there is a topotaxial crystallographic relationship between product and reactant phases (Putnis & Putnis, 2007). This onset stage of garnet nucleation and growth was characterized by stable planar surfaces and might correspond to a first stage of a two-dimensional nucleation growth mechanism (Sunagawa, 1987).

The second stage of growth is observed along the reaction front. It is characterized by development of garnet hopper crystal morphologies with numerous quartz inclusions (Fig. 10-3c). At the reaction front, hopper garnet morphologies are well developed where amphibole is exhausted, where metastable orthopyroxene is reacting, or where both precursor phases for garnet are absent. For a given mafic cluster, garnet hopper morphologies commonly develop inwards of the mafic clusters core, a textural location where orthopyroxene commonly occurs at the metastable hornblende-gabbronorite zone

(Fig. 10-1). This observation suggests that garnet hopper morphologies are somehow related to the breakdown reactions of metastable orthopyroxene after the garnet nucleation and growth stage. The development of mono-crystalline garnet after a single mafic cluster (Fig. 10-3), the remarkable epitatic orientation of rhombic dodecahedral garnet of hopper interfaces (Fig. 10-3b), and the lack of independent nuclei of garnet within clusters point out that, for a given cluster, further growth of garnet nucleated in the first stage took place by a homoepitaxial growth mechanism (Quon & Potvin, 1972; Robertson, 1978; Markov & Stoyanov, 1987; Markov, 1995; Hibiya & Görnert, 2007; Spiess et al., 2007) after exhaustion of amphibole.

Hopper garnet morphologies are known in magmatic crystallization under high undercooling (Kirkpatrick, 1981; Faure et al., 2003) and in prograde regional metamorphism (Jamtveit & Andersen, 1992; Wilbur & Ague, 2006). Hopper crystal morphologies are produced by very fast rates of growth ("disequilibrium growth"; Kuroda et al., 1987). The growth rate increases with variations of the somehow related magnitudes: the reaction affinity, heating rate (Ridley, 1985), supersaturation (Kuroda et al., 1987) and the absolute temperature (Walther & Wood, 1984). It is unlikely that variations in absolute temperature or heating rate at the centimetre-scale may account for the observed disequilibrium growth of garnet inwards the core of mafic cluster. The development of garnet hopper textures is most likely related to supersaturation triggered by the high affinity of the disequilibrium breakdown reaction of metastable orthopyroxene in mafic clusters (Eqs 6 & 7).

A first requirement is to understand why the kinetic barriers for the orthopyroxene-consuming reaction were overcome just at the reaction front. The textural sequence observed at the reaction front and the sharp front between metastable precursor assemblages at the thin-section scale point to the release of a fluid/melt phase by amphibole breakdown (Fig. 10-7) in the reaction front as the key factor expediting the breakdown of metastable orthopyroxene. The amphibole-breakdown reaction not only helped to surmount the critical step for the early nucleation of the garnet-forming reaction after orthopyroxene, but also released a fluid/melt phase. The main rate-limiting factor in solid-state garnet-forming reactions is the intergranular diffusion of the slowest diffusing major element participating in the reaction, which is Al in most garnet-forming metamorphic reactions (Ashworth & Sheplev, 1997; Ashworth et al., 1998). The presence of an intergranular fluid phase increases the intergranular diffusion coefficient for Al by several orders of magnitude (Carlson et al., 1995; Carlson, 2002). The enhanced intergranular diffusion of Al in a fluid/melt phase most likely overcome the kinetic barrier that had promoted the orthopyroxene metastability so far. The high affinity of the garnet-in reaction after orthopyroxene (Fig. 10-7) enhanced the dissolution rate of metastable orthopyroxene, generating a supersaturated solution at the interface between earlier nucleated garnet and orthopyroxene.

The mechanism of interfacial growth in fluid/melt epitaxy depends on various factors controlling the growth rate of the precipitating phase such as supersaturation, misfit (lattice mismatch) and strain (smooth or rough interface) with the substrate phase, and the presence of surfactants, among others (Sunagawa, 1987; Markov, 1995; Hibiya & Görnert, 2007). In a reaction mediated by a fluid/melt phase, the interfacial growth rate of the reaction product is directly proportional to the diffusion coefficient of the slowest

diffusion element in the reaction and the supersaturation, and inversely proportional to the thickness of the diffusion boundary layer. A departure from the 2D growth mechanism of the interface with increasing supersaturation and growth rate is observed successively from step bunching, formation of inclusions, edge nucleation and surface dendrites, and hopper growth and bulk dendrites in the transition from stable growth to growth instability (Sunagawa, 1987; Markov, 1995; Hibiya & Go¨ rnert, 2007).

The 3D epitaxial growth implied by the hopper garnet interfaces was most likely caused by supersaturation. Once the kinetic barrier for the metastable garnet-in reaction after orthopyroxene was overcome, the high reaction rates – driven by the high affinity of the reaction – produced supersaturation of garnet components at the garnet–orthopyroxene interfaces. Supersaturation in garnet components sparked the growth rate (Kuroda et al., 1987) of the garnet interface towards the core of mafic cluster by a homoepitaxial 3D growth mechanism resulting in the observed garnet single crystals with hopper morphologies at the reaction front. Supersaturation also accounts for enhanced growth rate of garnet crystal corners relative to crystal edges (Donaldson, 1976; Kirkpatrick, 1981; Kuroda et al., 1987; Faure et al., 2003) observed at the TEM nanoscale (Fig. 10-4). Fast garnet growth facilitated the formation of inclusions of quartz generated during orthopyroxene-breakdown reaction (Eqs 6 & 7). The development of faceted garnet commonly observed at the plagioclase–garnet interfaces is characteristic of 2D growth mechanisms, which are favoured by slow growth rates and reduced supersaturation (Kuroda et al., 1987; Hibiya & Görnert, 2007).

The third stage of garnet growth was related to the final development of garnet porphyroblasts free of quartz inclusions observed in the GZ. The similar orientation between hopper garnet in the RF and large garnet porphyroblasts in the GZ, along with the close spatial relationship of porphyroblasts with mafic clusters, demonstrates that polyhedral garnet porphyroblasts derived from hopper garnet observed at the RF. The most likely mechanism whereby monocrystalline polyhedral garnet porphyroblasts may form after hopper garnet is by solution precipitation of quartz inclusions and coalescence of garnet hopper interfaces driven by a reduction of interfacial energy. Coalescence was favoured by the completion of garnet-producing net transfer reactions that reduced supersaturation and growth rate and by the high temperature at the granulite peak conditions (825–875ºC, Padrón-Navarta et al., submitted). Both factors, enhanced by a fluid-phase, promoted annealing and coalescence, forming faceted garnet porphyroblasts, which represent the final equilibrium texture in the GZ.

Coalescence and clustering of initial randomly oriented nuclei to a preferred bulk orientation because of misorientation-driven rotation (Spiess et al., 2001) has been proposed as a mechanism to produce garnet porphyroblasts with a strong CPO (Spiess et al., 2001). However, polycrystalline garnet aggregates with high-angle boundaries (Whitney et al., 2008) and garnet single crystals with identical orientation (Hirsch et al., 2003) observed using orientation contrast imaging partially contradict this interpretation. The rotation mechanism predicted in the hypothesis of Spiess et al. (2001) is a function of temperature and it is expected to operate effectively under high-temperature conditions at granulite facies relevant to this study (>750 ºC). However, detailed EBSD orientation maps of garnet of the Jijal Complex do not reveal any

microstructural feature implying that the misorientation of initial nuclei at plagioclase–amphibole boundaries was small or alternatively that high-angle boundaries were suppressed by misorientation-driven rotation at the initial stages of growth. The lack of structural Complexity observed in garnet coronas or in garnet porphyroblasts is indeed better explained by topotactic nucleation of garnet at mafic cluster rims.

10.7 Summary and conclusions

Mafic garnet granulites of the Jijal Complex (Kohistan Complex, north Pakistan) preserve a unique natural example of porphyroblast garnet nucleation and growth during high-pressure amphibole dehydration melting of hbl-gabbronorite, where the LPO fabric of precursor mafic minerals led to oriented growth of garnet. Garnet shows a strong LPO with two <111> axes on the foliation plane that can be accounted by the generalized topotaxial crystallographic relationships $<111>_{Grt}$ // $[001]_{Opx,Cpx,Amp}$.

The following sequence of garnet formation after the precursor mafic minerals can be inferred:

1. A first stage of garnet nucleation on amphibole at the amphibole–plagioclase interface during the amphibole-breakdown reaction that led to a fast kinetic for garnet nucleation and growth favoured by the release of a fluid/melt phase. At this stage, the existence of a 3D fit between amphibole and garnet crystal lattices (topotaxy) allowed interface-controlled growth of garnet.

2. A second stage of skeletal garnet growth towards the inner part of single mafic clusters where garnet developed "hopper" morphologies enclosing quartz inclusions. These garnet morphologies are accounted for by fast, 3D homoepitaxial garnet growth because of the high affinity of the garnet-producing reaction after metastable orthopyroxene that led to local supersaturation. The breakdown of metastable orthopyroxene was triggered by an increase of the intergranular diffusion of Al due to the presence of a fluid-melt phase.

3. A final stage of Ostwald ripening or crystal sintering resulted in the formation of large inclusion-free garnet porphyroblasts commonly observed in garnet granulites farther away from the reaction front.

Acknowledgements
The authors highly appreciate the reviews of J.J. Ague, D. Whitney and one anonymous reviewer which helped to improve the final version of the manuscript. This work was supported by the Spanish "Ministerio de Ciencia e Innovación (MICINN)" through research grants CGL2006-04440, CGL2007-61205-BTE, and ACI2006-A9-0580, and by the "Junta de Andalucía" research groups RNM-145 and RNM-131. JAPN is supported by fellowship AP2005-060 from the "Programa de Formación del Profesorado Universitario" and CJG by a RyC fellowship, both granted by the Spanish MICINN.

PART FOUR

11. Conclusions/Conclusiones

11 CONCLUSIONS

This chapter briefly summarizes the main results of this Thesis, focussed on the study of two specific dehydration reactions that are fundamental in the volatile cycling of subduction zones: the breakdown of antigorite deeper in the mantle wedge-slab (Part II), and the breakdown of amphibole in the lower arc crust (Part III). The study of arrested reactions in the field offers a unique opportunity not only to accurately establish the pressure and temperature conditions at which they were formed, but also to explore the mechanisms of prograde mineral growth and, hence, to understand better the petrophysical response of rocks to metamorphic devolatilization reactions. In this Thesis it has been shown the influence of the reaction overstepping on the development of textures with strong crystal preferred orientation of the prograde phases. This kind of finding may enable to couple dehydration reactions with their petrophysical implications in subduction settings.

High-pressure antigorite dehydration in Cerro del Almirez ultramafic massif (Nevado-Filábride Complex, Betic Cordillera, SE Spain)

Antigorite microstrutural and chemical characterization. TEM observations have revealed that, prior to its transfomation, antigorite is highly ordered and consists of the polysome m = 17. Antigorite is characterized by high aluminium and chromium contents (up to 4.2 wt % Al_2O_3 and 1.3 wt % Cr_2O_3) and by the lack of polysomatic defects. This fact additionally supports that serpentinites were close to their maximal thermal stability conditions. Owing to their extreme order, and the high-aluminium content, the Cerro del Almirez antigorites may become an important reference material in the study of the FMASH system.

Close to the devolatilization front, antigorite shows evidences of the beginning of breakdown, such as common (001) twins, offset SAED patterns, wobbling of lattice fringes, dislocation modulations, and intracrystalline suture.

Pressure and temperature constrains. In this Thesis the pressure and temperature conditions for the protolith (Atg-serpentinite) and products (Chl-harzburgite), as well as for the antigorite dehydration reaction itself, have been constrained, based on thermodynamic calculations and experimental petrology.

a) **Antigorite-serpentinite.** Exceptionally well recrystallized antigorite from Cerro del Almirez ultramafic massif attests for the high-pressure and relatively high-temperature conditions at which serpentinite was annealed. The petrographic and TEM study of Ti-Chu breakdown in olivine veins in Atg-serpentinite is also in agreement with these pressure and temperature conditions. According to phase diagram sections and the calculated P-T evolution for the upper Nevado-Filábride sequence, formation of these veins occurred at maximum conditions of 1.3 GPa and 475 °C. The breakdown of Ti-Chu occurred in a probable P-T range of 1.7–2.0 GPa

and 620–640 °C. Maximum temperature conditions of wall rock antigorite were, at least, this 620–640 °C

b) **Antigorite dehydration reaction.** Piston cylinder experiments on serpentinites from the Cerro del Almirez ultramafic Complex constrain the maximum temperature stability for the highly polysomatic ordered antigorite and high-Al and Cr contents to 680ºC at 1.9 GPa. For the bulk composition considered, the olivine-in reaction occurs 20–30ºC below the antigorite-out reaction. At 1.8 GPa, Al and other trivalent cations in antigorite expand its stability 60–70ºC when compared with the Al-free system.

c) **Chl-harzburgite.** The antigorite stability field experimentally found constrains the minimum temperature for the chlorite harzburgite between 660 and 680ºC at temperatures between 1.6 and 2.5 GPa. The occurrence of tremolite in the Ol + Opx + Chl rocks limits the pressure below 1.9 GPa. The Tr-out reaction also constrains the maximum temperature, which ranges from 680 to 710ºC for 1.9 and 1.6 GPa, respectively.

Phase relationships in the devolatilization front. Transitional lithologies are found (Chl-serpentinite and Chl-Atg-Opx-Ol schist) in a narrow band separating Atg-serpentinite from Chl-harzburgite. Chl-serpentinite occurs in direct contact with Atg-serpentinite and is characterized by the sharp appearance of chlorite and by the growth of a second generation of highly recrystallized antigorite. First occurrence of orthopyroxene takes place several centimetres to decimetres away from the contact with Atg-serpentinite. Accordingly, two different discontinuous metamorphic reactions must be invoked, in the FeO-MgO-Al_2O_3-SiO_2-H_2O (FMASH) compositional system, in order to account for the first appearance of chlorite (Chl-in) and orthopyroxene (Opx-in) in these rocks with increasing temperature. First reaction occurs as a consequence of the high aluminium content of the antigorite. With increasing temperature, the maximum tschermaks content in antigorite decreases as being buffered by chlorite. At higher temperature, antigorite further breaks down to orthopyroxene and olivine through the second discontinuous reaction due to its dependence on the magnesium number (X_{Mg}) of product minerals.

Si-enriched compositions. A key finding of this Thesis is the discovery of silica-enriched serpentinite with an unusual mineral assemblage (orthopyroxene-bearing serpentinite) and its prograde counterpart (Chl-harzburgite with olivine and orthopyroxene relic porphyroblasts). It has been experimentally shown here that the appereance of orthopyroxene is due to the reaction between antigorite and talc at lower temperature than the terminal antigorite dehydration. Opx-serpentinite with or without olivine is stable between 640 and 680ºC and pressure higher than 1.6 GPa. This reaction might be particularly important for the fore-arc mantle wedge. The amount of water released by Opx-serpentinite breakdown would depend on the modal proportion of these two phases that is ultimately related with the degree of interaction of the ultramafic rocks with Si-rich metasomatic fluids. Surprisingly, the unusual mineral assemblage from this Si-enriched serpentinite is preserved beyond the complete antigorite breakdown in the form of orthopyroxene and olivine relics. These relic porphyroblasts are characterized by contrasting compositional features with respect to prograde olivine

and orthopyroxene from Chl-harzburgite. Peak metamorphic conditions attained in Cerro del Almirez ultramafic massif are in good agreement with the slow diffusion rates required for the preservation of olivine and orthopyroxene porphyroblasts in chemical disequilibrium with the Chl-harzburgite mineral assemblage.

Origin of granofelsic and spinifex-like textures. The prograde Chl-harzburgite assemblage shows two very contrasting textures: granofelsic (with coarse, round olivine and idioblastic prismatic orthopyroxene) and spinifex-like (dentritic-like, cm-sized olivine and orthopyroxene). Both textures occur as interspersed, dm- to m-sized boudins beyond the atg-dehydration front. Both textures, however, have the same bulk-rock composition and very similar mineral composition. Based on field relationships, textural evolution and mineral chemistry presented in this Thesis, these textures are interpreted as resulting from shifts of the growth rate due to temporal and spatial fluctuations of the affinity of the antigorite breakdown reaction. These fluctuations are driven by cyclic variations of the excess fluid pressure which are ultimately controlled by the hydrodynamics of deserpentinization fluid expulsion. Crystallization at a low affinity of the reaction, correspondig to the granofelsic texture, may be attained if fluids are slowly drained out from the dehydration front. During the advancement of the dehydration front, overpressured domains are left behind preserving highly metastable atg-serpentinite domains. Brittle failure results in a sudden drop of the fluid pressure, and a displacement of antigorite equilibrium towards the prograde products that crystallizes at a high affinity of the reaction (spinifex-like texture).

Origin of Chl-harzburgite recrystallization. Evidences for the above mentioned brittle deformation can be found along grain-size reduction zones (GSRZ), a few mm to meters wide, which form roughly planar conjugate structures in the Chl-harzburgite. Granofelsic and spinifex-like metamorphic textures are partially obliterated by these GSRZ. Analysis of olivine crystal-preferred orientations (CPO) in GSRZ affecting the spinifex-like texture shows similar patterns, but a higher dispersion than in the non-deformed domains. It also reveals mm- to cm-scale discrete domains with rather homogeneous crystallographic orientations. suggesting inheritance from the preexisting spinifex-like olivines in the host peridotite. Misorientation angles between neighboring grains in the GSRZ show peaks at ~5-10º and ~20º, but the rotations are not crystallographically controlled. Based on these observations, the formation of the GSRZ is interpreted as record of brittle deformation (microcraking) of the chlorite-harzburgites, probably induced by hydrofracturing at high pressure. High-pressure hydrofracturing can, thus, explain very fast drainage rates of highly metastable domains and enhance the fast reaction rates responsible of the spinifex-like texture.

This textural bimodality (granofelsic and spinifex-like), together with GSRZ (ascribed to brittle deformation), hence attest for a unique example of the feedbacks taking place in the antigorite dehydrating system between the cyclic dynamic of metamorphic fluid expulsion, the reaction rate and crystallisation processes.

High-pressure amphibole dehydration-melting in Jijal Complex (Kohistan paleo-arc Complex, NW Pakistan)

Metastability of hbl-gabbronorite in the lower arc-crust. This Thesis presents a detailed study of composite samples of hbl-gabbronorite and grt-granulite, showing that the arrested amphibole and orthopyroxene breakdown occurs along a narrow transition zone (2-3 cm). In this reaction front, relic mineral compositions from the precursor assemblage are preserved. Isopleths thermobarometry after a melt-present pseudosection is consistent with conventional thermobarometry, yielding equilibration pressures of P ≈ 1.1-1.2 GPa and T ≈ 800-850 ºC for the Jijal upper GGU grt-granulite. These PT conditions imply differences in depth of ≥12 km between the precursor hbl-gabbronorite and the attainment of the high-P equilibration conditions of the grt-granulite. These PT estimates, together with phase diagram considerations, indicate that low-P hbl-gabbronorite remained metastable, due most likely to the persistence of fluid/melt-absent conditions during burial until attaining PT conditions of the lower arc crust. At these depths, amphibole dehydration (fluid-absent) melting occurred, enhancing kinetics and triggering the transformation of metastable, low-P assemblages to high-P, opx-free, grt-granulite.

Epitaxial growth of garnet in granulites. The garnet growth mechanism was further investigated in this Thesis by a combination of EBSD-SEM and TEM microstructural study. It is proposed that garnet nucleated on amphibole, this producing a strong crystallographic orientation in garnet. These granulites preserve the magmatic foliation from the precursor hbl-gabbronorite and lack evidence for deformation. This allowed the garnets to retain a strong preferred orientation. Two of the four <111> axes are within the magmatic foliation plane and the density maximum is subparallel to the precursor magmatic lineation. The crystallographic relationship $<111>_{Grt}//[001]_{Opx,Cpx,Amp}$ deduced from EBSD was confirmed by TEM observations. The sharp and discontinuous modal and compositional variations observed at the reaction front attest to the kinetic inhibition of prograde solid-state reactions predicted by equilibrium-phase diagrams

This abrupt transformation of low-P metastable assemblages to denser, high-P, granulitic assemblages in the lower arc crust has important implications for the mechanical stability of the lower arc crust as it may trigger its delamination and lead to intra-crustal differentiation of the island arcs.

12 CONCLUSIONES

En este último capítulo se resumen, brevemente, los principales resultados de esta Tesis Doctoral, en la que se aborda el estudio de dos reacciones de deshidratación. Estas dos reacciones son especialmente importantes en el reciclado de volátiles en las zonas de subducción. La primera de ellas (segunda parte de esta Tesis) corresponde a la deshidratación de la antigorita que tiene lugar tanto en la parte hidratada de la placa que subduce como en la cuña mantélica serpenitizada. La segunda concierne a la deshidración/fusión del anfíbol en la corteza inferior de arcos de islas (tercera parte de esta Tesis). El estudio de frentes de reacción abortados y observables a la escala del afloramiento ofrece una oportunidad única para establecer de manera precisa las condiciones de presión y temperatura a las que estas reacciones tuvieron lugar. Asimismo, permiten descifrar los mecanismos mediante los cuales se produce el crecimiento de minerales prograd os y comprender, de esta manera, la respuesta petrofísica que producen las reacciones de deshidratación. En esta Tesis se muestra la influencia del grado de inhibición de una reacción (en términos de energía libre) en el desarrollo textural de fuertes orientaciones preferentes de las fases progradas. Estas observaciones pueden permitir relacionar el efecto de las reacciones de deshidratación con la respuesta petrofísica a las mismas a mayor escala (zonas de subducción).

Deshidratación en condiciones de alta presión de la antigorita en el macizo ultramáfico del Cerro del Almirez (Complejo Nevado-Filábride, Cordilleras Béticas, SE España).

Caracterización microestructural y química de la antigorita. Observaciones realizadas mediante microscopía de transmisión electrónica (TEM) han permitido caracterizar el alto grado de ordenamiento cristalino de la antigorita (mineral principal de las serpentinitas), que está constituida principalmente por el polisoma m = 17. La antigorita de esta localidad es especialmente rica en aluminio y cromo (hasta 4.2 % y 1.3 % en peso de Al_2O_3 y Cr_2O_3, respectivamente) y se caracteriza por la ausencia de defectos polisomáticos. Este hecho sostiene que las serpentinitas estuvieron muy cerca de las máximas condiciones de estabilidad térmica. Debido a su ordenamiento cristalográfico extremo y a su alto contenido de aluminio, las antigoritas del Cerro del Almirez pueden llegar a constituir un excelente material de referencia para el estudio las relaciones de fase en el sistema FMASH.

En las cercanías al frente de deshidratación, las antigoritas comienzan a mostrar evidencias de la desestabilización, como maclas paralelas a los planos (001), descompensación de los patrones de difracción, oscilación de las imágenes estructurales de alta resolución, modulaciones debidas a dislocaciones o suturas intracristalinas.

Estimaciones de presión y temperatura. En la presente Tesis se han estimado las condiciones de formación del protolito hidratado (serpentinitas con antigorita), de sus

equivalentes prograd os (harzburgitas con clorita), así como de la propia reacción de deshidratación de la antigorita. Dichas estimaciones están basado en cálculos termodinámicas y en trabajos experimentales:

a) **Serpentinitas con antigorita.** El excepcional grado de recristalización de las antigoritas del macizo ultramáfico del Cerro del Almirez da testimonio de las altas condiciones de presión y temperatura a las que fueron sometidas las serpentinitas. El estudio petrográfico y mediante microscopía electrónica de transmisión de la desestabilización de la clinohumita titanífera en las venas de olivino de las serpentinitas confirma estas condiciones de presión y temperatura. Las condiciones de formación de estas venas han sido estimada en 1.3 GPa y 475 ºC, a partir de cálculos de secciones de diagramas de fase y de las restricciones impuestas por la evolución P-T para la parte superior de la secuencia Nevado-Filábride. Por otra parte, las condiciones de desestabilización de la clinohumita titanífera tuvieron lugar, muy probablemente entre los 1.7-2.0 GPa y los 620-640ºC. Ésta fue, como mínimo, la máxima temperatura alcanzada por la antigorita de las serpentinitas adyacentes.

b) **Reacción de deshidratación de la antigorita**. La estimación de la condiciones de presión y temperatura a las que tuvo lugar la desestabilización de la antigorita han sido calibradas mediante experimentos de alta presión (Piston Cylinder). La máxima estabilidad térmica para esta antigorita con un alto grado de ordenamiento y elevados contenidos de aluminio y cromo se encontró a 680 ºC para 1.9 GPa. Para las composiciones de roca total considerada, la reacción de aparición del olivino tuvo lugar unos 20-30 ºC por debajo de la curva de desestabilización de la antigorita. Para una presión de 1.8 GPa, la presencia de aluminio y otros cationes trivalentes en la antigorita, hace expandir su campo de estabilidad unos 60-70 ºC en comparación con los sistemas libres de aluminio.

c) **Harzburgitas con clorita.** El campo de estabilidad de la antigorita encontrado experimentalmente permite restringir las condiciones de temperatura de formación de la asociación prograda (harzburgitas con clorita) entre los 660 y los 680 ºC para presiones de 1.6 a 2.5 GPa. La presencia de tremolita en las asociación anterior limita la presión a valores inferiores a los 1.9 GPa. La reacción de desaparición de la tremolita, restringe, igualmente, las máximas temperaturas que han podido ser alcanzadas. Éstas varían entre los 680 y los 710 ºC para presiones de 1.9 y 1.6 GPa respectivamente.

Relaciones de fase en el frente de deshidratación. Entre las serpentinitas con antigorita y las harzburgitas con clorita se ha encontrado una estrecha banda constituida por una serie de litologías transicionales (serpentinitas con clorita y rocas esquistosas con Chl-Atg-Opx-Ol). Las serpentinitas con clorita están en contacto directo con las serpentinitas con antigorita y se caracterizan por la aparición brusca de clorita y por el crecimiento de una segunda generación de antigorita. La primera aparición de ortopiroxeno tiene lugar a pocos centímetros o decímetros del contacto con las serpentinitas con antigorita. La aparición de clorita (Chl-in) y ortopiroxeno (Opx-in) en estas rocas se produce debido a dos reacciones metamórficas discontinuas en el sistema

composicional FeO-MgO-Al_2O_3-SiO_2-H_2O (FMASH) como resultado de un incremento en la temperatura. La primera reacción tiene lugar debido al alto contenido en aluminio de la antigorita. Como consecuencia del aumento de la temperatura, el contenido máximo del componente tschermaks en la antigorita se reduce, quedando tamponado por la aparición de clorita. A temperaturas algo mayores la antigorita se desestabiliza finalmente para dar ortopiroxeno y olivino a través de una segunda reacción discontinua, controlada en este caso por el intercambio Fe-Mg entre los minerales ferromagnesianos.

Composiciones enriquecidas en sílice. Un descubimiento importante de esta Tesis doctoral es la presencia de serpentinitas con composiciones ricas en Si y con una inusual asociación mineral (serpentinitas con ortopiroxeno), así como de sus equivalentes progrados (harzburgitas con clorita con porfiroblastos relictos de ortopiroxeno y olivino). Se ha demostrado experimentalmente que la aparición de ortopiroxeno en estas rocas se debe a la reacción de antigorita con talco a temperaturas inferiores a las de la desestabilización completa de la antigorita. Las serpentinitas con ortopiroxeno y/o olivino son estables entre 640 y 680ºC para presiones por encima de 1.6 GPa. Esta reacción, aquí descrita, podría ser de particular importancia para el manto ante-arco, donde se cree que rocas con composiciones enriquecidas en sílice son más abundantes. La cantidad de agua liberada durante esta reacción depende de las proporciones modales iniciales entre talco y antigorita; dicha proporción que ligada en última instancia al grado de interacción de las rocas ultramáficas con fluidos metasomatizantes ricos en Si. Sorprendentemente, parte de esta asociación tan inusual aparece preservada en forma de relictos de ortopiroxeno y olivino en la asociación prograda (harzburgitas con clorita). Estos porfiroblastos relictos están caracterizados por composiciones químicas muy diferentes a las de los ortopiroxenos y olivinos de las harzburgitas con clorita. Las condiciones, de relativamente baja temperatura, del pico de metamorfismo alcanzadas en el macizo ultramáfico del Cerro del Almirez concuerdan con las bajas velocidades de difusión requeridas para la preservación del desequilibrio composicional entre los olivinos y porfiroblastos relictos con la composición de la asociación de las harzburgitas con clorita.

Origen de las texturas granofélsicas y de tipo spinifex. La asociación prograda se presenta en forma de dos tipos texturales muy contrastados: con una textura de "granofels" (con olivinos subredondeados y de gran tamaño y ortopiroxeno prismático) y de tipo spinifex (olivinos y ortopiroxenos dendríticos de tamaño centimétrico). Ambas texturas afloran como intercalaciones de niveles de potencia métrica a decamétrica, más allá del frente de deshidratación de la antigorita. A pesar de las diferencias texturales, ambos tipos tienen la misma composición de roca total y composiciones muy similares de los mineral. Atendiendo a las relaciones de campo, la evolución textural y la composición química de los minerales descritas en esta tesis, estas texturas se interpretan como consecuencia de cambios en la velocidad de crecimiento de los minerales debidos a fluctuaciones espaciales y temporales de la afinidad química de la reacción de desestabilización de la antigorita. Estas fluctuaciones son consecuencia de las variaciones cíclicas de la presión de fluidos. Dichas fluctuaciones están, en último término, controladas por la hidrodinámica de la expulsión de los fluidos de deshidratación de la antigorita. La cristalización en condiciones de baja afinidad química de la reacción, correspondiente a la textura granofélsica, podría tener lugar si los fluidos

son drenados lentamente del frente de reacción. Durante el avance del frente de deshidratación, se aíslan también dominios sobrepresionados, en los que se preservan serpentinitas con antigorita de manera metaestable. En el caso de producirse deformación frágil tendría lugar un descenso brusco de la presión de fluidos y del desplazamiento del equilibrio de la antigorita hacia la asociación programa, que cristalizaría bajo condiciones de alta afinidad química (textura de tipo spinifex).

Origen de la recristalización de las harzburgitas con clorita. También se pueden encontrar evidencias de la deformación frágil antes mencionada en lo que se han denominado en este trabajo, Zonas de Reducción de Tamaño de Grano (GSRZ de sus siglas en inglés). Estas zonas, de potencia de milimétrica a métrica, forman estructuras conjugadas en las harzburgitas con cloritas. Tanto las texturas granofélsicas como las de tipo spinifex pueden estar parcialmente obliteradas por estas GSRZ. El análisis de la orientación cristalina preferente del olivino en las GSRZ que afecta a rocas con textura tipo spinifex, muestra un patrón muy similar, aunque más disperso con respecto a los dominios no deformados. Se ha puesto de manifiesto, igualmente, la presencia de dominios discretos de tamaño milimétrico a centimétrico con orientaciones cristalográficas relativamente uniformes que sugieren que los olivinos tipo spinifex se han heredado de la metaperidotita preexistente. Los ángulos de desorientación entre granos vecinos en las GSRZ están comprendidos entre los 5-10º y los 20º, pero las rotaciones entre ellos no están cristalográficamente controladas. Atendiendo a estas observaciones, la formación de las GSRZ es interpretada aquí como una consecuencia de la deformación frágil (microcraking) de las harzburgitas con clorita, probablemente producidas por hidrofracturación en condiciones de alta presión. Dicha hidrofracturación podría, por tanto, explicar las altas tasas de drenaje de fluidos de las zonas altamente metaestables, contribuyendo, de este modo, a producir las altas velocidades de reacción responsables de la formación de la textura de tipo spinifex.

Esta alternancia bimodal de la texturas granofélsicas y de tipo spinifex, junto con la presencia de GSRZ, constituyen, por tanto, un ejemplo único en el que se establece una interrelación entre la dinámica de la expulsión de los fluidos metamórficos y las velocidades de reacción y de cristalización en un sistema controlado por la deshidratación de la antigorita.

Deshidratación/fusión del anfíbol en el complejo de Jijal (Complejo del Paleo-arco de Kohistán, NO de Pakistán).

Metaestabilidad de las gabbronoritas con hornblenda en la corteza inferior de arcos de islas. En esta Tesis se presenta un estudio detallado de muestras compuestas de gabbronoritas con hornblenda y granulitas con granate que muestran la reacción 'congelada' de desestabilización del anfíbol y del ortopiroxeno. Dicho frente de reacción se encuentra como una zona de transición de 2-3 cm entre ambas litologías. En este frente de reacción, se preservan composiciones relictas de las asociaciones precursoras. La termobarometría mediante isopletas, obtenidas a partir de pseudosecciones (diagramas de fase calculados para una composición de roca específica), es coherente con la termobarometría convencional. Las presiones de equilibrio calculadas son de P ~ 1.1-1.2 GPa y T ~ 800-850 ºC para las granulitas con granate de la parte superior del Complejo de Jijal. Estas condiciones de presión y temperatura implican diferencias en

profundidad de hasta ≥ 12 km entre las condiciones de estabilidad de la grabronorita con hornblenda y el metamorfismo de alta presión que dio lugar a las granulitas con granate. Estas estimaciones de PT, junto con las consideraciones de los diagramas de fase, indican que la asociación de baja presión permaneció metaestable, debido probablemente a la ausencia persistente de fluidos/fundidos durante el soterramiento, hasta alcanzar las condiciones PT de la corteza inferior del arco. A estas profundidades la deshidratación-fusión del anfíbol, en condiciones de ausencia de fluido, permitió que se superaran las barreras cinéticas y que ocurriera la rápida transformación de la asociación metaestable en la asociación de alta presión (granulitas con grante sin ortopiroxeno).

Crecimiento epitaxial en las granulitas con granate. En esta Tesis se han estudiado los mecanismos microestructurales de crecimiento de granate en las granulitas mediente el uso combinado de las técnicas de EBSD y de TEM. A partir de los resultados obtenidos, se propone que el granate nucleó sobre el anfíbol produciendo una fuerte orientación cristalográfica preferente. Las granulitas preservan una foliación magmática del precursor (gabronorita con hornblenda) y se caracterizan por una ausencia casi total de deformación. Dos de los cuatro ejes <111> del granate se encuentran incluidos en el plano marcado por la foliación magmática, mientras que el máximo es subparalelo a la lineación magmática del precursor. La relación cristalográfica $<111>_{Grt}//[001]_{Opx,Cpx,Amp}$, deducida con EBSD, fue también confirmada mediante el uso de TEM. Las bruscas y discontinuas variaciones modales y composicionales observadas en el frente de reacción atestiguan la inhibición cinética de las reacciones progradas predichas mediante diagramas de fase en equilibrio.

Esta abrupta transformación de asociaciones de baja presión a asociaciones granulíticas de alta presión y más densas, posee importantes implicaciones para la estabilidad de la corteza inferior de arcos de islas, ya que puede inducir delaminación y diferenciación intracortical del arco.

13. References

Abers, G. A., MacKenzie, L. S., Rondenay, S., Zhang, Z., Wech, A. G. & Creager, K. C., 2009. Imaging the source region of Cascadia tremor and intermediate-depth earthquakes. *Geology*, **37**(12), 1119-1122.

Afonso, J. C., Fernàndez, M., Ranalli G, Griffin WL & JAD, C., 2008. Integrated geophysical-petrological modeling of the lithosphere and sublithospheric upper mantle: Methodology and applications. *Geochemistry, Geophysics, Geosystems*, **9**.

Ague, J. J., 2003. Fluid Flow in the Deep Crust. In: *Treatise on Geochemistry*, pp. 195-228, Pergamon, Oxford.

Aharonov, E., Whitehead, J. A., Kelemen, P. B. & Spiegelman, M., 1995. Channeling instability of upwelling melt in the mantle. *Journal of Geophysical Research*, **100**.

Alonso-Perez, R., Müntener, O. & Ulmer, P., 2009. Igneous garnet and amphibole fractionation in the roots of island arcs: experimental constraints on andesitic liquids. *Contributions to Mineralogy and Petrology*, **157**(4), 541-558.

Alt, J. C., Shanks, W. C., Bach, W., Paulick, H., Garrido, C. J. & Beaudoin, G., 2007. Hydrothermal alteration and microbial sulfate reduction in peridotite and gabbro exposed by detachment faulting at the Mid-Atlantic Ridge, 15 degrees 20 ' N (ODP Leg 209): A sulfur and oxygen isotope study. *Geochemistry, Geophysics, Geosystems*, **8**.

Allibone, A. H., Milan, L. A., Daczko, N. R. & Turnbull, I. M., 2009. Granulite facies thermal aureoles and metastable amphibolite facies assemblages adjacent to the Western Fiordland Orthogneiss in southwest Fiordland, New Zealand. *Journal of Metamorphic Geology*, **27**(5), 349-369.

Amelinckx, S. & Dekeyser, W., 1959. The structure and properties of grain boundaries. *Solid State Physics-Advances in Research and Applications*, **8**, 325-499.

Ancey, M., Bastenaire, F. & Tixier, R., 1978. Application des méthodes statistiques en microanalyse. In: *Microanalyse, microscopie électronique à balayage* (eds Maurice, F., Meny, L. & Tixier, R.), pp. 323-347, Les éditions du Physicien, Orsay.

Anczkiewicz, R., Burg, J. P., Villa, I. M. & Meier, M., 2000. Late Cretaceous blueschist metamorphism in the Indus suture zone, Shangla region, Pakistan Himalaya. *Tectonophysics*, **324**, 111-134.

Anczkiewicz, R., Thirlwall, M. & Platt, J., 2002. Influence of inclusions and leaching techniques on Sm-Nd and Lu-Hf garnet chronology. *Geochimica et Cosmochimica Acta*, **66**(15A), A19-A19.

Andersen, T. B., Mair, K., Austrheim, H., Podladchikov, Y. & Vrijmoed, J. C., 2008. Stress release in exhumed intermediate and deep earthquakes determined from ultramafic pseudotachylyte. *Geology* **36**, 995-998.

Andriessen, P. A. M., Hebeda, E. H., Simon, O. J. & Verschure, R. H., 1991. Tourmaline K-Ar ages compared with other radiometric dating systems in Alpine anatectic leucosomes and metamorphic rocks (Cyclades and southern Spain). *Chemical Geology*, **91**, 33-48.

Arai, S., 1975. Contact metamorphosed dunite-harzburgite Complex in the Chugoku district, western Japan. *Contributions to Mineralogy and Petrology*, **52**(1), 1-16.

Arcay, D., Doin, M. P., Tric, E., Bousquet, R. & de Capitani, C., 2006. Overriding plate thinning in subduction zones: Localized convection induced by slab dehydration. *Geochemistry, Geophysics, Geosystems*, **7**.

Arcay, D., Tric, E. & Doin, M. P., 2005. Numerical simulations of subduction zones Effect of slab dehydration on the mantle wedge dynamics. *Physics of the Earth and Planetary Interiors*, **149**, 133-153.

Arcay, D., Tric, E. & Doin, M. P., 2007. Slab surface temperature in subduction zones: Influence of the interplate decoupling depth and upper plate thinning processes. *Earth and Planetary Science Letters*, **255**(3-4), 324-338.

Arculus, R., J. & Wills, K., J,A., 1980. The petrology of plutonic blocks and inclusions from the Lesser Antilles Island Arc. *Journal of Petrology*, **21**(4), 743-799.

Arculus, R. J., Johnson, R. W., Chappell, B. W., McKee, C. O. & Sakai, H., 1983. Ophiolite-Contaminated Andesites, Trachybasalts, and Cognate Inclusions of Mount Lamington, Papua-New-Guinea - Anhydrite-Amphibole-Bearing Lavas and the 1951 Cumulodome. *Journal of Volcanology and Geothermal Research*, **18**(1-4), 215-247.

Ashworth, J. R. & Sheplev, V. S., 1997. Diffusion modelling of metamorphic layered coronas with stability criterion and consideration of affinity. *Geochimica et Cosmochimica Acta*, **61**, 3671-3689.

Ashworth, J. R., Sheplev, V. S., Bryxina, N. A., Kolobov, V. Y. & Reverdatto, V. V., 1998. Diffusion-controlled corona reaction and overstepping of equilibrium in a garnet granulite, Yenisey Ridge, Siberia. *Journal of Metamorphic Geology*, **16**(2), 231-246.

Asta, M., Beckermann, C., Karma, A., Kurz, W., Napolitano, R., Plapp, M., Purdy, G., Rappaz, M. & Trivedi, R., 2009. Solidification microstructures and solid-state parallels: Recent developments, future directions. *Acta Materialia*, **57**, 941-971.

Audet, P., Bostock, M. G., Christensen, N. I. & Peacock, S. M., 2009. Seismic evidence for overpressured subducted oceanic crust and megathrust fault sealing. *Nature*, **457**(7225), 76-78.

Augier, R., Agard, P., Monie, P., Jolivet, L., Robin, C. & Booth-Rea, G., 2005. Exhumation, doming and slab retreat in the Betic Cordillera (SE Spain): in situ Ar-

40/Ar-39 ages and P-T-d-t paths for the Nevado-Filabride Complex. *Journal of Metamorphic Geology*, **23**(5), 357-381.

Auzende, A.-L., Guillot, S., Devouard, B. & Baronnet, A., 2006. Serpentinites in an Alpine convergent setting: Effects of metamorphic grade and deformation on microstructures. *European Journal of Mineralogy*, **18**, 21-33.

Auzende, A. L., Devouard, B., Guillot, S., Daniel, I., Baronnet, A. & Lardeaux, J. M., 2002. Serpentinites from Central Cuba: petrology and HRTEM study. *European Journal of Mineralogy*, **14**(5), 905-914.

Azañón, J. M., Galindo-Zaldívar, J., García-Dueñas, V. & Jabaloy, A., 2002. Alpine Tectonics II: Betic Cordillera and Balearic Islands. In: *Geology of Spain* (eds Gibbons, W. & Moreno, T.), pp. 401-416, Geological Society, London.

Azañón, J. M. & Goffé, B., 1997. Ferro- and magnesiocarpholite assemblages as record of high-P, low-T metamorphism in the Central Alpujarrides, Betic Cordillera (SE Spain). *European Journal of Mineralogy*, **9**(5), 1035-1051.

Bach, W., Garrido, C. J., Paulick, H., Harvey, J. & Rosner, M., 2004. Seawater-peridotite interactions: First insights from ODP Leg 209, MAR 15 degrees N. *Geochemistry, Geophysics, Geosystems*, **5**.

Bach, W., Paulick, H., Garrido, C. J., Ildefonse, B., Meurer, W. P. & Humphris, S. E., 2006. Unraveling the sequence of serpentinization reactions: petrography, mineral chemistry, and petrophysics of serpentinites from MAR 15ºN (ODP Leg 209, Site 1274). *Geophysical Research Letters*, **33**(13).

Baker, J. & Holland, T. J. B., 1996. Experimental reversals of chlorite compositions in divariant $MgO+Al_2O_3+SiO_2+H_2O$ assemblages. *American Mineralogist*, **81**(5-6), 676-684.

Bakker, H. E., De Jong, K., Helmers, H. & Biermann, C., 1989. The geodynamic evolution of the Internal Zone of the Betic Cordilleras (south-east Spain): a model based on structural analysis and geothermobarometry. *Journal of Metamorphic Geology*, **7**(3), 359-381.

Bard, J.-P., 1983a. Metamorphic evolution of an obducted island arc: example of the Kohistan sequence (Pakistan) in the Himalayan collided range. *Geol. Bull. Univ. Peshawar*, **16**, 105-184.

Bard, J.-P., 1983b. Metamorphism of an obducted island arc: example of the Kohistan sequence (Pakistan) in the Himalayan collided range. *Earth and Planetary Science Letters*, **65**, 133-144.

Barrois, C. H. & Offert, A., 1889. Mémoire sur la constitution géologique du Sud de l'Andalousie, de la Sierra Tejeda à la Sierra Nevada. *Mémoires de l'Académie des Sciences*, **30**(2), 79-167.

Bascou, J., Tommasi, A. & Mainprice, D., 2002. Plastic deformation and development of clinopyroxene lattice preferred orientations in eclogites. *Journal of Structural Geology*, **24**(8), 1357-1368.

Baxter, E. F. & DePaolo, D. J., 2002. Field measurement of high temperature bulk reaction rates II: Interpretation of results from a field site near Simplon Pass, Switzerland. *American Journal of Science*, **302**(6), 465-516.

Bea, F., Montero, P. & Ortega, M., 2006. A LA-ICP-MS evaluation of Zr reservoirs in common crustal rocks: Implications for Zr and Hf geochemistry, and zircon-forming processes. *Canadian Mineralogist*, **44**, 693-714.

Bebout, G. E. & Barton, M. D., 1989. Fluid-flow and metasomatism in a subduction zone hydrothermal system - Catalina-Schist Terrane, California. *Geology*, **17**(11), 976-980.

Bebout, G. E. & Barton, M. D., 2002. Tectonic and metasomatic mixing in a high-T, subduction-zone mélange--insights into the geochemical evolution of the slab-mantle interface. *Chemical Geology*, **187**(1-2), 79-106.

Behn, M. D. & Kelemen, P. B., 2006. Stability of arc lower crust: Insights from the Talkeetna arc section, south central Alaska, and the seismic structure of modern arcs. *Journal of Geophysical Research-Solid Earth*, **111**(B11), 20.

Bell, D. R. & Rossman, G. R., 1992. Water in Earth's Mantle: The Role of Nominally Anhydrous Minerals. *Science*, **255**(5050), 1391-1397.

Berry, A. J., Hermann, J., O'Neill, H. S. C. & Foran, G. J., 2005. Fingerprinting the water site in mantle olivine. *Geology*, **33**(11), 869-872.

Blattner, P., 1976. Replacement of Hornblende by Garnet in Granulite Facies Assemblages near Milford-Sound, New-Zealand. *Contributions to Mineralogy and Petrology*, **55**(2), 181-190.

Blattner, P., 2005. Transport of low-aH_2O dehydration products to melt sites via reaction-zone networks, Milford Sound, New Zealand. *Journal of Metamorphic Geology*, **23**(7), 569-578.

Blumenthal, M., 1927. Versuch einer tektonischen Gliederung der Betischen Kordilleren von Central und Südwest Andalusien. *The Eclogae Geologicae Helvetiae*, **20**, 487-592.

Bodinier, J. L., Puga, E., Díaz de Federico, A., Leblanc, M. & Morten, L., 1993. Secondary harzburgites with spinifex-like textures in the Betic Ophiolitic Association (Southeastern Spain)(abstract). *Terra Abstract*, **5**, 3.

Bohlen, S. R. & Liotta, J. J., 1986. A Barometer for Garnet Amphibolites and Garnet Granulites. *Journal of Petrology*, **27**(5), 1025-1034.

Boillot, G., Feraud, G., Recq, M. & Girardeau, J., 1989. Undercrusting by serpentinite beneath rifted margins. *Nature*, **341**(6242), 523-525.

Booth-Rea, G., Azanon, J. M., Martinez-Martinez, J. M., Vidal, O. & Garcia-Duenas, V., 2005. Contrasting structural and P-T evolution of tectonic units in the southeastern Betics: Key for understanding the exhumation of the Alboran Domain HP/LT crustal rocks (western Mediterranean). *Tectonics*, **24**(2).

Bowen, N. L. & Tuttle, O. F., 1949. The system MgO—SiO2—H2O. *Geological Society of America Bulletin*, **60**(3), 439-460.

Brodie, K., Fettes, D., Harte, B. & Schmid, R., 2007. A systematic nomenclature for metamorphic rocks: 3. Structural terms including fault rock terms. In: *Recommendations by the IUGS Subcommission on the Systematics of Metamorphic Rocks. Recommendations, web version of 01.02.2007*.

Bromiley, G. D. & Pawley, A. R., 2003. The stability of antigorite in the systems MgO-SiO2-H2O (MSH) and MgO-Al2O3-SiO2-H2O (MASH): The effects of Al3+ substitution on high-pressure stability. *American Mineralogist*, **88**(1), 99-108.

Brown, E. H., 1996. High-pressure metamorphism caused by magma loading in Fiordland, New Zealand. *Journal of Metamorphic Geology*, **14**, 441-452.

Brown, E. H. & McClelland, W. C., 2000. Pluton emplacement by sheeting and vertical ballooning in part of the southeast Coast Plutonic Complex, British Columbia. *Geological Society of America Bulletin*, **112**, 708-719.

Brown, K. M., Tryon, M. D., DeShon, H. R., Dorman, L. M. & Schwartz, S. Y., 2005. Correlated transient fluid pulsing and seismic tremor in the Costa Rica subduction zone. *Earth and Planetary Science Letters*, **238**(1-2), 189-203.

Bunge, H. J., 1982. *Texture analysis in Materials Sciences*. Butterworths, London.

Burg, J.-P., Arbaret, L., Chaudhry, N., Dawood, H., Hussain, S. & Zeilinger, G., 2005. Shear strain localization from the upper mantle to the middle crust of the Kohistan arc (Pakistan), Geological Society of London.

Burg, J. P., Bodinier, J. L., Chaudhry, S., Hussain, S. & Dawood, H., 1998. Infra-arc mantle-crust transition and intra-arc mantle diapirs in the Kohistan Complex (Pakistani Himalaya); petro-structural evidence. *Terra Nova*, **10**(2), 74-80.

Burgos, J., Díaz de Federico, A., Morten, L. & Puga, E., 1980. The ultramafic rocks from the Cerro del Almirez, Sierra Nevada Complex, Betic Cordilleras, Spain: preliminary report. . *Cuadernos de Geología*, **11**, 157-165.

Capitani, G. & Mellini, M., 2004. The modulated crystal structure of antigorite: The m=17 polysome. *American Mineralogist*, **89**(1), 147-158.

Capitani, G. & Mellini, M., 2006. The crystal structure of a second antigorite polysome (m = 16), by single crystal synchrotron diffraction. *American Mineralogist*, **91**, 394-399.

Carlson, W. D., 1989. The significance of intergranular diffusion to the mechanisms and kinetics of porphyroblast crystallization. *Contributions to Mineralogy and Petrology*, **103**(1), 1-24.

Carlson, W. D., 1991. Competitive diffusion-controlled growth of porphyroblasts. *Mineralogical Magazine*, **55**(380), 317-330.

Carlson, W. D., 2002. Scales of disequilibrium and rates of equilibration during metamorphism. *American Mineralogist*, **87**(2-3), 185-204.

Carlson, W. D., Denison, C. & Ketcham, R. A., 1995. Controls on the nucleation and growth of porphyroblasts: Kinetics from natural textures and numerical models. *Geological Journal*, **30**(3-4), 207-225.

Carson, C. J., Clarke, G. L. & Powell, R., 2000. Hydration of eclogite, Pam Peninsula, New Caledonia. *Journal of Metamorphic Geology*, **18**(1), 79-90.

Carson, C. J., Powell, R. & Clarke, G. L., 1999. Calculated mineral equilibria for eclogites in CaO-Na_2O-FeO-MgO-Al_2O_3-SiO_2-H_2O: application to the Pouebo Terrane, Pam Peninsula, New Caledonia. *Journal of Metamorphic Geology*, **17**(1), 9-24.

Cesare, B., Poletti, E., Boiron, M.-C. & Cathelineau, M., 2001. Alpine metamorphism and veining in the Zentralgneis Complex of the SW Tauern Window: a model of fluid-rock interactions based on fluid inclusions. *Tectonophysics*, **336**(1-4), 121-136.

Clarke, G. L., Aitchison, J. C. & Cluzel, D., 1997. Eclogites and blueschists of the Pam Peninsula, NE New Caledonia: A reappraisal. *Journal of Petrology*, **38**(7), 843-876.

Clarke, G. L., Klepeis, K. A. & Daczko, N. R., 2000. Cretaceous high-P granulites at Milford Sound, New Zealand: metamorphic history and emplacement in a convergent margin setting. *Journal of Metamorphic Geology*, **18**(4), 359-374.

Clemens, J. D. & Watkins, J. M., 2001. The fluid regime of high-temperature metamorphism during granitoid magma genesis. *Contributions to Mineralogy and Petrology*, **140**(5), 600-606.

Cliff, G. & Lorimer, G. W., 1975. Quantitative-analysis of thin specimens. *Journal of Microscopy - Oxford*, **103**, 203-207.

Coe, R. S. & Kirby, S. H., 1975. Orthoenstatite To Clinoenstatite Transformation By Shearing And Reversion By Annealing - Mechanism And Potential Applications. *Contributions to Mineralogy and Petrology*, **52**(1), 29-55.

Coleman, R. G., Lee, D. E., Beatty, L. B. & Brannock, W. W., 1965. Eclogites and Eclogites - Their Differences and Similarities. *Geological Society of America Bulletin*, **76**(5), 483-508.

Comas, M. C., Platt, J. P., Soto, J. I. & Watts, A. B., 1999. The origin and tectonic history of the Alboran Basin: Insights from Leg 161 results. *Proceedings of the Ocean Drilling Program - Scientific Results*, **161**, 555-580.

Condie, K. C. & Chomiak, B., 1996. Continental accretion: contrasting Mesosoic and Early Proterozoic tectonic regimes in North America. *Tectonophysics*, **265**(1-2), 101-126.

Connolly, J., A. D. & Thompson, A., B. , 1989. Fluid and enthalpy production during regional metamorphism. *Contributions to Mineralogy and Petrology*, **102**(3), 347-366.

Connolly, J. A. D., 1990. Multivariable Phase-Diagrams - an Algorithm Based on Generalized Thermodynamics. *American Journal of Science*, **290**(6), 666-718.

Connolly, J. A. D., 1997. Devolatilization-generated fluid pressure and deformation-propagated fluid flow during prograde regional metamorphism *Journal of Geophysical Research*, **112**(B8), 18,149-18,173.

Connolly, J. A. D., 2005. Computation of phase equilibria by linear programming: A tool for geodynamic modeling and its application to subduction zone decarbonation. *Earth and Planetary Science Letters*, **236**(1-2), 524-541.

Connolly, J. A. D., 2009. The geodynamic equation of state: What and how. *Geochemistry, Geophysics, Geosystems*, **10**(10).

Connolly, J. A. D., 2010 (in press). The mechanics of metamorphic fluid expulsion. *Elements*.

Connolly, J. A. D. & Petrini, K., 2002. An automated strategy for calculation of phase diagram sections and retrieval of rock properties as a function of physical conditions. *Journal of Metamorphic Geology*, **20**(7), 697-708.

Connolly, J. A. D. & Podladchikov, Y., 1998. Compactation-driven fluid flow in viscoelastic rock. *Geodinamica Acta*, **11**(2-3), 55-84.

Connolly, J. A. D. & Podladchikov, Y., 2004. Fluid flow in compressive tectonic settings: Implications for midcrustal seismic reflectors and downward fluid migration. *Journal of Geophysical Research*, **109**(B04201).

Conrad, W. K. & Kay, R. W., 1984. Ultramafic and Mafic Inclusions from Adak-Island - Crystallization History, and Implications for the Nature of Primary Magmas and Crustal Evolution in the Aleutian Arc. *Journal of Petrology*, **25**(1), 88-125.

Costa, F., Dungan, M. A. & Singer, B. S., 2002. Hornblende- and phlogopite-bearing gabbroic xenoliths from Volcan San Pedro (36 degrees S), Chilean Andes: Evidence for melt and fluid migration and reactions in subduction-related plutons. *Journal of Petrology*, **43**(2), 219-241.

Coward, M. P., Rex, D. C., Khan, M. A., Windley, B. F., Broughton, R. D., Luff, I. W., Petterson, M. G. & Pudsey, C. J., 1986. Collision tectonics in the NW Himalayas. *Geological Society, London, Special Publications*, **19**(1), 203-219.

Currie, C. A., Wang, K., Hyndman, R. D. & He, J., 2004. The thermal effects of steady-state slab-driven mantle flow above a subducting plate: the Cascadia subduction zone and backarc. *Earth and Planetary Science Letters*, **223**(1-2), 35-48.

Chernosky, J. V., Day, H. W. & Caruso, L. J., 1985. Equilibria in the system MgO-SiO2-H2O - experimental-determination of the stability of Mg-anthophyllite. *American Mineralogist*, **70**(3-4), 223-236.

Christensen, N. I. & Fountain, D. M., 1975. Constitution of lower continental crust based on experimental studies of seismic velocities in granulite. *Geological Society of America Bulletin*, **86**, 227-236.

Daczko, N. R., Clarke, G. L. & Klepeis, K. A., 2001a. Transformation of two-pyroxene hornblende granulite to garnet granulite involving simultaneous melting and fracturing of the lower crust, Fiordland, New Zealand. *Journal of Metamorphic Geology*, **19**(5), 547-560.

Daczko, N. R., Clarke, G. L. & Klepeis, K. A., 2002. Kyanite-paragonite-bearing assemblages, northern Fiordland, New Zealand: rapid cooling of the lower crustal root to a Cretaceous magmatic arc. *Journal of Metamorphic Geology*, **20**(9), 887-902.

Daczko, N. R. & Halpin, J. A., 2009. Evidence for melt migration enhancing recrystallization of metastable assemblages in mafic lower crust, Fiordland, New Zealand. *Journal of Metamorphic Geology*, **27**(2), 167-185.

Daczko, N. R., Klepeis, K. A. & Clarke, G. L., 2001b. Evidence of Early Cretaceous collisional-style orogenesis in northern Fiordland, New Zealand and its effects on the evolution of the lower crust. *Journal of Structural Geology*, **23**(4), 693-713.

Daczko, N. R., Milan, L. A. & Halpin, J. A., 2009. Metastable persistence of pelitic metamorphic assemblages at the root of a Cretaceous magmatic arc – Fiordland, New Zealand. *Journal of Metamorphic Geology*, **27**(3), 233-247.

Dahlen, F. A., 1992. Metamorphism of nonhydrostatically stressed rocks. *American Journal of Science*, **292**, 184-198.

De Jong, K., 1993. The tectono-metamorphic evolution of the Veleta Complex and the development of the contact with the Mulhacen Complex (Betic Zone, SE Spain). *Geologie en Mijnbouw*, **71**, 227-237.

Denison, C. & Carlson, W. D., 1997. Three-dimensional quantitative textural analysis of metamorphic rocks using high-resolution computed X-ray tomography: Part II. Application to natural samples. *Journal of Metamorphic Geology*, **15**(1), 45-57.

Denison, C., Carlson, W. D. & Ketcham, R. A., 1997. Three-dimensional quantitative textural analysis of metamorphic rocks using high-resolution computed X-ray tomography: Part I. Methods and techniques. *Journal of Metamorphic Geology*, **15**(1), 29-44.

Dewey, J. F., Helman, M. L., Turco, E., Hutton, D. H. W. & Knott, S. D., 1989. Kinematics of the western Mediterranean. In: *Alpine Tectonics* (eds Coward, M. P., Dietrich, V. J. & Park, R. G.), pp. 265-283, Geological Special Publication.

Dewey, J. F., Pitman, W. C., III, Ryan, W. B. F. & Bonnin, J., 1973. Plate Tectonics and the Evolution of the Alpine System. *Geological Society of America Bulletin*, **84**(10), 3137-3180.

Dhuime, B., Bosch, D., Bodinier, J. L., Garrido, C. J., Bruguier, O., Hussain, S. S. & Dawood, H., 2007. Multistage evolution of the Jijal ultramafic-mafic Complex (Kohistan, N Pakistan): Implications for building the roots of island arcs. *Earth and Planetary Science Letters*, **261**(1-2), 179-200.

Dhuime, B., Bosch, D., Garrido, C. J., Bodinier, J.-L., Bruguier, O., Hussain, S. S. & Dawood, H., 2009. Geochemical Architecture of the Lower- to Middle-crustal Section of a Paleo-island Arc (Kohistan Complex, Jijal-Kamila Area, Northern Pakistan): Implications for the Evolution of an Oceanic Subduction Zone. *Journal of Petrology*, **50**(3), 531-569.

Diener, J. F. A., White, R. W. & Powell, R., 2008. Granulite facies metamorphism and subsolidus fluid-absent reworking, Strangways Range, Arunta Block, central Australia. *Journal of Metamorphic Geology*, **26**(6), 603-622.

Dobrzhinetskaya, L., Green, H. W. & Wang, S., 1996. Alpe Arami: A peridotite massif from depths of more than 300 kilometers. *Science*, **271**(5257), 1841-1845.

Donaldson, C. H., 1976. Experimental investigation of olivine morphology. *Contributions to Mineralogy and Petrology*, **57**, 187-213.

Dornbush, H. J., Weber, K. & Skrotzki, W., 1994. Development of microstructure and texture in high-temperature mylonites from the Ivrea Zone. In: *Textures of Geological Materials* (eds Burg, J. P., Siegesmund, D., Skrotzki, W. & Weber, K.), pp. 187-201, DGM Informationsgesellschaft, Oberursel

Eckert, J. O., Newton, R. C. & Kleppa, O. J., 1991. The Delta-H of Reaction and Recalibration of Garnet-Pyroxene-Plagioclase-Quartz Geobarometers in the Cmas System by Solution Calorimetry. *American Mineralogist*, **76**(1-2), 148-160.

Egeler, C. G., 1963. On the tectonics of the eastern Betic Cordilleras (SE Spain). *Geologische Rundschau*, **53**, 260-269.

Egeler, C. G. & Simon, O. J., 1969. Orogenic evolution of the Betic Zone (Betic Cordillera, Spain), with emphasis on the nappe structures. *Geologie En Mijnbouw*, **48**(3), 296-305.

Ellis, D. J. & Green, D. H., 1979. An experimental study of the effect of Ca upon garnet-clinopyroxene Fe-Mg exchange equilibria. *Contributions to Mineralogy and Petrology*, **71**(1), 13-22.

Evans, B., Johannes, W., Oterdoom, H. & Trommsdorff, V., 1976. Stability of crystotile and serpentinite in the serpentine multisystem. *Schweizerische Mineralogische Und Petrographische Mitteilungen*, **56**, 79-93.

Evans, B. W., 1977. Metamorphism of Alpine Peridotite and Serpentinite. *Annual Review of Earth and Planetary Sciences*, **5**(1), 397-447.

Evans, B. W., 2008. Control of the Products of Serpentinization by the Fe2+Mg-1 Exchange Potential of Olivine and Orthopyroxene. *Journal of Petrology*, **49**(10), 1873-1887.

Evans, B. W. & Trommsdorff, V., 1983. Fluorine hydroxyl titanian clinohumite in alpine recrystallized garnet peridotite: compositional controls and petrologic significance. *American Journal of Science*, **283-A**, 355-369.

Faure, F., Trolliard, G., Nicollet, C. & Montel, J.-M., 2003. A developmental model of olivine morphology as a function of the cooling rate and the degree of undercooling. *Contributions to Mineralogy and Petrology*, **145**(2), 251-263.

Feenstra, A. & Wunder, B., 2002. Dehydration of diasporite to corundite in nature and experiment. *Geology*, **30**(2), 119-122.

Fichaut, M., Marcelot, G. & Clocchiatti, R., 1989. Magmatology of Mt Pelee (Martinique, Fwi) .2. Petrology of Gabbroic and Dioritic Cumulates. *Journal of Volcanology and Geothermal Research*, 171-187.

Figlarz, M., Gerand, B., Delahaye-Vidal, A., Dumont, B., Harb, F., Coucou, A. & Fievet, F., 1990. Topotaxy, nucleation and growth. *Solid State Ionics*, **43**, 143-170.

Franz, L. & Harlov, D. E., 1998. High-grade K-feldspar veining in granulites from the Ivrea-Verbano Zone, northern Italy: Fluid flow in the lower crust and implications for granulite facies genesis. *Journal of Geology*, **106**(4), 455-472.

Frost, R., 1975. Contact Metamorphism of Serpentinite, Chloritic Blackwall and Rodingite at Paddy-Go-Easy Pass, Central Cascades, Washington. *Journal of Petrology*, **16**(2), 272-313.

Fullea, J., Afonso, J. C., Connolly, J. A. D., Fernández, M., García-Castellanos, D. & Zeyen, H., 2009. LitMod3D: An interactive 3-D software to model the thermal, compositional, density, seismological, and rheological structure of the lithosphere and sublithospheric upper mantle. *Geochemistry, Geophysics, Geosystems*, **10**(8).

Fumagalli, P. & Poli, S., 2005. Experimentally Determined Phase Relations in Hydrous Peridotites to 6.5 GPa and their Consequences on the Dynamics of Subduction Zones. *Journal of Petrology*, **46**(3), 555-578.

Furukawa, Y., 1993. Depth of the decoupling plate interface and thermal structure under arcs. *Journal of Geophysical Research-Solid Earth*, **98**(B11), 20005-20013.

Furukawa, Y., 2009. Convergence of aqueous fluid at the corner of the mantle wedge: Implications for a generation mechanism of deep low-frequency earthquakes. *Tectonophysics*, **469**(1-4), 85-92.

Fyfe, W. S., 1973a. Dehydration reactions. *American Association of Petroleum Geologists Bulletin*, **57**, 190-197.

Fyfe, W. S., 1973b. Granulite facies partial melting and archaean crust. *Philosophical Transactions of the Royal Society of London Series A-Mathematical Physical and Engineering Sciences* **273**, 457-461.

Gaidies, F., Abart, R., De Capitani, C., Schuster, R., Connolly, J. A. D. & Reusser, E., 2006. Characterization of polymetamorphism in the Austroalpine basement east of the Tauern Window using garnet isopleth thermobarometry. *Journal of Metamorphic Geology*, **24**(6), 451-475.

Galindo-Zaldívar, J., González-Lodeiro, F. & Jabaloy, A., 1989. Progressive extensional shear structures in a detachment contact in the western Sierra Nevada (Betic Cordilleras, Spain). *Geodinámica Acta*, **3**, 73-85.

Ganguly, J. & Saxena, S. K., 1984. Mixing Properties of Aluminosilicate Garnets - Constraints from Natural and Experimental-Data, and Applications to Geothermo-Barometry. *American Mineralogist*, **69**(1-2), 88-97.

Garcia-Casco, A., Torres-Roldan, R. L., Millan, G., Monie, P. & Schneider, J., 2002. Oscillatory zoning in eclogitic garnet and amphibole, Northern Serpentinite Melange, Cuba: a record of tectonic instability during subduction? *Journal of Metamorphic Geology*, **20**(6), 581-598.

Garrido, C. J., Bodinier, J.-L., Burg, J.-P., Zeilinger, G., Hussain, S. S., Dawood, H., Chaudhry, M. N. & Gervilla, F., 2006. Petrogenesis of Mafic Garnet Granulite in the Lower Crust of the Kohistan Paleo-arc Complex (Northern Pakistan): Implications for Intra-crustal Differentiation of Island Arcs and Generation of Continental Crust. *Journal of Petrology*, **47**(10), 1873-1914.

Garrido, C. J., Bodinier, J. L., Dhuirne, B., Bosch, D., Chanefo, I., Bruguier, O., Hussain, S. S., Dawood, H. & Burg, J. P., 2007. Origin of the island arc Moho transition zone via melt-rock reaction and its implications for intracrustal differentiation of island arcs: Evidence from the Jijal Complex (Kohistan Complex, northern Pakistan). *Geology*, **35**(8), 683-686.

Garrido, C. J., López Sánchez-Vizcaíno, V., Gómez-Pugnaire, M. T., Trommsdorff, V., Alard, O., Bodinier, J. L. & Godard, M., 2005. Enrichment of HFSE in chlorite-harzburgite produced by high-pressure dehydration of antigorite-serpentinite: Implications for subduction magmatism. *Geochemistry, Geophysics, Geosystems*, **6**, -.

Gerya, T., Connolly, J. A. D. & Yuen, D. A., 2008. Why is terrestrial subduction one-sided? *Geology* **36**(1), 43-46.

Gerya, T. & Stockhert, B., 2006. Two-dimensional numerical modeling of tectonic and metamorphic histories at active continental margins. *International Journal of Earth Sciences*, **95**, 250-274.

Gerya, T. V., Stockhert, B. & Perchuk, A. L., 2002. Exhumation of high-pressure metamorphic rocks in a subduction channel: A numerical simulation. *Tectonics*, **21**(6).

Gerya, T. V. & Yuen, D. A., 2003. Rayleigh-Taylor instabilities from hydration and melting propel 'cold plumes' at subduction zones. *Earth and Planetary Science Letters*, **212**(1-2), 47-62.

Goldsmith, R., 1959. Granofels, a new metamorphic rock name. *Journal of Geology*, **67**(1), 109-110.

Gómez-Pugnaire, M. T., Braga, J. C., Martin, J. M., Sassi, F. P. & Del Moro, A., 2000. Regional implications of a Palaeozoic age for the Nevado-Filabride Cover of the Betic Cordillera, Spain. *Schweizerische Mineralogische Und Petrographische Mitteilungen*, **80**(1), 45-52.

Gómez-Pugnaire, M. T., Chacón, J., Mitrofanov, F. & Timofeev, V., 1982. First report on pre-Cambrian roks in the graphite-bearing series of the Nevado-Filabride Complex (Betic Cordilleras, Spain). *Neues Jahrbuch Fur Geologie Und Palaontologie-Abhandlungen*, **3**, 176-180.

Gómez-Pugnaire, M. T. & Fernández-Soler, J. M., 1987. High-pressure metamorphism in metabasites from the Betic Cordilleras (S.E. Spain) and its evolution during the Alpine orogeny. *Contributions to Mineralogy and Petrology*, **95**(2), 231-244.

Gómez-Pugnaire, M. T. & Franz, G., 1988. Metamorphic evolution of the palaezoic series of the Betic Cordillera (Nevado-Filabride Complex, SE Spain) and its relationship with the alpine orogeny. *Geologische Rundschau*, **77**(3), 619-640.

Gómez-Pugnaire, M. T., Franz, G. & López Sánchez-Vizcaíno, V., 1994. Retrograde formation of NaCl-scapolite in high pressure metaevaporites from the Cordilleras Béticas (Spain). *Contributions to Mineralogy and Petrology*, **116**(4), 448-461.

Gómez-Pugnaire, M. T., Galindo-Zaldivar, J., Rubatto, D., Gonzalez-Lodeiro, F., Sanchez-Vizcaino, V. L. & Jabaloy, A., 2004. A reinterpretation of the Nevado-Filabride and Alpujarride Complexes (Betic Cordillera): field, petrography and U-Pb ages from orthogneisses (western Sierra Nevada, S Spain). *Schweizerische Mineralogische Und Petrographische Mitteilungen*, **84**(3), 303-322.

González-Lodeiro, F., Aldaya, F., Galindo-Zaldívar, J. & Jabaloy, A., 1996. Superposition of extensional detachments during the Neogene in the internal zones of the Betic cordilleras. *International Journal of Earth Sciences*, **85**(2), 350-362.

Grant, J. A., 2009. Thermocalc and experimental modelling of melting of pelite, Morton Pass, Wyoming. *Journal of Metamorphic Geology*, **27**(8), 571-578.

Green, H. W., Dobrzhinetskaya, L. & Bozhilov, K., 1997. Response to determining the origin of ultrahigh-pressure lherzolites. *Science*, **278**, 704-707.

Grobéty, B., 2003. Polytypes and higher-order structures of antigorite: A TEM study. *American Mineralogist*, **88**(1), 27-36.

Gueguen, Y. & Palciauskas, V., 1994. *Introduction to the Physics of Rocks*. Princeton University Press, Princeton.

Guillot, S., Hattori, K. H. & de Sigoyer, J., 2000. Mantle wedge serpentinization and exhumation of eclogites: Insights from eastern Ladakh, northwest Himalaya. *Geology*, **28**(3), 199-202.

Guillot, S., Hattori, K. H., de Sigoyer, J., Nagler, T. & Auzende, A. L., 2001. Evidence of hydration of the mantle wedge and its role in the exhumation of eclogites. *Earth and Planetary Science Letters*, **193**(1-2), 115-127.

Guiraud, M., Powell, R. & Cottin, J. Y., 1996. Hydration of orthopyroxene-cordierite-bearing assemblages at Laouni, Central Hoggar, Algeria. *Journal of Metamorphic Geology*, **14**(4), 467-476.

Hacker, B. R., 1997. Diagenesis and fault valve seismicity of crustal faults. *Journal of Geophysical Research*, **102**.

Hacker, B. R., 2008. H_2O subduction beyond arcs. *Geochemistry, Geophysics, Geosystems*, **9**.

Hacker, B. R., Mehl, L., Kelemen, P. B., Rioux, M., Behn, M. D. & Luffi, P., 2008. Reconstruction of the Talkeetna intraoceanic arc of Alaska through

thermobarometry. *Journal of Geophysical Research-Solid Earth*, **113**(B3).

Hacker, B. R., Peacock, S. M., Abers, G. A. & Holloway, S. D., 2003. Subduction factory - 2. Are intermediate-depth earthquakes in subducting slabs linked to metamorphic dehydration reactions? *Journal of Geophysical Research-Solid Earth*, **108**(B1), art. no.-2030.

Harley, S. L., 1987. Origin and Growth of Continents. *Nature*, **329**(6135), 108-109.

Harlov, D. E. & Forster, H.-J., 2002. High-Grade Fluid Metasomatism on both a Local and a Regional Scale: the Seward Peninsula, Alaska, and the Val Strona di Omegna, Ivrea-Verbano Zone, Northern Italy. Part I: Petrography and Silicate Mineral Chemistry. *Journal of Petrology*, **43**(5), 769-799.

Harlov, D. E., Hansen, E. C. & Bigler, C., 1998. Petrologic evidence for K-feldspar metasomatism in granulite facies rocks. *Chemical Geology*, **151**(1-4), 373-386.

Harlov, D. E. & Wirth, R., 2000. K-feldspar-quartz and K-feldspar-plagioclase phase boundary interactions in garnet-orthopyroxene gneiss's from the Val Strona di Omegna, Ivrea-Verbano Zone, northern Italy. *Contributions to Mineralogy and Petrology*, **140**(2), 148-162.

Hartel, T. H. D. & Pattison, D. R. M., 1996. Genesis of the Kapuskasing (Ontario) migmatitic mafic granulites by dehydration melting of amphibolite: The importance of quartz to reaction progress. *Journal of Metamorphic Geology*, **14**(5), 591-611.

Hartman, P. & Perdok, W. G., 1955. On the relations between structure and morphology of crystals. *Acta Crystallographica*, **8**, 49-52.

Healy, D., Reddy, S. M., Timms, N. E., Gray, E. M. & Brovarone, A. V., 2009. Trench-parallel fast axes of seismic anisotropy due to fluid-filled cracks in subducting slabs. *Earth and Planetary Science Letters*, **283**(1-4), 75-86.

Hermann, J., Gerald, J. D. F., Malaspina, N., Berry, A. J. & Scambelluri, M., 2007. OH-bearing planar defects in olivine produced by the breakdown of Ti-rich humite minerals from Dabie Shan (China). *Contributions to Mineralogy and Petrology*, **153**(4), 417-428.

Hermann, J., Müntener, O. & Scambelluri, M., 2000. The importance of serpentinite mylonites for subduction and exhumation of oceanic crust. *Tectonophysics*, **327**(3-4), 225-238.

Hermann, J., Spandler, C., Hack, A. & Korsakov, A. V., 2006. Aqueous fluids and hydrous melts in high-pressure and ultra-high pressure rocks: Implications for element transfer in subduction zones. *Lithos*, **92**(3-4), 399-417.

Hermann, J. & Spandler, C. J., 2008. Sediment Melts at Sub-arc Depths: an Experimental Study. *Journal of Petrology*, **49**(4), 717-740.

Hibiya, T. & Görnert, P., 2007. Liquid phase epitaxy of garnets. In: *Liquid Phase Epitaxy of Electronic, Optical and Optoelectronic Materials* (eds Capper, P. & Mauk, M.), pp. 305-337, John Wiley & Sons, London.

Hilairet, N., Daniel, I. & Reynard, B., 2006a. Equation of state of antigorite, stability field of serpentines, and seismicity in subduction zones. *Geophysical Research Letters*, **33**(2).

Hilairet, N., Daniel, I. & Reynard, B., 2006b. P-V Equations of State and the relative stabilities of serpentine varieties. *Physics and Chemistry of Minerals*, **33**, 629-637.

Hilairet, N., Reynard, B., Wang, Y. B., Daniel, I., Merkel, S., Nishiyama, N. & Petitgirard, S., 2007. High-pressure creep of serpentine, interseismic deformation, and initiation of subduction. *Science*, **318**, 1910-1913.

Hirsch, D. M., Prior, D. J. & Carlson, W. D., 2003. An overgrowth model to explain multiple, dispersed high-Mn regions in the cores of garnet porphyroblasts. *American Mineralogist*, **88**(1), 131-141.

Hirth, G. & Kohlstedt, D. L., 1996. Water in the oceanic upper mantle: implications for rheology, melt extraction and the evolution of the lithosphere. *Earth and Planetary Science Letters*, **144**(1-2), 93-108.

Holness, M. B. & Watt, G. R., 2001. Quartz recrystallization and fluid flow during contact metamorphism: a cathodoluminescence study. *Geofluids*, **1**(3), 215-228.

Holtzman, B. K., Kohlstedt, D. L., Zimmerman, M. E., Heidelbach, F., Hiraga, T. & Hustoft, J., 2003. Melt Segregation and Strain Partitioning: Implications for Seismic Anisotropy and Mantle Flow. *Science*, **301**(5637), 1227-1230.

Holland, T. & Powell, R., 1991. A Compensated-Redlich-Kwong (CORK) equation for volumes and fugacities of CO2 and H2O in the range 1 bar to 50 kbar and 100–1600°C. *Contributions to Mineralogy and Petrology*, **109**(2), 265-273.

Holland, T. & Powell, R., 2001. Calculation of phase relations involving haplogranitic melts using an internally consistent thermodynamic dataset. *Journal of Petrology*, **42**(4), 673-683.

Holland, T. J. B. & Powell, R., 1998. An internally consistent thermodynamic data set for phases of petrological interest. *Journal of Metamorphic Geology*, **16**, 309-343.

Honda, S. & Saito, M., 2003. Small-scale convection under the back-arc occurring in the low viscosity wedge. *Earth and Planetary Science Letters*, **216**(4), 703-715.

Hürlimann, R., 1999. *Die Hochdruckmetamorphose der Ultramafika und der angrenzenden Nebengesteine am Cerro de Almirez, Sierra Nevada, Su¨ dspanien. Teil II. Unpublished Diplomarbeit.*, ETH, Zürich.

IGME, 1981. Mapa Geológico de España escala 1/50,000 (MAGNA). Hoja núm. 1028 Instituto Geológico y Minero de España.

Indares, A. D., 2003. Metamorphic textures and P-T evolution of high-P granulites from the Lelukuau terrane, NE Grenville Province. *Journal of Metamorphic Geology*, **21**, 35-48.

Indares, A. D. & Martignole, J., 2003. Towards the upper limits of the granulite facies. *Journal of Metamorphic Geology*, **21**(1-2).

Irving, A. J. & Ashley, P. M., 1976. Amphibole-olivine-spinel, cordierite-anthophyllite and related hornfelses associated with metamorphosed serpentinites in the goobarragandra district, near Tumut, New South Wales. *Australian Journal of Earth Sciences*, **23**(1), 19 - 43.

Iwamori, H. & Zhao, D. P., 2000. Melting and seismic structure beneath the northeast Japan arc. *Geophysical Research Letters*, **27**(3), 425-428.

Jabaloy, A., 1993. *La estructura de la región occidental de la Sierra de los Filabres (Cordilleras Béticas): mapas y cortes geológicos*, Universidad de Granada, Granada.

Jabaloy, A., Galindo-Zaldivar, J. & González-Lodeiro, F., 1993. The Alpujárride-Nevado-Filábride extensional shear zone, Betic Cordillera, SE Spain. *Journal of Structural Geology*, **15**(3-5), 555-569.

Jamtveit, B. & Andersen, T. B., 1992. Morphological instabilities during rapid growth of metamorphic garnets. *Physics and Chemistry of Minerals*, **19**(3), 176-184.

Jamtveit, B., Malthe-Sorenssen, A. & Kostenko, O., 2008. Reaction enhanced permeability during retrogressive metamorphism. *Earth and Planetary Science Letters*, **267**(3-4), 620-627.

Jamtveit, B., Putnis, C. & Malthe-Sørenssen, A., 2009. Reaction induced fracturing during replacement processes. *Contributions to Mineralogy and Petrology*, **157**(1), 127-133.

Jan, M. Q., 1979. Petrography of the Jijal Complex, Kohistan. In: *Geology of Kohistan, Karakoram Himalaya, Northern Pakistan* (eds Tahirkheli, R. A. K. & Jan, M. Q.) *Special issue of the Geological Bulletin*, pp. 31-49, University of Peshawar, Peshawar.

Jan, M. Q. & Howie, R. A., 1981. The Mineralogy and Geochemistry of the Metamorphosed Basic and Ultrabasic Rocks of the Jijal Complex, Kohistan, Nw Pakistan. *Journal of Petrology*, **22**(1), 85-126.

Jan, M. Q. & Windley, B. F., 1990. Chromian Spinel Silicate Chemistry in Ultramafic Rocks of the Jijal Complex, Northwest Pakistan. *Journal of Petrology*, **31**(3), 667-715.

Jansen, H., 1936. *De Geologie van de Sierra de Baza en van aagrenzende gebieden der Sierra Nevada en Sierra de los Filabre (Zuid-Spanje)*, Amsterdam, Amsterdam.

Jenkins, D. M., 1981. Experimental phase relations of hydrous peridotites modelled in the system H2O-CaO-MgO-Al2O3,-SiO2. *Contributions to Mineralogy and Petrology*, **77**(2), 166-176.

Jessell, M. W., Kostenko, O. & Jamtveit, B., 2003. The preservation potential of microstructures during static grain growth. *Journal of Metamorphic Geology*, **21**(5), 481-491.

Jochum, 2006. MPI-DING reference glasses for in situ microanalysis: New reference values for element concentrations and isotope ratios. *Geochemistry, Geophysics, Geosystems*, **7**(2).

Johannes, W., 1975. Zur synthese and thermischen stabilität von antigorite. *Fortschritte Der Mineralogie*, **53**, 36.

Johannes, W. & Koepke, J., 2001. Incomplete reaction of plagioclase in experimental dehydration melting of amphibolite. *Australian Journal of Earth Sciences*, **48**(4), 581-590.

John, T., Scherer, E. E., Haase, K. & Schenk, V., 2004. Trace element fractionation during fluid-induced eclogitization in a subducting slab: trace element and Lu-Hf-Sm-Nd isotope systematics. *Earth and Planetary Science Letters*, **227**(3-4), 441-456.

Jull, M. & Kelemen, P. B., 2001. On the conditions for lower crustal convective instability. *Journal of Geophysical Research-Solid Earth*, **106**(B4), 6423-6446.

Kawakatsu, H. & Watada, S., 2007. Seismic evidence for deep-water transportation in the mantle. *Science*, **316**(5830), 1468-1471.

Kawamoto, T. & Holloway, J. R., 1997. Melting temperature and partial melt chemistry of H_2O-saturated mantle peridotite to 11 Gigapascals. *Science*, **276**(5310), 240-243.

Kelemen, P. B., 1995. Genesis of High Mg-Number Andesites and the Continental-Crust. *Contributions to Mineralogy and Petrology*, **120**(1), 1-19.

Kelemen, P. B., Rilling, J. L., Parmentier, E. M., Mehl, L. & Hacker, B. R., 2003. Thermal structure due to solid-state flow in the mantle wedge beneath arcs. In: *Inside the Subduction Factory* (ed Eiler, J. M.) *AGU Monographs*, American Geophysical Union, Washington DC.

Kelsey, D. E., White, R. W. & Powell, R., 2003a. Orthopyroxene-sillimanite-quartz assemblages: distribution, petrology, quantitative P-T-X constraints and P-T paths. *Journal of Metamorphic Geology*, **21**(5), 439-453.

Kelsey, D. E., White, R. W., Powell, R., Wilson, C. J. L. & Quinn, C. D., 2003b. New constraints on metamorphism in the Rauer Group, Prydz Bay, east Antarctica. *Journal of Metamorphic Geology*, **21**(8), 739-759.

Ketcham, R. A., 2005. Three-dimensional grain fabric measurements using high-resolution X-ray computed tomography. *Journal of Structural Geology*, **27**(7), 1217-1228.

King, R. L. & Bebout, G. E., 2006. Metamorphic evolution along the slab/mantle interface within subduction zones. *Geochimica et Cosmochimica Acta*, **70**(18), A319-A319.

Kirby, S. H., Durham, W. B. & Stern, L. A., 1991. Mantle phase changes and deep-earthquake faulting in subducting lithosphere. *Science*, **252**, 216-225.

Kirby, S. H., Stein, S., Okal, E. A. & Rubie, D. C., 1996. Metastable mantle phase transformations and deep earthquakes in subducting oceanic lithosphere. *Reviews of Geophysics*, **34**(2), 261-306.

Kirkpatrick, R. J., 1981. Kinetics of crystallization of igneous rocks. In: *Kinetics of Geochemical Processes*

(eds Lasaga, A. C. & Kirkpatrrick, R. J.), pp. 321-398, Mineralogical Society of America, Washington, DC.

Kitamura, M., Kondoh, S., Morimoto, N., Miller, G. H., Rossman, G. R. & Putnis, A., 1987. Planar OH-bearing defects in mantle olivine. *Nature*, **328**(6126), 143-145.

Kleinschrodt, R. & Duyster, J. P., 2002. HT-deformation of garnet: an EBSD study on granulites from Sri Lanka, India and the Ivrea Zone. *Journal of Structural Geology*, **24**(11), 1829-1844.

Kleinschrodt, R. & McGrew, A., 2000. Garnet plasticity in the lower continental crust: implications for deformation mechanisms based on microstructures and SEM-electron channeling pattern analysis. *Journal of Structural Geology*, **22**(6), 795-809.

Ko, S.-C., Olgaard, D. L. & Wong, T.-F., 1997. Generation and maintenance of pore pressure excess in a dehydrating system: 1. Experimental and microstructural observations. *Journal of Geophysical Research*, **102**, 825-839.

Kodaira, S., Iidaka, T., Kato, A., Park, J.-O., Iwasaki, T. & Kaneda, Y., 2004. High Pore Fluid Pressure May Cause Silent Slip in the Nankai Trough. *Science*, **304**(5675), 1295-1298.

Kohlstedt, D. L., Goetze, C., Durham, W. B. & Vandersande, J., 1976. New Technique For Decorating Dislocations In Olivine. *Science*, **191**(4231), 1045-1046.

Koss, M. B., LaCombe, J. C., Chait, A., Pines, V., Zlatkowski, M., Glicksman, M. E. & Kar, P., 2005. Pressure-mediated effects on thermal dendrites. *Journal of Crystal Growth*, **279**, 170-185.

Kostenko, O., Jamtveit, B., Austrheim, H., Pollok, K. & Putnis, C., 2002. The mechanism of fluid infiltration in peridotites at Almklovdalen, western Norway. *Geofluids*, **2**(3), 203-215.

Kovacs, I., Hermann, J., O'Neill, H. S. C., Gerald, J. F., Sambridge, M. & Horvath, G., 2008. Quantitative absorbance spectroscopy with unpolarized light: Part II. Experimental evaluation and development of a protocol for quantitative analysis of mineral IR spectra. *American Mineralogist*, **93**(5-6), 765-778.

Kretz, R., 1969. On the spatial distribution of crystals in rocks. *Lithos*, **2**(1), 39-65.

Kretz, R., 1983. Symbols for Rock-Forming Minerals. *American Mineralogist*, **68**(1-2), 277-279.

Kuroda, T., Irisawa, T. & Ookawa, A., 1987. Transition from polyhedral to dendritic morphology. In: *Morphology of Crystals* (ed Sunagawa, I.), pp. 589-612, Terra Scientific Publishing, Tokyo.

La Rocca, M., Creager, K. C., Galluzzo, D., Malone, S., Vidale, J. E., Sweet, J. R. & Wech, A. G., 2009. Cascadia Tremor Located Near Plate Interface Constrained by S Minus P Wave Times. *Science*, **323**(5914), 620-623.

Lafuste, J. & Pavillon, M. J., 1976. Discovery of Eifelian fossils in internal zones - metamorphic series of Cordilleres Betiques (Southern Spain) - importance of this stratigraphical data. *Comptes Rendus Hebdomadaires Des Seances De L Academie Des Sciences Serie D*, **283**(9), 1015-1018.

Lagabrielle, Y. & Bodinier, J.-L., 2008. Submarine reworking of exhumed subcontinental mantle rocks: field evidence from the Lherz peridotites, French Pyrenees. *Terra Nova*, **20**(1), 11-21.

Lallemand, S., 1999. *La subduction Océanique.* Gordon and Breach Science Publishers, London.

Lamoureux, G., Ildefonse, B. & Mainprice, D., 1999. Modelling the seismic properties of fast-spreading ridge crustal Low-Velocity Zones: insights from Oman gabbro textures. *Tectonophysics*, **312**(283-301).

Lasaga, A. C., 1998. *Kinetic Theory in the Earth Sciences* Princeton University Press, Princeton, NJ.

Le Gleuher, M., Livi, K. J. T., Veblen, D. R., Noack, Y. & Amouric, M., 1990. Serpentinization of enstatite from Pernes, France - reaction microstructures and the role of system openness. *American Mineralogist*, **75**(7-8), 813-824.

Le Roux, V., Tommasi, A. & Vauchez, A., 2008. Feedback between melt percolation and deformation in an exhumed lithosphere-asthenosphere boundary. *Earth and Planetary Science Letters*, **274**(3-4), 401-413.

Leake, B. E., Woolley, A. R., Arps, C. E. S., Birch, W. D., Gilbert, M. C., Grice, J. D., Hawthorne, F. C., Kato, A., Kisch, H. J., Krivovichev, V. G., Linthout, K., Laird, J., Mandarino, J. A., Maresch, W. V., Nickel, E. H., Rock, N. M. S., Schumacher, J. C., Smith, D. C., Stephenson, N. C. N., Ungaretti, L., Whittaker, E. J. W. & Guo, Y. Z., 1997. Nomenclature of amphiboles: Report of the subcommittee on amphiboles of the International Mineralogical Association, commission on new minerals and mineral names. *American Mineralogist*, **82**(9-10), 1019-1037.

López Sánchez-Vizcaíno, V., 1994. *Evolución petrológica y geoquímica de las rocas carbonáticas y litologías asociadas en el área de Macael-Cóbdar (Almería), Complejo Nevado-Filábride, Cordilleras Béticas, SE España.*, Universidad de Granada, Granada.

López Sánchez-Vizcaíno, V., Gómez-Pugnaire, M. T., Garrido, C. J., Padrón-Navarta, J. A. & Mellini, M., 2009. Breakdown mechanisms of titanclinohumite in antigorite serpentinite (Cerro del Almirez massif, S. Spain): A petrological and TEM study. *Lithos*, **107**, 216-226.

López Sánchez-Vizcaíno, V., Rubatto, D., Gómez-Pugnaire, M. T., Trommsdorff, V. & Müntener, O., 2001. Middle Miocene high-pressure metamorphism and fast exhumation of the Nevado-Filabride Complex, SE Spain. *Terra Nova*, **13**(5), 327-332.

López Sánchez-Vizcaíno, V., Trommsdorff, V., Gómez-Pugnaire, M. T., Garrido, C. J., Müntener, O. & Connolly, J. A. D., 2005. Petrology of titanian clinohumite and olivine at the high-pressure breakdown of antigorite serpentinite to chlorite harzburgite (Almirez Massif, S. Spain). *Contributions to Mineralogy and Petrology*, **149**(6), 627-646.

Lund, M. G. & Austrheim, H., 2003. High-pressure metamorphism and deep-crustal seismicity: evidence

from contemporaneous formation of pseudotachylytes and eclogite facies coronas. *Tectonophysics*, **372**(1-2), 59-83.

Lyubetskaya, T. & Ague, J. J., 2009. Effect of metamorphic reactions on thermal evolution in collisional orogens. *Journal of Metamorphic Geology*, **27**, 579-600.

Mackwell, S. J., Kohlstedt, D. L. & Paterson, M. S., 1985. The Role of Water in the Deformation of Olivine Single Crystals. *Journal of Geophysical Research*, **90**.

Mainprice, D., 1990. A FORTRAN program to calculate seismic anisotropy from the lattice preferred orientation of minerals. *Computers & Geosciences*, **16**(3), 385-393.

Mainprice, D., 2007. ftp://www.gm.univ-montp2.fr/mainprice//CareWare_Unicef_Programs/.

Mainprice, D., Bascou, J., Cordier, P. & Tommasi, A., 2004. Crystal preferred orientations of garnet: comparison between numerical simulations and electron back-scattered diffraction (EBSD) measurements in naturally deformed eclogites. *Journal of Structural Geology*, **26**(11), 2089-2102.

Mainprice, D. & Humbert, M., 1994. Methods Of Calculating Petrophysical Properties From Lattice Preferred Orientation Data. *Surveys in Geophysics*, **15**(5), 575-592.

Mainprice, D. & Silver, P. G., 1993. Interpretation of SKS-waves using samples from the subcontinental lithosphere. *Physics of The Earth and Planetary Interiors*, **78**(3-4), 257-280.

Malaspina, N., Hermann, J. & Scambelluri, M., 2009. Fluid/mineral interaction in UHP garnet peridotite. *Lithos*, **107**(1-2), 38-52.

Manning, C. E., 1994a. Fractal clustering of metamorphic veins. *Geology* **22**, 335-338.

Manning, C. E., 1994b. The solubility of quartz in H_2O in the lower crust and upper mantle. *Geochimica et Cosmochimica Acta*, **58**(22), 4831-4839.

Manning, C. E., 1995. Phase-Equilibrium controls on SiO_2: Metasomatism by Aqueous Fluid in subduction zones: reaction at constant pressure and temperature. *International Geology Review*, **37**, 1074-1093.

Manning, C. E., 2004. The chemistry of subduction-zone fluids. *Earth and Planetary Science Letters*, **223**(1-2), 1-16.

Marchesi, C., Garrido, C., Godard, M., Proenza, J., Gervilla, F. & Blanco-Moreno, J., 2006. Petrogenesis of highly depleted peridotites and gabbroic rocks from the Mayarí-Baracoa Ophiolitic Belt (eastern Cuba). *Contributions to Mineralogy and Petrology*, **151**(6), 717-736.

Markov, I., 1995. *Crystal Growth for Beginners. Fundamentals of Nucleation, Crystal Growth and Epitaxy*. World Scientific, Singapore.

Markov, I. & Stoyanov, S., 1987. Mechanisms of epitaxial growth. *Contemporary Physics*, **28**, 267-320.

Martin, J. M. & Braga, J. C., 1987. Alpujárride carbonate deposits (Southern Spain) - marine sedimentation in a Triassic Atlantic. *Palaeogeography, Palaeoclimatology, Palaeoecology*, **59**(4), 243-260.

Martínez-Martínez, J. M., Soto, J. I. & Balanya, J. C., 2002. Orthogonal folding of extensional detachments: Structure and origin of the Sierra Nevada elongated dome (Betics, SE Spain). *Tectonics*, **21**(3).

Matthes, S. & Knauer, E., 1981. The phase petrology of the contact metamorphic serpentinite nera Erbendorf, Oberpfalz, Bavaria. *Neues Jahrbuch Fur Geologie Und Palaontologie-Abhandlungen*, **141**(1), 59-89.

McInnes, B. I. A., Gregoire, M., Binns, R. A., Herzig, P. M. & Hannington, M. D., 2001. Hydrous metasomatism of oceanic sub-arc mantle, Lihir, Papua New Guinea: petrology and geochemistry of fluid-metasomatised mantle wedge xenoliths. *Earth and Planetary Science Letters*, **188**(1-2), 169-183.

McLaren, A. C. & Etheridge, M. A., 1976. A transmission electron microscope study of naturally deformed orthopyroxene. *Contributions to Mineralogy and Petrology*, **57**(2), 163-177.

McLelland, J. M. & Whitney, P. R., 1977. Origin of Garnet in Anorthosite-Charnockite-Suite-of-Adirondacks. *Contributions to Mineralogy and Petrology*, **60**(2), 161-181.

Meagher, E. P., 1975. Crystal-Structures Of Pyrope And Grossularite At Elevated-Temperatures. *American Mineralogist*, **60**(3-4), 218-228.

Mei, S., Bai, W., Hiraga, T. & Kohlstedt, D. L., 2002. Influence of melt on the creep behavior of olivine-basalt aggregates under hydrous conditions. *Earth and Planetary Science Letters*, **201**(3-4), 491-507.

Mei, S. & Kohlstedt, D. L., 2000. Influence of water on plastic deformation of olivine aggregates 2. Dislocation creep regime. *Journal of Geophysical Research*, **105**.

Melekhova, E., Schmidt, M. W., Ulmer, P. & Guggenbuhl, E., 2006. The reaction talc plus forsterite = enstatite plus H2O revisited: Application of conventional and novel experimental techniques and derivation of revised thermodynamic properties. *American Mineralogist*, **91**(7), 1081-1088.

Mellini, M., Fuchs, Y., Viti, C., Lemaire, C., Linar, egrave & s, J., 2002. Insights into the antigorite structure from Mossbauer and FTIR spectroscopies. *European Journal of Mineralogy*, **14**, 97-104.

Mellini, M., Trommsdorff, V. & Compagnoni, R., 1987. Antigorite polysomatism - behavior during progressive metamorphism. *Contributions to Mineralogy and Petrology*, **97**(2), 147-155.

Mercier, J. C., 1985. Olivine and pyroxenes. In: *Preferred Orientation in Deformed Metals and Rocks* (ed Wenk, H. R.), Academic Press, Orlando.

Merlet, C. & Bodinier, J.-L., 1990. Electron microprobe determination of minor and trace transition elements in silicate minerals: A method and its application to mineral zoning in the peridotite nodule PHN 1611. *Chemical Geology*, **83**(1-2), 55-69.

Michibayashi, K. & Mainprice, D., 2004. The Role of Pre-existing Mechanical Anisotropy on Shear Zone Development within Oceanic Mantle Lithosphere: an Example from the Oman Ophiolite. *Journal of Petrology*, **45**(2), 405-414.

Miller, D. J. & Christensen, N. I., 1994. Seismic signature and geochemistry of an island arc: a multidisciplinary study of the Kohistan accreted terrane, northern Pakistan. *Journal of Geophysical Research*, **99**, 11,623-11,642.

Miller, G. H., Rossman, G. R. & Harlow, G. E., 1987. The natural occurrence of hydroxide in olivine. *Physics and Chemistry of Minerals*, **14**(5), 461-472.

Miller, J. A., Buick, I. S., Cartwright, I. & Barnicoat, A., 2002. Fluid processes during the exhumation of high-P metamorphic belts. *Mineralogical Magazine*, **66**, 93-119.

Miller, S. A. & Nur, A., 2000. Permeability as a toggle switch in fluid-controlled crustal processes. *Earth and Planetary Science Letters*, **183**(1-2), 133-146.

Miller, S. A., van der Zee, W., Olgaard, D. L. & Connolly, J. A. D., 2003. A fluid-pressure feedback model of dehydration reactions: experiments, modelling, and application to subduction zones. *Tectonophysics*, **370**(1-4), 241-251.

Moecher, D. P., Essene, E. J. & Anovitz, L. M., 1988. Calculation and Application of Clinopyroxene-Garnet-Plagioclase-Quartz Geobarometers. *Contributions to Mineralogy and Petrology*, **100**(1), 92-106.

Moore, D. & Lockner, D., 2007. Comparative Deformation Behavior of Minerals in Serpentinized Ultramafic Rock: Application to the Slab-Mantle Interface in Subduction Zones. *International Geology Review*, **49**(5), 401-415.

Morimoto, N., Fabries, J., Ferguson, A. K., Ginzburg, I. V., Ross, M., Seifert, F. A., Zussman, J., Aoki, K. & Gottardi, G., 1988. Nomenclature of pyroxenes. *American Mineralogist*, **73**(9-10), 1123-1133.

Morten, L. & Puga, E., 1984. Blades of olivines and orthopyroxenes in ultramafic rocks from the Cerro del Almirez, Sierra Nevada Complex, Spain: relics of quench-textured harzburgites? *Neues Jahrbuch für Mineralogie, Abhandlungen*, **5**, 211-218.

Müntener, O. & Ulmer, P., 2006. Experimentally derived high-pressure cumulates from hydrous arc magmas and consequences for the seismic velocity structure of lower arc crust. *Geophysical Research Letters*, **31**(21).

Muko, A., Yoshioka, N., Ogasawara, Y., Zhu, Y. & Liou, J., 2001. Petrography and mineral chemistry of Ti-clinohumite-bearing garnet rock from Kokchetav ultra high-pressure belt. In: *UHPM Workshop, Waseda University*, pp. 190-193.

Muntener, O. & Hermann, J., 1994. Titanian andradite in a metapyroxenite layer from the Malenco ultramafics (Italy) - implications for Ti-mobility and low-oxygen fugacity. *Contributions to Mineralogy and Petrology*, **116**(1-2), 156-168.

Nestola, F., Angel, R., Zhao, J., Garrido, C., López Sánchez-Vizcaíno, V., Capitani, G. & Mellini, M., in press. Antigorite equation of state and anomalous softening at 6 GPa: an in situ single-crystal X-ray diffraction study. *Contributions to Mineralogy and Petrology*, **DOI: 10.1007/s00410-009-0463-9**.

Newton, R. C. & Perkins, D., 1982. Thermodynamic Calibration of Geobarometers Based on the Assemblages Garnet-Plagioclase-Orthopyroxene (Clinopyroxene)-Quartz. *American Mineralogist*, **67**(3-4), 203-222.

Nicolas, A. & Ildefonse, B., 1996. Flow mechanism and viscosity in basaltic magma chambers. *Geophysical Research Letters*, **23**(16), 2013-2016.

Nieto, J. M., Puga, E., Monié, P., Díaz de Federico, A. & Jagoutz, E., 1997. High-pressure metamorphism in metagranites and orthogneiss from the Mulhacén Complex (Betic Cordillera, Spain). *Terra Nova*, **9**(abstr. supl. 1), 22-23.

Nijhuis, H. J., 1964. *Plurifacial alpine metamorphism in the south-eastern Sierra de los Filabres, South of Lubrín*, University of Amsterdam, Amsterdam.

Nishiyama, T., 1989. Kinetics of hydrofracturing and metamorphic veining. *Geology* **17**, 1068-1071.

Nozaka, T. & Shibata, T., 1995. Mineral paragenesis in thermally metamorphosed serpentinites, Ohsa-yama, Okayama Prefecture. *Okayama University Earth Science Reports, 2, 1-11.*, **2**, 1-11.

O'Brien, P. J., 2006. Type-locality granulites: high-pressure rocks formed at eclogite-facies conditions. *Mineralogy and Petrology*, **86**, 161-175.

O'Brien, P. J. & Rotzler, J., 2003. High-pressure granulites: formation, recovery of peak conditions and implications for tectonics. *Journal of Metamorphic Geology*, **21**(1), 3-20.

O'Hanley, D., 1996. *Serpentinites: Records of petrologic and tectonic history*. Oxford University Press.

Obara, K., 2002. Nonvolcanic Deep Tremor Associated with Subduction in Southwest Japan. *Science*, **296**(5573), 1679-1681.

Olgaard, D. L., Ko, S. C. & Wong, T. F., 1995. Deformation and pore pressure in dehydrating gypsum under transiently drained conditions. *Tectonophysics*, **245**, 237-248.

Otten, M. T., 1993. High-resolution transmission electron-microscopy of polysomatism and stacking defects in antigorite. *American Mineralogist*, **78**(1-2), 75-84.

Padrón-Navarta, J. A., Garrido, C. J., López Sánchez-Vizcaíno, V., Bodinier, J., Gomez-Pugnaire, M. T., Hussain, S. S. & Dawood, H., submitted-a. Metamorphism of the Arrested Transformation of Hornblende Gabbronorite into Mafic Opx-Free, Garnet Granulite in the Lower Crust of An Paleo-Island Arc (Jijal Complex, Kohistan, NW Pakistan). *Journal of Petrology*. (Chapter 9, this Thesis)

Padrón-Navarta, J. A., Hermann, J., Garrido, C., López Sánchez-Vizcaíno, V. & Gómez-Pugnaire, M. T., 2010. An experimental investigation of antigorite dehydration in natural silica-enriched serpentinite. *Contributions to Mineralogy and Petrology*, **159**(1), 25-42.

Padrón-Navarta, J. A., López Sánchez-Vizcaíno, V., Garrido, C. J., Gómez-Pugnaire, M. T., Jabaloy, A., Capitani, G. & Mellini, M., 2008. Highly ordered antigorite from Cerro del Almirez HP–HT serpentinites,

SE Spain. *Contributions to Mineralogy and Petrology*, **156**(5), 679-688.

Padrón-Navarta, J. A., Tommasi, A., Garrido, C., López Sánchez-Vizcaíno, V., Gómez-Pugnaire, M. T., Jabaloy, A. & Vauchez, A., submitted-b. Fluid transfer into the wedge controlled by high-pressure hydrofracturing in the cold top-slab mantle. *Earth and Planetary Science Letters*. (Chapter 8, this Thesis)

Pattison, D. R. M., 2003. Petrogenetic significance of orthopyroxene-free garnet + clinopyroxene + plagioclase ± quartz-bearing metabasites with respect to the amphibolite and granulite facies. *Journal of Metamorphic Geology*, **21**, 21-34.

Pattison, D. R. M. & Newton, R. C., 1989. Reversed Experimental Calibration of the Garnet-Clinopyroxene Fe-Mg Exchange Thermometer. *Contributions to Mineralogy and Petrology*, **101**(1), 87-103.

Paulick, H., Bach, W., Godard, M., De Hoog, J. C. M., Suhr, G. & Harvey, J., 2006. Geochemistry of abyssal peridotites (Mid-Atlantic Ridge, 15°20'N, ODP Leg 209): Implications for fluid/rock interaction in slow spreading environments. *Chemical Geology*, **234**(3-4), 179-210.

Pawley, A., 2003. Chlorite stability in mantle peridotite: the reaction clinochlore+enstatite=forsterite+pyrope+H2O. *Contributions to Mineralogy and Petrology*, **144**(4), 449-456.

Pawley, A. R., 1998. The reaction talc plus forsterite = enstatite plus H_2O: New experimental results and petrological implication. *American Mineralogist*, **83**(1-2), 51-57.

Peacock, S. M., 1990. Fluid processes in subduction zones. *Science*, **248**(4953), 329-337.

Peacock, S. M., 2001. Are the lower planes of double seismic zones caused by serpentine dehydration in subducting oceanic mantle? *Geology*, **29**(4), 299-302.

Peacock, S. M. & Hyndman, R. D., 1999. Hydrous minerals in the mantle wedge and the maximum depth of subduction thrust earthquakes. *Geophysical Research Letters*, **26**(16), 2517-2520.

Peacock, S. M. & Wang, K., 1999. Seismic consequences of warm versus cool subduction metamorphism: Examples from southwest and northeast Japan. *Science*, **286**(5441), 937-939.

Pennacchioni, G., 1996. Progressive eclogitization under fluid-present conditions of pre-Alpine mafic granulites in the Austroalpine Mt Emilius Klippe (Italian Western Alps). *Journal of Structural Geology*, **18**(5), 549-561.

Perchuk, L. L. & Gerya, T. V., 1993. Fluid Control of Charnockitization. *Chemical Geology*, **108**(1-4), 175-186.

Perchuk, L. L., Safonov, O. G., Gerya, T. V., Fu, B. & Harlov, D. E., 2000. Mobility of components in metasomatic transformation and partial melting of gneisses: an example from Sri Lanka. *Contributions to Mineralogy and Petrology*, **140**(212-232).

Perrillat, J. P., Daniel, I., Koga, K. T., Reynard, B., Cardon, H. & Crichton, W. A., 2005. Kinetics of antigorite dehydration: A real-time X-ray diffraction study. *Earth and Planetary Science Letters*, **236**(3-4), 899-913.

Phipps Morgan, J., 2001. The Thermodynamics of Pressure-Release Melting of a Veined Plum-Pudding Mantle. *Geochemistry, Geophysics, Geosystems*, **2**(4).

Phipps Morgan, J. & Holtzman, B. K., 2005. Vug waves: A mechanism for coupled rock deformation and fluid migration. *Geochemistry, Geophysics, Geosystems*, **6**.

Pickering, J. M., Schwab, B. E. & Johnston, A. D., 1998. Off-center hot spots: Double thermocouple determination of the thermal gradient in a 1.27cm (1/2in) CaF2 piston-cylinder furnace assembly. *American Mineralogist*, **83**(3-4), 228-235.

Pinsent, R. H. & Hirst, D. M., 1977. The Metamorphism of the Blue River Ultramafic Body, Cassiar, British Columbia, Canada. *Journal of Petrology*, **18**(4), 567-594.

Platt, J. P. & Vissers, R. L. M., 1989. Extensional collapse of thickened continental lithosphere: A working hypothesis for the Alboran Sea and Gibraltar arc. *Geology*, **17**(6), 540-543.

Poli, S. & Schmidt, M. W., 2002. Petrology of subducted slabs. *Annual Review of Earth and Planetary Sciences*, **30**, 207-235.

Powell, R., 1985. Regression Diagnostics and Robust Regression in Geothermometer Geobarometer Calibration - the Garnet Clinopyroxene Geothermometer Revisited. *Journal of Metamorphic Geology*, **3**(3), 231-243.

Powell, R. & Holland, T. J. B., 1988. An Internally Consistent Dataset with Uncertainties and Correlations .3. Applications to Geobarometry, Worked Examples and a Computer-Program. *Journal of Metamorphic Geology*, **6**(2), 173-204.

Priem, H., Boelrijk, N., Hebeda, E. & RH, V., 1966. Isotopic age determinationson tourmaline granite-gneisses and a metagranite in the eastern Betic Cordilleras (southeastern Sierra de los Filabres, SE Spain). *Geology in Mijnbouw*, **45**, 184-187.

Prigogine, I. & Defay, R., 1954. *Chemical Thermodynamics*. Longmans, London.

Prior, D. J., Boyle, A. P., Brenker, F., Cheadle, M. C., Day, A., Lopez, G., Peruzzo, L., Potts, G. J., Reddy, S., Spiess, R., Timms, N. E., Trimby, P., Wheeler, J. & Zetterstrom, L., 1999. The application of electron backscatter diffraction and orientation contrast imaging in the SEM to textural problems in rocks. *American Mineralogist*, **84**(11-12), 1741-1759.

Prior, D. J., Wheeler, J., Brenker, F. E., Harte, B. & Matthews, M., 2000. Crystal plasticity of natural garnet: New microstructural evidence. *Geology*, **28**(11), 1003-1006.

Prior, D. J., Wheeler, J., Peruzzo, L., Spiess, R. & Storey, C., 2002. Some garnet microstructures: an illustration of the potential of orientation maps and misorientation analysis in microstructural studies. *Journal of Structural Geology*, **24**(6-7), 999-1011.

Puga, E., De Federico, A. D. & Nieto, J. M., 2002. Tectonostratigraphic subdivision and petrological characterisation of the deepest Complexes of the Betic zone: a review. *Geodinamica Acta*, **15**(1), 23-43.

Puga, E., Díaz de Federico, A., Fediukova, E., Bondi, M. & Morten, L., 1989. Petrology, geochemistry and metamorphic evolution of the ophiolitic eclogites and related rocks from the Sierra Nevada (Betic Cordilleras, Southeastern Spain). *Schweizerische Mineralogische Und Petrographische Mitteilungen*, **69**, 435-455.

Puga, E., Nieto, J. M., de Federico, A. D., Bodinier, J. L. & Morten, L., 1999. Petrology and metamorphic evolution of ultramafic rocks and dolerite dykes of the Betic Ophiolitic Association (Mulhacen Complex, SE Spain): evidence of eo-Alpine subduction following an ocean-floor metasomatic process. *Lithos*, **49**(1-4), 23-56.

Putnis, A., 1992. *Introduction to Mineral Sciences*. Cambridge University Press, New York.

Putnis, A. & Putnis, C. V., 2007. The mechanism of reequilibration of solids in the presence of a fluid phase. *Journal of Solid State Chemistry*, **180**, 1783-1786.

Quon, H. H. & Potvin, A. J., 1972. Growth of single crystal rare-earth garnet films by liquid phase epitaxy. *Materials Research Bulletin*, **7**(5), 463-472.

Raleigh, C. B. & Paterson, M. S., 1965. Experimental Deformation of Serpentinite and Its Tectonic Implications. *Journal of Geophysical Research*, **70**.

Ranero, C. R., Morgan, J. P., McIntosh, K. & Reichert, C., 2003. Bending-related faulting and mantle serpentinization at the Middle America trench. *Nature*, **425**(6956), 367-373.

Regenauer-Lieb, K., Yuen, D. A. & Branlund, J., 2001. The Initiation of Subduction: Criticality by Addition of Water? *Science*, **294**(5542), 578-580.

Reynard, B. & Wunder, B., 2006. High-pressure behavior of synthetic antigorite in the MgO-SiO2-H2O system from Raman spectroscopy. *American Mineralogist*, **91**(2-3), 459-462.

Ridley, J., 1985. The effect of reaction enthalpy on the progress of a metamorphic reaction. In: *Metamorphic Reactions Kinetics, Textures and Deformation* (eds Thompson, A. B. & Rubie, D. C.), pp. 80-97, Springer, New York.

Ridley, J. & Thompson, A. B., 1986. The role of mineral kinetics in the development of metamorphic microtextures. In: *Fluidrock Interactions during Metamorphism* (eds Walther, J. V. & Wood, B. J.), pp. 154-193, Springer, New York.

Ringuette, L., Martignole, J. & Windley, B. F., 1999. Magmatic crystallization, isobaric cooling, and decompression of the garnet-bearing assemblages of the Jijal Sequence (Kohistan Terrane, western Himalayas). *Geology*, **27**(2), 139-142.

Risold, A. C., Trommsdorff, V. & Grobety, B., 2003. Morphology of oriented ilmenite inclusions in olivine from garnet peridotites (Central Alps, Switzerland). *European Journal of Mineralogy*, **15**(2), 289-294.

Risold, A. C., Trommsdorff, V. & Grobéty, B., 2001. Genesis of ilmenite rods and palisades along humite-type defects in olivine from Alpe Arami. *Contributions to Mineralogy and Petrology*, **140**(5), 619-628.

Robertson, J. M., 1978. Liquid-phase epitaxy of garnets. *Journal of Crystal Growth*, **45**, 233-242.

Robinson, K., Gibbs, G. V. & Ribbe, P. H., 1973. Crystal-structures of humite minerals .4. Clinohumite and titanoclinohumite. *American Mineralogist*, **58**(1-2), 43-49.

Rogers, G. & Dragert, H., 2003. Episodic Tremor and Slip on the Cascadia Subduction Zone: The Chatter of Silent Slip. *Science*, **300**(5627), 1942-1943.

Rosenberg, C. L. & Handy, M. R., 2000. Syntectonic melt pathways during simple shearing of a partially molten rock analogue (Norcamphor-Benzamide). *Journal of Geophysical Research-Solid Earth*, **105**(B2), 3135-3149.

Rubie, D. C., 1998. Disequilibrium during metamorphism: the role of nucleation kinetics. In: *What drives metamorphism and metamorphic reactions* (eds Treloar, P. J. & O'Brien, P. J.), pp. 199-214, Geological Society of London, Special Publications, London.

Rudnick, R. L., 1992. Restites, Eu Anomalies, and the Lower Continental-Crust. *Geochimica et Cosmochimica Acta*, **56**(3), 963-970.

Rudnick, R. L., 1995. Making Continental-Crust. *Nature*, **378**(6557), 571-578.

Rudnick, R. L. & Presper, T., 1990. Geochemistry of intermediate to high-pressure granulites. In: *Granulites and Crustal Evolution* (ed Vidal, P.), pp. 523-550, Kluwer Academic Publishers, the Netherlands.

Rüpke, L. H., Morgan, J. P., Hort, M. & Connolly, J. A. D., 2004. Serpentine and the subduction zone water cycle. *Earth and Planetary Science Letters*, **223**(1-2), 17-34.

Ruiz Cruz, M. D., Puga, E. & Nieto, J. M., 1999. Silicate and oxide exsolution in pseudo-spinifex olivine from metaultramafic rocks of the Betic Ophiolitic Association: A TEM study. *American Mineralogist*, **84**(11-12), 1915-1924.

Scambelluri, M., Bottazzi, P., Trommsdorff, V., Vannucci, R., Hermann, J., Gómez-Pugnaire, M. T. & López Sánchez-Vizcaíno, V., 2001a. Incompatible element-rich fluids released by antigorite breakdown in deeply subducted mantle. *Earth and Planetary Science Letters*, **192**(3), 457-470.

Scambelluri, M., Fiebig, J., Malaspina, N., Muntener, O. & Pettke, T., 2004a. Serpentinite subduction: Implications for fluid processes and trace-element recycling. *International Geology Review*, **46**(7), 595-613.

Scambelluri, M., Malaspina, N. & Hermann, J., 2007. Subduction fluids and their interaction with the mantle wedge: a perspective from the study of high-pressure ultramafic rocks. *Periodico Di Mineralogia*, **76**(2-3), 253-265.

Scambelluri, M., Muntener, O., Hermann, J., Piccardo, G. B. & Trommsdorff, V., 1995. Subduction of water into

the mantle - history of an alpine peridotite. *Geology*, **23**(5), 459-462.

Scambelluri, M., Muntener, O., Ottolini, L., Pettke, T. T. & Vannucci, R., 2004b. The fate of B, Cl and Li in the subducted oceanic mantle and in the antigorite breakdown fluids. *Earth and Planetary Science Letters*, **222**(1), 217-234.

Scambelluri, M. & Philippot, P., 2001. Deep fluids in subduction zones. *Lithos*, **55**(1-4), 213-227.

Scambelluri, M., Rampone, E. & Piccardo, G. B., 2001b. Fluid and element cycling in subducted serpentinite: A trace-element study of the Erro-Tobbio high-pressure ultramafites (Western alps, NW Italy). *Journal of Petrology*, **42**(1), 55-67.

Schilling, F. & Wunder, B., 2004. Temperature distribution in piston-cylinder assemblies: Numerical simulations and laboratory experiments. *European Journal of Mineralogy*, **16**(1), 7-14.

Schmidt, M. W. & Poli, S., 1998. Experimentally based water budgets for dehydrating slabs and consequences for arc magma generation. *Earth and Planetary Science Letters*, **163**(1-4), 361-379.

Schneider, M. E. & Eggler, D. H., 1986. Fluids in equilibrium with peridotite minerals: Implications for mantle metasomatism. *Geochimica et Cosmochimica Acta*, **50**(5), 711-724.

Schönbächer, M., 1999. Die Hochdruckmetamorphose der Ultramafika und der angrenzenden Nebengesteine am Cerro de Almirez, Sierra Nevada, Südspanien. Unpublished Diplomarbeit, pp. 113, ETH Zürich.

Shelly, D. R., Beroza, G. C., Ide, S. & Nakamula, S., 2006. Low-frequency earthquakes in Shikoku, Japan, and their relationship to episodic tremor and slip. *Nature*, **442**(7099), 188-191.

Sibson, R. H., 2004. Controls on maximum fluid overpressure defining conditions for mesozonal mineralisation. *Journal of Structural Geology*, **26**, 1127-1136.

Sibson, R. H. 1992. Fault-valve behavior and the hydrostatic lithostatic fluid pressure interface. *Earth-Science Reviews*, **32**, 141-144.

Sorensen, S. S. & Grossman, J. N., 1989. Enrichment of trace elements in garnet amphibolites from a paleo-subduction zone: Catalina Schist, southern California. *Geochimica et Cosmochimica Acta*, **53**(12), 3155-3177.

Sorensen, S. S. & Grossman, J. N., 1993. Accessory minerals and subduction zone metasomatism - a geochemical comparison of 2 melanges (Washington and California, USA). *Chemical Geology*, **110**(1-3), 269-297.

Soustelle, V., Tommasi, A., Demouchy, S. & Ionov, D., 2010. Deformation and fluid-rock interactions in the supra-subduction mantle: Microstructures and water contents in peridotite xenoliths from the Avacha Volcano, Kamchatka. *Journal of Petrology*, **doi:10.1093/petrology/egp085**.

Spandler, C., Hermann, J., Arculus, R. & Mavrogenes, J., 2003. Redistribution of trace elements during prograde metamorphism from lawsonite blueschist to eclogite facies; implications for deep subduction-zone processes. *Contributions to Mineralogy and Petrology*, **146**(2), 205-222.

Spandler, C., Hermann, J., Faure, K., Mavrogenes, J. & Arculus, R., 2008. The importance of talc and chlorite "hybrid" rocks for volatile recycling through subduction zones; evidence from the high-pressure subduction mélange of New Caledonia. *Contributions to Mineralogy and Petrology*, **155**(2), 181-198.

Spear, F. S. & Kohn, M. A., 2001. GTB: Program Geothermobarometry, version 2.1. February 2001. Computer program. http://ees2.geo.rpi.edu/MetaPetaRen/Frame_software.html.

Spiess, R. & Bell, T. H., 1996. Microstructural controls on sites of metamorphic reaction: A case study of the inter-relationship between deformation and metamorphism. *European Journal of Mineralogy*, **8**(165-186).

Spiess, R., Groppo, C. & Compagnoni, R., 2007. When epitaxy controls garnet growth. *Journal of Metamorphic Geology*, **25**(4), 439-450.

Spiess, R., Peruzzo, L., Prior, D. J. & Wheeler, J., 2001. Development of garnet porphyroblasts by multiple nucleation, coalescence and boundary misorientation-driven rotations. *Journal of Metamorphic Geology*, **19**(3), 269-290.

Springer, R. K., 1974. Contact Metamorphosed Ultramafic Rocks in the Western Sierra Nevada Foothills, California. *Journal of Petrology*, **15**(1), 160-195.

Springer, W. & Seck, H. A., 1997. Partial fusion of basic granulites at 5 to 15 kbar: implications for the origin of TTG magmas. *Contributions to Mineralogy and Petrology*, **V127**(1), 30-45.

Spry, A., 1969. Metamorphic Textures, Pergamon Press, Oxford.

Stern, R. J., 2002. Subduction zones. *Reviews of Geophysics*, **40**(4).

Stevenson, D. J., 1989. Spontaneous small-scale melt segregation in partial melts undergoing deformation. *Geophysical Research Letters*, **16**(9), 1067-1070.

Stipska, P. & Powell, R., 2005. Constraining the P-T path of a MORB-type eclogite using pseudosections, garnet zoning and garnet-clinopyroxene thermometry: an example from the Bohemian Massif. *Journal of Metamorphic Geology*, **23**(8), 725-743.

Storey, C. D. & Prior, D. J., 2005. Plastic deformation and recrystallization of garnet: A mechanism to facilitate diffusion creep. *Journal of Petrology*, **46**(12), 2593-2613.

Strating, E. H. H. & Vissers, R. L. M., 1991. Dehydration-induced fracturing of eclogite-facies peridotites: Implications for the mechanical behaviour of subducting oceanic lithosphere. *Tectonophysics*, **200**(1-3), 187-198.

Sunagawa, I., 1987. Morphology of minerals. In: *Morphology of Crystals* (ed Sunagawa, I.), pp. 509-587, Terra Scientific Publishing, Tokyo.

Tahirkheli, R. A. K., 1979. Geotectonic evolution of Kohistan. In: *Geology of Kohistan, Karakoram*

Himalaya, northern Pakistan, Geological Bulletin (ed Jan, M. Q. e.), pp. 113-130, University of Peshawar, Peshawar, Pakistan.

Takei, Y., 2005. Deformation-induced grain boundary wetting and its effects on the acoustic and rheological properties of partially molten rock analogue. *Journal of Geophysical Research*, **110**.

Tatsumi, Y., 1989. Migration of fluid phases and genesis of basalt magmas in subduction zones. *Journal of Geophysical Research-Solid Earth and Planets*, **94**(B4), 4697-4707.

Tatsumi, Y., 2005. The subduction factory: How it operates in the evolving Earth. *GSA Today*, **15**(7), 4-10.

Tatsumi, Y. & Eggins, S. M., 1995. *Subduction zone magmatism*. Blackwell, Cambridge.

Taylor, S. R. & McLennan, S. M., 1985. *The continental crust: its composition and evolution.* Blackwell Scientific, Oxford.

Taylor, S. R. & McLennan, S. M., 1995. The geochemical evolution of the continental crust. *Reviews of Geophysics*, **33**(2), 241-265.

Tenthorey, E. & Cox, S. F., 2003. Reaction-enhanced permeability during serpentinite dehydration. *Geology*, **31**(10), 921-924.

Tenthorey, E. & Hermann, J., 2004. Composition of fluids during serpentinite breakdown in subduction zones: Evidence for limited boron mobility. *Geology*, **32**(10), 865-868.

Terry, M. P. & Heidelbach, F., 2006. Deformation-enhanced metamorphic reactions and the rheology of high-pressure shear zones, Western Gneiss Region, Norway. *Journal of Metamorphic Geology*, **24**(1), 3-18.

Thompson, A. B., 1990. Heat, fluids and melting in the granulite facies. In: *Granulties and Crustal Differentiation* (eds Vielzeuf, D. & Vidal, P.), pp. 37-57, Kluwer Academic Publishers.

Thompson, A. B. & Connolly, J. A. D., 1990. Metamorphic fluids and anomalous porosities in the lower crust. *Tectonophysics*, **182**(1-2), 47-55.

Thompson, J. B. J., 1978. Biopyriboles and polysomatic series. *American Mineralogist*, **63**, 239-249.

Tommasi, A., Godard, M., Coromina, G., Dautria, J.-M. & Barsczus, H., 2004. Seismic anisotropy and compositionally induced velocity anomalies in the lithosphere above mantle plumes: a petrological and microstructural study of mantle xenoliths from French Polynesia. *Earth and Planetary Science Letters*, **227**(3-4), 539-556.

Tommasi, A., Mainprice, D., Canova, G. & Chastel, Y., 2000. Viscoplastic self-consistent and equilibrium-based modeling of olivine lattice preferred orientations: Implications for the upper mantle seismic anisotropy. *Journal of Geophysical Research-Solid Earth*, **105**(B4), 7893-7908.

Tommasi, A., Vauchez, A., Godard, M. & Belley, F., 2006. Deformation and melt transport in a highly depleted peridotite massif from the Canadian Cordillera: Implications to seismic anisotropy above subduction zones. *Earth and Planetary Science Letters*, **252**(3-4), 245-259.

Tommasi, A., Vauchez, A. & Ionov, D. A., 2008. Deformation, static recrystallization, and reactive melt transport in shallow subcontinental mantle xenoliths (Tok Cenozoic volcanic field, SE Siberia). *Earth and Planetary Science Letters*, **272**(1-2), 65-77.

Toriumi, M. & Hara, E., 1995. Crack geometries and deformation by the crack-seal mechanism in the Sambagawa metamorphic belt. *Tectonophysics*, **245**(3-4), 249-261.

Torres-Roldán, R. L., García-Casco, A. & García-Sanchez, P. A., 2000. CSpace: an integrated workplace for the graphical and algebraic analysis of phase assemblages on 32-bit wintel platforms. *Computers & Geosciences*, **26**(7), 779-793.

Treloar, P. J., Broughton, R. D., Williams, M. P., Coward, M. P. & Windley, B. F., 1989. Deformation, Metamorphism and Imbrication of the Indian Plate, South of the Main Mantle Thrust, North Pakistan. *Journal of Metamorphic Geology*, **7**(1), 111-125.

Trommsdorff, V. & Evans, B., 1974. Alpine metamorphism of peridotitic rocks. *Schweizerische Mineralogische Und Petrographische Mitteilungen*, **72**, 229-242.

Trommsdorff, V. & Evans, B. W., 1972. Progressive metamorphism of antigorite schist in the Bergell tonalite aureole (Italy). *Am J Sci*, **272**(5), 423-437.

Trommsdorff, V. & Evans, B. W., 1980. Titanian hydroxyl-clinohumite: Formation and breakdown in antigorite rocks (Malenco, Italy). *Contributions to Mineralogy and Petrology*, **72**(3), 229-242.

Trommsdorff, V., López Sánchez-Vizcaíno, V. L., Gómez-Pugnaire, M. T. & Müntener, O., 1998. High pressure breakdown of antigorite to spinifex-textured olivine and orthopyroxene, SE Spain. *Contributions to Mineralogy and Petrology*, **132**(2), 139-148.

Trommsdorff, V., Risold, A. C., Reusser, E., Connolly, J. A. D. & Ulmer, P., 2001a. Titanian chlinohumite, ilmenite rod inclusions and phase relations, Central Alps. *UHPM Workshop, Waswda University*, 84-85.

Trommsdorff, V., Risold, A. C., Reusser, E., Connolly, J. A. D. & Ulmer, P., 2001b. Titanian chlinohumite, ilmenite rod inclusions and phase relations, Central Alps. *UHPM Workshop,Waswda University*, 84-85.

Uehara, S., 1998. TEM and XRD study of antigorite superstructures. *Canadian Mineralogist*, **36**, 1595-1605.

Uehara, S. & Kamata, K., 1994. Antigorite with a large supercell from Saganoseki, Oita prefecture, Japan. *Canadian Mineralogist*, **32**, 93-103.

Ulmer, P. & Stalder, R., 2001. The Mg(Fe)SiO3 orthoenstatite-clinoenstatite transitions at high pressures and temperatures determined by Raman- spectroscopy on quenched samples. *American Mineralogist*, **86**(10), 1267-1274.

Ulmer, P. & Trommsdorff, V., 1995. Serpentine stability to mantle depths and subduction-related magmatism. *Science*, **268**(5212), 858-861.

Ulmer, P. & Trommsdorff, V., 1999. Phase relations of hydrous mantle subducting to 300 km. In: *Mantle Petrology: Field Observations and High Pressure Experimentation* (eds Fei, Y., Bertka, C. M. & Mysen, B. O.), pp. 259-281, The Geochemical Society.

Urai, J. L. & Feenstra, A., 2001. Weakening associated with the diaspore-corundum dehydration reaction in metabauxites: an example from Naxos (Greece). *Journal of Structural Geology*, **23**(6-7), 941-950.

Van Baalen, M. R., 1993. Titanium mobility in metamorphic systems - a review. *Chemical Geology*, **110**(1-3), 233-249.

Van Bemmelen, R. W., 1927. *Bijdrage tot de geologie der Betisch Ketens in de provincie Granada.*, Delft University, Delft.

Vance, J. A. & Dungan, M. A., 1977. Formation of peridotites by deserpentinization in the Darrington and Sultan areas, Cascade Mountains, Washington. *Geological Society of America Bulletin*, **88**(10), 1497-1508.

Veblen, D. R., 1991. Polysomatism and polysomatic series - a review and applications. *American Mineralogist*, **76**(5-6), 801-826.

Veblen, D. R., 1992. Electron microscopy applied to nonstoichiometry, polysomatism, and replacement reactions in minerals. In: *Reviews in Mineralogy* (ed Buseck, P. R.), pp. 181-230, Mineralogical Society of America, Washington, D.C.

Veblen, D. R. & Buseck, P. R., 1979. Serpentine Minerals: Intergrowths and New Combination Structures. *Science*, **206**(4425), 1398-1400.

Vera, J. A., 2004. Cordillera Bética y Baleares. In: *Geología de España* (ed Vera, J. A.), pp. 345-464, SGE-IGME, Madrid.

Vielzeuf, D., Clemens, J. D., Pin, C. & Moinet, E., 1990. Granites, granulites, and crustal differentiation. In: *Granulites and Crustal Evolution* (eds Vielzeuf, D. & Vidal, P.) *NATO ASI Series. Serie C: Mathematical and Physical Sciences*, pp. 59-86, Kluwer Academic Publishers, Dordrecht / Boston / London.

Vielzeuf, D. & Schmidt, M. W., 2001. Melting relations in hydrous systems revisited: application to metapelites, metagreywackes and metabasalts. *Contributions to Mineralogy and Petrology*, **141**(3), 251-267.

Viti, C. & Mellini, M., 1996. Vein antigorites from Elba Island, Italy. *European Journal of Mineralogy*, **8**(2), 423-434.

Vollmer, F. W., 1990. An Application Of Eigenvalue Methods To Structural Domain Analysis. *Geological Society of America Bulletin*, **102**(6), 786-791.

Von Drasche, R., 1879. Bosquejo geológico de la zona superior de Sierra Nevada. *Boletín de la Comisión del Mapa Geológico de España, TOMO 8º*, **6**, 353-388.

Vrijmoed, J. C., Smith, D. C. & Van Roermund, H. L. M., 2008. Raman Confirmation of Microdiamond in the Svartberget Fe-Ti type garnet peridotite, Western Gneiss Region, Western Norway. *Terra Nova*, **20**, 295-301.

Vrijmoed, J. C., Van Roermund, H. L. M. & Davis, G. R., 2006. Evidence for diamond-grade ultra-high pressure metamorphism and fluid interaction in the Svartberget Fe-Ti garnet peridotite-websterite body, Western Gneiss Region, Norway. *Mineralogy and Petrology*, **88**, 381-405.

Waard, D. d., 1965. The Occurrence of Garnet in the Granulite-Facies Terrane of the Adirondack Highlands *Journal of Petrology*, **6**, 165-191.

Walther, J. V. & Wood, B. J., 1984. Rate and Mechanism in Prograde Metamorphism. *Contributions to Mineralogy and Petrology*, **88**(3), 246-259.

Wang, W. H. & Wong, T.-F., 2003. Effects of reaction kinetics and fluid drainage on the development of pore pressure excess in a dehydrating system. *Tectonophysics*, **370**, 227-239.

Waters, D. J. & Lovegrove, D. P., 2002. Assessing the extent of disequilibrium and overstepping of prograde metamorphic reactions in metapelites from the Bushveld Complex aureole, South Africa. *Journal of Metamorphic Geology*, **20**(1), 135-149.

Waters, D. J. & Wales, C. J., 1984. Dehydration melting and the granulite transition in metapelites from southern Namaqualand, S. Africa. *Contributions to Mineralogy and Petrology*, **88**, 269-275.

Watson, E. B., Wark, D. A., Price, J. D. & Van Orman, J. A., 2002. Mapping the thermal structure of solid-media pressure assemblies. *Contributions to Mineralogy and Petrology*, **142**(6), 640-652.

Watt, G. R., Oliver, N. H. S. & Griffin, B. J., 2000. Evidence for reaction-induced microfracturing in granulite facies migmatites. *Geology* **28**, 327-330.

Weiss, M., 1997. Clinohumites: a field and experimental study. PhD Thesis. ETH, Zurich, pp 168.

White, D. A., Roeder, D. H., Nelson, T. H. & Crowell, J. C., 1970. Subduction. *Geological Society of America Bulletin*, **81**(11), 3431-3432.

White, R. W., Powell, R. & Holland, T. J. B., 2001. Calculation of partial melting equilibria in the system Na_2O-CaO-K_2O-FeO-MgO-Al_2O_3-SiO_2-H_2O (NCKFMASH). *Journal of Metamorphic Geology*, **19**(2), 139-153.

Whitney, D. L., Goergen, E. T., Ketcham, R. A. & Kunze, K., 2008. Formation of garnet polycrystals during metamorphic crystallization. *Journal of Metamorphic Geology*, **26**(3), 365-383.

Wicks, F. J. & Whittaker, E. J. W., 1977. Serpentine textures and serpentinization. *The Canadian Mineralogist*, **15**(4), 459-488.

Wilbur, D. E. & Ague, J. J., 2006. Chemical disequilibrium during garnet growth: Monte Carlo simulations of natural crystal morphologies. *Geology*, **34**(8), 689-692.

Wilshire, H. G. & Kirby, S. H., 1989. Dikes, joints, and faults in the upper mantle. *Tectonophysics*, **161**(1-2), 23-31.

Wirth, R., Dobrzhinetskaya, L. F. & Green, H. W., 2001. Electron microscope study of the reaction olivine plus H_2O+TiO_2 $\rightarrow$ titanian clinohumite plus Titanian

chondrodite synthesized at 8 GPa, 1300 K. *American Mineralogist*, **86**(5-6), 601-610.

Wong, T. F., Ko, S. C. & Olgaard, D. L., 1997. Generation and maintenance of pore pressure excess in a dehydrating system: 2. Theoretical analysis. *Journal of Geophysical Research-Solid Earth*, **102**, 841-852.

Woodcock, N. H. & Naylor, M. A., 1983. Randomness testing in three-dimensional orientation data. *Journal of Structural Geology*, **5**(5), 539-548.

Worden, R. H., Champness, P. E. & Droop, G. T. R., 1987. Transmission electron-microscopy of the pyrometamorphic breakdown of phengite and chlorite. *Mineralogical Magazine*, **51**, 107-121.

Worden, R. H., Droop, G. T. R. & Champness, P. E., 1991. The reaction antigorite = olivine + talc + H_2O in the Bergell aureole, N. Italy. *Mineralogical Magazine*, **55**(380), 367-377.

Wunder, B. & Schreyer, W., 1997. Antigorite: High-pressure stability in the system MgO-SiO_2-H_2O (MSH). *Lithos*, **41**(1-3), 213-227.

Wunder, B., Wirth, R. & Gottschalk, M., 2001. Antigorite: Pressure and temperature dependence of polysomatism and water content. *European Journal of Mineralogy*, **13**(3), 485-495.

Yamamoto, H., 1993. Contrasting metamorphic P-T-time paths of the Kohistan granulites and tectonics of the western Himalayas. *Journal of the Geological Society of London*, **150**(Part 5), 843-856.

Yamamoto, H., Kobayashi, K., Nakamura, E., Kaneko, Y. & Kausar, A. B., 2005. U-Pb zircon dating of regional deformation in the lower crust of the Kohistan arc. *International Geology Review*, **47**, 1035-1047.

Yamamoto, H. & Nakamura, E., 1996. Sm-Nd dating of garnet granulites from the Kohistan Complex, northern Pakistan. *Journal of the Geological Society of London*, **153**(6), 965-969.

Yamamoto, H. & Nakamura, E., 2000. Timing of magmatic and metamorphic events in the Jijal Complex of the Kohistan are deduced from Sm-Nd dating of mafic granulites. In: *Tectonics of the Nanga Parbat Syntaxis and the Western Himalaya* (eds Khan, M. A., Treloar Peter, J., Searle Michael, P. & Jan, M. Q.), pp. 313-319, Geological Society of London, London.

Yamamoto, H. & Yoshino, T., 1998. Superposition of replacements in the mafic granulites of the Jijal Complex of the Kohistan arc, northern Pakistan: dehydration and rehydration within deep arc crust. *Lithos*, **43**(4), 219-234.

Yamasaki, T. & Seno, T., 2003. Double seismic zone and dehydration embrittlement of the subducting slab. *Journal of Geophysical Research*, **108**.

Yoshino, T. & Okudaira, T., 2004. Crustal growth by magmatic accretion constrained by metamorphic P-T paths and thermal models of the Kohistan arc, NW Himalayas. *Journal of Petrology*, **45**(11), 2287-2302.

Yoshino, T., Yamamoto, H., Okudaira, T. & Toriumi, M., 1998. Crustal thickening of the lower crust of the Kohistan arc (N. Pakistan) deduced from Al zoning in clinopyroxene and plagioclase. *Journal of Metamorphic Geology*, **16**(6), 729-748.

Yoshinobu, A. S. & Harper, G. D., 2004. Hypersolidus deformation in the lower crust of the Josephine ophiolite: evidence for kinematic decoupling between the upper and lower oceanic crust. *Journal of Structural Geology*, **26**, 163-175.

Zeh, A. & Holness, M. B., 2003. The effect of reaction overstep on garnet microtextures in metapelitic rocks of the Ilesha Schist belt, SW Nigeria. *Journal of Petrology*, **44**(6), 967-994.

Zeilinger, G., 2002. *Structural and Geochronological Study of the Lowest Kohistan Complex, Indus Kohistan Region in Pakistan, NW Himalaya*. Unpub. Ph. D. Thesis, ETH, Zurich.

Zeilinger, G., Burg, J. P., Chaudhry, N., Dawood, H. & Hussain, S., 2000. Fault systems and Paleo-stress tensors in the Indus Suture Zone (NW Pakistan). *Journal of Asian Earth Sciences*, **18**(5), 547-559.

Ziebold, T. O., 1967. Precision and sensitivity in electron microprobe analysis. *Analytical Chemistry*, **39**(8), 858-861.

14. APPENDIX

14.1 Abbreviations
14.2 Localization and description of samples
14.3 EDS analyses of minerals in the experimental runs (cf. chapter 7).

14.1 Mineral abbreviation and formulae

where possible after Kretz (1983).

Ab	albite	$NaAlSi_3O_8$
Alm	almandine	$Fe^{2+}{}_3Al_2(SiO_4)_3$
Am	amesite	$Mg_4Al_4Si_2O_{10}(OH)_8$
An	anorthite	$Ca(Al_2Si_2O_8)$
Ap	apatite	$Ca_5(PO_4)_3(Cl,F,OH)$
Atg*	antigorite	$M_{3m-3}T_{2m}O_{5m}(OH)_{4m-6}$
Atg	antigorite (m=17)	$Mg_{2.824}Si_2O_5(OH)_{3.647}$
Brc	brucite	$Mg(OH)_2$
Cal	calcite	$CaCO_3$
Chl	chlorite (MASH)	$(Mg_{6-x}Al_x)Si_{4-x}Al_xO_{10}(OH)_8$ $(0<x<2)$
Chr	chromite	$Fe^{2+}Cr_2O_4$
Clin	clinocholore	$(Mg_5Al)Si_3AlO_{10}(OH)_8$ $(x = 1)$
Ti-Chu*	clinohumite	$4(M_2SiO_4)M_{1-x}Ti_x(OH,F)_{2-2x}O_{2x}$ $(0<x<0.5)$
Ctl	chrysotile	$Mg_3Si_2O_5(OH)_4$
Di	diopside	$CaMgSi_2O_6$
Dol	dolomite	$CaMg(CO_3)_2$
En	enstatite (ortho)	$Mg_2Si_2O_6$
Fa	fayalite	$Fe^{2+}{}_2SiO_4$
Fo	forsterite	Mg_2SiO_4
Fs	ferrosilite (ortho)	$(Fe^{2+},Mg)_2Si_2O_6$
Grs	grossular	$Ca_3Al_2(SiO_4)_3$
Grt	garnet	$(Mg,Fe^{2+},Mn,Ca)_3Al_2(SiO_4)_3$
Hbl	hornblende	$Ca_2(Mg,Fe)_4AlSi7AlO_{22}(OH)_2$
Hem	hematite	Fe_2O_3
Ilm	ilmenite	$Fe^{2+}TiO_3$
Kfs	K-feldspar	$(K,Na)AlSi_3O_8$
Mag	magnetite	$Fe^{2+}Fe^{3+}{}_2O_4$
Ol	olivine	$(Mg,Fe^{2+})_2SiO_4$
Opx	orthopyroxene	$(Mg,Fe^{2+})_2SiO_3$
Or	orthoclase	$KAlSi_3O_8$
Pl	plagioclase	$Na(AlSi_3O_8)$-$Ca(Al_2Si_2O_8)$
Pn	pentlandite	$(Fe,Ni)_9S_8$
Po	pyrrhotite	$Fe_{1-x}S$ $(x=0\text{-}0.17)$
Prg	pargasite	$NaCa_2(Mg_4Al)Si_6Al_2O_{22}(OH)_2$
Prp	pyrope	$Mg_3Al_2(SiO_4)_3$
Qtz	quartz	SiO_2
Rt	rutile	TiO_2
Sps	spessartine	$Mn^{2+}{}_3Al_2(SiO_4)_3$
Spl	spinel	$MgAl_2O_4$
Srp	serpentine	$Mg_3Si_2O_5(OH)_4$
Sud	sudoite	$Mg_2Al_4Si_3O_{10}(OH)_8$
Tlc	talc	$Mg_3Si_4O_{10}(OH)_2$
Tr	tremolite	$Ca_2Mg_5Si_8O_{22}(OH)_2$
Ts	tschermakite	$Ca_2(Mg_3AlFe^{3+})Si_6Al_2O_{22}(OH)_2$
Usp	ulvospinel	$TiFe^{2+}{}_2O_4$

* M: octahedral site, T: tetahedral site

14.2 Sample description

Short description for the whole sampling concerning to Part II. Coordinate frame system is ED50 (European datum 1950), UTM.

Sample Nr	Short description	TS	XRF	EMP	FTIR	EBSD	Coordinates (x,y)	GPS code
AI06-01	Spinifex textured harzburgite	●	○	○	○	○	30S 506652 4103979	021
AI06-02	Orthopyroxene-chlorite vein	●	●	●	●	○	30S 506652 4103979	021
AI06-03	Completely recrystallized harzburgite	●	○	○	○	●	30S 506684 4104003	022
AI06-04	Partially recrystallized harzburgite	●	○	○	○	○	30S 506671 4104029	023
AI06-05	Partially recrystallized harzburgite	●	●	●	○	●	30S 506646 4103983	025
AI06-06	Spinifex textured harzburgite	●	○	○	○	○	30S 506692 4103993	026
AI06-07	Chloritoid-Garnet metapelite	●	○	○	○	○	30S 506802 4104284	X59
AI06-08	Spinifex textured harzburgite	●	○	○	○	○	30S 506872 4104193	027
AI06-09	Diopside-Tremolite bearing serpentinite	●	●	○	○	●	30S 506876 4104176	030
AI06-10	Tremolite vein	○	○	○	○	○	30S 506883 4104134	031
AI06-11	Opx-Chl-Ol granofelse	●	○	○	○	○	30S 507419 4104596	033
AI06-12	Opx-Chl-Ol granofelse	●	●	●	●	●	30S 507419 4104596	033
AI06-13	Orthopyroxene-chlorite vein	○	○	○	○	○	30S 507430 4104599	034
AI06-14	Spinifex textured harzburgite	○	○	○	○	○	30S 507457 4104646	035
AI06-15	Partially recrystallized harzburgite	●	○	○	○	○	30S 507577 4104808	037
AI06-16	Fine grained spinifex textured harzburgite	●	●	○	○	○	30S 507639 4104813	039
AI06-17	Spinifex textured harzburgite	●	●	○	○	○	30S 507639 4104813	039
AI06-18	Opx-Chl-Ol granofelse	●	●	○	○	○	30S 507639 4104814	040
AI06-19	Spinifex textured harzburgite with Opx relic	●	●	●	●	○	30S 507639 4104814	040
AI06-20	Opx-bearing serpentinite	●	●	○	○	●	30S 507639 4104814	040
AI06-21	Recrystallized harzburgite	○	○	○	○	○	30S 508254 4104626	042
AI06-22	Spinifex textured harzburgite	○	○	○	○	○	30S 508248 4104641	043
AI06-23	Atg-serpentinite	○	○	○	○	○	30S 508210 4104814	044
AI06-25	Dp-serpentinite with TiChu-Ol vein	●	○	●	○	○	30S 508251 4104966	047
AI06-26	Tremolite-rich harzburgite	●	○	○	●	○	30S 508309 4105023	048
AI06-27	Atg-serpentinite	●	○	○	○	○	30S 508318 4105105	049
AI06-28	Uvarovite-bearing chlorite schist	●	●	●	○	○	30S 508318 4105105	049
AI06-29	Ophicarbonate	●	○	○	○	○	30S 508349 4105124	051
AI06-30	Partially recrystallized harzburgite	●	●	○	●	○	30S 506640 4103975	A24
AI06-31	Rodingite chlorite blackwall	●	○	○	○	○	30S 506678 4103985	A26
AI06-32	Spinifex textured harzburgite	○	○	○	○	○	30S 506671 4103977	A27
AI06-33	TiChu vein in Chl-harzburgite	●	○	●	○	○	30S 506671 4103977	A27
AI06-34	Partially recrystallized harzburgite	●	○	○	○	●	30S 506671 4103977	A27
AI06-35	Partially recrystallized harzburgite	●	○	○	○	●	30S 506671 4103977	A27
AI06-36	Orthopyroxene-bearing serpentinite	○	○	○	○	○	30S 506671 4103977	A27
AI06-37	Orthopyroxene-bearing serpentinite	●	●	●	●	○	30S 507639 4104814	040
AI06-38	Orthopyroxene-bearing serpentinite	○	●	○	○	○	30S 507639 4104814	040
AI06-39	Spinifex textured harzburgite	○	○	○	○	○	30S 507639 4104814	040
AI06-40	Orthopyroxene-bearing serpentinite	○	○	○	○	○	30S 507639 4104814	040
AI06-41	Spinifex textured harzburgite	○	○	○	○	○	30S 507639 4104814	040
AI06-42	Spinifex textured harzburgite	●	○	●	●	●	30S 507657 4104805	A31
AI06-4½	Atg-serpentinite	●	○	○	○	○	30S 507707 4104825	A33
AI06-43	Chl-Atg serpentinite	●	●	●	○	●	30S 507707 4104825	A33
AI06-44	Atg-serpentinite	●	●	○	○	○	30S 507707 4104825	A33
AI06-45	Chl-Atg serpentinite	●	○	●	○	○	30S 507707 4104825	A33
AI06-46	Atg-serpentinite	○	●	○	○	○	30S 507768 4104855	A34

Sample Nr	Short description	TS	XRF	EMP	FTIR	EBSD	Coordinates (x,y)	GPS code
Al06-47	Spinifex textured harzburgite with Opx relic	●	○	○	○	○	30S 507494 4104712	054
Al06-48	Recrystallized harzburgite with TiChu grains	○	○	○	○	○	30S 508039 4103841	058
Al06-49	Tr-Ol vein	●	○	●	●	○	30S 507368 4104564	A28
Al07-01	Partially recrystallized harzburgite	●	○	○	○	○	30S 506573 4103912	J02
Al07-02	Partially recrystallized harzburgite	○	○	○	○	○	30S 506573 4103911	060
Al07-03	Partially recrystallized harzburgite	●	○	○	○	○	30S 506573 4103911	060
Al07-04	Partially recrystallized harzburgite	●	○	○	○	○	30S 506573 4103911	060
Al07-05	Spinifex textured harzburgite	○	○	○	○	○	30S 506573 4103911	060
Al07-06	Chl-Atg serpentinite	●	●	○	○	○	30S 506626 4104039	061
Al07-07	Completely recrystallized harzburgite	●	○	○	○	○	30S 506689 4104048	062
Al07-08	Recrystallized harzburgite with TiChu grains	○	○	○	○	○	30S 508023 4103867	063
Al07-09	Opx-Chl-Ol granofelse	●	●	○	○	○	30S 507426 4104603	C4
Al07-10	Tremolite vein with chlorite blackwall	●	○	○	○	○	30S 507426 4104603	C4
Al07-11	Chl-Atg serpentinite	●	●	○	○	○	30S 507643 4104792	C5
Al07-12	Spinifex textured harzburgite	●	●	●	●	○	30S 507673 4104785	C6
Al07-13	Spinifex textured harzburgite with Ol-relic	●	●	●	○	○	30S 507673 4104785	C6
Al07-14	Spinifex textured harzburgite	○	○	○	○	○	30S 507673 4104785	C6
Al07-15	Opx-Chl-Ol granofels	●	○	●	○	○	30S 507712 4104832	C7
Al07-17	Chl-Atg serpentinite	●	○	○	○	○	30S 506585 4104023	M17
Al07-18	Chl-Atg serpentinite	●	○	○	○	○	30S 506585 4104028	M18
Al07-19	Chl-Atg serpentinite	●	○	○	○	○	30S 506615 4104042	M19
Al07-20	Completely recrystallized harzburgite	●	○	○	○	○	30S 506617 4104030	M20
Al07-21	Completely recrystallized harzburgite	●	○	○	○	○	30S 506621 4104020	M21
Al07-22	Partially recrystallized harzburgite	●	○	○	○	○	30S 506627 4104010	M22
Al07-23	Completely recrystallized harzburgite	●	○	○	○	○	30S 506639 4104001	M23-26
Al07-24	Partially recrystallized harzburgite	●	○	○	○	○	30S 506639 4104001	M23-26
Al07-25	Partially recrystallized harzburgite	●	○	○	○	○	30S 506639 4104001	M23-26
Al07-26	Partially recrystallized harzburgite	●	○	○	○	○	30S 506639 4104001	M23-26
Al07-27	Completely recrystallized harzburgite	●	○	○	○	○	30S 506663 4104007	M27
Al07-28	Completely recrystallized harzburgite	●	○	○	○	○	30S 506680 4104019	M28
Al07-29	Partially recrystallized harzburgite	●	○	○	○	○	30S 506700 4104033	M29
Al07-30	Opx-Chl-Ol granofelse	●	○	○	○	○	30S 506727 4104068	M30
Al08-01	Quartzite	○	○	○	○	○	30S 507694 4105181	X001
Al08-02	Slate	○	○	○	○	○	30S 507689 4105179	X002
Al08-03	Atg-serpentinite	○	○	○	○	○	30S 507747 4104833	002
Al08-04	Atg-serpentinite	●	○	○	○	○	30S 507709 4104835	003
Al08-05	Chl-Atg serpentinite	●	○	○	○	○	30S 507709 4104835	003
Al08-06	Opx-Chl-Atg-Ol schist	●	○	○	○	○	30S 507709 4104835	003
Al08-07	Opx-Chl-Ol granofelse	●	●	●	○	○	30S 507709 4104835	003
Al08-08	Chlorite-orthopyroxene vein	●	●	○	○	○	30S 507709 4104843	004
Al08-09	Spinifex textured harzburgite	●	○	○	○	○	30S 507709 4104843	004
Al08-10	Spinifex textured harzburgite	●	●	○	○	○	30S 507696 4104856	005
Al08-11	Spinifex textured harzburgite	○	○	○	○	○	30S 507696 4104856	005
Al08-12	Completely weathered harzburgite	●	○	○	○	○	30S 507506 4104717	010
Al08-13	Spinifex textured harzburgite with Ol-relic	●	●	●	○	○	30S 507570 4104786	012
Al08-14	Opx-Chl-Atg-Ol schist	●	●	●	○	○	30S 507646 4104665	014
Al08-15	Opx-Chl-Atg-Ol schist	●	○	○	○	○	30S 507679 4104414	017
Al08-16	Opx-Chl-Ol granofelse	●	●	●	○	○	30S 507634 4104336	018
Al08-17	Spinifex textured harzburgite	●	●	○	○	○	30S 507634 4104336	018
Al08-18	Atg-serpentinite	●	○	○	○	○	30S 507813 4104163	020
Al08-19	Opx-Chl-Atg-Ol schist	●	○	○	○	○	30S 507746 4104107	021
Al08-20	Opx-Chl-Atg-Ol schist	●	○	○	○	○	30S 507746 4104107	021

Sample Nr	Short description	TS	XRF	EMP	FTIR	EBSD	Coordinates (x,y)	GPS code
AI08-21	Spinifex textured harz. with Ol-relic	●	●	●	○	○	30S 507720 4104129	022
AI08-22	Spinifex textured harz. with Opx-Ol-relic	●	○	●	○	○	30S 507612 4104045	024
AI08-23	Partially recrystallized harzburgite	●	●	○	○	○	30S 507722 4103831	025
AI08-24	Diopside-Tremolite bearing serpentinite	●	○	○	○	○	30S 507727 4103889	026
AI08-25	Diopside-Tremolite bearing serpentinite	●	○	○	○	○	30S 507698 4103875	027
AI08-26	Diopside-Tremolite bearing serpentinite	●	●	○	○	○	30S 507709 4103883	028
AI08-27	Diopside-Tremolite bearing serpentinite	●	○	○	○	○	30S 507709 4103883	028
AI08-28	Clinopyroxenite	●	●	●	○	○	30S 507937 4103809	031
AI08-29	Diopside-Tremolite bearing serpentinite	●	○	○	○	○	30S 507910 4103871	043
AI08-30	Diopside-Tremolite bearing serpentinite	●	○	○	○	○	30S 507895 4103853	045
AI08-31	Diopside-Tremolite bearing serpentinite	●	○	○	○	○	30S 507924 4103846	047
AI08-32	Tremolite-Olivine granofelse	●	●	○	○	○	30S 507924 4103846	047
AI08-33	Diopside-Tremolite bearing serpentinite	●	○	●	○	○	30S 507920 4103865	034
AI08-34	Opx-Chl-Ol granofelse	●	○	○	○	○	30S 507920 4103865	034
AI08-35	Completely recrystallized harzburgite	●	○	○	○	○	30S 507895 4103876	048
AI08-36	Diopside-Tremolite bearing serpentinite	●	○	○	○	○	30S 508152 4104416	056
AI08-37	Opx-Chl-Ol granofelse	●	●	○	○	○	30S 508155 4104519	063
AI08-38	Opx-Chl-Ol granofelse	●	●	○	○	○	30S 508155 4104519	063
AI08-39	Completely recrystallized harzburgite	●	○	○	○	○	30S 508195 4104800	076
AI08-40	Diopside-Tremolite bearing serpentinite	●	○	○	○	○	30S 508195 4104800	076
AI08-41	Diopside-Tremolite bearing serpentinite	●	○	○	○	○	30S 508190 4104838	077
AI08-42	Talc-Magnesite-Chlorite-Opx schist	●	○	○	○	○	30S 508190 4104838	077
AI08-43	Talc-Magnesite-Chlorite-Opx schist	●	●	●	○	○	30S 508185 4104847	078
AI08-44	Diopside-Tremolite bearing serpentinite	●	○	○	○	○	30S 508160 4104843	081
AI08-45	Talc-Magnesite-Chlorite-Opx schist	●	○	●	○	○	30S 508160 4104843	081
AI08-46	Chloritite layer	●	●	○	○	○	30S 508184 4104849	083
AI08-47	Completely recrystallized harzburgite	●	○	○	○	○	30S 508204 4104851	084
AI08-48	Tremolite-rich recrystallized harzburgite	●	○	○	○	○	30S 508180 4104842	085
AI08-49	Talc-Magnesite-Chlorite-Opx-TiChu schist	●	○	○	○	○	30S 508184 4104849	083
AI08-50	Talc-Magnesite-Chlorite-Opx schist	●	○	○	○	○	30S 508222 4104923	088
AI08-51	Diopside-Tremolite bearing serpentinite	●	○	○	○	○	30S 508279 4105103	099
AI08-52	Chlorite-Antigorite serpentinite	●	●	○	○	○	30S 508279 4105103	099
AI08-53	Chlorite-Antigorite serpentinite	●	○	○	○	○	30S 508279 4105103	099
AI08-54	Dp-Tr-Chl-TiChl-layered serpentinite	●	●	○	○	○	30S 508288 4105121	100
AI08-55	Dp-Tr-Chl-schist	●	●	○	○	○	30S 508288 4105121	100
AI08-56	Tr-Chl-TiChu shists	●	●	○	○	○	30S 508288 4105121	100
AI08-57	Dp-serpentinite/Chloritite	●	○	○	○	○	30S 508288 4105121	100
AI08-58	Folded Marble	○	○	○	○	○	30S 508347 4105166	104
AI08-59	Completely recrystallized harzburgite	●	○	○	○	○	30S 508284 4105151	107
AI08-60	Chlorite-Antigorite serpentinite	●	○	○	○	○	30S 508284 4105151	107
AI08-61	Cpx-chlorite schists	●	○	○	○	○	30S 508287 4105134	108
AI08-62	Chlorite-Antigorite serpentinite	●	○	○	○	○	30S 508241 4105174	110
AI09-01	Partially recrystallized harzburgite	●	○	○	○	○	30S 507532 4104555	033
AI09-02	Rodingite	○	○	○	○	○	30S 507769 4104648	035
AI09-03	Olivine-rich serpentinite	○	○	○	○	○	30S 507907 4104146	040
AI09-04	Olivine-rich serpentinite	●	○	○	○	○	30S 507955 4104135	041
AI09-05	Olivine-rich serpentinite	○	○	○	○	○	30S 507769 4104648	035
AI09-06	Ophicarbonate	●	○	○	○	○	30S 508239 4105203	043
AI09-07	Chlorite vein	●	○	○	○	○	30S 508239 4105203	043
AI09-08	Chlorite-Tremolite vein	●	○	○	○	○	30S 508239 4105203	043
AI09-09	Magnesite vein	●	○	○	○	○	30S 508239 4105203	043
AI09-10	Serpentinite-carbonate breccha	●	○	○	○	○	30S 508186 4105207	045

Sample Nr	Short description	TS	XRF	EMP	FTIR	EBSD	Coordinates (x,y)	GPS code
Al09-11	Chlorite-bearing metapelite	○	○	○	○	○	30S 508162 4105203	049
Al09-12	Completely recrystallized harzburgite	●	○	○	○	○	30S 508164 4105190	050
Al09-13	Completely recrystallized harzburgite	●	○	○	○	○	30S 508164 4105190	050
Al09-14	Opx-Chl-Ol granofelse with Opx relic	●	○	○	○	○	30S 507527 4104577	059
Al09-15	Opx-Chl-Ol granofelse with Opx relic	●	○	○	○	○	30S 507527 4104577	059
Al09-16	Opx-Chl-Ol granofelse	●	○	○	○	○	30S 507527 4104577	059
Al09-17	Olivine-serpentinite	●	○	○	○	○	30S 507591 4104604	074
Al09-18	Opx-Chl-Ol granofelse	●	○	○	○	○	30S 507598 4104601	075
Al09-19	Spinifex textured harzburgite	●	○	○	○	○	30S 507598 4104601	075
Al09-20	Clinopyroxenite	●	○	○	○	○	30S 507659 4104632	090
Al09-21	Diopside-Tremolite bearing serpentinite	●	○	○	○	○	30S 508133 4104735	093
Al09-22	Olivine-rich serpentinite	●	○	○	○	○	30S 508018 4104760	102
Al09-23	Metadunite	●	○	○	○	○	30S 508017 4104759	101
Al09-24	Metadunite	●	○	○	○	○	30S 508017 4104759	101
Al09-25	Metadunite	●	○	○	○	○	30S 508017 4104759	101
Al09-26	Clinopyroxene-rich serpentinite	●	○	○	○	○	30S 508025 4104764	100
Al09-27	Chlorite-blackwall	○	○	○	○	○	30S 507998 4105040	109

14.3 EDS analyses of minerals in the experimental runs corresponding to Chapter 7

Electonic table 1. Composition (average and 1σ) of the different phases observed in the runs.

RUN	C2967						D912								C2978									
	Opx (n=6)		Ol (n=7)		Chl (n=6)		Ol (n=5)		Atg (n=5)		Tlc (n=5)		Tr (n=5)		Opx (n=5)		Ol (n=7)		Atg (n=6)		Tr (n=5)		Tlc (n=5)	
	mean	stdev	mean	stdev	mean	stdev	mean	stdev	mean	stdev	mean	stdev	mean	stdev	mean	stdev	mean	stdev	mean	stdev	mean	stdev	mean	stdev
SiO_2	56.52	0.73	40.86	0.39	32.07	0.65	40.81	0.29	40.65	0.75	60.60	0.84	58.33	0.37	57.64	0.35	40.64	0.20	40.80	0.28	58.34	0.45	61.61	1.04
Al_2O_3	1.62	0.48	*bdl*		13.71		*bdl*		3.61	0.34	*bdl*		*bdl*		*bdl*		*bdl*		3.50	0.20	*bdl*		*bdl*	
Cr_2O_3	0.38	0.23	*bdl*		1.88	0.12	*bdl*		0.74	0.06	*bdl*		*bdl*		*bdl*		*bdl*		0.79	0.08	*bdl*		*bdl*	
FeO	6.64	0.34	10.65	0.53	3.18	0.09	10.79	0.36	4.58	0.44	1.33	0.20	1.98	0.24	7.93	0.08	10.81	0.53	4.51	0.30	2.02	0.19	1.58	0.17
NiO	*bdl*		0.30	0.15	0.32	0.14	0.28	0.13	*bdl*		0.15	0.11	*bdl*		*bdl*		0.24	0.09	*bdl*		*bdl*		0.18	0.08
MgO	33.71	0.62	47.86	0.68	32.10	0.76	48.08	0.48	35.25	0.72	29.47	0.53	23.83	0.15	33.73	0.33	47.65	0.80	35.37	0.45	23.77	0.22	30.13	0.57
MnO	*bdl*		*bdl*		*bdl*		0.21	0.14	*bdl*		*bdl*		*bdl*		0.41	0.04	0.31	0.25	*bdl*		*bdl*		*bdl*	
CaO	*bdl*		*bdl*		*bdl*		*bdl*		*bdl*		*bdl*		12.35	0.21	*bdl*		*bdl*		*bdl*		12.50	0.20	*bdl*	
Na_2O	*bdl*		*bdl*		*bdl*		*bdl*		0.18	0.03	0.23	0.07	0.27	0.08	*bdl*		*bdl*		0.19	0.04	0.23	0.11	0.19	0.04
H2O					12.11	0.24			12.43	0.16	4.55	0.07	2.18	0.01					12.46	0.07	2.18	0.02	4.64	0.08
Total	98.87	2.69	99.67	2.12	95.36	2.92	100.18	1.57	97.45	2.68	96.56	2.16	98.96	1.44	99.71	1.05	99.64	2.11	97.61	1.65	99.05	1.47	98.55	2.24
O	6		4		14		4		7		11		23		6		4		7		23		11	
OH					8				4		2		2						4		2		2	
Si	1.97	0.01	1.01	0.01	3.18	0.03	1.00	0.00	1.96	0.01	3.99	0.02	8.02	0.02	2.00	0.00	1.00	0.00	1.96	0.01	8.01	0.01	3.98	0.02
Al	0.07	0.02	-		1.60	0.07	-		0.21	0.02	0.02	0.02	-		-		-		0.20	0.01	-		0.02	0.01
Cr	0.01	0.01	-		0.15	0.01	-		0.03	0.00	-		-		-		-		0.03	0.00	-		-	
Fe	0.19	0.01	0.22	0.01	0.26	0.01	0.22	0.01	0.18	0.02	0.07	0.01	0.23	0.03	0.23	0.00	0.22	0.01	0.18	0.01	0.23	0.02	0.09	0.01
Ni	-		0.01	0.00	0.03	0.01	0.01	0.00	-		0.01	0.01	-		-		-		-		-		0.01	0.00
Mg	1.75	0.02	1.76	0.01	4.74	0.04	1.76	0.01	2.54	0.03	2.89	0.02	4.88	0.01	1.75	0.01	1.76	0.02	2.54	0.02	4.87	0.01	2.90	0.02
Ca	-		-		-		-		-		-		1.82	0.03	-		-		-		1.84	0.03	-	
Mn	-		-		-		-		-		-		-		0.01	0.00	0.01	0.01	-		-		-	
Na	-		-		-		-		0.02	0.00	0.03	0.01	0.07	0.02	-		-		0.02	0.00	0.06	0.03	0.02	0.00
OH			-		8.00		-		4.00		2.00		2.00						4.00		2.00		2.00	
Sum	3.99	0.00	2.99	0.01	9.95	0.02	3.00	0.00	4.93	0.00	7.01	0.02	15.02	0.02	4.00	0.00	3.00	0.00	4.93	0.01	15.02	0.02	7.02	0.02
XMg	0.90	0.01	0.89	0.01	0.94	0.00	0.88	0.00	0.93	0.01	0.97	0.00	0.96	0.00	0.88	0.00	0.88	0.01	0.93	0.01	0.95	0.00	0.97	0.00

water concentration is based on the mineral stoichiometry

bdl. Below detection limit (typically 0.10-0.15 wt.% in EDS)

Low totals in hydrous phases (specially chlorite) are due to their irregular surface nevertheless the total cations sum is close to the expected for their structural formula.

Electonic table 1. Continuation

RUN	C2989										C2990								C3003									
	Ol (n=6)		Atg (n=5)		Tlc (n=6)		Tr (n=6)		Opx (n=5)		Ol (n=5)		Atg (n=6)		Tlc (n=5)		Tr (n=6)		Opx (n=5)		Ol (n=5)		Atg (n=6)		Tr (n=5)		Chl (n=4)	
	mean	stdev	mean	stdev	mean	stdev	mean	stdev	mean	stdev	mean	stdev	mean	stdev	mean	stdev	mean	stdev	mean	stdev	mean	stdev	mean	stdev	mean	stdev	mean	stdev
SiO_2	40.39	0.56	41.18	1.10	60.18	1.02	58.66	0.70	57.72	0.40	40.43	0.19	40.78	0.90	62.04	0.88	58.48	0.32	57.12	0.72	41.01	0.91	41.16	0.82	58.02	0.71	36.76	2.13
Al_2O_3	*bdl*		3.21	0.79	*bdl*		0.19	0.11	*bdl*		*bdl*		3.75	0.33	*bdl*		0.24	0.06	0.47	0.15	*bdl*		3.43	0.51	0.29	0.28	11.06	0.75
Cr_2O_3	*bdl*		0.51	0.32	*bdl*		*bdl*		*bdl*		*bdl*		0.69	0.01	*bdl*		*bdl*		0.25	0.12	*bdl*		0.69	0.28	*bdl*		0.83	0.10
FeO	10.97	0.43	4.19	0.25	1.15	0.18	1.99	0.22	7.91	0.22	10.78	0.39	4.59	0.20	1.33	0.24	2.22	0.13	8.16	1.43	10.41	0.51	4.27	0.27	2.68	1.38	3.09	0.32
NiO	0.24	0.24	0.16	0.15	*bdl*		*bdl*		*bdl*		*bdl*		*bdl*		*bdl*		*bdl*		*bdl*		0.37	0.13	0.20	0.07	*bdl*		0.28	0.12
MgO	47.61	0.88	35.98	0.78	28.94	0.64	23.98	0.38	33.93	0.53	47.72	0.39	35.17	0.89	29.98	0.49	24.01	0.15	32.73	1.04	48.43	1.18	35.75	0.79	23.50	0.73	33.19	0.81
MnO	0.28	0.17	*bdl*		*bdl*		*bdl*		0.32	0.09	0.19	0.09	*bdl*		*bdl*		*bdl*		*bdl*		*bdl*		*bdl*		*bdl*		*bdl*	
CaO	*bdl*		*bdl*		*bdl*		12.45	0.12	*bdl*		*bdl*		*bdl*		*bdl*		12.38	0.34	0.49	0.43	*bdl*		*bdl*		12.10	0.71	0.32	0.39
Na_2O	*bdl*		*bdl*		*bdl*		0.34	0.21	*bdl*		*bdl*		*bdl*		*bdl*		0.19	0.08	*bdl*		*bdl*		*bdl*		0.29	0.18	0.21	0.04
H2O			12.50	0.29	4.48	0.08	2.20	0.03	*bdl*				12.45	0.25	4.63	0.07	2.20	0.01					12.53	0.17	2.18	0.02	12.58	0.24
	99.49	2.52	97.73	3.78	94.76	2.30	99.80	2.04	99.88	1.72	99.13	1.16	97.44	2.71	97.99	1.89	99.71	1.20	99.22	4.19	100.23	2.89	98.03	3.05	99.06	4.46	98.32	4.99
O	4		7		11		23		6		4		7		11		23		6		4		7		23		14	
OH			4		2		2						4		2		2						4		2		8	
Si	1.00	0.00	1.98	0.03	4.03	0.01	8.00	0.03	2.00	0.01	1.00	0.00	1.96	0.01	4.02	0.01	7.98	0.01	2.00	0.01	1.01	0.00	1.97	0.01	7.99	0.03	3.50	0.15
Al	-		0.18	0.04	-		0.03	0.02	-		-		0.21	0.02	-		0.04	0.01	0.02	0.01	-		0.19	0.03	0.05	0.05	1.24	0.11
Cr	-		0.02	0.01	-		-		-		-		0.03	0.01	-		-		0.01	0.00	-		0.03	0.01	-		0.06	0.01
Fe	0.23	0.01	0.17	0.01	0.06	0.01	0.23	0.02	0.23	0.01	0.22	0.01	0.18	0.01	0.07	0.01	0.25	0.02	0.24	0.04	0.21	0.01	0.17	0.01	0.31	0.16	0.25	0.03
Ni	-		0.01	0.01	-		-		-		-		-		-		-		-		0.01	0.00	0.01	0.00	-		0.02	0.01
Mg	1.76	0.01	2.57	0.03	2.89	0.02	4.87	0.01	1.76	0.02	1.77	0.00	2.53	0.02	2.89	0.02	4.89	0.01	1.71	0.04	1.77	0.01	2.55	0.03	4.82	0.11	4.72	0.13
Ca	-		-		-		1.82	0.03	-		-		-		-		1.81	0.05	0.02	0.02	-		-		1.78	0.10	0.03	0.04
Mn	0.01	0.00	-		-		-		0.01	0.00	-		-		-		-		-		-		-		-		-	
Na	-		-		-		0.09	0.06	-		-		-		-		0.05	0.02	-		-		-		0.08	0.05	0.04	0.01
OH			4.00		2.00		2.00						4.00		2.00		2.00						4.00		2.00		8.00	
Sum	3.00	0.01	4.92	0.01	6.97	0.01	15.03	0.05	4.00	0.01	3.00	0.00	4.92	0.01	6.98	0.01	15.02	0.01	3.99	0.00	2.99	0.00	4.92	0.01	15.03	0.05	9.86	0.09
XMg	0.88	0.00	0.94	0.01	0.98	0.00	0.96	0.00	0.88	0.01	0.89	0.00	0.93	0.00	0.98	0.00	0.95	0.00	0.88	0.02	0.89	0.01	0.93	0.00	0.94	0.03	0.95	0.00

water concentration is based on the mineral stoichiometry

b.d.l. Below detection limit (typically 0.10-0.15 wt.% in EDS)

Low totals in hydrous phases (specially chlorite) are due to their irregular surface nevertheless the total cations sum is close to the expected for their structural formula.

Electonic table 1. Continuation

RUN	C3004								C3011								C3012							
	Opx (n=5)		Ol (n= 5)		Tr (n=5)		Chl (n=6)		Opx (n=9)		Ol (n=8)		Di (n=4)		Chl (n=7)		Opx (n=8)		Ol (n=5)		Di (n=3)		Chl (n=5)	
	mean	stdev	mean	stdev	mean	stdev	mean	stdev	mean	stdev	mean	stdev	mean	stdev	mean	stdev	mean	stdev	mean	stdev	mean	stdev	mean	stdev
SiO_2	58.40	0.78	41.83	0.52	58.07	1.39	32.76	0.71	57.71	0.75	41.94	0.95	55.40	1.90	34.02	1.17	57.38	0.99	40.62	0.45	52.85	1.10	33.29	1.48
Al_2O_3	0.54	0.10	*bdl*		0.19	0.11	12.48	1.31	0.92	0.18	*bdl*		0.41	0.01	13.78	0.93	0.62	0.28	*bdl*		0.86	0.67	12.89	1.24
Cr_2O_3	*bdl*		*bdl*		*bdl*		1.24	0.17	0.22	0.13	*bdl*		0.21	0.24	1.37	0.19	0.19	0.11	*bdl*		0.18	0.03	1.24	0.16
FeO	7.29	0.31	10.66	0.70	2.01	0.13	3.55	0.57	6.05	0.31	10.90	0.74	6.11	0.19	3.15	0.15	6.65	0.62	10.61	0.52	5.55	3.88	2.93	0.23
NiO	*bdl*		0.31	0.16	0.24	0.19	0.34	0.17	*bdl*		0.27	0.20	*bdl*		0.27	0.23	*bdl*		0.22	0.19	0.16	0.07	0.26	0.07
MgO	34.39	0.67	48.56	0.91	23.67	0.69	32.61	0.81	34.67	0.57	48.96	1.24	17.10	2.83	33.53	1.37	33.88	0.62	47.64	0.84	17.16	1.65	32.00	1.17
MnO	*bdl*		*bdl*		*bdl*		*bdl*		*bdl*		*bdl*		*bdl*		*bdl*		0.18	0.16	0.18	0.10	*bdl*		*bdl*	
CaO	0.29	0.08	*bdl*		12.62	0.38	*bdl*		0.34	0.08	*bdl*		20.94	2.19	*bdl*		0.29	0.09	*bdl*		20.90	1.37	*bdl*	
Na_2O	*bdl*		*bdl*		0.16	0.15	*bdl*	0.11	*bdl*		*bdl*		*bdl*		*bdl*		*bdl*		*bdl*		*bdl*		*bdl*	
H2O					2.18	0.06	12.07	0.12							12.58	0.49							12.10	0.36
	100.91	2.25	101.36	2.41	99.14	3.36	95.04	4.17	99.92	2.22	102.06	3.34	100.16	7.56	98.71	4.57	99.18	3.00	99.27	2.28	97.65	8.90	94.69	4.85
O	6		4		23		14		6		4		6		14		6		4		6		14	
OH					2		8								8								8	
Si	2.00	0.01	1.01	0.02	7.98	0.04	3.26	0.05	1.99	0.01	1.01	0.00	2.02	0.00	3.24	0.03	1.99	0.01	1.01	0.01	1.98	0.02	3.30	0.13
Al	0.02	0.00	-		0.03	0.02	1.46	0.16	0.04	0.01	-		0.02	0.00	1.55	0.07	0.03	0.01	-		0.04	0.03	1.51	0.13
Cr	-		-		-		0.10	0.01	0.01	0.00	-		0.01	0.01	0.10	0.02	0.01	0.00	-		0.01	0.00	0.10	0.01
Fe	0.21	0.01	0.22	0.01	0.23	0.01	0.29	0.05	0.17	0.01	0.22	0.01	0.19	0.01	0.25	0.01	0.19	0.02	0.22	0.01	0.17	0.12	0.24	0.02
Ni	-		0.01	0.00	0.03	0.02	0.03	0.01	-		0.01	0.00	-		0.02	0.02	-		-		-		0.02	0.01
Mg	1.75	0.02	1.75	0.02	4.85	0.02	4.83	0.11	1.78	0.02	1.76	0.02	0.93	0.12	4.76	0.05	1.76	0.01	1.76	0.01	0.96	0.08	4.73	0.06
Ca	0.01	0.00	-		1.86	0.04	-		0.01	0.00	-		0.82	0.11	-		0.01	0.00	-		0.84	0.04	-	
Mn	-		-		-		-		-		-		-		-		0.01	0.00	-		-		-	
Na	-		-		0.04	0.04	-		-		-		-		-		-		-		-		-	
OH					2.00		8.00								8.00								8.00	
Sum	3.99	0.01	2.99	0.02	15.02	0.03	9.97	0.05	3.99	0.01	2.99	0.00	3.97	0.00	9.93	0.02	3.99	0.00	2.99	0.01	4.00	0.01	9.90	0.06
XMg	0.89	0.01	0.89	0.01	0.95	0.00	0.94	0.01	0.91	0.00	0.89	0.01	0.83	0.03	0.95	0.00	0.90	0.01	0.89	0.01	0.84	0.10	0.95	0.00

water concentration is based on the mineral stoichiometry

b.d.l. Below detection limit (typically 0.10-0.15 wt.% in EDS)

Low totals in hydrous phases (specially chlorite) are due to their irregular surface nevertheless the total cations sum is close to the expected for their structural formula.

Electonic table 1. Continuation

RUN	C3044										C3219											
	Opx (n=9)		Ol (n=5)		Tr (n=7)		Chl (n=6)		Atg (n=5)		Opx (n=5)		Ol (n=7)		Atg (n=6)		Tr (n=6)		Chl (n=5)		Tlc (n=5)	
	mean	stdev	mean	stdev	mean	stdev	mean	stdev	mean	stdev	mean	stdev	mean	stdev	mean	stdev	mean	stdev	mean	stdev	mean	stdev
SiO_2	57.31	0.43	41.08	0.37	58.41	0.92	33.46	0.83	40.37	2.45	57.41	0.71	40.00	0.40	41.04	1.28	58.03	2.44	34.80	0.87	60.55	1.17
Al_2O_3	0.63	0.20	*bdl*		*bdl*		12.67	0.61	3.63	0.49	*bdl*		*bdl*		3.18	0.65	0.25	0.08	10.98	0.67	*bdl*	
Cr_2O_3	*bdl*		*bdl*		*bdl*		0.94	0.36	0.67	0.12	*bdl*		*bdl*		0.52	0.24	*bdl*		*bdl*		*bdl*	
FeO	7.56	0.59	10.79	0.39	1.80	0.29	3.36	0.39	4.29	0.45	7.83	0.20	10.41	0.51	4.33	0.26	2.08	0.12	6.98	0.47	1.53	0.18
NiO	*bdl*		0.38	0.08	*bdl*		0.39	0.04	*bdl*		*bdl*		0.31	0.11	*bdl*		*bdl*		0.32	0.09	*bdl*	
MgO	33.47	0.40	47.92	0.54	23.73	0.54	32.78	0.85	35.24	2.02	33.49	0.62	47.13	0.60	35.68	0.77	23.62	1.08	31.18	1.05	29.64	0.46
MnO	*bdl*		0.24	0.22	0.18	0.11	*bdl*	0.03	*bdl*		0.38	0.08	0.22	0.09	*bdl*		*bdl*		*bdl*		*bdl*	
CaO	0.31	0.09	*bdl*		12.61	0.25	*bdl*		*bdl*		*bdl*		*bdl*		*bdl*		12.25	0.47	*bdl*		0.20	0.11
Na_2O	*bdl*		*bdl*		*bdl*		*bdl*		*bdl*		*bdl*		*bdl*		0.18	0.03	0.46	0.15	0.18	0.03	0.21	0.04
H2O					2.18	0.04	12.20	0.26	12.34	0.66					12.45	0.33	2.18	0.09	12.15	0.34	4.56	0.06
	99.28	2.05	100.41	1.79	98.91	2.23	95.80	3.52	96.55	6.47	99.11	1.95	98.06	1.93	97.36	3.87	98.87	4.71	96.59	3.83	96.97	2.58
O	6		4		23		14		7		6		4		7		23		14		11	
OH					2		8		4						4		2		8		2	
Si	2.00	0.00	1.01	0.00	8.03	0.04	3.29	0.03	1.96	0.02	2.01	0.00	1.00	0.00	1.98	0.02	7.99	0.02	3.44	0.04	3.98	0.04
Al	0.03	0.01	-		-		1.47	0.07	0.21	0.04	-		-		0.18	0.04	0.04	0.01	1.28	0.05	0.02	0.03
Cr	-		-		-		0.07	0.03	0.03	0.00	-		-		0.02	0.01	-		-		-	
Fe	0.22	0.02	0.22	0.01	0.21	0.03	0.28	0.03	0.17	0.01	0.23	0.01	0.22	0.01	0.17	0.01	0.24	0.02	0.58	0.05	0.08	0.01
Ni	-		0.01	0.00	-		0.03	0.02	-		-		0.01	-		0.01	-		0.03	0.01	-	
Mg	1.74	0.02	1.75	0.01	4.86	0.06	4.80	0.05	2.55	0.02	1.75	0.01	1.76	0.01	2.56	0.03	4.85	0.04	4.59	0.05	2.90	0.04
Ca	0.01	0.00	-		1.86	0.01	-		-		-		-		-		1.81	0.03	-		0.01	0.01
Mn	-		0.01	0.00	0.02	0.01	-		-		0.01	0.00	-		-		-		-		-	
Na	-		-		-		-		-		-		-		0.02	0.00	0.12	0.04	0.03	0.01	0.03	0.01
OH					2.00		8.00		4.00						4.00		2.00		8.00		2.00	
Sum	3.99	0.00	2.99	0.00	14.97	0.04	9.94	0.02	4.92	0.01	3.99	0.00	3.00	0.00	4.93	0.01	15.05	0.04	9.94	0.04	7.03	0.03
XMg	0.89	0.01	0.88	0.00	0.96	0.00	0.94	0.01	0.94	0.00	0.88	0.00	0.88	0.01	0.94	0.00	0.95	0.00	0.88	0.01	0.97	0.00

water concentration is based on the mineral stoichiometry

b.d.l. Below detection limit (typically 0.10-0.15 wt.% in EDS)

Electonic table 1. Continuation

RUN	C3220										D756							
	Opx (n=6)		Ol (n=6)		Atg (n=5)		Di (n=5)		Chl (n=5)		Opx (n=12)		Ol (n=11)		Di (n=5)		Chl (n=5)	
	mean	stdev	mean	stdev	mean	stdev	mean	stdev	mean	stdev	mean	stdev	mean	stdev	mean	stdev	mean	stdev
SiO_2	57.51	0.82	40.62	0.38	41.47	2.55	54.98	1.24	33.64	0.37	57.90	0.66	41.09	0.40	53.61	0.92	33.24	0.35
Al_2O_3	0.60	0.11	*bdl*		3.40	0.20	0.33	0.09	11.41	1.54	0.82	0.17	*bdl*	0.03	0.48	0.20	14.13	0.25
Cr_2O_3	*bdl*		*bdl*		0.60	0.21	*bdl*		0.92	0.13	0.24	0.14	*bdl*		0.16	0.11	1.06	0.30
FeO	7.45	0.75	11.23	0.34	4.16	0.34	6.68	0.68	3.32	0.14	6.78	0.71	10.68	0.49	6.56	1.66	3.07	0.14
NiO	*bdl*		0.20	0.16	*bdl*		*bdl*		0.27	0.13	*bdl*		0.16	0.16	*bdl*		0.40	0.02
MgO	33.67	1.05	47.20	0.57	36.11	2.39	17.26	2.61	32.53	0.68	34.26	0.65	48.21	0.57	15.17	1.60	32.77	0.30
MnO	*bdl*		0.22	0.05	*bdl*		*bdl*		*bdl*		*bdl*		0.24	0.09	*bdl*		*bdl*	
CaO	0.26	0.05	*bdl*		*bdl*		18.98	2.02	*bdl*		0.30	0.07	*bdl*		22.57	1.45	*bdl*	
Na_2O	*bdl*		*bdl*		0.21	0.08	*bdl*		*bdl*		*bdl*		*bdl*		*bdl*		*bdl*	
H2O					12.61	0.71			12.00	0.18							12.38	0.06
	99.48	3.23	99.46	1.75	98.57	6.75	99.59	8.67	94.08	3.34	100.30	2.60	100.38	1.88	98.55	5.95	97.04	1.61
O	6		4		7		6		14		6		4		6		14	
OH					4				8								8	
Si	2.00	0.00	1.01	0.00	1.97	0.01	2.02	0.02	3.36	0.08	1.99	0.00	1.01	0.00	2.00	0.01	3.22	0.02
Al	0.02	0.00	-		0.19	0.02	0.01	0.00	1.34	0.17	0.03	0.01	-		0.02	0.01	1.61	0.04
Cr	-		-		0.02	0.01	-		0.07	0.04	0.01	0.00	-		0.00	0.00	0.08	0.02
Fe	0.22	0.02	0.23	0.01	0.17	0.01	0.21	0.02	0.28	0.02	0.19	0.02	0.22	0.01	0.21	0.05	0.25	0.01
Ni	-		-		-		-		0.02	0.01	-		-		-		0.03	0.02
Mg	1.74	0.04	1.74	0.01	2.56	0.03	0.94	0.13	4.85	0.07	1.76	0.02	1.76	0.01	0.85	0.08	4.73	0.03
Ca	0.01	0.00	-		-		0.75	0.09	-		0.01	0.00	-		0.90	0.06	-	
Mn	-		-		-		-		-		-		-		-		-	
Na	-		-		0.02	0.01	0.08	0.11	-		-		-		-		-	
OH					4.00				8.00								8.00	
Sum	3.99	0.00	2.99	0.00	4.93	0.01	4.02	0.07	9.93	0.03	3.99	0.00	2.99	0.00	3.98	0.01	9.93	0.01
XMg	0.89	0.01	0.88	0.01	0.94	0.00	0.82	0.03	0.94	0.00	0.90	0.01	0.89	0.01	0.80	0.06	0.94	0.00

water concentration is based on the mineral stoichiometry

b.d.l. Below detection limit (typically 0.10-0.15 wt.% in EDS)

Low totals in hydrous phases (specially chlorite) are due to their irregular surface nevertheless the total cations sum is close to the expected for their structural formula.